Design and development of calorimetry at SHiP and SND@LHC

DISSERTATION

ZUR ERLANGUNG DES GRADES

"Doktor der Naturwissenschaften"

AM FACHBEREICH PHYSIK, MATHEMATIK UND INFORMATIK
DER
JOHANNES GUTENBERG UNIVERSITÄT

MAINZ

Matei A.V. Climescu
aus Lausanne, Schweiz

Mainz, 2025

Abstract

This thesis focuses on calorimetry in the context of searches for rare particle interactions at the SHiP and SND@LHC experiments at CERN.

The SHiP (Search for Hidden Particles) experiment at CERN SPS is going to be the flagship experiment for investigating low-coupling physics in the $\mathcal{O}(10\,\mathrm{MeV})$ to a couple of GeV range. Its calorimeter system will achieve very good particle identification capabilities and be able to reconstruct the directionality of electromagnetic shower with excellent precision. This will enable significant background reduction and the ability to reconstruct neutral final states arising from possible new physics decays. For this, it relies on plastic scintillator bars traversed by wavelength-shifting fibres and readout by SiPMs on the one hand and high-precision layers on the other. The physics requirements of the calorimeter have been studied with Monte Carlo simulations. The plastic scintillator layers' light yield was optimised both in simulations and laboratory studies, yielding a design for usage in the final experiment. The readout electronics must cover a very large dynamic range, four systems were investigated with the KLauS chip being identified as having potential for usage in the end experiment. Three test beams were lead using a modular and custom-built prototype of the SHiP electromagnetic calorimeter system. There, different readout electronics and detector configurations were evaluated. Preliminary results allow to establish the robustness of the design for energy reconstruction and particle identification. These studies are in use for the final design of the energy reconstruction and particle identification.

The SND@LHC (Scattering Neutrino Detector at the Large Hadron Collider) is a running experiment placed off-axis at the ATLAS interaction point at $7.2 < \eta < 8.6$. The experiment's position enhances the charm parentage of final state ν_e and ν_τ from decays inside of ATLAS. A hadronic calorimeter based on scintillator bars readout by SiPMs is used to identify muons and measure the energy of hadronic final states from interactions in an emulsion target. The performance of the hadronic calorimeter has been studied. Its response to hadronic showers as well as the development and testing of tagging algorithms used for the calorimeter calibration are presented. In addition, muon deep inelastic scattering and catastrophic muon bremsstrahlung background studies have been performed in the emulsion detector together with the development of electromagnetic calorimetry techniques. These evaluations are currently being used for searches for ν_e in the emulsion detector at SND@LHC.

Zusammenfassung

Die vorliegende Arbeit befasst sich mit Kalorimetrie im Rahmen der Suche nach seltenen Teilchenwechselwirkungen in den SHiP- und SND@LHC-Experimenten am CERN.

Das geplante SHiP-Experiment *(Search for Hidden Particles)* am CERN-SPS soll schwach wechselwirkende Teilchen im Energiebereich zwischen $\mathcal{O}(10)$ MeV) und einigen GeV nachweisen. Das SHiP-Kalorimeter muss über eine sehr gute Teilchenidentifikation verfügen und in der Lage sein, die Richtung elektromagnetischer Schauer mit hoher Präzision zu rekonstruieren. Dies ermöglicht eine starke Unterdrückung von Hintergrundprozessen und die Rekonstruktion neutraler Endzustände aus Zerfällen möglicher neuer Teilchen. Dafür werden Plastikszintillatorstreifen eingesetzt, die einerseits von wellenlängenverschiebenden Fasern durchzogen und mit SiPMs ausgelesen werden und andererseits auf hochpräzise Lagen. Die physikalischen Anforderungen an das Kalorimeter wurden mit Monte-Carlo-Simulationen untersucht. Die Lichtausbeute der Szintillatoren wurde sowohl in Simulationen als auch in Laborstudien optimiert. Das daraus folgende Design ist für die Verwendung im endgültigen Experiment vorgesehen. Für die Ausleseelektronik, die einen sehr großen dynamischen Bereich abdecken muss, wurden vier verschiedene Systeme untersucht. Der von der Universität Heidelberg stammende ASIC *KLauS* wurde dabei als geeignet für den Einsatz im endgültigen Experiment identifiziert. Drei Teststrahlkampagnen wurden mit einem speziell entwickelten, modularen Prototypen des elektromagnetischen SHiP-Kalorimeters durchgeführt. Dabei wurden verschiedene Detektorkonfigurationen und Datenauslesesysteme getestet. Die Ergebnisse belegen die Eignung des Designs für die Energierekonstruktion und Teilchenidentifikation.

Das zur Zeit laufende SND@LHC-Experiment *(Scattering and Neutrino Detector at the Large Hadron Collider)* befindet sich nahe des ATLAS-Wechselwirkungspunkts im Bereich $7.2 < \eta < 8.6$ außerhalb der LHC-Strahlachse. Durch die Position des Experiments stammt ein großer Anteil an ν_e- und ν_τ-Neutrinos aus Charmproduktion bei ATLAS. Ein hadronisches Kalorimeter, basierend auf Szintillatorstreifen mit SiPM-Auslese, wird verwendet, um Myonen zu identifizieren und die Energie hadronischer Endzustände zu messen. Die Leistungsfähigkeit des hadronischen Kalorimeters wurde eingehend untersucht. Sowohl der Nachweis von hadronischen Schauern als auch die Entwicklung und der Test von Softwarealgorithmen zum *Tagging*, das für die Kalibrierung des Kalorimeters verwendet wird, werden vorgestellt. Zusätzlich wurden Studien zu tief-inelastischer Myonstreuung und katastrophaler Myon-Bremsstrahlung im Emulsionsdetektor durchgeführt, ebenso wie zur Rekonstruktion von elektromagnetischen Schauern. Die Ergebnisse werden derzeit zur Suche nach ν_e-Neutrinos im SND@LHC-Emulsionsdetektor genutzt.

Contents

June 5, 1953

Important decisions about the future development of particle physics must frequently be made by people who do not necessarily have an intimate knowledge of the technical aspects of detectors. These people are, nonetheless, interested in what a detector unit will do, how much it will cost, how long it will take to build and how long and how well it will operate. When they attempt to learn these things, they become aware of confusion existing in the detector business. There appears to be unresolved conflict on almost every issue that arises.

I believe that this confusion stems from a failure to distinguish between the academic and the practical. These apparent conflicts can usually be explained only when the various aspects of the issue are resolved into their academic and practical components. To aid in this resolution, it is possible to define in a general way those characteristics which distinguish the one from the other.

An academic detector or detector unit almost always has the following basic characteristics: (1) It is simple. (2) It is small. (3) It is cheap. (4) It is light. (5) It can be built very quickly. (6) It is very flexible in purpose ("omnibus detector"). (7) Very little development is required. It will use mostly "off the shelf" components. (8) The detector is in the study phase. It is not being built now.

On the other hand, a practical detector unit can be distinguished by the following characteristics: (1) It is being built now. (2) It is behind schedule. (3) It is requiring an immense amount of development on apparently trivial items. Glue, in particular, is a problem. (4) It is very expensive. (5) It takes a long time to build because of the engineering development problems. (6) It is large. (7) It is heavy. (8) It is complicated.

The tools of the academic detector designer are a piece of paper and a pencil with an eraser. If a mistake is made, it can always be erased and changed. If the practical detector designer errs, he wears the mistake around his neck; it cannot be erased. Everyone can see it.

The academic detector designer is a dilettante. He has not had to assume any real responsibility in connection with his projects. He is free to luxuriate in elegant ideas, the practical shortcomings of which can be relegated to the category of "mere technical details". The practical detector designer must live with these same technical details. Although recalcitrant and awkward, they must be solved and cannot be put off until tomorrow. Their solutions require manpower, time and money.

Unfortunately for those who must make far reaching decisions without the benefit of an intimate knowledge of detector technology and unfortunately for the interested public, it is much easier to get the academic side of an issue than the practical side. For a large part those involved with the academic detectors have more inclination and time to present their ideas in reports and orally to those who will listen. Since they are innocently unaware of the real but hidden difficulties of their plans, They speak with great facility and confidence. Those involved with practical detectors, humbled by their experiences, speak less and worry more.

Yet it is incumbent on those in high places to make wise decisions, and it is reasonable and important that the public be correctly informed. It is consequently incumbent on all of us to state the facts as forth rightly as possible. Although it is probably impossible to have detector ideas labelled as "practical" or "academic" by the authors, it is worth while for both the authors and the audience to bear in mind this distinction and to be guided thereby.

Yours faithfully,

Adapted from H. G. Rickover, Naval Reactors Branch Division of Reactor Development U. S. Atomic Energy Commission

Introduction

"Nature is wont to hide herself"- Heraclitus

In Summer 2023 during a conference held at a resort town somewhere in Eastern Europe, an eager physics PhD student asked a seasoned theoretical physicist whether there was any indication, beyond that it was massive, did not interact much with known physics and tended to be concentrated within halos and clusters universe-wide, as to what Dark Matter was. His answer was curt but short "No".

This episode can be seen as a good representation of the state of modern particle physics: What is understood can be verified to very high levels of precision, sometimes up to the 10^{-8} level and beyond [1, 2]. The fundamental theory, known as the Standard Model of Particle Physics (SM) describing this understanding was completed in 2012 with the discovery of a scalar particle displaying properties compatible with those of the so-called Higgs Boson [3, 4], predicted nearly 50 years prior [5–7] and last missing piece of the theory's proverbial jigsaw puzzle [8, 9]. On the other hand, no explanation can be verified as having any veracity for describing any phenomenon *not* described by the SM, particularly in the area of neutrino masses [10, 11], dark matter or matter-antimatter asymmetry [11]. As such, the Higgs detection can be seen as yielding more questions than answers, and while impressive, could be described as being evolutionary rather than revolutionary: The last decades have seen particles be discovered using machines of larger size and ever powerful than their predecessors as particles left to discover would get increasingly heavier and/or with more subtle signatures. The W and Z boson were discovered at the UA1 and UA2 experiments thanks to the Super Proton Synchrotron (SPS) accelerator [12], the top quark was observed at DØ and CDF utilising the Tevatron Accelerator facility [13, 14] and more recently the Higgs Boson was seen at LHC [3, 4]. It now appears that the Higgs discovery was the last of a series. Despite a remarkable increase in searching power enabled by the LHC [15, 16], which is expected to rise even further in the future [17], and a variety of complementary studies both direct [18–20] or indirect [1, 21, 22] studies, no sign of new physics has been found despite abundant evidence of its existence. While these searches have so far yielded no observed signal that would definitively suggest discovery of new physics, it is now quite apparent that the current searches require an expansion in both scope and depth. For this purpose, new experiments need to be designed [23] which themselves have imperative needs of new detector technologies [24]. Existing physics facilities are thus used to their maximum potential to extract as much physics data as possible from their operation [25, 26].

This work sets itself coherently within these goals and describes the development of a novel detector aimed at innovative searches for new physics: the *SplitCal* as well as the development of calorimetry in searches for collider neutrinos.

First a summary description of the theoretical framework of particle physics, the *Standard Model* will be given for context, then a presentation of the *Search for Hidden Particles* and the *Scattering Neutrino Detector at LHC* experiments will be provided, with their underlying principles and motivation. A presentation and the SplitCal follows with the development of the detector itself, its components, its electronics being exposed followed by a presentation of test beam results. This work ends with a presentation of calorimetry techniques developed for collider neutrino searches and a general conclusion.

Chapter 1

Modern particle physics and the Standard Model

The description of the Universe's behaviour at a quantum level has been achieved by a theory called the *Standard Model* (SM). It is the state-of-art theory for describing matter and interaction at the most fundamental level to the best of our understanding. The SM was completed in the 1970's and proven experimentally in the 1990's, mainly at the Large Electron-Positron Collider (LEP) at CERN [27] through four experiments (ALEPH [28], DELPHI [29], OPAL [30] and L3 [31]) and at the Tevatron at Fermilab through two experiments (DØ [32] and CDF [33]). It provides an explanation of the basic laws of Nature through very elegant symmetry principles. These symmetries at the core of the SM will be summarised, as it is today entirely discovered in its most minimal incarnation. An overview of physics done with neutrinos as it relates to this work will follow. The self-consistency of the SM does not prevent it from having limitations which will be explained with an exploration of means to overcome these limitations closing this chapter. Einstein's notation will used to contract equations and fundamental constants (c and $\hbar$ notably) are taken as equal to 1. The formalism is mainly adopted from [34] and [35].

1.1 Introduction to the Standard Model

1.1.1 Fermions

The SM describes elementary matter, as excitations of fermion fields with intrinsic angular momentum (spin) $\frac{1}{2}$. They propagate through free space according to Dirac's equation:

$$\left(i\gamma^\mu \partial_\mu - m\right)\psi = 0, \tag{1.1}$$

with m the fermion's mass, γ^μ the gamma matrices and ψ the Dirac spinor, the solutions to the equation. Said spinors manifest under four forms, two of which have positive helicity (the projection of spin on momentum), two of which have negative helicity, two of which have "positive energy", two of which have "negative energy". For this last distinction, it is useful to note that the negative energy solutions are interpreted as antiparticles (negative excitations, application of a destruction operator onto the field), whereas positive energy solutions are viewed as particles (positive excitations, application of a creation operator onto the field). The particles helicity eigenstates $\mathbf{h}$ manifest as:

$$\mathbf{h} \equiv \frac{\hat{S}\cdot\hat{p}}{|\hat{p}|} \qquad \text{taking eigenstates} \qquad h = \pm\frac{1}{2} \tag{1.2}$$

with $\hat{S}$ the spin and $\hat{p}$ the momentum. More explicitly, helicity spinors are identified by:

$$\mathbf{u}_\uparrow = \sqrt{E+m}\begin{bmatrix} 1 \\ se^{i\phi} \\ \frac{p}{E+m} \\ \frac{p}{E+m}se^{i\phi} \end{bmatrix} \qquad \mathbf{u}_\downarrow = \sqrt{E+m}\begin{bmatrix} -s \\ e^{i\phi} \\ \frac{p}{E+m}s \\ -\frac{p}{E+m}e^{i\phi} \end{bmatrix} \tag{1.3}$$

$$\mathbf{v}_\uparrow = \sqrt{E+m}\begin{bmatrix} \frac{p}{E+m}s \\ \frac{p}{E+m}e^{i\phi} \\ -s \\ e^{i\phi} \end{bmatrix} \qquad \mathbf{v}_\downarrow = \sqrt{E+m}\begin{bmatrix} \frac{p}{E+m} \\ \frac{p}{E+m}se^{i\phi} \\ 1 \\ se^{i\phi} \end{bmatrix} \tag{1.4}$$

with ϕ the azimuthal angle, E the (anti-)particle's energy and s its spin, normalised to twice the energy. Helicity however, being relative to a particles momentum, is a bad quantum number for massive particles as it is not Lorentz invariant: it is possible to find a frame of reference where the particle momentum is facing the opposite direction, flipping helicity. Chirality is the Lorentz invariant quantum number and is defined through whether a particle transforms into a *right* or *left handed* (RH and LH respectively) representation of the Poincaré group by defining $\gamma^5 \equiv i\gamma^0\gamma^1\gamma^2\gamma^3$. The γ^5 operator notably has the following properties:

$$(\gamma^5)^2 = 1 \tag{1.5}$$

$$\gamma^{5\dagger} = \gamma^5 \tag{1.6}$$

$$\gamma^5\gamma^\mu = -\gamma^\mu\gamma^5. \tag{1.7}$$

The eigenstates of Equations 1.3 and 1.4 are also eigenstates of γ^5 where the eigenvalue sign follows the spin's. The right-handed spinor can be written as:

$$u_\uparrow(p,\theta,\phi) = \sqrt{E+m}\begin{bmatrix} 1 \\ se^{i\theta} \\ \kappa \\ \kappa se^{i\theta} \end{bmatrix} \qquad \text{with } \kappa = \frac{p}{E+m}. \tag{1.8}$$

This gives rise to a decomposition into right- and left-handed chiral components:

$$u_R = P_R u_\uparrow = \frac{1}{2}(1+\kappa)\sqrt{E+m}\begin{bmatrix} 1 \\ se^{i\phi} \\ 1 \\ se^{i\phi} \end{bmatrix} \text{ and } u_L = P_L u_\uparrow = \frac{1}{2}(1-\kappa)\sqrt{E+m}\begin{bmatrix} 1 \\ se^{i\phi} \\ -1 \\ -se^{i\phi} \end{bmatrix} \tag{1.9}$$

As such, the right-handed helicity spinor, Lorentz variant, can be expressed in terms of its chiral components:

$$u_\uparrow(p,\theta,\phi) = \frac{1}{2}(1+\kappa)\sqrt{E+m}\begin{bmatrix} 1 \\ se^{i\theta} \\ 1 \\ se^{i\theta} \end{bmatrix} + \frac{1}{2}(1-\kappa)\sqrt{E+m}\begin{bmatrix} 1 \\ se^{i\theta} \\ -1 \\ -se^{i\theta} \end{bmatrix} \tag{1.10}$$

where u_R and u_L are chiral eigenstates. In the limit where $\kappa \to 1$, helicity eigenstates and chiral eigenstates are identical. Although, unlike helicity, chirality does not have a simple instinctive interpretation, it is the invariant quantum number present in the Standard Model.

1.1.2 Quantum Electrodynamics

1.1.2.1 The foundations of Quantum Electrodynamics

Quantum Electrodynamics (QED) is the Quantum Field Theory (QFT) describing the behaviour of electromagnetism at quantum level. It is articulated around a Lagrangian defined as:

$$\mathcal{L} = -\overline{\psi}\left(\gamma_\mu \frac{\partial}{\partial x_\mu} + m\right)\psi - \frac{1}{4}F_{\mu\nu}F^{\mu\nu} - ie\overline{\psi}\gamma_\mu A_\mu \psi \tag{1.11}$$

with $F_{\mu\nu}$ Faraday's electromagnetic field strength tensor containing the electric and magnetic field components [36] whereas A_μ is the *photon* field defined as:

$$A_\mu = \frac{1}{\sqrt{V}}\sum_{k\alpha}\sqrt{\frac{1}{2\omega}}\epsilon^{(\lambda_\mu)}\left(a_{k,\alpha}(t)e^{i\mathbf{k}\cdot\mathbf{x}} + a^\dagger_{k,\alpha}(t)e^{-i\mathbf{k}\cdot\mathbf{x}}\right), \tag{1.12}$$

with $\epsilon^{(\lambda_\mu)}$ denoting the polarisation, k the momentum and a and $a^\dagger$ the creation and destruction operators respectively.

The $-ie\overline{\psi}\gamma_\mu A_\mu\psi$ term of Equation 1.11 implies that while photons can be created or annihilated one at the time, e^- however may only be created in conjunction with a e^+. Gauge symmetries are rather trivial in QED, the general gauge transformation

$$\psi \to e^{i\lambda(x)}\psi, \qquad A_\mu \to A_\mu - \frac{1}{e}\frac{\partial\lambda(x)}{\partial x_\mu}. \tag{1.13}$$

It affects the Lagrangian as follows:

$$\mathcal{L} \to \mathcal{L} - i\overline{\psi}\gamma_\mu\frac{\partial\lambda}{\partial x_\mu}\psi - ie\overline{\psi}\gamma_\mu\frac{1}{e}\frac{\partial\lambda}{\partial x_\mu}\psi = \mathcal{L}, \tag{1.14}$$

leaving it invariant. If a mass term $-m^2A_\mu A^\mu$ were to be added, the Lagrangian would no longer be invariant. Thus, quite elegantly, gauge invariance implies a massless vector (spin ~ 1) mediator (the photon γ) in QED and the $\mathcal{L}$ is invariant, *symmetrical*, under a $U(1)$, namely $\psi \to e^{i\lambda(x)}\psi$.

1.1.2.2 Scattering processes

The experimental observation of physical phenomena requires prediction of observables. Fermi's Golden Rule defines the transition rate from an initial state $|i\rangle$ to a final state $|f\rangle$:

$$\Gamma_{fi} = 2\pi|T_{fi}|^2\rho(E_i) \tag{1.15}$$

where T_{fi} is the transition matrix element determined by the Hamiltonian and $\rho(E_i)$ the density of states. This is quantised to

$$\Gamma_{fi} = \frac{(2\pi)^4}{2E_a}\int|\mathcal{M}_{fi}|^2\delta(E_a - E_1 - E_2)\delta^3(\mathbf{p_a} - \mathbf{p_1} - \mathbf{p_2})\frac{\mathrm{d}^3\mathbf{p}_1}{(2\pi)^3 2E_1}\frac{\mathrm{d}^3\mathbf{p}_2}{(2\pi)^3 2E_2}, \tag{1.16}$$

for transitions from energy states E_a to E_1 and E_2. This becomes for a two body decay

$$\Gamma_{fi} = \frac{p^*}{32\pi^2 m_a}\int|\mathcal{M}_{fi}|^2 d\Omega. \tag{1.17}$$

The total cross section $\sigma \equiv \frac{N}{\phi}$, with N the number of interactions per unit time and ϕ the incident particle flux, of a scattering process is related to Γ_{fi} by $\sigma = \frac{\Gamma_{fi}}{v_a + v_b}$ with v_a and v_b the velocities of the incoming particles and can thus generally be described as such:

$$\sigma = \frac{1}{64\pi^2 s}\frac{p_f^*}{p_i^*}\int|\mathcal{M}_{fi}|^2 d\Omega^*. \tag{1.18}$$

Here, s is the so-called *Mandelstam variable* corresponding to the centre of mass of the process, p_f^* and p_i^* are the final and initial momentum of the system and most interestingly, $\mathcal{M}_{fi}$ is the S-matrix element corresponding to the transition from the initial to the final state.

The *differential cross section* is defined by:

$$\frac{\mathrm{d}\sigma}{\mathrm{d}\Omega *} = \frac{1}{64\pi^2 s}\frac{p_f^*}{p_i^*}|\mathcal{M}_{fi}|^2. \tag{1.19}$$

While all other elements are a matter for the experiment to determine (which is its own challenge!), the determination of $\mathcal{M}_{fi}$ requires input from phenomenology derived, for instance, from QED. Thus, making use of elements from Sections 1.1.1 and 1.1.2, it is possible to write, for a scattering process involving one fermion and its antifermion (for instance e^- and e^+) in the initial state, another (possibly different!) fermion-antifermion pair in the final state (for instance, a heavier cousin of the electron, the muon μ^-, μ^+) and a photon propagating through space time being created at the annihilation of the first pair, and being annihilated at the creation of the second, the following matrix element at the lowest order:

$$\mathcal{M} = -\frac{e^2}{q^2} g_{\mu\nu} \left(\overline{v}(p_2)\gamma^\mu u(p_1)\right) \left(\overline{u}(p_3)\gamma^\mu v(p_4)\right). \tag{1.20}$$

This equation, while long, can be instinctively be re-written as a so-called Feynman diagram which allows to visualise the different components as shown in Figure 1.1.

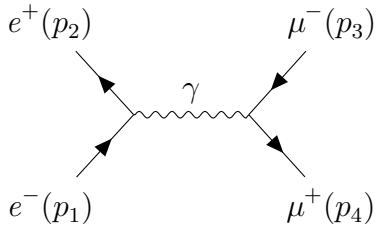

Figure 1.1: Fermion-fermion scattering Feynman diagram in QED.

Naturally, this transition must account for all possible initial and final states to be transposable to any experiment, thus, summing over chirality states:

$$\langle|\mathcal{M}_{fi}|\rangle = \frac{1}{4}\left(|\mathcal{M}_{RR}|^2 + |\mathcal{M}_{RL}|^2 + |\mathcal{M}_{LR}|^2 + |\mathcal{M}_{LL}|^2\right) = \frac{1}{4}\sum_{\text{spin}} |\mathcal{M}|^2. \tag{1.21}$$

These different initial and final states can be evaluated in different ways, they all lead however to the differential cross section:

$$\frac{\mathrm{d}\sigma}{\mathrm{d}\Omega} = \frac{\alpha^2}{4s}(1 + \cos^2\theta) \tag{1.22}$$

with α the fine structure constant and θ the angle of the outgoing particle 3 with respect to the incoming particle 1, which matches experimental observations as shown in Figure 1.2.

The calculation can be done in a pertubative regime as higher order contributions such as particle loops are taken into account:

$$\mathcal{M}_{fi} = \sum_{i,j} \alpha^i M_{i,j} \tag{1.23}$$

with i the order of perturbation theory whose contributions are taken into account and j the contribution in question. While these contribution may diverge, they are expected to be renormalisable via the use of corrections [38].

1.1.3 Electroweak unification

1.1.3.1 Weak theory

While QED governs a vast majority of known phenomena, at least at a macroscopic level, there is a particular variety of phenomenon which finds no explanation in electromagnetic theory, namely radioactivity. β-radioactivity in particular, although involving charged fermions which can otherwise be well-described by the gauge invariant $\mathcal{L}_{\text{QED}}$. The issue of 4-momentum conservation implies the existence of another, neutral particle, which would therefore not be described by QED [39]. This thus requires an extension of QED to explain such phenomena as well. Similarly to how QED derives from a $U(1)$ symmetry, a new interaction, the *weak interaction* derives from a $SU(2)$ symmetry, a non-abelian Lie algebra [40] [41]. The underlying gauge theory, which describes

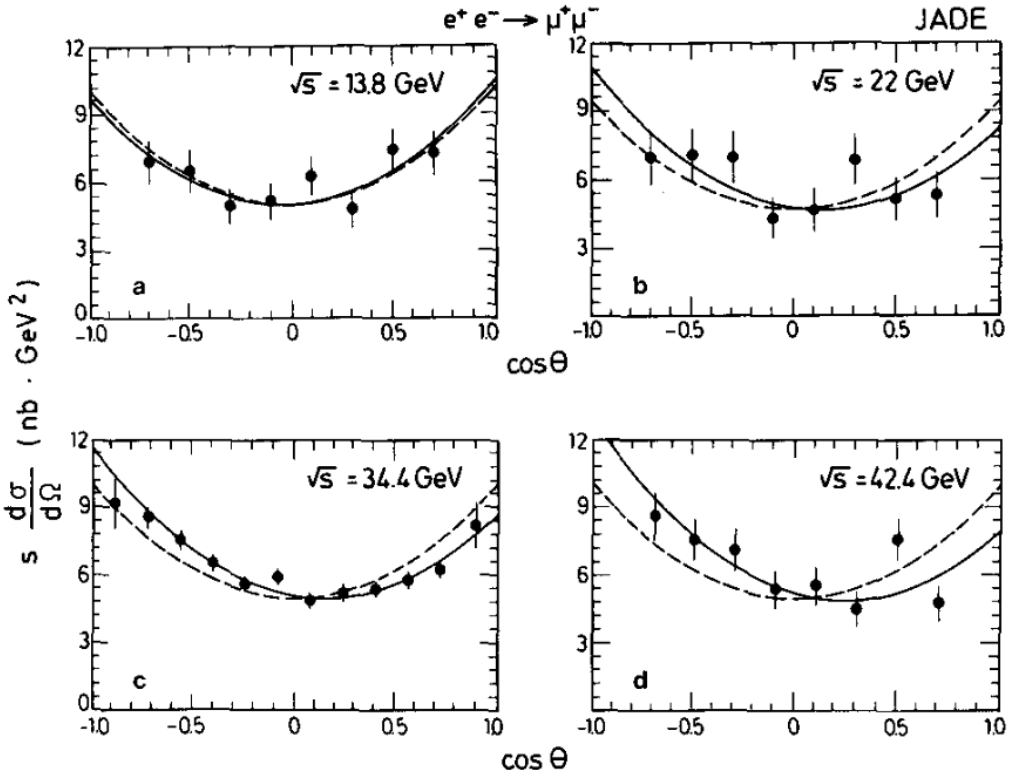

Figure 1.2: $e^- e^+ \to \mu^- \mu^+$ differential cross section as observed by the JADE experiment [37]. The dots correspond to experimental observations while the full lines are fits allowing for an asymmetry, the dashed lines are symmetric fits.

particle interactions through compact Lie groups is dubbed a *Yang-Mills Theory* [42] and can be made to apply to other interactions as well although it must be renormalisable. The implied neutrino was discovered in 1953 in the landmark Cowan-Reines experiment [43] [44] and allows for the information of the corresponding charged fermion, described by the *flavour* quantum number to be conserved. This gives rise to the following effective interaction:

$$\mathcal{M}_{fi} = G_{\mathrm{F}} g_{\mu\nu} \left(\overline{\psi}_3 \gamma^\mu \psi_1\right) \left(\overline{\psi}_4 \gamma^\nu \psi_2\right), \tag{1.24}$$

known as the Fermi 4-point interaction shown in Figure 1.3a. G_{F} being the *Fermi constant* measurable experimentally [45] [11]. It is notable as it lacks a propagator altogether.

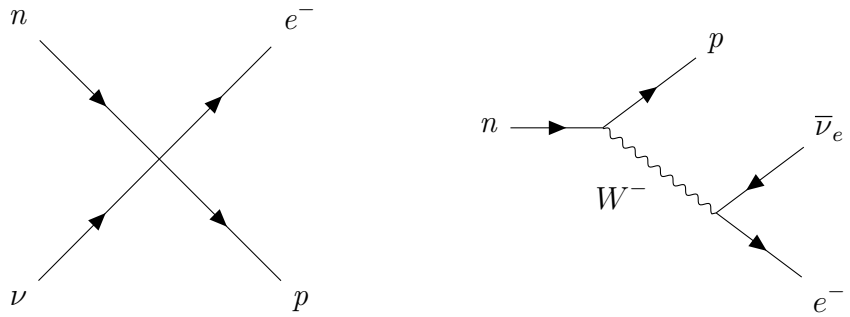

(a) Fermi 4-point interaction for a β^- decay.

(b) Propagator-mediated β^- decay.

Figure 1.3

While this contact interaction works extremely well at lower energies [11] and despite the fact that such-*Effective Field Theories* (EFT) approaches, formalising dimensional analysis and Taylor expansions to describe the effective behaviour of a fundamental theory operating below the energy scale of certain of its constituants,

have been in wide and continued use in all fields of theoretical and experimental physics [46–52], it does not scale at higher energies as G_{F} having dimensions of E^{-2} implies a scaling of the interaction with $E^2 G_{\mathrm{F}}$. The *weak* interaction is indeed weak at low energies but increases quadratically. This however cannot continue infinitely and necessitates the introduction of a propagator, analogous to the photon of QED as shown in Figure 1.3b which leads to:

$$\mathcal{M}_{fi} = -\left(\frac{g_{\mathrm{W}}}{\sqrt{2}}\overline{\psi}_3 \frac{1}{2}\gamma^{\mu}(1-\gamma^5)\psi_1\right)\cdot\left(\frac{g_{\mu\nu} - q_\mu q_\nu / m_{\mathrm{W}}^2}{q^2 - m_{\mathrm{W}}^2}\right)\cdot\left(\frac{g_{\mathrm{W}}}{\sqrt{2}}\overline{\psi}_4 \frac{1}{2}\gamma^{\nu}(1-\gamma^5)\psi_2\right), \tag{1.25}$$

with g_{W} the weak coupling constant relative to the interaction and q the momentum transfer. The term m_{W} should be noted, it is the mass of the propagator which may not be massless (and could explain the weakness of the weak interaction at low energies and would serve as cutoff scale for the EFT) and which must be electrically charged (in both positively and negatively charged variants) to preserve charge conservation. In the limit where $q^2 \ll m_{\mathrm{W}}^2$, Fermi's 4-point interaction reemerges with $\frac{G_{\mathrm{F}}}{\sqrt{2}} = \frac{g_{\mathrm{W}}^2}{8 m_{\mathrm{W}}^2}$. The range of the weak interaction should be very small [53] [54], of the order of $r_{\mathrm{W}} = \frac{\hbar}{m_{\mathrm{W}}} \sim 2.5\,\mathrm{am}$, corresponding to a $m_{\mathrm{W}} \sim 80\,\mathrm{GeV}$: This is radically different from QED's massless and infinite range photon.

Another property of the weak interaction was noted: it appears that only *left-handed fermions* couple to the W mediator. Additionally, the $e^- e^+ \to W^+ W^-$ interaction sees its cross section diverging at high energy, leading to the introduction of another heavy photon-like weak-interacting mediator (shown in Figure 1.4) [55], the Z^0 boson whose existence was put forward by Gargamelle's bubble chamber [56] and subsequently discovered at the CERN SPS [57–59].

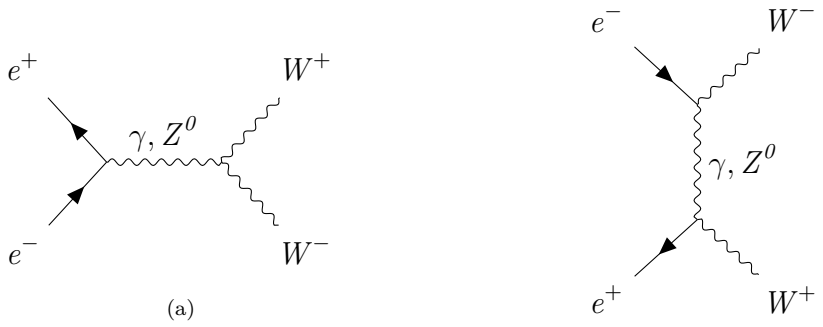

Figure 1.4: Feynman diagrams for $e^- e^+ \to W^+ W^-$

.

1.1.3.2 Unification

Looking at gauge invariance in $SU(2)$ $\varphi(x) \to \varphi(x)' = e^{i g_{\mathrm{W}} \alpha(x)\cdot \mathbf{T}}\varphi(x)$, where $\mathbf{T}$ are the three generators of the $SU(2)$ group with $\mathbf{T}_i = \frac{1}{2}\sigma_i$, with σ_i being the Pauli spin matrices, and $\alpha(x)$ are the three functions specifying local phase at each point of space-time. This implies that the local gauge invariance may only be satisfied with the introduction of three distinct gauge fields W_μ^k, with $k = 1, 2, 3$. The 2×2 nature of the Pauli spin matrices implies that $\varphi(x)$ requires a minimum of two components and is thus dubbed a *doublet* in terms of *weak isospin* $\mathrm{I_W}$, the new quantum number pertaining to $SU(2)$.

$$\varphi(x) = \begin{bmatrix} \nu_e(x) \\ e^-(x) \end{bmatrix}, \tag{1.26}$$

with $\mathrm{I_W^3}(\nu_e) = \frac{1}{2}$ and $\mathrm{I_W^3}(e^-) = -\frac{1}{2}$. In order for weak charged propagators to only couple to LH particles and RH antiparticles, they are given a singlet state with $\mathrm{I_W} = 0$. Thus emerges $SU(2)_{\mathrm{L}}$ which, for electron particles is:

$$\begin{bmatrix} \nu_e \\ e^- \end{bmatrix}_L, \tag{1.27}$$

defining doublets, RH particles are alone in a singlet, for instance ${e^-}_R$. The weak isospin singlets are not affected by the $SU(2)_\mathrm{L}$ local gauge transformation relative to the weak interaction, which permits an absence of RH couplings of particles to charged propagators to be achieved. This means the interaction term becomes:

$$ig_\mathrm{W} T_k \gamma^\mu W_\mu^k \varphi_L, \tag{1.28}$$

with φ_L the LH weak isospin doublet. This yields three weak *currents* of W^k, $k = 1, 2, 3$, corresponding to the actual particle exchange and defined in terms of the $\mathbf{T}$ generators as:

$$j_k^\mu = g_\mathrm{W} \overline{\varphi}_L \gamma^\mu \mathbf{T}_i \varphi_L. \tag{1.29}$$

The couplings to the $W^\pm$ fields are defined as

$$\mathbf{j}^\mu \cdot \mathbf{W}_\mu = j_1^\mu W_\mu^{(1)} + j_2^\mu W_\mu^{(2)} + j_3^\mu W_\mu^{(3)} = j_+^\mu W_\mu^+ + j_-^\mu W_\mu^- + j_3^\mu W_\mu^{(3)}. \tag{1.30}$$

The positive current j_+^μ couples exclusively to right-handed antiparticles through $\sigma_+ = \frac{1}{2}(\sigma_1 + i\sigma_2)$ and j_-^μ analogously couples only to left-handed particles.

This however, implies the existence of a further neutral $W^{(3)}$ which has a current $j_3^\mu = g_\mathrm{W} \overline{\varphi}_L \gamma^\mu \frac{1}{2} \sigma_3 \varphi_L$ and would only couple to particles with $\mathrm{I_W} = \pm\frac{1}{2}$, which RH particles or LH antiparticles do not, in contradiction with the neutral current described in Section 1.1.3.1. Considering the commonalities between the observed neutral current and QED's γ, Glashow, Salam and Weinberg replaced $U(1)$ by $U(1)_\mathrm{Y}$ [60–62] around *hypercharge* $Y = 2\left(Q - I_\mathrm{W}^{(3)}\right)$ analagous to Equation 1.13:

$$\psi(x) \to \psi'(x) = e^{ig' \frac{Y}{2} \zeta(x)} \psi(x). \tag{1.31}$$

This thus involves a new field B_μ which couples to Y with $g' \frac{Y}{2} \gamma^\mu B_\mu \psi$ and is entirely equivalent to that of QED: $Qe\gamma^\mu A_\mu \psi \to \frac{Y g'}{2} \gamma^\mu A_\mu \psi$. In this unified theory, boson fields and their respective currents can be written as linear combinations:

$$\begin{aligned} A_\mu &= B_\mu \cos\theta_\mathrm{W} + W_\mu^{(3)} \sin\theta_\mathrm{W}, \\ Z_\mu &= -B_\mu \sin\theta_\mathrm{W} + W_\mu^{(3)} \cos\theta_\mathrm{W}, \\ j_\mathrm{em}^\mu &= j_\mathrm{Y}^\mu \cos\theta_\mathrm{W} + j_3^\mu \sin\theta_\mathrm{W}, \\ j_\mathrm{Z}^\mu &= -j_\mathrm{Y}^\mu \sin\theta_\mathrm{W} + j_\mathrm{Z}^\mu \cos\theta_\mathrm{W}, \end{aligned} \tag{1.32}$$

θ_W is the *electroweak mixing angle* or *Weinberg angle* which describes the ratio of weak to electromagnetic coupling constants $\frac{\alpha}{\alpha_\mathrm{W}} = \frac{e^2}{g_\mathrm{W}^2} = \sin\theta_\mathrm{W} \simeq 0.23$ [63–65].

While electroweak theory is now seemingly complete, a Yang-Mills theory yielding two charged vector bosons and two neutral ones, three significant problems persist: the mixing of $U(1)_\mathrm{Y}$ and $SU(2)_\mathrm{L}$ is not particularly instinctive and may seem contrived, there remains no explanation for the masses of W and Z^0 (nor that of any fermion for that matter) nor any mechanism to introduce it without breaking gauge invariance and perhaps more problematic yet: $W^+ + W^- \to W^+ + W^-$ scattering is entirely divergent at higher energies which is non-physical. Two solutions seem to exist for this last issue: either vector bosons also appear in another Yang-Mills theory (for instance $SU(3)$ described in Section 1.1.4 [66]) or there exists another field with different (non-Yang-Mills) couplings whose interference would bring the interaction cross section to converge.

1.1.3.3 Spontaneous symmetry breaking

Confronted with the lack of evidence for extra Yang-Mills couplings in W bosons [11, 67–69], the hypothesis of scalar i.e.*spinless* fields is attractive, with a potential for a real field ϕ:

$$V(\phi) = \frac{1}{2}\mu^2\phi^2 + \frac{1}{4}\lambda\phi^4. \tag{1.33}$$

The derived Lagrangian is therefore:

$$\mathcal{L} = \frac{1}{2}\left(\partial_\mu\phi\right)\left(\partial^\mu\phi\right) - \frac{1}{2}\mu^2\phi^2 - \frac{1}{4}\lambda\phi^4. \tag{1.34}$$

The $\left(\partial_\mu \phi\right)\left(\partial^\mu \phi\right)$ term is the dynamics term, $\frac{1}{2}\mu^2\phi^2$ is the rest mass of the particle whereas the $\lambda\phi^4$ is the self interaction term of the field, specifically in this case, the *4-point interacting* term corresponding to the Feynman diagram shown in Figure 1.5.

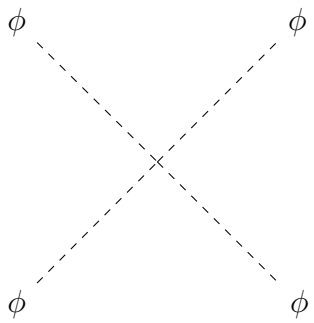

Figure 1.5: Scalar field 4-point coupling.

The lowest energy state of ϕ, called the vacuum state is the minimum of $V(\phi)$ from Equation 1.33, finiteness requires that λ be positive. If μ^2 is positive as well, the absolute minimum is found at $\phi = 0$, the mass of the particle is μ and the vertex from Figure 1.5 is proportional to ϕ^4. However, if μ^2 is negative, μ cannot be the mass of the associated particle as squared masses cannot be negative. The potential minima are occuring for non-zero ϕ:

$$\phi = \pm v = \pm\left|\sqrt{\frac{-\mu^2}{\lambda}}\right|. \tag{1.35}$$

The vacuum expectation value (vev), v the value at which $\phi = 0$ is therefore non-zero, which for a symmetric potential such as $V(\phi)$, two distinct minima emerge, $\phi = \pm v$. Since these lowest-energy states are distinct from the vacuum expectation value, this gives rise to a symmetry which cannot remain whole as it will break under any quantum fluctuation, and is thus *spontaneously broken* [70–72].

In an analagous manner, this can be applied to a complex field with $V(\phi) = \mu^2(\phi^*\phi) + \lambda(\phi^*\phi)^2$ and $\mathcal{L} = (\partial_\mu\phi)(\partial^\mu\phi) - V(\phi)$. It can be noted that gauge invariance implies that $\mathcal{L}$ is invariant under $\phi \to \phi' = e^{i\alpha}\phi$ and thus is symmetric under global $U(1)$. If $\mu^2 < 0$, an infinite amount of minimas is generated visualised in Figure 1.6:

$$\mathfrak{Re}(\phi)^2 + \mathfrak{Im}(\phi)^2 = \frac{-\mu^2}{\lambda} = v^2. \tag{1.36}$$

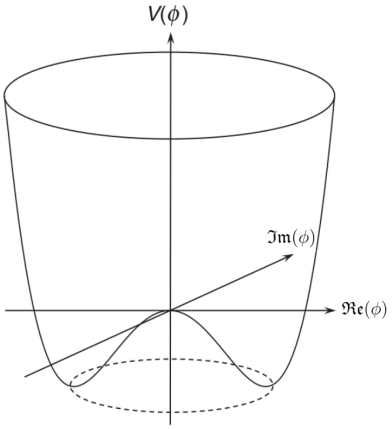

Figure 1.6: Visualisation of spontaneous symmetry breaking in a complex scalar field [34]. The dashed circle represents the minima.

Identically to the real scalar field case, the $U(1)$ symmetry is spontaneously broken. The field can be rewritten as $\phi = \frac{1}{\sqrt{2}}(\eta + v + \xi)$ with $\mathfrak{Re}(\phi) = \eta(x) + v$ and $\mathfrak{Im}(\phi) = \xi(x)$. This gives rise to the Lagrangian:

$$\mathcal{L} = \frac{1}{2}(\partial_\mu\eta)(\partial^\mu\eta) - \frac{1}{2}m_\eta^2\eta^2 + \frac{1}{2}(\partial_\mu\xi)(\partial^\mu\xi) - \lambda v\eta^3 + \frac{1}{4}\lambda\eta^4 + \frac{1}{4}\lambda\xi^4 + \lambda v\eta\xi^2 + \frac{1}{2}\lambda\eta^2\xi^2, \tag{1.37}$$

where $m_\eta = \sqrt{2\lambda v^2}$. $\mathcal{L}$ yields a massive scalar field η and a massless field ξ. Excitations of ξ do not affect the potential and the massless boson emerging from it is called a Nambu-Goldstone boson (NGB) [73–75].

The SM's complex field $V(\phi)$ is present within the local $U(1)_\mathrm{Y} \times SU(2)_\mathrm{L}$, not the global $U(1)$ with ϕ_SM as:

$$\phi_\mathrm{SM} = \begin{pmatrix} \phi^+ \\ \phi^0 \end{pmatrix} = \frac{1}{\sqrt{2}} \begin{pmatrix} \phi_1 + i\phi_2 \\ \phi_3 + i\phi_4 \end{pmatrix}, \tag{1.38}$$

with the two components of the doublet differing by one unit of charge. The potential and Lagrangian of the SM scalar boson are defined:

$$\begin{aligned} \mathcal{L} &= \left(\partial_\mu \phi\right)^\dagger \left(\partial^\mu \phi\right) - V(\phi), \\ V(\phi) &= \mu^2 \phi^\dagger \phi + \lambda \left(\phi^\dagger \phi\right). \end{aligned} \tag{1.39}$$

Spontaneous symmetry breaking yields a circle of minima analogous to those of Figure 1.6 with $\phi^\dagger\phi = -\frac{\mu^2}{2\lambda}$ corresponding to one massive self-coupling scalar particle as well as three NGBs. These NGBs acquire mass by dynamically coupling to the aforementionned scalar field, using the covariant derivative $\partial_\mu \rightarrow D_\mu = \partial_\mu + ig_\mathrm{W}\mathbf{T}\cdot\mathbf{W}_\mu + ig'\frac{\mathrm{Y}}{2}B_\mu$, with B_μ the massless gauge field corresponding to Y

$$\begin{aligned} &\frac{1}{2}\left(\partial_\mu h\right)\left(\partial^\mu h\right) + (v+h)^2 \left[\frac{1}{8}v^2 g_\mathrm{W}^2 \left(W_\mu^{(1)} W^{(1)\mu} + W_\mu^{(2)} W^{(2)\mu}\right)\right. \\ &\left. + \frac{1}{8}v^2 \left(g_\mathrm{W} W_\mu^{(3)} - g' B_\mu\right)\left(g_\mathrm{W} W^{(3)\mu} - g' B^\mu\right)\right] - V(\phi). \end{aligned} \tag{1.40}$$

The mass terms for $W^{(1)}$ and $W^{(2)}$ appear in $\frac{1}{2}m_\mathrm{W}^2 W_\mu^{(1,2)} W^{(1,2)\mu}$ relating the $W^\pm$ mass to the vacuum expectation value:

$$m_W = \frac{1}{2} g_\mathrm{W} v. \tag{1.41}$$

The $W^{(3)}$ terms of Equation 1.40 can be rewritten as as function of the mass matrix $\mathbf{M}$: $\frac{v^2}{8}\left(W_\mu^{(3)}\ B_\mu\right)\mathbf{M}\begin{pmatrix} W^{(3)\mu} \\ B^\mu \end{pmatrix}$. In order to allow for mixing with QED's photon, $\mathbf{M} = \frac{1}{2}\left(A_\mu\ Z_\mu\right)\begin{pmatrix} m_A^2 & 0 \\ 0 & M_{Z^0}^2 \end{pmatrix}\begin{pmatrix} A^\mu \\ Z\mu \end{pmatrix}$ is non-diagonal, which in combination with Equation 1.40 yields the γ and Z^0 masses:

$$m_A = 0 \text{ and } m_{Z^0} = \frac{1}{2}\sqrt{g_W^2 + g'^2}. \tag{1.42}$$

Fermion masses, if they were introduced through a Dirac $-m\left(\overline{\psi}_\mathrm{R}\psi_\mathrm{L} + \overline{\psi}_\mathrm{L}\psi_\mathrm{R}\right)$ term would not be gauge invariant. Fortunately, the SM scalar field produces them through *Yukawa couplings* [76] [77], for instance for the $SU(2)$ electron doublet as:

$$\mathcal{L}_e = -g_e \left[\begin{pmatrix} \overline{\nu}_e & \overline{e} \end{pmatrix}_L \begin{pmatrix} \phi^+ \\ \phi^0 \end{pmatrix} e_R + \overline{e}_R \begin{pmatrix} \phi^{+*} & \phi^{0*} \end{pmatrix} \begin{pmatrix} \nu \\ e \end{pmatrix}_L\right]. \tag{1.43}$$

which allows the introduction of gauge-invariant mass terms via the couplings to the scalar field, for instance in the unitary gauge:

$$\mathcal{L}_e = -\frac{g_e}{\sqrt{2}} v \left[\overline{e}_L e_R + \overline{e}_R e_L\right] - \frac{g_e}{\sqrt{2}} h \left[\overline{e}_L e_R + e_R e_L\right]. \tag{1.44}$$

The mass of the underlying fermion (here an electron) is then defined as:

$$m_\ell = \frac{v g_e}{\sqrt{2}} \tag{1.45}$$

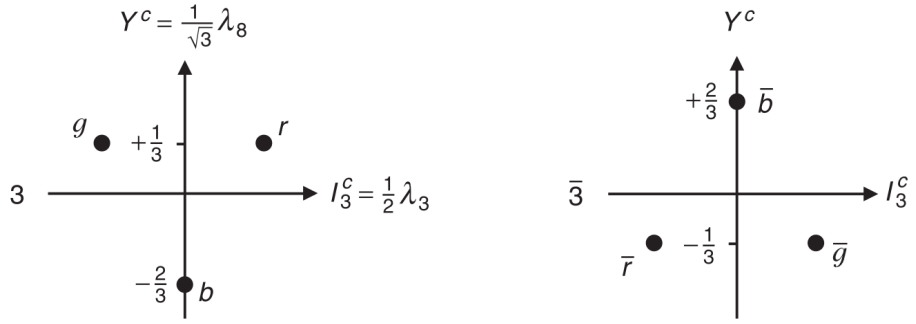

Figure 1.7: Representation of Eighfold path $SU(3)$ algebra applied to quarks [34].

The scalar field is called the Higgs field and its excitation is interpreted as the so-called Higgs boson [5–7].

Significantly, it can be observed from the Lagrangian 1.44 that both fermion chiralities are involved in the Higgs fermion mass acquisition mechanism.

1.1.4 Quantum Chromodynamics and deep-inelastic-scattering

The unified electroweak force covers a majority of easily-accessible objects but provides no explanation to the existence of nuclei and much less a description of their interaction with other nuclei.

The strong interaction is the final force covered by the Standard Model. This theory was born from the experimental observation of a great variety of strong-interacting particles, giving rise to a *particle zoo* [78] [11]. The great variety of particles and the study of their properties (particularly mass, spin and *strangeness* [79] [80]) led to the organisation of strong interacting particles into a special unitary group known as the eightfold way [81]. This solution was however incapable of describing quite all observed particles. Thus *Quantum ChromoDynamics* (QCD) was introduced.

QCD can be defined as a *limited range QED-like theory with 8 self-interacting messenger particles* based around a complex $SU(3)$ Yang-Mills local gauge symmetry instead of $U(1)$. This implies that the gauge invariance $\psi(x) \rightarrow \psi'(x) = e^{ig_S\alpha(x)\cdot\mathbf{T}}\psi(x)$ has eight generators with $\mathrm{T}^a = \frac{1}{2}\lambda^a$ with λ^a the eight *Gell-Mann matrices* [81]. The three new degrees of freedom are provided by adding *colour*, a new quantum number which allows the content of strongly interacting particles, *the quarks*, not to violate the Pauli exclusion principle. Colours (unrelated to optical colours beyond basic properties) are present for three values and three "antivalues": red $r^T = \begin{bmatrix}1 & 0 & 0\end{bmatrix}$, green $g^T = \begin{bmatrix}0 & 1 & 0\end{bmatrix}$ and blue $b^T = \begin{bmatrix}0 & 0 & 1\end{bmatrix}$, anti-red (also known as cyan), anti-blue (also known as yellow) and anti-green (also known as magenta). These colours operate through a quantum number formally called *colour isospin* I_k^C and *colour hypercharge* Y^C analogous to $\mathrm{I_W}$, albeit with 3 components and anticomponents, as can be visualised in Figure 1.7.

Massive nuclear elementary matter is present through fermions called *quarks* which, analogous to electroweak fermions, display distinct flavours such as *upness*, *downness* or the aforementioned *strangeness* which allows them to participate in electroweak interactions such as the β decay described in Section 1.1.3.1. Each of these flavour eigenstates displays different masses which are not aligned with their mass eigenstates and related to one another through the Cabbibbo Kobayashi Maskawa (CKM) matrix [11, 82, 83]. The eight generators of SU(3) imply the presence of eight mediator *gluon* particles, analogous to the photon of QED which couple to quarks through $-ig_S\frac{1}{2}\lambda^a\gamma^\mu G_\mu^a\psi$. They are distinct from QED through their coupling constant $g_S(\mu^2)$ which weakens for higher energy scales μ^2 and the use of colour interactions through λ^a. The gluon-quark vertex emerges as $-\frac{1}{2}ig_S\lambda_{ji}^a\gamma^\mu$ and the gluon propagator is associated with $-i\frac{g_{\mu\nu}}{q^2}\delta^{ab}$. The high value of the coupling constant g_S [84] compared to electroweak ones [85] might suggest that quarks and gluons should be dominant all over the universe, leaving little space for other interactions.

This is limited by a few mechanisms: First, quarks are unable to exit a composite object in a process known as *colour confinement*, gluons, carrying colour charge, self interact [86], as such creating an attractive force which increases pseudo-linearly with distance [87], thus energy put into the separation of quarks will only create new bound quarks in a process known as *asymptotic freedom* [88] [89]. Such strongly interacting objects are named *hadrons* are composed of *valence quarks* which must sum up to a colourless object, gluons which maintain the object, and *sea-quarks* created and annihilated constantly within the object by gluons. If an object has 2 valance quarks, it is called a *meson*, if it has 3 it is called a *baryon*.

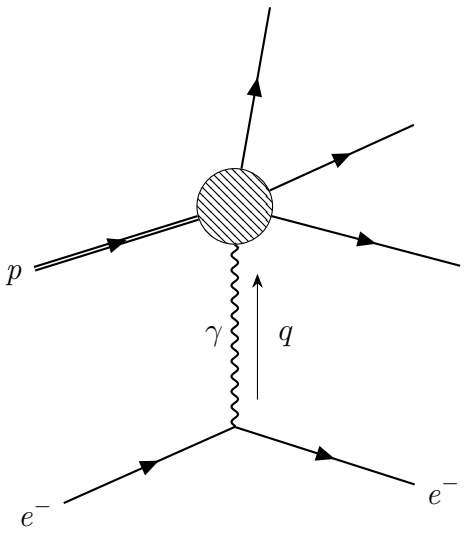

Figure 1.8: DIS of an electron on a proton.

Among mesons, an interesting case is that of the π, as the chiral $\mathrm{SU}(3)_L \times \mathrm{SU}(3)_R$ symmetry of QCD is broken by the quarks not being massless, a NGB-like scalar emerges analogous to that of Section 1.1.3.3, instead of it being massless however, it has a small mass which tends to 0 as the symmetry gets more exact. The π is thus created, much lighter than its other hadron cousins. The pion is here a *Pseudo-Nambu-Goldstone-Boson* (PNGB). A more in depth description of the chiral symmetry breaking and the eight PNGB that emerge from it may be found in [90].

The fraction of momentum carried by each of these *partons* is determined by the Dokshitzer-Gribov-Lipatov-Altarelli-Parisi (DGLAP) equations [91] [92], has been verified experimentally and give rise to *parton distribution functions* (PDF) which indicate the distribution of momentum fraction within the strongly interacting object [93–95]. Said momentum fraction is denoted as the Bjørken x:

$$x \equiv \frac{Q^2}{2p_2 q} \tag{1.46}$$

where q is the momentum of the virtual photon in a deep inelastic scattering (DIS) process for instance for instance shown in Figure 1.8, $Q^2 = -q^2$ and p_2 is the momentum of the incoming hadron.

1.1.4.1 The Standard Model

The Minimal Standard Model is the full theory combining the minimal electroweak and QCD descriptions into a single $U(1) \times SU(2)_L \times SU(3)$ symmetry. The full Standard Model Lagrangian is as follows:

Fermions			Bosons
up quark u $m = 2.16^{+0.49}_{-0.26}$ MeV q_{EM} =2/3	charm quark c $m = 1.27 \pm 0.02$ GeV q_{EM} =2/3	top quark t $m = 172.69 \pm 0.30$ GeV q_{EM} =2/3	gluon g $m = 0$ eV q_{EM} =0
down quark d $m = 4.67^{+0.48}_{-0.17}$ MeV q_{EM} =-1/3	strange quark s $m = 93.4^{+8.6}_{-3.4}$ MeV q_{EM} =-1/3	bottom quark b $m = 4.18^{+0.03}_{-0.02}$GeV q_{EM} =-1/3	photon γ $m = 0$ eV q_{EM} =0
electron e^- $m = 511$ keV q_{EM} =-1	muon μ^- $m = 105.658$ MeV q_{EM} =-1	tau τ^- $m = 1776.86 \pm 0.12$ MeV q_{EM} =-1	W bosons $W^{\pm}$ $m = 80.369 \pm 0.013$ GeV $q_{\text{EM}} = \pm 1$
electron neutrino ν_e $m = 0$ eV q_{EM} =0	muon neutrino ν_μ $m = 0$ eV q_{EM} =0	tau neutrino ν_τ $m = 0$ eV q_{EM} =0	Z boson Z^0 $m = 91.1876 \pm 0.0021$ GeV q_{EM} =0
			Higgs boson H $m = 125.25 \pm 0.17$ GeV q_{EM} =0

Table 1.1: SM particles, their masses and their electric charge, values taken from [11]. Neutrino masses are observed to be non-zero which is contrary to the SM prediction.

$$
\begin{aligned}
&\mathcal{L} = -\frac{1}{4}\mathbf{B}_{\mu\nu}\mathbf{B}^{\mu\nu} - \frac{1}{8}\mathrm{Tr}(\mathbf{W}_{\mu\nu}\mathbf{W}^{\mu\nu}) - \frac{1}{2}\mathrm{Tr}(\mathbf{G}_{\mu\nu}\mathbf{G}^{\mu\nu}) \\
&\text{U(1), SU(2) and SU(3) gauge terms. } \mathbf{B}\text{, } \mathbf{W} \text{ and } \mathbf{G} \text{ are the associated vector potentials.} \\
&+ (\overline{\nu}_L, \overline{e}_L)\tilde{\sigma}^\mu i D_\mu \begin{pmatrix} \nu_L \\ e_L \end{pmatrix} + \overline{e}_R \sigma^\mu i D_\mu e_R + \overline{\nu}_R \sigma^\mu i D_\mu \overline{\nu}_R + (\text{h.c.}) \\
&\text{lepton dynamics term. } (h.c.) \text{ is the hermitian conjugate of the previous expression} \\
&- \frac{\sqrt{2}}{v}\left[\overline{e}_L \phi M^e e_R + \overline{e}_R \overline{M}^e \overline{\phi}\, e_L\right] \\
&\text{charged leptons mass term} \\
&+ (\overline{u}_L, \overline{d}_L)\tilde{\sigma}^\mu i D_\mu \begin{pmatrix} u_L \\ d_L \end{pmatrix} + \overline{u}_R \sigma^\mu i D_\mu u_R + \overline{d}_R \sigma^\mu i D_\mu d_R + (\text{h.c.}) \\
&\text{quark dynamics term.} \\
&- \frac{\sqrt{2}}{v}\left[(\overline{u}_L, \overline{d}_L)\phi M^d d_R + \overline{d}_R \overline{M}^d \overline{\phi} \begin{pmatrix} u_L \\ d_L \end{pmatrix}\right] \\
&\text{down-type quarks mass term} \\
&- \frac{\sqrt{2}}{v}\left[(-\overline{d}_L, \overline{u}_L)\phi^* M^u u_R + \overline{u}_R \overline{M}^u \overline{\phi}^T \begin{pmatrix} -d_L \\ u_L \end{pmatrix}\right] \\
&\text{up-type quarks mass term} \\
&+ \overline{(D_\mu \phi)} D^\mu \phi - \frac{m_h^2\left[\overline{\phi}\phi - \frac{v^2}{2}\right]^2}{2v^2}. \\
&\text{Higgs dynamics and mass term}
\end{aligned}
\tag{1.47}
$$

which gives rise to the particles and interactions seen in Table 1.1 and Figure 1.9.

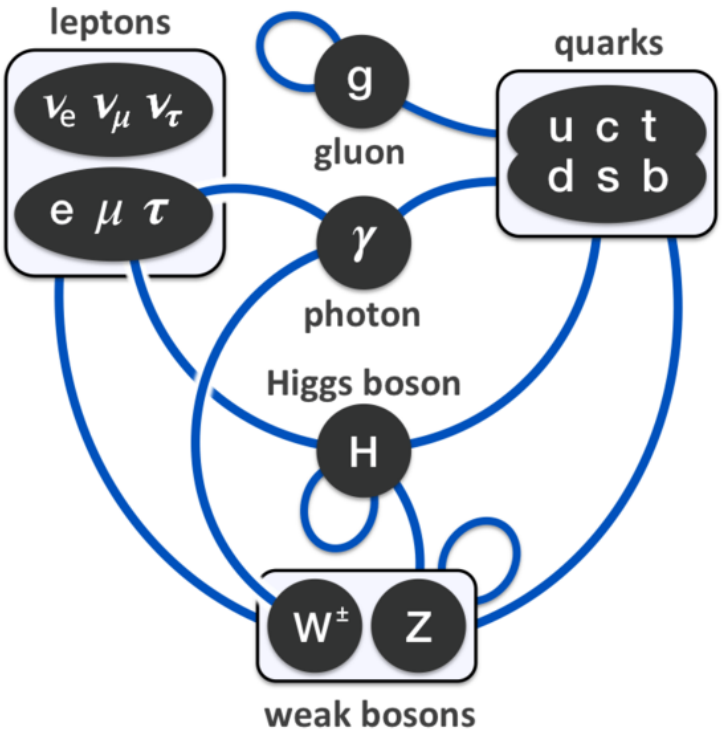

Figure 1.9: Visualisation of particles and their interactions in the SM [96]. The dark ellipses represent particles, the blue lines indicate which particles they interact with.

1.1.5 Standard Model studies using neutrinos

Neutrinos are a particularly studied particle in modern particle physics [11, 97–99]. Of particular interest to this work are neutrinos from particle colliders (see Section 2.2.1) which are discussed below. High intensity neutrino fluxes from beam dump experiments are also covered (see Section 2.3.2).

1.1.5.1 Physics using collider neutrino

Neutrinos may be used in DIS experiments [100, 101] which allows the effective constraint of PDFs, particularly in the strange quark sector [102]. Neutrinos have the peculiarity that they may only interact weakly which implies that on-shell s-channel interactions have a final state invariant mass equal to the mass of the W or the Z^0 which facilitate reconstruction.

Interaction can occur with electrons and hadrons in charged and neutral current (CC, NC) interactions. Nuclear interactions of neutrinos come in two variants: quasi-elastic, where momenta change but free particle counts do not, and deep inelastic (DIS), where the neutrino interacts with a parton with a large energy-momentum transfer causing the hadron to break up inelastically. The tree level diagrams for these different scattering processes are shown in Figure 1.10.

The total cross sections of electron neutrino scattering on electrons are given in Table 1.2.

Process	Cross section
$\nu_e + e^- \to \nu_e + e^-$	$\sigma_{\text{tot}} = \frac{G_F^2 s}{4\pi}\left[(2\sin^2(\theta_W - 1)^2 + \frac{4}{3}\sin^4(\theta_W)\right]$
$\bar{\nu_e} + e^- \to \bar{\nu_e} + e^-$	$\sigma_{\text{tot}} = \frac{G_F^2 s}{4\pi}\left[\frac{1}{3}(2\sin^2(\theta_W + 1)^2 + 4\sin^4(\theta_W)\right]$

Table 1.2: Cross section of (anti-)neutrino elastic interactions with electrons.

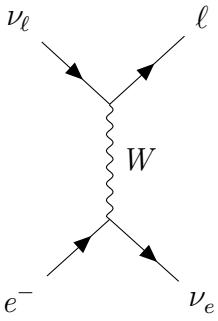

(a) CC interaction of an (anti)neutrino and an electron.

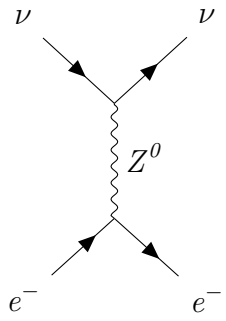

(b) NC interaction of an (anti)neutrino and an electron.

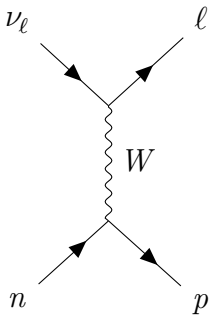

(c) CC quasi-elastic interaction of a neutrino and a neutron.

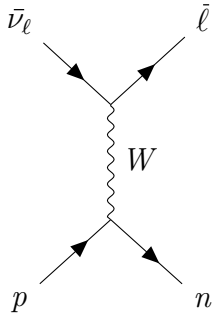

(d) CC quasi-elastic interaction of an antineutrino and a proton.

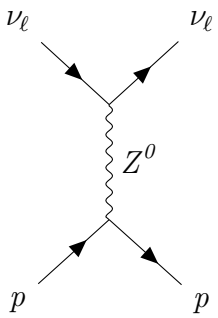

(e) NC quasi-elastic interaction of an (anti)neutrino and a proton.
A similar interaction may take place with a neutron.

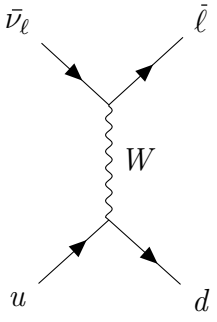

(f) CC DIS interaction of an antineutrino and an up quark.
An analogue interaction may take place with the associated antiparticles.

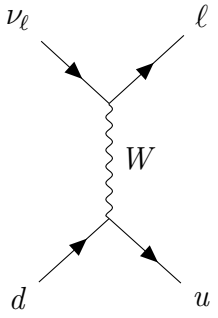

(g) CC DIS interaction of a neutrino and an up quark.
An analogue interaction may take place with the associated antiparticles.

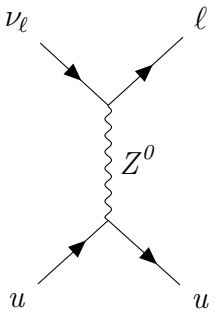

(h) NC DIS interaction of a neutrino and an up quark. An analogue interaction may take place with antineutrinos and/or down type quarks.

Figure 1.10

A useful number here is $\sigma(\nu_e e^-) = \frac{G_F^2 s}{\pi}[(\frac{1}{2} + \sin^2\theta_W)^2 + \frac{1}{3}\sin^4\theta_W] \sim 0.09(\frac{E}{10\,\text{MeV}})$ ab. For neutrino DIS however, the cross section depends on difficult-to-model parton behaviour which is often regrouped under so called *structure functions* [103]:

$$\frac{d\sigma_{\nu,\bar{\nu},\text{DIS}}}{dxdy} = \frac{G_F^2 ME}{\pi}\Big[(1-y)F_2^{\nu N} + y^2 x F_1^{\nu N} \mp \big(y - \frac{y^2}{2}F_3^{\nu N}\big)\Big], \tag{1.48}$$

$$F_1 = d(x) + \bar{u}(x), \tag{1.49}$$

$$F_2 = 2x\left[d(x) + \bar{u}(x)\right], \tag{1.50}$$

$$F_3 = 2x\left[d(x) - \bar{u}(x)\right] \tag{1.51}$$

where F_1, F_2, F_3 are dimensionless structure functions of the Bjørken x of Section 1.1.4 and the associated relative presence of quarks in the composite object. $d(x)$ and $\bar{u}(x)$ are the quark distribution functions. Two more structure functions F_4 and F_5 emerge from more general parametrisations, they are however not measurable with good precision at the current generation of colliders as they are proportional to m_ℓ^2 which renders them measurable only when a large ν_τ flux is achieved [104]. The determination of these structure functions is of high value in describing composite particle behaviour, for instance in hadron collisions (Section 2.1.1) where the final state is dependent on the cross section of the parton-parton initial state which itself is dependent on the parton flavour and energy. This can be done through the observation of the cross section as a function of $y = \left(1 - \frac{E_\mu}{E_\nu}\right)$.

1.1.5.2 Physics using high intensity neutrino fluxes

Large neutrinos fluxes may be used to perform ν_τ phenomenology and allow the determination of the F_4 and F_5 structure functions [105]. In addition neutrino-induced charm production in the detector could be observed in such conditions due to statistics with adequate tracking detector. This would allow for high granularity neutrino-induced calorimetric observation of the charm quark with final states other than $\mu^-\mu^+$ [106]. Furthermore, the precise measurement of quark sea strange flavour content could be achieved leveraging the large V_{cs} CKM matrix element [11] (see Section 2.2.2).

A large amount of ν_τ would further permits measurements of the ν_τ magnetic moment using neutrino-electron scattering processes where the scattered neutrino remains unobserved [107].

1.2 Limits of the Standard Model

The SM is in very good agreement with experimental observations. It however displays some issues with its underlying theory, furthermore, while the SM has seldom been proved wrong in any of its predictions, a variety of phenomena are observed in nature albeit unexplained by the SM. This suggests the existence of Beyond the Standard Model (BSM) Physics to extend or replace the SM in order for these issues to be resolved.

1.2.1 Universe expansion acceleration

Astronomical observations display an accelerated expansion of the Universe [108–110]. There exists no process in the SM for such an acceleration in a Universe dominated by gravity which is a supposedly purely attractive force. Consequently there is a need for some form of new repulsive process which would adequately act at larger energy scales. This is referred under the umbrella term of Dark Energy, as its behaviour is so far unexplained [111].

1.2.2 Gravity anomalies

While performing astronomical observations, misbehaviours in gravity which are incompatible with observed matter and/or the current understanding of gravity, general relativity, are observed. In particular, spiral galaxies seem to maintain their rotation speeds even at high radii [112–114], significant gravitational lensing anomalies

are observed [115–117] where massive objects appear to be present in area of the cosmos which are observed to otherwise be empty. The preferred explanation for those anomalies would be the existence of a form of massive matter which interacts weakly or even not at all with SM objects. Constraints on so-called *Dark Matter* (DM) are generally loose [11] or model-dependent [118]. It generally can be said that (some) DM would have to be heavier than $\sim 10^{-22}$ eV in order for their wavelength to fit inside of galaxies [119, 120] and be lighter than $\mathcal{O}(10^{70}\,\text{eV}) \sim 10^{4}\ \text{M}_{\odot}$ (solar masses) [121–124] because of tidal stability of structures immersed within DM halos (such as dwarf galaxies or galaxy disks) [125].

Alternative explanations to gravity anomalies exist as well [126–128] but are not seen to be as well supported by theory and experiment [129–132].

1.2.3 Baryonic asymmetry

Observations of the ratio of matter to antimatter in the universe suggest that very little antimatter exists compared to matter [133]. While production in equal amounts of both could be expected as a result of symmetry, the breaking of these and the experimental absence of any clear delimitation of particle and antiparticle regions within the galaxy indicate that there is a sizeable amount of CP violation, i.e. that the some imaginary components are present in SM mixing matrices such as the CKM matrix. While CP violation is present in the SM and has been found as mentioned in Section 1.1.3.1, it is not sufficiently significant to account for the observed matter/antimatter asymmetry [134]. Sources of extra CP violation are therefore a significant point for BSM Physics.

1.2.4 Description of neutrinos

Neutrinos, being capable of oscillations [135, 136], need to be massive [137] and, analogous to quarks, do not have their mass eigenstates aligned with their flavour eigenstates. Since they only interact through the weak interaction of Section 1.1.3.1 and have only been observed to couple to the W and Z^0 bosons, the only observed neutrinos have been *left-handed neutrinos* (and *right-handed antineutrinos*). The mechanism through which neutrinos acquire mass is, however, entirely unknown. It could be the Higgs mechanism from Section 1.1.3.3 implying $\mathcal{L}_D = -m_D(\overline{\nu}_R\nu_L + \overline{\nu}_L\nu_R)$, but this would give rise to opposite-chirality neutrinos that would not interact and are not present within the SM. Any additional field terms in the SM Lagrangian wouldn't break gauge invariance as ν_R and $\overline{\nu_L}$ transform as singlets. Thus, through a CP operation $\psi^c = \hat{C}\hat{P}\psi = i\gamma^2\gamma^0\psi^*$ which yields ν_R^c when applied to ν_R, producing the left-handed antineutrino without adding any new particles. The antineutrino becomes the right-handed neutrino which implies an extra *Majorana* mass term M:

$$\mathcal{L}_{\text{M}} = -\frac{1}{2}\text{M}\left(\overline{\nu_R^c}\nu_R + \overline{\nu_R}\nu_R^c\right) \tag{1.52}$$

Searches for signs of this Majorana nature of neutrinos are particularly acute in *neutrinoless double β decay* [138–141]. Searches for the neutrinos' absolute mass are active through experimental means [142, 143], as well as cosmological constraints [144]. Preliminary results from neutrino oscillation experiments suggest that leptonic CP violation could be transferred to the baryon section and thus explain the mystery of Section 1.2.3.

A significant experimental gap of neutrino physics relates to their cross section, indeed, while observations have been made at energies lower than 500 GeV and over 10 TeV, there is an absence of neutrino cross section measurements in the $\mathcal{O}$(TeV) range as displayed in Figure 1.11.

1.2.5 Strong CP Problem

A curiosity arises when computing the neutron's electrical dipole moment (eDM): indeed, using the classical formula, a naive computation of eDM would yield $\mathbf{d} = \sum q\mathbf{r}$; $|d_n| = 10^{-13}\sqrt{1-\cos\theta}\ e$ cm with θ the CP-violating phase which leads to an expectation of eDM being $\sim 10^{-13}e$ cm. Experimental checks, using measurements of Larmor precession find a very different upper bound of $\sim 10^{-28}e$ cm [146, 147] which implies a physical CP violating angle $\overline{\theta} < 10^{-10}$ [148]. In a simplified case, a Yang-Mills theory Lagrangian for a single massive quark would be:

$$\mathcal{L} = -\frac{1}{4}F_{\mu\nu}F^{\mu\nu} + \theta\frac{g^2}{32\pi^2}F_{\mu\nu}\widetilde{F}^{\mu\nu} + \overline{\psi}\left(i\gamma^\mu D_\mu - me^{i\theta'\gamma^5}\right)\psi. \tag{1.53}$$

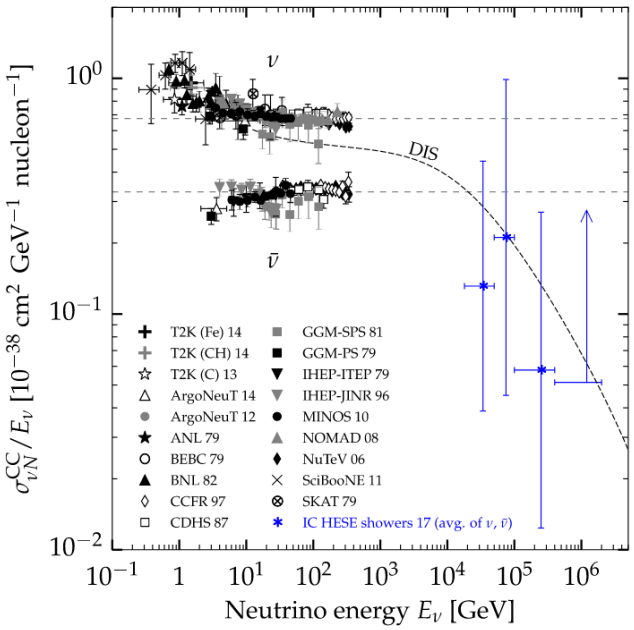

Figure 1.11: Reported neutrino cross sections from experimental data [145].

The θ and mass terms being CP violating, any chiral transformation with angle α leads to $\theta' \to \theta' - \alpha$ and $\theta \to \theta + \alpha$. The so-called *Strong CP problem* arises from the existence of these two CP-violating terms and the impossibility to eliminate them as there would have to be $\theta = -\theta'$ which would cause the full CP violation $\theta + \theta'$ to remain invariant under any chiral transformation and CP is observed to be conserved by the strong interaction in the SM. The simplest solution to the Strong CP problem, namely setting one quark to be massless (allowing the redefinition of fields in a CP conserving fashion) [149] is ruled out [11]. Leaving the SM with an unexplainably unbroken SU(3) symmetry.

1.2.6 Gravity

Gravity has yet to be described satisfactorily quantum mechanically. While the existence of a gauge symmetry mediated by a graviton g [150, 151] could be expected, this mediator has yet to be described satisfactorily theoretically [152, 153] as the Yang-Mills theory is found to be non-renormalisable [154]. While alternative approaches exist [155–162] , none satisfy renormalisability, gauge invariance, phenomenological description and experimental consistency, even as an EFT, giving rise to the so-called *Swampland* [163] of QFTs that aren't consistent with quantum gravity. This on its own implies that the SM is not a *Theory of everything*.

1.2.7 Hierarchy

In the SM, the Higgs mass term is $\mu H^\dagger H$, set as a free parameter and invariant under gauge or global symmetry. This implies that the term is susceptible to radiative corrections which may thus modify it proportionally at every scale where the Higgs field interacts through particle loops. These corrections take the form $\frac{\Lambda^2}{16\pi^2}\left(6\lambda + \frac{9}{4}g_2^2 + \frac{3}{4}g_{\mathrm{Y}_{12}} - 6y_t^2 + ...\right)$ where Λ is crucially the *UV* cutoff scale used to regularize the integral and representing the scale above which the theory is no longer thought to be valid (for example, classical physics is effective above a certain *infrared* cutoff). The SM is renormalisable and as such in principle scales until a higher energy, be it the Grand Unification Scale [164, 165] where all three forces undergo unification analogous to what is observed in the electroweak case $\Lambda_{\mathrm{GUT}} \sim 10^{16}$ GeV or the Plank Scale, where the energy level yielded by dimensional analysis of fundamental constant combinations where gravitational effects are no longer negligible, for instance a photon with $E_\gamma \sim E_{\mathrm{Planck}}$ has $\lambda_\gamma < R_{\gamma,\mathrm{Schwarzschild}}$, $\Lambda_{\mathrm{Planck}} \sim 10^{19}$ GeV which is then the UV-cutoff. This issue is circumvented for fermions as they are subject to chiral symmetry while gauge bosons are subject to gauge symmetry, protecting their mass.

The Higgs boson mass however enjoys no such mechanism in the SM and would have to be comparable to the Planck/GUT energy scale which is in sharp contrast with its modest observed mass. This issue can be

solved by heavily fine-tuning the Higgs mass [166], reducing it through extensive use of loops, for instance, for the top quark $\delta m^2_{\mathrm{H|top}} \sim \frac{3G_{\mathrm{F}}}{2\sqrt{2}\pi^2} m_t^2 \Lambda^2 \sim -(0.2\Lambda)^2$. A similar exercise can be done with scalar bosons which may substantially enter these corrections. If this fine-tuning is motivated by the existence of new physics, the correction should not exceed the observed Higgs mass, therefore $\Lambda \sim \mathcal{O}(\mathrm{TeV})$, effectively reducing the cutoff scale and a sign that there may be new physics as close as the TeV scale, in reach of the LHC.

The Hierarchy problem is therefore an issue of naturalness [167]: It seems unnatural that such large amounts of unmotivated fine-tuning be needed to provide the Higgs with its observed mass, reasons for the non-proportionality of the Higgs mass to the cutoff scale are therefore the core of the SM Hierarchy problem.

1.2.8 Model generalness

The central role played by the S-matrix in QFT invites the question of the symmetry generators which commute with it, bringing single particle states to single particle states and bringing multi-particle states to a sum of single particle states. Poincaré group generators P_μ (for translations) and $M_{\mu\nu}$ (for Lorentz transformations) have been proven to be the only generators, along with internal symmetry group generators commuting with one another [168]. This however, is only the case based on some assumptions such as locality, causality, positivity of energy and finiteness of particles count. If those assumptions were to be weakened, another group would become the most general symmetry group of the S-matrix [169], giving rise to a more general model. S-matrix space-time degrees of freedom and internal symmetry degrees of freedom being factorisable, any type of new physics, which are required to explain aforementioned phenomena, may only emerge from new symmetries, not from any external new degrees of freedom.

1.3 Possible approaches for Beyond the Standard Model physics

The limitations displayed by the SM imply the existence of new physics, which may require a complete rework of the SM. For instance by inducing a composite Higgs in so-called technicolour models [170], therefore inducing elementary masses dynamically, solving the Higgs Hierarchy problem and creating new alleyways for DM and constraining neutrino mass acquisition mechanisms. Another solution would be the introduction of extra dimensions [171] which would imply the propagation of forces in more dimensions, explaining their different relative strengths. There is generally a great variety in the field of non-SM physics [172–174] and constraints on said models [11, 175, 176].

Overall the SM remains a highly effective description, its limitations may be overcome with extensions, some of which will be described here. In particular, two approaches can be used when describing BSM physics: the introduction of new symmetries analogous to the QFTs of the SM, often yielding a vast array of new physics and predictions or more minimal extensions, often focusing on solving a specific set of SM issues. Both alleyways have in common the introduction of new sets of particles and will be explored here. The key issue is the coupling and the mass of new physics, as they were not yet observed, the new particles must either be heavy enough not to have been produced (the focus of high-energy searches) or feebly interacting enough not to have been seen yet (the focus of high-intensity searches), this can be seen in Figure 1.12.

For experimental searches however, sensitivity channels are the most important output of a given theory and the ones which are particularly of interest in this thesis here are neutral decays such as $\gamma\gamma$ final states. As such, a particular focus in extracting the $\gamma\gamma$ decays of BSM candidates at energies up to $\sim 28\,\mathrm{GeV}$ will shape the coming section.

1.3.1 Supersymmetric expansions

Symmetric extensions of Yang-Mills theories have displayed incredible success in the SM, therefore further success may be expected by the use of further symmetric expansions. The how a popular such extra symmetry, *Supersymmetry* can yield neutral final states in the region of interest will be explored. Complements to Supersymmetry can be found in [177].

Any supersymmetry (SUSY) would have to be spontaneously broken as particle masses would otherwise be preserved, which does not match experimental observations [178, 179]. No sign of SUSY, minimal or otherwise has been observed however, not even at higher energy [179] which suggests a rethink of the way SUSY is viewed

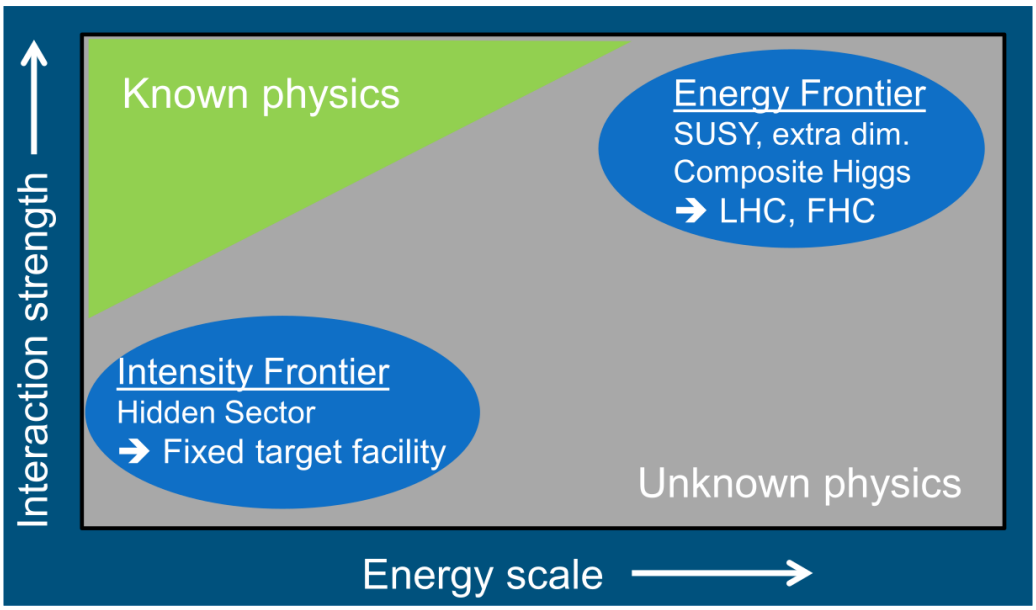

Figure 1.12: New physics must be either too heavy to have been produced or too weakly interacting to have been observed [104].

[104] as chiral and vector superfields may indeed be numerous and NGBs may emerge from symmetries being broken, analogous to the situation described in Section 1.1.3.3 and particularly in relation to the gravitino $\widetilde{g}$, the superpartner to the graviton which would mediate gravity [150, 180]. Indeed the massless gravitino $\widetilde{g}$ may acquires mass through the superhiggs mechanism [181] when SUSY is a local symmetry:

$$\widetilde{g}_\mu \rightarrow \widetilde{g}_\mu + \frac{i}{m_{\widetilde{g}_\mu}}\sqrt{\frac{2}{3}}\partial_\mu\psi, \qquad m_{\widetilde{g}} = \sqrt{\frac{8\pi}{3}}\frac{F}{\mathrm{M}_{\mathrm{Planck}}}. \tag{1.54}$$

The Majorana spin $\frac{3}{2}$ $\widetilde{g}$ has only $\pm\frac{3}{2}$ chirality states before becoming massive, its $\pm\frac{1}{2}$ chiralities are yielded by the goldstino G which therefore would imply that the on-shell amplitudes with chirality $\pm\frac{1}{2}$ gravitinos are asymptotically equivalent to amplitudes with corresponding external goldstinos.

Generically the supersymmetric chiral superfield Φ is known as the Goldstone supermultiplet [182] [104], whose component F_Φ must have non-zero vacuum-expectation-value and is thus responsible for SUSY spontaneous breaking:

$$\Psi = \phi + \sqrt{2}\theta\psi + F_\phi\theta\theta \tag{1.55}$$

This breaking induces a G and its superpartner the spin-0 component ϕ forming scalar S, pseudoscalar P sgoldstino $\widetilde{G}$. If SUSY becomes a local symmetry, the G vanishes but depending on how the model is built, scalar and pseudoscalar $\widetilde{G}$ remain massless at leading order $S \equiv \frac{1}{\sqrt{2}}(\phi + \phi^\dagger)$, $P \equiv \frac{1}{i\sqrt{2}}(\phi - \phi^\dagger)$ [183], with their masses being induced by higher-order processes which can in principle take any value depending on the model, making them a generic particle of a SUSY model.

At leading order in $\frac{1}{F}$, G couples to all fields through the Goldberger-Treiman formula [184]:

$$\mathcal{L} = \frac{1}{F}J^\mu_{\mathrm{SUSY}}\partial_\mu\psi, \tag{1.56}$$

J^μ_{SUSY} is here the supercurrent, while Equation 1.54 induces couplings of the gravitino to other inverse-SUSY violating parameter $\frac{1}{F}$ suppressed fields, this implies couplings of the gravitino mostly through the $\widetilde{G}$, its longitudinal chirality component for $\Lambda_{\mathrm{SUSY}} \sim \sqrt{F}$. Its effective interactions can be derived using spurion techniques [185]:

$$\frac{\mathrm{M}_\lambda}{F}\int d\theta^2 \Psi W^\alpha W_\alpha + h.c. \tag{1.57}$$

This yields SUSY violation in gaugino mass terms when the vev is introduced in Equation 1.55 which provides couplings of the $\widetilde{G}$ to gauge bosons, in particular to $\gamma\gamma$:

$$\mathcal{L}_{\widetilde{G}\to\gamma\gamma} = -\frac{1}{2\sqrt{2}}\frac{\mathrm{M}_{\gamma\gamma}}{F}SF^{\mu\nu}F_{\mu\nu} + \frac{1}{4\sqrt{2}}\frac{\mathrm{M}_{\gamma\gamma}}{F}P\epsilon^{\mu\nu\rho\sigma}F^{\mu\nu}F_{\mu\nu} \tag{1.58}$$

$F_{\mu\nu}$ can clearly be identified as the electromagnetic field tensor, with $M_{\gamma\gamma} = \mathrm{M}_1 + \sin^2\theta_\mathrm{W} + \mathrm{M}_2 + \cos^2\theta_\mathrm{W}$, M_1 and M_2 being the SM $U(1)_\mathrm{Y}$ and $SU(2)_\mathrm{W}$ gaugino SUSY breaking mass terms.

Sgoldstinos with $m_{\widetilde{G}} < 1.2\,\mathrm{GeV}$ may also decay into π^0 pairs [186] leading to a decay width of:

$$\Gamma_{\widetilde{G}\to\pi^0\pi^0} \simeq \frac{\alpha_s^2(M_3)}{\beta^2(\alpha_s(M_3))}\cdot\frac{\pi m_{\widetilde{G}}^3 M_3^2}{4F^2}\cdot\left(1-\frac{\beta(\alpha_s(M_3))}{\alpha_s(M_3)}\cdot\frac{9}{4\pi}\cdot\frac{B_0(m_u+m_d)A_Q}{m_{\widetilde{G}}M_3}\right)^2\cdot\sqrt{1-\frac{4m_{\pi^0}^2}{m_{\widetilde{G}}^2}} \tag{1.59}$$

where $\beta(\alpha_s)$ is the QCD beta function, M_3 the mass of the $\widetilde{g}$, $\alpha_S(M_3)$ is the strong coupling evaluated at the scale of M_3 and B_0 defined by the ratio of kaon and quark masses by $B_0 = \frac{M_K^2}{m_d+m_s}$ [187].

SUSY models are however incredibly varied and may manifest also in the cases described below.

1.3.2 Hidden Sectors

As extra symmetries, be they SUSY or others have yet to be found if they exist, more minimal extensions of the SM have been considered. Among the most generic ones are so-called Dark or Hidden Sectors (HS). There, dark matter does not couple directly to the SM but does so through "portals", renormalisable interactions with small dimensionless coupling constants or through Λ^{-n} suppressed higher-dimensional operators. Generally however, 3 types of portals can be identified depending on the mass dimension of the SM singlet operator: Scalar, Neutrino and Vector portals. These will be examined in the scope of interest, a more complete review of dark sectors may be found in [104].

1.3.2.1 Scalar portals

The discovery of the Higgs boson [4] [3] at LHC definitely confirms the existence of scalar particles in nature. Strong motivations exist for extra scalars however as possible solutions for baryonic asymmetry (see Section 1.2.3) [188], dark matter candidates (see Section 1.2.2) [189] [190] or answers to the hierarchy problem (Section 1.2.7) [191]. Extra scalars may emerge as extra singlets under the SM gauge group, as Pseudo Nambu-Goldstone bosons which may include Axion-Like-Particles. Each of these three options will be discussed.

1.3.2.2 Extra SM gauge singlet

BSM scalars S_i may exist in their most clear form if they are singlets under SM gauge transformations. They would generally couple to the Higgs field $|\Psi|^2$ through the Lagrangian extension:

$$\mathcal{L}_{\text{Scalar-portal}} = \left(\lambda_i S_i^2 + g_i S_i\right)(\Psi^\dagger\Psi). \tag{1.60}$$

The general effective Lagrangian for such an extension would emerge as:

$$\mathcal{L}_{\text{Scalar}} = \frac{1}{2}\partial_\mu S\partial^\mu S + \left(\alpha_1 S + \alpha S^2\right)(H^\dagger H) + \lambda_2 S^2 + \lambda_3 S^3 + \lambda_4 S^4, \tag{1.61}$$

where portal couplings are denoted λ_i, $i \in \{2,3,4\}$ whereas α_1 and α are the portal couplings to the Higgs H. As H^2 is capable of mediating leading order interactions between the SM and HS, being the lowest-dimension-gauge and Lorentz singlet that may emerge from SM fields, is it quite possible for such a portal mediator to exist. The interactions of Equation 1.61 are renormalisable which removes the issue of high-scale emergence of the Higgs-scalar interaction in addition to having the potential of playing a role in dark sector physics while connecting the HS to the SM. A notable example of HS are the so-called Hidden Valleys [192] [193] involving elaborate dark sector physic which may include extra dark gauge groups, composite QCD-like dark matter [194], to the SM. The sensitivity to those sectors may involve a "dark pion" (see Section 1.3.2.3), which, being uncharged under the extra DM symmetry may decay into SM particles and add an extra layer of sensitivity to the model.

The scalar mediator phenomenology is highly dependent on whether $\alpha_1 \neq 0$ in Equation 1.61. If so and if a non-zero vacuum expectation value $\alpha_1 = 4\alpha\langle S\rangle$ is present for S, a linear mixing is induced between S and H. The mixing angle $\theta = \frac{\alpha_1 v}{m_h^2}$ determines the decay length of S in an experiment. In the absence of other light states, S should decay into SM particles, for instance into a pair of photons through a particle loop as shown in Figure 1.13. It thus also couples to SM fermions.

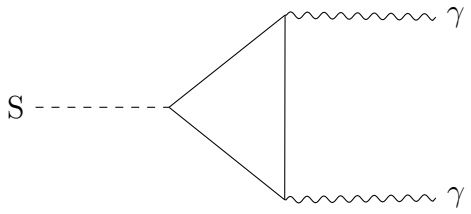

Figure 1.13: Example Scalar portal decay to 2 photons.

In the case where S has no vacuum expectation value and cannot mix with H ($\alpha_1 = 0$), the scalar may mediate exotic decays of the Higgs into BSM states. At lower energies (under $m_{\mathrm{H}} \sim 125\,\mathrm{GeV}$) light BSM states mix with the SM and thus inherit some level of SM coupling [195] which allow for $\gamma\gamma$ final states analogous to previously [196].

1.3.2.3 Pseudo Nambu-Goldstone bosons

In models that include a QCD-like dark sector which contain a broken symmetry creating dark pions analogous to the light ones of Section 1.1.4. In this frame, the theory may contain extra dark flavours of Dirac fermions ψ_i transforming under some SU(N) symmetry ($N > 1$) but singlets under SM symmetries. This can give rise to N EW Dirac fermion doublet $(Q_u Q_d)_i^T$ with Y= $\frac{1}{2}$ which transform under SU(N) thus inducing the Lagrangian:

$$\mathcal{L} = \overline{Q}_L \mathbf{Y} \psi_R H - \overline{Q}_R \widetilde{\mathbf{Y}} \psi_L H - \overline{Q}_L \mathbf{M} Q_R - \overline{\psi}_L \boldsymbol{\omega} \psi_R - h.c. \tag{1.62}$$

where $\mathbf{Y}$, $\widetilde{\mathbf{Y}}$, $\mathbf{M}$ and $\boldsymbol{\omega}$ are $N \times N$ coupling and mass matrices in flavour, space respectively. Similarly to the SM QCD, the chiral SU(N)×SU(N) symmetry is spontaneously broken which results in $N^2 - 1$ PNGB dark pions ϕ. They may decay in a variety of fashions such as through tree-level Higgs exchanges, in Flavour-Changing-Neutral-Currents (FNCN) or, most relevant here, into $\gamma\gamma$, somewhat analogous to π^0 with a width:

$$\Gamma_{\phi\to\gamma\gamma} = \frac{s_\theta \alpha^2 m_\phi^3}{256\pi^3 v^3} \left| \sum_{i\in \text{fermions}} 2N_c^i Q_i^2 x_i \left(1 + (1-x_i) f(x_i)^2\right) \left(2 + 3x_W + 3x_W(2-x_W) f(x_W)^2\right) \right|^2, \tag{1.63}$$

where $x_i = \frac{4m_i}{m_\phi}$, $f(x) = \arcsin \frac{1}{\sqrt{(x)}}$ if $x \geq 1$ and $f(x) = \frac{\pi}{2} + \frac{i}{2} \log \frac{1+\sqrt{1-x}}{1-\sqrt{1-x}}$ if $x < 1$; s_θ being the sine of the mixing angle between the ϕ and the Higgs, v being the vev of the ϕ.

More generally, these models offer a rich phenomenology, more details and precisions may be found in [104, 195–197].

1.3.2.4 Axion-Like-Particles

The Strong CP problem of Section 1.2.5 can be solved in different ways such as a soft P/CP breaking, where these symmetries imply $\overline{\theta} = 0$ in the UV [198–200] or with infrared dynamics of QCD [201] [202]. These solutions are however difficult to test experimentally, limiting their appeal.

Thus emerges the so-called axion solution [203] [204]. In this scenario a new scalar field $a(x)$ is introduced through the Chern-Simons Lagrangian:

$$\mathcal{L}_{\text{QCD ax}} = \frac{\theta}{32\pi^2} \mathrm{Tr}(G_{\mu\nu} \widetilde{G}^{\mu\nu}), \tag{1.64}$$

where G is the gluon field tensor and $\widetilde{G}^{\mu\nu} = \varepsilon^{\alpha\beta\mu\nu} G_{\alpha\beta}$ is the dual whereas the trace is running over the SU(3) colour indices. The solution to the Strong CP Problem relies on the introduction of a U(1) symmetry

which affects some quarks, inducing a chiral anomaly $\mathcal{C}$. The symmetry breaks, inducing a NGB ϕ with vacuum expectation value $\frac{f_a}{\sqrt{2}}$, f_a being the axion decay constant. Through an anomalous chiral rotation of $\frac{\phi}{f_a}$ which rotates left- and right-handed components of the fermion oppositely, its measure of the path integral is modified which leads to an action change:

$$S \to S + \int \frac{\mathcal{C}}{32\pi^2}\frac{\phi}{f_a}\mathrm{Tr}(G_{\mu\nu}\widetilde{G}^{\mu\nu})\mathrm{d}^4x.$$

Because of the shift symmetry of ϕ, S only contains terms of $\partial\phi$ and ϕ may be shifted by any constant, absorbing θ by redefining the field. This effectively cleans up the Strong CP Problem.

The axion couples to electromagnetism:

$$\mathcal{L}_{\text{int}} = -\frac{g_{\phi\gamma}}{4}\phi F_{\mu\nu}\widetilde{F}^{\mu\nu},\ g_{\phi\gamma} = \frac{\alpha_{\text{EM}}}{2\pi f_a}\left(\mathcal{C} - \mathcal{C}\frac{2}{3}\frac{4+\frac{\mathrm{m}_u}{\mathrm{m}_d}}{1+\frac{\mathrm{m}_u}{\mathrm{m}_d}}\right) \tag{1.65}$$

$\mathcal{C}$ being the $\mathrm{U}(1)_{\text{EM}}$ anomaly. The axion as such decays into $\gamma\gamma$ through the electromagnetic interaction with a width:

$$\Gamma_{\phi\to\gamma\gamma} = \frac{g_{\phi\gamma}m_\phi}{64\pi}. \tag{1.66}$$

This solution is called the Peccei-Quinn axion [203], which is now excluded in its simplest form [205]. Other axion solutions exist, particularly the *Kim-Shifman-Vainshtein-Zakharov* (KSVZ) [206, 207] which function by mediating the anomaly using extra heavy quarks charged under Peccei-Quinn, and the *Dine-Fischler-Srednicki--Zhitnitsky* (DFSZ) which mediate it through SM quarks which would be charged under Peccei-Quinn [208, 209].

While QCD-axions are PNGB, which by definition emerge from QCD anomalies, there is no intrinsic requirement for the broken symmetry creating the PNGB to be a QCD anomaly. The explicit symmetry breaking would then provide the PNGB its mass. As long as the PNGB's mass is significantly larger than that of the QCD-axion, it may couple to QCD without displacing the axion. Since those particles would emerge similarly to QCD-axions without solving the Strong CP problem, they are called *Axion-Like-Particles* (ALPs).

ALPs may emerge according to the theory described in Section 1.3.2.2 through an extended Higgs sector, or perhaps in a so-called *axiverse* where ALPs span up to 30 orders of magnitude in mass [210]. Such an axiverse may also be considered as derived from a dark-pion like ALP which is analogous to that of Section 1.3.2.3.

ALPs are quite significant in the context of Dark Matter as they could mediate interactions between SM and HS, if the ALP is a mediator in the HS while weakly coupling to the SM with $m_{\text{ALP}} < 1\,\text{GeV}$. It would be capable of matching cosmological constraints [104, 211] without being excluded by LHC searches [212, 213].

Interactions between an ALP a and the SM can be described through the Lagrangian:

$$\mathcal{L}_{\text{ALP-SM}} = \sum_f \frac{C_{af}}{2f_a}\overline{f}\gamma^\mu\gamma^5 f\partial_\mu a - \sum_i \frac{\alpha_i}{8\pi}\frac{C_{ai}}{f_a}F^{b(i)}_{\mu\nu}\widetilde{F}^{(i)\mu\nu}_b a, \tag{1.67}$$

where f corresponds to the SM fermions (quarks q, charged leptons l, neutrinos ν) and $i = \{Y, 2, 3\}$. a couples to gauge fields with $g_a i \equiv \frac{\alpha_i}{2\pi}\frac{C_{ai}}{f_a}$. The extra ALP mass term is assumed to be large enough to dominate and not place any competition between the ALP and the QCD-axion.

ALPs may be produced in three ways in beam dumps: coherent scattering where a particle scatters elastically on a target nucleus, incoherent scattering where individual quarks or gluons from the beam and/or target scatter off-one another and non-perturbative processes through the decay of hadronic final states. The most significant example of coherent scattering is the so-called Primakoff scattering process [214] where ALP photon couplings in an analogous way to π^0 (a PNGB), would allow it to be formed, as can be seen in Figure 1.14.

Coherent scattering cross section scales with Z^2 and is expected to be significant compared to other possible production mechanisms [215–217]. Incoherent scattering, while mostly sub-dominant, is expected to become important when the photon virtuality of [215, 217] defined by $Q_i^2 = \frac{q_{\perp,i}^2 + x_i^2 m_i^2}{1-x_i}$ (m_i being the mass of the impinged nucleus, x_i and $q_\perp$ the longitudinal and transverse momentum of the photon respectively), becomes large, and occur by standard Drell-Yan processes [218] as in Figure 1.14. Hypothesised perturbative processes would likely have small cross sections and are neglected here but are explored in [219].

ALP decays may be modelled by re-using the Lagrangian of Equation 1.65. The width of an ALP decaying

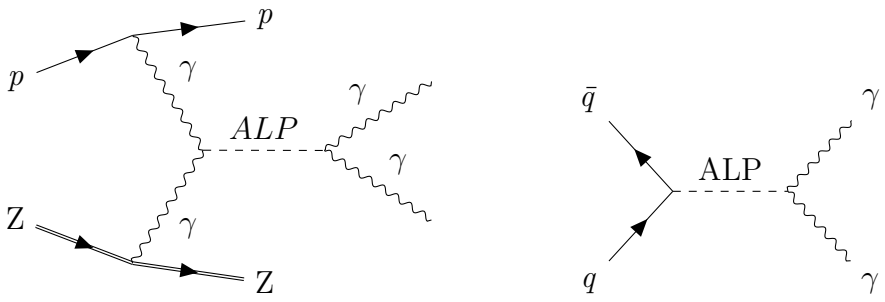

Figure 1.14: Primakoff production and subsequent decay of an ALP in a proton on nuclear scattering (left) and Drell-Yan production and subsequent decay of an ALPs in incoherent scattering (right).

into two SM gauge bosons is then:

$$\Gamma_{a\to g_b g_b} = \frac{d(G) g_{ai}^2 m_a^3}{64\pi}, \tag{1.68}$$

with $d(G)$ the group generator count. The gauge bosons in question could of course be $\gamma\gamma$ but ALPs may also couple to gg or to SM fermions [104].

1.3.2.5 Neutrino portal

The neutrino portal is an extremely well-motivated physics solution [104, 220, 221], particularly from the fundamental question of the origin of neutrino masses discussed in Section 1.2.4 and by questions left in suspense by anomalies in short baseline neutrino experiments [222–225]. It would manifest through:

$$\mathcal{L}_{\text{Portal neutrino}} = F_{\alpha I}\left(\overline{L}_\alpha \cdot \widetilde{\Psi}\right) N_I + h.c., \tag{1.69}$$

$F_{\alpha I}$ is the Yukawa coupling (C.f. Section 1.1.3.3), L_α is the left lepton doublet with α being the SM lepton flavour, Φ is the Higgs doublet, and $\tilde{\Psi}_a = \epsilon_{ab}\Psi_b$ with only the right-handed N_I coupling to the SM.

The neutrino portal particle is commonly called a *Heavy Neutral Lepton* (HNL), and may acquire mass unrelated to the Yukawa coupling through, for instance, explaining the lack of right-handed neutrinos in the SM by a (here type-I) seesaw mechanism. The Lagrangian inducing it being an extension of Equation 1.69:

$$\mathcal{L}_{HNL_{\text{seesaw}}} = i\bar{N}_I \partial\!\!\!/ N_I - \left(F_{\alpha I}\bar{L}_\alpha \bar{N}_I \tilde{\psi} + \frac{M_I}{2}\bar{N}_I^C N_I + h.c.\right). \tag{1.70}$$

Here, N_I is a Majorana particle (see Section 1.2.4) and a singlet under all SM gauge symmetry, thus being a form of *sterile neutrino*. In the Higgs phase $(\bar{L}_\alpha \widetilde{\Psi}) = \bar{\nu}_\alpha$. This implies that N_I mixes with ν_α, as such Lagrangian 1.70 is not aligned with the N_I mass eigenstates, thus the mass matrix

$$\mathcal{M}_{\nu,N} = \begin{pmatrix} 0 & m_{\text{D}} \\ m_{\text{D}}^T & M_I \end{pmatrix},$$

containing the Dirac $3\times\mathcal{N}$ mass matrix m_{D} and the Majorana $\mathcal{N}\times\mathcal{N}$ mass matrix M_I. It can be diagonalised to obtain the mass eigenstates. In the limit where $m_{\text{D}} \ll M_I$, a 5-dimension *Weinberg Operator* [226] emerges:

$$\frac{c_{\alpha\beta v^2}}{\Lambda} \equiv -\sum_I (m_{\text{D}})_{\alpha I}\frac{1}{M_I}(m_{\text{D}})_{\beta I}. \tag{1.71}$$

The seesaw mechanism takes advantage of the difference between m_D and M_I. Through mass matrix rotation, the SM neutrino masses (3 eigenstates of the Weinberg operator matrix of Equation 1.71) become very small compared to M_I, allowing the HNL to be much heavier. SM neutrino masses have only been measured down to 0.8 eV [142] or estimated to be lower than 0.54 eV [108] down to lower than 0.082 eV [227] from different cosmology models.

HNLs couple via Yukawa to SM neutrinos. These couplings are related to their mass eigenstates, but as several HNL flavours (for $\mathcal{N}_{\text{flavour}} \leq 2$) can cancel each other's contribution, no strict limit can be placed on

the coupling based on their mass [104]. Their number should be $\mathcal{N}_{\text{flavour}} \leq 2$ to explain the mass differences for active neutrinos [11] [104]. These couplings, identical to active neutrinos are explicit in the Lagrangian:

$$\mathcal{L}_{\text{HNL couplings}} = \frac{g}{2\sqrt{2}} W_\mu^+ \overline{N^c} \sum_\alpha U_\alpha^* \gamma^\mu (1-\gamma^5) \ell_\alpha^- + \frac{g}{4\cos\theta_W} Z_\mu \overline{N^c} \sum_\alpha U_\alpha^* \gamma^\mu (1-\gamma^5) \nu_\alpha + h.c, \tag{1.72}$$

with l_α the charged SM leptons. The SM couplings of the HNLs are heavily suppressed by the small mixing angles $U_\alpha = M_\alpha^D M_N^{-1}$. This, however, allows HNLs to be produced in meson decays [228], particularly weak decaying-hadrons (thus the lightest hadron of each flavour, B, D, K or even π) and to decay typically either through a hidden charged current into $\ell^\pm \pi^\mp$ or through a hidden neutral current into $\nu\pi^0$ (π^0 may be substituted for any other pseudo scalar neutral meson). The π^0 would then promptly decay into $\gamma\gamma$. The width of such neutral semileptonic decays is given by:

$$\Gamma(N \to \nu_\alpha h_P^0) = \frac{G_F^2 f_h^2 M_N^3}{32\pi} |U_\alpha|^2 \left[1 - \left(\frac{m_h}{m_N}\right)^2\right]^2. \tag{1.73}$$

HNLs are a powerful tool for explaining baryonic asymmetry (Section 1.2.3) [133, 229–231], neutrino oscillations (Section 1.2.4) [104, 231, 232] or Dark Matter (Section 1.2.2) [104, 231, 233].

1.3.2.6 Vector portal

Portals emerging from extra U(1) symmetric fields which kinetically mix with the SM U(1) photon field to give rise to extra vector "dark" mediators dubbed *Dark Photons* (DP). They emerge from two U(1) group theory Lagrangians:

$$\mathcal{L}_{\text{kinetic}} = \mathcal{L}_{\psi,A} + \mathcal{L}_{\chi,A'} - \frac{\varepsilon}{2} F^{\mu\nu} F'_{\mu\nu} + \frac{1}{2} m_{A'}^2 (A'_\mu)^2. \tag{1.74}$$

where $\mathcal{L}_{\psi,A}$ and $\mathcal{L}_{\chi,A'}$ are the standard and extra QED-like Lagrangians, which can be found in Equation 1.47. $\varepsilon \ll 1$ is a dimensionless mixing parameter which is assumed to be small and A' is the DP field. The DP may couple to the SM photon through the Lagrangian:

$$\mathcal{L}_{\text{DP}\gamma} = -\frac{e\varepsilon}{\sqrt{1-\varepsilon^2}} J_\mu A'^\mu \sim -e\varepsilon J_\mu A'^\mu. \tag{1.75}$$

It may acquire mass either through spontaneous breaking of the gauge symmetry, which locks the mixing angle and creates a dark Higgs bosons, or through the so-called Stueckelberg process [234] with Lagrangian:

$$\mathcal{L}_{\text{Stueckelberg}} = -\frac{1}{2} M_a^2 A_{a\mu} A_a^\mu - \frac{1}{2} M_b^2 A_{b\mu} A_b^\mu - M_a M_b A_{a\mu} A_b^\mu. \tag{1.76}$$

The DP phenomenology mainly derives from its interaction term:

$$\mathcal{L}_{\text{DP int}} = -\varepsilon e J^\mu A'_\mu. \tag{1.77}$$

As a result, the DP couples to SM particles as the SM EM current J^μ. The DP can thus be produced through meson decays, but also in (quasi)elastic scattering processes, bremsstrahlung or Drell-Yan processes [218] and gluon excitation [235] processes if m_{DP} is large. The DP may decay into lepton pairs, a particularly clean channel, or into quark pairs [236], particularly into sets of π including π^0 which would then decay into $\gamma\gamma$. The width of the process is:

$$\Gamma_{\text{DP}\to\text{quarks}} = \frac{1}{3}\alpha\epsilon^2 m_{DP} \sqrt{1 - \frac{4m_\mu^2}{m_{DP}}} \left(1 + \frac{2m_\mu^2}{m_V^2}\right) R(S = m_{DP}^2) \tag{1.78}$$

DPs are relevant in the area of DM (Section 1.2.2) [11, 104, 237, 238], and is a favoured solution to the μ $g-2$ problem [1] if it were confirmed [239].

1.3.2.7 Dark axion portal

An interesting case arises when the DP of Section 1.3.2.6 and an axion of 1.3.2.4 coexist: rather than simply obtaining new vertices as a product of the two portals, entirely new couplings emerge as new fermions are charged under both the DP's $\mathrm{U}(1)_{\mathrm{Dark}}$ and the axion's $\mathrm{U}(1)_{\mathrm{PQ}}$ (part of KSVZ axion models [240] [206]). This implies a direct "real" coupling not induced by any form of mixing to the vector portal [241]. The Lagrangian for the emerging dark axion portal (DAP) reads as:

$$\mathcal{L}_{\mathrm{DAP}} = \frac{g_{\phi\gamma A'}}{2} a F_{\mu\nu} \widetilde{F}'^{\mu\nu} + \frac{g_{aA'A'}}{4} a F'_{\mu\nu} \widetilde{F}'^{\mu\nu}, \tag{1.79}$$

with $F_{\mu\nu}$ and $F'_{\mu\nu}$ the photon and dark photon field strength tensors, respectively, and a the ALP (which may be a QCD axion). The implication is that the ALP may couple indeed to two photons as normally the case (Section 1.3.2.4), but also to a DP and a photon or to two DP through loop diagrams analogous to that shown in Figure 1.13. A key characteristic is the carrying of both $\mathrm{U}(1)_{\mathrm{PQ}}$ and $\mathrm{U}(1)_{\mathrm{Dark}}$ charges by the loop fermions. The DP, identically to the case of Section 1.3.2.6, may mix kinetically to the SM photon. The $g_{\phi\gamma A'}$ mixing implies the existence of a possible decay of the DP to an ALP and a photon through the DAP with the width.

$$\Gamma(\mathrm{DP} \to \gamma a) = \frac{g_{a\gamma A'}}{96\pi} m_{\mathrm{DP}}^3 \left(1 - \frac{m_a^2}{m_\gamma^2}\right)^3 \tag{1.80}$$

DAP decays may be induced through $\pi^0, \eta \to a\gamma\mathrm{DP}$ decays where the visible photon may be detected in a beam dump setup [242].

1.3.2.8 Leptophobic mediators

Leptophobic mediators are hypothetical particles that couple to quarks but not leptons. They are particularly compelling candidates in the search for physics beyond the Standard Model. Their lack of coupling to leptons allows them to evade many existing experimental constraints, which often rely on leptonic final states, thereby opening regions of parameter space that remain largely unexplored. These mediators naturally arise in various dark matter models where interactions occur primarily with hadrons rather than electrons or photons. Ongoing experiments are uniquely suited to probe such particles through hadronic scattering signatures [243], offering a complementary approach to traditional searches. By enabling the detection of weakly coupled, hadron-interacting particles, studies of leptophobic mediators provide valuable insights into the structure of hidden sectors and the possible nature of dark matter. Experimental constraints on those leptophobic mediators are relatively weak [244, 245] and are thus within improvement range (see Section 2.2.2 [245]). Their interactions are shown in Figure 1.15 and have Lagrangian:

$$\mathcal{L}_{\mathrm{leptophob}} = -g_B V^\mu J_\mu^B + g_\chi V^\mu (\partial_\mu \chi^\dagger \chi - \chi^\dagger \partial_\mu \chi), \quad J_\mu^B = \frac{1}{3} \sum_q \bar{q} \gamma_\mu q \tag{1.81}$$

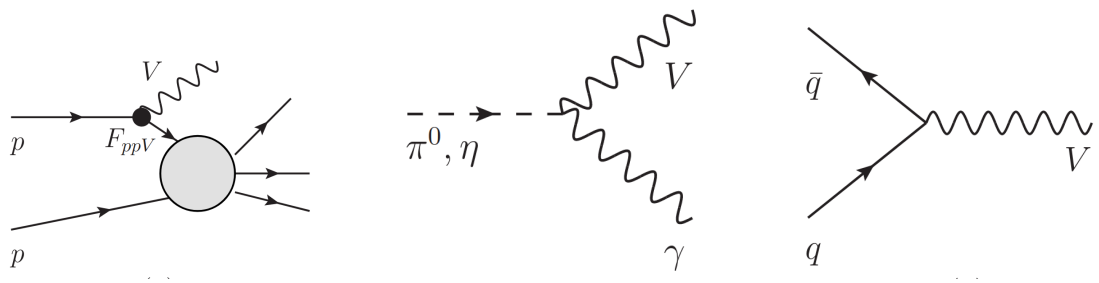

Figure 1.15: Production of leptophobic mediators V through proton Bremsstrahlung (left), through decays of flavourless mesons (centre) and in Drell-Yan processes (right) [243].

1.3.2.9 Conclusion

As shown above, a great variety of BSM physics may exist with highly attractive experimental photon-signatures. Such new physics may allow the explanation of many limitations of our understanding of nature expressed in Section 1.2. The means to observe such signatures will be the focus of the next chapter by the examination of two modern experiments which are dedicated to advancing our knowledge of nature: The Scattering Neutrino Detector at the Large Hadron Collider (SND@LHC) and the Search for Hidden Particles (SHiP).

Chapter 2

Searching for hidden particles and neutrinos at SND@LHC and SHiP

In this chapter the experimental modes of production and observation of collider neutrino and high intensity searches for BSM particle will be exposed. In particular the process of acceleration and collisions as well as the two flagship experiments relevant to this work: SND@LHC and SHiP.

2.1 The CERN accelerator complex

Particle accelerators are nowadays used to obtain the highest energies in a controlled setting. The are the only known mean to achieve energies of several hundreds of GeV, at high intensity and with high concentration. The production of new physics requires some combination of high energies and high intensities, making accelerators ideal in this pursuit. Simultaneously, the study of nuclear effects in partons at small-x necessitates very asymmetric collisions, hence large energies. These also allow for the study of high energy neutrinos with large fluxes. A contextualisation of particle acceleration is provided in Appendix A.

The CERN Accelerator Complex houses some of the world's largest and highest energy accelerators. It makes use of linear accelerators and mostly synchrotons as shown in Figure 2.1 used to accelerate a variety of particles. Protons are the most popular particle for acceleration due to its mass and abundance. The operation of the largest accelerator, the LHC, is divided into Runs which are numbered and interleaved by long shutdowns (LS). At the time of writing, the LHC is operating in Run 3 until 2026, it will be followed by LS3 which should last 3 and a half years.

2.1.1 Particle collisions

The key reason why particles are made to collide with one another is the direct result of Einstein's famous equation:

$$E^2 = m^2c^4 + p^2c^2, \tag{2.1}$$

where E is the total particle energy, m is the particle mass, p the particle momentum in the given frame of reference and c the speed of light in vacuum (which is otherwise taken as equal to 1). The direct consequence of this equation is that mass and momentum are but a particular manifestation of energy, as such, momentum, through energy conservation, may be converted into mass, enabling the creation of heavier particles with higher energy particle beams. The way to maximize this energy is to utilise same energy particle beams and run one into another to allow for collisions with a centre of mass energy:

$$E_{\text{Centre of Mass}} = E_1 + E_2 = 2E_{\text{beam}}, \tag{2.2}$$

where $E_1 = E_2$ are the beam energies. The LHC at CERN is the most powerful contemporary particle collider, designed to reach up to 7 TeV proton beams, allowing it to effectively probe the right hand side of

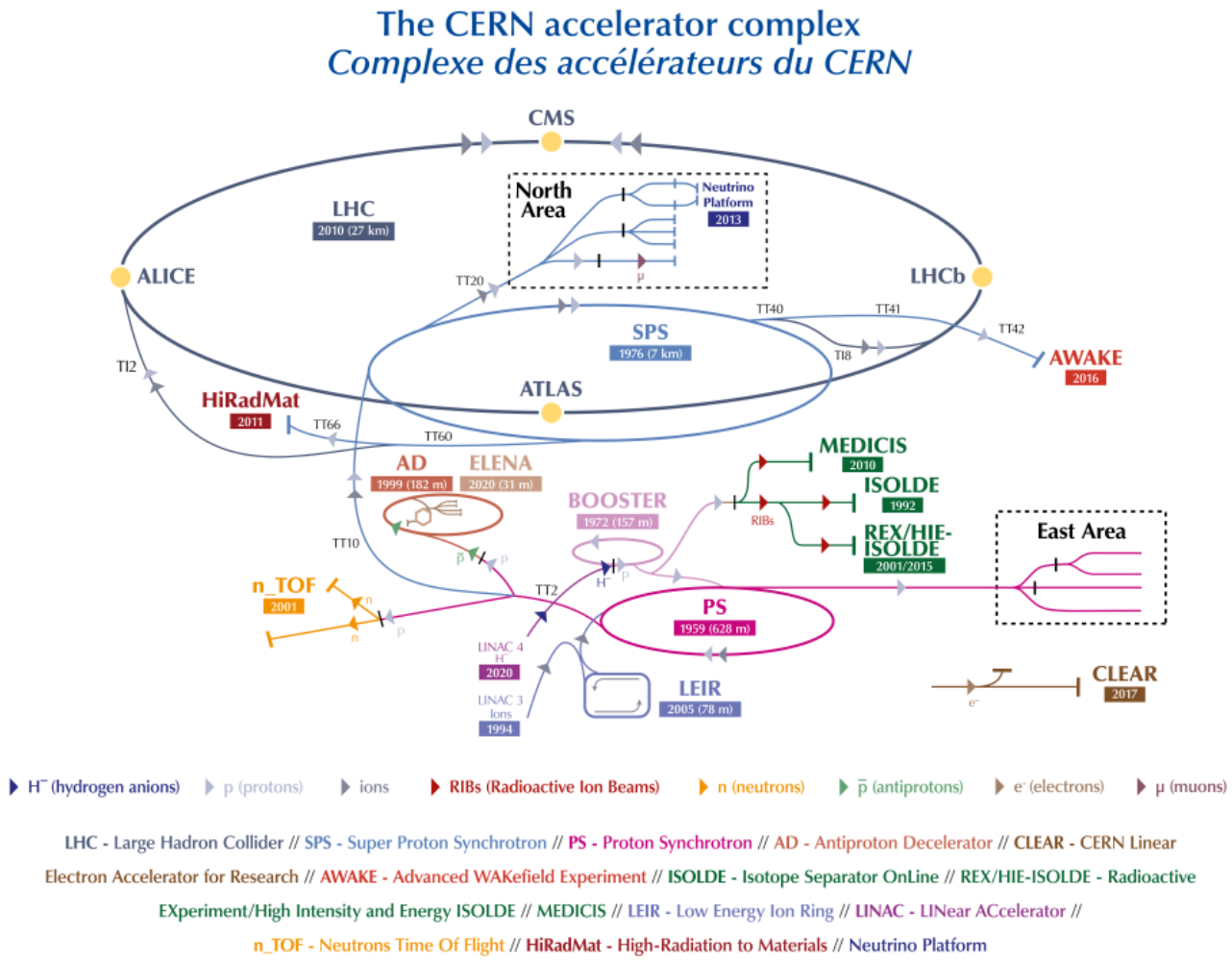

Figure 2.1: The CERN accelerator complex. The proton beam begins in a hydrogen bottle before being accelerated in the LINAC4 previous to them entering the Booster, being further accelerated in the Proton Synchrotron (PS) and entering the most relevant accelerators for this work: the Super Proton Synchrotron (SPS) and the Large Hadron Collider (LHC) [246].

Figure 1.12. LHC interactions are dominated by gluon-gluon fusion although certain Drell-Yann processes also occur, both processes are shown in Figure 2.2 [247].

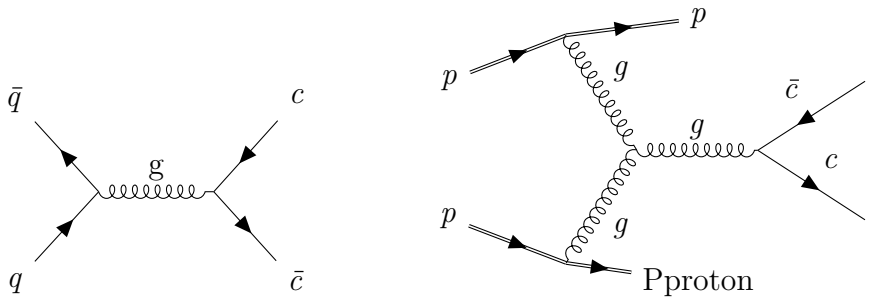

Figure 2.2: Drell-Yan production of a charm quark pair preferred at the Tevatron (left). Gluon-gluon fusion production of charm quark pairs preferred at the LHC (right).

The expected number of collisions is determined through a variable called *Luminosity*, measured in b^{-1}, $\mathcal{L}$ which is an expression of the number of expected collisions:

$$N_{\text{event}} = \mathcal{L}\sigma_{\text{FS}}, \tag{2.3}$$

where σ_{FS} is the cross section of the final state. $\mathcal{L}$ is in the case of LHC determined by:

$$\mathcal{L} = \frac{N_b^2 n_b f_{\text{rev}} \gamma_r}{4\pi\epsilon_n \beta^*} F, \tag{2.4}$$

where N_b is the particle count per bunch, n_b the number of bunches per beam, f_{rev} the revolution frequency of the beam around the ring, γ_r the beam's relativistic gamma factor, ϵ_n is the area occupied by the beam in position and momentum space known as *emittance* [248] and β^* is the beam's amplitude function.

Four Large Experiments operate at the LHC: A Toroidal LHC Apparatus (ATLAS) [249], the Compact Muon Solenoid (CMS) [250], A Large Ion Collider Experiment (ALICE) [251] and the Large Hadron Collider beauty (LHCb) [252] whose positions in the CERN accelerator complex are shown on Figure 2.1. Each of them take place at an interaction point where the bunches forming the particle beam collide and produce a vast variety of particles which are observed and recorded by the 4 detectors. Particles fly at every conceivable angle from a centre of mass frame. The longitudinal momentum of the colliding parton-parton system is given by $(x_1 - x_2)E_p$, particles emerging from a collision are boosted in the beam direction which define *rapidity* $y = \frac{1}{2}\ln\frac{E+p_z}{E-p_z}$, where E is the outgoing particle energy projected on the z-axis and p_z is the corresponding particle momentum. Rapidity has the convenient property that it is invariant under Lorentz boosts and the z-axis. A practical approximation is the assumption $p_z \sim E\cos\theta$ with θ the particle polar angle with respect to the z-axis, this leads to pseudorapidity η, visualised in Figure 2.3 and defined by:

$$\eta = -\ln\tan\frac{\theta}{2} \tag{2.5}$$

Large amounts of neutrinos are produced in these collisions, a large majority of which remain undetected as a result of their small interaction cross-section. Dedicated detectors are however capable of observing them. This is the primary goal of SND@LHC.

2.2 The Scattering neutrino detector at the LHC

2.2.1 Forward neutrino production at colliders

Production of neutrinos at the LHC emerges mainly from prompt W, Z^0 leptonic decays and beauty and charm decays as well as subsequent decays of kaons and pions. They have a broad energy spectrum that extends well into the TeV range which is underexplored in experimental neutrino measurements (Figure 1.11). Collider neutrinos have been considered for physics studies for over 30 years [254–256] but it is only somewhat recently

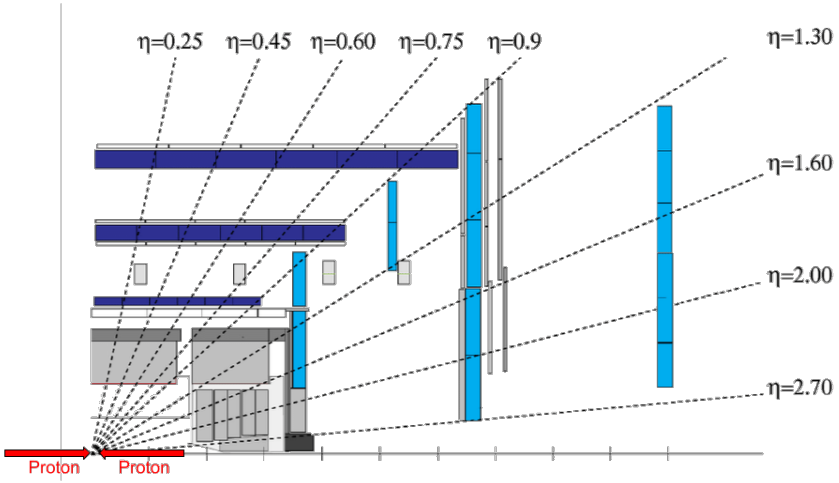

Figure 2.3: Proton-collision representation of the ATLAS experiment at the CERN LHC. η is the pseudo rapidity [253].

that their physics potential was truly made clear [257, 258] as they allow for a controlled flux of high energy neutrinos. The key characteristic of neutrino fluxes at the LHC is their pseudo-rapidity dependence:

- For $4 < \eta < 5$, neutrinos are mostly produced in leptonic decays of W bosons with a roughly even flavour distribution due to lepton universality [259].
- For $6.5 < \eta < 9.5$, neutrinos mostly emerge from c and b decays with the rarely observed ν_τ [260] [261] representing $\sim 5\%$.

As a direct consequence, collider neutrinos cannot only serve to determine the ν interaction cross section in the $\mathcal{O}(100\,\text{GeV}) - \text{TeV}$ range but can also be used to probe heavy-flavour physics in the high-η range: the forward region [262]. LHC detectors are typically not well-instrumented in this range as shown in Figure 2.3. This can be used to constrain the very loosely known gluon PDF in the very-small x region (see Section 1.1.4) through prompt charm production in pp collisions [263] due to the asymmetrical collision implying a low gluon x. The strange sea quark contribution may also be studied through W-mediated neutrino interactions within the detector volume. This contribution is unique to neutrinos as they may only interact weakly, not electromagnetically unlike e.g. electrons at HERA [95, 264, 265]. The charm may therefore be produced and its large mass implies a very short lifetime comparable to that of the τ lepton which is produced in ν_τ interactions. This constitutes an important proof of concept in its observation. In addition, the measurement of the underlying flux of ν_τ enables lepton flavour universality tests through the determination of the lepton flavour ratios $\frac{\nu_e}{\nu_\mu}$ and $\frac{\nu_e}{\nu_\tau}$. These are only sensitive to the source quark hadronisation fraction provided all three neutrino flavours can be identified.

2.2.2 Experiment and detector system

The goals of observing collider neutrinos, constraining the gluon and strange PDFs, the charm hadronisation function and the F_1, F_2 and F_3 structure functions as well as BSM physics searches are pursued by the Scattering Neutrino Detector at the LHC (SND@LHC) experiment [266] [267]. The experiment is located in the $7.2 < \eta < 8.6$ range, 480 m away from the ATLAS interaction point within the TI18 access tunnel and is expected to collect data from $250\,\text{fb}^{-1}$ of pp collisions between 2022 and 2025, providing it with particular sensitivity to charm quark neutrino decays as shown in Figure 2.4.

As a result, around 90% of ν_e in SND are produced by charm quark decays (as pions, $K^\pm$ and K_S^0 seldom decay into ν_e due to helicity and isospin suppression) whereas ν_τ are almost exclusively produced by D_s decays

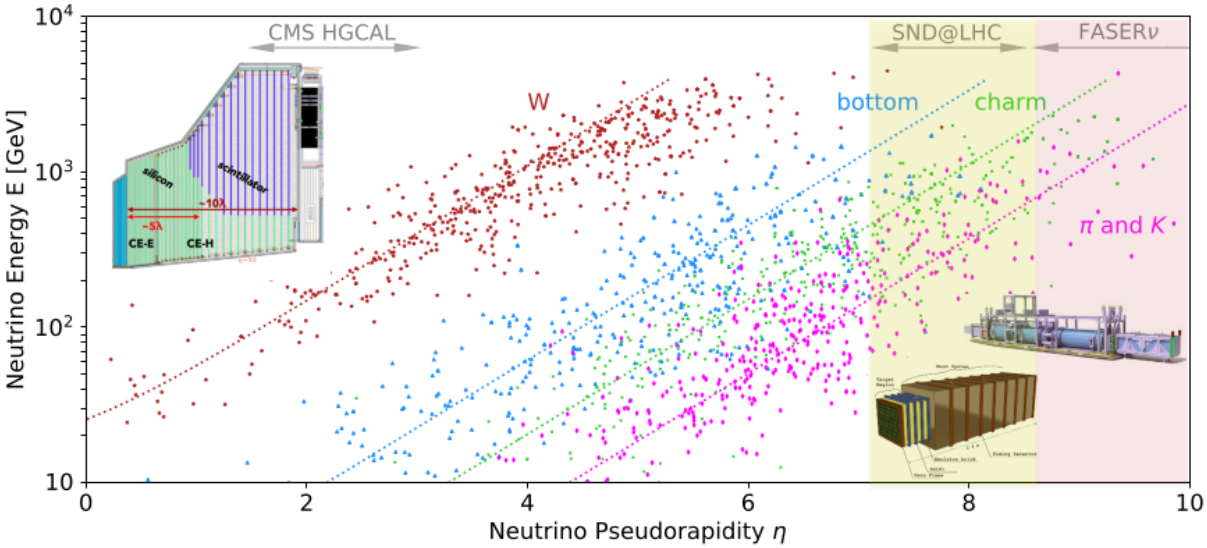

Figure 2.4: Neutrino production mechanisms as a function of their energy and pseudorapidity in an LHC pp collider experiment [268].

(considering that no other sufficiently heavy particle has significant presence in this η region to produce a substantial τ flux). ν_μ have a greater variety of production mechanisms considering the many kaons and pions produced in this region as well as charm in particular. The main observed particle however remains the μ, it abundantly traverses the $\sim 100\,\text{m}$ of concrete wall separating the collision point from the SND detector. Muons occasionally undergo catastrophic Bremsstrahlung radiation [269] and DIS interactions [270]. Muon fluxes are thus studied in detail [271] whereas the total neutrino fluxes can be seen in Figure 2.5.

2.2.3 Detector system

The SND@LHC detector can be subdivided in three sections which can be seen in Figure 2.6: a *veto detector*, a *vertex detector and electromagnetic calorimeter*, and a *hadronic calorimeter and muon system*.

2.2.3.1 Veto detector

The first element of the SND detector is a veto detector which serves to reject charged particles entering the detector acceptance, particularly muons [271] from the ATLAS interaction point. The veto detector comprises three (two until 2024) parallel planes made of *plastic scintillator*, a material which emits light when traversed by ionising radiation (see Section 3.3.4). They are each composed of seven stacked EJ-200 [272] scintillator bars, each $1 \times 6 \times 42\,\text{cm}^3$ wrapped in aluminised mylar foil allowing for light tightness and isolation from any light coming from a neighbouring bar or outside. Each plane is located 4.3 cm apart from one another. Each scintillator is readout by 8 *Silicon Photomultiplers* (SiPMs, see Section 3.3.5.3), of type Hamamatsu S14160-6050HS ($6 \times 6\,\text{mm}^2$). There are 112 SiPM channels per plane housed onto Printed Circuit Boards (PCB) for a total of 336 (224 until 2024) channels over the entire veto system.

The SiPM signals are digitised by TOFPET2 application specific integrated electronics (ASIC) [273].

2.2.3.2 Vertex detector and electromagnetic calorimeter

The *vertex detector and electromagnetic calorimeter* is based on two technologies: the highly position-accurate *Emulsion Cloud Chamber* [274, 275] and coarser position reconstructing *Scintillating fibres trackers* [276], also provide timing information. The emulsion detector consists of 5 walls each containing 2×2 bricks which themselves are made of 60 $19.2 \times 19.2\,\text{cm}^2$ emulsion films interleaved with 1 mm thick tungsten plates shown in Figure 2.7 for a total detector mass of 830 kg. The emulsion film thickness varies depending on whether the films are being produced by the University of Nagoya (195 μm plastic base, $\sim$70 μm emulsion layer) or by the Slavich company in Russia (175 μm plastic base, $\sim$70 μm emulsion layer). The emulsion walls themselves are

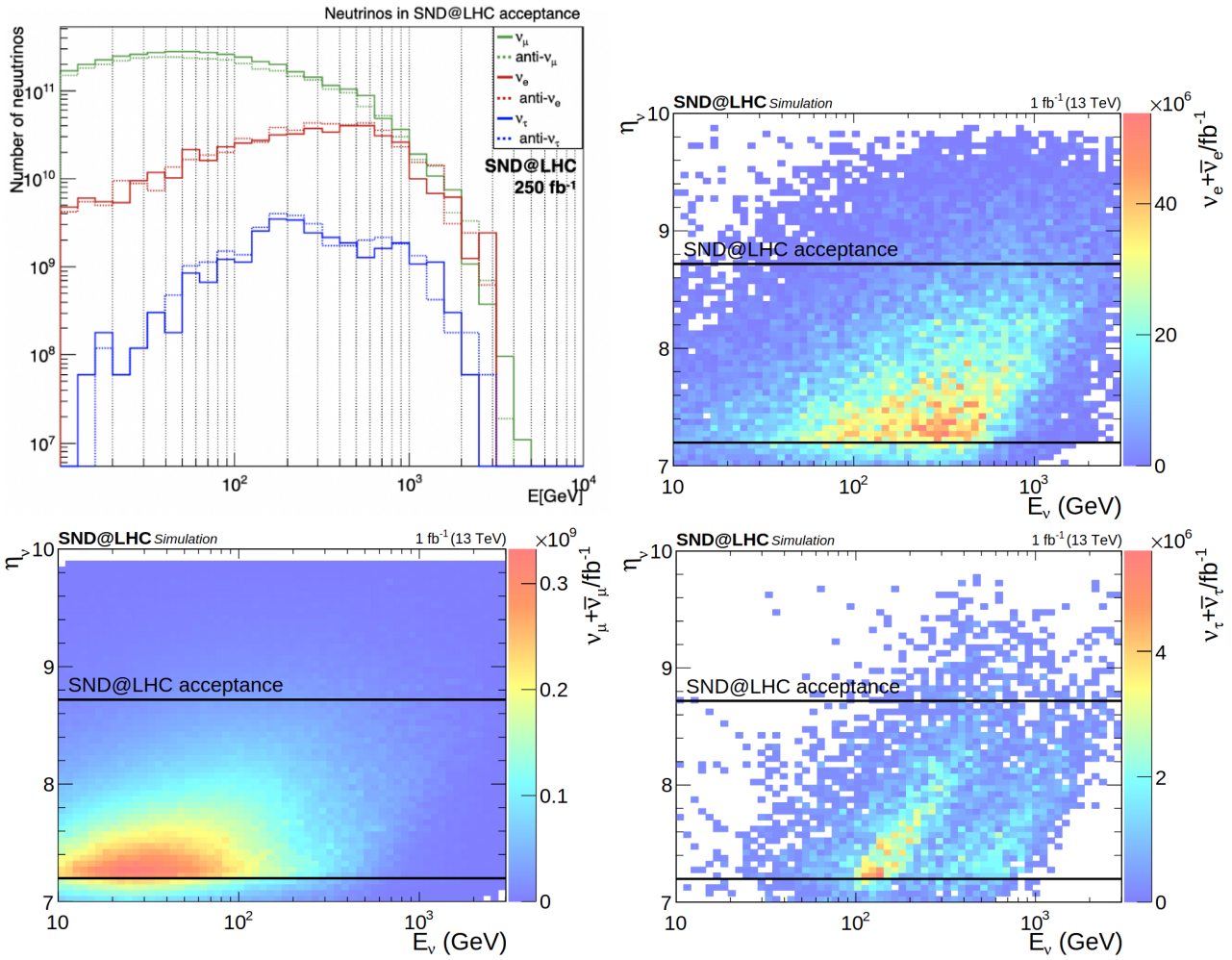

Figure 2.5: Neutrino fluxes according to flavour in SND@LHC normalised to 250 fb^{-1} (top left), Electron (anti-)neutrino flux as a function of their energy and η (top right), Muon (anti-)neutrino flux as a function of their energy and η (bottom left), Tau (anti-)neutrino flux as a function of their energy and η (bottom right) [267].

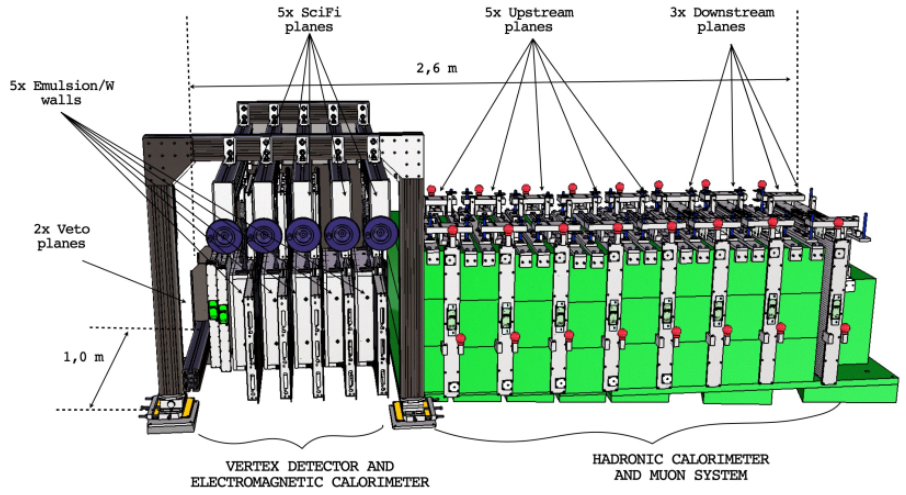

Figure 2.6: Visualisation of the SND@LHC detector system [267]. The ATLAS interaction point is 480 m to the left of the apparatus.

interleaved with the scintillating fibre trackers as shown in Figure 2.6 which serve to provide a timestamp to the emulsion detector. The SciFi detectors are separated by ∼130 mm of air each.

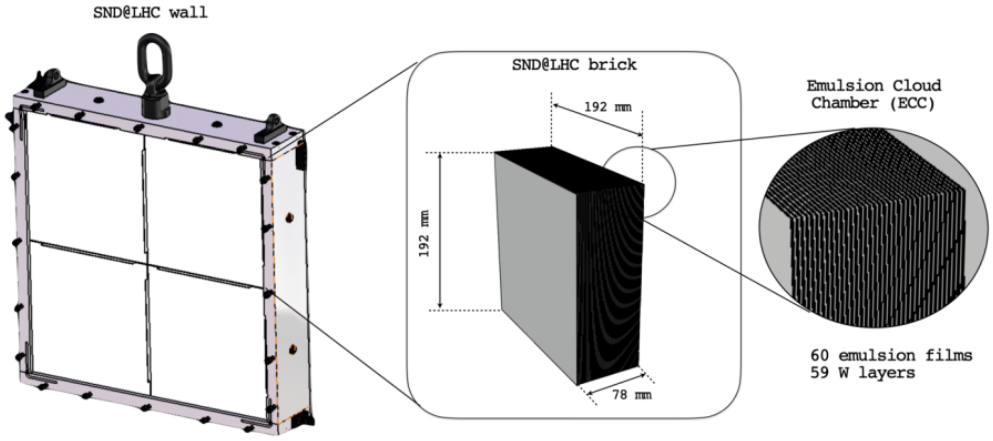

Figure 2.7: Schematic view of an SND emulsion wall consisting of 60 emulsion films interleaved with 59 tungsten sheets [267].

Emulsion detectors Emulsion detectors are an old technology [277]. They possess no online digital readout, require substantive preparation and processing, are fragile, provide no timing information and possess relatively low efficiency, up to ∼ 95% in most applications. Yet nuclear emulsions are exceptional in their unmatched spatial resolution which allows for outstanding precision in the observation of charged particle tracks. They provide single hit spatial resolution below 1 μm (with contemporary works underway to improve it even further down to 50 nm [278]), an order of magnitude better than the best pixel detectors [279, 280], rendering them the ideal candidate for the search of particles with short lived decay products: neutrinos [260, 261] and certain forms of Dark Matter [26, 243, 281].

Emulsion detectors are comprised of thin emulsion films, which are composed of an emulsion substrate and a plastic or glass base. The current emulsion substrate workhorse is constituted of a large number of 200 ± 16 nm halide silver crystals shown in Figure 2.8, each an independent detection channel. They are very uniformly dispersed in a gelatine. The result is an extremely high-channel density of $\mathcal{O}(10^{14})$ channels cm^{-3}. AgBr crystals have a band gap of 2.684 eV, which implies that charged particle passage causes electrons in the valence band to pass into the conduction band. The electron trap is rather shallow however ($\sim 21 - 25$ meV) which implies diffusion within the crystal until trapping in one of the sensitisation centres located on the crystal surface, which itself is artificially created chemically (typically gold-sulphur sensitisation [282]). Once an electron has been trapped, it is negatively charged and thus attracts the surrounding positively charged interstitial silver ions which then migrate in the crystal lattice. The ion reacts with the trapped electron and thus forms a silver atom through $Ag^+ + e^- \rightarrow Ag$, thus rendering the sensitisation centre positively charged again and once again ready to trap an electron. These processes take place multiple times and form an aggregate of silver atoms, any aggregate containing 4 or more silver atoms is large enough to be developed and is called the *latent image centre* at this stage.

The image may be amplified chemically in a dark room through a development procedure by soaking the emulsion film in a reduction chemical implying the RedOx reaction

$$\mathrm{Red} + n\mathrm{Ag}^+ \rightleftharpoons n\mathrm{Ag} + \mathrm{Ox} + m\mathrm{H}^+,$$

Red and Ox are the developing agent and the oxidised developed agent respectively , n is the number of ions and m the number of protons produced. This process leaves a metallic silver filament at the position of the crystal with a latent image centre while latent imageless crystals are unaffected. The filament is called a track segment whereas the assembly of multiple segments from multiple emulsion plates are called tracks. This induces a gain $\mathcal{O}(10^8)$ which renders the particle tracks visible (see Figure 2.8) through a microscope. The individual detection efficiency of a single crystal for a MIP is 0.17 [284] and there are typically 30–50 grains per 100 μm, the total crystal occupancy in terms of total emulsion volume is around 30–55%. A convenient consequence of the mechanism is the proportionality of grains to particle ionisation meaning that low-energy

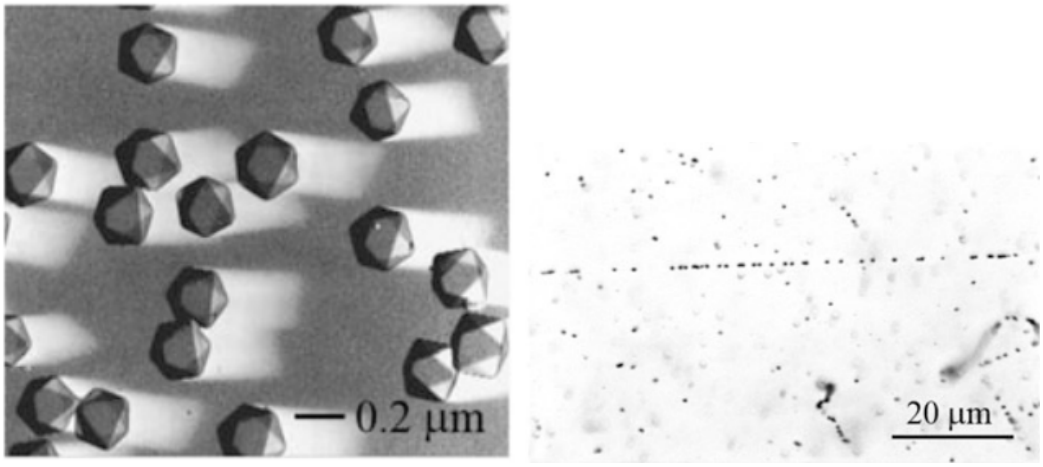

Figure 2.8: 0.2 μm Silver bromide crystals as seen with an electronic microscope (left) and 0.2 μm Emulsion track left by a MIP as seen by an electronic microscope[283]. There are 36 grains/100 μm [284] (right).

electrons are more visible than MIPs, allowing the measurement of dE/dx for each track. However, as can be seen in Figure 2.8, a random "fog" appears due to gelatine impurity, thermal effects and over-sensitisation. A fog density < 5 grains $\cdot$ μm^3 is deemed low enough not to impede measurements. The intrinsic point spatial resolution of an emulsion detector assuming spherical crystals is close to 50 nm and 0.35 mrad angular resolution [285].

The scanning of an emulsion plate is done through an optical microscope and relies on adjusting the focal plane of the objective lens through the whole thickness of the emulsion to obtain an optical tomography of each view field as shown in Figure 2.9. The emulsion plate is placed on a movable stage and illuminated with a short wavelength ($\lambda_{\text{scan}} = 405$ nm) lightsource which allow the optical observation of the silver grains by the microscope's camera which can be observed down to $\frac{\lambda_{\text{scan}}}{2}$.

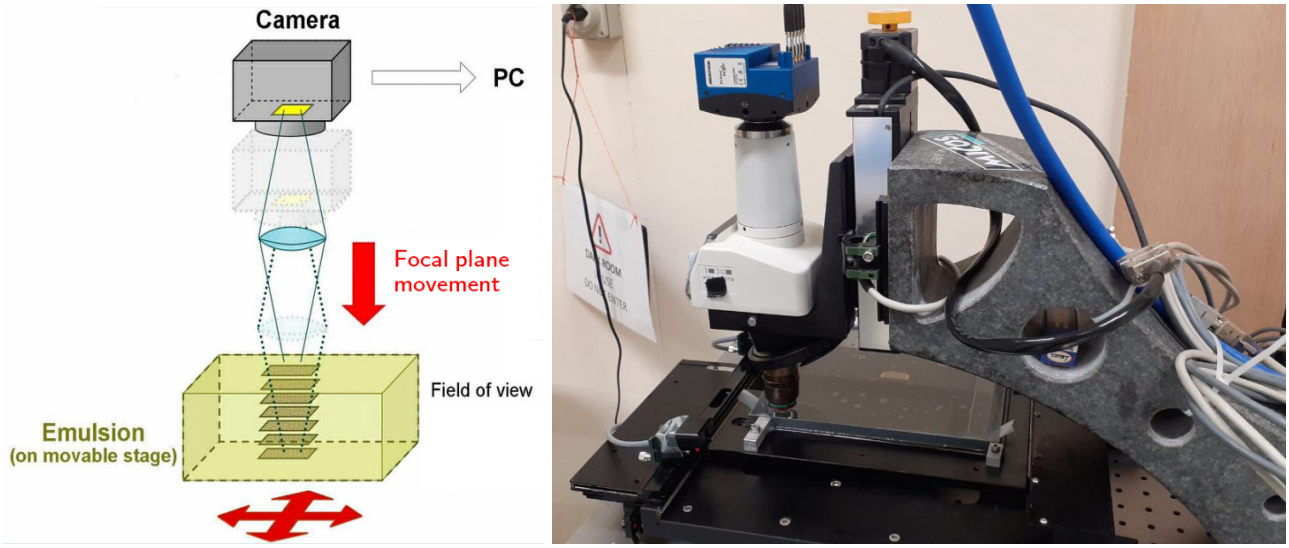

Figure 2.9: Schematic view of an emulsion microscope at SND@LHC [286] (left) and SND scanning microscope (right). The plate is tapped to the stage and the optical transmission between microscope and plate is ensured by utilising a transparent oil (typically lineseed oil).

In the case of SND@LHC, the films are scanned automatically by a microscope with minimal human intervention with only steps such as placing the film onto the stage, parametrising the microscope and replacing the film only taking place at the start and end of the scanning. One to two films are scanned per day depending on the microscope. The full scanning of an emulsion brick by a single microscope would therefore take one to two months. This leads to ten microscopes being used with four operating at CERN, three at the university of Naples in Italy, two at the University of Bologna in Italy and one at the university of Santiago in Chile. Segments are identified thanks to the LASSO software [287] and assembled into tracks then analysed using the

Framework for Emulsion Data Reconstruction and Analysis (FEDRA) [288]. The emulsion films are exchanged every $\sim 10-25\,\mathrm{fb}^{-1}$ depending on the LHC beam optics. A fully exposed plate will display $\sim 10^5$ tracks cm^{-2}.

Scintillating fibre detectors Scintillating fibre detectors (SciFi) are used to match tracks from the emulsion detector and provide a timestamp in SND. They feature mats of scintillating fibres very similar to the ones used in LHCb [276]. The fibres used are 250 µm diameter blue-emitting double-cladded polystyrene SCSF-78MJ scintillating fibres from Kuraray which have a decay time of 2.8 ns. The fibres are arranged in 6-tightly packed staggered layers glued with reflective titan oxide loaded epoxy glue called mats of 1.35 mm thickness. These mats are assembled in modules that may be readout in the X or Y direction. In the case of SND, the active area of a SciFi module is $40 \times 40\,\mathrm{cm}^2$ with 5 XY planes, the mats and modules may be seen in Figure 2.10.

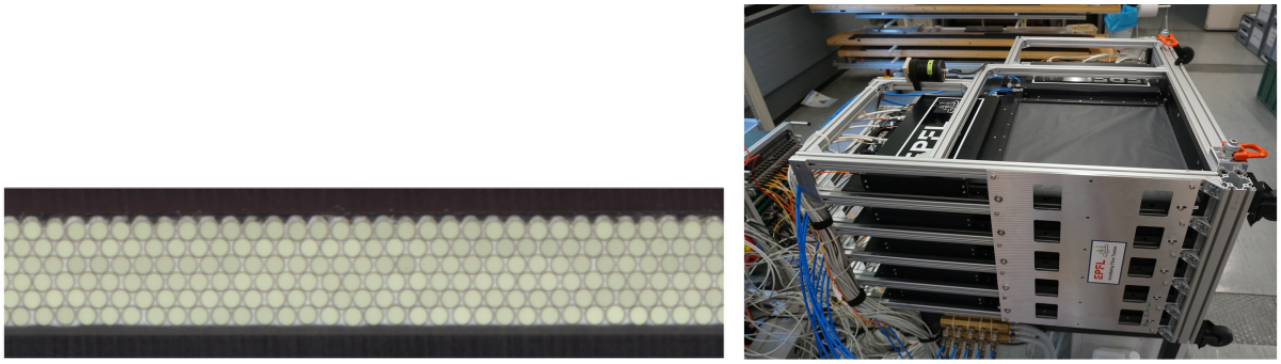

Figure 2.10: Picture of a SciFi mat (left) and of the SND SciFi tracker layers (right) [267].

The SiPMs used are Hamamatsu S13552 SiPM multichannel arrays [289] and are positioned at the end of a given fibre module. They are placed on kapton flex PCBs and kept light-tight through a seal on the Kapton flex, the aluminium module frame and an opaque Tedlar plastic sheet on each side of the module. The SiPMs are operated at 15 °C which allows acceptable noise conditions of $\sim$ 25 Hz/channel. The full detector thus achieves an overall efficiency of $\sim$ 99% [267]. The SiPM array has a channel area of $0.25 \times 1.625\,\mathrm{mm}^2$ with peak photodetection effiency $\sim$ 47% using a 3.5 V overvoltage for a gain of 3.6×10^6. This induces a signal of 25 photoelectrons/MIP (see Section 3.1 and 5.4) whereas the dynamic range linearity stretches to $\sim$ 50 PE. Similarly to the veto detector, the SciFi is readout by TOFPET2 boards.

The SciFi's time resolution is limited by the detected photon counts and the scintillator decay time. It has been determined to be $\sim$ 330 ps on each fibre layer which implies $\sim$ 230 ps per plane and $\sim$ 100 ps over the entire tracker while the track spatial resolution is around 90 µm [267].

2.2.3.3 Hadronic calorimeter and muon system

The *hadronic calorimeter (HCAL) and muon system* is located downstream of the vertex detector. It is present to identify muons and provide energy reconstruction for hadronic showers that leak out of the emulsion walls (see Section 3). It is made of 8 layers of scintillator bars interleaved with 20 cm iron blocks. This yields an 11 nuclear interaction length calorimeter. The system has two major components. The first 5 layers have coarse position resolution and are called the *Upstream System* (US), using $82.5 \times 6 \times 1\,\mathrm{cm}^3$ of EJ-200 scintillator wrapped in aluminised Mylar foil similar to the veto system. The bars are readout by 16 SiPMs each with 6 Hamamatsu S14160-6050HS and two Hamamatsu S14160-3010PS [290] SiPMs ($3 \times 3\,\mathrm{mm}^2$) on each end which in turn see their signals digitised and further readout by a TOFPET2 readout board similar to that of Section 2.2.3.1. The SiPM are arranged onto custom PCBs in a pattern alternating 2 large SiPM for every small SiPM per bar side. The smaller SiPMs are used to compensate for the saturation of the large SiPM channels through their superior pixel density and reduced area (see Section 5.5.2) as the calorimeter needs to be sensitive to large hadronic showers inducing great amounts of light. In order to maximise light collection, the $\sim$ 1 mm space between scintillator and SiPM is filled with silicon epoxy gel (see Section 5.5.4).

Behind the 5 US layers are 3 Downstream System layers (DS) which are used primarily for muon identification. Each DS station consists of a horizontal plane and a vertical plane of 60 thin scintillating bars each measuring $82.5 \times 1 \times 1\,\mathrm{cm}^3$ and $63.5 \times 1 \times 1\,\mathrm{cm}^3$ respectively with the third station having an extra vertical plane. The bars are readout by single large SiPMs analogous to the US ones, horizontal ones being readout on

both sides whereas vertical bars are only readout on the upper end in order to allow for the placing of the bar as close as possible to the floor as to maximise detector acceptance, they are readout by 60 SiPMs placed on a PCB at a regular 1.1 cm interval from one another for a total of 600 SiPMs DS-wide readout through TOFPET2 boards in a similar way to the US. Each bar is tightly wrapped in aluminised mylar foil which extends to the SiPM-less side of the vertical layers the DS bars. The full US and DS system can be seen in 2.11.

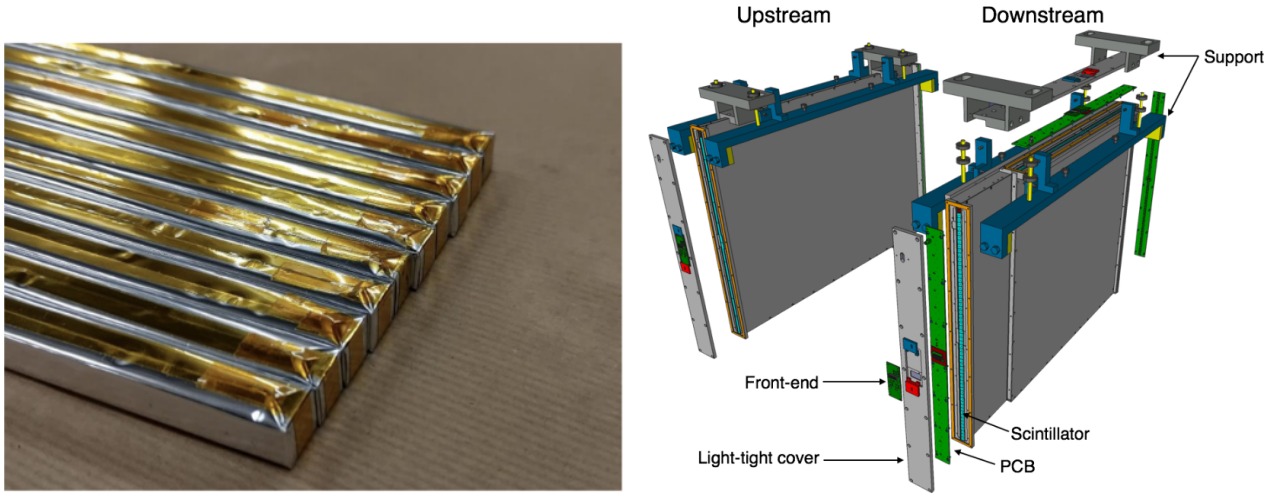

Figure 2.11: DS bars (left) and US and DS single layer visualisation (right) [267].

2.2.3.4 Neutron shield

In January and February 2022 a neutron shield was built in order to reduce the incoming flux of thermal neutrons from particle interactions in the cavern walls which increased the emulsion fog. The neutron shield is composed of 4 cm thick borated polyethylene and 5 cm thick acrylic layers. It reduces unwanted interactions by a factor 10^{-7}. In addition to this significant reduction in background rates, the neutron shield provides effective insulation which is beneficial for the long-term stability of the emulsion films, it is therefore accompanied by a cooling system which preserves the target temperature at $15 \pm 1\,^{\circ}\mathrm{C}$ and the relative humidity in a range of $40 - 50\%$. The full system can be seen in Figure 2.12.

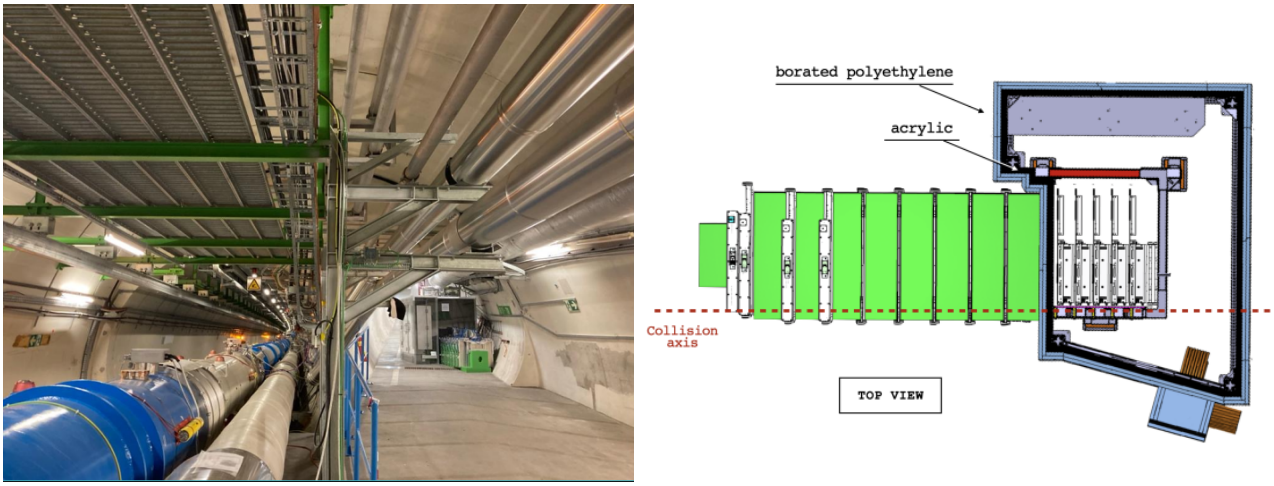

Figure 2.12: Picture of SND@LHC after February 2022, the ATLAS interaction point lies outside the picture, 480 m towards the viewer [291] (left) and schematic drawing of the neutron shield [100]. The interaction point is there to the left. (right).

2.2.4 SND data acquisition, trigger and software

2.2.4.1 Online data acquisition

The data from the electronic detectors, all readout through TOFPET2 boards and acquired by the DAQ boards is recorded on a surface DAQ computer. The recorded information includes timestamps, integrated charge and channel and board numbers. The full detector uses 37 DAQ boards which each concentrate the data of 4 TOFPET2 (FE) boards. The full system is synchronised to the LHC bunch crossing clock signal and operates triggerless, that is to say, no input trigger signal is provided to the detector system to begin or otherwise influence data acquisition and all recorded hits are transmitted to the DAQ server. In such a configuration, noise reduction is crucial to avoid a saturation of the readout. This is done at the FE level through threshold setting and at the DAQ server level in the event building step. The LHC clock (40.079 MHz bunch crossing frequency) and orbit signals (11.245 kHz revolution frequency) from the LHC Beam Synchronous Timing (BST) are received by a Trigger Timing Control (TTC) [292] through optical fibres and extracted by a dedicated BST-TTC board sends it further to the detector units using the TTC. The boards receive the signals thanks to TTCvia and TTCex modules housed in a VME crate. The TTCvia ensures reception of clock and orbit signals as well as generation of trigger signals and (a)synchronous command signals which are then encoded and transmitted to the front end by the TTCex.

An Experiment Control System (ECS) is established to ensure the smooth and automatic running of the experiment. It encompasses a Detector Control System (DCS) which controls and monitors power supplies, cooling, humidity, temperatures and fire alarm, a Data Quality Monitoring (DQM) which produces data histograms and updates them every 10^5 events while also reading and converting the online data format into an offline analysis format. In addition the ECS comprises logging of the state configuration and conditions of the DAQ systems which allows for effective and speedy recovery when needed. The ECS as a whole, being the top level experiment control, hence provides a unified framework for hardware control and software processing. It functions using an ECS Process Manager (EPM) which runs on the main server and links every online system element, ensuring the smooth start and monitoring of their status as needed. The EPM restarts processes if it is found not to be running and is notably capable of starting DAQ automatically when the LHC declares stable beams, it is operated through the ECS Graphical User Interface (GUI) which allows for easy and clear access to the EPM components.

2.2.4.2 Offline software, simulation and data analysis

The official SND software is called `sndsw` [293] and is a fork of the `FairShip` framework which functions similarly for the SHiP experiment [294]. FairShip itself is based on `FairRoot` [295] which is used for simulation, data analysis, interpretation and event display.

Simulation Simulation is crucial to allow the testing of analysis techniques in a controlled environment, where interactions and their participants are identified a priori and generated from a list of known physics behaviour, making use of pseudo-random generation techniques where needed [296]. They are done through the GEANT4 [297, 298] package. Detector geometries are defined by including active and passive volumes, incoming particles as well as their energy depositions in matter. Depending on the targeted physics case, different simulation engines are used to handle critical effective interactions of matrix elements: Muons from pp collisions are transported through the LHC magnets, materials, collimators using a FLUKA model [299, 300]. Their interactions are generally simulated using GEANT4 whereas their DIS are handled by Pythia6 [301], DPMJET3 [302] or Pythia8 [303]. Neutrino production is handled by DPMJET3 and their interactions in the detector are handled using GENIE [304]. Each of these engines provides a precise description of the physics in questions (Pythia typically works for most elementary interactions but only describes them at leading order whereas others may be preferred for descriptions where Pythia would be too imprecise) The GEANT4 simulation can notably generate particles originating from the IP's proton collision or from a particle gun which can be set to a certain species, momentum, angle and/or origin point. Data, whether simulated or taken by electronic detectors is handled identically and is stored as *hits* which can then be assembled into *tracks*.

Neutrino identification The determination of particles species observed in SND@LHC is of primordial interest, particularly for leptons. Particles exiting the tunnel wall such as muons (MIPs or having interacted

through DIS) are vetoed out using the aforementioned veto detector. ν_μ are observed as discussed earlier whereas ν_e CC interactions are observed through the showers they produce in the EM calorimeter. ν_τ CC interactions are most difficult to observe and require fine usage of the EM calorimeter's emulsions to observe the *kink* produced by the τ decay interactions taking place in the tunnel walls. All of these interactions are shown in Figures 2.13, 2.14 and 2.15.

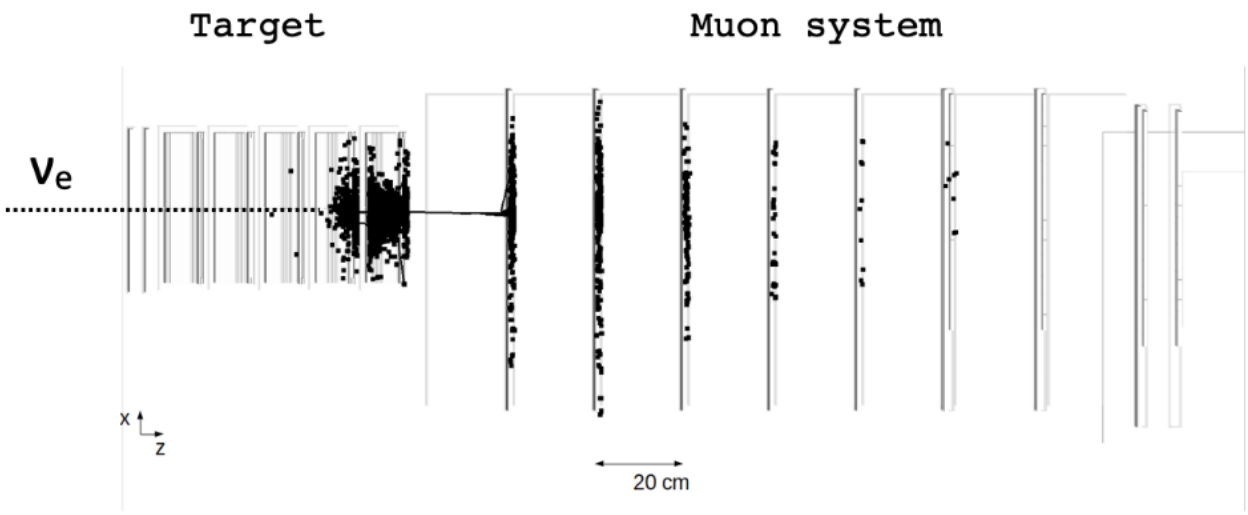

Figure 2.13: Event display of simulated observation of a collider ν_e by SND@LHC using electronic detectors [305].

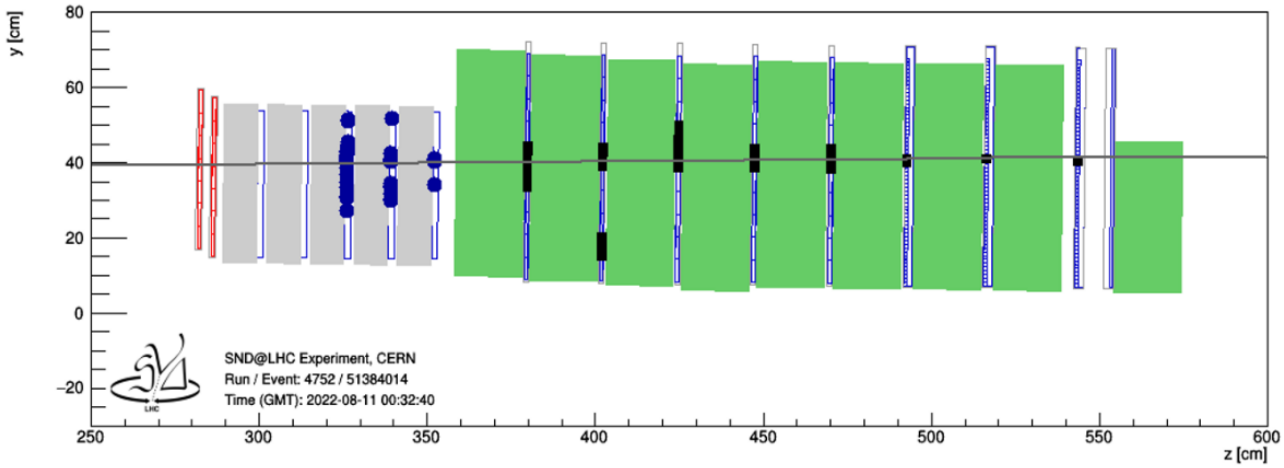

Figure 2.14: Event display of first observation of a collider ν_μ by SND@LHC using electronic detectors [305].

SND expects a total of ~ 2500 neutrino interactions over $290\,\mathrm{fb}^{-1}$ of which ~ 50 would be ν_τ interactions all shown in Table 2.1. While this constitutes a significant increase compared to historical observations (19 at the time of writing) it remains an extremely statistically limited search. This is, among others, a limit which should be lifted with the Search for Hidden Particles experiment.

2.3 The Search for Hidden Particles

Searches for BSM physics necessitate a combination of high enough energies and high enough intensities to be observed (Section 1.3). High-intensity searches are limited by their achievable decay modes and thus benefit from energies large enough in order to produce heavy flavour particles that expand their sensitivity into higher energy ranges.

The flagship example for these high-intensity searches implementing this approach is the recently approved Search for Hidden Particles (SHiP) at the Beam Dump Facility (BDF) [26, 104, 306–310] which will be located

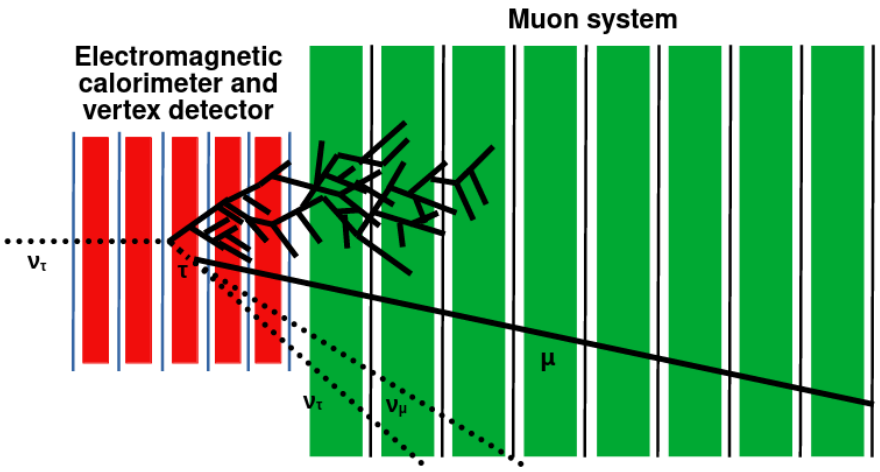

Figure 2.15: Visualisation of a ν_τ reconstruction, dotted lines are unseen particles. The shower structure has been simplified and scales have been adjusted for maximum clarity.

Flavour	**Neutrinos in acceptance**	**CC neutrino $\langle E \rangle$ [GeV]**	**Interactions yield**	**NC neutrino $\langle E \rangle$ [GeV]**	**Interactions yield**
ν_μ	3.4×10^{12}	450	1028	480	310
$\bar{\nu}_\mu$	3.0×10^{12}	480	419	480	157
ν_e	4.0×10^{11}	760	292	720	88
$\bar{\nu}_e$	4.4×10^{11}	680	158	720	58
ν_τ	2.8×10^{10}	740	23	740	8
$\bar{\nu}_\tau$	3.1×10^{10}	740	11	740	5
All	7.3×10^{12}	500	1930	540	625

Table 2.1: Expected neutrino interactions in SND@LHC over $290\,\mathrm{fb}^{-1}$ [100].

in the CERN North Area in the ECN3 hall as visible in Figures 2.16 and 2.17, making use of 4×10^{19} 400 GeV slow-extracted SPS protons on target (PoT) over 200 days of operation per year with 5000 spills a day (see Figure 2.1), beginning its data taking around 2030 and operating for 15 years. The experiment uses protons as they are easiest to accelerate at high energies and intensities while having the greatest diversity of possible interactions. When interacting, the proton should produce as many heavy flavours as possible. The top is inaccessible due to its very high mass, beauty and charm quarks, mainly manifesting in D and B mesons, are hence preferred. The exact yield of each production channel is influenced by the cascade effect, causing heavy flavour to not only be produced in prompt collisions, but also for them to emerge from subsequent interactions of promptly produced particles with the thick target [275]. These production mechanisms are shown in Figure 2.18 whereas the sensitivity of SHiP to benchmark BSM models are shown in Appendix B.

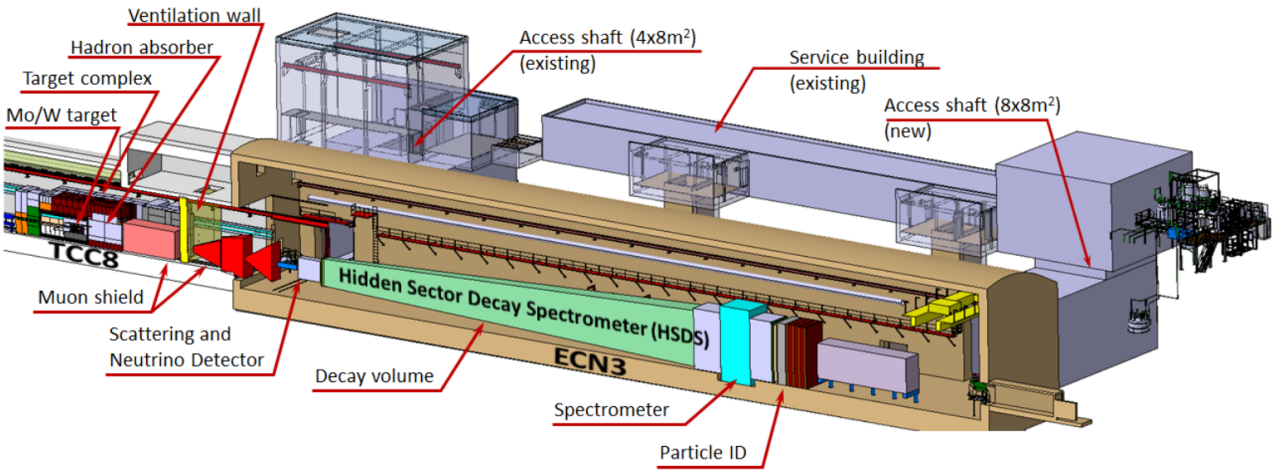

Figure 2.16: Overview of the BDF/SHiP infrastructure and detector components [26].

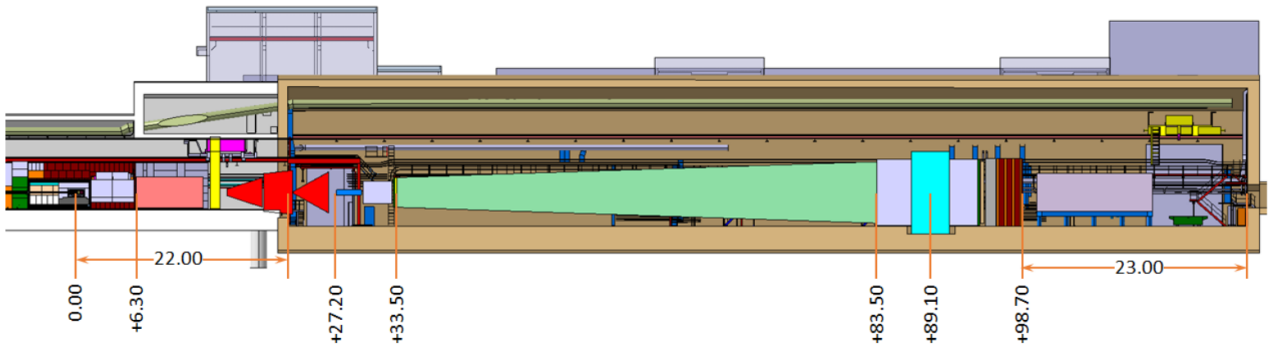

Figure 2.17: BDF/SHiP component sizes [26].

The extreme intensity of the dump implies an equally large production of associated particles which cannot be allowed to become a significant source of background as the searched for signals are extremely faint and could very well constitute no more than a couple of events over the entire 15 years of SHiP physics runs if they were to be observed. This induces the need for dedicated filter and veto systems.

The SHiP detectors systems will be introduced in order while descending the beam line.

2.3.1 SHiP upstream systems

The SHiP experiment is divided into 4 primary sections, the first of which is composed of upstream systems meant to dump the beam and allow for the rest of the detector systems to pursue the physics program. This is done with a beam and target complex and a muon shield which are discussed in the following section.

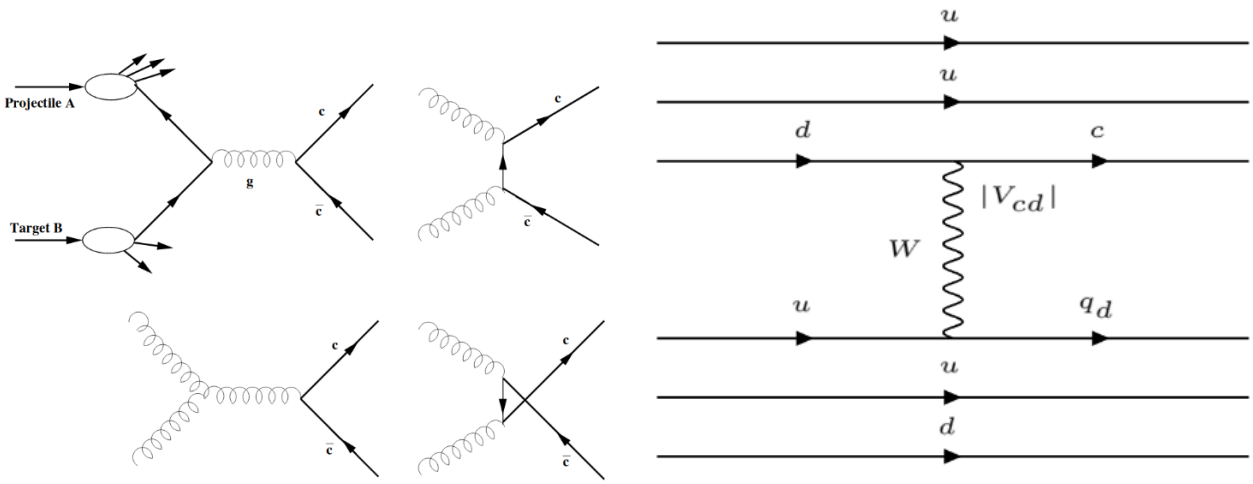

Figure 2.18: Production of two charmed particles in fixed target experiments at leading order [311] (left) and example production of single charm [296] (right).

2.3.1.1 SHiP beam and target complex

The SHiP proton beam is the starting point of the physics program and is thus optimised for maximum proton yield. The high intensity of the proton beam renders an increase of the beam spot desirable to diffuse the heat induced by the collisions. Hence, the SHiP/BDF would utilise a large beam with $\sigma_b \sim 35\,\text{mm}$ with studies being under way to increase it further while keeping beam tails under control [26].

The beam arrives on a tungsten target to maximise charm and beauty production [306]. The target blocks are spaced by 5 mm, allowing for water-cooling, necessary to prevent a target meltdown caused by the intense $2.6\,\text{MJ/pulse}^{-1}$ every 7 seconds, corresponding to around 350 kW of average beam power. The target itself can be seen in 2.19 whereas the full SHiP target system can be seen in Figure 2.20.

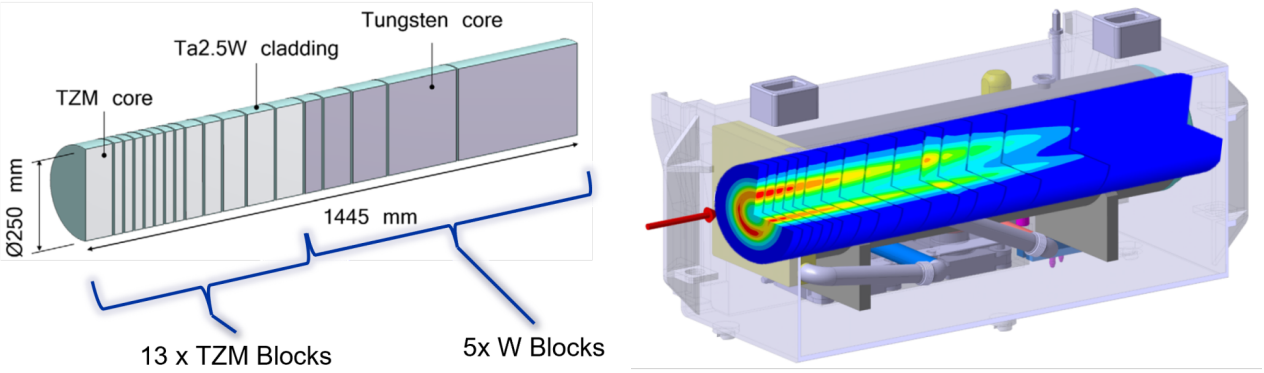

Figure 2.19: SHiP target composition and design (left) and expected temperature rise during pulse from simulation (right) [26].

The consequence of the dump's intensity is a large muon flux ($\mathcal{O}(10^{10})\mu$/spill) with more than 10 GeV momentum focused in the forward region. This flux, to eliminate combinatorial background and limit muon DIS background, must be limited. Low-energy muons, hadrons and electromagnetic components are stopped using a 5 m long hadron absorber made of magnetised iron, possibly followed by extra shielding if necessary.

2.3.1.2 SHiP active muon shield

While low-energy muons are be stopped by the hadron absorber, the outgoing muon flux does not stop at low energies as shown in Figure 2.21. In order to reduce it, the most effective solution was shown to be using an active *Muon Shield* (MS) made of a series of custom magnets [307]. The muons are swept out utilising an alternating polarity scheme [312]. The working principle allows to deflect both high and medium energy muons:

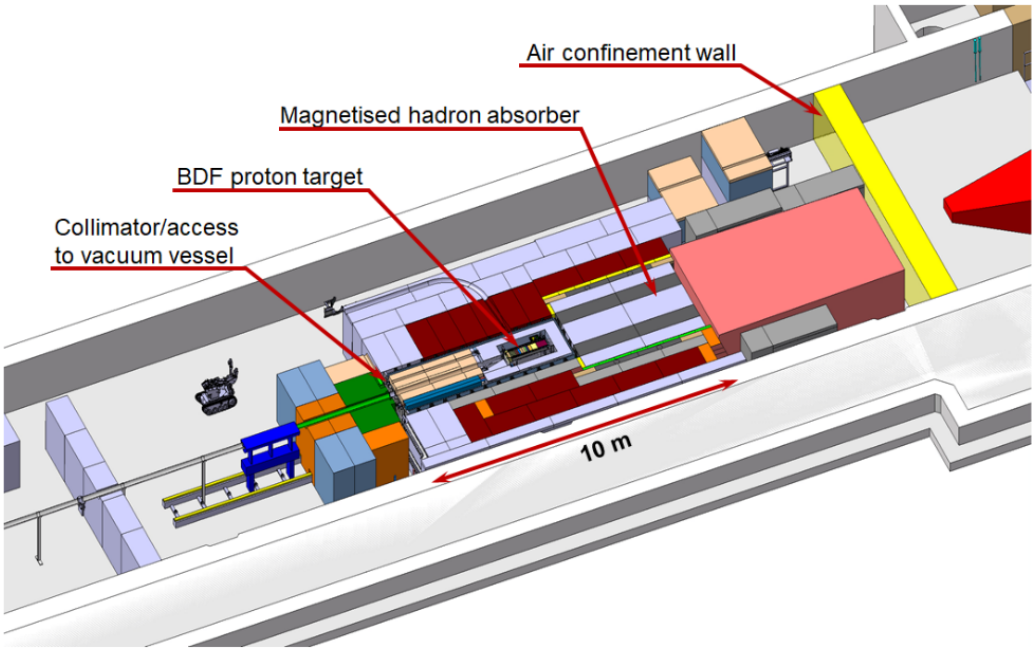

Figure 2.20: SHiP target complex in ECN3 and design [26].

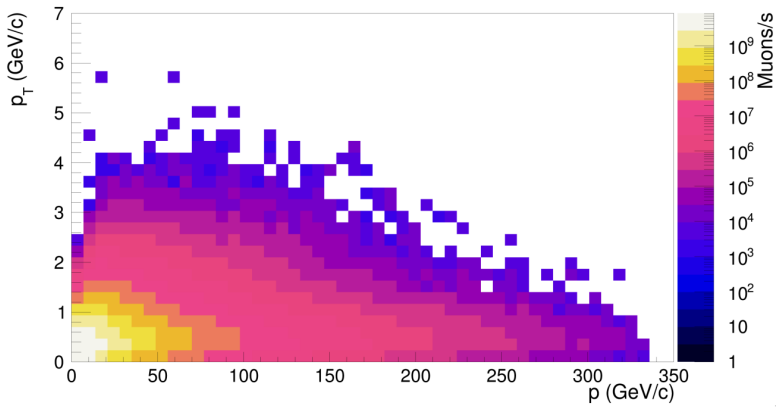

Figure 2.21: Expected muon flux exiting the hadron absorber as a function of total momentum p and transverse momentum p_{T} [26].

- High-energy muons are deflected in the core of a first section and then further deflected by the return field induced by the yoke of the second section.
- Medium-energy muons are refocused by the first section's return field onto the yoke of the second section then deflected outwards.

Both sections have alternating polarity and allow the suppression of the muon rate in the detector region by $\sim 10^6$. The scheme can be seen in Figure 2.22

Two configurations are under study for the MS: a 1.7 T normal conducting 6-magnet section configuration and a 5.1 T hybrid superconducting/normal conducting scheme. The latter allows for a shorter muon shield. The full optimisation of the MS is still ongoing at the time of writing but the overall length of the muon shield should be ~ 10 m.

2.3.2 SHiP scattering and neutrino detector detectors

The SHiP SND is where a large portion of the physics program is pursued: neutrino physics, searches for light ($\mathcal{O}$(100MeV)) dark matter, lepton flavour universality violation searches and hadron flavour physics are done using the intense neutrino and muon flux.

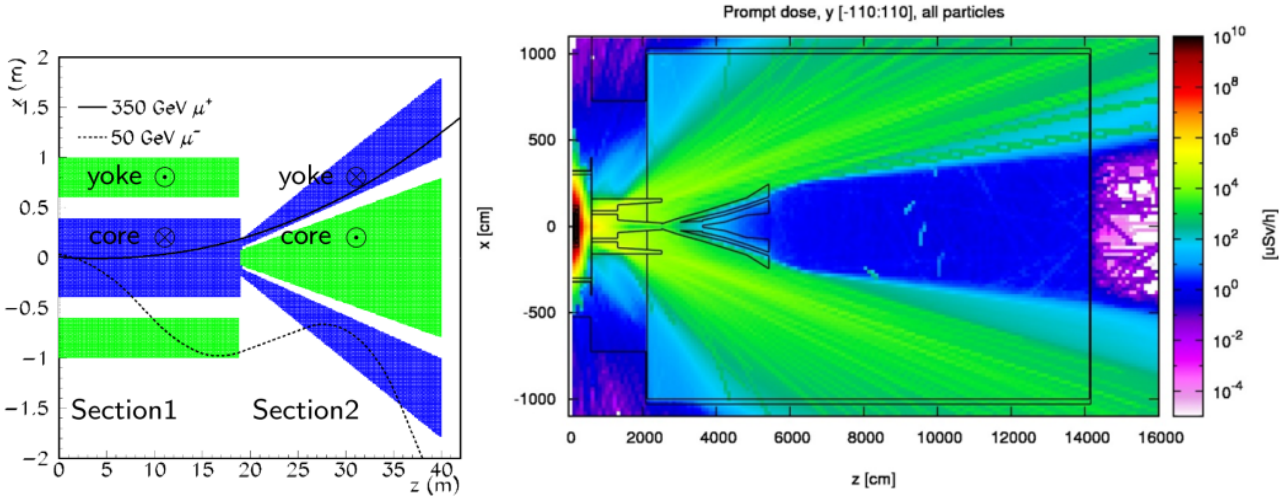

Figure 2.22: SHiP muon shield deflection scheme (left) and expected prompt dose (essentially muon-induced) at SHiP (right) [307]. The detector apparatus is placed in the low dose region at the centre. 1 µSv is estimated to correspond to $\sim 10^6 \mu$.

2.3.2.1 Emulsion section

The complementarity between SND@LHC and the SHiP SND (or SND@SHiP) encourages a very similar detector system for the latter compared to its collider neutrino counterpart. It is as such consisting of an initial section of five ECC walls made of 180 $20 \times 20\,\text{cm}^2$ emulsion films (standard Nagoya emulsions) interleaved with 1 mm tungsten plates for a ~ 7.8 cm and ~ 500 kg target, benefiting from the return on experience of its LHC cousin. These ECCs are interleaved with SciFi tracking stations which would be used to provide electronic timing information and tagging to the SND@SHiP forming the target tracker.

2.3.2.2 Silicon section

A second section would utilise high-resolution silicon strip detectors and would be based on interleaving them with tungsten plates based on the SND@LHC planned upgrade [262].

2.3.2.3 SND magnetised tracking calorimeter

The SND@SHiP is completed with a hadronic calorimeter which would combine SciFi tracking stations analogous of those of Section 2.3.2.1 with scintillator tiles readout by wavelength-shifting fibres and SiPMs.

The detector is pictured in Figure 2.23.

2.3.3 SHiP decay volume detector system

The large particle intensity found in SHiP may produce a variety of weakly coupled BSM particles which themselves would be long lived enough to travel several tens of meters within the detector before decaying back into visible SM final states. This implies the need for a detector system allowing for the undisturbed decay of BSM particles as well as sufficient background taggers ensuring that no stray particles from the dump of cosmic radiation be confused for a signal. Those roles are filled by the SHiP decay volume as well as its associated detector systems.

2.3.3.1 SHiP decay volume

Immediately downstream from the SND ~33 m from the proton target centre is the SHiP decay volume. It is a vessel, seen in Figure 2.24, which defines the decay acceptance for BSM signatures in a wide variety of models to optimise the overall sensitivity of the experiment. The tank would be made of aluminium and filled with helium. The helium is contained inside of a balloon, itself encased into an aluminium supporting structure. The choice of helium is made as it removes the need for difficult and expensive vacuum sealing and pressure robustness of

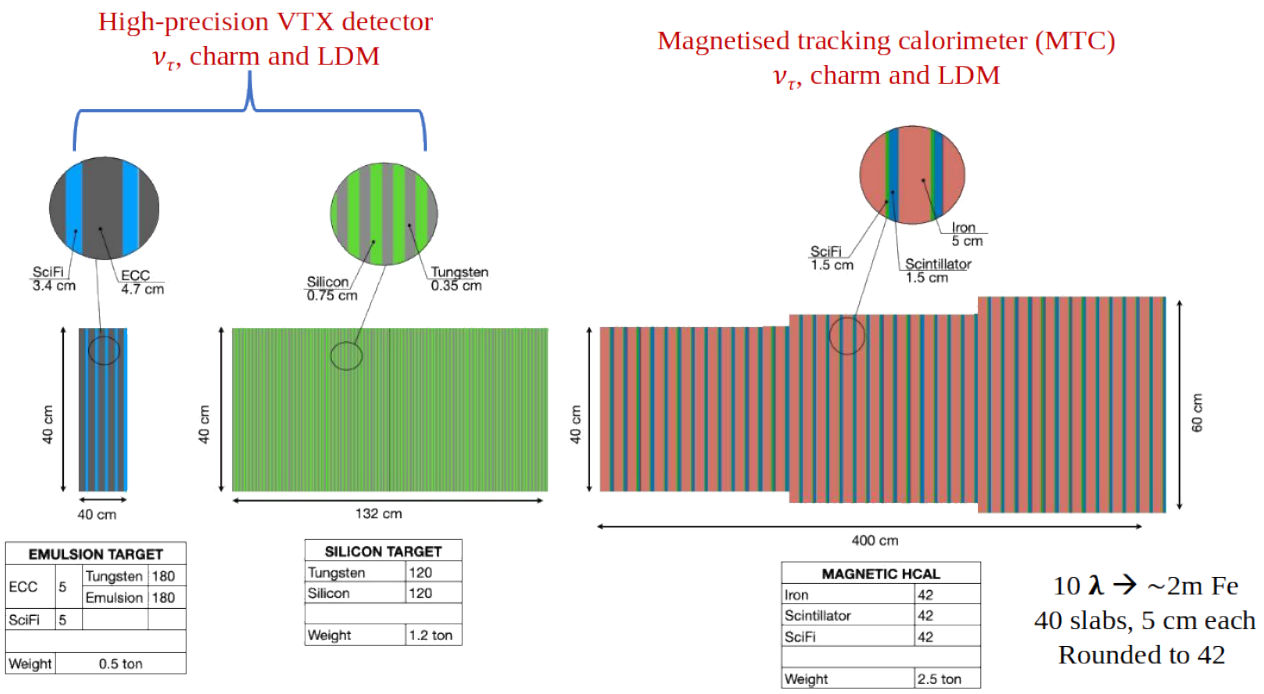

Figure 2.23: SND@SHiP Magnetised tracking calorimeter.

the vessel. It comes with the significant disadvantage of increased background, although the background was found not to be insurmountable [313, 314].

A key characteristic of the decay volume is its double wall structure, with an inner wall of 20 mm, to which are added azimuthal and longitudinal strengthening members, 200 mm height and 15 mm thickness each, and an 20 mm thick outer wall.

The decay volume is divided in ~ 1400 cells of varying size which contain the Surround Background Tagger described in Section 2.3.3.3 and represent a volume of $\sim 145\,\mathrm{m}^3$.

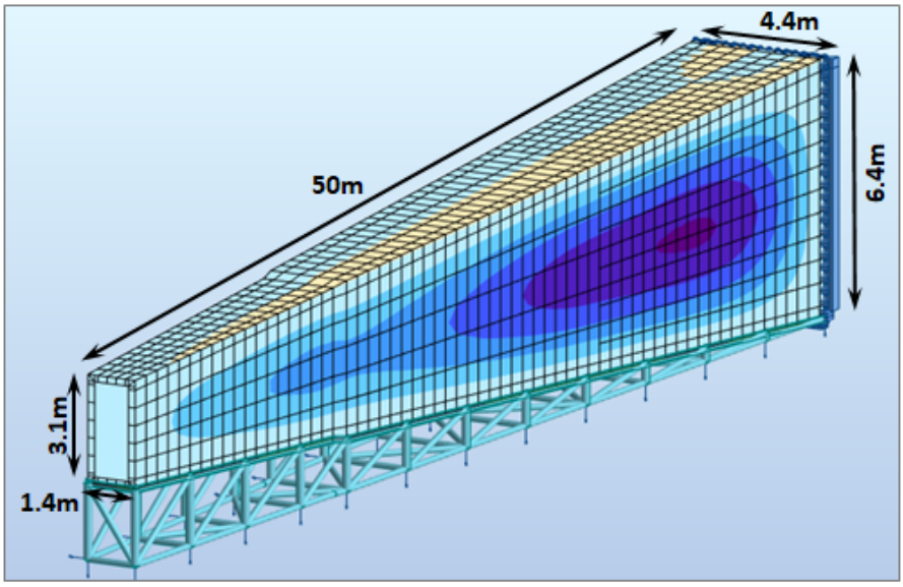

Figure 2.24: SHiP decay vessel [26]. The color code represents the load on different sections in a FEM analysis.

2.3.3.2 SHiP Upstream Background Tagger

Certain particles from the dump, primarily muons, pass the MS's deflection and make it into the decay vessel. This background is vetoed using an Upstream Background Tagger (UBT). The SHiP UBT tags the timing

and position of incoming background charged particles using gas detectors based on Multigap Resistive Plate Chambers (MRPC) [26]. Each RPC is a plane capacitor filled with a gas mixture and readout using strips, yielding excellent timing and good position resolution.

The SHiP UBT would consist of three planes of vertical MRPCs which would cover the decay vessel entrance. Each plane include seven $1500 \times 1200 \times 1\,\mathrm{mm}^3$ highly resistive (hence the name) glass electrodes readout by $1600 \times 37.5\,\mathrm{mm}^2$ copper strips. Correspondingly six gas gaps using a 98% $C_2H_2F_4$, 2% SF_6 mixture and operated with a constant flow of $5\,\mathrm{cm}^3\,\mathrm{min}^{-1}\,\mathrm{m}^2$ constitute the UBT's sensitive volume. A $\sim 20\,\mathrm{cm}$ overlap is foreseen to eliminate the impact of dead regions (used for mechanics or readout for instance).

Utilising the combination of the MRPCs's excellent timing resolution ($\sim 50\,\mathrm{ps}$) and its good position resolution ($\mathcal{O}(\mathrm{mm})$), the background may be effectively vetoed.

2.3.3.3 SHiP Surround Background Tagger

Although the UBT effectively tags background induced by the dump's central area, there remain muons outside of the UBT's acceptance which are significant as seen from Figure 2.22. In addition, muons may undergo backward-scattering with the cavern's walls back into the decay volume. Particularly problematic is muon deep inelastic scattering on the decay vessel's walls and the electromagnetic debris created in the process. These forms of backgrounds are tagged by the SHiP Surround Background Tagger (SBT) [315].

The SBT utilises the gap between both decay vessel walls which is filled with liquid scintillator [316] a wavelength shifter (see Section 3.3.4). The light emitted by the liquid scintillator is captured by a Wavelength-shifting Optical Module (WOM) [317, 318], a transparent PMMA hollow tube coated with wavelength shifting organic luminophore paint. The light captured by the WOM is totally internally reflected by its walls and arrives to the tube's end where it is readout by a ring of 40 SiPMs. The overall spatial resolution achieved is around 10 cm whereas the timing resolution is $\sim 1\,\mathrm{ns}$ with an overall efficiency of 99.9% over the entire volume for energy depositions above 45 MeV [26].

There would be around 4000 WOMs over the entire SBT, ensuring full coverage around the acceptance leading to the Hidden Sector Spectrometer (HSS).

2.3.4 SHiP Hidden Sector Spectrometer

Particles exiting the decay vessel must be observed, tracked, tagged identified and measured. This is done through the $4 \times 6\,\mathrm{m}^2$ HSS which consists of a magnet, a main tracker, a timing detector and most relevantly for this work, a calorimeter system. This last element will be the focus of Chapters 3 and 4 while the other three are summarised below.

2.3.4.1 Spectrometer magnet

The spectrometer magnet is used in conjunction with the tracker to measure the momenta of outgoing charged particles (see Section 2.3.2). It would be a superferric H-type yoke magnet utilising two symmetric flat coils with a target central field of 0.15 T and a bending strength of $\sim 0.6\,\mathrm{T\,m}$. The magnet will be built out of MgB_2 cables similar to the High Luminosity LHC work package 6a's [319] and would be operated in gaseous helium at $20 - 30\,\mathrm{K}$. A visualisation of the magnet may be seen in Figure 2.25.

2.3.4.2 SHiP Spectrometer Straw Tracker

The Spectrometer Straw Tracker (SST) is based on 4 m long and 2 cm drift tubes are made of ultrasonically welded BoPET, a technique developed for NA62 [321] which significantly reduces multiple scattering within the tubes and thus improves their spatial resolution. They are operated with Ar/CO_2 (70/30%) at one bar in a proportional regime, that is, the amount of charge produced in the discharge is proportional to the initial ionisation ($G \sim 10^5 - 10^8$) and biased with a HV of $\sim 2\,\mathrm{kV}$.

The SST's timing resolution will be $\sim 5\,\mathrm{ns}$, allowing it to achieve its tracking purposes. The fine timestamp will be provided by the SHiP Timing Detector.

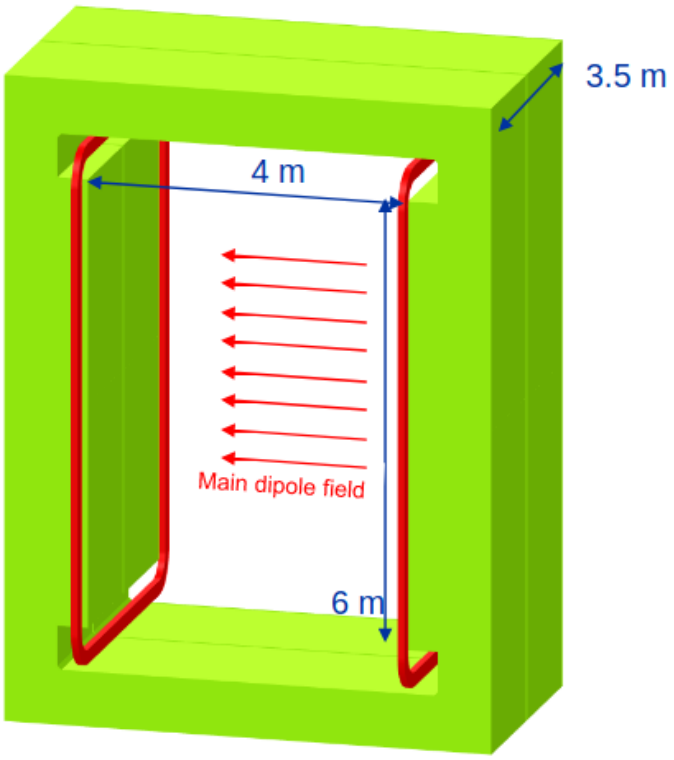

Figure 2.25: SHiP spectrometer magnet, in red are the coils whereas the yoke is displayed in green [320].

2.3.4.3 SHiP Timing detector

The Timing Detector is present to reduce muon combinatorial background to manageable levels through the measurement of a time coincidence between two particles and provide particle identification (PID) through time of flight for charged particles with $p < 10\,\text{GeV}$. For these purposes to be achieved, a timing resolution $\sigma_t < 100\,\text{ps}$ or even $\sigma_t < 50\,\text{ps}$ if necessary.

The Timing Detector will consist of sets of three vertically staggered columns of plastic scintillator, each $144 \times 6 \times 1\,\text{cm}^3$ and readout by an array of eight SiPMs equipped with a custom pre-amplifier and a SAMPIC [322] or FASTIC [323] based front end. There would be 110 rows of bars and the bars would overlap by 5 mm vertically and $\sim 10\,\text{cm}$ horizontally.

2.3.5 SHiP DAQ & Trigger

SHiP is characterised by a very long detector with low-radiation levels of conservatively $\sim 50\,\text{kHz}$ over a $4 \times 6\,\text{m}^2$ plane at the HSS level. The data flow is relatively modest. In addition, there is a complete impossibility to rely on any form of external trigger, considering the length of the extraction (1 s). This implies the use of a fully triggerless readout where hits are provided channel by channel, each containing a channel ID, a coarse time ($\sim 25\,\text{ns}$) and a fine time ($\sim 1\,\text{ns}$) which is sufficient for most detector systems. Certain detectors require either an extra single value in their data stream (ADC for the TT, ultra fine time ($\sim 100\,\text{ps}$), useful for the Timing Detector), an extra fixed amount of information (such as ADC values) or a variable amount of extra data for when the amount of channels firing per event is not fixed [324]. Timing information is particularly crucial as it is what will allow the system to sort data entries and build events.

Thus the system's Common Detector Electronics (CDE) will be defined through three main components: the Timing and Fast Control (TFC) system, which delivers the clock and fast commands; the Experiment Control System (ECS), in charge of the slow control (FE registers and memory access), the monitoring of the detector and the firmware reconfiguration and the Data Transport and Concentration (DTC) system, which is in charge of performing the readout of the physics data produced by the sub-detectors [325].

SHiP is as such divided in autonomous partitions which are all readout during SHiP data cycles (which for instance contain SPS extractions spills). Partition data is merged by concentrators into data streams and sent

to the Partition Front End Host Computer where all data is merged into a final partition data stream. This architecture can be seen in Figures 2.26 and 2.27.

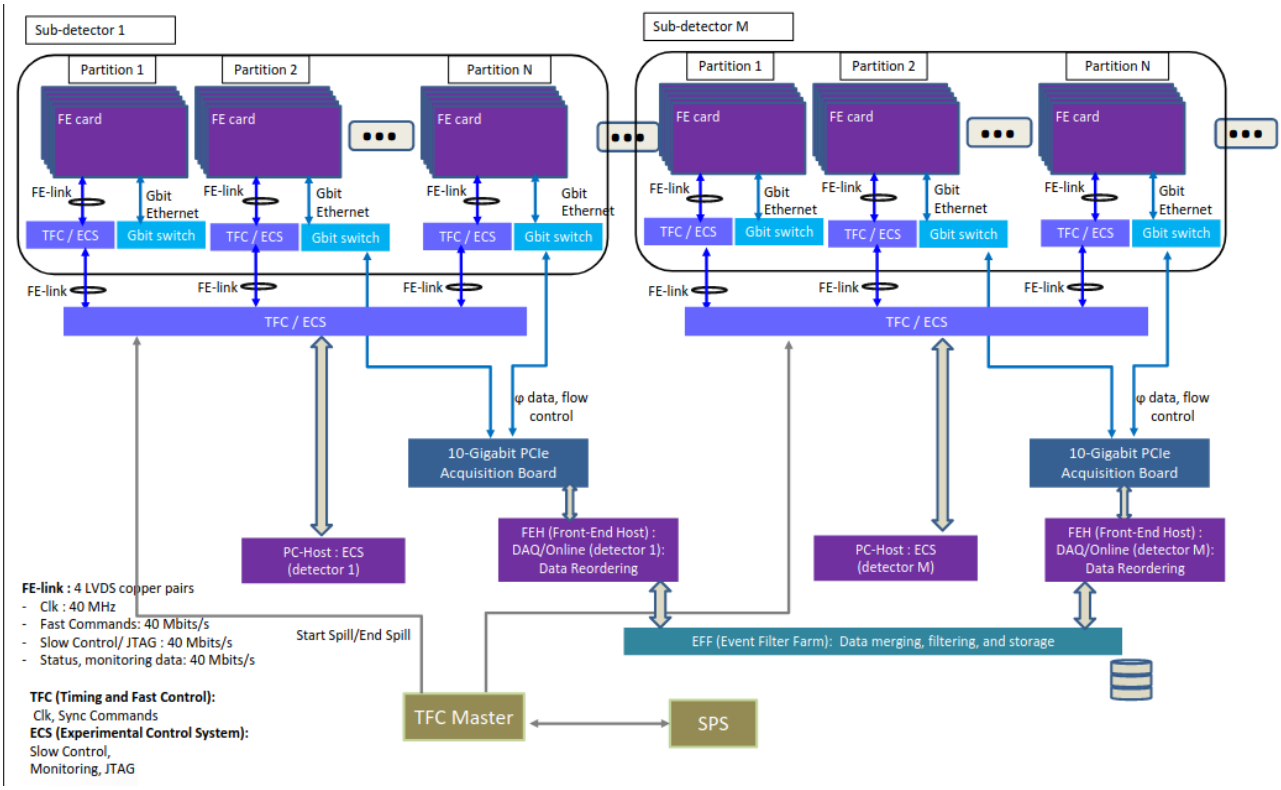

Figure 2.26: SHiP partition system architecture [325].

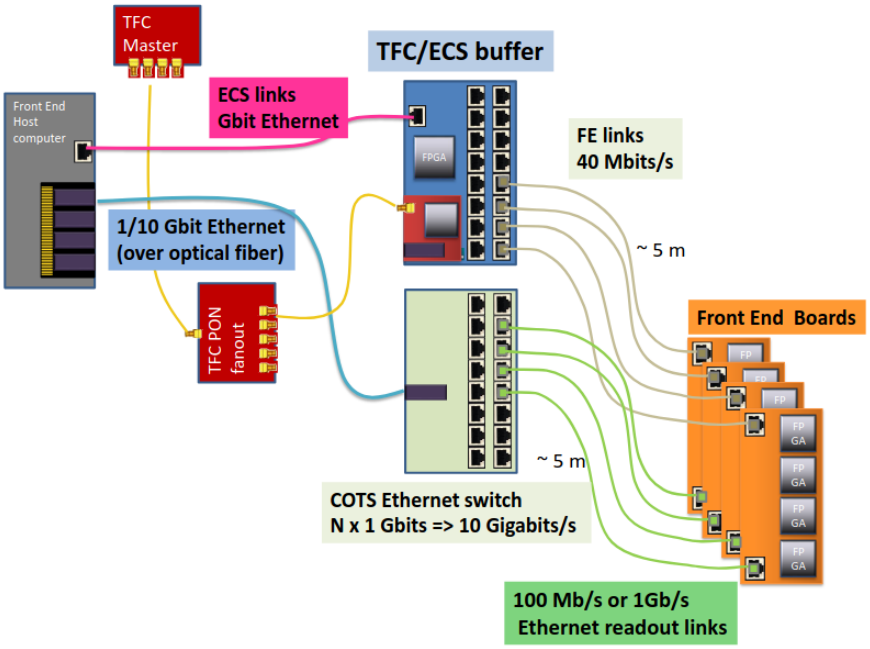

Figure 2.27: SHiP readout scheme [325].

Chapter 3

Particle detectors, calorimetry and the SHiP calorimeter

The observation of particles, whether they be known or new, requires the usage of a particle detector. While detector technologies are incredibly varied, ranging from thin solid state semiconductive layers equipped with readout implants [296, 326, 327] to gaseous volumes [328, 329], the basic physical principles governing these detectors remain mostly common in between them: a particle passes through a sensitive area defined as the detection volume and leaves behind energy. This energy deposition may manifest in different ways which leads to different detector technologies. This chapter will expose different particle interaction mechanisms as well as the principles of a particular type of detectors called calorimeter. Formalism is mainly taken from [330–332], unless otherwise indicated, all fundamental constants, notably c and $\hbar$ are taken as equal to 1.

3.1 Particle interactions with matter

The interactions of particles with matter vary depending on whether they are done by charged particles, photons or other particles. The first two cases are particularly relevant to calorimetry and will thus be presented in the following.

3.1.1 Ionisation

The most common interaction with matter is *ionisation*, governed by the so-called Bethe-Bloch formula:

$$-\left\langle \frac{\mathrm{d}E}{\mathrm{d}x} \right\rangle = Kz^2 \frac{Z}{A}\frac{1}{\beta}\left[\frac{1}{2}\ln\frac{2m_\mathrm{e}c^2\beta^2\gamma^2 T_\mathrm{max}}{I^2} - \beta^2 - \frac{\delta}{2}\right], \tag{3.1}$$

with $\left\langle \frac{\mathrm{d}E}{\mathrm{d}x} \right\rangle$ representing the average ionisation, the proportionality constant $K = 4\pi N_\mathrm{A} r_e^2 m_e c^2$, with $\mathrm{N_A}$ the Avogadro number, r_e the classical electron radius, m_e, the electron mass and c the speed of light, being a proportionality constant, z the charge number of the incoming particle, Z the charge content of the impinged atomic structure, A the mass content of the nuclear structure, T_max the maximum kinetic energy that may be imparted to an electron in a single collision. β is the Lorentz ratio of particle speed and speed of light, γ is the Lorentz relativistic factor, δ is a function of $\beta\gamma$ is the density effect correction term while I is the mean excitation energy.

A key peculiarity of the Bethe-Bloch equation is its complete invariance when set as a function of $\beta\gamma \sim \frac{p}{m}$ in a relativistic approximation. The other remarkable feature is the absolute minimum in energy deposition around $\beta\gamma \sim 3$ as well as the very slow rise of the energy deposition as a function of $\beta\gamma$. As a result of this behaviour, particles with $\beta\gamma > 3$ are typically called *MIPs* (Minimum Ionising Particles). As an example, a muon μ^- (chosen for its limited ability to interact otherwise than through the Bethe-Bloch-described-mechanisms) with a $\beta\gamma \sim 3$ would have $p \sim 300\,\mathrm{MeV}$ and would deposit around 1.5 MeV in 10 cm of a 20–80% $\mathrm{Ar} - \mathrm{CO_2}$ admixture at 1 bar. The same muon, were it to have $p \sim 30\,\mathrm{GeV}$ energy, would deposit a scarce 1.9 MeV in the

same configuration, that is to say, 2 orders of magnitude more energy lead to a mere 30% increase in energy deposition.

A useful approximation is the assumption that all MIPs deposit $\sim 1.4\,\mathrm{MeV\,cm^2\,g^{-1}}$ in materials with $Z \sim 0.5A$. These characteristics are exemplified in Figure 3.1.

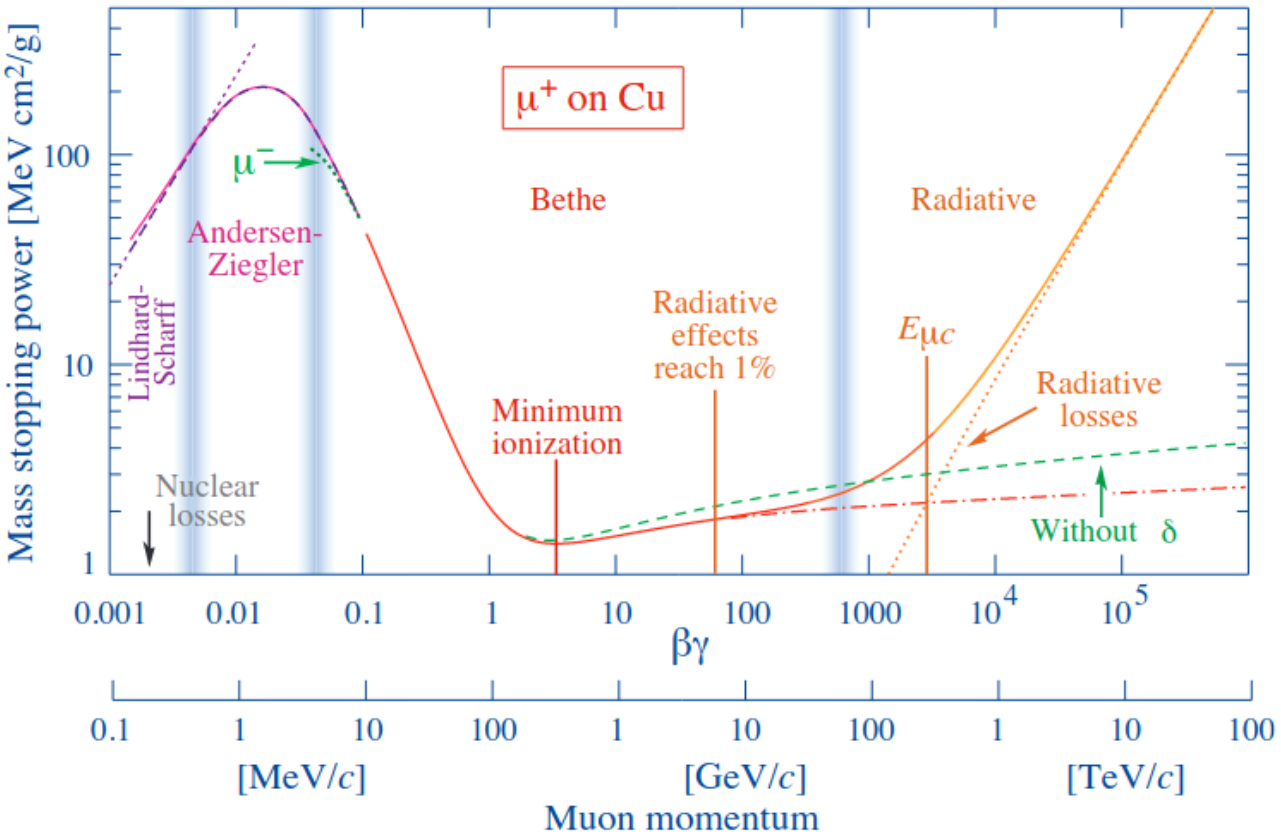

Figure 3.1: Energy deposition in matter for positive muons as a function of $\beta\gamma$. Solid curves indicate total energy loss, dotted lines illustrate the dependence of energy loss on charge at very low energies [11].

The energy deposition of a single MIP follows a Landau distribution:

$$f_L(\lambda) = \frac{1}{\pi}\int_0^\infty e^{-t\ln t - \lambda t}\sin(\pi t)dt \sim f_M(\lambda) = \frac{1}{\sqrt{2\pi}}e^{-0.5(\lambda+e^{-\lambda})}. \tag{3.2}$$

with a most probably value (MPV) given at $\lambda = -0.22278$ and a full width at half maximum (FWHM) given by $\Delta\lambda = 4.018$ in the canonical form. Practically, the Landau distribution is often parametrised as:

$$L(x,\mu,\sigma) = \frac{A}{\pi\sigma}\int_{-\infty}^{\infty}\frac{e^{-\frac{((x-\mu)/\sigma-t)^2}{2}}}{t-\frac{x-\mu}{\sigma}}dt. \tag{3.3}$$

with μ the MPV, σ the width of the distribution and A a scaling factor for the distribution. The Landau distribution in this parametrisation is visualised in Figure 3.2.

The asymmetric shape of the Landau is due to so-called $\delta-$electrons, which are knocked off atoms in the ionisation process and lead to increased ionisation yields.

Ionisation, while common, is however only limited to charged particle interactions and evidently cannot apply to neutral particles such as photons.

3.1.2 Photon interactions in matter

Photons, interact differently than other particles. They have three different behaviours when in matter: *photo-electric effect*, *Compton scattering* and *pair creation*.

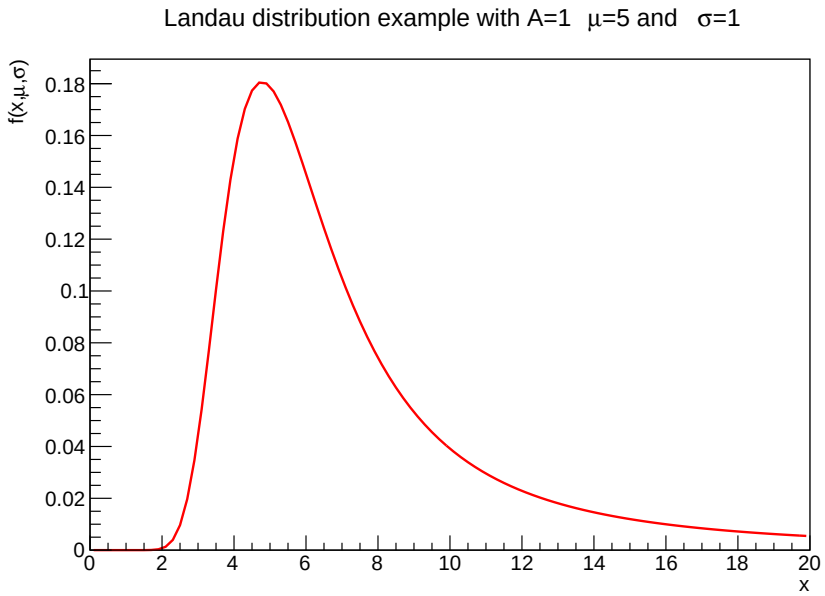

Figure 3.2: Representation of a Landau function parametrised with $\mu = 5$, $\sigma = 1$, A= 1.

3.1.2.1 Photoelectric effect

The photoelectric effect (also called photoeffect) takes places at low energies, it corresponds to the interaction of a photon with an atomic structure, where the photon is absorbed, promoting an electron called *photoelectron* (PE) outside of the atomic shell. The photoelectron energy is described by:

$$E_{e^-} = h\nu - E_{\mathrm{b}}, \tag{3.4}$$

where h is the Planck constant, ν the photon frequency and E_{b} the bonding energy of the electron within the atom. The probability of photoelectric interaction $\tau \propto \frac{Z^{\mathrm{n}}}{(h\nu)^3}$ where n varies between 3 and 4 over the energies of interest [11].

This form of interaction is utilised in all manners of photon detectors, such as *Photomultiplier tubes* (see [333]) or particularly *Silicon Photomultipliers* (see Section 3.3.5.3).

3.1.2.2 Compton scattering

Compton scattering is the deflection of the incoming photon accompanied with the emission of a *Compton electron*. The scattering process is kinematically described by the energy of the outgoing photon E'_γ:

$$E'_\gamma = \frac{E_\gamma}{1 + \varepsilon(1 - \cos\theta)}, \tag{3.5}$$

where θ is the outcoming photon's angle with respect to the incoming photon's angle and $\varepsilon = \frac{E_\gamma}{m_e c^2}$. The energy of the Compton electron is defined:

$$E_{e^-} = h\nu \frac{\alpha(1 - \cos\theta)}{1 + \alpha(1 - \cos\theta)}. \tag{3.6}$$

The Compton scattering cross section is largely (but not entirely) independent of Z and generally falls as a function of photon energy $\sigma \sim \frac{1}{E}$. It is directly proportional to the medium's electron density which varies very little from material to material (only $\sim 20\%$ variation from the lightest to the heaviest elements, hydrogen excluded).

3.1.2.3 Electron pair creation and bremstrahlung

The by-far dominant process for photons with energies above $2m_e$ is pair creation, where $\gamma \rightarrow e^- e^+$. Pair creation takes place when a photon is in the field of a charged particle, typically a nuclear electromagnetic field.

It is possible to average the radiated bremstrahlung energies to obtain the mean energy loss per path length:

$$\frac{\mathrm{d}E}{\mathrm{d}x} = \frac{N_\mathrm{A}}{A} \int_0^E E_\gamma \frac{\mathrm{d}\sigma}{\mathrm{d}E_\gamma} dE_\gamma. \tag{3.7}$$

The electron's mass is here neglected, A is the nuclear mass number and N_A the Avogadro number. The characteristic length for energy loss through bremstrahlung, X_0, is given by:

$$\left(\frac{\mathrm{d}E}{\mathrm{d}x}\right)_\mathrm{rad} = -\frac{E}{X_0} \quad ; \quad E(x) = E_0 e^{\frac{x}{X_0}}, \tag{3.8}$$

where X_0 is called the material dependent *radiation length* and implies that the average electron will only retain $1/e$ ($\sim$37%) of its initial energy after passing through one radiation length.

As pair creation and bremstrahlung are similar concepts as mentioned previously, it is possible to express the pair production cross section as a function of X_0 as:

$$\sigma_\mathrm{pair} \sim \frac{7}{9} \frac{1}{X_0} \frac{A}{N_\mathrm{A} \rho}, \tag{3.9}$$

ρ being the material density, which implies a photon absorption length for pair production or mean free path λ_γ:

$$\lambda_\gamma = \frac{A}{\sigma_\mathrm{pair} \rho N_\mathrm{A}} = \frac{9}{7} X_0. \tag{3.10}$$

This translates to X_0 being the length over which pair creation takes place with a probability of $P(\gamma \rightarrow e^+ e^-) = 1 - e^{\frac{7}{9}} = 54\%$, smaller than that of bremstrahlung for an electron.

These main defining features of both bremstrahlung and pair creation processes give rise to *electromagnetic showers* (EM showers) formed by electrons and photons which are the core feature in (electromagnetic-)calorimeters.

3.1.2.4 Hadron interactions

Compared to leptons and apart from ionisation and bremstrahlung, hadron interactions in materials are significantly more complex, particularly as they have access to a much wider variety of interactions. It is however possible to treat them with limited analogy to EM processes, in particular with a nuclear absorption length λ_a:

$$N(x) = N_0 e^{-\frac{x}{\lambda_a}} \quad ; \quad \lambda_a = \frac{A}{N_A \rho \sigma_\mathrm{inelas}}, \tag{3.11}$$

with N_0 the number of hadrons entering the medium, σ_inelas the inelastic scattering cross section of the hadron and x the distance.

The key characteristic of hadron interactions is that $\lambda_a \gg X_0$ as $X_0 \sim \frac{A}{Z^2}$ whereas $\lambda_a \sim A^{1/3}$. This implies that a considerably greater amount of material is necessary to stop a hadronic shower than a photon or electron showers. This implies large differences in hadronic showers topologies compared to their EM counterparts.

3.2 Calorimetry

Calorimeters are versatile detectors as they may, depending on chosen technologies, provide information in particle identification, timing resolution and position determination. Nonetheless the main added value of calorimeters in a detector system is their energy reconstruction which will be described here.

3.2.1 Introduction

Although their name may suggest otherwise, calorimeters in high-energy physics are not effective in the reconstruction of temperatures. Although eventually nearly all of the energy lost in a material through the processes described in Section 3.1 is done in the form of a temperature rise, an impressive 1 TeV energy loss in a material would only corresponds to around 10^{-7} cal. Calorimeters in high-energy physics are *destructive* detectors in that the measured particle typically doesn't escape the detector volume. As a result they are often placed at the end of the detection chain, followed only by detectors meant to observe what particles may survive the calorimeter (see Section 2.2.3.3).

Since calorimeters aim to stop particles, the crucial question of its composition is asked. If the calorimeter is to be made entirely with sensitive volumes, it may end up being fairly large and quite expensive but may attain extremely good energy resolution. On the other hand, should most of the stopping power be provided by dense (comparatively) inexpensive passive material such as iron, tungsten, lead or uranium, it will lose in resolution but will be more affordable. This distinction defines *homogenous calorimeters* [334, 335] on the one hand and *sampling calorimeters* [336, 337] on the other, which are both visualised in Figure 3.3. Furthermore, calorimeters are often distinguished between electromagnetic calorimeters (ECAL) and hadronic ones (HCAL) as the significantly larger λ_a implies a need for significantly more material than EM calorimeter. For this reason, hadronic calorimeters are also rarely homogenous calorimeters.

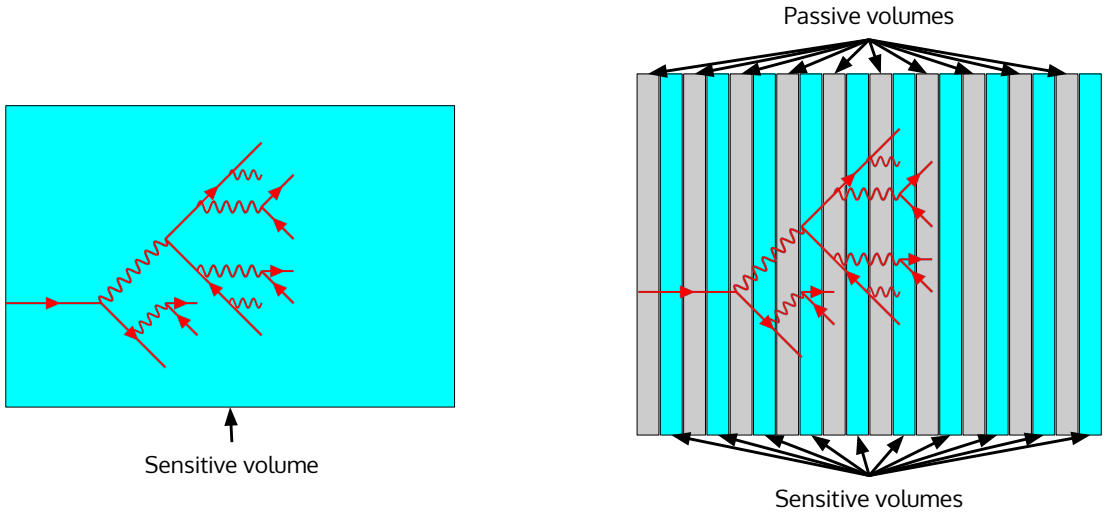

Figure 3.3: Visualisation of a homogenous calorimeter (left) and of a sampling calorimeter (right).

The resolution of a calorimeter would in principle be limited by the particle number $\sqrt{N} \sim \sqrt{E}$ assuming every particle is seen as a direct consequence of Poisson statistics. In practice, however, it is limited by the three factors:

$$\frac{\sigma}{E} = \sqrt{\frac{a^2}{E} + \frac{b^2}{E^2} + c^2} = \frac{a}{\sqrt{E}} \oplus \frac{b}{E} \oplus c. \tag{3.12}$$

- a is the so called *stochastic term* and is directly derived from Equations 3.8 and 3.9 which encompasses the Poisson statistics inherent to particle showers $N_{\text{particle}} \propto E_0$ therefore $\sigma(E) \propto \sqrt{N}$. a therefore regroups uncertainty due to the intrinsic random nature of shower fluctuations, the fluctuations in the sampling for sampling calorimeters as well as signal quantum fluctuations. The stochastic term is as such mitigated by using a homogenous calorimeter and utilising detectors with high-quantum efficiency (see Section 3.3.5).
- b is known as the *constant term*, it regroups inhomogeneities in hardware variations (in dimensions, response...) or calibration uncertainties, non-linearities in readout electronics (see Chapter 6), fluctuations in longitudinal containment of the showers and fluctuations in the energy lost in passive material before or within the calorimeter. b is the main limitation in energy resolution at low energies and is typically dominated by electronic noise.

- c is denominated the *noise term* as it arises from imperfections in the calorimeter, be they electronic or mechanical in origin. Notable among those imperfections is energy leakage which is significant for thinner calorimeters. c is the ultimate uncertainty at high energies and is reduced by minimising the noise within the readout electronics as well as detector radioactivity and simultaneous events within the readout window (also known as *pile-up*).

The resolution of calorimeters becomes instrumental for larger energies as, unlike trackers, their relative energy resolution *improves* as energies get larger. c is the ultimate liming factor at high energies as it remains constant while all other terms see their contribution to energy reconstruction uncertainty decrease as a function of energy.

Sampling calorimeters typically suffer from large stochastic terms. This is determined by the so called *sampling fraction* which is defined as the ratio of visible and total deposited energy:

$$f_{\mathrm{s}} = \frac{E_{\mathrm{vis}}}{E_{\mathrm{dep}}}. \tag{3.13}$$

which is typically of the order of a few percent. Hadronic calorimeters are exclusively sampling whereas electromagnetic calorimeters often make use of sampling techniques as an effective mean to reduce their costs.

3.2.2 Reconstruction of electromagnetic showers

3.2.2.1 Electromagnetic shower development

Electromagnetic showers develop primarily through the processes described in Section 3.1.2.3 and are the basis of electromagnetic calorimetry. They are initiated by either (anti-)electrons which then develop into shower through bremstrahlung, or photons which undergo pair creation. This then cascades into a shower. While the internal dynamics of an electromagnetic shower are rather complex, a common approximation known as *Rossi's approximation B* [338] is often used as it displays a good match with observed data. In this hypothesis, only bremstrahlung and pair creation are considered, multiple scattering is neglected, the shower is assumed to propagate in a single direction and it is assumed that path-wise energy loss is energy independent and may be approximated as:

$$\left(\frac{\mathrm{d}E}{\mathrm{d}x}(E_c)\right)_{\mathrm{ion}} X_0 = -E_{\mathrm{c}}. \tag{3.14}$$

where E_{c} is defined as the critical energy, at which ionisation becomes the largest energy loss mechanism for electrons, rather than bremstrahlung. Important is the scaling: namely that the shower development profile is largely independent from the material for a given radiation length count (see Equation 3.8). An assumption shown in Figure 3.4 is made that for each particle and after each radiation length, either bremstrahlung or pair creation occurs once on average and each final particle carries half of the energy of the initial particle:

Under this assumption, $\frac{1}{X_0} \propto Z^2$, implying a performance improvement for elements higher in the periodic table such as lead, tungsten or uranium. As the shower progresses in the longitudinal direction, the number of particles, proportional to the total shower energy increases:

$$N = 2^t, \quad E = \frac{E_0}{2^t}, \tag{3.15}$$

where t is the path length in units of X_0. This induces a maximum number of particles N_{max}, corresponding to the shower maximum at t_{max}:

$$E = E_c = \frac{E_0}{2^{t_{\mathrm{max}}}}; \quad N_{\mathrm{tot}} = \frac{E_0}{E_c}; \quad t_{\mathrm{max}} = \frac{\ln \frac{E_0}{E_c}}{\ln 2}. \tag{3.16}$$

Significantly, N_{max} is proportional to the initial energy E_0 while t_{max} logarithmically increases with E_0.

3.2.2.2 Longitudinal shower profile and Longo formula

The containment of the shower within the calorimeter is of primary concern to detector design, indeed it is not possible to reconstruct shower energy if the shower maximum is reached in the last sensitive layer or beyond it.

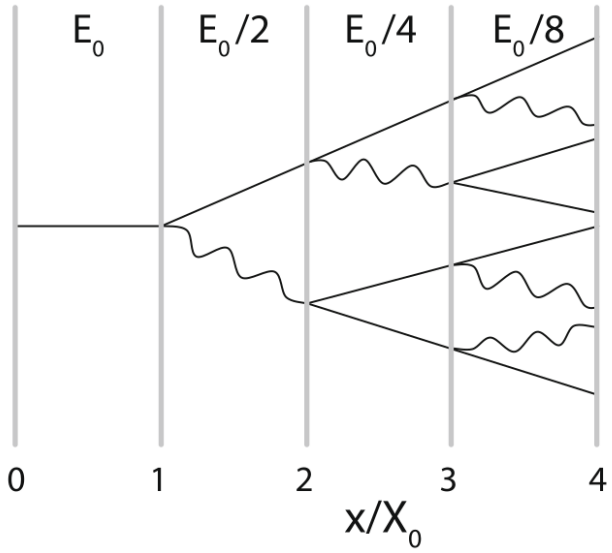

Figure 3.4: Visualisation of shower evolution according to Rossi's approximation B. Each X_0 causes a doubling in particle count and thus a halving of particle energy [330].

Simultaneously, the channel number typically increases with calorimeter length leading to a need to optimise the length to contain the shower while minimising readout channel count and thus cost.

The longitudinal profile of EM showers has been parametrised by Longo and Sestili in 1975 [339] in the semi-empirical *Longo formula*:

$$\frac{\mathrm{d}E}{\mathrm{d}t} = E_0 \frac{b^a}{\Gamma(a)} t^{a-1} e^{-bt}, \tag{3.17}$$

where a, b depend on E_0 and Z. Looking for the function roots it is possible to derive $t_{\max} = \frac{a-1}{b} = \ln \frac{E_0}{E_c} \pm \frac{1}{2}$ with the negative sum for electron-induced showers and the positive one for photon-induced ones.

3.2.2.3 Transverse shower profile

The angles θ of scattered electrons and photons with respect to the initial particle's path are typically quite small in EM showers as $\theta \propto \frac{1}{\gamma} = \frac{m_e}{E}$, since the electron mass is small compared to their kinetic energy. The transverse shower profile is therefore mainly given by processes such as multiple scattering for electrons and Compton scattering for photons.

The transverse shower profile is characterised by the *Molière radius* R_M which defines the radius of a cylinder containing 90% of the shower's energy. The shower transverse profile decreases rapidly with distance, thus a cylinder with a radius $r = 2R_\mathrm{M}$ contains 95% and a cylinder with $r = 3.5R_\mathrm{M}$ will contain 99% of the shower energy.

The relative shower width tends to be wider for lighter elements, this can be seen in Table 3.1 which lists the materials most relevant for this work.

Material	Z	X_0 [cm]	E_c [MeV] (e^-)	E_c [MeV] (e^+)	R_M	λ_a [cm]	Minimum ionisation [MeV cm^{-1}]
polystyrene	3.5	41.31	93.11	90.65	9.409	77.07	2.052
polyvinyltoluene	3.37	42.54	94.11	91.62	9.586	78.80	2.019
iron	26	1.757	21.68	21.00	1.719	16.77	11.43
tungstene	74	0.3504	7.97	7.68	0.9327	9.946	22.10
lead	82	0.5612	7.43	7.16	1.602	17.59	12.74

Table 3.1: Calorimetric characteristics of relevant materials [11].

3.2.3 Reconstruction of Hadronic showers

Hadron-induced showers have different properties with respect to electromagnetic showers. Incoming particles undergo inelastic scattering with nucleons within nuclei. This leads to most of the energy inducing the emission of hadrons in the forward direction. A smaller portion of the energy is transferred to other nucleons inducing processes called an *intranuclear cascade* with neutrons being ejected about $\sim$ 1.5 times more frequently to protons as a result of differing relative abundances within the nuclei. This process repeats with dynamics akin to those of EM showers but may be interrupted when the produced particle is a π^0 (which quickly decays almost exclusively into $\gamma\gamma$) or an η (which decays exclusively into some combination of π^0 and γ) [11]. In this case, the shower obtains an electromagnetic component which is independent from the hadronic contribution. The nuclei left over from these processes are excited and undergoes spallation processes until around 100 MeV are lost.

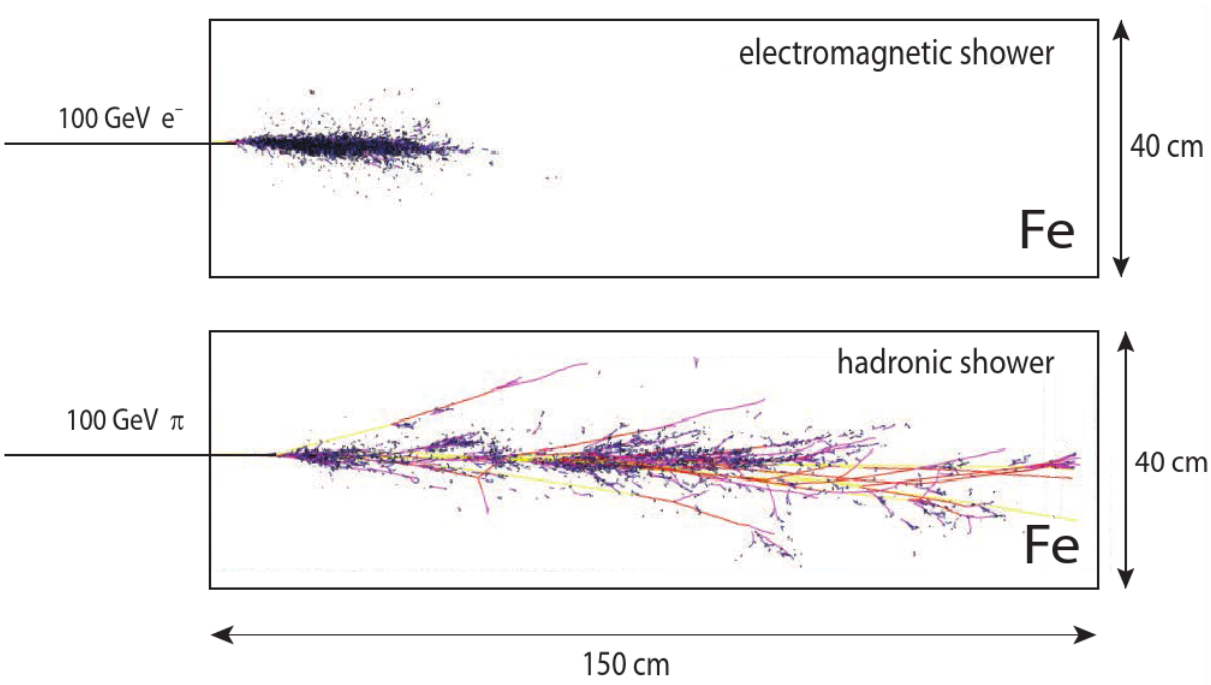

Figure 3.5: Simulation of showers in an iron block. Only ionising particles are plotted [330].

The hadronic shower deposited energy is thus split into *electromagnetic*, *ionisation*, *neutron*, *photon* and *nuclei breaking* contributions and fluctuates considerably more than EM ones. The energy resolution of HCALs is typically much worst than that of ECALs as a result of greater losses in fluctuating invisible processes (such as nuclei breaking or neutrino emission) and the fluctuations in the electromagnetic fraction in hadronic showers [331, 340, 341].

The longitudinal profile of the hadronic shower is dictated by the *nuclear interaction length* λ_a with $\frac{\lambda_a}{X_0} \sim 0.37Z$for most common materials such as iron. Standard hadronic calorimeters are generally around $5\lambda_a$ long [267] [340] which allow for satisfactory containment. Transverse sizes of hadronic showers are extremely variable from event to event, the rule of thumb $R_{95\%} \sim \lambda_a$ is generally valid with precise values depending on the material [331].

3.2.4 Particle identification with calorimeters

Particle identification (PID) is an essential role of calorimeters. It is done by isolating the particle type based on its unique characteristics. In high energy physics, these are primarily the particle's charge, its mass and main interactions. Calorimeters are instrumental in PID performance as they allow for the precise identification of electrons, photons, hadrons and muons which will interact differently with the calorimeter materials. Electrons, charged hadrons and muons are seen in the tracing system whereas photons and neutral hadrons are not. Electrons and photons shower and are stopped inside of the ECAL section of the calorimeter system whereas

hadrons usually shower and be stopped in the HCAL section. Muons mostly escape the detector entirely while being observed by every subsystem. These behaviours allow for PID to occur, shown in Figure 3.6.

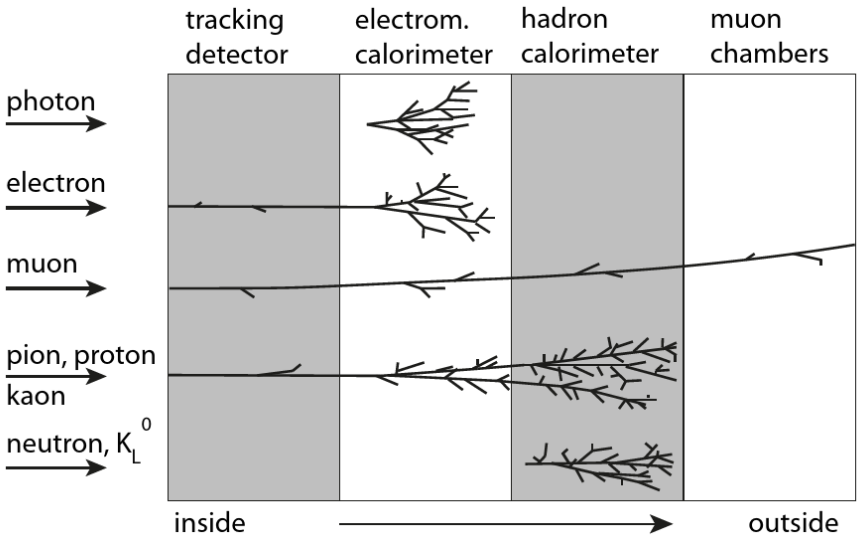

Figure 3.6: Illustration of particle identification in different detectors [330].

While this allows to obtain good performance, rarer events (for instance pions showering significantly in the ECAL) remain. These prevent the system from reaching PID performance at the level of 10^5 rejection or better [342]. This imposes the use of more refined PID techniques.

Calorimeters can obtain additional e/μ/hadron separation through the measurement of the shower shape. As described in Section 3.2, shower widths and depths are significantly different between hadronic and electromagnetic showers with the latter being both wider and deeper. In addition, EM showers start earlier inside a material than hadronic showers. It thus becomes possible to perform PID by discriminating over the shower starting point and the ratio of deposited energy in the front and at the back of the calorimeter, or reconstructing containment cylinders: in iron, a cylinder with 3.4 cm radius contains 95% of an EM shower's energy, whereas a 16.8 cm cylinder will be required for a hadronic shower. Another useful technique consists in observing differences in the E/p ratio, with the calorimeter observing the energy E and the spectrometer observing the momentum p. Finally, machine learning techniques have become increasingly popular in the past years, with the finest separation coming out of these techniques. They leverage multivariate analysis to well capture the correlations between the evolution of different variables such as the ratio of deposited energy in the front and at the back of the calorimeter or E/p to finely discriminate between different incident particles.

The SHiP calorimeter system has to perform these PID roles, particularly ensuring separation between electrons, pions and especially muons as the latter will form the large majority of visible incoming particles. Muon rejection must therefore be brought to excellent levels.

Muon/electron separation, beyond the techniques described above, is mainly worsened by catastrophic muon bremstrahlung: in this rare process, the muon showers and loses the entirety of its energy electromagnetically, making it impossible to distinguish from electrons [342]. In these cases, amongst the most effective approaches consist in tagging the starting point of the bremstrahlung development within the calorimeter system.

Muon/pion can be performed well with separation mainly being limited by pions decaying in flight into muons.

Pion/electron separation is primarily performed through longitudinal shower profiles (see Sections 3.2.2 and 3.2.3) and E/p. Certain electrons will however shower late whereas certain pions will shower early, creating some overlap in shower profiles, which is detrimental to PID performance. This is problematic particularly in the case of higher energy particles for which $\frac{E}{p}$ separation is more difficult. In these extreme cases, using the HCAL allows to be more sensitive to the hadronic fraction, as transversal shower analysis may be performed. This can help in identifying early-showering pions. These PID roles are to be performed by the SHiP calorimeter system, together with the reconstruction of neutral final states, particularly $\gamma\gamma$.

3.3 Calorimeter technologies

The great breadth of calorimeter technologies implies very different advantages and disadvantages. The build and calibration of a calorimeter determines to a large extent the b and c terms of its resolution (see Section 3.2.1). Relevant technologies will be the focus of the ensuing discussion.

3.3.1 Homogenous calorimeters

Homogenous calorimeters stand out for their exceptional energy resolution [334, 343, 344], therefore being closest to the primary purpose of calorimeters as a result of the minimisation of unseen stochastic variations. This leads to an integral reconstruction of energy deposition without any unseen shower elements. The intrinsic shower stochastics then become the limiting factor for energy resolution.

3.3.2 Sampling Calorimeters

Sampling calorimeters generally display inferior energy resolution to their homogenous counterparts, nonetheless they are easier to build mechanically, partially recovering through a better b and perhaps c what they loose in a (see Section 3.2.1). They are ubiquitous among hadronic calorimeter. Sampling calorimeter are made of passive, heavy material interleaved with sensitive material. Common passive materials are iron, brass, lead or uranium.

The effects of the sampling on the stochastic term can be parametrised in Rossi's Approximation B (Section 3.2.2.1) which directly provides the poissonian sampling uncertainty:

$$\left(\frac{\sigma_E}{E}\right)_{\text{sampling}} = \frac{1}{\sqrt{N_{\text{vis}}}} = \sqrt{\frac{tE_c}{E_0}} = 0.032\sqrt{\frac{tE_c[\,\text{MeV}]}{E[\,\text{GeV}]}} = a_t\sqrt{\frac{t}{E[\,\text{GeV}]}}. \tag{3.18}$$

The stochastic term is determined by the sampling t, $a_t \equiv \frac{a}{\sqrt{t}}$, the sampling frequency is defined by $\nu_s = \frac{1}{t} = \frac{X_0}{d}$ with d being the geometrical thickness of a passive layer.

3.3.3 Gas sampling calorimeters

Gas-filled calorimeters have been in wide use until the 1990s as a result of their great segmentation flexibility and low cost. They are notable also for their very low sampling fraction, often smaller than 1%. They are ordinarily operated in proportional mode (see Section 2.3.4.2). Deploying gas detectors in calorimeters is only possible in a sampling calorimeter as the radiation length of such a homogenous device would make it prohibitively large. These detectors suffer from large Landau fluctuations as a result of small N (see Section 3.1.1). In addition, the constant term reduction tends to be challenging beyond a certain point as gain is extremely sensitive to difficult-to adjust factors such as readout wire diameter and position, gas pressure, temperature and purity and high voltage setting. Gas-filled calorimeters were very common at LEP, with in particular the ALEPH lead-gas ECAL calorimeter [28] and the DELPHI time projection chamber ECAL [29].

3.3.4 Scintillators

Scintillators are materials which emit light when exposed to ionising radiation and are a particularly popular technology for calorimetry: they combine a wide variety of valuable properties: robustness, fairly large emission of signal particles (photons) which increases N and thus minimises the stochastic term. Depending on the choice of technology, can be found for a relatively low cost which allows for simple assembly of large scale calorimeters by collecting the produced photons in dedicated photosensors. Important scintillator properties include linearity of light yield L_γ defined as $\langle N_\gamma \rangle = L_\gamma \times E$.

3.3.4.1 Scintillation

Scintillators are broadly divided into organic and inorganic types, each with distinct light-emission mechanisms. Organic scintillators are typically based on aromatic molecules—such as those found in certain crystals or plas-

tics—which emit visible or UV light after absorbing high-energy radiation. This emission, called luminescence, arises from molecular structures with alternating double bonds (conjugated systems) and is influenced by how carbon atoms bond within the molecule. Light absorption promotes electrons to higher-energy singlet states, and the subsequent return to the ground state results in fluorescence. This process is fast (nanoseconds) and produces a characteristic spectrum that depends on the molecule's structure but not on the exact excitation path, due to rapid internal energy redistribution. Other slower emissions can also occur, such as phosphorescence, which involves longer-lived states, and delayed fluorescence, which follows non-radiative pathways. Inorganic scintillators, on the other hand, rely on the band structure of crystals. When doped with impurities, these crystals form energy states that allow visible light emission. Unlike organic materials, their light yield is generally higher because less energy is lost in non-radiative processes.

3.3.4.2 Plastic scintillators

An important property of scintillators is their transparency as reabsorption of emitted photons is undesirable. This implies the need for a large Stokes shift: the partial overlap between fluorescence and absorption spectra with the difference between peaks. This is achieved rather inexpensively using a plastic base (polyvinyltoluene [PVT] or polystyrene) and the addition of wavelength shifters (WLS). The primary WLS agent or dye is meant to ensure a larger overall light yield with a shorter emission rise time than the base material, they have good quantum efficiencies (see Section 3.3.5) and spectral conformity: the overlap between the base's emission spectrum and that of the primary agent's absorption spectrum is large. The strongest and fastest couplings between plastic base and primary agent provide a fast emission rise time of $\mathcal{O}$(ns) while typical absorption length are of the order of a couple of meters. The concentration in primary agents remains small and is further reduced for the secondary agent to minimise self reabsorption.

A classical example of plastic scintillator is the PVT/p-terphenyl/POPOP combination shown in Figure 3.7.

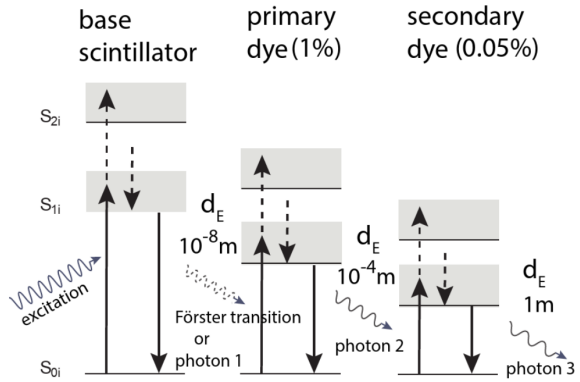

(a) Schematical representation of wavelength shifting: the base scintillator (here PVT) is excited and its deexcitation photon or Förster transition excites the primary agent (here p-terphenyl) the deexcitation photon of which excites the secondary agent (here POPOP). Spatial distances d_E are also shown [330].

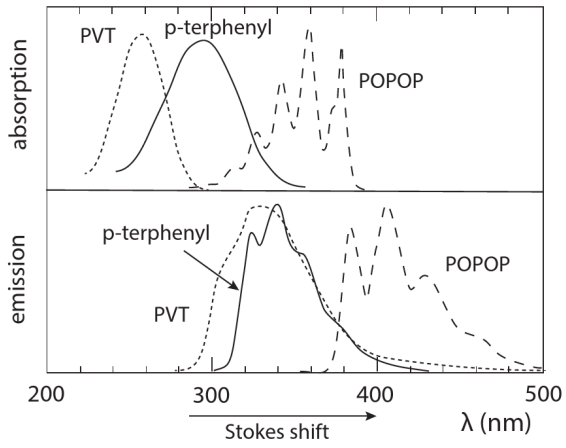

(b) Absorption and emission spectra of PVT, p-terphenyl and POPOP. The y axis is in arbitrary albeit linear units [330]. The good absorption spectrum coverage and large Stokes shift achieved implies good final light yield and transparency making it a good plastic scintillator.

Figure 3.7

Plastic scintillators are extremely common in particle detectors as a result of their good performance and low price point as well as flexible geometry. Their main disadvantage is their low radiation hardness, with their light yield decreasing notably after $\mathcal{O}$(kGy) doses which has lead the CMS experiment for instance to use radiation harder silicon sensors in the inner regions of its High Granularity Calorimeter while preferring plastic scintillators in the outer regions which are subject to lower fluences [345]. Plastic scintillators are used in particle detectors as bars (see Section 4), plates [346], tiles [347] or fibres, as will be shown in the following.

3.3.4.3 Scintillating and wavelength-shifting fibres

Scintillating fibres make use of a mixture of scintillating and optical properties to *trap* light within them and guiding it to its ends. The typical fibre revolves around a scintillating core and one or more cladding layers as shown in Figure 3.8, although other geometries also do exist [348] [349].

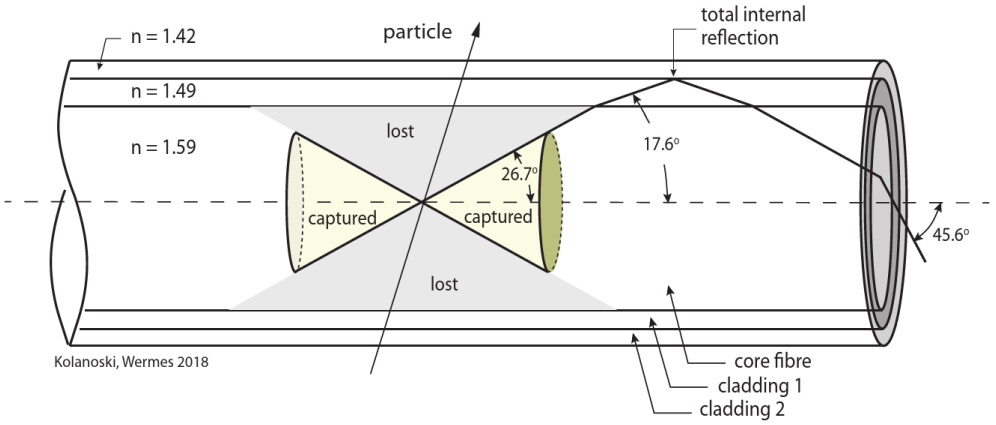

Figure 3.8: Representation of a scintillating fibre and the process of light trapping [330].

Light trapping is done by enhancing total internal reflection induced by the Snell-Descartes law used when light crosses between two media:

$$n_1 \sin\theta_1 = n_2 \sin\theta_2, \tag{3.19}$$

where n_1 and n_2 are the optical indices of the initial and final medium respectively and θ_1 and θ_2 are the incoming and outgoing photon angles. This implies a *critical angle* $\theta_{\text{crit}} = \frac{n_2}{n_1} = \frac{n_{\text{clad}}}{n_{\text{core}}}$ above which light is trapped within the first medium, the aforementioned total internal reflection. A compromise is found between better trapping, induced by high (outer) cladding optical indices comparatively to base material and core optical indices, and good capture induced by low (outer) cladding optical index relative to the core, as too high cladding indices may prevent scintillation from occurring in the core. The total trapped fraction is:

$$f_{\text{trap}} = \frac{1}{4\pi}\int_0^{\pi-\theta_{\text{crit}}} 2\pi \sin\theta d\theta = \frac{1}{2}\left(1 - \frac{n_{\text{clad}}}{n_{\text{core}}}\right). \tag{3.20}$$

Light produced in the fibre is attenuated through the usual $I(x) = I_0 e^{-\frac{x}{\Lambda_{\text{att}}}}$ with Λ_{att} being an effective wavelength dependent value.

3.3.5 Photodetectors

Photodetectors are here taken as the detection of photons in the near-UV, visible and near-infrared range and are essential to all experiments relying on any form of light production, be it obtained through scintillation or Cherenkov. They function around absorbing photons and converting them into some form of electronic signal, be it as a chemical modification (in human eyes or photographic emulsion films for instance) or as an analogue electrical signal.

In (modern) particle physics detectors however, two large families of photodetectors exist: photocathode and semiconductor-based ones with some more niche ones also being used, those including gas detectors or photoemulsion (see Sections 2.3.4.2 and 2.2.3.2 respectively).

3.3.5.1 Photocathode photodetectors and photomultipler tubes

Photocathode-based detector rely on a *photocathode* to convert the incoming photon into an electron. The electron then migrates to the photocathode's surface and (iii) escapes from the photocathode surface to the vacuum. This allows the definition of *quantum efficiency* (QE):

$$Q = \frac{N_{\gamma \mathrm{em}}}{N_{\gamma \mathrm{in}}}, \tag{3.21}$$

with $N_{\gamma \mathrm{em}}$ and $N_{\gamma \mathrm{in}}$ being the amount of emitted and incoming photons respectively. This technique is used in *Photomultiplier Tubes* (PMT) shown in Figure 3.9.

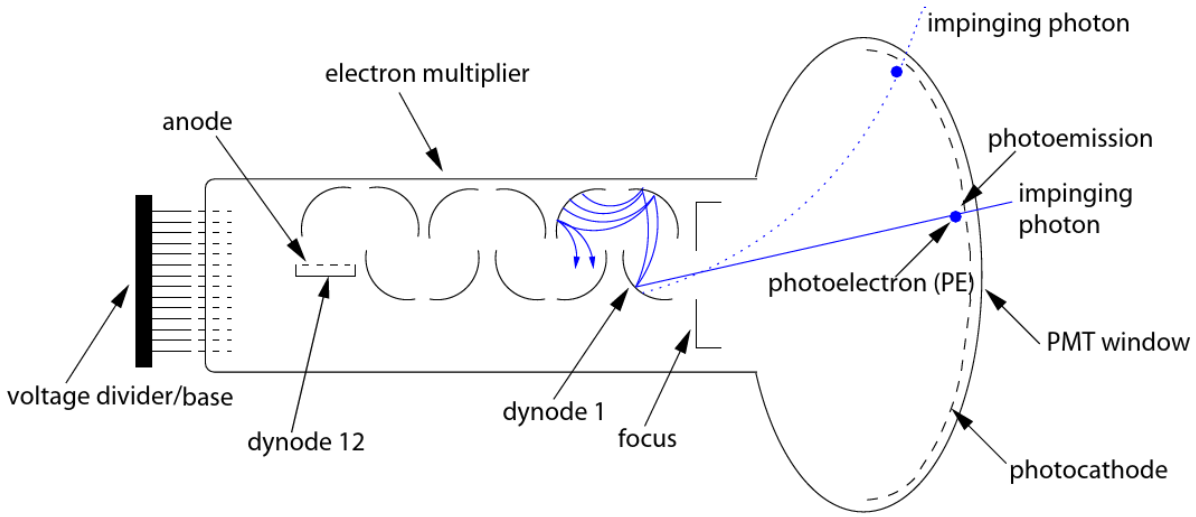

Figure 3.9: Working principle of a PMT: the incoming photon is converted into an electron by the photocathode and then stage-amplified by dynodes of increasing bias voltage until the analogue signal is collected by an anode [330].

PMTs perform excellently in low intensity applications as a result of their low noise rating. They can also be very fast [350] and reach large footprints for large detectors [351]. They can however be expensive, are very sensitive to magnetic fields, require high voltage (in excess of 1 kV) to operate and are fairly delicate as a result of their vacuum content, making them an implosion hazard.

3.3.5.2 Semiconductor photosensors and PIN photodiodes

Photodetection may be achieved without a photocathode but by using the photoeffect to promote an electron from the valence to the conduction band and thus creating an electron-hole pair (e/h) which are then separated by an electric field which also depletes the medium of free charge carriers. The charge carriers, e and h then migrate to the readout electrodes, their movement inducing a voltage which can then be readout. In the most commonly used semiconductor, Silicon, the required minimal photon energy is $E_{\mathrm{min}} \sim 1.12\,\mathrm{eV}$ corresponding to $\lambda_{\mathrm{max}} \sim 1100\,\mathrm{nm}$.

Silicon is an indirect bandgap semiconductor however, leading to a momentum requirement to bridge the bandgap. Thushus a typical needed photon energy of $E_{G,\mathrm{typ}} \sim 3.4\,\mathrm{eV} \rightarrow \lambda_{\mathrm{typ}} \sim 360\,\mathrm{nm}$. Quantum efficiency peaks around 400 nm for silicon-based photosensors.

These properties lead to the PIN (positive-intrinsic-negative) photodiode, the simplest semiconductor photodetector. The photodiode functions by applying reverse-bias to an PN junction interleaved with an undoped region where free charge carrier density derives from impurity density called the *intrinsic zone* (the I in PIN diode), thus depleting the material, including the intrinsic zone from free charge carriers. An incoming photon with the required energy can thus create e/h pairs which are separated by the E-field in the diode, as such inducing currents in the readout electrodes. The principle is showed in Figure 3.10.

Photodiodes have much larger quantum efficiency integrated over a much broader wavelength range ($\sim 190 - 1100\,\mathrm{nm}$) than PMTs with the typical $Q_{\mathrm{PIN}} > 50\% > 25\% \sim Q_{\mathrm{PMT}}$. They in addition require much lower operating voltages of $\mathcal{O}(10\,\mathrm{V})$ and are largely immune to magnetic field effects. The main disadvantage is the worse time resolution (σtiming,PIN $\sim 2\,\mathrm{nm} >$ σtiming,PMT$\sim$200 ps), their small sensitive area and particularly their lack of any form of intrinsic amplification leading to smaller light sensitivity at low intensities. This last disadvantage is the dominant one for photodiodes as their noise profile is dominated by amplification electronics which leverage dark current and capacitance (see Chapter 6).

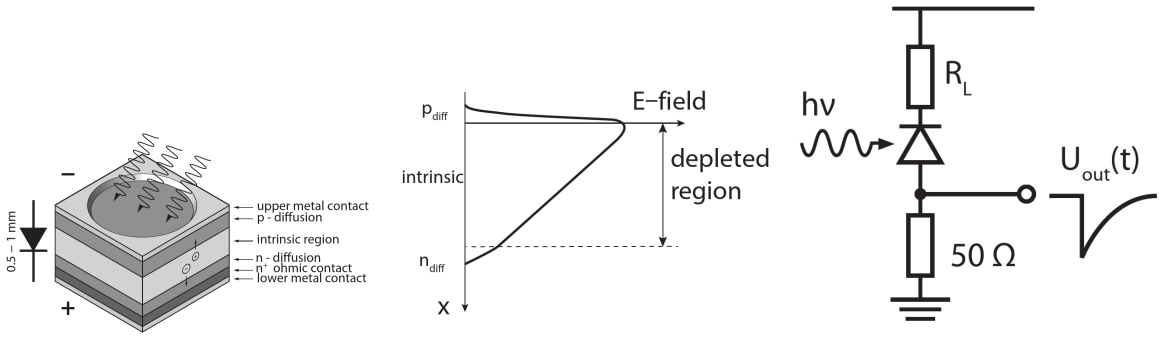

Figure 3.10: PIN diode composition (layer thickness not to scale) (left), PIN diode electric field as a function of thickness (centre), PIN diode electric circuit (right) [330].

3.3.5.3 Avalanche Photodiodes

The lack of intrinsic amplification in photodiodes may be counteracted by adding an additional PN junction called the *metallurgical junction* with high p and n profiles. This implies higher E-fields in the junction region with a magnitude proportional to the doping concentration. This E-field induces intrinsic amplification of electron signals, attaining gains of $\mathcal{O}(10^2)$. This solution is called the *Avalanche Photodiode* (APD). Geometrically, they are most sensitive to photons in the largest, weakly doped and depleted n region (see Figure 3.11): the initial e/h pair is created with the electron drifting towards the readout anode, traversing the metallurgical junction with its strong E-field inducing avalanche amplification, hence the name. The avalanche then induces a signal in the anode.

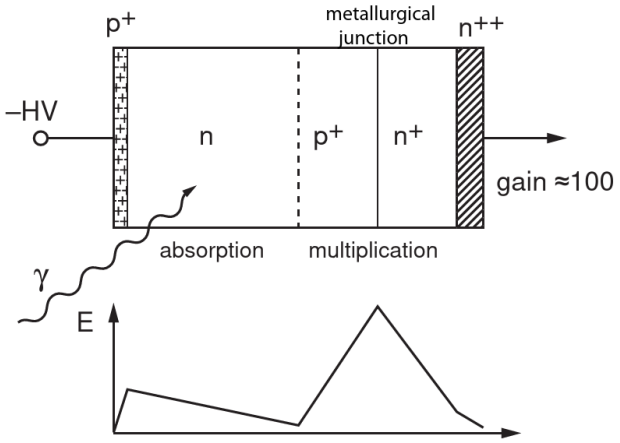

Figure 3.11: Doping regions and corresponding E-fields in an APD, not to scale [330].

In APDs, noise is induced primarily by the sensors rather than by subsequent electronics. This generally puts them at an advantage to PIN diodes although nominally above single photon levels.

Nonetheless, it is possible to operate APDs in linear or Geiger regime. In this last case, the avalanche size is fixed for any signal size and the APD as such acquires sensitivity to single photons, making it a single photon avalanche diode (or SPAD). The discharge breakdown is quenched by either a resistor or a transistor circuit which allows the bias voltage to decrease during avalanche collection. This operation mode induces a gain of $\mathcal{O}(10^5 - 10^6)$ and excellent timing resolution smaller than 1 ns. These detectors can be used in conjunction with one another in SPAD arrays, implying a *photodetection efficiency* (PDE):

$$\text{PDE} = Q \times f_\text{A} \times P_\text{G}, \tag{3.22}$$

where f_A is the fraction of photosensitive surface on the array and P_G is the probability to induce a Geiger avalanche related to the mechanisms described in Section 3.3.5.2. The typical PDE values are around 50% at the optimal wavelength. The functioning of these APD arrays is the basis for one of the most commonly used photodetectors in high energy physics: the Silicon Photomultiplier.

Silicon photomultipliers Silicon photomultipliers, also sometimes called multi-pixel photon counter (MPPC) or even metal resistive layer semiconductor APD (MRS-APD), have become ubiquitous in many photon counting detectors in particle physics. They are matrices of APDs operated in Geiger mode for an intrinsic gain of $\mathcal{O}(10^6)$ with a merged single readout. Each APD cell is capable of detecting the presence of photons, irrespective of their number with their dead time being $\mathcal{O}(50\,\text{ns})$ [352]. The APD cells, hereafter referred to as *pixels* are spaced by $15-75\,\mu\text{m}$, each of them producing a large enough signal to be processed and digitised, even without external amplification. Each fired pixel corresponds to one photoelectron (PE). SiPM geometry, cells and photosensitivity are shown in Figure 3.12a and 3.14.

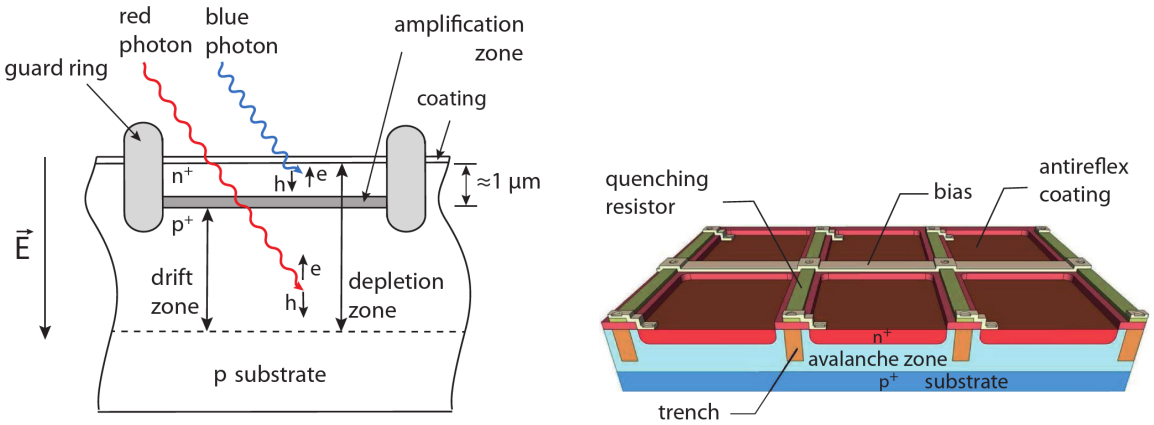

(a) SiPM array structure [353] (left) and schematic representation of a single SiPM APD pixel[330] (right).

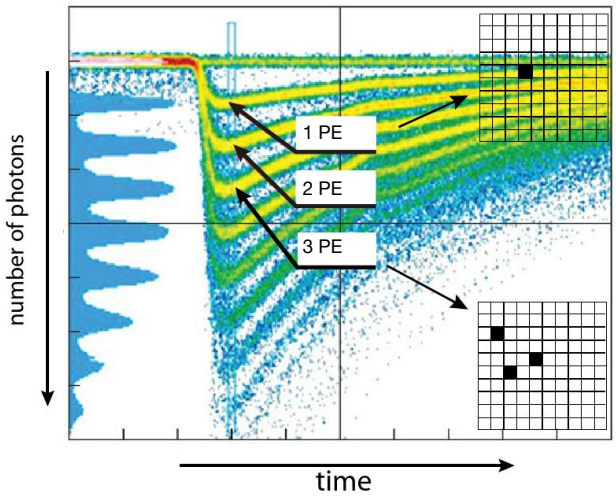

Figure 3.13: SiPM output pulses for different PE counts. One PE corresponds to one pixel firing, two PE correspond to two pixels firing and three PE correspond to three pixels firing [330].

Figure 3.14

SiPMs is a series of pixel cells in parallel. Each pixel cell is composed of an APD and a quenching resistor R_{pix}. The APD circuit is composed of a combination of a switch, a voltage source V_{BD} representing the breakdown voltage), a resistor R_S representing the resistance of the entire APD during a discharge with a capacitor C_j in parallel representing the junction capacitance. When an incoming photon creates an e/h pair, it closes the switch due to the Geiger avalanche breakdown, allowing for current to flow. The junction then capacitance discharges into R_S which produces a current pulse. The current flow through R_S causes a voltage drop below V_{BR} which quenches the avalanche. Afterwards, the junction capacitance is recharged through R_{pix}: the pixel is ready for another event. This circuit is shown in Figure 3.15. The single pixel gain is determined by its junction capacitance with $Q_{\text{pix}} = C_{\text{pix}}\Delta V$, C_{pix} being the pixel capacitance (typically $\sim 100\,\text{fF}$) and $\Delta V = V_{\text{operation}} - V_{\text{BR}}$ the overvoltage, typically of the order of $2-5\,\text{V}$ with $V_{\text{BR}} \sim 50\,\text{V}$. The bulk capacitance of a SiPM can however be much larger, based on its size and the number of cells, which may affect rise time and

decay time of the waveform (see Figures 3.18 and 3.17). As a result, the typical charge output from a single PE would be 100 fC which limits the noise induced by readout electronics as a result of the high gain. The total charge produced is thus proportional to the pulse amplitude at first order as a result of pixel linearity.

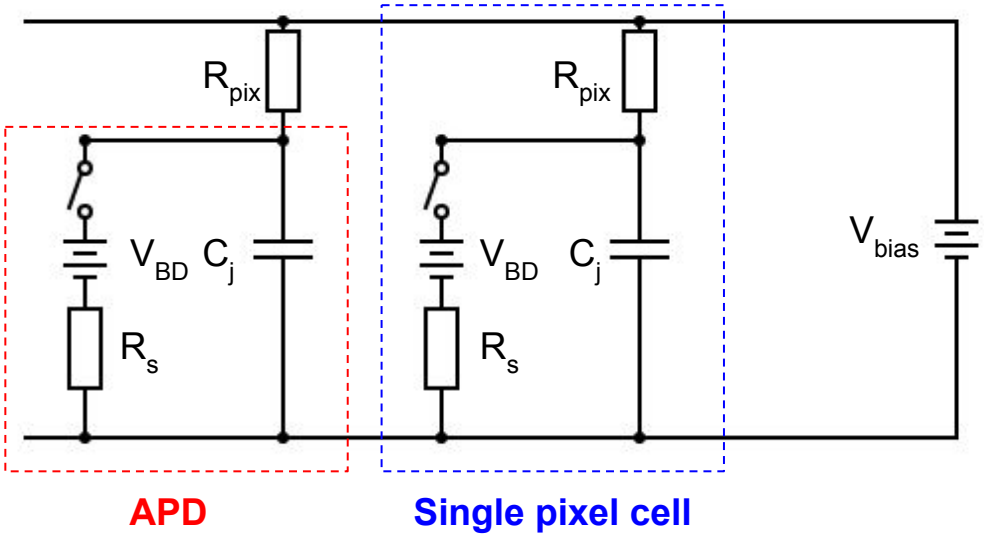

Figure 3.15: Simplified circuit of SiPM elements. R_s, C_j, R_{pix} V_{bias} and V_{BD} are the SiPM's series resistor, junction capacitance, quenching resistor, bias and breakdown voltage respectively.

While it is possible to directly digitise SiPM signals already on the matrix [354], analogue SiPMs are by far more common. This enables proportionality between number of fired pixels and cell number, the *dynamic range*, defined by the number of different amplitudes that can be produced by the system, is therefore equal to the pixel count.

It should however be noted that the output is not strictly *linear*: for any non-single photon count, there is a probability that multiple photons hit the same pixel, creating a geometrical uncertainty that is added to the stochastic uncertainty on each pixel to fire determined primarily by its single photon PDE this is studied in Chapter 5.

This stochastic uncertainty can be exemplified with a SiPM with a single-photon PDE of 0.5. Neglecting all other effects, the likelihood of a pixel hit by one photon to fire would be 0.5, that of the same pixel hit by n photons would be $1 - 0.5^n$.

The loss in linearity is called *saturation*.

The limits of SiPMs mainly manifest under the form of *dark current*, *cross-talk* and *afterpulsing*. Dark current, also known as *dark count*, originates from sensitive areas of the SiPM substrate or its surface creating spontaneous breakdowns as a result of high E-fields in the amplification region. This effect is thus very dependent on temperature and bias voltage.

Cross talk is caused by photons created during the amplification process in a pixel reaching a neighbouring pixel where another avalanche is created. This effect is mitigated by the use of isolating trenches around each cell. These trenches, however, reduce the geometrical fill factor of the SiPM, corresponding to the fraction of sensitive area and thus reduce the overall PDE.

Afterpulsing is caused by delayed pulses created by electrons or holes trapped during the avalanche amplification and release a couples of 100 ns later, thus creating new pulses.

SiPMs may be biased in one of four ways, as shown in Figure 3.19, leading to flexibility on the readout side as both polarities and bias directions are possible.

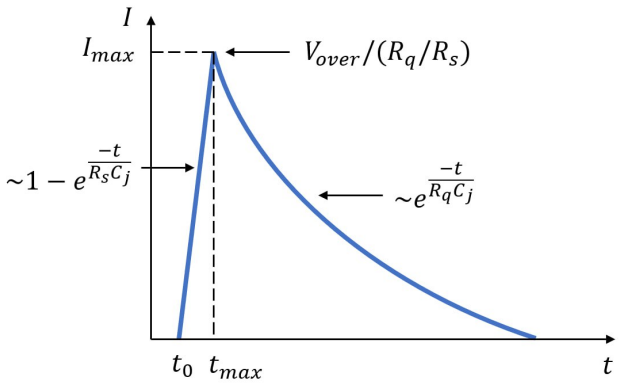

Figure 3.16: Example of a SiPM output pulse as a function of its parameters. V_{over} is the SiPM overvoltage.

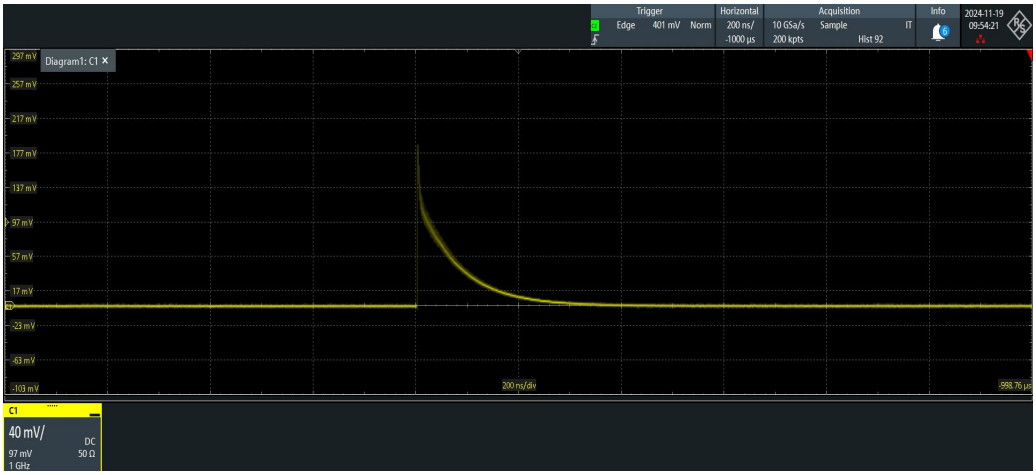

Figure 3.17: Output of a $3 \times 3\,\text{cm}^2$ SiPM firing with a set amount of light for an equivalent of ~ 1000 PE. The amount of light on the SiPMs and the overvoltage is identical to that of Figure 3.18.

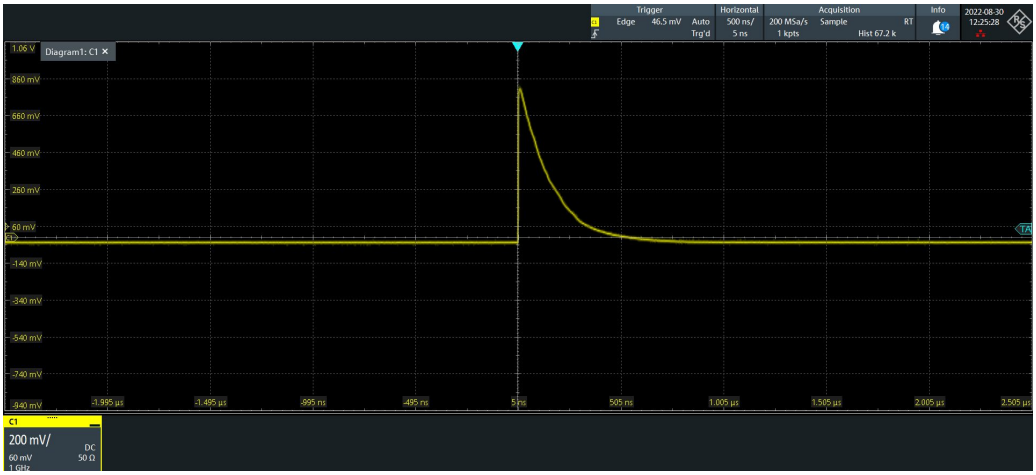

Figure 3.18: Output of a $6 \times 6\,\text{cm}^2$ SiPM firing with a set amount of light for an equivalent of ~ 4000 PE. The amount of light on the SiPMs and the overvoltage is identical to that of Figure 3.17.

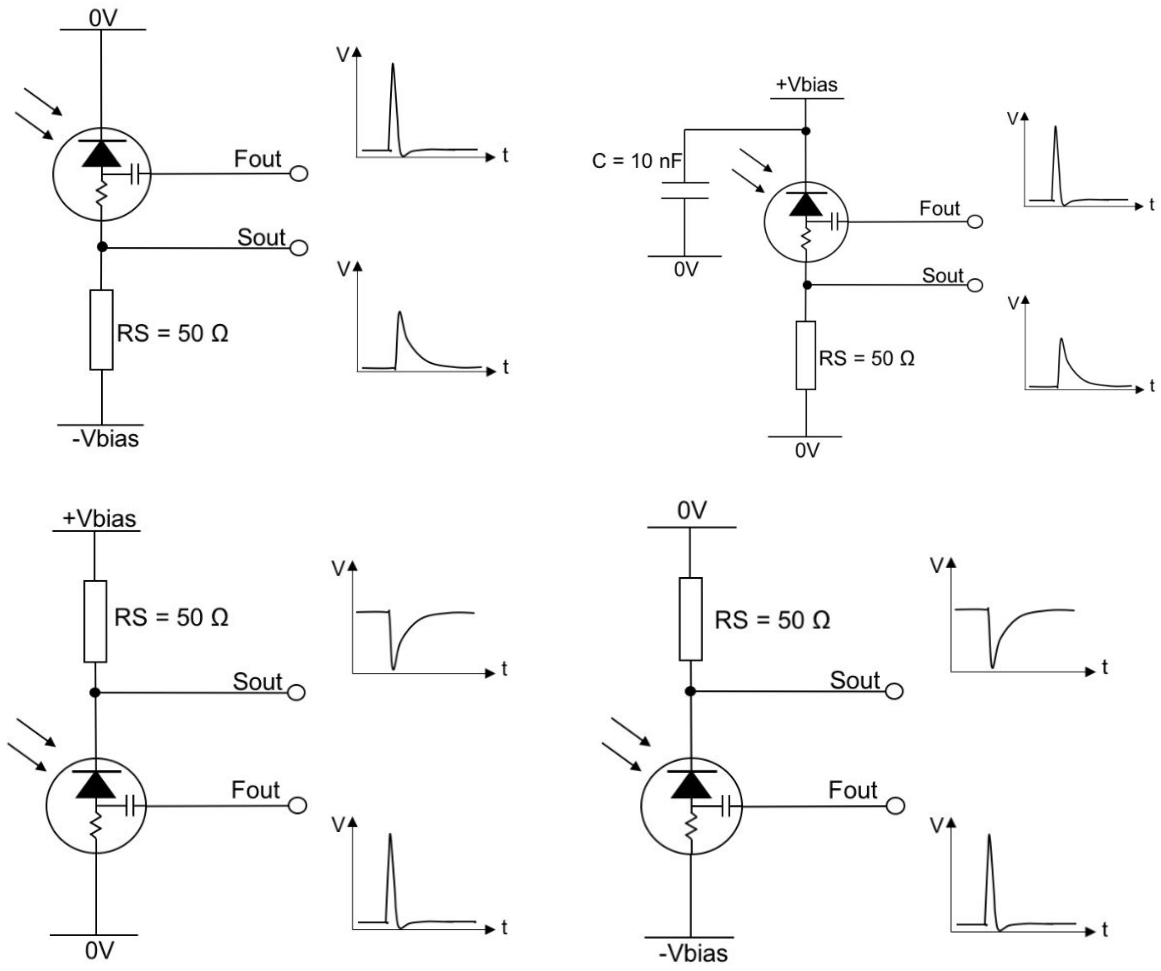

Figure 3.19: SiPM biasing with inverting biasing and positive polarity (top left), with forward biasing and positive polarity (top right), these two configurations lead to improved timing resolution. SiPM biasing with forward biasing and negative polarity (bottom left) and with inverted biasing and negative polarity (bottom right). The fast output F_{out} is specific to SensL SiPMs, the regular output S_{out} is otherwise commonly used [355].

Chapter 4

The SHiP calorimeter system and the SplitCal

The SHiP calorimeter system (also known as the SHiP PID detector) is the most downstream detector in the SHiP experiment and is based on a 20 X_0 ECAL and a 5 λ_a HCAL section. Its primary goal is to allow for particle identification of final states entering the detector, particularly distinguishing between electrons, pions and muons. In addition, the SHiP calorimeter system uniquely allows the detection of possible BSM particles with in neutral final states, particularly photons, as described in Section 1.3.

4.1 Physics of the SHiP calorimeter system

4.1.1 $\gamma\gamma$ final state reconstruction

ALPs or sgoldstinos are examples of particles susceptible to decaying into neutral final states. Particles undergoing such decays will be generically denominated $\gamma\gamma$-decaying particles ($X \to \gamma\gamma$). Their observation is a crucial goal of the SHiP experiment and the only subdetector capable of observing these finals states is the SHiP ECAL.

The reconstruction of the initial state is done by measuring the shower directionalities to determine the origin point of the decay. The invariant mass defined of the decaying particle is given by:

$$m_X = \sqrt{(\sum E_i)^2 - (\sum \mathbf{p}_i)^2} \tag{4.1}$$

$$p_x = E \cdot \sin\theta \cdot \cos\phi \tag{4.2}$$

$$p_y = E \cdot \theta \cdot \sin\phi \tag{4.3}$$

$$p_z = E \cdot \cos\theta \tag{4.4}$$

with E_i the energies of each photon, whereas p_i are the $3-$momentum components between them, θ is the polar angle with respect to the positive z axis and ϕ is the azimuthal angle with respect to the xy plane, $m_{\gamma\gamma}$ is the mass of the initial state particle reconstructed kinematically. It can be seen that the invariant mass resolution is directly linked to the detector's angular resolution insofar as it allows for the reconstruction of $\mathbf{p}_i$. Simultaneously, the energy resolution of the calorimeter to individual photons is also primordial in this reconstruction as it will influence E_1 and E_2. The final state mass resolution thus depends on the calorimeter's angular resolution σ_θ, its energy resolution σ_E E, the X mass m_X (m_{ALP} in the case of the particle being an ALP) and the particle boost in the z direction p_z or B determined by its production kinematics.

4.1.1.1 Particle separation

Particle separation is a crucial aspect of $X \to \gamma\gamma$ decay reconstruction. It consists of isolation of both electromagnetic showers created by both photons. This is favoured by the relatively large lever arm available between

the end of the decay volume and the start of the calorimeter, as well as the ECAL's granularity. The importance of lever arm is portrayed in Figure 4.1.

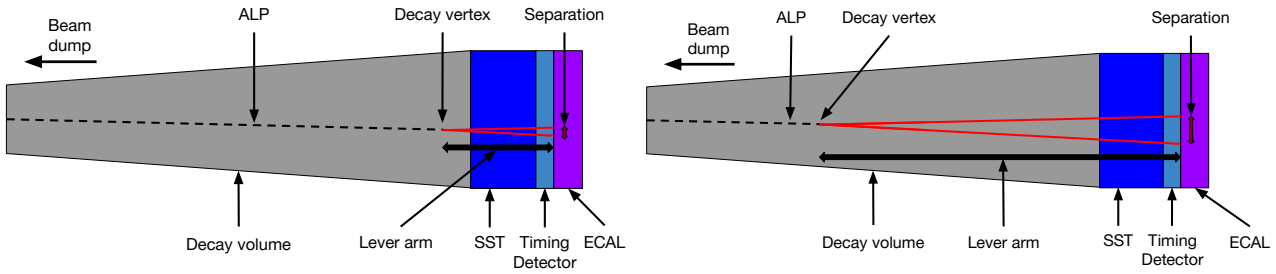

(a) Effect of a short lever arm for a late decaying ALP in particle separation: the separation is reduced.

(b) Effect of a long lever arm for an early decaying ALP in particle separation: the separation is increased.

Figure 4.1: The representations are not to scale.

Better separation is achieved for larger angles created by heavier initial state masses, short lifetimes, causing the initial state to preferably decay early in the decay volume, and lower boosts. If separation is very conservatively assumed to only be possible between two showers for a full 2 *Molière radii* (in lead) and a short lever arm of 10 m separating the end of the decay vessel and the start of the ECAL is taken (see Figure 2.17), the minimal output angle that would still be reconstructable would be 3.2 mrad. $X \to \gamma\gamma$s having a fairly large 70 GeV forward boost can be separated and thus kinematically reconstructed down to below 100 MeV masses, as shown in Figure 4.2. This importantly implies that photons from π^0 decays which may be produced in late particle decays (see Section 4.1.1.4) are also largely separable until boosts nearing 100 GeV.

It is found that under the investigated conditions, tension only exists in the reconstruction of 100 MeV $X \to \gamma\gamma$ decays, which would lead to a reduction of the fiducial volume by ~ 40 cm in z as more lever arm would be required. Every other case can be separated without issue.

If effective particle separation can be guaranteed, precise studies of both model-dependent and model-independent $X \to \gamma\gamma$ decays are enabled, both of which are examined below.

4.1.1.2 Model-independent reconstruction of particles decaying to $\gamma\gamma$

Model-independent studies of $X \to \gamma\gamma$ decays are by essence very general and therefore cover considerable amounts of phase-space. They allow to cover regions not constrained by any particular model and only rely on kinematics for their constraints. Following this logic, in order to design and optimise the SHiP ECAL to enable the reconstruction of as many $X \to \gamma\gamma$ decays as possible, 10 000 $X \to \gamma\gamma$ decays were generated using the `phasepace` python package at the end of the decay volume and kinematically reconstructed using a wide array of X masses m_X, forward boosts B, calorimeter angular resolutions σ_θ and calorimeter energy resolution σ_E, in particular:

- $m_X \in \{0.1, 0.2, 0.3, 0.4, 0.5, 0.6, 0.7, 0.8, 0.9, 1, 2, 3, 4, 5\}$ GeV as the heaviest new particles expected are from B hadron decays.
- $B \in \{1., 3., 5., 7.5, 10, 12.5, 15., 20., 25., 30., 40., 50., 60., 70., 100, 150, 200\}$ GeV. Larger boosts were not considered as they mostly improve calorimeter energy and angular resolution and thus enjoy better detector performance and are not expected to be significant given the 400 GeV incoming beam energy.
- $\sigma_\theta \in \{0, 0.001, 0.002, 0.003, 0.004, 0.005, 0.01, 0.02, 0.03, 0.04, 0.05\}$ rad plus an additional angular resolution which is deemed to be realistic with current angular resolution studies with a dependence on particle energy. These angles are extrapolated from existing and ongoing studies (see Section 4.2) and are shown as being negative in the corresponding figures.
- $\sigma_E \in$\{0,0.05,0.1,0.15,0.2\}, these values are taken to reflect achievable performance and to guide potential upgrades to the calorimeter if they were needed.

The assumption is made that all photons can be resolved and have both their polar and azimuthal angles resolved by calorimetric reconstruction. This assumption seems to generally hold well for heavier particles

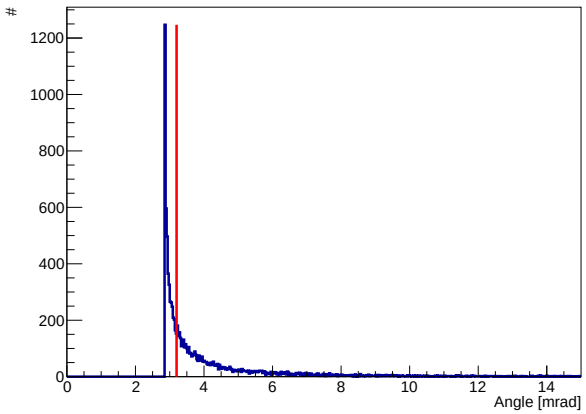

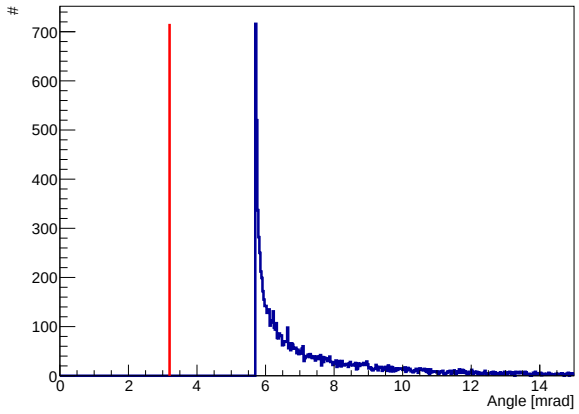

(a) 200 MeV particle decay.

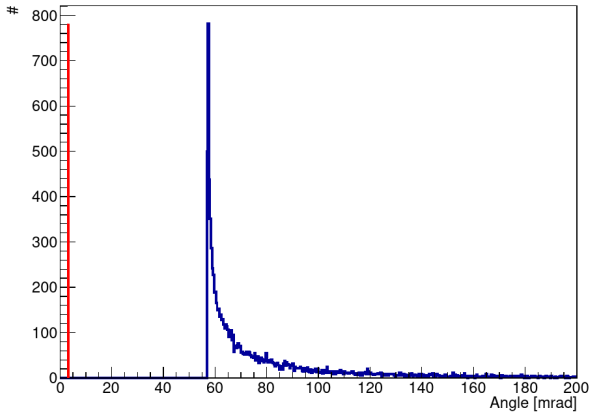

(b) 2 GeV particle decay.

Figure 4.2: Separation angle between both photons produced in particle decays with 100 MeV (top), 200 MeV (middle) and 2 GeV (bottom) mass with 70 GeV forward momentum. The orange lines display the conservative limit explained in the text.

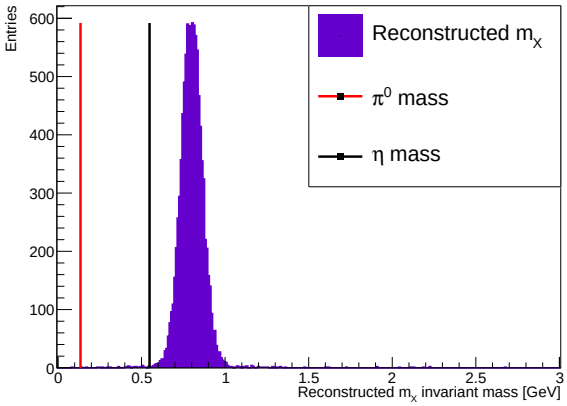

(a) $\sigma_\theta = 5\,\text{mrad}$, $\sigma_E = 10\%\sqrt{E}$.

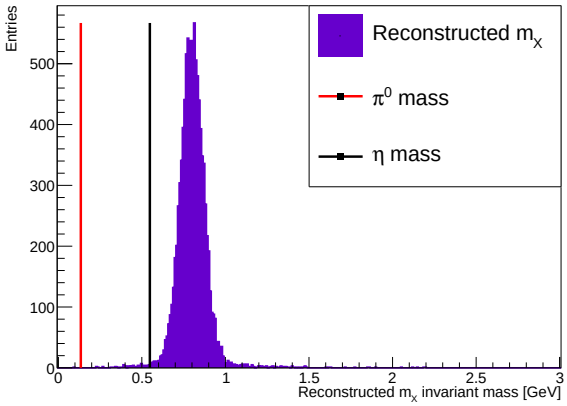

(b) $\sigma_\theta = 5\,\text{mrad}$, $\sigma_E = 20\%\sqrt{E}$.

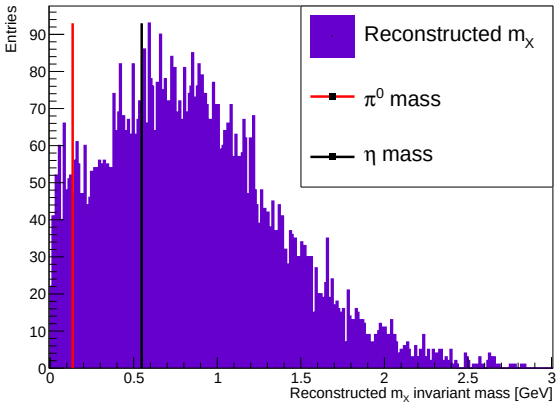

(c) $\sigma_\theta = 50\,\text{mrad}$, $\sigma_E = 10\%\sqrt{E}$.

Figure 4.3: Invariant mass resolution for $X \to \gamma\gamma$s with 800 MeV mass and 20 GeV forward boost reconstructed from their $\gamma\gamma$ final state using different detector configurations. The red and black line represent the π^0 and η backgrounds' masses respectively.

but may be challenged in the case of lighter ones due to acceptance and phase space (see Section 4.1.1.1 and Appendix B). This leads to 14280 parameter combinations, the results of 3 of them being shown in Figure 4.3.

The reconstructed invariant masses are fitted with a gaussian distribution. The fits results as a function of various parameters are shown in Figures 4.4-4.8.

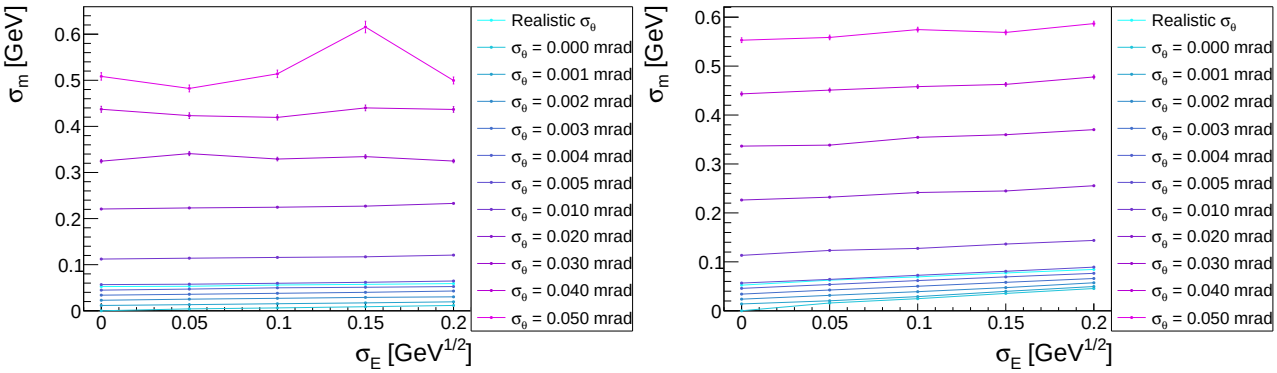

(a) $m_{\text{inv}}(\sigma_E)$, $m_X = 500\,\text{MeV}$, $B = 20\,\text{GeV}$, for different σ_θ. (b) $m_{\text{inv}}(\sigma_E)$, $m_X = 2\,\text{GeV}$, $B = 20\,\text{GeV}$, for different σ_θ.

Figure 4.4: Absolute invariant mass resolution as a function of calorimetric energy resolution, for medium boosts, lighter and heavier X, for different calorimeter angular resolutions.

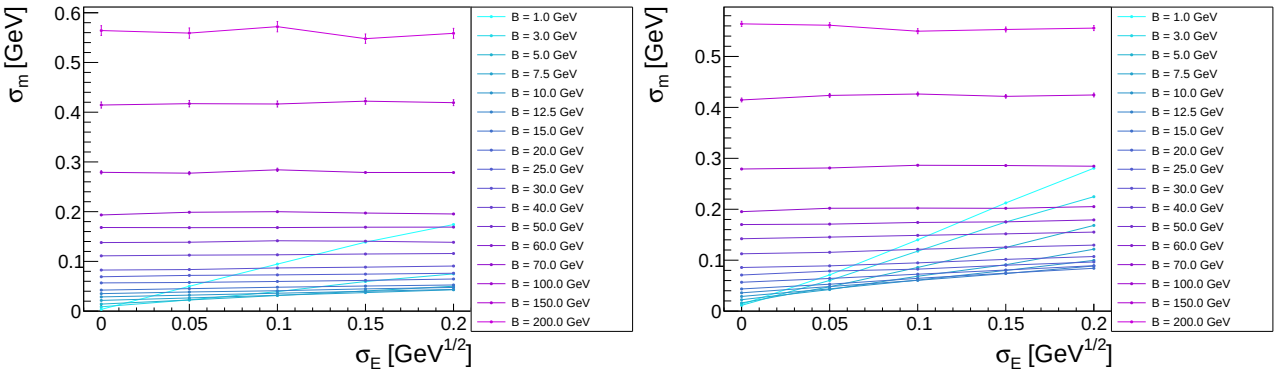

(a) $m_{\text{inv}}(\sigma_E)$, $m_X = 500\,\text{MeV}$ $\sigma_\theta = 5\,\text{mrad}$, for different boosts. (b) $m_{\text{inv}}(\sigma_E)$, $m_X = 2\,\text{GeV}$ $\sigma_\theta = 5\,\text{mrad}$, for different boosts.

Figure 4.5: Absolute invariant mass resolution as a function of calorimetric energy resolution, for good calorimeter angular resolution, lighter and heavier X, for different X boosts.

It can be from there seen that better calorimetric energy resolution (σ_E) improves the mass resolution for different levels of boost (see Figure 4.5). Angular resolution (σ_θ) on the other hand, improves mass resolution for all combinations of parameters (Figures 4.6 and 4.8), irrespective of σ_E (Figure 4.4). Absolute mass resolution degrades with higher boosts. The reconstruction of lighter X with higher boosts (which may also include photon-coupling ALPs with short lifetimes as shown in Section 4.1.1.3) is challenging and would thus require improved angular resolution and energy resolution (Figure 4.8). This is due to both σ_E and σ_θ linearly improving mass resolution. Angular resolution has a stronger effect, therefore developments in this area are being pursued (see Section 4.2).

The main background for new particles decaying into photon pairs are $\gamma\gamma$ decays of SM particles, mainly from π^0 or η. The proximity of the $\gamma\gamma$ decaying particle's mass to these backgrounds as well as detector angular and energy resolution are the main drivers of exclusion.

In addition to mass resolution, the position of the vertex is of extreme importance in $\gamma\gamma$ reconstruction in SHiP to ensure that the decay originates in the decay volume and does not come from background. This is done by matching tracks to find a common point of origin in space for a given event as illustrated in Figure 4.1. In the case of photons, the EM shower directions are used to form a vertex. The vertex resolution is driven primarily by angular resolution. Higher photon energies imply longer showers which allow for better measurements of photon directions.

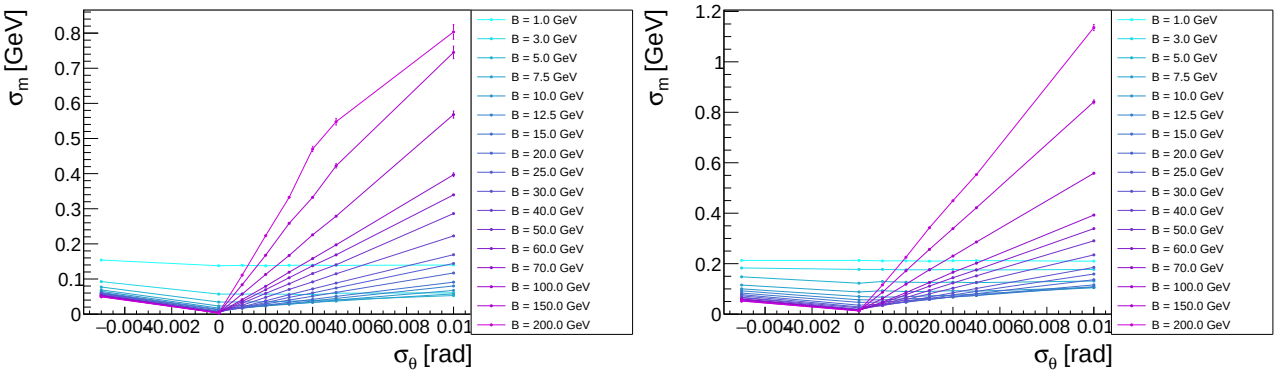

(a) $m_{\text{inv}}(\sigma_\theta)$, $m_X = 500\,\text{MeV}$ $\sigma_E = 15\%\sqrt{\text{GeV}}$, for different boosts.

(b) $m_{\text{inv}}(\sigma_\theta)$, $m_X = 2\,\text{GeV}$ $\sigma_E = 15\%\sqrt{\text{GeV}}$, for different boosts.

Figure 4.6: Absolute invariant mass resolution as a function of calorimeter angular resolution, given standard calorimeter energy resolution, lighter and heavier X, for different X boosts. Negative angular resolutions are used for "realistic" values for ease of visualisation (see Section 4.2)

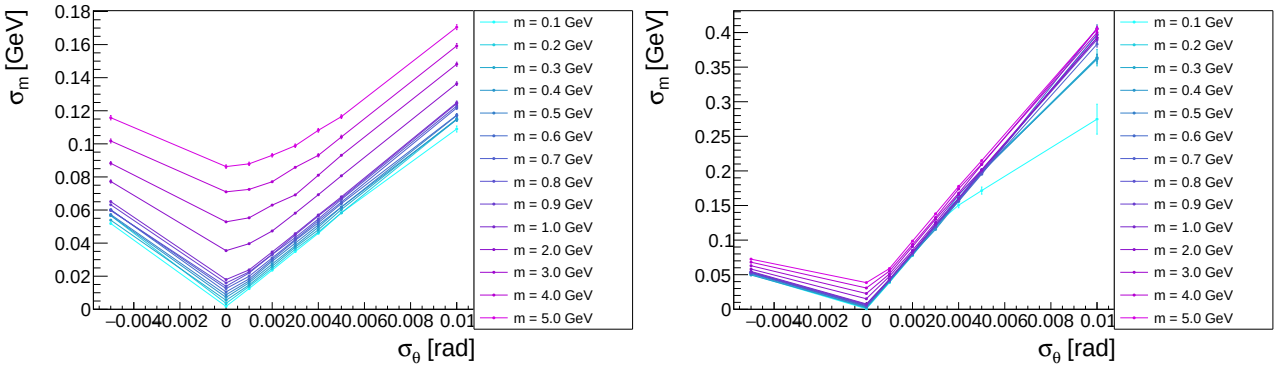

(a) $m_{\text{inv}}(\sigma_\theta)$, $B = 20\,\text{GeV}$ $\sigma_E = 15\%\sqrt{\text{GeV}}$, for different m_X.

(b) $m_{\text{inv}}(\sigma_\theta)$, $B = 70\,\text{GeV}$ $\sigma_E = 15\%\sqrt{\text{GeV}}$, for different m_X.

Figure 4.7: Absolute invariant mass resolution as a function of calorimeter angular resolution, given standard calorimeter energy resolution, lower and higher X boosts, for different X masses. Negative angular resolutions are used for "realistic" values for ease of visualisation.

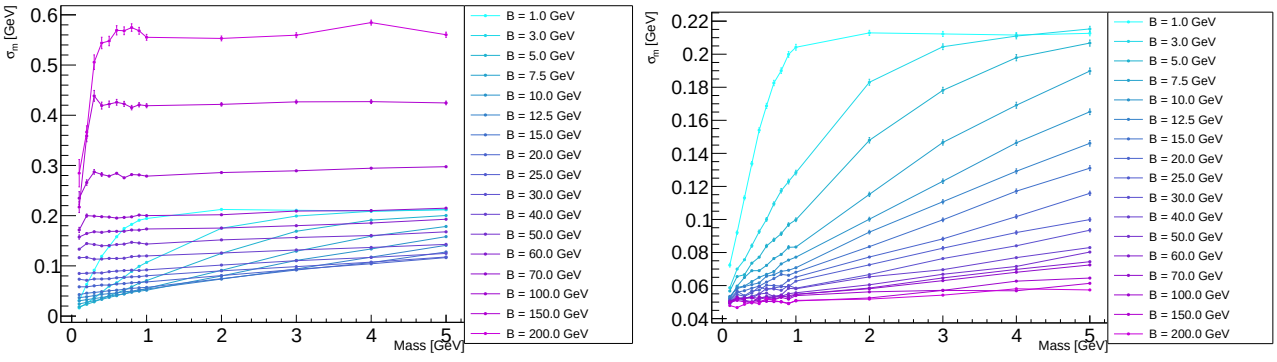

(a) $m_{\text{inv}}(m_X)$, $\sigma_\theta = 5\,\text{mrad}$ $\sigma_E = 15\%\sqrt{\text{GeV}}$, for different boosts.

(b) $m_{\text{inv}}(m_X)$, "realistic" σ_θ $\sigma_E = 15\%\sqrt{\text{GeV}}$, for different boosts.

Figure 4.8: Absolute invariant mass resolution as a function of X mass, given standard calorimeter energy resolution, good and realistic calorimeter angular resolutions, for different X boosts.

4.1.1.3 Reconstructibility of ALPs decaying to photon pairs

Specific ALP models constrain their masses and lifetimes differently, with implications on the higher energy mass scales they are related to (see Section 1.3.2.4). These constraints allow for a reduction in the phase space needed to be studied. SHiP, through its ECAL, aims to cover as many $ALP \to \gamma\gamma$ scenarios as possible and has as such developed a specialised custom generator called `EventCalc` [356, 357] which enables accurate studies of particular regions of parameter space. Using `EventCalc`, ALPs coupling to photons with different masses m_{ALP} and lifetimes τ were generated in the SHiP topology through Primakoff production (see Section 1.3.2.4), leading to different boost distributions as a function of mass with examples shown in Figure 4.9.

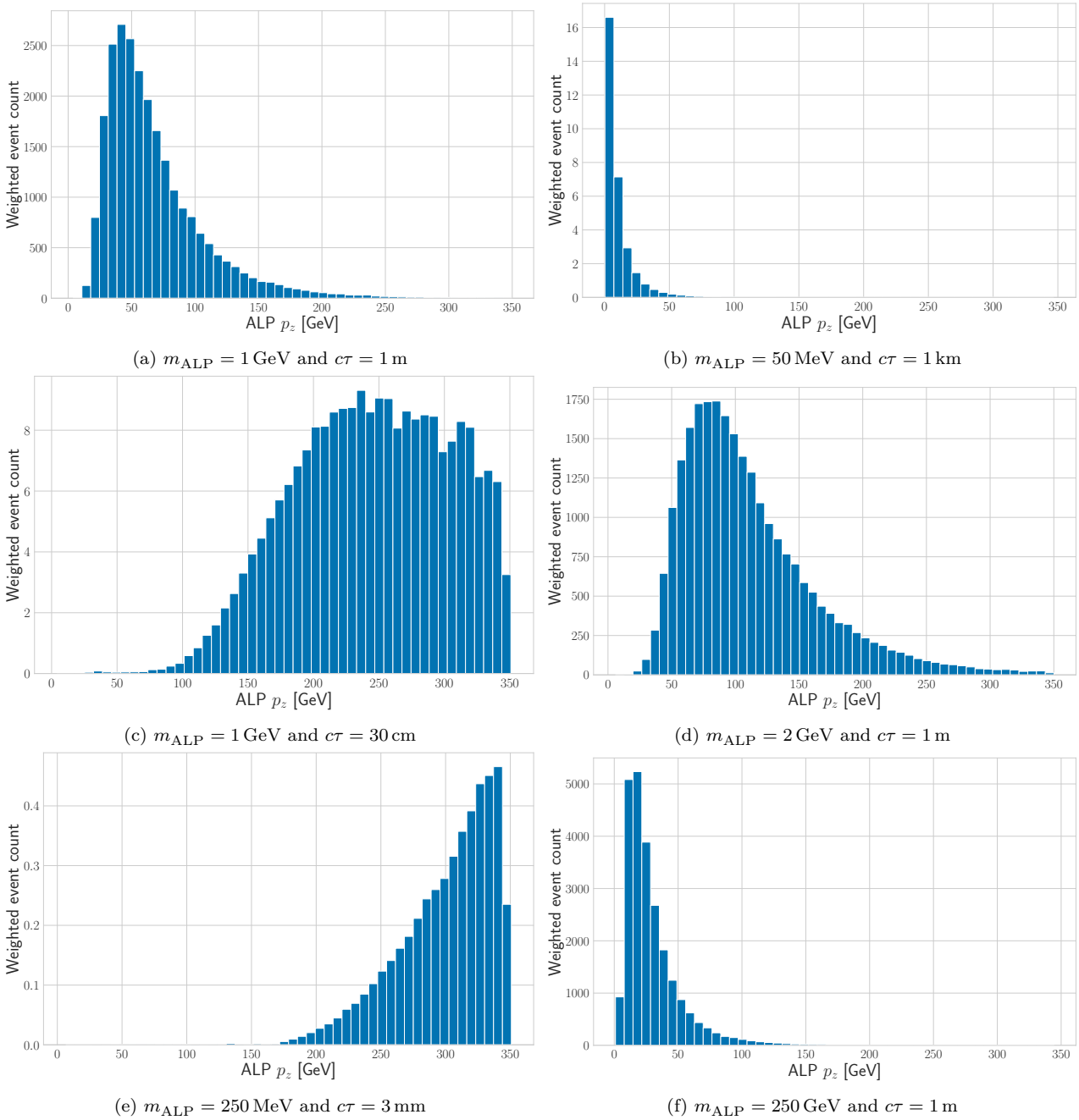

(a) $m_{\text{ALP}} = 1\,\text{GeV}$ and $c\tau = 1\,\text{m}$

(b) $m_{\text{ALP}} = 50\,\text{MeV}$ and $c\tau = 1\,\text{km}$

(c) $m_{\text{ALP}} = 1\,\text{GeV}$ and $c\tau = 30\,\text{cm}$

(d) $m_{\text{ALP}} = 2\,\text{GeV}$ and $c\tau = 1\,\text{m}$

(e) $m_{\text{ALP}} = 250\,\text{MeV}$ and $c\tau = 3\,\text{mm}$

(f) $m_{\text{ALP}} = 250\,\text{GeV}$ and $c\tau = 1\,\text{m}$

Figure 4.9: Forward boost distribution of ALPs coupling to $\gamma\gamma$ with different masses and lifetimes in SHiP.

Integration of the respective decay probability of the event as:

$$\frac{\mathrm{d}P}{\mathrm{d}z} = e^{-\frac{z}{c\tau\cos\theta}}, \quad (4.5)$$

over longitudinal decay vertex positions z, ALP production polar angles θ and energies, provides the relative event rate for a given combination. As the ALP has to decay while being within the decay volume, large boost is

required for shorter lifetime ALPs, similarly, lower boosts are needed for longer lived ALPs. The exact possible rates are enabled by the photon distribution within the target complex which enable Primakoff production. The mass of the produced ALP thus increases with forward momentum as a result of Primakoff kinematics. By construction, the separation between photons will be tend to be larger and the travelled distance, determined by $\gamma c\tau$ with $\gamma = \frac{E}{m}$ is thus reduced. Heavier particles will have larger boost while seeing large angles between outgoing particles. This allows for their reconstruction in the ECAL as shown in Figure 4.10, allowing for an wide explorable phase space which make beam dump experiments and particularly SHiP ideal ALP-factories in this mass range.

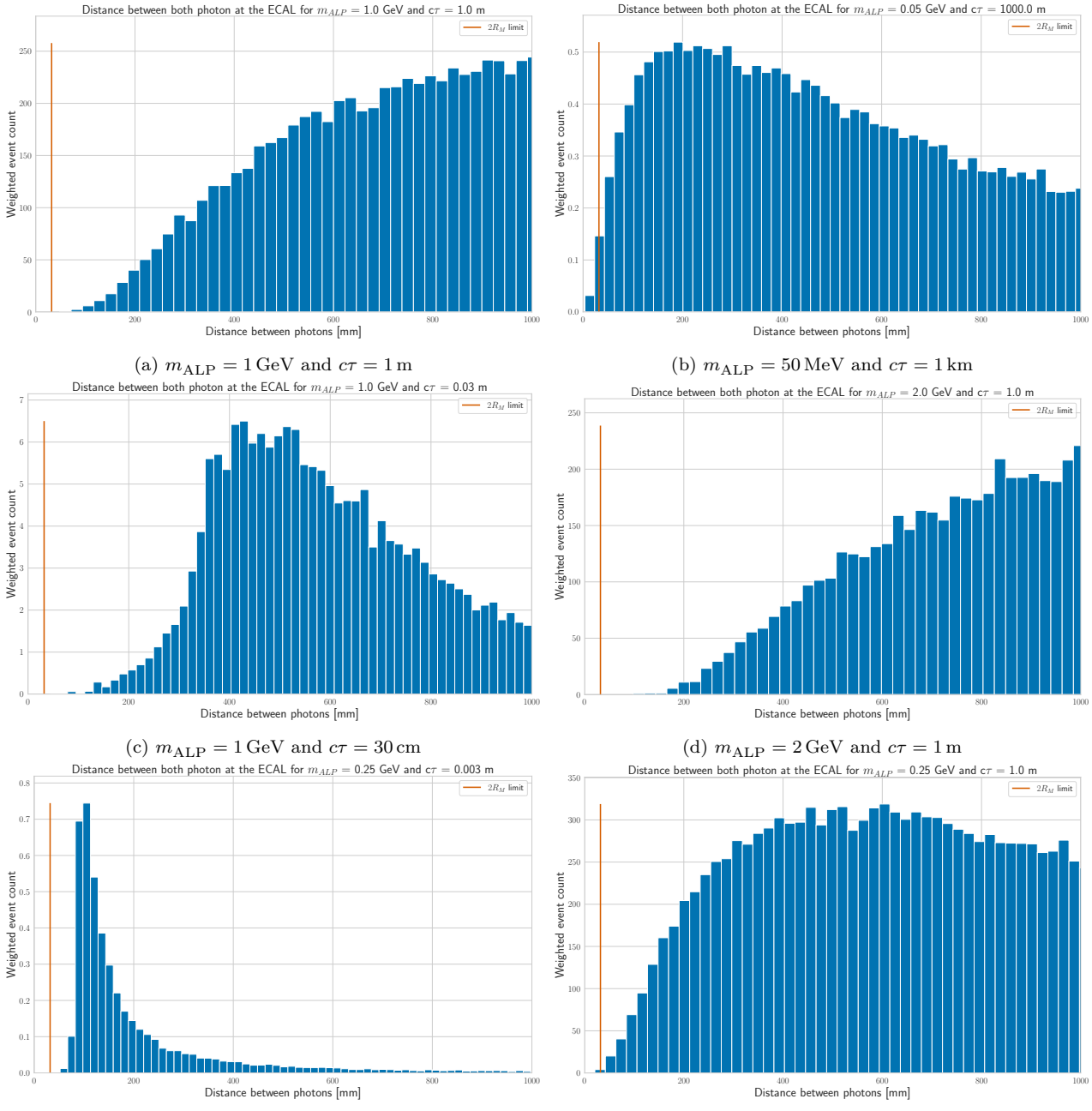

(a) $m_{\text{ALP}} = 1\,\text{GeV}$ and $c\tau = 1\,\text{m}$

(b) $m_{\text{ALP}} = 50\,\text{MeV}$ and $c\tau = 1\,\text{km}$

(c) $m_{\text{ALP}} = 1\,\text{GeV}$ and $c\tau = 30\,\text{cm}$

(d) $m_{\text{ALP}} = 2\,\text{GeV}$ and $c\tau = 1\,\text{m}$

(e) $m_{\text{ALP}} = 250\,\text{MeV}$ and $c\tau = 3\,\text{mm}$

(f) $m_{\text{ALP}} = 250\,\text{GeV}$ and $c\tau = 1\,\text{m}$

Figure 4.10: Separation between both final state photons from ALP decays with different masses and lifetimes coupling to $\gamma\gamma$ in SHiP. The red line displays the conservative limit expressed in Section 4.1.1.

4.1.1.4 π^0 reconstruction

The reconstruction of π^0 is essential for a number of final states (see Section 1.3). It requires determining that the $\gamma\gamma$ final state does originate from a π^0, as well as determining the distance d_v of the vertex to the

calorimeter. The former may be achieved through invariant mass reconstructions while the primary way of doing the latter in the limit of small opening angles [358] is:

$$d_v = \frac{1}{m_{\pi^0}} \sqrt{E_1 E_2} d_{12}, \tag{4.6}$$

where E_1 and E_2 are the photons' reconstructed energies and d_{12} is the distance separating them from one another on the calorimeter front layer the calorimetric XY-plane. The energy resolution is here the driving factor for the accurate reconstruction of the π^0 decay distance to the calorimeter as the resolution for d depends linearly on energy resolution [358]. This strategy can be combined with traditional vertexing and invariant mass reconstruction to allow for the optimisation of the π^0 parameters using a kinematic fit [359].

Certain decays (for instance HNLs with mass $> 1\,\text{GeV}$) feature mixtures of $\pi 0$ and charged tracks. The shower directionality of the π^0 decay $\gamma\gamma$ must then be reconstructed well enough to allow for vertex matching together with the charged tracks.

4.2 Calorimeter design

The challenge of attaining the required combination of PID performance, primarily driven by energy-resolution and the HCAL, as well as $X \to \gamma\gamma$ reconstruction, primarily driven by angular resolution, have led to the development of a unique detector for the ECAL. It manifests as a sampling calorimeter using plastic scintillator layers for energy reconstruction, lead as passive material in the ECAL section to improve on energy resolution (see Equation 3.18), while the mechanically simpler iron will be used as passive material for the larger HCAL section. A combination of either higher-resolution plastic scintillator detectors and dedicated *High Precision Layers* (HPLs), which are sensitive layers based on detectors with excellent position resolution, may allow for an excellent angular resolution to be achieved. Both the plastic scintillator and HPL options are presented below.

4.2.1 Energy-reconstructing scintillator layers

The SHiP calorimeter system, consisting of an ECAL and HCAL is planned to use sets of 2 m long scintillator bars. The bars would be 6 cm wide and 1 cm thick. The bars will be traversed by two wavelength shifting fibres (see Chapter 5), sealed in reflective foil and readout on both sides by large $6 \times 6\,\text{mm}$ SiPMs using an optimised fibre-sensor interface. This is done to yield a large dynamic range. This allows to measure both muons and large EM showers while reducing the stochastic term (see Sections 3.2.1 and 3.3.5.3). The choice of 6 cm bars is made as it corresponds to roughly twice the Molière diameter of the passive material and thus allows cost-effective separation of nearby showers. 34 such bars ($34 \times 6\,\text{cm} \simeq 2\,\text{m}$) are grouped in layers and are aligned vertically and horizontally (up to 20 layers each) with alternating orientations to enable the reconstruction of *clusters*. A cluster is a group of energy depositions that are spatially close and likely to originate from a single initial particle. Clusters are useful when multiple energy depositions occur in different locations of the calorimeter. The use of alternating orientations allows to reconstruct X and Y spatial coordinates for single showers but is confronted with *ambiguities* when multiple showers take place. This is due to the fact that for simultaneous clusters, the X-information of the cluster is not matched with a Y-position, unlike in pixel or tile detectors. This may be resolved by using longitudinal information and timing since two showers may originate at different longitudinal depths or using the asymmetry in the dual sided-readout. The Z-position of an energy deposition is ensured by an independent readout of each bar, corresponding to two channels (one for each side) for each scintillator bar.

In the case of small opening angles, a single cluster is reconstructed. This then requires information from higher-granularity layers to disentangle the showers.

The HCAL section is planned to be similarly built but to consist of only 5 readout layers, one every λ_a. It will primarily be used for PID and will only provide modest energy resolution, estimated analytically to be $\sim 200\% \sqrt{\text{E}}$.

The calorimeter will transversally be built in 6 $2 \times 2\,\text{m}^2$ modules, spanning the entire cross section of $6 \times 4\,\text{m}^2$ at the end of the SHiP detector system. The design is shown in Figure 4.11.

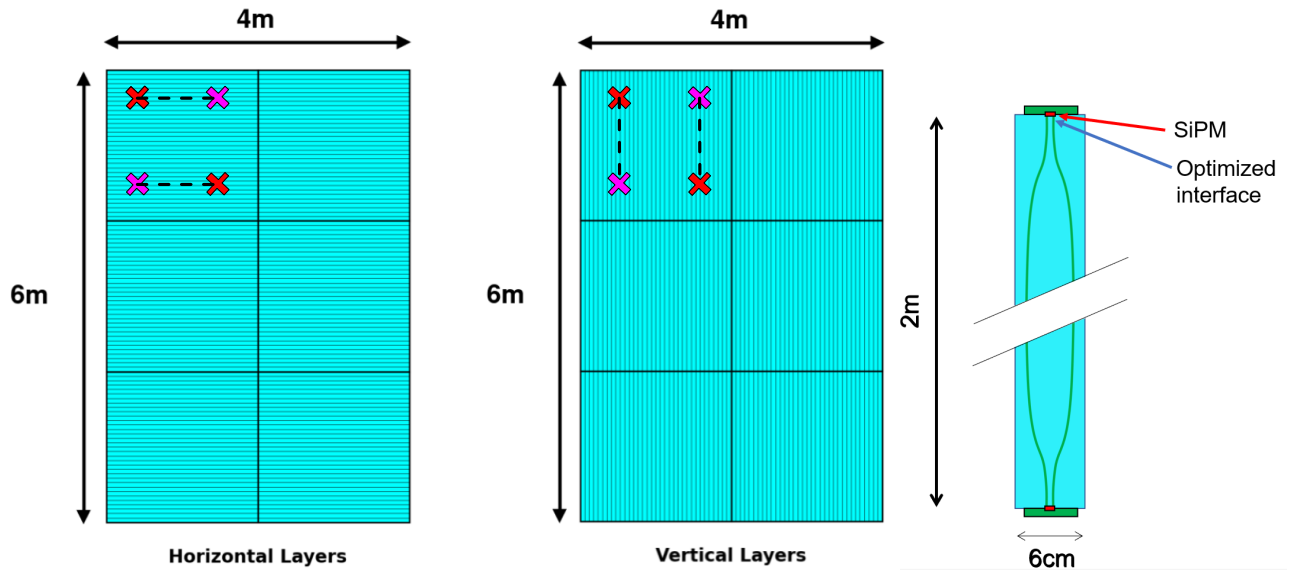

Figure 4.11: SHiP calorimeter system module and single bar design for the energy reconstruction layers. The red crosses represent real hits whereas the pink ones represent ambiguities.

4.2.2 The SplitCal: HPLs and scintillator layers

The SplitCal [360] is a calorimeter concept which improve shower directionality reconstruction capabilities by introducing a longitudinal split. The angular resolution is provided by 2-3 HPLs which use the lever arm to reconstruct the shower origin. The HPLs also allow to separate shower components in the case of close-by showers. They also complement the SST in reconstructing the momentum of hard muons.

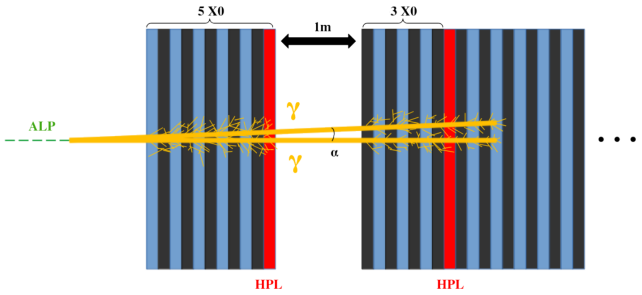

Figure 4.12: Schematic representation of the SplitCal using 2 HPLs. Radiation and segmentation length is not final.

The considered technologies for the HPLs are primarily cost-effective gas detectors such as Gas-Electron-Multiplier (GEM) detectors [361], MicroMegas [329] or Multi-wire-proportional chambers [362]. The former two have sensor pitches of around 300 µm, with their resolution being well improved for showers where centroid reconstruction is enabled [296] and reaching $\sim$ 70 µm track resolution. The latter technology reaches similar track resolutions, being only more rate-sensitive, about $\mathcal{O}(\mathrm{kHz\,cm^{-2}})$ whereas the micro-pattern detectors that are GEMs and MicroMegas may withstand rates up to $\mathcal{O}(100\,\mathrm{kHz\,cm^{-2}})$ without significant efficiency loss.

Each HPL would be integrated to the calorimeter modules, with 12 slightly overlapping $60 \times 72\,\mathrm{cm}^2$ GEM detectors on each module being proposed.

A limitation of the HPLs is the potential reduced efficiency, estimated to be a loss of up to $\mathcal{O}$(few%), due to late-showering photons, which may thus initiate shower development after the HPLs. As a result, optimisation of HPL positioning within the calorimeter to maximise the angular resolution and efficiency. The option of three HPLs would thus preferentially see a single HPL placed at the front section of the SplitCal with the other two placed at the back to allow for maximum track resolution. This issue is not affecting electrons which leave ionisation signals in the first calorimeter planes.

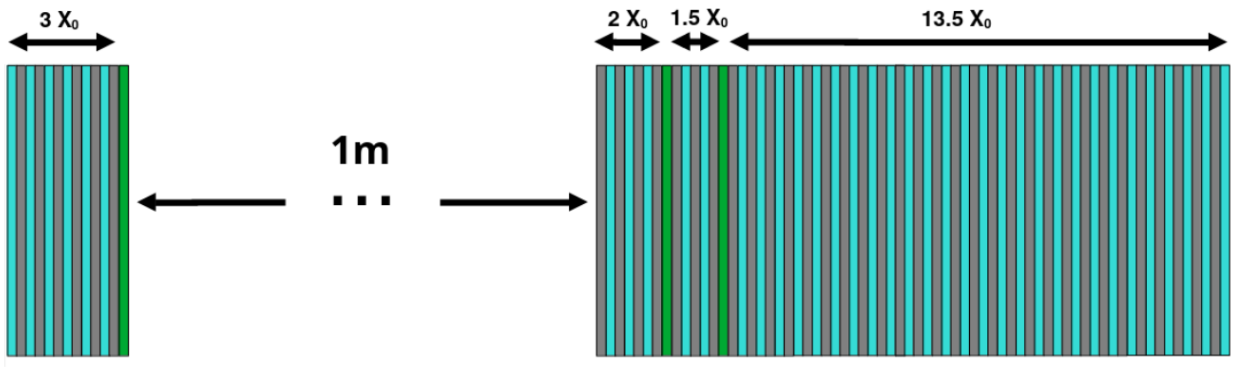

Figure 4.13: Schematic representation of the SplitCal using 3 high-precision-layers. Radiation and segmentation length is not final.

4.2.3 Thin scintillator bars

Recently, the option of thinner 1 cm scintillator bars has been explored and will here be denominated precision layers (PLs) in opposition to HPLs. They function similarly to HPLs in their role, albeit with coarser position resolution and more layers. They are similar to the wider scintillators but are traversed by a single WLS fibre and use smaller SiPMs as a result. This enables a potential for better timing measurements which in turn could be used for 4D tracking [363] and perhaps even time-of-flight PID for lower energy particles if the gap can be made sufficiently wide.

A single PL is cheaper than a HPL. PLs can therefore be more numerous and mitigate efficiency loss for late-showering photons if adequately placed. In addition, the ECAL's angular resolution benefits from a greater number of PLs [364] while energy resolution and thus certain aspects of PID performance are somewhat reduced by their greater use to the expense of wide scintillators (see Chapter 7). A visualisation of an ECAL section using PLs is shown in Figure 4.14.

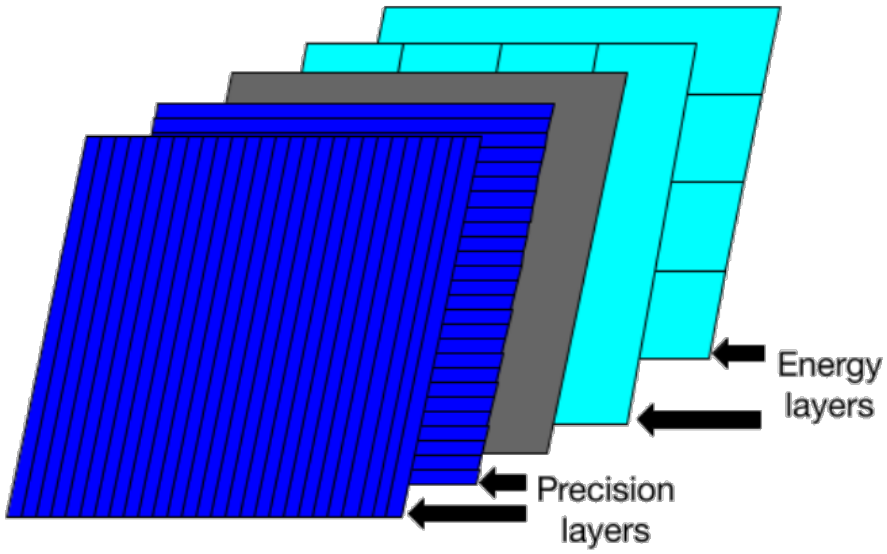

Figure 4.14: Schematic representation of a SHiP ECAL section using precision layers.

Limitations to the use of PLs, which could otherwise be used to built the entire ECAL include the poorer angular resolution which is shown in Figure 4.15. Compared to the wide scintillators, they have poorer energy resolution as a result of the reduced total SiPM pixel count and individual bars' light yields. In addition, the difference in SiPM capacitances to the wider layers has repercussions on the front-end readout electronics as discussed in Chapter 6. The main limitation however is their high cost which increases with the number of readout channels. This issue can be minimised by the use of the wide scintillator layers of Section 4.2.1. As a result, the PLs would be restricted to up to half of the total layer count, the exact amount of which remaining to be determined as an optimum of cost, angular resolution and PID performance. PLs finally suffer from SiPM

saturation for large showers which limits their charge weighing capabilities and hence their position resolution. This can be mitigated by using larger SiPMs with more pixels to readout the PLs, but this is expensive given the channel count.

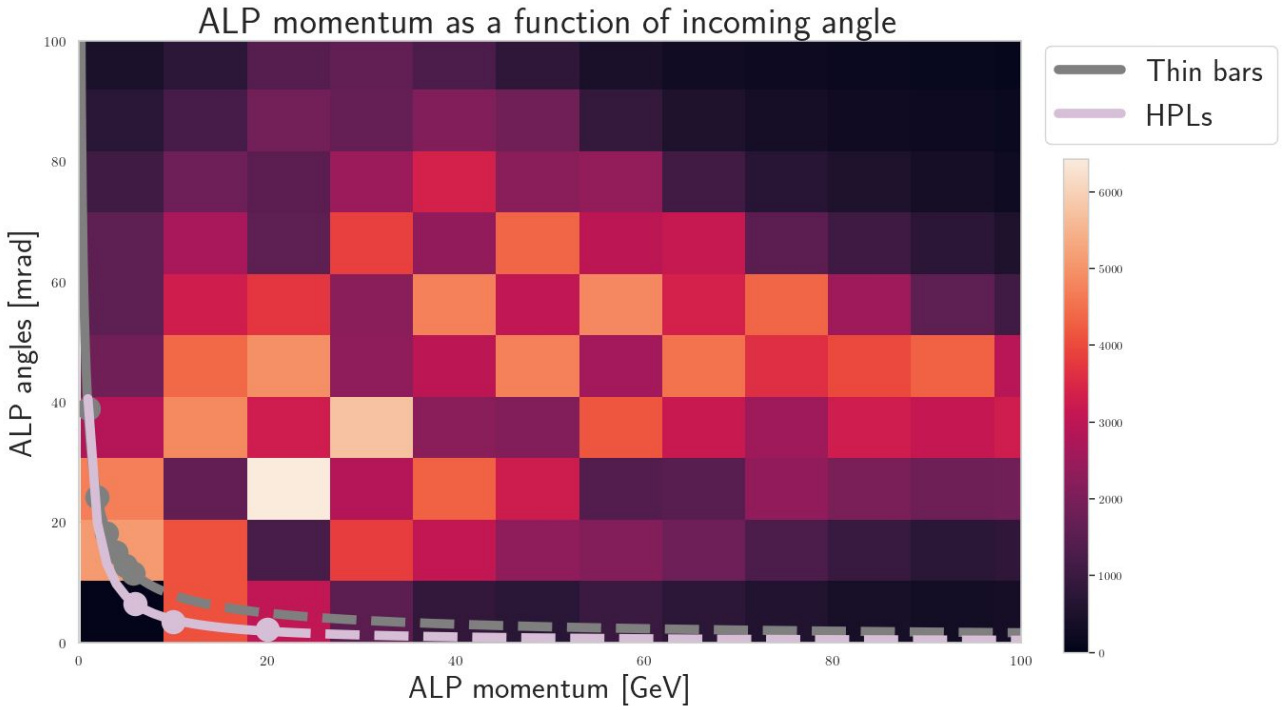

Figure 4.15: The resolution using HPLs is fitted from the tests performed in [360] while the resolution using PLs is fitted from data points extracted from test beams using 9 PLs (see [364] and Chapter 7). The HPL fit was deemed a realistic performance for physics studies.

The optimised SHiP ECAL would be using a combination of wide scintillators, PLs and HPLs, with the bulk of the detector relying on the first, the PLs being placed rather at the very front and at the back of the detector to minimise SiPM saturation. HPLs would be placed around the shower maximum, with at least one such layer in the front section, to maximise PID performance, angular resolution and energy resolution.

4.2.4 Detector integration

The integration of the SHiP calorimeters presents significant challenges due to their large size, high channel count (up to ~ 1.1 million for the HPLs), and complex service requirements such as cabling, readout electronics, and channel accessibility. These factors complicate accurate simulation, reducing calorimetric resolution. The total calorimeter weight ($\sim 250\,\mathrm{t}$) necessitates ceiling support, mitigated by a modular design limiting individual module weight to $40\,\mathrm{t}$. The readout scheme is optimised to reduce cable count, with transverse access via rail-mounted modules and vertical movement using a $45\,\mathrm{t}$ crane. Additional structural challenges arise in the ECAL due to the mechanical weakness of $2.8\,\mathrm{mm}$ lead sheets; thin aluminium or carbon steel backing plates are considered to provide support with minimal impact on shower development.

4.2.4.1 Electronic integration and SHiP calorimeter system DAQ & Trigger

The SHiP calorimeter system DAQ must comply with the requirements set out in Section 2.3.5. Similar to CMS [250], preference is given towards digitising analogue signal as close to the sensors as possible, with plans to integrate ADC information directly onto the SiPM and HPL PCBs respectively.

As a result, a single readout cable will be outgoing from each sensitive layer with the total data rate being estimated to be $\sim 500\,\mathrm{Mbit\,s^{-1}}$.

The ADCs signals will be processed by custom data acquisition computation boards (CALODAQ boards) which will assign channel numbers, both timestamps and final ADC values using software solutions, FPGA-

solutions being seen as unnecessary and overly complex given the low rates. The CALODAQs will include sufficient buffering to allow for all information to be processed without loss, the estimated total rate being $\mathcal{O}(2\,\text{MHz})$ for the scintillator layers and $\mathcal{O}(100\,\text{kHz})$ for the HPLs. In addition, they will be capable of assigning different formats to scintillator and HPL data if needed. The HCAL section, consisting of comparatively few channels represents a data flow substantially smaller than a single ECAL module and will thus either be combined for its data acquisition to other modules or will have its CALODAQs function without module differentiation.

Depending on the final SHiP DAQ architecture, the CALODAQ output will either be streamed to another processor-based concentrator board which would further align the data streams before they are sent to the higher level DAQ or be streamed to it directly. The considered DAQ scheme is shown in Figure 4.16.

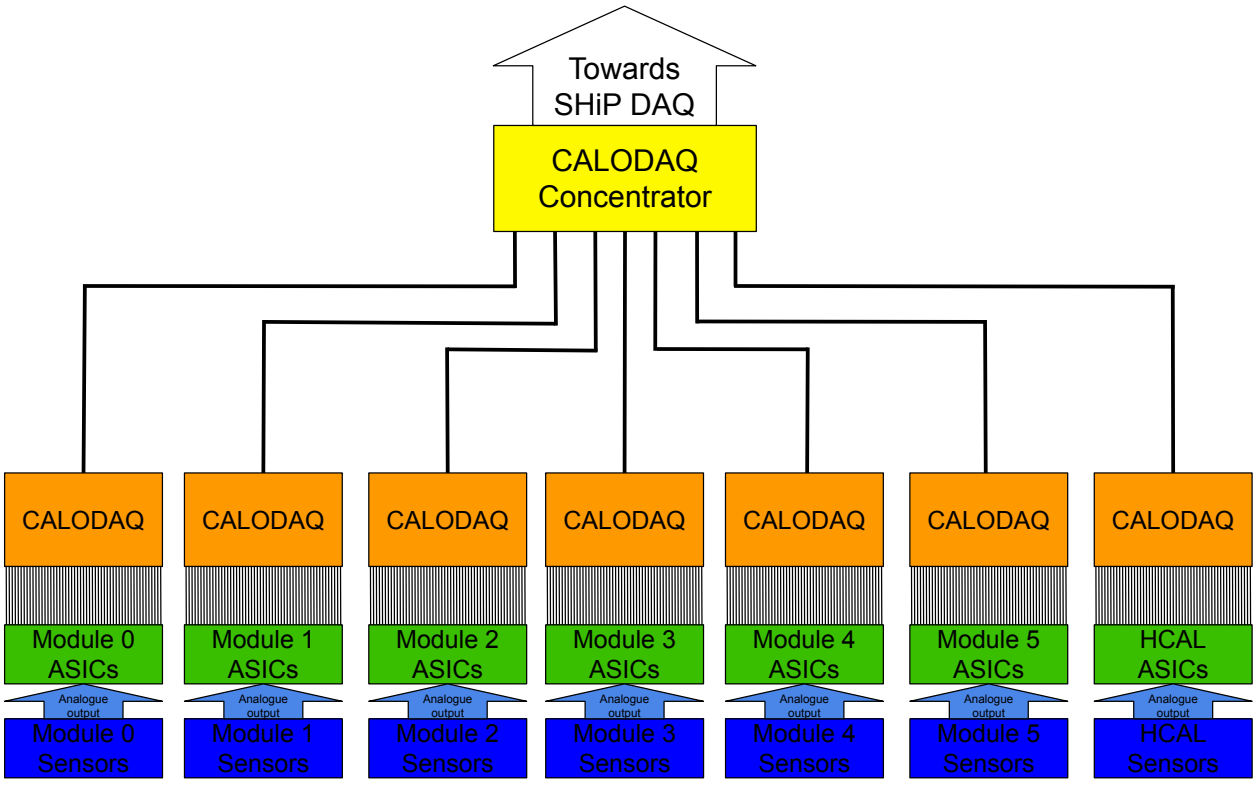

Figure 4.16: Example of the proposed DAQ scheme for the SHiP calorimeter system.

Chapter 5

Optimisation of scintillator light yield

The SHiP calorimeter system, relying on scintillators readout by SiPMs, needs to ensure adequate performance in terms of light yield. This therefore requires the linearity in response of the system, the adequate selection and matching of scintillator and SiPMs. This is presented in this chapter, followed by a study of scintillator light yield improvements and one of the scintillator-SiPM interface. The readout-electronics are presented in the following Chapter 6 and into the build-up and subsequent testing of a prototype, in Chapter 7. All fibres used hereafter are polished at their ends using sandpaper unless otherwise stated.

5.1 Motivation and infrastructure

5.1.1 Introduction and initial prototype

The scintillator bars, primarily the wide 6 cm bars of Section 4.2.1 are used in both the SHiP ECAL and HCAL sections. Their performance is instrumental in ensuring PID capabilities. A larger light yield translates to higher PE counts which leads to better stochastic energy resolution. The goal of the studies led in this chapter is the optimisation of the light yield of the SHiP calorimeter system's scintillator to achieve the best possible energy resolution. This can be done by increasing the amount of light produced inside of the scintillator, the amount captured by the WLS fibres, the amount reaching the scintillator's readout end, the amount that effectively exits the scintillator and the amount of light converted into photoelectrons.

This has led to a substitute over the NA62 scintillator towards a newer scintillator, the EJ-200 which better integrates its plastic base with wavelength shifters. An examination of the importance of foil evenness has also been carried out as well. Greater light levels induce increased SiPM saturation (Section 3.3.5.3). Hence keeping the fibres close to the photosensing surface will not make full use of the SiPM's pixels. As a result, a gap between fibres and SiPMs is introduced to increase dynamic range.

The optimisation studies started from an initial prototype which was operated in 2017, 2018 and 2019 in a series of test beams at CERN PS and DESY [359]. The prototype detector components are shown in Figure 5.1. Sensitive and passive layers may easily be slotted into the prototype using a slot system. The initial prototype notably included two HPLs (MicroMegas)[365], which were operated to great success. The energy reconstructing layers were 6 cm leftover scintillators bars from the NA62 MUV1 [366] wrapped in aluminised foil, traversed by 2 Y11 Kuraray WLS fibres [367] and readout on both sides by S13360-3050PE and S13360-6050PE SiPMs, $3 \times 3\,\mathrm{mm}^2$ and $6 \times 6\,\mathrm{mm}^2$ [368] respectively. The initial prototype readout electronics are covered in Chapter 6.

This prototype, while demonstrating the underlying soundness of the chosen design, needed to be optimised to provide greater light yields and a single type of SiPM to optimise cost and performance. This was done through optimisation of the scintillator bars themselves, of the SiPM and of the interface between WLS fibres and SiPMs, the principles of which are detailed hereafter. In accordance with usage in the SHiP calorimeter system, all scintillator used in the following bars are 6 cm wide unless otherwise specified.

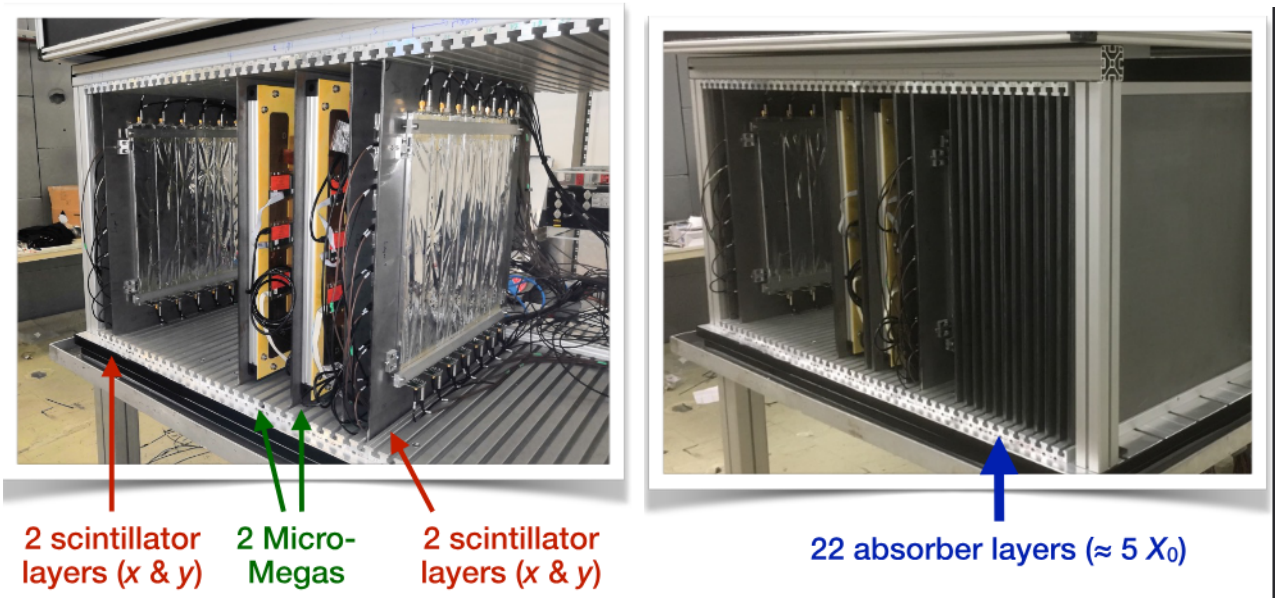

Figure 5.1: Initial prototype [369].

5.2 Laboratory infrastructure

The studies towards calorimeter development performed in this and the next chapter were conducted in the University of Mainz's PRISMA detector photonics laboratory, which are detailed below.

5.2.1 Laser test stand and dark room

The laboratory is divided into two primary sections: a lit laboratory and a dark room which is hermetic to external photons and limits photon propagation in itself thanks to its black walls. The dark room is isolated from the outside using a set of dark curtains and an interlocked door. An additional access exists to allow for cables to be brought from the outside.

The dark room is equipped with an optical table as well as an Advanced Laser Diode Systems tunable laser system. The laser itself has a 377 nm wavelength, adequate to excite plastic scintillators and irradiate SiPMs directly. It has tunable power, up to 1000 mW through both an external and internal attenuator. The laser pulses are 29 ps long and may be emitted at a tunable frequency up to 1 MHz. The laser attenuation is known not to be linear accross its entire range, and the size of the laser irradiation region is known to decrease with attenuation. The stand is pictured in Figure 5.2. The laser output can be displaced using a 3D-movement system which has sub-mm accuracy, allowing for fine alignements of the laser relative to the SiPM.

5.2.2 Cosmic ray test stand

Cosmic muons, having fluxes of $\sim 1\,\mathrm{cm}^{-2}\,\mathrm{min}^{-1}$ and being good approximations of MIPs, may be used to perform measurements in conjunction with scintillators and SiPMs or PMTs. This type of setup may be compact but still requires perfect darkness, leading to a specially created dark box as cosmic test stand used in the laboratory, pictured in Figure 5.3. The stand is sealed with black tar paint ensuring light hermeticity. It has bent pipes equipped with black cloth to allow power and readout cables to be inserted inside the box while preventing any light from reaching the inside of the box.

5.2.3 Data acquisition

For the laboratory setup, a 4-channel Rohde & Schwarz RTO6 oscilloscope [370] was used which, thanks to its high sampling rate and functionalities, allows for visualisation and measurement of waveforms. The used functionalities are:

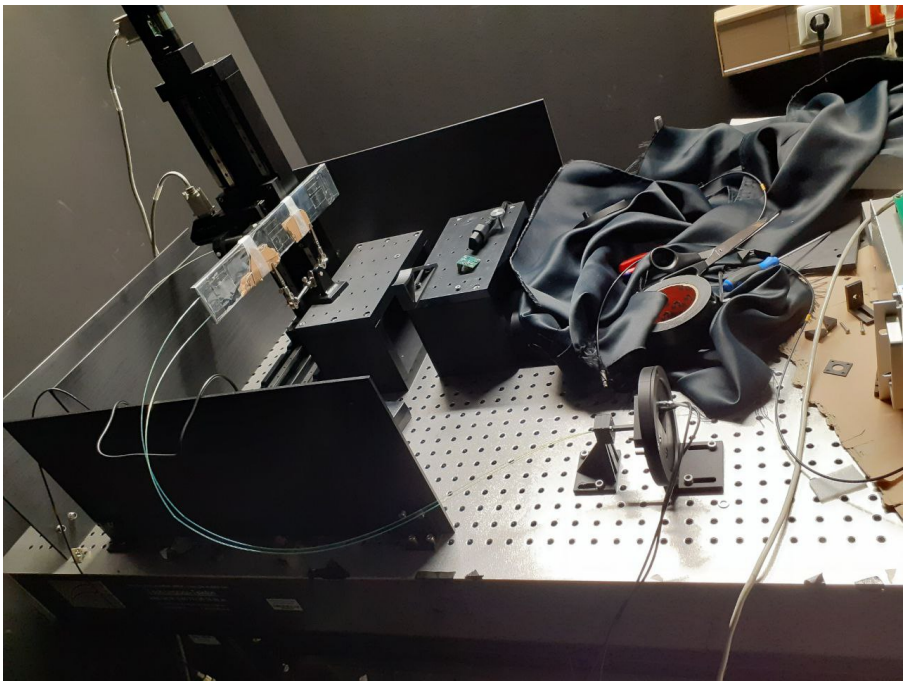

Figure 5.2: Laser stand in the dark room. The laser is pulsed onto a scintillator bar from which WLS fibres are sent towards a SiPM situated on the shown device below.

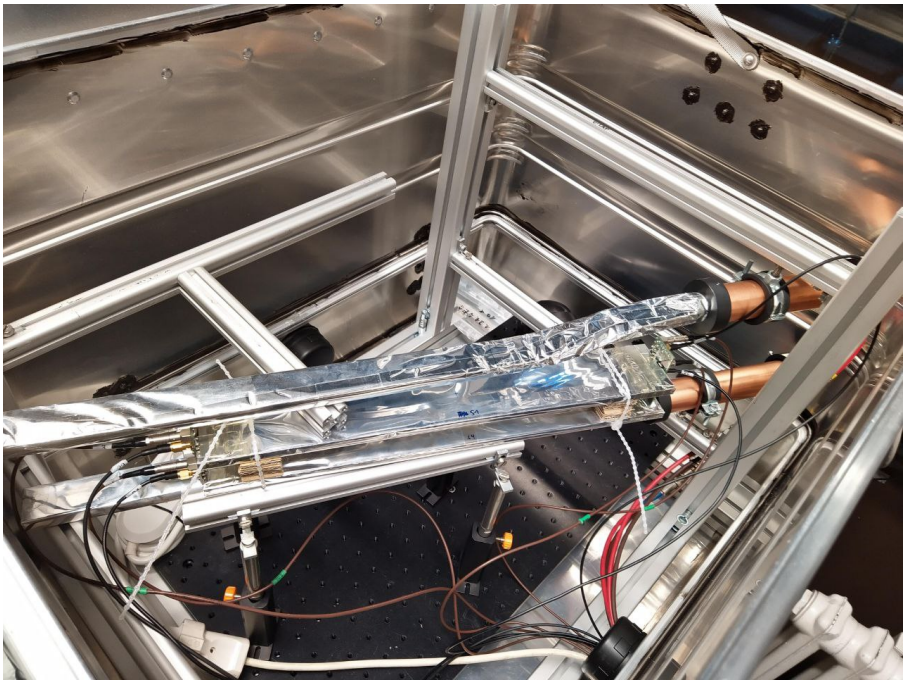

Figure 5.3: Inside of the cosmic box which here contains two scintillators readout, by two SiPMs each, and using two extra scintillators readout by PMTs as a trigger.

- A rising edge trigger which records a pulse if its amplitude is larger than a set amount. It is used to trigger on the laser itself whenever the laser is used.
- Measurements of the amplitude mean and the root mean squared (RMS) standard deviation
- Long term measurements of amplitudes and RMS standard deviations, which allows to record up to several billions of waveforms.

5.3 Photoelectron calibration

A direct consequence of the capacitor-like behaviour of SiPMs (see Section 3.3.5.3) is that their output manifests as a pulse with a width fixed by the SiPM circuit capacitance and an amplitude proportional to the PE count. Calibrating this voltage is necessary to determine the SiPM response and ensure that changes in operation reliably bring improvements independently of operation conditions. This calibration is done using the relation $N_{\mathrm{PE}} = C_{\mathrm{PE}} A_{\mathrm{SiPM}}$, with N_{PE} the number of photoelectrons, A_{SiPM} the amplitude of the SiPM pulse in mV and C_{PE} the calibration constant to be determined. C_{PE} is specific to each SiPM for each bias voltage and operating temperature. The characteristic energy deposition calibrations are typically given in PE/MIP for a given detector system (such as a scintillator bar readout by SiPMs), rendering PE calibration essential for inter-SiPM comparisons and the operation of multi-channels detectors.

The calibration has here been done in three different fashions: *unamplified SiPM dark count pulses*, *amplified SiPM dark count pulses* and *Digitised SiPM pulses*, which are described below.

5.3.1 Unamplified SiPM dark count pulses

As explained in Section 3.3.5.3, SiPM suffer from so-called dark current which is the spontaneous emergence of pulses from SiPMs operated above breakdown voltage. While these pulses are typically small, they may be observed and identified on an oscilloscope. Because of their small amplitude, triggering on these pulse without specialised equipment is challenging as the typical resolution of most oscilloscopes does not extend below 1 mV because of electronic noise. Nonetheless, the pulses are normally distinguishable by eye as they are identical for a given amplitude and appear with frequencies higher than 1 kHz for most voltages. The preferred solution is thus the optical selection of such pulses on the oscilloscope's screen. Larger pulses are considerably more rare than smaller ones and they always have an amplitude which is an integer multiple of the smallest pulse. An example of the selection procedure is shown in Figure 5.4. The selection statistics is limited by the measurement time. Still this remains a simple and quick way to determine C_{PE}.

This technique, despite being quick and simple, suffers from a lack of accuracy related to the optical selection of peaks and the limited resolution of the oscilloscope. These factors may be improved upon though the other two techniques. Indicatively, the single PE amplitude using this technique with a $6 \times 6\,\mathrm{mm}^2$ SiPM operated near the optimal voltage provided by manufacturer ($\sim 55\,\mathrm{V}$ and $\sim 42\,\mathrm{V}$ for the S13360-6050PE and S14160-6050HS respectively), yields $C_{\mathrm{PE}} \sim 0.18\,\mathrm{mV/PE}$.

5.3.2 Amplified SiPM dark count pulses

The smallness of the pulse are the limiting factor for the reconstruction of single PE peaks. This naturally invites the amplification of the SiPM signals to allow for an increased amplitude that will lie within the oscilloscope's resolution. The underlying principle for measuring C_{PE} is thus identical to the previous section.

The main difference lies in the use of the custom voltage-controlled amplifier (VCA) adapted to be powered externally. The amplifier PCBs are shown in Figure 5.5. The VCA receives an input voltage which determines its gain. The gain profile is evaluated by connecting to a test SiPM illuminated using the laser at a fixed low intensity before and after amplification and computing the ratio of the two corresponding to the VCA's gain, shown in Figure 5.6.

With the gain profile known, it is possible to observe dark count pulses by eye with much greater ease and thus more easily determine C_{PE} by dividing the observed pulse amplitude by the gain at the corresponding amplifier bias: $C_{\mathrm{PE}} = \frac{A_{\mathrm{obs}}}{G_V \times N_\gamma}$. This is performed on a large number of pulses for each bias voltage to reduce statistical uncertainty while keeping the measurement short enough. When performed across 20 pulses for each

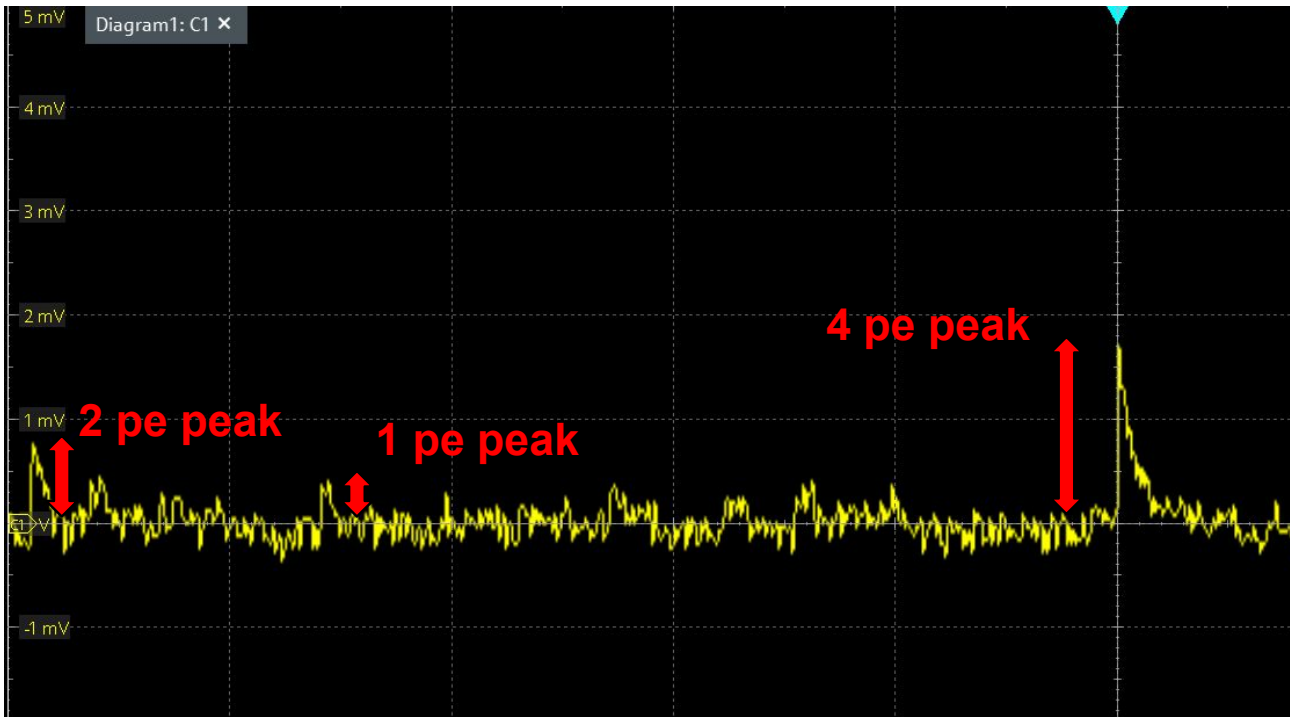

Figure 5.4: Example selection procedure for PE calibration. The S14160-6050HS SiPM is left inside the dark room. The SiPM is powered using a custom power supply and its signals are measured on the oscilloscope. It can be seen that in this case, that $C_{\mathrm{PE}} \sim 0.4\,\mathrm{mV/PE}$. This example is deliberately operated at higher levels of HV than normally used for illustration, which significantly increases the amplitude of the PE peaks.

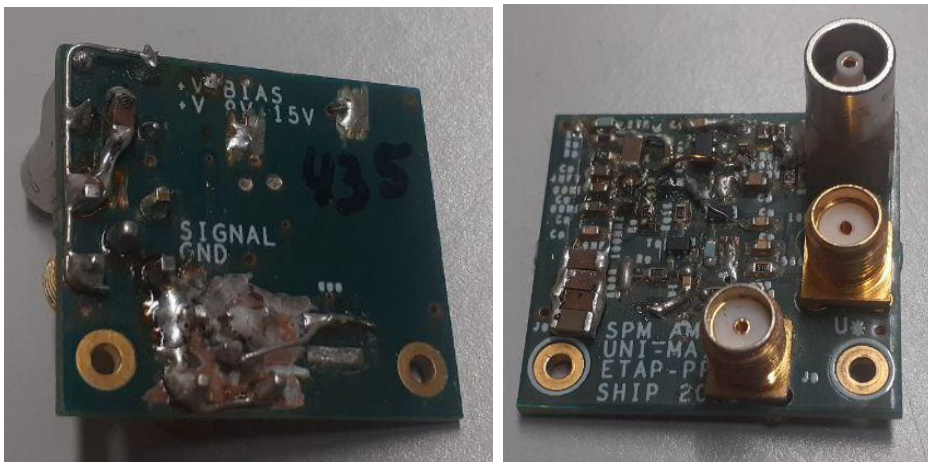

Figure 5.5: Adapted VCA PCB front (left) and back (right) side.

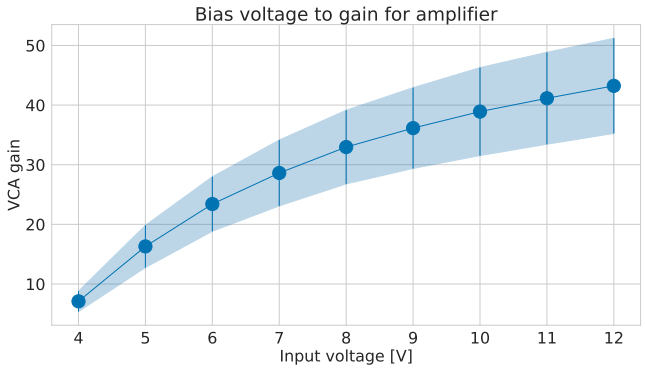

Figure 5.6: Gain profile of the used VCA. The VCA is known to saturate at high input charges is and thus best suited to operate at low SiPM irradiation.

voltage, it yields distributions such as shown in Figure 5.7. The key issue is the increased amplifier noise at higher voltages which significantly increases the systematic error on the measurements. The correlation, is found to be $\rho = 0.97$, the noise is almost fully correlated to the VCA's input voltage. It then becomes possible to compute a calibration constant which in the example case yields 0.174 ± 0.078, consistent with the unamplified case. While this allow for calculation instead of observation of C_{PE}, the uncertainties related to the amplifier limit the reliability of this method, in the absence of a less noisy amplifier, this leads to the digitised SiPM pulses PE calibration.

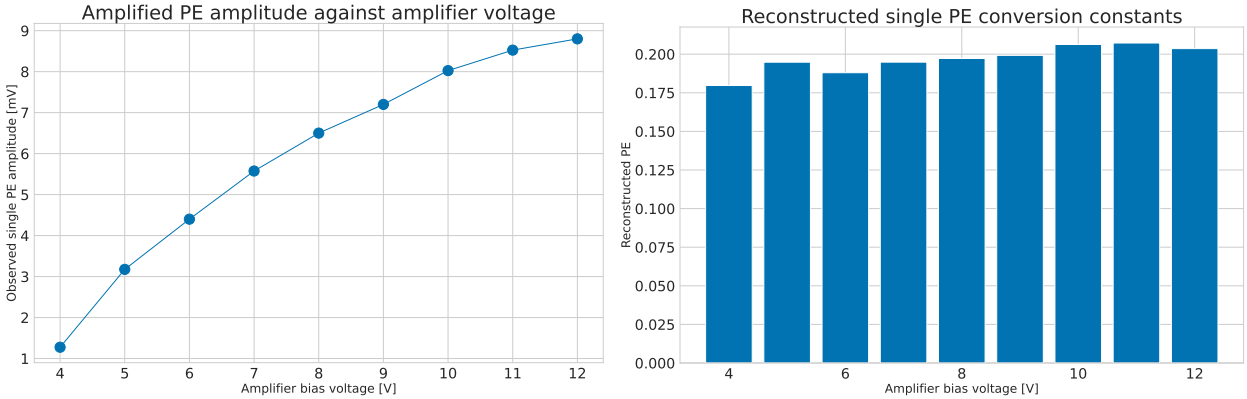

Figure 5.7: Observed single PE amplitude as a function of amplifier voltage (left) and distribution of reconstructed SiPM C_{PE} as a function of amplifier bias voltage (right).

5.3.3 Digitised SiPM pulses

The most accurate method utilised here uses an analogue to digital converter (ADC) (see Appendix E). These readout electronics convert the amount of charge yielded by the SiPM over a pulse into a digital, numerical entry and can be designed to be made highly sensitive and linear. For instance, the amount of charge contained within a 100 ns and 1 mV SiPM pulse is ~ 2 pC which could for example be digitised as 50 ADC counts. A 5 mV pulse, representing ~ 10 pC of charge would then, assuming good linearity and enough ADC channels be digitised as 250 ADC counts (the pedestal is neglected in this simple example).

Using a fine enough ADC, possibly operated with a low-noise amplifier, it becomes possible to visualise the difference in voltages created by the discrete nature of the SiPM response. This can be visualised through a histogram in which each peak will correspond to a single PE count. If the SiPM PDE were 1, there would be a single value of N_{PE} taken by the SiPM signal, assuming no variation in illuminated area. If the SiPM and ADC were perfect, there would in addition be no overlap between peaks. Thermal effects on the SiPM and electronic noise on the ADC cause each Dirac comb corresponding to a single PE count to be smeared into a gaussian. Nonetheless, provided that these effects are not too significant, it is possible to define a SiPM *resolution* $R = \frac{\langle \mu_{i+1} - \mu_i \rangle}{\sqrt{\sigma_{i+1}^2 - \sigma_i^2}}$, where μ_i is the average ADC value of the i^{th} peak and σ_i its standard deviation. This is shown in Figure 5.8.

Provided the resolution is high enough, it becomes possible to separate PEs on the ADC histogram as shown in Figure 5.8. Irradiating the SiPM to a set laser illumination and measuring the induced pulse amplitude on the oscilloscope yields an average amplitude (2.66 ± 0.69 mV in the example case). This amplitude may be matched to a PE count and further to an ADC count, using the dark count as the start of the PE spectrum. The consistency of the technique is ensured by verifying that the selected starting point on the dark count spectrum is correctly spaced from its neighbours, with the first peak with inconsistent spacing interpreted as the pedestal corresponding to the electronic noise emerging from the ADC. The dark count being below the set oscilloscope trigger, it must be cut which is done using a $5\,\sigma$ cut to the right of the dark count peak. This is seen as acceptable as dark count is otherwise dominating the ADC distribution. In addition, the amplitude distribution quickly decreases away from the average in the signal region. The average of the ADC distribution is thus matched to an amplitude which is itself matched to a PE count.. This yields $C_{\mathrm{PE}} = \frac{A_{\mathrm{osc}}}{N_{\mathrm{PE}}}$ which in the example case yields $C_{\mathrm{PE}} = 0.172 \pm 0.045$ mV/PE consistent with both previous methods but much more accurate.

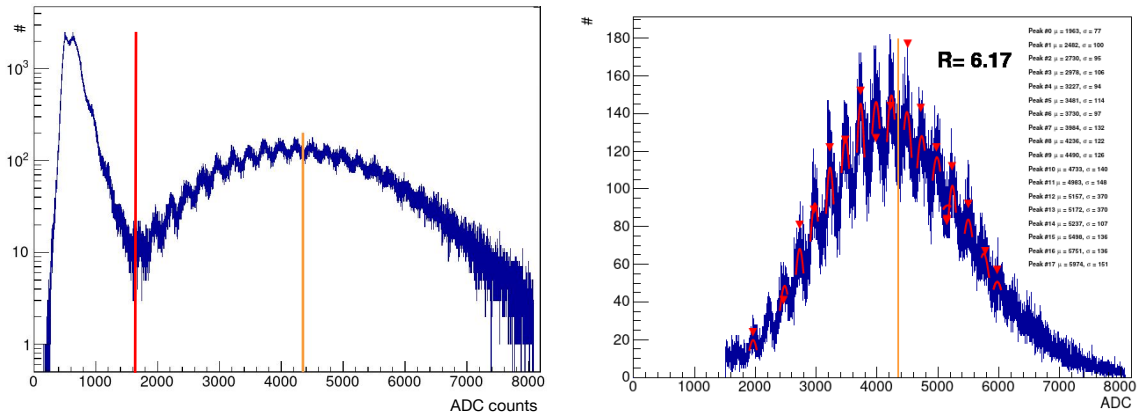

Figure 5.8: ADC spectrum of the example SiPM including the pedestal and dark count (left) and after dark count removal (right). The red line indicates the $5\,\sigma$ cut on the dark count, the orange line represents the average laser-induced signal.

Digitised pulse PE calibration is thus the more accurate technique. It is, however, more time-consuming and complex to apply. As a result, the unamplified pulse technique, due to its simplicity and relative accuracy is preferred and is used in what follows unless otherwise stated.

5.4 Scintillator optimisation

The amount of light yielded by a scintillator element is dependent on the material itself but also the way it is readout. It is relevant to determine whether the scintillator performance can be enhanced to increase the light output. The light yield optimisation has been examined through a characterisation of base scintillator characteristics as well as determining whether the scintillator foil can be a factor for improved performance, as presented below.

5.4.1 Scintillator characteristics

Two distinct scintillators were used in this context: the NA62 custom polysterene/p-terphernyl/POPOP scintillator and the Eljen EJ-200 scintillator [272]. The Eljen scintillator's spectral profile is known with good precision from the manufacturer and many other experiments including SND [272]. That of the NA62 scintillator is known *a priory* but only at the time of the NA62 build and not to the extent that it may have aged since. This is a known concern for plastic scintillators [371]. It is in particular known that the plastic base substrate may lose transparency at higher wavelengths. It was thus reexamined to ensure performance using a spectrometer. The spectrometer functions by sending light from 250 nm until 500 nm and measuring the difference between sent and measured intensities. This allows to form an absorption spectrum which is expected to display high levels of absorption at low wavelengths due to fluorescence mechanisms (Section 3.3.4.1) and a much lower amount of it at higher wavelengths as it becomes transparent. This spectrum was measured and is shown in Figure 5.9.

While the NA62 scintillator had been machined to great regularity with the University of Mainz's workshop, the Eljen one was directly supplied by the Scionix company, thus requiring an evaluation of its regularity to ensure performance homogeneity. This was done investigating the thickness in different locations using a pair of calipers and scintillator bar segments. Each scintillator segment section is expected to be precisely 1 cm thick and was investigated twice, the results can be found in Figures 5.10 and 5.11. The thickness distribution is not centred on the nominal 1 cm. This is taken as introducing a $\frac{0.19}{9.7} = 2\%$ systematic uncertainty on light intensity in the following measurements using this scintillator.

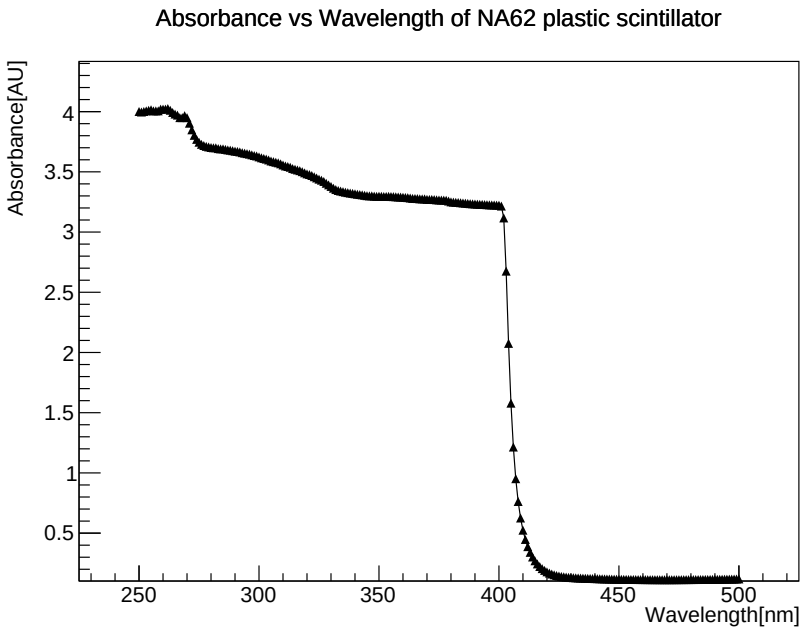

Figure 5.9: Absorption of a 1 cm thick NA62 scintillator given as a function of injected wavelength. The initial plateau until 270 nm is dominated by the polysterene base substrate. Afterwards come the p-Terphernyl until 320 nm and POPOP until 420 nm respectively. The irregularity of the distribution around 270 nm is understood as being aging which, regarding the irregularity, is low and thus unlikely to significantly affect performance.

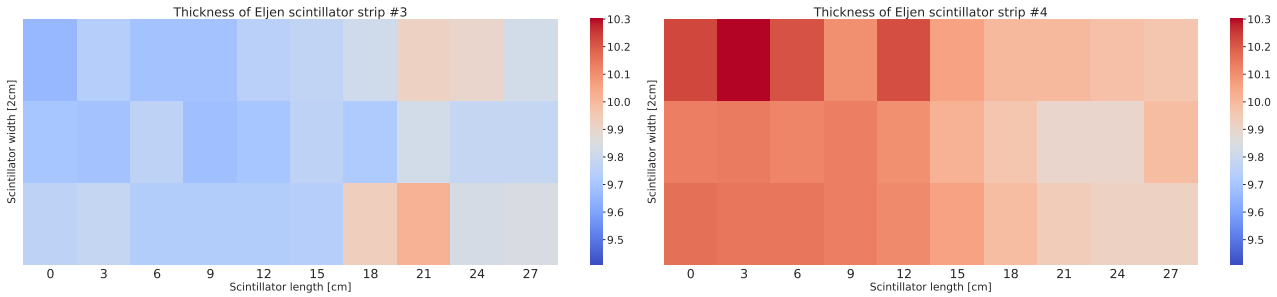

Figure 5.10: EJ-200 scintillator thickness examples as measured across segments, the thickness is given in mm.

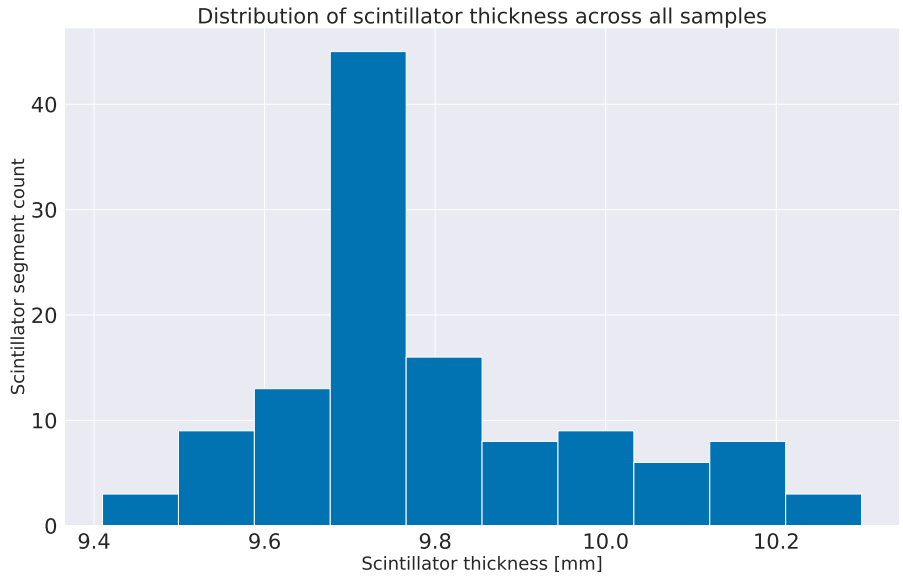

Figure 5.11: Scintillator segment distribution. The thickness is found to vary with a standard deviation of 0.19 mm.

5.4.2 Fibre efficiency

Wavelength shifting fibres, used to trap the scintillator light and to route it to a SiPM, have different spectral profiles based on the dyes used and the exact manufacturing techniques used. It should be noted that this is assumed to mainly affect the output wavelength distribution and not the spatial or angular distribution of the light output as the underlying principles of cladding-bonding are expected not to change, although this is confidential to the producing company. The emission spectrum is here provided by the Kuraray company [367] and may be convoluted with the spectral PDE response of the Hamamatsu SiPMs to determine which fibre model, given a SiPM model, would yield the best match between PDE and emitted light wavelength. This is done by matching, for every provided wavelength (given in this case with a 10 nm binning) the SiPM PDE at the same wavelength in question while normalising by the relative light intensity at the same wavelength while assuming that the total photon count remains identical between fibres (which is implied by [367]). This was done for the three most promising available models (Y11, YS1, YS2) for a S14160-6050HS SiPM, leading to Figure 5.12.

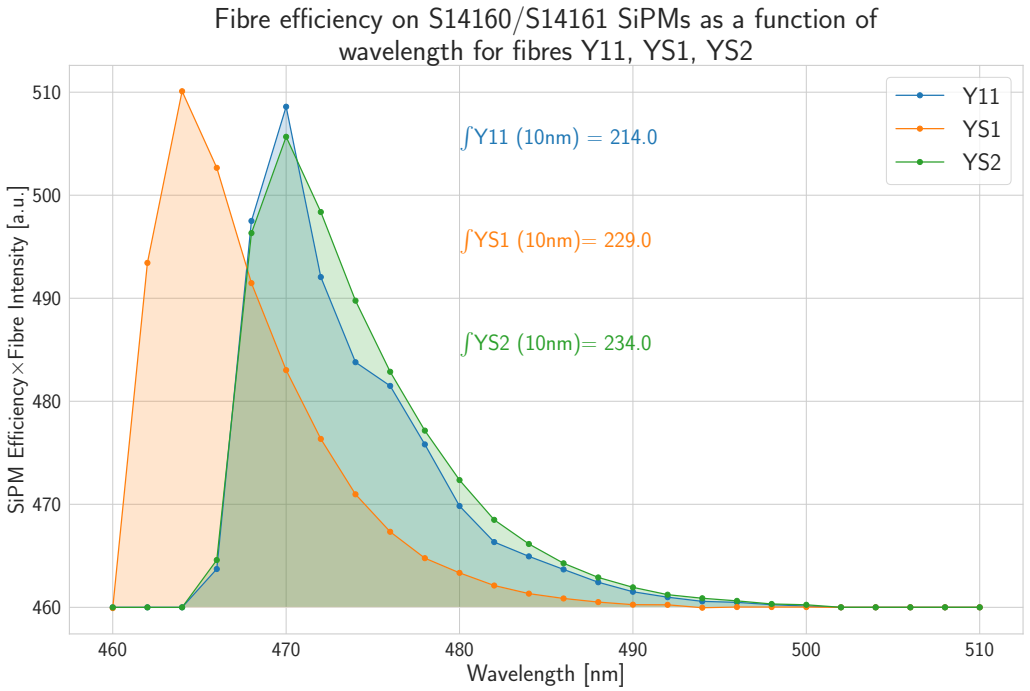

Figure 5.12: Integrated efficiency of the Kuraray Y11, YS1, YS2 WLS fibres together with a Hamamatsu S14160-6050HS SiPM.

It can be observed that the YS2 fibres provide the best integrated efficiency in the examined case, although their spectral efficiency peaks lower than, for instance the YS1 fibres.

5.4.3 Optimisation of the scintillator foil

The scintillator foil plays the essential role of maintaining the scintillation light within the scintillator and ensuring bar-wise isolation. Whether the foil should be crumpled or kept smooth has been a debate amongst detector physicists. The argument in favour of creasing the foil used to pack the bars is to allow for a greater diversity in light angles, thus allowing more light to be trapped within the fibres and/or to reach the SiPM readout window. The argument against is that induced degradation of the foil, leading to worst reflection. To determine whether either case is preferred, a measurement has been led using 3 EJ-200 $6 \times 36 \times 1\,\mathrm{cm}^3$ scintillator bars wrapped into smooth reflective foil, the foil for each was then removed and crumpled by packing them into a ball by hand, then smoothing it back by hand and using it to wrap the bar again as shown in Figure 5.13. Protective latex gloves were used during the operation to minimize any contamination of the foil while the scintillator was kept on protective high-quality washing paper during the operation for similar reasons. Since it is difficult to ensure that the packing is entirely identical, the use of a hole in the foil for laser irradiation was not utilised. As a result, the use of cosmic radiation was preferred. The scintillator bars were therefore

put into the cosmic box with its broad side facing up and readout on both sides by two S14160-6050HS SiPMs. A coincidence circuit with a window width of 50 ns was programmed into the oscilloscope to ensure that the data was only recorded if both SiPMs have a signal above 20 PE with the system left to run precisely 10 h each. The means of each SiPM channel were averaged and compared in both the crumpled and smooth foil case. A correction factor to the lowest performing of the two channels was applied to equalise performance on both sides of the scintillator, it is determined by irradiating both SiPMs using the laser at a fixed intensity and observing the difference in response between the two SiPMs due to PDE. The correction is defined as $c = \frac{N_{\mathrm{PE,higher}}}{N_{\mathrm{PE,lower}}}$ with A the amplitudes of the higher and lower performing channels respectively. The results for each case are shown in Appendix C.3.

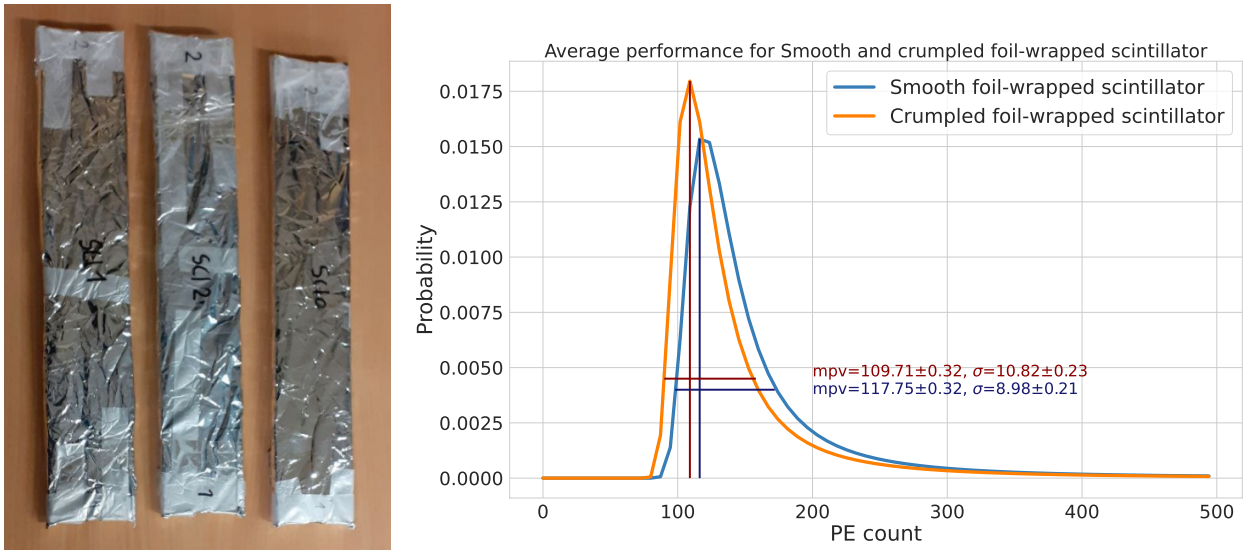

(a) Picture of the three scintillator bars used for the measurement in crumpled foil.

(b) Aggregated results of runs for all three cases. The smooth foil case performs 7.33 ± 0.43 % better than the crumpled foil case.

Figure 5.13

Within uncertainties and as shown in Figure 5.13, smooth foil performs better than crumpled foil by around 7%. Smooth foil should thus generally be preferred as it is easier to use and less likely to induce cracks in the scintillator structure.

5.4.4 Conclusion and outlook of scintillator optimisation studies

The studies made in this section suggest that scintillator aging is not a major issue at the time scales examined. Furthermore, scintillator irregularities from the manufacturer are a source of minor concern and can be avoided by ordering thicker scintillators that are then polished to the right thickness in house or performing specific calibration for each scintillator. The WLS fibres available from Kuraray best suited for the SHiP calorimeter system are expected to be the YS2, assuming that S14160-6050HS SiPMs are used. Lately, some other AFBR-S4N66C013 SiPMs from FBK-Broadcom [372] have come under consideration which are also likely to match the SHiP calorimeter system's requirements. The evaluation of the best WLS fibre model would have to be repeated for these SiPMs if they were to be used, especially seeing as the spectral performance profile of these SiPMs is different from the Hamamatsu ones with more efficiency at shorter wavelengths, make YS1 fibres potentially competitive in this range.

Finally, it has been determined that within uncertainties, smooth reflective foil is to be preferred when packing scintillators and are thus preferred.

The YS2-WLS fibres and smooth foil are thus preferred for usage in the SHiP calorimeter system.

5.5 Optimisation of fibre-SiPM interface connection

The interface connection between WLS fibre and SiPM allows to spread the photons outcoming from the fibre's facet. This allows to limit saturation induced by large amounts of photons. The optimisation of this interface connection can be done through Monte Carlo simulation but requires:

- A description of the photon behaviour along the WLS fibre: this is done through a Zeemax simulation [373]
- A description of the photons on the fibre's facet: this is done through the custom *Fibresim* toolkit [374]
- A propagation of the photons onto the SiPM surface: this is done through the custom *Fibresim* toolkit
- A description of the SiPM response to incoming photons: this is done through the custom *Fibresim* toolkit

The Zeemax and Fibresim simulations are described in the following.

5.5.1 Simulation studies of the WLS fibre

The Zeemax simulation [318] is based on setting optical indices in space and generating photons. As such, a 200 cm cylinder surrounded by two levels of cladding are setup to mimic the WLS fibre following Figure 5.14. Photons are isotropically generated within the fibre centre within a 30 cm length which has its centre 100 cm away from both fibre facets. These photons may then:

- Not be totally internally reflected: they then escape the fibre layer. If the photon escapes the outer cladding, it escapes the fibre and is considered lost
- Propagate in the wrong direction: the photon propagates away from the SiPM while remaining inside of the fibre. It is considered lost
- Be absorbed by the WLS fibre, they are then lost
- Remain within the fibre and reach the facet equipped with a SiPM. These photons may then induce a signal.

Only $\sim 2.3\,\%$ of all photons are found to reach the fibre's end. Those photons may either have propagated "straight" to the facet if they were emitted with a small polar angle with respect to the fibre axis or spiral around the fibre if they were emitted with a large polar angle. These phenomena can be seen in Figures 5.15 and 5.16.

The spatial and angular distributions of the photons reaching the fibre facet determine whether the photons may exit the fibre and reach the SiPM. Photons with a large polar angle at the fibre facet will be totally internally reflected and remain trapped within the fibre, those photons are also effectively lost. The photons with small polar angles can exit the fibre. The spatial and angular distribution of photons on the fibre's facet are shown in Figure 5.17. The correlation between both distributions is shown in Figure 5.18. The photon angular distribution is found to peak near 40°. The photons at angles beyond 45° are mostly spiralling photons.

Photons totally internally reflected on the fibre facet have larger angles which leads to losses dependent on the optical index of the medium outside of the facet. These are shown in Figure 5.19. Accounting for these losses, the correlation between position on the fibre and angle after exiting the fibre assuming an optical index of 1 (air) outside of the facet is shown in Figure 5.20.

This leads to a modified angle-position correlation distribution for the photons exiting the fibre, shown in Figure 5.20.

These studies suggest that light yield can be significantly increased by reducing photon losses from the fibres to the SiPM as large photon amounts are lost to total internal reflection at the fibre facet. This could be done by reducing the optical index of the optical cement used to bound the fibres to the scintillator. In addition, the angle of photons reaching the fibre facet indicates that large amounts of light $\sim 60\,\%$ is lost to total internal reflection and could be recovered by increasing the optical index at the fibre facet. This type of optimisation can be simulated using the FibreSim toolkit, which uses these distributions and is described below.

Materials

		Materials	Refractive index	Density (g/cm³)	No. of atom per cm³
Core		Polystylene(PS)	n_D=1.59	1.05	C: 4.9x10²² H: 4.9x10²²
Cladding	for single cladding inner for multi-cladding	Polymethylmethacrylate (PMMA)	n_D=1.49	1.19	C: 3.6x10²² H: 5.7x10²² O: 1.4x10²²
	outer for multi-cladding	Fluorinated polymer (FP)	n_D=1.42	1.43	

Cross-section and Cladding Thickness

	Single Cladding	Multi-Cladding (M)
Round Fiber (D)	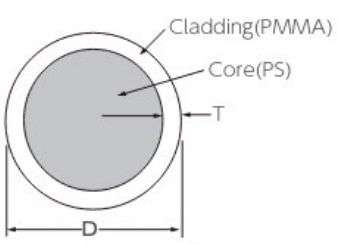 Cladding Thickness[1]: T=2% of D Numerical Aperture: NA=0.55 Trapping Efficiency : 3.1%	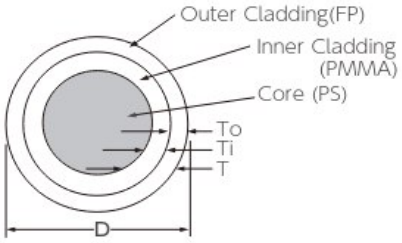 Cladding Thickness[2]: T=2%(To)+2%(Ti) =4% of D Numerical Aperture : NA=0.72 Trapping Efficiency : 5.4%

Figure 5.14: Technical characteristics of the Y11 fibres [367]. These were used instead of YS2 because of documentation availability.

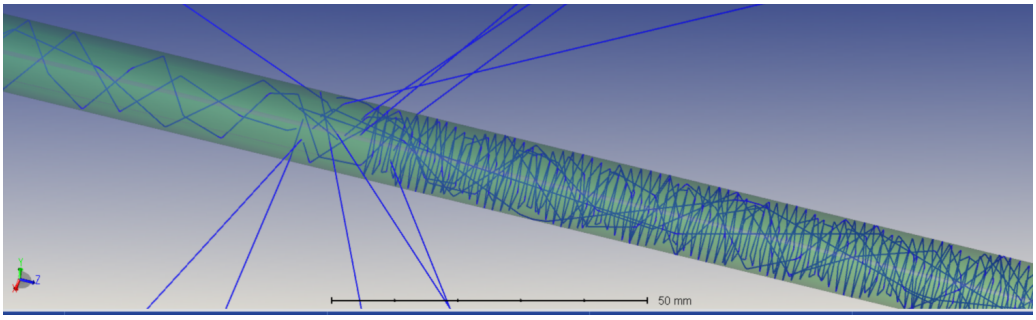

Figure 5.15: Visualisation of the Zeemax simulation. Very high polar angle photons, represented by the blue lines, exit the fibre whereas lower angle photons are trapped either spiralling or propagating straight [373].

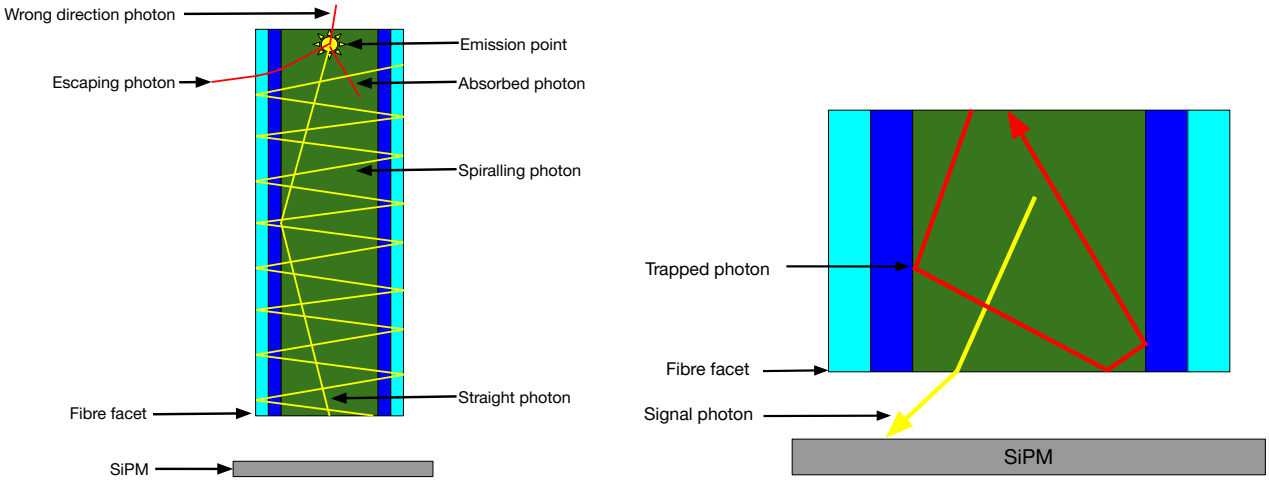

Figure 5.16: Fibre effects on photons during the propagation (left) and on the fibre facet (right). Yellow photons are susceptible to induce a signal, red ones are lost. The green area represents the fibre core, the blue and cyan represent the inner and outer cladding respectively.

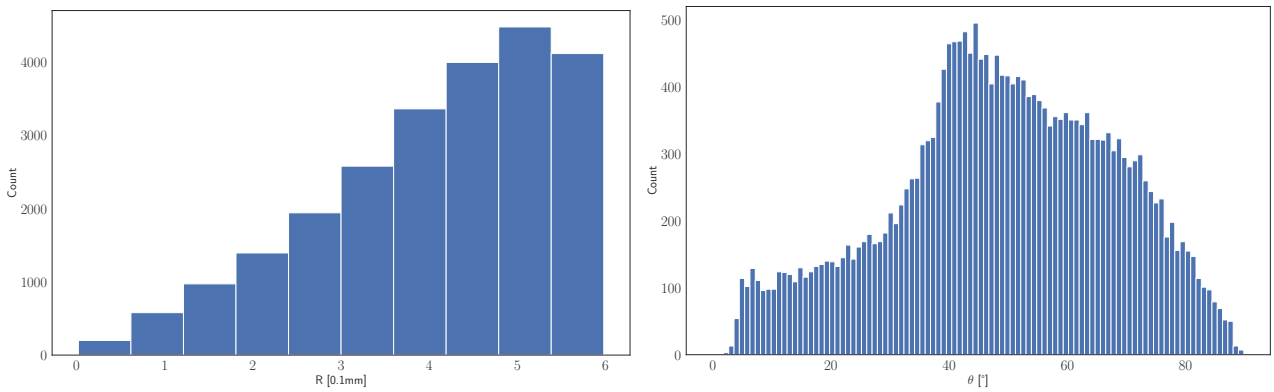

Figure 5.17: Radial position of photon (left) and Angular distribution of photons (right) at the fibre's output.

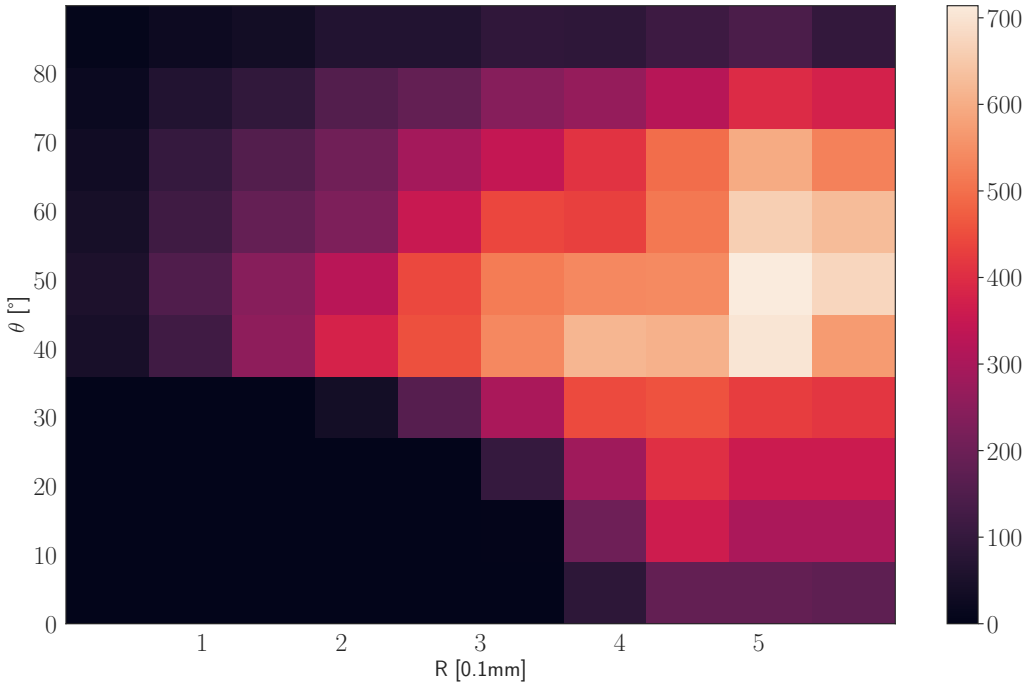

Figure 5.18: Correlation between position and angular distribution of photons at the fibre's output inside the fibre, for a 1 m fibre, with a 2 cm photon generation source in its centre.

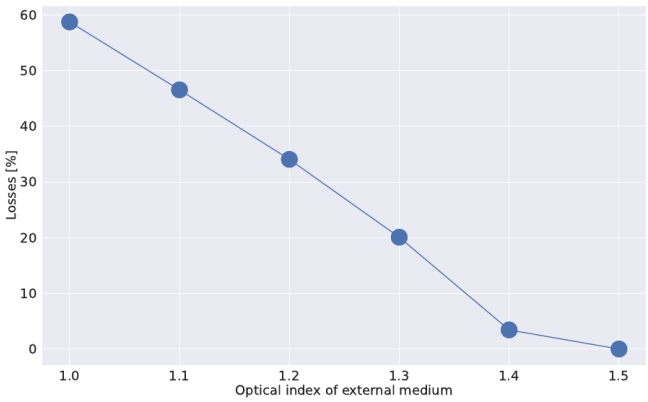

Figure 5.19: Photon total internal reflection losses at fibre facet.

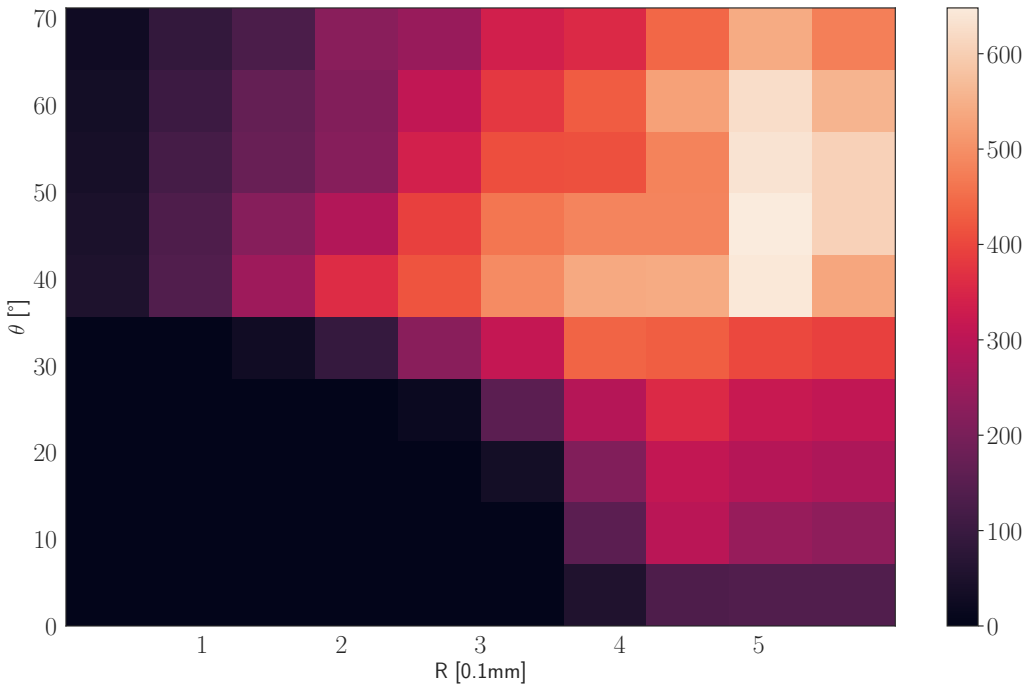

Figure 5.20: Correlation between position and angular distribution of photons outside of the fibre's facet assuming an external optical index of 1.

5.5.2 SiPM-fibre interface connection simulation

For the scintillator optimisation studies, a simulation toolkit called *FibreSim* was developed in the framework of this thesis. This toolkit is written in C++ and is designed to study the interface between WLS fibres and SIPMs. It can run on any Linux PC with CERN ROOT version 6.14 or higher. It reproduces laboratory results and has been extensively used to optimise the fibre-SiPM interface connection leading to greater light yields.

5.5.2.1 Principles of FibreSim

FibreSim functions using an input distribution of light inside the fibres or at the fibre facet as provided for instance by the Zeemax studies. An environment is defined as well through an external optical index (EOI) and the addition of reflective walls. Finally a SiPM is defined.

Fibresim takes the following input parameter which can be set freely inside of a initialisation file:

- The event count: `nev`
- The amount of times the simulation should be run for a given set of parameters: `occperstep`
- The amount of WLS fibres: `nfibre` (1 or 2 at the time of writing)
- The distance between the fibres and the SiPM: `zdim`
- A positioning variable for the fibres: `optifibre`
- A cutoff for high angle photons to study only low angle photons which can also be used to speed up the simulation: `anglecutoff`
- The side length of the SiPM: `sipmside` (The SiPM is assumed to be square)
- The amount of pixels on the SiPM: `n_pixel` (The pixel count will also be rounded down to a value the square root of which is an integer)
- The optical index outside of the fibres: `oie`
- The fibres' attenuation length: `att_l`
- The PDE of the SiPM pixels: `pixelefficiency`

- The presence or absence of rectangular reflective walls around the SiPM: `iswall`

The optical index inside of the fibre as well as alternative reflective wall shapes and positions can also be set inside of the simulation.

The simulation then runs through the following steps:

- The photon are generated on the fibre surfaces
- They are propagated through the external medium
- They reach the SiPM plane
- A PE may be generated from the SiPM
- The process is repeated until the defined photon count is reached

In addition, the user has control over the walls' reflectivity and the photon distribution inside of the fibre which can be input. By default the distribution used is derived from Figure 5.23, but custom distributions derived from laboratory measurements and Zeemax simulations are also available.

Each generated photon is assigned to a fibre, a position on the fibre cross section and a polar and azimuthal angle according to the input distributions. The photon travels along the z direction and is reflected by any defined reflective walls. It may in that case be absorbed by the walls according to their reflectivity. If the photon reaches the SiPM, it may fire the corresponding pixel with a probability set by `pixelefficiency`. Photon overlap, corresponding to multiple photons reaching the same pixel is present and will adequately saturate the SiPM as described in Section 3.3.5.3. Pixel cross talk is not present in the simulation as pixel isolation is assumed to make it negligible.

FibreSim has flexible outputs, capable of displaying events for a single set of parameters as histograms such as shown in Figures 5.22 or 5.21. For analysis purposes, its output are *real PEs* (rPEs) and *perfect PEs* (pPEs). pPEs correspond to the amount of SiPM PEs, if the pixels had a perfect 1.0 efficiency, rPEs are the real reconstructed photon counts. This allows to evaluate the SiPM saturation based on the amount of incoming photons in different configurations.

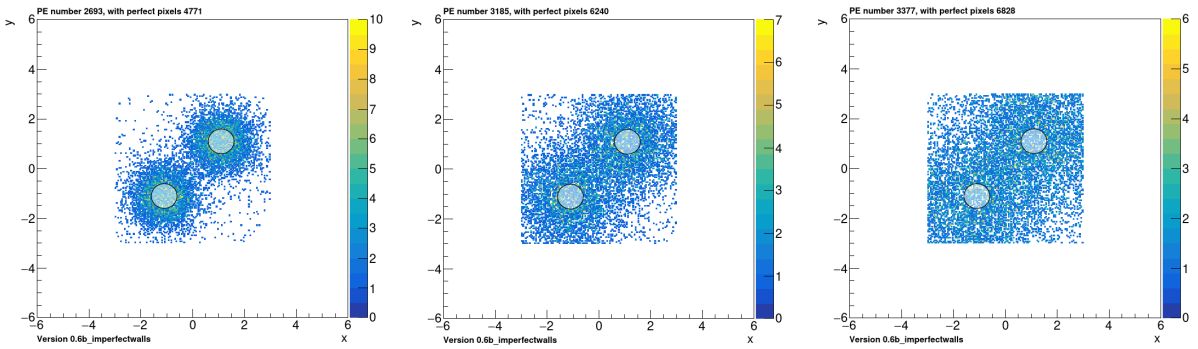

(a) 1 mm distance between fibre and SiPM.

(b) 2 mm distance between fibre and SiPM.

(c) 3 mm distance between fibre and SiPM.

Figure 5.21: 10 000 simulated photon onto a 6×6 mm SiPM with a 50 µm pixel pitch, a 0.5 PDE, with different distances between fibre and SiPM and a $n = 1$ external optical index. Each bin represents a pixel.

FibreSim, while providing good performance and well matching the data at close distances, can still be improved in a few ways. In particular, the photon distributions used are derived from studies performed in Aachen [375] and Dortmund [376]. Alternatively, the distributions inferred in Section 5.5.1 are used, which, while not explicitly contradicted by laboratory measurements, are not validated in laboratory measurements either.

In addition, the SiPM modelling used in FibreSim is simplified with only a stochastic model being used. Over-saturation phenomena [377] are for instance not covered which therefore prevents large light levels from being properly simulated. The approximation that a pixel receiving n photons will have a firing probability of $1-p^n$, with $p = 1-\text{PDE}$ can be challenged. While de-excitations of electrons failing to pass into the conduction band after photo-excitation take place within $\mathcal{O}$(fs) [378], the (optical) phonons generated by the de-excitation

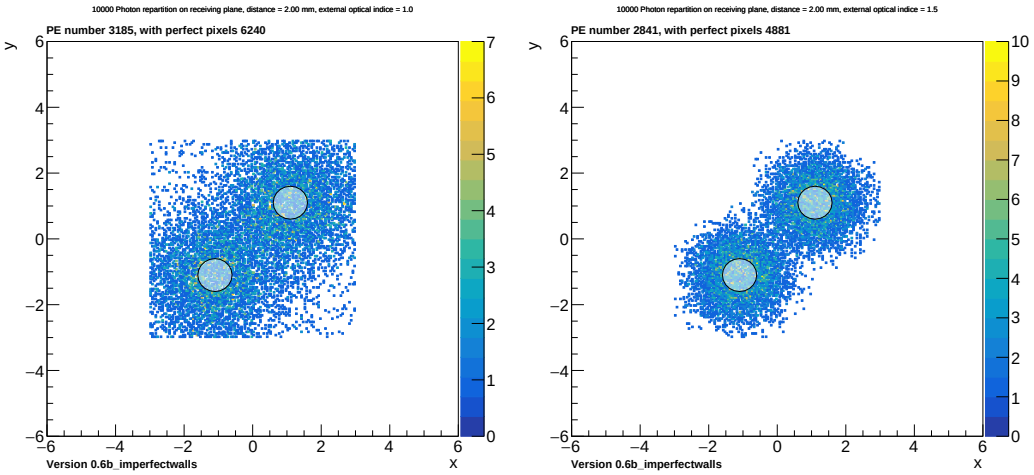

(a) $n = 1$ EOI.

(b) $n = 1.5$ EOI.

Figure 5.22: 10 000 simulated photon onto a 6×6 mm SiPM with a 50 µm pixel pitch, a 0.5 PDE, a 2 mm distance between fibre and SiPM and for different EOIs. Each bin represents a pixel.

may contribute towards higher excitation probability either in the pixel itself or a neighbouring one. Detailed studies have yet to be made for this last phenomenon which is thus not implemented.

Finally, the introduction of complex geometries with varying external optical index is currently done by hand in FibreSim. While experimental tools allowing for the definition of rectangular, trapezoidal exist, allowing also for the removal of material using rectangles or spheres, they are at the time of writing not at a level of maturity allowing for easy volume definitions.

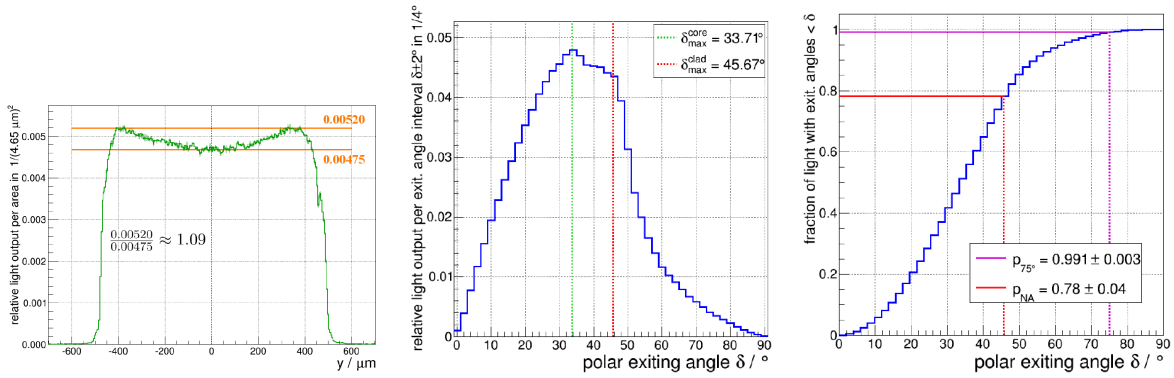

Figure 5.23: Measured position (left), angles (centre) and cumulative angle (right) of photons on round, multi-clad fibres [376].

5.5.3 Optimisation of fibre-to-SiPM interface connection for fibres in air

Simulation results indicate that significant potential for reducing SiPM saturation effects by increasing the distance between SiPM and fibres. These measurements on fibres in air were made in two ways: firstly optically, in order to determine general behaviour, then digititally using a SiPM, as detailed below.

5.5.3.1 Optical measurement of the fibre light output

These measurements were conducted together with Elisa Ruis Chòliz in the dark room to provide a first constraint of the light output distribution of the fibres. They were done using different distances. The 3 m long, 1.2 mm Y11 fibre (see Figure 5.14) was illuminated using an intense white light source coming from a smartphone torch function at one end of the fibre which was duck taped to the phone's torch and kept clear from the measurement area. The fibre was fixed to the markers using black duck tape to ensure that the marker's

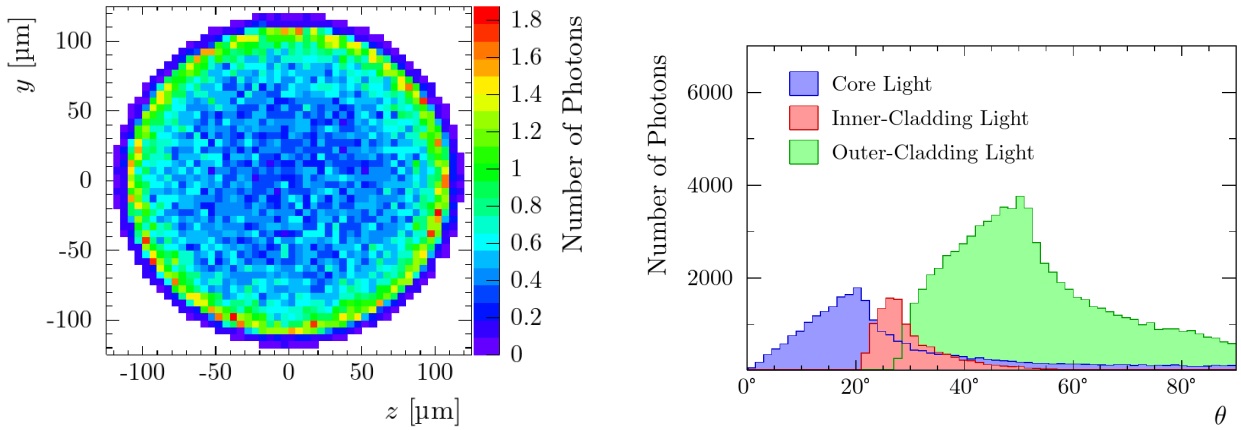

Figure 5.24: Simulated positions (left) and angles (right) of photons on the fibre facet [375].

Figure 5.25

distance to its end was as close as possible to the real marker value and to minimise the reflection from the tape itself. The measurement was done twice using two different techniques. First the gradated white paper placed on the optical table and marked with the size of the two concentric light rings observed during the measurement was used to determine the size of the circles. Secondly the pictures were pixel calibrated using the gradations on the paper and pixel measurements were made, correcting for the camera angle as shown in Figure 5.26. Measurement results are shown in Figure 5.27.

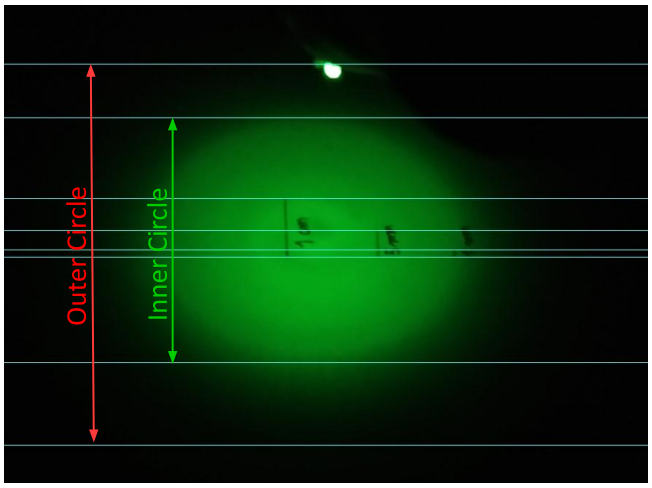

Figure 5.26: Visualisation of the measured objects. The fibre can be seen at the top. Two concentric light circles are observed with a break in intensity between the two.

The light output is observed to be separated into two concentric circles, implying a near-linear regime of increasing light amounts for smaller photon polar angles with a critical polar angle above which the light distribution is no longer evolving linearly. Using the fit results, it is possible to compute the critical angle θ_{crit}. This yields a $\theta_{\text{crit}} = 0.6338\,\text{rad} = 36.32^{\circ}$ consistent with the behaviour of Figure 5.23 and the Zeemax studies of Section 5.5.1.

5.5.3.2 Digital measurement of the fibre light output

The measurements of the fibre-SiPM separation were made with the help of Asa Nehm, Sebastian Ritter and Elisa Ruis-Chòliz who assisted in taking the data and operating the setup. The light output is measured by consistently varying the distance between two fibres and a SiPM for a given fibre illumination. This is done using a scintillator traversed by two WLS fibres ans excited by the laser. The fibres are fed into a 3D-printed hollow tube (T1) with a custom 3D-printed end-cap letting them illuminate the SiPM placed in front of them. The tube with the end cap enter a corresponding larger tube (T2) attached to the SiPM PCB, with T2 3D-printed

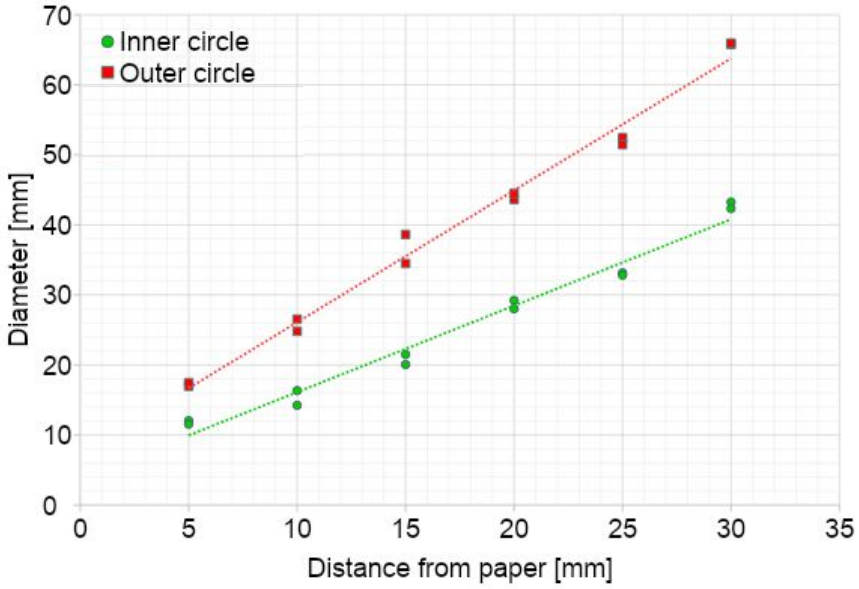

Figure 5.27: Observed diameter of the fibre light spot as a function of distance. Plot courtesy of Elisa Ruis-Chòliz.

to perfectly fit T1. A screw device allows to change the distance between the fibre facets and the SiPM. Each full turn of the screw linearly increases or decreases the distance by 0.5 mm. T1 and T2 are 3D-printed to have the tubes centred on the SiPM's sensitive surface. The fibres themselves emerge from T1 with a 1 mm offset each to allow the full angular range of photons to emerge from the fibres unimpeded. The errors on the offsets are estimated to be 0.2 mm and fully correlated as a rigid and smooth piece of 3D-printed plastic was used to push the fibres into position. All 3D-printed parts are made of black obsidian plastic to minimise reflections. The setup is pictured in Figure 5.28.

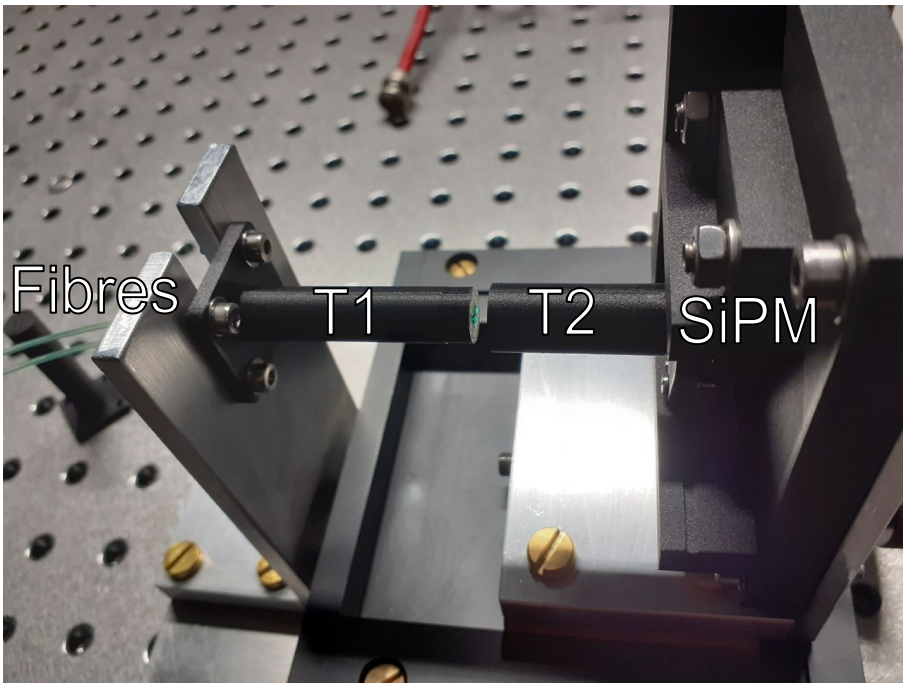

Figure 5.28: Fibre screw device. The fibres enter T1 which is inserted into T2 fixed to the SiPM.

In particular, T2 is manufactured in two variants. One is round (rT2), with an outer radius of 6 mm and an inner radius of 5 mm, minimally sized to fully contain the Hamamatsu S13360-6050PE SiPM footprint while remaining centred on the sensitive surface. The other T2 variant is square (sT2) and precisely $6 \times 6\,\mathrm{mm}^2$ again centred on the sensitive surface of the SiPM. A visualisation from above is shown in Figure 5.29.

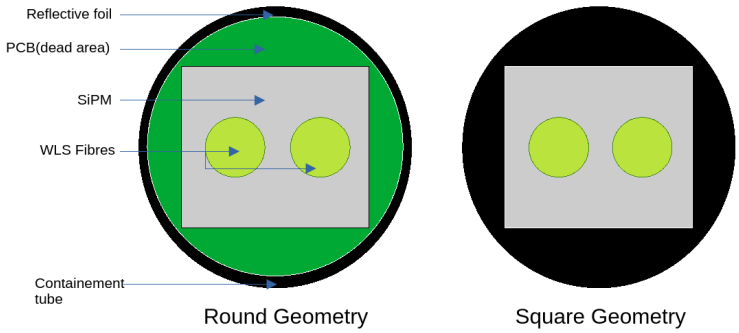

Figure 5.29: Fibre and SiPM system as seen from above.

Figure 5.30: From left to right: the SiPM used for the measurement, T1, sT2 (with foil), rT2 (no foil), rT2 (with foil) used for the measurements of the light output of fibres in air.

In addition, in order to determine the importance of reflectivity, versions of T1 and T2 are rendered reflective. This was attempted in two ways: first sputtering using aluminium particles was tried, the results were however inconclusive as the sputtered thickness was found to be far insufficient to reliably reflect photons. Therefore, another solution was chosen, with reflective foil being used and fixed with a very light layer of fluid glue to the sides of the tube as pictured in Figure 5.30.

Unless indicated otherwise, the fibres are passing through a $6\times40\,\mathrm{cm}^2$ scintillator bar where they are separated by 2 cm and glued using BC-600 optical cement ($n = 1.56$). The bar is irradiated by the laser running at a low 10 kHz frequency through a hole in the foil. Varying laser intensities are used, defined by different laser tune parameters and modified using the internal laser attenuator. The distance is changed by turning the screw device without interrupting laser irradiation which was observed to be slightly irregular immediately after startup before it stabilised. The screw device was turned by an operator inside the dark room. Each combination of distance, corresponding to a data point, and intensity, varied between datasets, is recorded on the oscilloscope for 30 s or 300 000 pulses. The mean and RMS standard deviation are recorded and compared for different configurations. The distance is increased from 1 mm away from the SiPM surface to avoid direct contact between fibres, which could be misaligned, and sensor, which could be damaged. The measurement output can be found in Figure 5.32.

Good agreement is observed with the FibreSim simulation and an optimal distance is observed, being 2 mm and 3 mm for foil and foil-less T2. This corresponds to the ideal distance between fibre and SiPM where the most light is collected by the SiPM. As expected, the presence of foil allows for better conservation of light particularly at longer distances. No significant loss is observed in the round T2 beyond 8 mm which indicates that the foil reflectivity is indeed close to 100%. The primary causes of light loss at larger distance are the dead regions around the SiPM.

At close distances, the maximum amplitude of the setup with reflective T2 is around 15 % higher than with dark T2. This indicates that over ∼15 % of light is present at angles $\theta > 45^\circ$. Those photons, based on Figure 5.25 should mostly be concentrated in the outer cladding region. The simulation estimates indicate that the outer cladding would have a greater amount of photons, about 60 % of the total fibre photon count. This

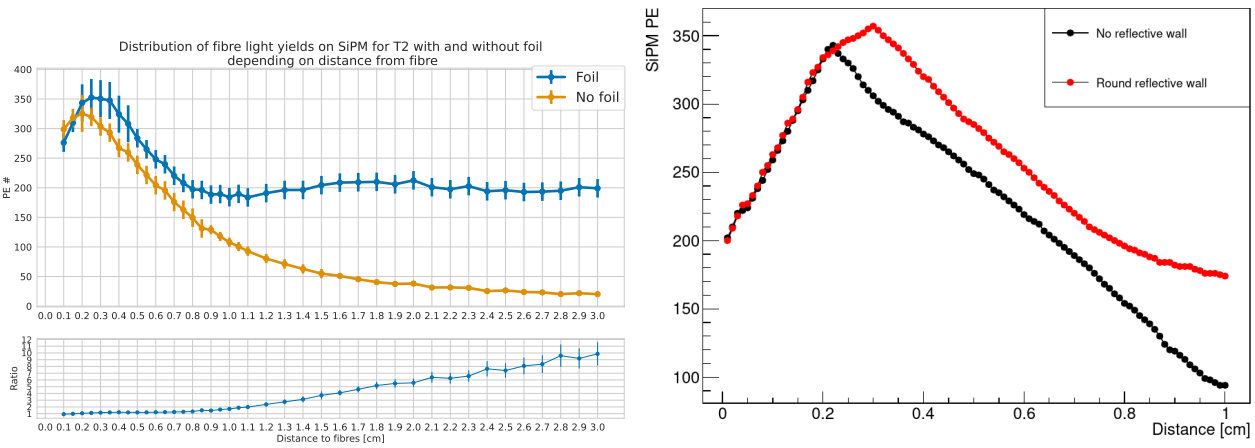

Figure 5.31: SiPM average PE counts as a function of distance to the fibres as a function of distance for a fixed laser setting (left) and in FibreSim for 840 generated photons (right).

Figure 5.32

difference is due to the loss of all of the photons initially produced in the core and reaching the outer cladding within the initial scintillator because of the higher optical index of the optical cement and scintillator (both at 1.56). In the case of the SHiP calorimeter system, seeing as the fibres are embedded inside of the scintillator, the determination of the outer cladding light distribution is not significant in this context. It is however valuable to see if more photons with larger polar angles can be collected by the SiPM by changing the geometry of T2 from round to square to minimise dead regions. This comparison is shown in Figure 5.33.

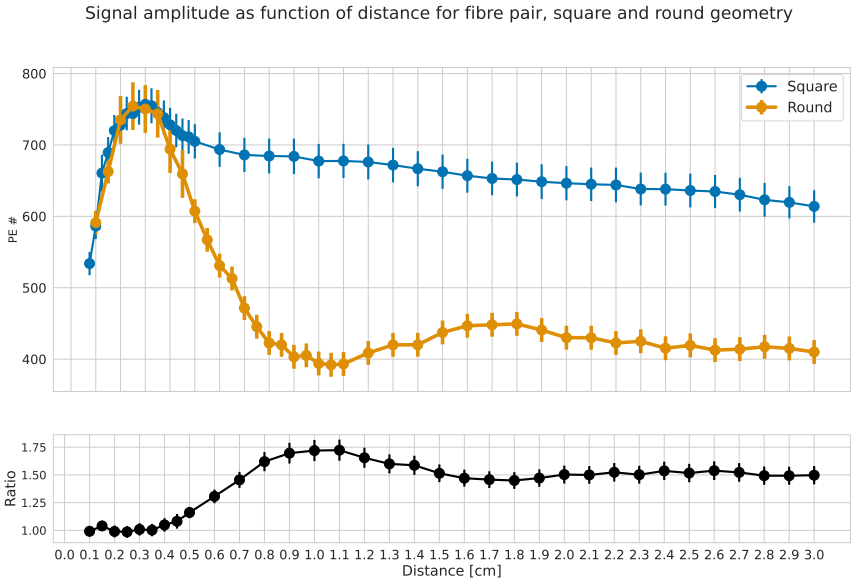

Figure 5.33: SiPM average PE counts as a function of distance for square and round geometries of T2.

While light is better conserved in square geometries due to the significant reduction in gaps leading to dead regions, the peaks however are located at the same distance and have the same amplitude. This implies that there is no added value in using a square reflective surface rather than a round one. The exact angular distributions are ill represented analytically given the large amount of modes enabled by multiple reflections. Those are therefore better simulated as is done in Section 5.5.2.

The angles in fibres in air which were directly irradiated by the laser were also investigated, due to the lack of relevance of the study to the SHiP calorimeter however, the study was not concluded. In particular, while the distribution with reflective T2 was measured, the one with non-reflective T2 was not, thus not allowing to determine the angles in fibres in air. These distribution can be found in Appendix C.3.

Conclusion and outlook It is possible to improve the SiPM light collection by a factor up to ~ 2 by increasing the distance between fibre and sensor to 2 mm for $6\times6\,\mathrm{mm}^2$ SiPMs if no further reflections are placed around the fibre. If such reflective elements are placed parallel to the fibre direction and around the fibre, it is possible to improve the light output by a further $\sim 15\%$ by increasing the distance further at 3 mm thanks to photons with normal exit angles above 56°. No variation in performance at the optimal distance was found whether the reflection geometry was circular or square.

The investigated photons come primarily from the fibre core and fibre inner cladding, those in the outer cladding are lost within the scintillator bar and are expected to be more numerous, but also at typically much higher angles, than their inner layers counterparts. It is possible to investigate the distribution including the outer cladding by removing the scintillator and irradiating the fibres directly. The correlation between the incoming photon direction and outgoing re-emitted photon in WLS fibres implies that usage of highly collimated fibre illumination such as lasers is not realistic to usage within a scintillator. Radioactive sources or cosmic radiation are preferable for such studies which have not been made due to their lack of applicability for the SHiP calorimeter system.

Furthermore, a complete measurement indicating the full correlation of photon angles to the their position at fibre facet could provide further insights to the light distribution in the fibre and be useful to write accurate fibre simulation codes.

5.5.4 Optimisation of interface connection between SiPM and fibres inside of scintillator

The light output in fibres traversing a scintillator is theoretically similar to that of fibres exiting a scintillator into air, as light trapped inside of the core and inner cladding can only escape through second order phenomena. These can be verified experimentally to determine whether an optimisation may significantly improve the fibre light yield. In addition, as shown in Sections 5.5.1 and 5.5.2, large amounts of light are expected to remain trapped within the WLS fibre because of its heightened external optical index compared to the optical index of air, up to 60 %. Simultaneously, an increase in the external optical index would imply an increased focus of the light onto fewer SiPM pixels, which would decrease the PE count as a result of increased SiPM saturation. These two competing effects are evaluated in the following.

5.5.4.1 High EOI evaluation of light output onto SiPMs

The experiment is using a 36 cm long EJ-200 scintillator bar traversed by two fully contained YS2 WLS fibres which reach a S14160-6050HS SiPM (see Section 5.5.5) and are separated by 2 mm in the transversal plane. The SiPM is placed on a PCB which is screwed onto the scintillator using different 3D-printed masks, thus allowing to vary the distance between fibres and SiPM. In addition to the distance, the interface is also varied, using different thicknesses of "active" materials in PMMA[1] and glass ($n = 1.5$ and $n = 1.45$ respectively) cut and polished on all sides using sandpaper to meet the dimensions requirements. The plexiglas has a base cross section of $6.5 \times 6.5\,\mathrm{mm}^2$ to cover the sensitive area of the SiPM and a variable thickness Z. In order to preserve as much light as possible, a trapezoid PMMA geometry was investigated in addition to the typical square cuboid shape. Both are shown in Figure 5.34. Glass, being more difficult to machine, has only been investigated in the configuration it could be obtained, namely 1 mm thickness with unpolished sides. In order to minimise optical losses to total internal reflection, Luxlite optical grease ($n = 1.517$) is deployed in certain test runs to evaluate the light output gains that can be made by reducing losses to total internal reflection within the fibre. This solution, while workable and simple, could be improved as it doesn't match the optical index of the Plexiglas and more significantly neither that of any of the fibre components. Nonetheless it is deemed to allow a satisfactory study of achievable light yield gains.

The measurement of the light output of fibres connected to high external optical index mediums is made utilising a scintillator irradiated through the laser through a small hole in the foil equidistant from both fibres. The direct comparison between different setups was deemed hazardous due to the possible changes in the difficult to reproduce setup on the laser stand, with exact orientation of the scintillator being a particular concern. The measurement is hence made as a ratio of a measured SiPM to a reference SiPM set on the opposite end of the

[1] Plexiglas

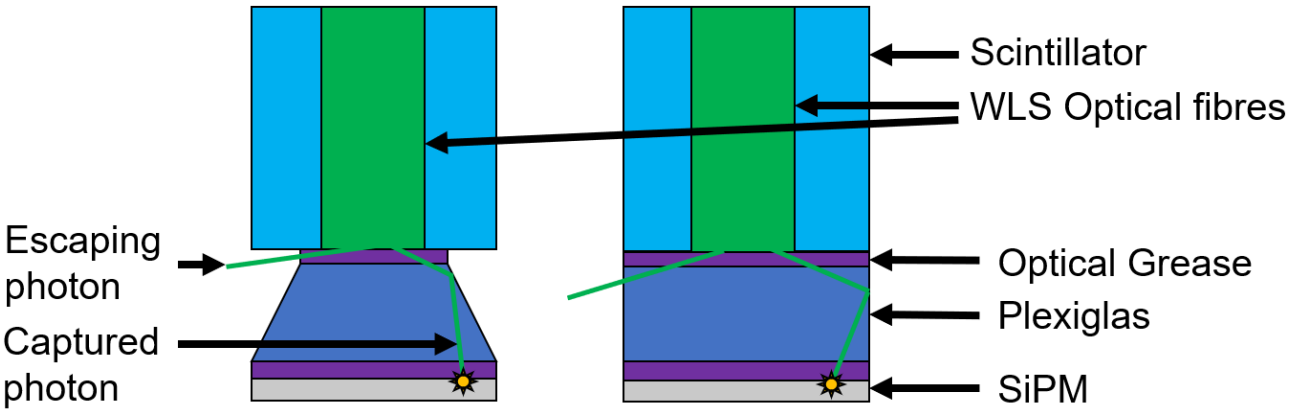

Figure 5.34: Trapezoidal Plexiglas interface (left) and cuboid interface (right). The potential gains from varying the geometry from the Plexiglas at the fibre's exit by increasing the photon angle that would be capable of exiting is shown. In the trapezoidal case, escaping photons preferentially escape through the optical grease which, due to its smaller thickness, allows to reduce the loss of photons with high polar angles.

scintillator bar utilising an unchanged interface. The reference SiPM is operated using a set voltage using the best known air interface without extra reflections, namely with a 2 mm air gap. The interface on the test side is varied with each interface variant being evaluated at different laser intensities. Both SiPMs' signal amplitudes A_{test} and A_{ref} and standard deviation σ_{test} and σ_{ref} are taken in 30 s measurements using the oscilloscope and the ratio of their amplitudes is taken as figure of merit. The trapezoid geometries are defined by a larger ($S = 6.5\,\text{mm}$) square and a smaller one, whose sides' length L are manufactured to be either 4 mm or 4.5 mm. An $L = 5\,\text{mm}$ square was attempted but proved difficult to manufacture with the required precision.

The optical grease was applied using a 1 mm diameter syringe either on only the fibre side of the interface, one both sides or not at all. It was reasoned that a test with grease on only the SiPM side will not yield better results than its greased fibre counterpart and would be comparable to an air gap as total internal reflection would still prevent many photons from leaving the fibre in the absence of optical grease at the interface. All different setups are summarised in Table 5.1.

Each piece of glass/PMMA is placed onto the SiPM laterally using a set of thin tweezers and a 3D-printed mold which can be separated into two parts to perfectly match the SiPM shape and then be easily removed to ensure regular behaviour. Each setup is inspected visually before the ratio measurement started. The measured ratios of test to reference SiPM signals as a function of laser intensity can be found in Appendix C.3.

The ratios are observed to be stable until the laser exits its linear regime around $T_{\text{laser}} = 70$, indicating limited SiPM saturation for most setups. Systematic errors are difficult to estimate but are expected to be small and not significantly shift the experiment given the utilised means. They would mostly stem from differences in the setups regarding the placing of the high EOI material and the illumination of the scintillator as well as from the laser itself. A 5% symmetric and uncorrelated systematic error is assumed on each setup which is deemed conservative. Indeed the systematics which do not cancel out as a result of the ratio approach are expected to be positively correlated if at all such as if the glass/PMMA piece slid out of alignment because of gravity, implying that only a reduction in the uncertainty may be achieved in this case as $\sigma_{A_1/A_2} = (\frac{\sigma_1}{A_1})^2 + (\frac{\sigma_2}{A_2})^2 - 2\rho_{A_1A_2}\frac{\sigma_1\sigma_2}{A_1A_2} = \sigma_{A_1/A_2,\text{uncorr}} - 2\rho_{A_1A_2}\frac{\sigma_1\sigma_2}{A_1A_2}$. The 3D-printed parts are accurate to less than 1 % and the alignment of all parts is verified before each measurement, rendering 5 % prudent. A visualisation of the setup is provided in Figure 5.35

As expected, setups using optical grease, whether single or double sided perform best overall. However, given the large number of examined setups, a performance ratio of ratios was taken by computing the ratio of each setup on the *Airgap_ref* setup corresponding to an optimised interface without high optical index material. These ratios are computing over the $[0, 60]$ laser range where performance is deemed most reliable and shown in Figure 5.36.

It can be observed that the best performing setups are those with a 2 mm space and that within uncertainties, it does not make a difference whether single or doubled sided grease is used. In the best performing setups, a $\sim 20\,\%$ signal increase is achieved compared to the optimised airgap setup. The trapezoidal shape is found to potentially provide a limited benefit but not to warrant its usage for small numbers.

Improvements to this study could be further brought through a careful experimental study of systematic

Setup name	Interface material	Material thickness	Grease setup	Setup code
Airgap_ref	Air	1 mm	_	AR
Dry cuboid 1 mm glass_test	Glass	1 mm	_	DR1G
Dry cuboid 1 mm PMMA_test	PMMA	1 mm	_	DR1
Dry cuboid 2 mm PMMA_test	PMMA	2 mm	_	DR2
Dry cuboid 3 mm PMMA_test	PMMA	3 mm	_	DR3
Dry cuboid 4 mm PMMA_test	PMMA	4 mm	_	DR4
Dry trapezoidal $L = 4$ mm $Z = 2$ mm PMMA_test	PMMA	2 mm	_	DT42
Dry trapezoidal $L = 4$ mm $Z = 3$ mm PMMA_test	PMMA	3 mm	_	DT43
Dry trapezoidal $L = 4$ mm $Z = 4$ mm PMMA_test	PMMA	3 mm	_	DT44
Dry trapezoidal $L = 4.5$ mm $Z = 2$ mm PMMA_test	PMMA	2 mm	_	DT52
Dry trapezoidal $L = 4.5$ mm $Z = 3$ mm PMMA_test	PMMA	3 mm	_	DT53
Dry trapezoidal $L = 4.5$ mm $Z = 4$ mm PMMA_test	PMMA	3 mm	_	DT54
One sided greased cuboid 1 mm glass_test	Glass	1 mm	Single sided	OR1G
One sided greased cuboid 1 mm PMMA_test	PMMA	1 mm	Single sided	OR1
One sided greased cuboid 2 mm PMMA_test	PMMA	2 mm	Single sided	OR2
One sided greased cuboid 3 mm PMMA_test	PMMA	3 mm	Single sided	OR3
One sided greased cuboid 4 mm PMMA_test	PMMA	4 mm	Single sided	OR4
One sided greased trapezoid $L = 4$ mm $Z = 2$ mm PMMA_test	PMMA	2 mm	Single sided	OR42
One sided greased trapezoid $L = 4$ mm $Z = 3$ mm PMMA_test	PMMA	3 mm	Single sided	OR43
One sided greased trapezoid $L = 4$ mm $Z = 4$ mm PMMA_test	PMMA	4 mm	Single sided	OR44
One sided greased trapezoid $L = 4.5$ mm $Z = 2$ mm PMMA_test	PMMA	2 mm	Single sided	OR52
One sided greased trapezoid $L = 4.5$ mm $Z = 3$ mm PMMA_test	PMMA	3 mm	Single sided	OR53
One sided greased trapezoid $L = 4.5$ mm $Z = 4$ mm PMMA_test	PMMA	4 mm	Single sided	OR54
Double sided greased cuboid 1 mm glass_test	Glass	1 mm	Double sided	AR1G
Double sided greased cuboid 1 mm PMMA_test	PMMA	1 mm	Double sided	AR1
Double sided greased cuboid 2 mm PMMA_test	PMMA	2 mm	Double sided	AR2
Double sided greased cuboid 3 mm PMMA_test	PMMA	3 mm	Double sided	AR3
Double sided greased cuboid 4 mm PMMA_test	PMMA	4 mm	Double sided	AR4
Double sided greased trapezoid $L = 4$ mm $Z = 2$ mm PMMA_test	PMMA	2 mm	Double sided	AR42
Double sided greased trapezoid $L = 4$ mm $Z = 3$ mm PMMA_test	PMMA	3 mm	Double sided	AR43
Double sided greased trapezoid $L = 4$ mm $Z = 4$ mm PMMA_test	PMMA	4 mm	Double sided	AR44
Double sided greased trapezoid $L = 4.5$ mm $Z = 2$ mm PMMA_test	PMMA	2 mm	Double sided	AR52
Double sided greased trapezoid $L = 4.5$ mm $Z = 3$ mm PMMA_test	PMMA	3 mm	Double sided	AR53
Double sided greased trapezoid $L = 4.5$ mm $Z = 4$ mm PMMA_test	PMMA	4 mm	Double sided	AR54

Table 5.1: Active EOI fibre light output setup summary. L corresponds to the side length of the material, Z corresponds to the material thickness.

Figure 5.35: Visualisation of the setup. The left SiPM is set with a reference interface which remains unmodified throughout the study. The right SiPM is connected to a custom interface which changes during the study. For the measurement where the interface under test is a simple airgap, the reference SiPM yields an amplitude $A_{\text{ref,Airgap\_ref}}$ whereas the test SiPM yields $A_{\text{test,Airgap\_ref}}$. When the interface under test is set to be "active", the reference SiPM records $A_{\text{ref,\_test}}$ whereas the test SiPM records $A_{\text{test,\_test}}$.

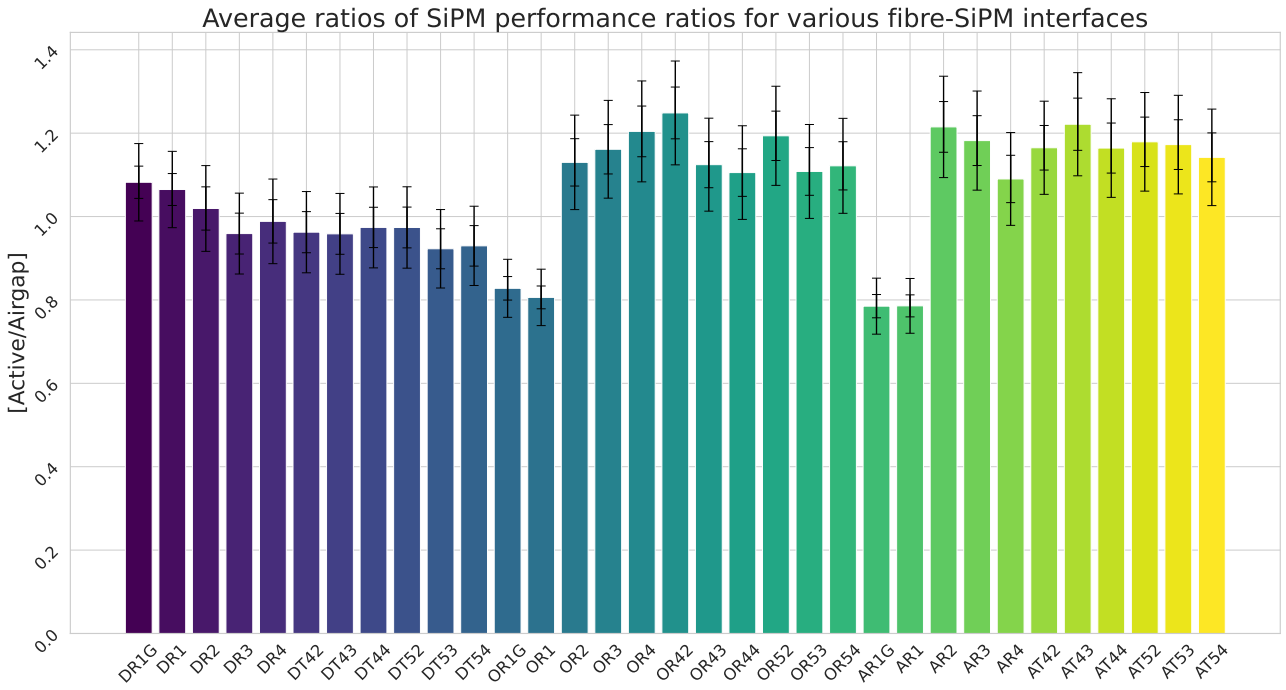

Figure 5.36: Evaluation of the ratio of the ratios between both sides of the SiPM for different interfaces $\frac{A_{\text{test,\_test}}/A_{\text{ref,\_test}}}{A_{\text{test,Airgap\_ref}}/A_{\text{ref,Airgap\_ref}}}$. The inner error bars are statistical whereas the outer ones are systematic.

uncertainties using perhaps different PMMA insertion techniques and having a more stable scintillator irradiation stand, perhaps through 3D-printing. In addition, the added benefit of glass was underexplored due to difficulties in its machining. More generally, this study could be done using a greater variety of materials with more optical indices which would also further contribute towards tuning FibreSim. Of particular import is also the optical grease: while its usage was proven to be beneficial, it would be valuable to vary its optical index, perhaps increasing it until $n = 1.59$ to match the fibre core, to extract maximum amounts of light, thus requiring higher n materials as well.

The value of optical grease in an optimal setup having been demonstrated, its performance in long-term measurements now needs to be as well. This is done in the next section.

5.5.4.2 Aging of optical grease

Optical grease is commonly used as a replaceable part of an optical apparatus. This is due to it being a silicone grease composed of several solvents meant to maintain its fluidity but tends to dry when certain solvents (alcohols in particular) evaporate. The ensuing degassing is largely harmless to a scintillator-based detector but may hinder the homogeneity of the grease and thus, through the formation of dry clumps, reduce the effective surface of the fibre-grease-PMMA interface. Nonetheless, optical grease has significant advantages over its most common replacement, namely optical cement [342], particularly in that its ease of use and replaceable nature allow for much easier maintenance of the underlying components. The significance of the drying effect is likely dependent on the materials with which the optical grease is in contact with. This has been studied in order to determine the usability of the optical grease interface in long term, multi-year operations of the SHiP calorimeter system.

PMMA is not expected to significantly age as the photons have wavelengths too long to be capable of interacting with the polymer structure of the PMMA (which would require X-rays to damage, not optical photons emitted by the fibres). It should be noted however that the following measurement nonetheless is not sensitive to aging from the PMMA or the optical grease separately but only to their combination.

The setup to determine the optical grease aging had to accommodate weektime usage of the dark room and was thus only used when the dark room was not used for other purposes, mostly on weekends. Each period where contiguous measurements were taken is denominated a measurement period. A 36 cm EJ-200 scintillator bar traversed by two Y11 WLS-fibres in a setup similar to that of the initial prototype were used for the measurement. The interface on one end was modified to the “One sided greased cuboid 3 mm PMMA_test”

setup (see Table 5.1). The bar was irradiated by the laser running at 1 kHz through a small hole within the foil. The SiPM signal amplitude and standard deviation were recorded on the oscilloscope for each pulse. The setup was removed from the optical table at the start of each next day with laboratory access (typically Monday) from the optical table and placed on another dark room table until the following day preceding time without laboratory access (typically Friday). It was placed back into the laser beam in identical conditions ensuring by using a set of markers set to the optical table screws. Exposure times varied by $\mathcal{O}$(h) most weeks with longer exposures times of 24 h being achieved on weeks 8 and 10. Starting the third week, a reference SiPM is placed on the other side of the scintillator bar using an interface identical to the reference interface of Section 5.5.4. It was used to provide a reference aging to compare with the interface aging. Certain variations occurred in single measurement periods as shown in Figure 5.38. The internal variations within a single measurement period were taken as statistical uncertainty leading to different statistical uncertainties for different measurement periods.

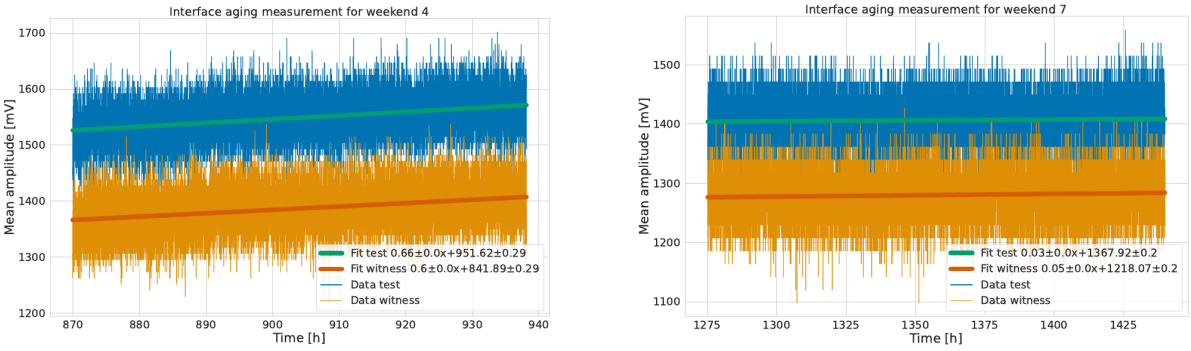

Figure 5.37: Aging measurement from Weeks 4 (left) and 7 (right).

Figure 5.38

The SiPM signal amplitude in time is thus used to determine the interface aging and is shown in Figure 5.39 whereas the reference SiPM signal amplitude in time is shown in Figure 5.40.

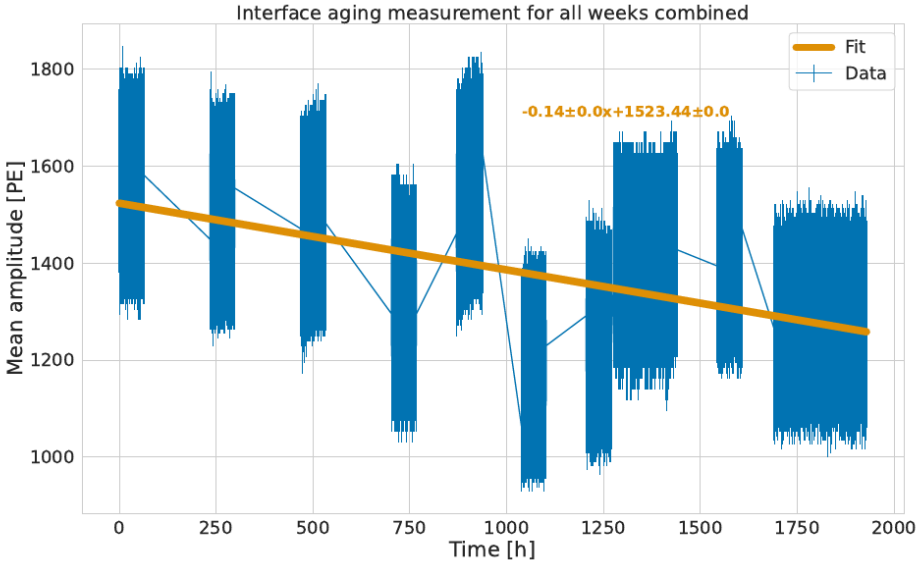

Figure 5.39: Test SiPM signal amplitude as a function of time.

Aging is observed to occur at an accelerated rate on the test interface compared to the reference but the loss is found to be small. Nonetheless, significant variations are observed in between measurements. This is interpreted as inducing a systematic error induced by setup reproducibility which is computed using the standard deviation between the achieved means in the reference case, where no interference from the interface may occur. Both test and reference full datasets are fitted using affine functions. The standard deviation from the reference is scaled by the ratio of the fitted affine functions' constants in both cases $r = \frac{1523.44}{1355.35} \simeq 1.12$,

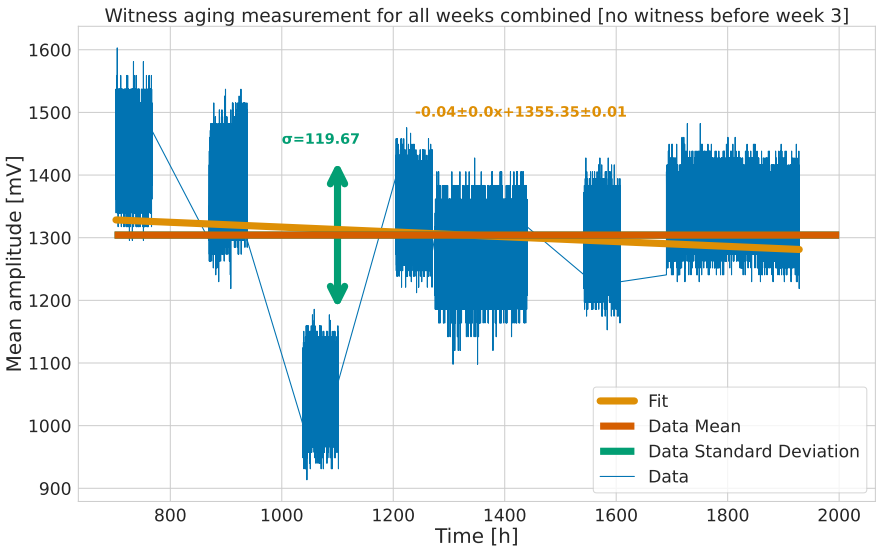

Figure 5.40: Reference SiPM signal amplitude as a function of time. The third measurement week is viewed as an outlier as a noticeable difference in positioning was observed.

the result of which, $\sigma_{\text{sys}} = 134.03$, is taken as a systematic error on the test case which is then fitted again. The correlation between uncertainties leads to low fit uncertainties, thus allowing for a statistically significant measurement of the aging. The aging is evaluated as a function of time using those two fits by substracting the fit slopes to one another, yielding an absolute loss rate of $L_{\text{aging,abs}} = 0.1\,\text{PE/h}$ or $2.4\,\text{PE/d}$ in this setup. Utilising the affine constant of the fit on the test data of Figure 5.39 it is possible to determine a final relative loss rate of $L_{\text{aging,rel}} = 0.16\,\%\,\text{d}^{-1}$ with negligible uncertainty.

This loss rate is small but is not suitable for an experiment which would have to run for months or years. Nonetheless, it is likely that the aging is not strictly linear and would slow down as surface solvents become scarce thus building a dry crust to the grease. The data taking length, stretching only over two and half months does not allow to extrapolate for this effect. Use of optical cement is thus preferred for experiments running for very long periods of time.

5.5.5 Orientation of SiPM relative to the fibres

The orientation of the SiPMs relative to the fibres was also examined. While instinctively, a $\frac{\pi}{4}$ rotation compared to the two fibres may be valuable to increase the light collection on the SiPM, FibreSim simulations only display a modest improvement as shown in Figure 5.41, within the margin of error.

For simplicity in PCB design, it is preferable to have the SiPM non-rotated to keep a distance between the SiPM edges and the PCB edges. The absence of gain in light collection performance, however, had to be validated in laboratory. This was done using two fibres in air aligned straight connected to a scintillator. Loose fibres display a larger angled light profile, implying that results for fibres in air are also valid for fibres fully in a scintillator in this case.

The scintillator was irradiated with the laser through a hole in its foil whereas the SiPM was placed inside of a device which allowed the sensor to be rotated in steps of 15° shown in Figure 5.44.

The fibres were then placed at given distances from the SiPM and exposed for 1 min at the time for combination of angle and distance. The average and RMS standard deviation are reported and plotted in polar coordinates shown in Figure 5.44c. The SiPM used were the S14160-6050HS which were perfectly square and are perfectly centred on the fibre beyond the systematics of their placement of the PCB which are fully correlated between measurements. The SiPM signal amplitude was thus expected to be identical modulo 90°.

The SiPM signal amplitude is observed to vary very little as a function of the angle, in order to determine this with better precision however, the difference between light yields at each angle modulo 90° is computed with regards to the average $\mu_\theta = \frac{\sum_{q=0}^{q<4} A_{\theta,q}}{4}$ where $\theta = 0, 15, 30, 45, 60, 75°$ is the SiPM inclination angle whereas q is the quadrant of the chosen polar distribution of Figure 5.44c. The residuals with respect to the average for

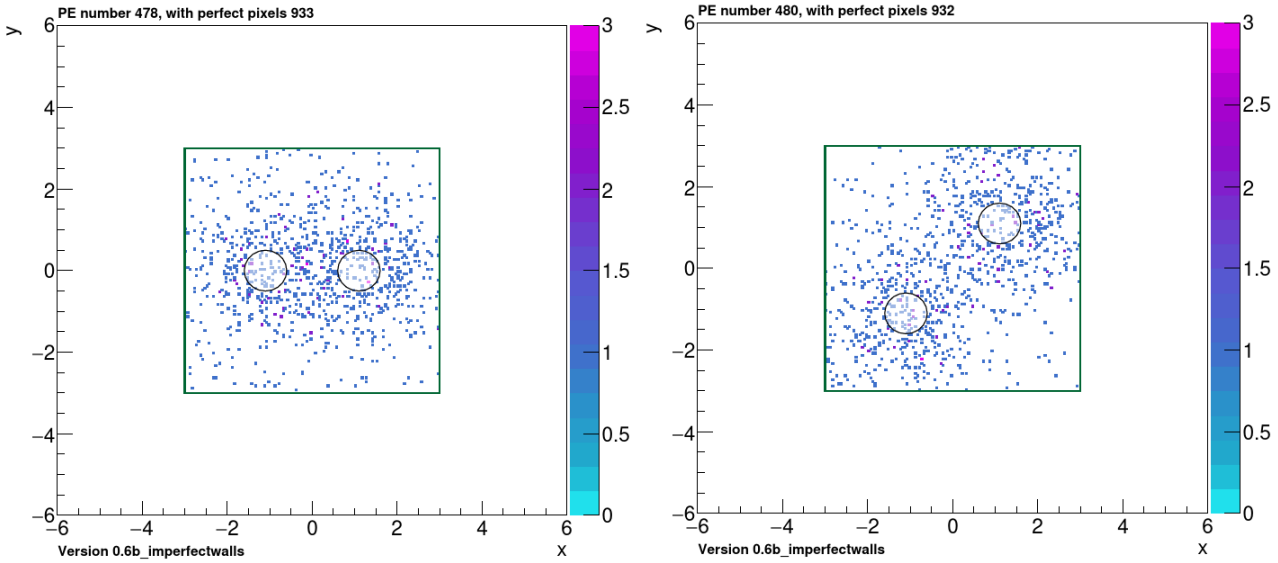

Figure 5.41: PE count for straight fibres (left) and fibre rotated by $\frac{\pi}{4}$ (right) for 1000 incoming photons: 478 and 480 rPEs are found respectively. The green square delimits the SiPM sensitive area.

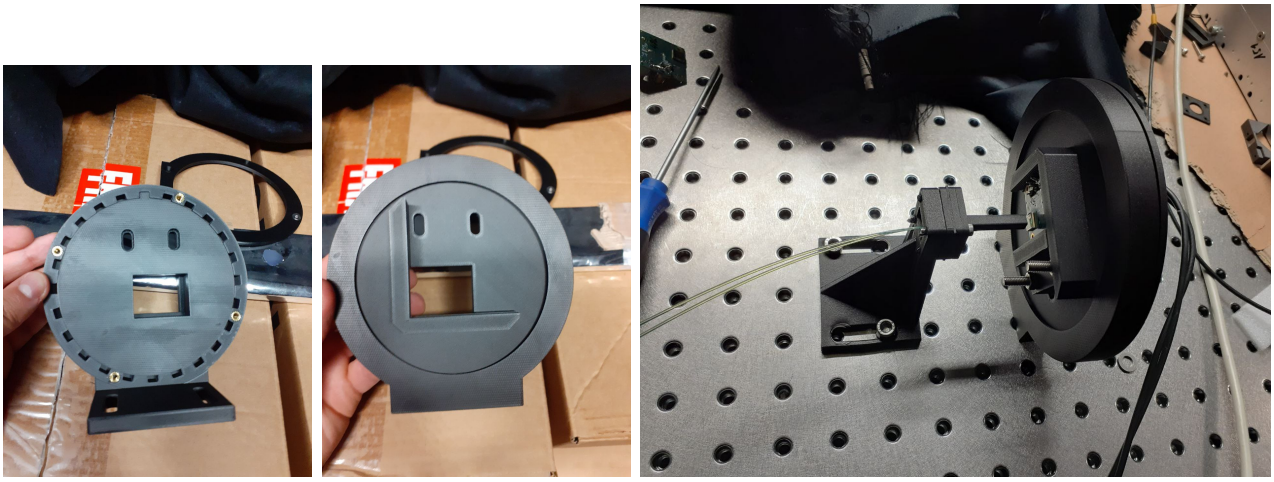

(a) (b) (c)

Figure 5.42: SiPM rotation device. Angles may be varied in steps of 15° with the SiPM remaining aligned on the fibres.

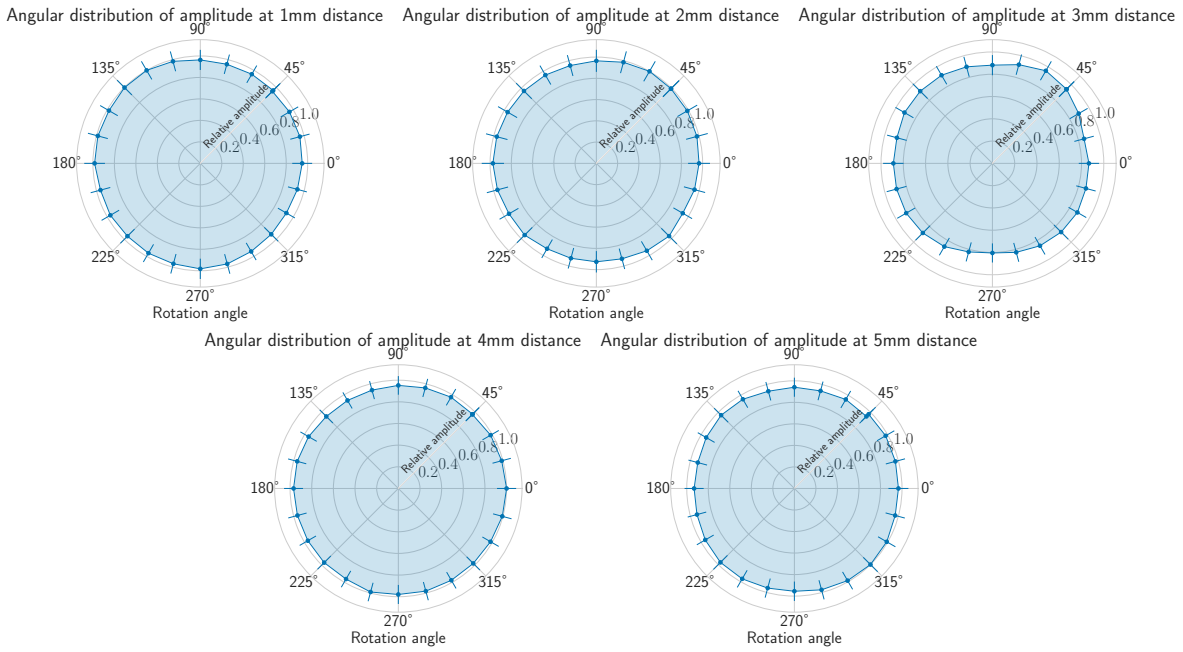

Figure 5.43: Amplitude of SiPM signals as a function of SiPM angle to fibres for different distances between fibre and SiPM.

each distance can be found in Figure 5.44. With residuals being consistent with 0, no significant benefit from inclining the SiPM compared to the fibres is found. Indicating that no orientation would have an impact on the SiPM light collection performance.

5.5.6 Conclusion and comparison to initial prototype

This chapter has covered means meant to optimise the light yield of scintillator bars for the SHiP calorimeter system. Optimisations can be divided in those that affect the scintillator bars themselves or the interface between fibres and SiPM. It has been demonstrated that using smooth foil improves the light yield by about 7%. Improvements in the interface between fibre and SiPM have also been made with laboratory measurements leading the path towards the development of the simulation toolkit FibreSim, which allows the study of optimal interfaces for different configurations. This has lead to an understanding of the light distribution in the fibre allowing for the development of optimised interfaces for both fibres in air and fibre in scintillator. This has been applied to optimise the SHiP calorimeter system's 6 cm scintillator bars, which doubles the total achieved signal with respect to the initial configuration as shown in Figure 5.45.

Furthermore, it has been shown that, given an optimal distance between fibres and SiPM, the orientation of the SiPM in relation to the fibres does not play a significant role.

These studies may be expanded to test more scintillator geometries, with notably cutoffs being applied to the scintillator sides in the longitudinal direction, allowing to improve light focussing towards the SiPMs and capture by the WLS fibres. Furthermore, simulations may be improved and fine-tuned through the measurement of the correlation between photon position on the fibre cross section and its position. This can be done using a setup shown in Figure 5.46. A further complement to these studies could involve tests of different optical cement indices to determine the relative value of higher prompt photon capture versus wavelength shifted photon loss.

Interface studies can also be pursued, with further studies dedicated to more interfaces including high optical index pads which have become increasingly common in the past years [379]. The study of more advanced high optical index interface material geometries may also yield further improvements, through more materials or fine tuning of the fibre-material interface such as by creating an "optical grease pool" to improve photon retention as shown in Figure 5.47. Most valuable here are however improved means of material manufacturing of the interface, which may be achieved for the material itself using developments in 3D-printing. Improvements in optical grease dispensing can also contribute to better ease of use of these improvements as well as determining the aging profile of these interfaces and their separate components in longer-term measurements.

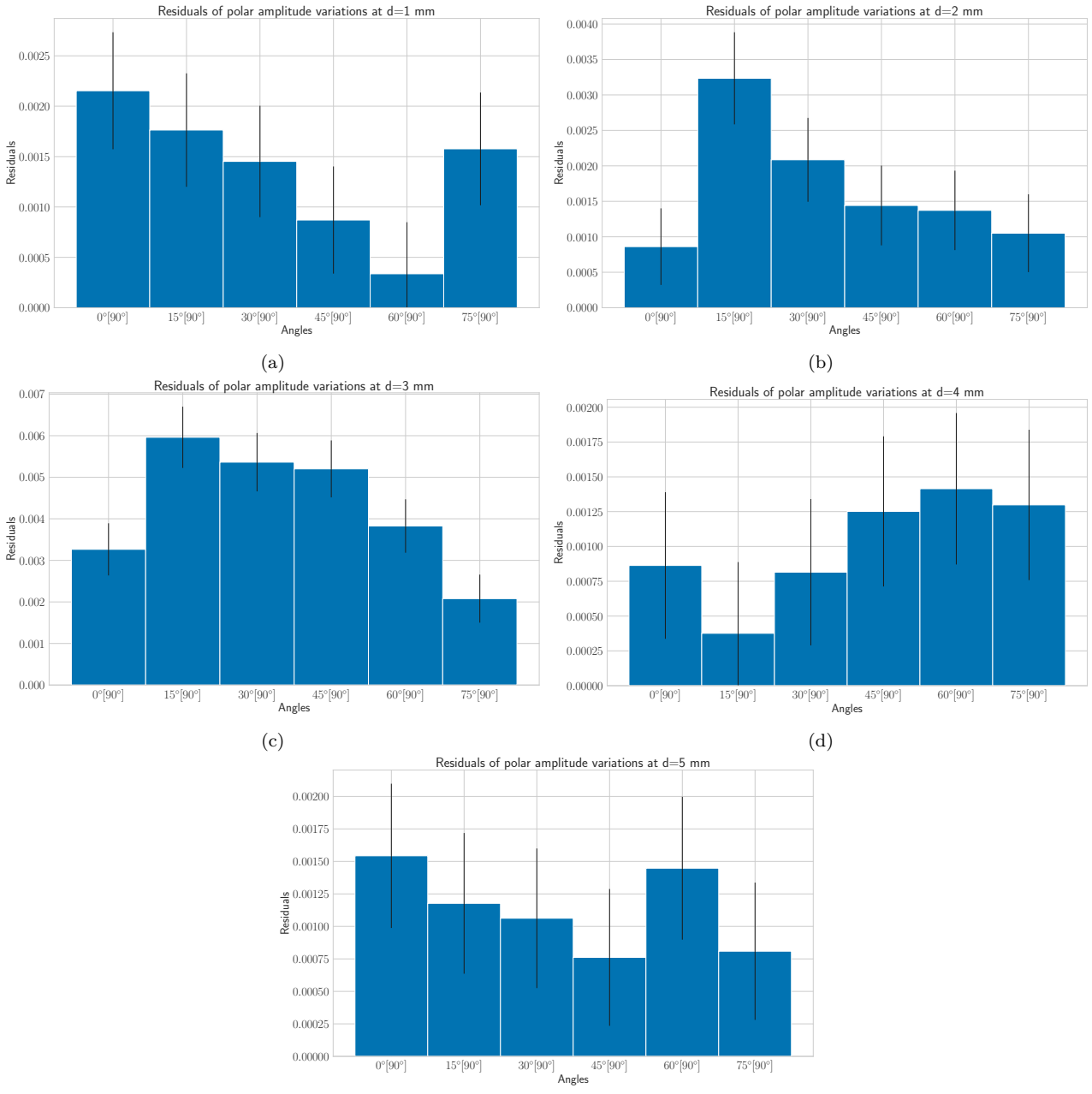

Figure 5.44: Amplitude of SiPM signals as a function of SiPM angle to fibres for different distances between fibre and SiPM.

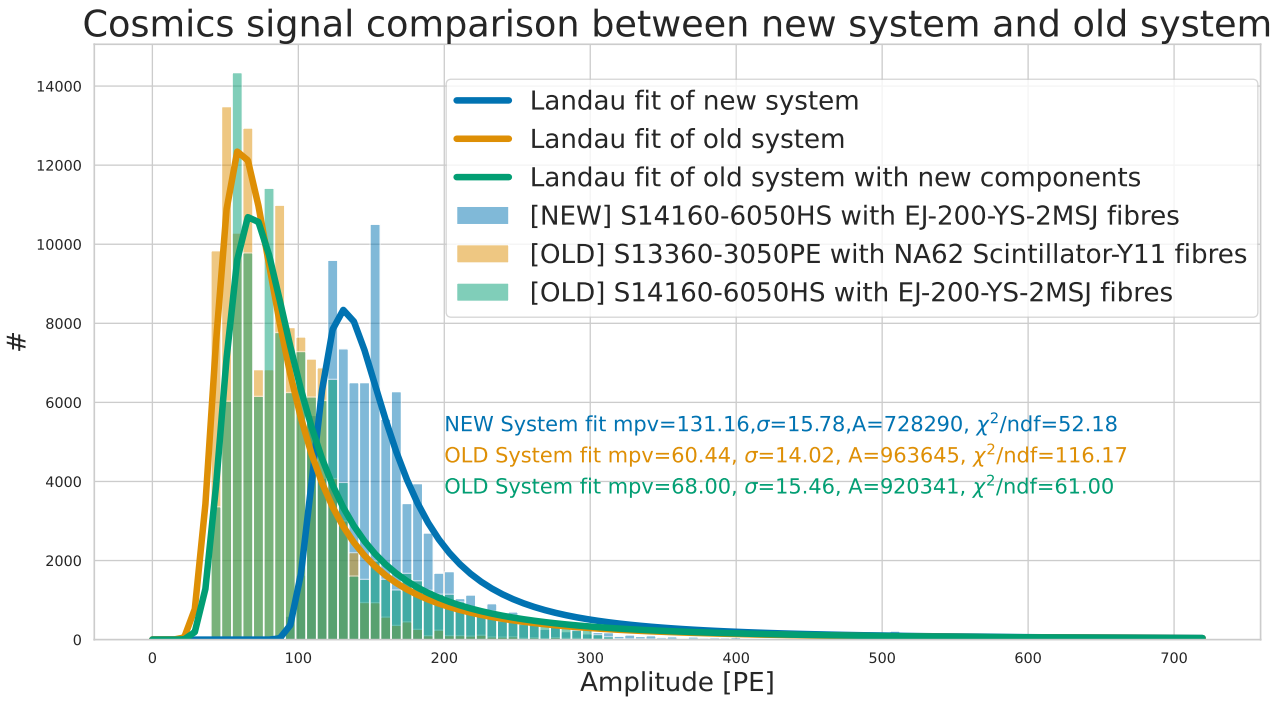

Figure 5.45: Signal yield from cosmic ray exposition of scintillator bars from the initial prototype, EJ-200 scintillator bars with YS2 fibres glued to the scintillator using EJ-500 optical cement otherwise using the initial prototype configuration and the same components used in the developed new and optimised configuration without optical grease or PMMA. Each scintillator was readout on both sides by two SiPMs readout using a 50 ns coincidence window on the oscilloscope with the average PE count from both sides being reported here.

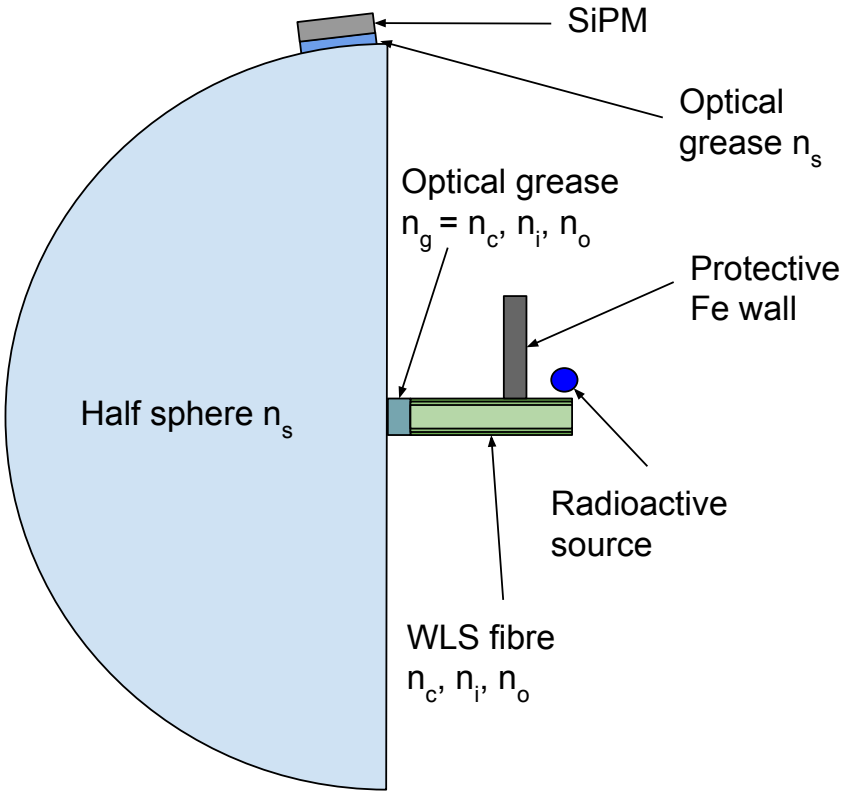

Figure 5.46: Proposed measurement of photon angle at fibre exit. Different optical greases would be used to allow the study of the fibre core, inner and outer cladding respectively. The half sphere would have an optical index equal or larger than the fibre core to avoid any photons to total internal reflection on the fibre cross section. The SiPM would be moved along the half-sphere to observe photons at different angles with the half sphere itself have an absorption length comparable to its radius to minimise background from internally reflected photon within the half-sphere.

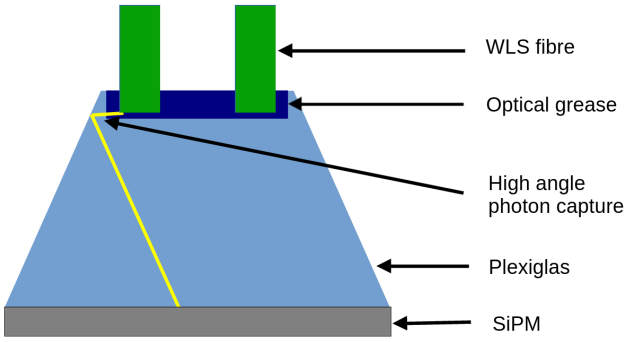

Figure 5.47: Suggested optical grease pool design. It could be used to improve the capture of high angle photons which are typically otherwise lost.

Chapter 6

Evaluation and development of calorimeter readout electronics

The optimisation of light yield, as explained in Chapter 5 allows for considerable improvement in the calorimetric stochastic term. This however requires adequate readout electronics, capable of processing the outcoming SiPM signals into usable data. The development of such electronics allowing for the data to be utilised to benefit the SHiP calorimeter system's physics case has been performed through a formulation of requirements. This was followed by the investigation of four separate readout systems which have led to the design of a custom readout solution, all of which are presented in the following.

6.1 SHiP PID detector physics-induced electronics requirements

The SHiP calorimeter system's physics requirements presented in Section 4 have direct repercussions on its readout electronics. An contextualisation of relevant analogue and digital electronics as they relate to the requirements is provided in Appendix E

The SHiP calorimeter system's role within SHiP is mainly determined by its PID requirements and overall experimental operating conditions. Crucial are the required dynamic range for the ECAL, the dead time, the sensor capacitance requirements, the output needs, the time resolution and rate capabilities, the output data rate and other services which are examined here with an emphasis on the scintillator layers.

6.1.1 Dynamic range

First and foremost, the SHiP calorimeter system must be capable of observing and identifying μ, π and showers from γ or e (see Sections 4). As a result it needs to be capable of observing MIP-like signals and electromagnetic showers. The results from Chapter 5 indicate that a MIP in a wide scintillator bar yields $\mathcal{O}(100)$ PE which corresponds to $\sim 1\,\text{pC}$ assuming a 10^5 gain. Thin scintillators bars in similar conditions yield $\mathcal{O}(10)$ PE [364] which then correspond to $\sim 100\,\text{fC}$. On the other hand, an electromagnetic shower originating from two γs at one of the highest achievable energies of $2 \times 200\,\text{GeV}$ implies ~ 18000 charged particles (see Equations 3.15 and 3.16) at the shower maximum, which, if approximated as MIPs yields a deposited charge of up to $\sim 20\,\text{nC}$ in the case of wide scintillators. This implies the need for a dynamic range of $\mathcal{O}(10^4 - 10^5)$ for which the SiPMs must also be adapted. If directly translated to ADC requirements, assuming that the MIP energy deposition peak is present at 100 ADC, implies that the largest shower peaks around $P_{\text{max}} \simeq 2 \times 10^6$ ADC counts with statistical fluctuations corresponding to $\sqrt{P}$ being small. This therefore necessitates a 21 bit ADC, which is very rare, complex to implement and expensive [380].

As precision at higher levels is not as crucial as $\frac{\sigma_P}{P}$ decreases, a gain switching mechanism can be implemented, allowing to lower the gain for large signals, thus adding considerable dynamic range at the cost of a single extra bit to the digital output. A gain switch of 10 allows to reduce the ADC bitcount to 18 whereas one of 100 allows to reduce the bitcount to 15. In the case of the SHiP ECAL, if a 10 bit ADC is assumed [381], the maximal required gain switch is then ~ 2000. This option however severely limits the readout bandwidth leading to a preference for readout electronics displaying multiple gain switches which allows to alleviate this

effect, allowing to scale detector resolution and readout bandwidth with energy. It should be noted that some amount of saturation is likely acceptable given the expected scarcity of $2 \times 200\,\text{GeV}$ shower events and the possibility to infer their energy if the saturation point is achieved, given the rest of the calorimetric layers and experimental conditions.

The option for hybrid ADC and time over threshold (ToT) [382] should be mentioned: it is an option that leaves the preamplification stage to saturate and only measures the length of the induced signal above a certain charge. This leads to moderately worst resolution at higher energies than full signal integration and is not currently available together with the desired parallel readout scheme. It should furthermore be stressed that this, while applicable in the ECAL, leads to worst PID in the HCAL with neutron signals being difficult to identify as a result of their delayed pulses for high energy deposition which would keep the preamplifier saturated.

The ability to observe single photopeaks is desirable for system calibration, although this will not used in the experiment operation itself.

6.1.2 Dead time

The final detector-wide rate will be determined once the final muon shield design will be complete (see Section 2.3.1.2). However, a conservative baseline rate of 50 kHz detector-wide is assumed based on previous studies [26]. The muon shield is expected to deflect particles towards the detector upper and lower modules (see Section 4.2), implying a non-homogenous rate. The module-wide rate is hence foreseen to reach $\sim 20\,\text{kHz}$ in the most exposed sections, implying an acceptable layer-wide average dead time of 20 µs. Poissonian uncertainty from the beam only very slightly modifies the acceptable dead-time. The beam is known not to be entirely normally distributed with significant variations induced. Furthermore, delayed decays from particles such as neutrons are a significant signal to certain BSM searches [383], thus modifying the dead-time requirements to be as low as achievable, ideally below 1 µs.

6.1.3 Sensor capacitance

The SHiP calorimeter system will be readout by two different SiPM types, estimated to be 60 pF and 2 nF for the thin and wide bars respectively. This has consequences on the analogue front-end (see Appendix D.0.1), with a low-impedance amplifier and tunable shaping times being required to allow proper integration and shaping of the analogue input no matter the sensor.

6.1.4 Output, rate and time resolution

In order to operate in SHiP conditions (see Sections 2.3.5 and 4.2.4.1), the CALODAQ readout board needs to be capable of acquiring an ADC value per output allowing physics to be reconstructed from the calorimeter. A TDC value is also necessary for event building and in particular output sorting. Finally, the channel number is also required to be able to locate the output origin. This is particularly crucial in the case of the HPLs and thin scintillator bars. This is expected to be included into a 32 bit output which is scaled to the full detector. Assuming that each scintillator bar ouputs two bitstreams per MIP (one for each bar side) and that each GEM layer outputs 7 bitstreams per MIP, the final data rate is expected to be a relatively modest $\sim 500\,\text{Mbit}\,\text{s}^{-1}$ detector wide. The timing resolution required is set by other subsystems, particularly the SST and is expected to be $\mathcal{O}(\text{ns})$.

6.1.5 Other services

In order to guarantee a uniform detector, individual SiPM channels are expected to require different bias voltages, implying the need for a tunable voltage system. In addition, noise removal from SiPM dark counts may be improved by enabling dual-sided coincidences for individual bars, which would be done at the CALODAQ level (see Section 4.2.4.1). This can be avoided if MIP peaks are large enough to severely minimise dark counts, enabling noise filtering through a simple threshold. In addition, the detector is expected to run 15 years and as such, channels are expected to suffer from degradation over this time. The dual readout of individual bars

enables compensation which can be achieved through the use of dual sided calibration LEDs. Slow control requirements is still being finalised at the time of writing but also needs to be fulfilled for the 10 000s of channels in the scintillator part of the detector as well as the 100 000s of channels of the HPLs.

6.2 Evaluation of readout electronics

In order to maximise compactness and reproducibility, modern detectors have come to rely on custom designed integrated circuit. As a result, the first stages of the readout, often including digitisation and even complete readout architecture, are nowadays done by an application specific integrated circuit (ASIC). These generally manifest as chips with all components engraved directly onto their constituent silicon via a CMOS process [384].

Four systems relying on such ASICs were investigated as options for the SHiP calorimeter system's frontend readout electronics: the commercial CAEN DT5702, the commercial CAEN DT5202, the TOFPET2 and the KLauS chip. These are presented in order.

6.2.1 CAEN DT5702

The DT5702 system, pictured in Figure 6.1, is built around the CITIROC-1A chip from the Weeroc company [385]. It is a 32 channel analogue ASIC which includes an amplifier with configurable gain (10-600), a fast and a slow shaper with 15 ns and $12.5 - 87.5$ ns shaping time respectively and a discriminator which is fed into a hold circuit and further into an analogue multiplexer for signal distribution. The TDCs are implemented by a Spartan-6 FPGA using the trigger ouputs of the CITIROC-1A whereas the 12-bit ADC is provided by a LPC4370 ARM processor using the ASIC's analogue outputs with power also being provided by the system. Communications with the DT5702 and data taking are done through an RJ-45 ethernet link. The block diagram is shown in Figure 6.1. The system is capable of taking an external trigger as input or may rely on self-triggering and is capable of operating under different analogue trigger levels. The self triggering mode is observed to bring efficiency down to $\sim 60\%$ compared to operation using an external trigger. The DT5702 was used as readout electronics in the initial prototype (see Section 5.1.1) as part of an integrated board which function with SiPMs, a two-stage common-collector/common-emmitter preamplifier which inverts the signal polarity. This renders them incompatible with the DT5702. The outcoming pulse polarity renders them incompatible with the DT5702, the board relied upon a set of inverters to feed positive polarity into the DT5702. They are powered using the shell of the LEMO connector from the sensor board which is fed a positive voltage, leaving only the SMA shell for grounding which is deemed inadequate for long-term operation. While the system functions well for small signals, for instance dark counts (see Figure 6.2), its gain-switch and single-channel-bias-voltage-switching-capabilities have been found not to be implemented, invalidating the board as a readout option for the SHiP calorimeter system.

In addition and as described earlier, the CITIROC, as an analogue chip, does not yield TDCs or ADCs and relies on external FPGA and microprocessor blocks for those outputs. Finally, the chip implements a serial readout, reading out all channels one by one after a trigger signal is received, inducing a chip-wide dead time which may last up to 10 µs during which it is blind to any incoming signals. This makes it ill-suited for a triggerless application. The limitations of the initial electronics, in particular regarding the complex analogue readout chain have motivated the development of a different readout electronics capable of better fulfilling the requirements set in Section 6.1.

6.2.2 TOFPET2

The TOFPET2, as described in Section 2.2.3 is the ASIC used to readout the SND electronics detectors. The chip is a 64-channel readout and digitisation designed for time of flight PET systems and includes amplification, discrimination, charge integration, analogue to digital converters (charge to digital QDC in this case) and time to digital converters (TDC). In SND@LHC, each front-end (FE) board contains two TOFPET2 ASICS for 128 channels in total. Each channel is equipped with a single preamplifier and two amplifier stages which are optimised for timing and charge measurements respectively, thus up to three discriminators with configurable thresholds may be used for timing (lowest threshold), low-amplitude repulse rejection and charge integration start. The TDCs include a ~ 40 ps bin size while the QDC remains linear up to 1500 pC incoming charge. The

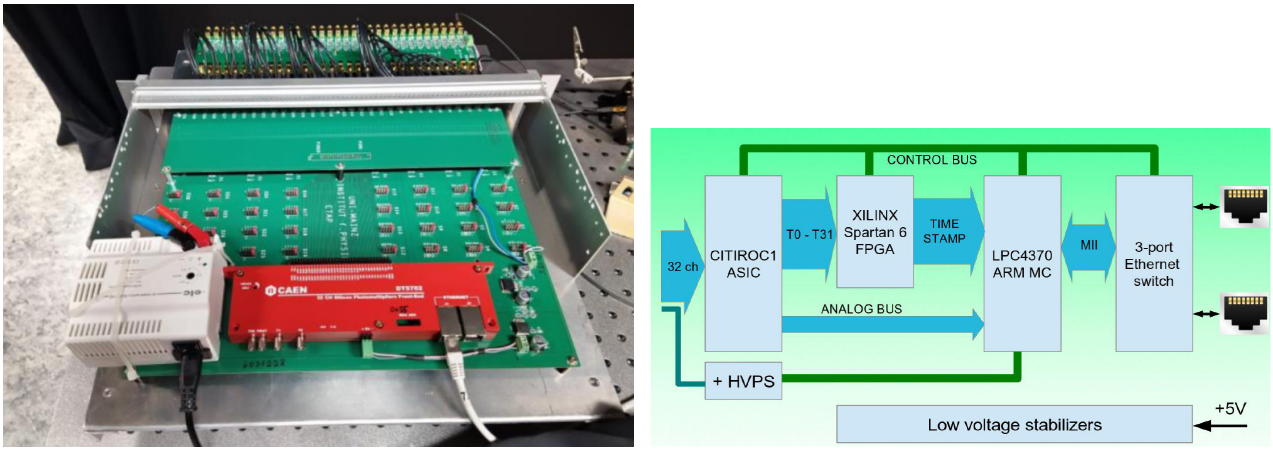

Figure 6.1: DT5702 as integrated as the initial prototype's readout electronics (left) and DT5702 block diagram (right) [386].

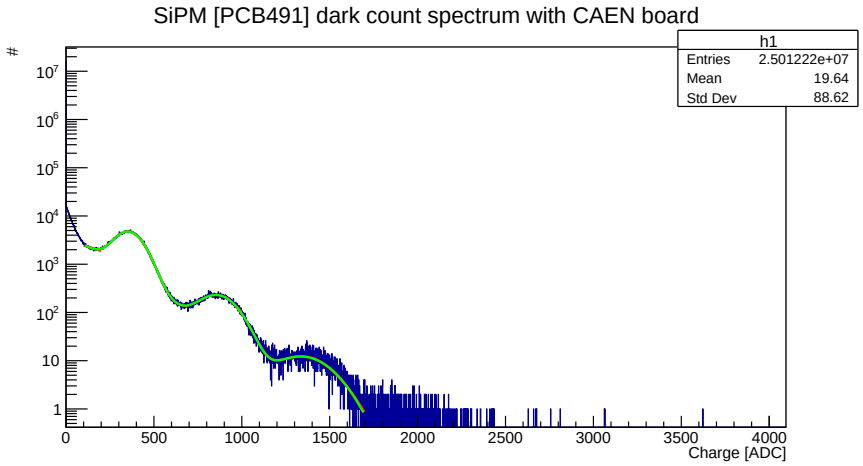

Figure 6.2: Dark counts from DT5702 after amplification. Dark counts peaks are found at 357, 863 and 1345 ADCs in a combined multi-Gaussian fit (green). The system is capable of readout out small signals but saturates around 12 PE far below the ~ 100 PE obtained for a MIP (see Section 5.5.6) requiring modifications for calorimetric operation.

QDC branch may be chosen to have an extratenuous gain of $1-3.65$ which allow further tuning between SiPM channels. The readout data acquisition (DAQ) board is based on a Mercury SA1 module from Enclustra [387] which include an Altera Cyclone V FPGA and collects the digitised data of 4 FE boards (512 channels) then further transmits the data to a DAQ PC located on the surface. The low voltage (LV) and high voltage (HV) supply powering the readout (12 V and 2 A each) and the SiPM (60 V and 300 µA per channel) respectively are provided by CAEN A2519 modules which are housed in two SY5527 mainframes [386].

TOFPET2 are effective for all electronic detectors in SND@LHC, the option to use it as part of the SHiP calorimeter system arose naturally as it has proven itself well insofar as different capacitance readout, 8bit-QDC (an acceptable alternative to ADC) and TDC yield, operating in triggerless conditions.

The TOFPET2 outputs have been validated in real conditions during the 2023 SND HCAL calibration testbeam, where a copy of the SND HCAL, missing only the last two DS layers, was exposed to π^+ beams of different energies (from 100 GeV up to 300 GeV). The QDC outputs of certain relevant channels are shown in Figure 6.3.

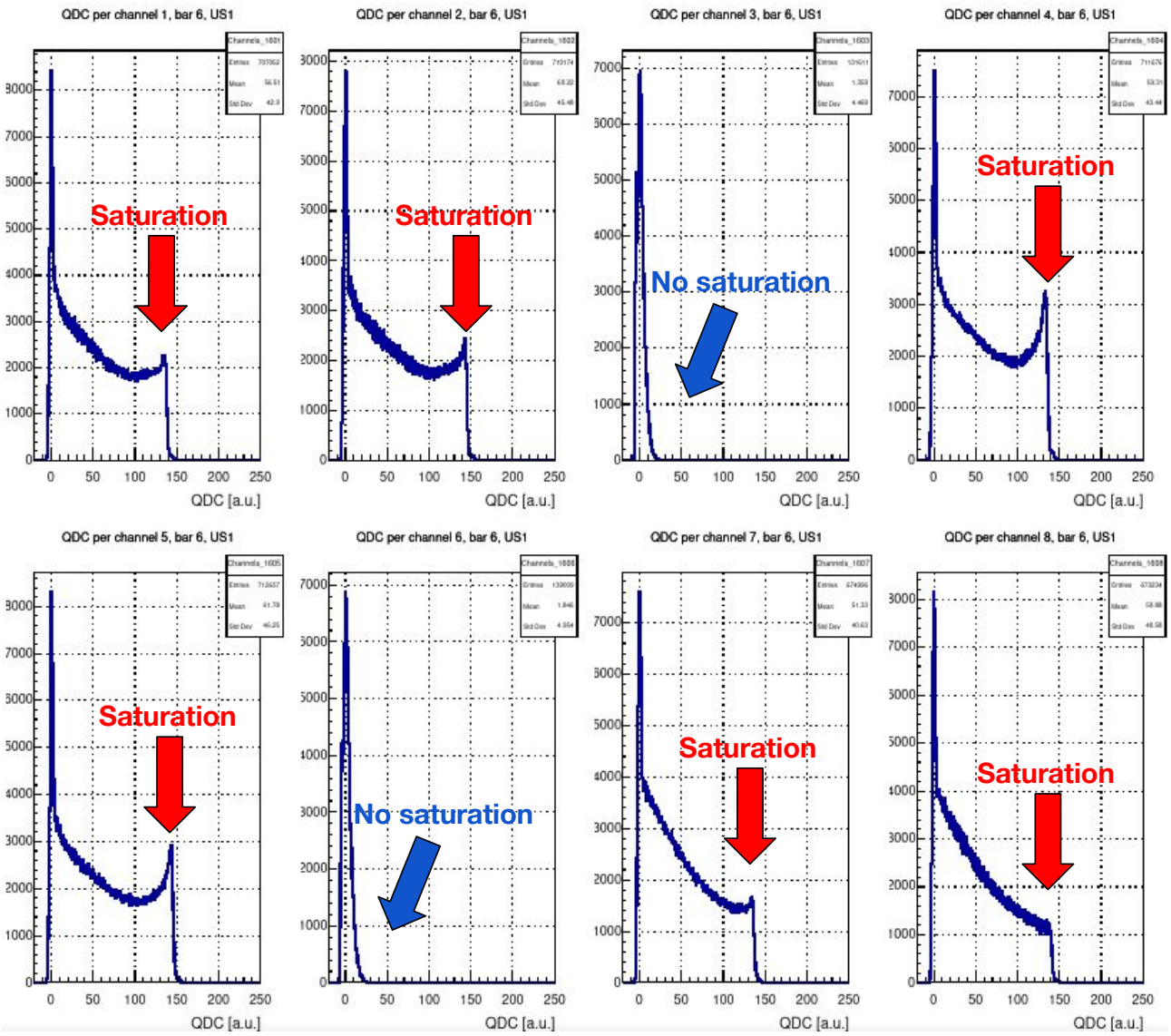

Figure 6.3: QDC outputs of channels on one side of a bar of US1, close to shower peak centred on the pion beam in the SND 2023 HCAL calibration test beam. Channels 3 and 6 correspond to small SiPM.

The QDC outputs show severe saturation around 150 QDC counts from the large SiPMs, rendering them inadequate for use in an ECAL targeting good PID performance as EM showers are denser than hadronic ones (see Chapter 3). The use of the TOFPET2 could be considered for the thin bars as they are equipped with small SiPMs which are shown not to saturate in such conditions. This may be seen as advantageous since its excellent TDC resolution improves the implementation a time-of-flight measurements described in Section

4.2.3 compared to readout electronics with poorer timing resolution. The TOFPET2 however likely is unable to display sufficient dynamic range, evaluated at 1500 pC [388] although this has to be proven in future test beams. Small SiPMs in addition have fewer pixels which leads to worst energy resolution. A TOFPETv3 is in preparation at the time of writing and may be considered as superseeding the TOFPET2 although it does not significantly improve on dynamic range considerations. In addition, the intercalibration of a gain switched ADC used by the wide scintillator layers with a QDC system, as well as their integration into a coherent data stream is an added complexity which may be better avoided should a more suitable option be found.

6.2.3 CAEN DT5202

The DT5202[386] integrated into the FERS-5200 system is the successor of the commercial DT5702 from CAEN, while it features multiple operation modes, the *Spectroscopy* mode is the only one of interest in the following. It similarly functions around two CITIROC-1A chips for 64 channels per DT5202 unit. It differs from its older sibling by its externally (tunable) 13 bit-ADC and TDC blocks feeding into a fully integrated FPGA which also controls the chip. Communications with the DT5202 may be handled either through RJ-45 ethernet or through optical link using a DT5215 concentrator board which streams the data and synchronises the board clocks. Sensors are connected to the board through a pair of standard 72-pin header connectors which allow for direct connection to the SiPM, including bias voltage with decoupling and amplification taking place directly on the board. The output data is a binary encoded stream which by default may be converted to CSV using a provided decoder or using a flexible custom ROOT decoder that was specially created as part of the front end (FE) evaluation and is now available for cloning [389]. This second option is systematically used in all studies of this work as it allows to compress the data files by a factor ~ 5 as well as giving access to the more powerful `.root` format. The DT5202 is equipped with a tunable amplifier (using a 6-bit digital setting) as well as a shaper which can use shaping times from 12.5 ns to 82.5 ns. It can be self-triggered using a basic logic implemented into the FPGA or using an external trigger.

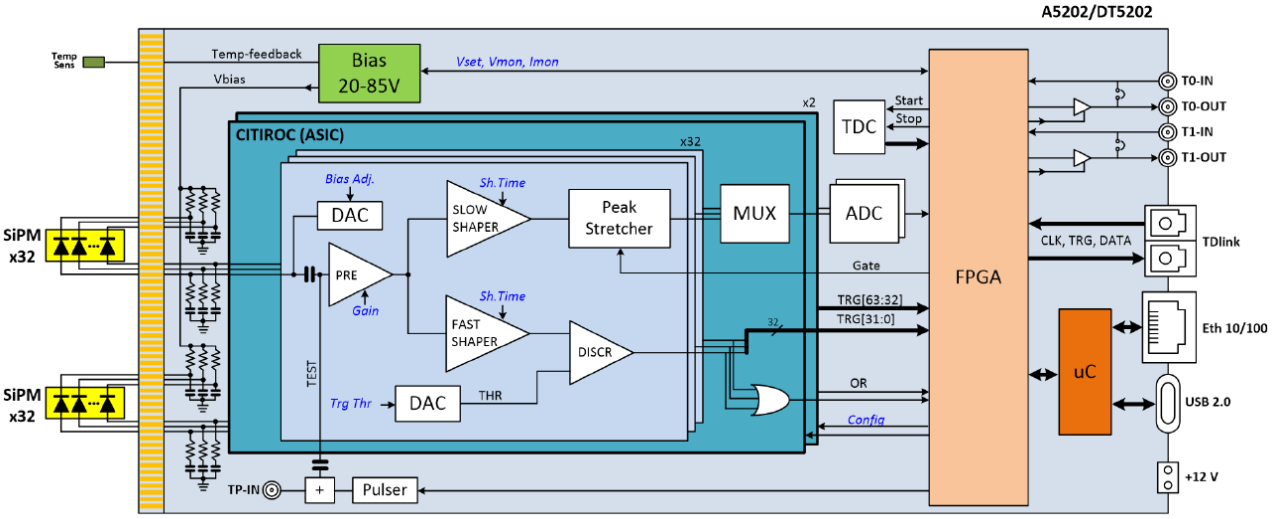

Figure 6.4: Block diagram of the CAEN DT5202 [386].

The DT5202 now implements channel bias voltage fine-tuning and a gain switch with two gains: high gain (HG) and low gain (LG). Thus makes it ill-suited for reading out the SHiP ECAL due to its persisting dead-time issue, somewhat insufficient dynamic range and its high price per channel. Nonetheless, it may be used in a prototype setting for physics tests (see Chapter 7) owing to its otherwise suitable characteristics.

6.2.3.1 DT5202 custom adapter board

In order for this evaluation to be conducted, a custom 4-layer adapter board has been designed, pictured in Figure 6.5. It allows to connect SiPM to SMA with anodes connecting onto the pin and cathodes onto the shielding.

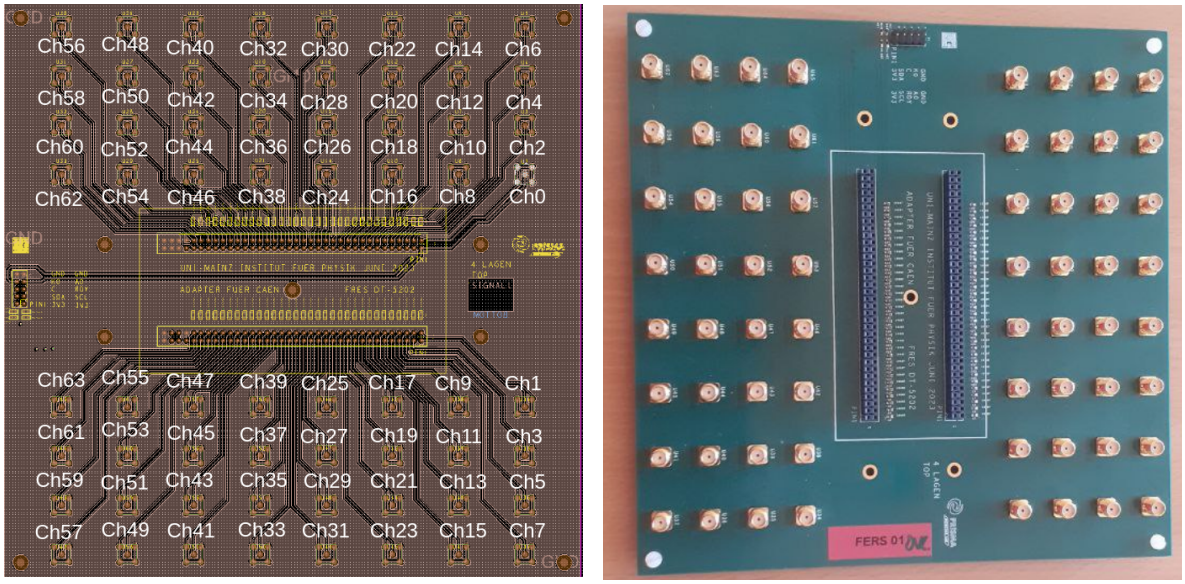

(a)

Figure 6.5: Layout (left) and top layer of the designed adapter board. The FERS system is plugged into it from the top

The adapter board has been designed without meandering for simplicity, therefore different channels suffer from somewhat different attenuations and delays. The impedance was not finely tuned in this first design and performance was evaluated through time domain reflectrometry (TDR) [390] using a digital serial analyser as shown in Figure 6.6.

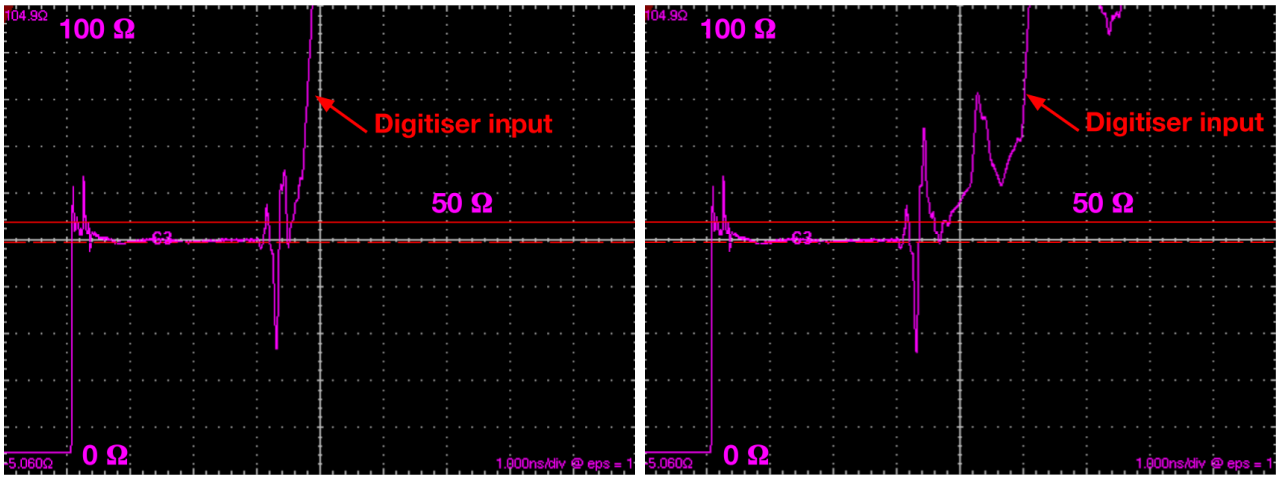

Figure 6.6: Impedance RC scan of channels 38 (left) a very short-line channel on the adapter board and 56 (right), a very long-line channel on the adapter board. The impedance is found to be workable.

It can be seen that the impedance breaks off after a given point and beyond that point, impedance levels are no longer stable and reflections may occur. The distances are quantified in Figure 6.7.

The effects of delay differences can be observed to induce variations in data at low amplitudes as the data as shown in Figure 6.8.

These effects are expected to be apparent also at higher amplitudes where MIP peaks may be smeared or displaced by reflections. This induces a reinforced need for channel wise calibration when using this adapter board with symmetrical channels expected to be otherwise identical.

6.2.3.2 Single photoelectron spectrum, gain and MIP calibration

Single PE spectrum The DT5202 can be used for calibration as shown in Section 5.3.3 and to observe the single PE spectrum induced from laser irradiation. This allows for a good measure of the system's PE

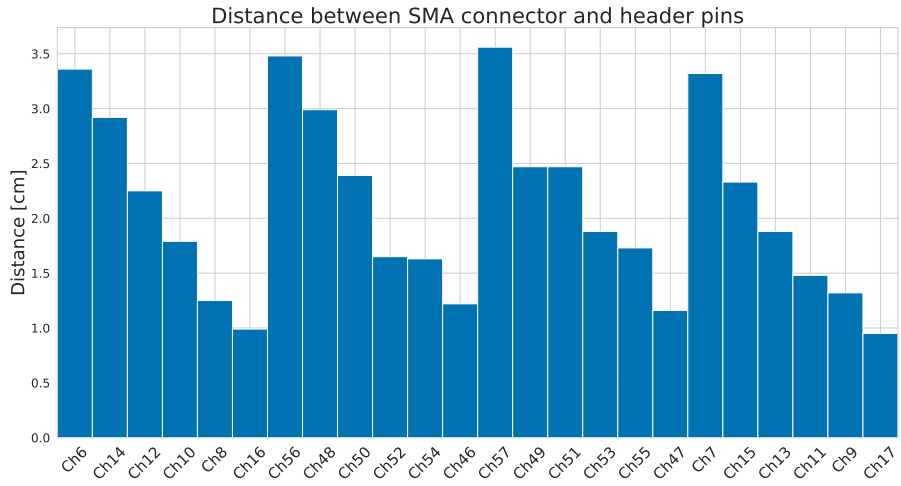

Figure 6.7: Distance between SMA pin and corresponding header pin input. Only 24 channels are shown as the board is symmetric.

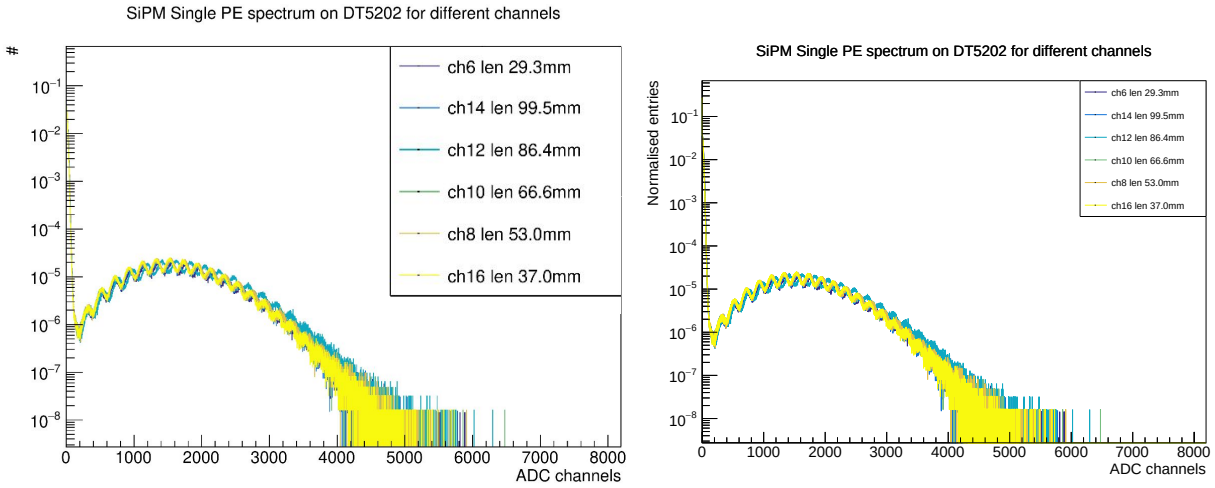

Figure 6.8: Single PE spectrum as seen from low intensity laser irradiation for different channels. Noise can be induced (left) and the PE spectrums are progressively dephased as higher amplitudes are reached (right). Different gains are used in both cases.

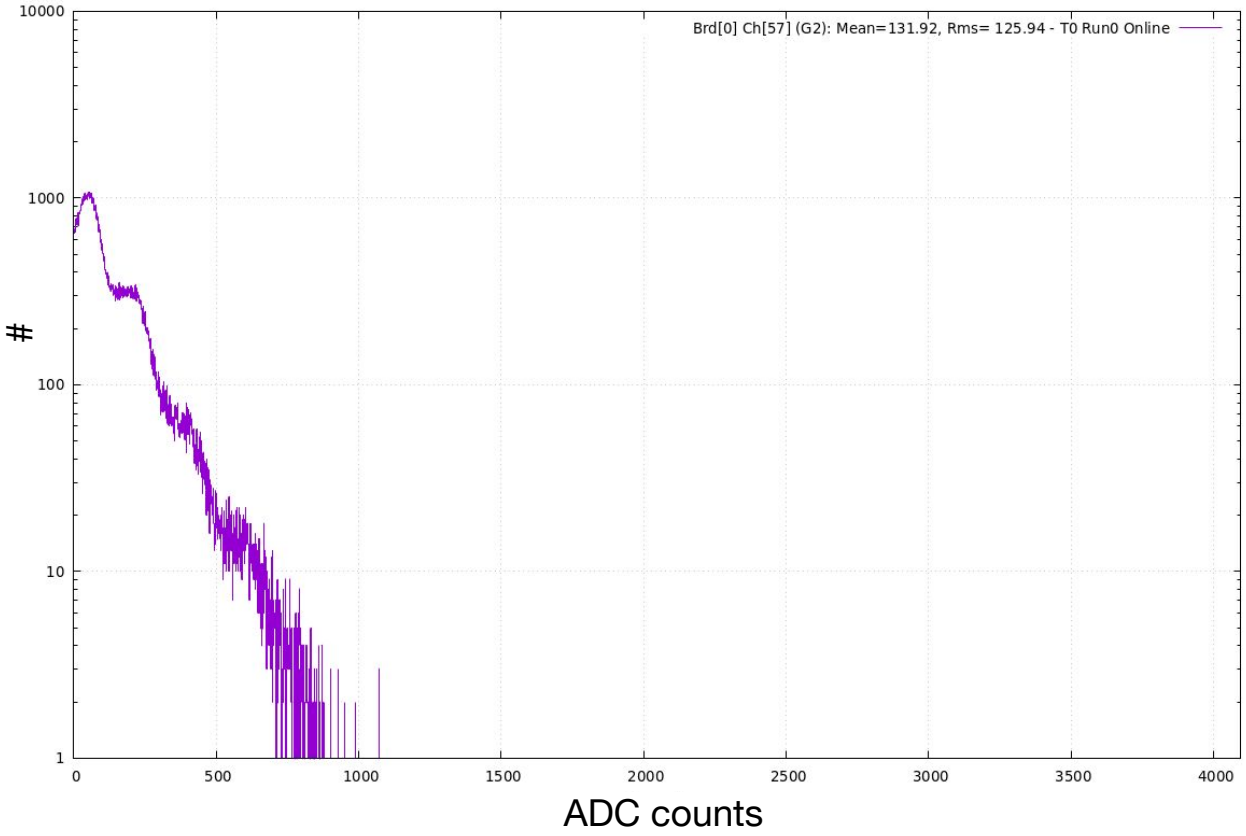

Figure 6.9: ADC output from dark counts from a S14160-6050HS SiPM operated at 42 V as seen by the DT5202 using the maximum gain value of 63 and self-triggering.

resolution and allows to optimise the output for resolution. The dark count can be measured as shown in Figure 6.9, allowing for a photoelectron calibration to ADCs. Similarly exposition to the laser operated at low intensities allows to complement the PE calibration as shown in Figure 6.10.

Gain study As the system produced in chapter 5 yields large amounts of light and thus large signals which can quickly lead to saturation the readout electronics' ADC, operation at low bias voltage, around 42 V (~ 3 V overvoltage) is preferred. The tunable gain may be used to further increase the system sensitivity which induces the need for a calibration of the gain for a given operating voltage. This is done by first calibrating the PE count using the digitised SiPM pulse method of Section 5.3.3 and then irradiating the SiPM with a stable amount of light yielding a known average PE count from the laser operated so as to be as stable as possible, while changing the gain value. This was done with a 10 kHz laser frequency, using an external trigger from the laser and having each run corresponding to a gain value last 10 s, the results of which are shown in Figure 6.11.

Different gain values lead to different PE resolutions. These can be examined by irradiating a SiPM readout by the DT5202 using the laser at low intensity similarly to Section 5.3.3. The resolution, a handle of detector photodetection precision, is expected to start high and decrease until a certain gain threshold beyond which PE peaks become smeared and indistinguishable. This examination is done in Figures 6.13 6.12.

The resolution is found to increase until the high gain setup reaches $HG = 61$ and plateau until $HG = 40$ before quickly decreasing afterwards.

The gain operation can be set to be always HG, LG, switching between the two depending on the analogue input or for both gain branches to be used in all circumstances. The transition between HG and LG, being most sensitive in an experimental setting is observed on a scintillator two sided coincidence is shown in Figure 6.18. The ratio between both gain values for different light inputs as applied by the laser is shown in Figure 6.14 and 6.15.

The overall effective dynamic range achieved by the system, with a HG/LG ratio of ~ 10 and a MIP around 600 ADC can be estimated to be around 10^2, two orders of magnitude below the minimum of 10^4 estimated to be necessary for the SHiP ECAL (see Section 6.1.1).

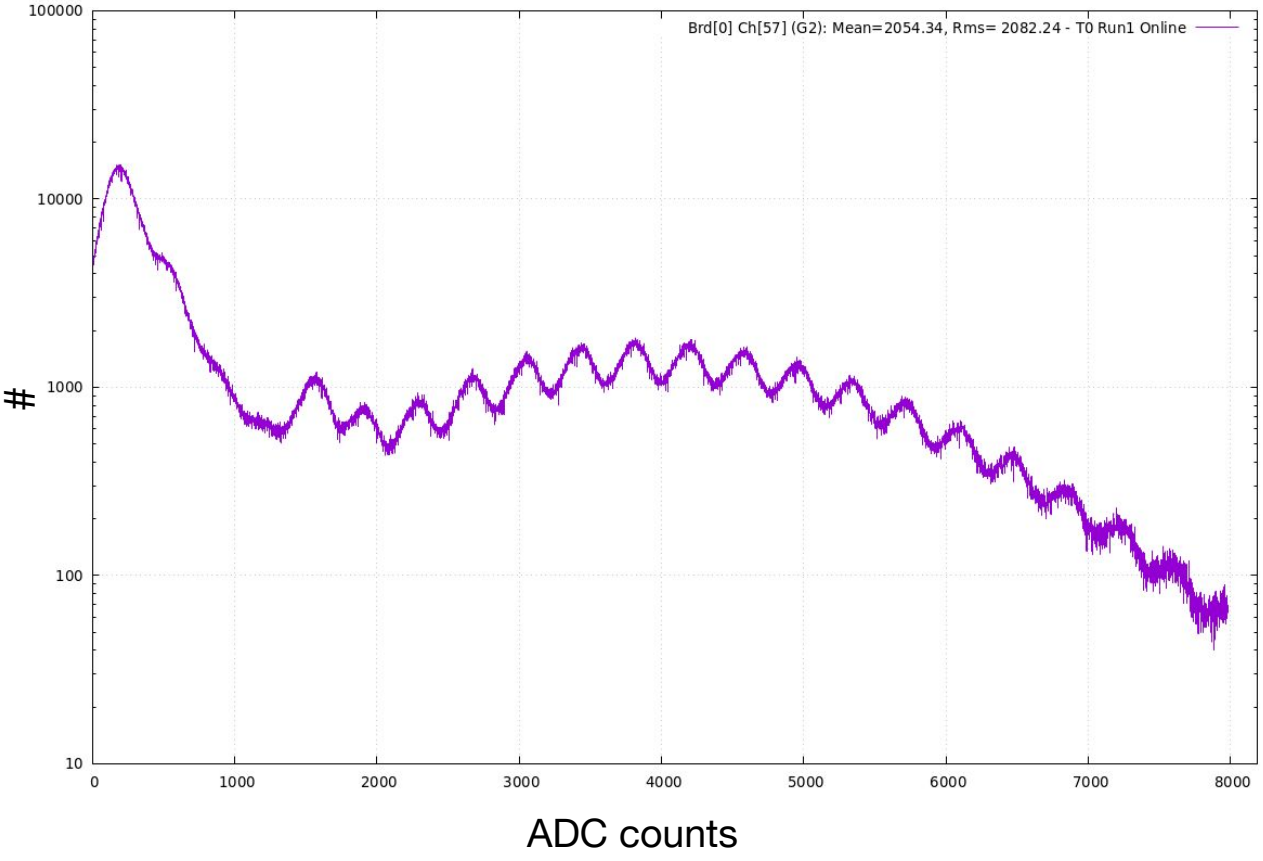

Figure 6.10: ADC output from a S14160-6050HS SiPM operated at 42 V as seen by the DT5202 using the maximum gain value of 63 and self-triggering.

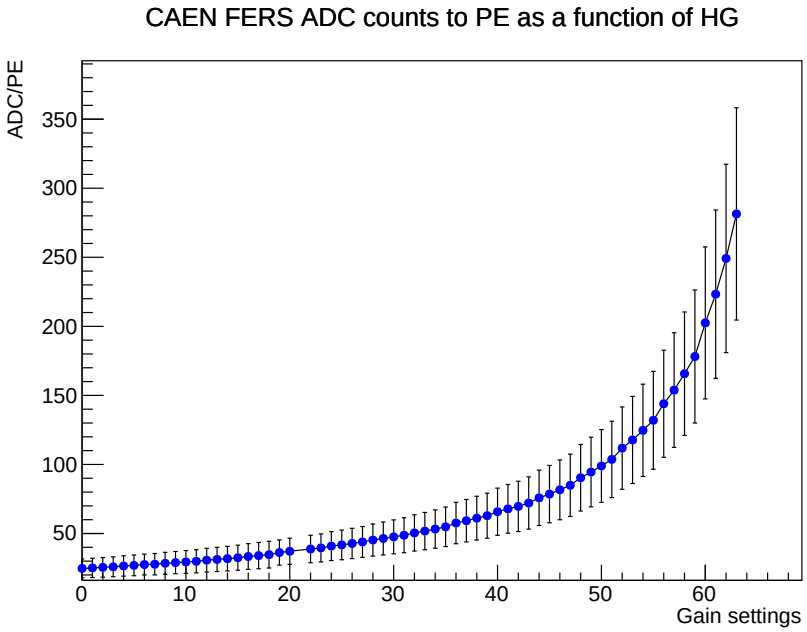

Figure 6.11: PE-gain calibration of the DT5202 from a S14160-6050HS SiPM operated at 42 V. Data for gain 21 was corrupted and thus removed.

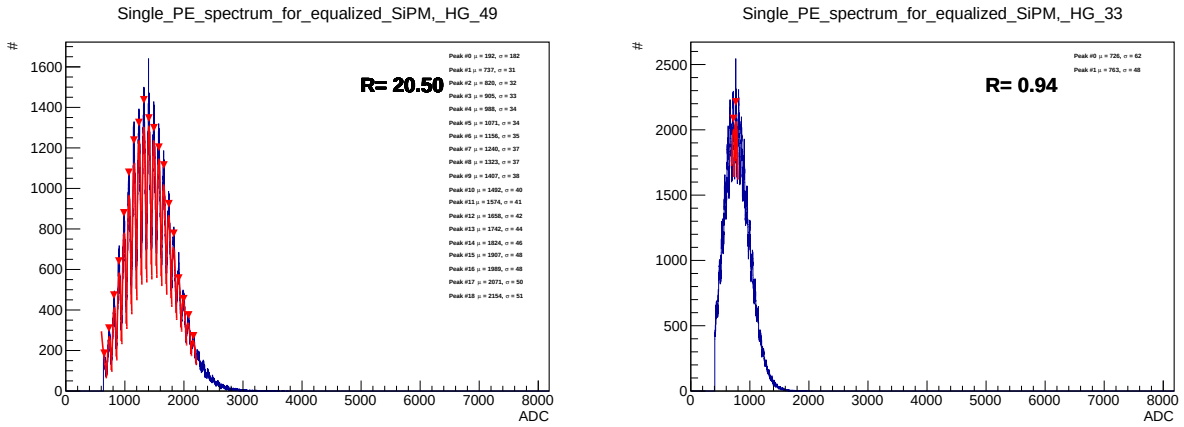

Figure 6.12: Single PE spectrum using the DT5202 with the HG setting at 49 (left) and 33 (right).

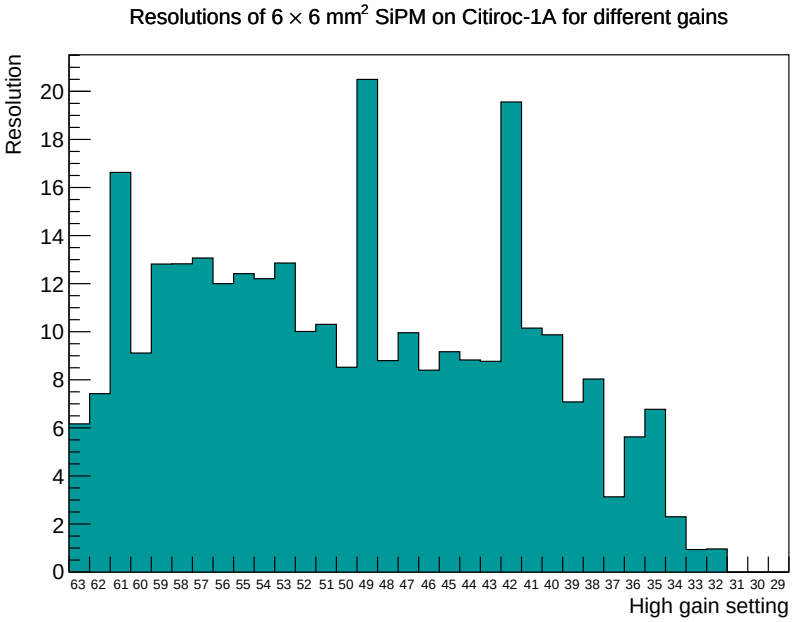

Figure 6.13: Resolution as a function of gain for a fixed laser setting. The x-axis represents the gain setting.

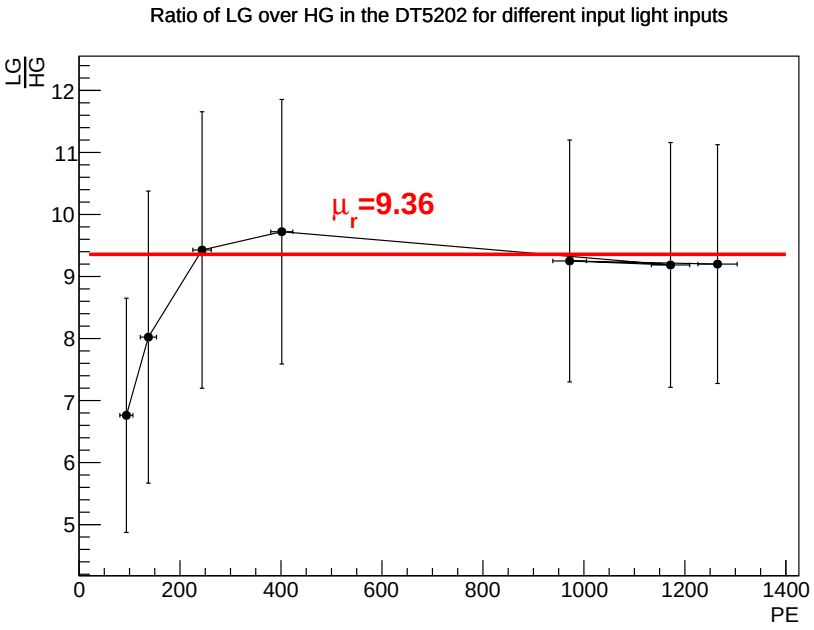

Figure 6.14: Ratio between HG and LG. The error bars are the standard deviation from the measured ADC distributions from laser irradiation. The ratio is found not to be stable in laboratory conditions. This is unlikely to be caused by variations in uncertainties and is thus the likely consequence of the electronics implementation itself.

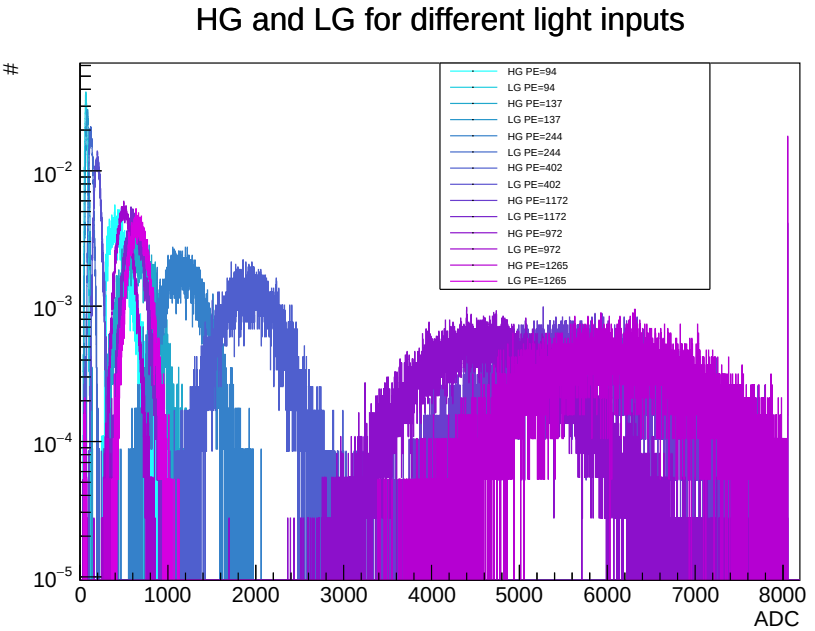

Figure 6.15: HG and LG spectra for different incoming PE counts.

MIP calibration Using the PE calibration and the principles explained in Section 3.1, it becomes possible to calibrate a scintillator bar system readout by a SiPM using the DT5202 as its readout electronics using cosmic muons. In order to restrict the angular variations of the incoming particles, this is done by using two $36 \times 6 \times 1\,\mathrm{cm}^3$ EJ-200 scintillator bars each equipped with a pair of WLS fibres and the SiPM-fibre interface described in Section 5.5.6. Both bars are vertically separated by 37 cm and kept perpendicularly overlapping in their centre, forming a cross pattern with the system placed inside of the cosmic box of Section 5.2.2 and shown in Figure 6.16. The bars are separated by 5 cm by 3D printed frame to limit the angular variety of muons traversing the bars. The remaining angles are approximated to take values around 0° according to a gaussian distribution with $\sigma = \frac{\theta_{\mathrm{cell,max}}}{3} = \arctan\left(\frac{6}{5}\right)/3$. This is taken as a systematic error above the $\sim 1.7\,\mathrm{MeV}$ average expected loss in 1 cm of the scintillator for a perpendicularly passing through MIP. A 100 ns coincidence between any two channels from different bars connected channels is then imposed (four channels coincidences were found not to be well implemented in the FERS-5200 system's FPGA firmware, a bug which has since been fixed), making it so that cosmic muons passing through the $6 \times 6\,\mathrm{cm}^2$ centre area of both bars will be recorded. The data-taking conditions restrict the rate, leading to a week long measurement with the result being shown in Figure 6.17. This allows for an energy deposition calibration by matching the (known) energy deposition of a MIP to ADC counts which can then be translated to calorimetric energy reconstruction. In the case of the built system, a MIP is known to deposit 1.785 MeV in the scintillator. It is noted that certain anomalies appear in the MIP spectrum at higher amplitudes. These are understood to stem from bugs in the electronics' firmware and to be fixed in a future update.

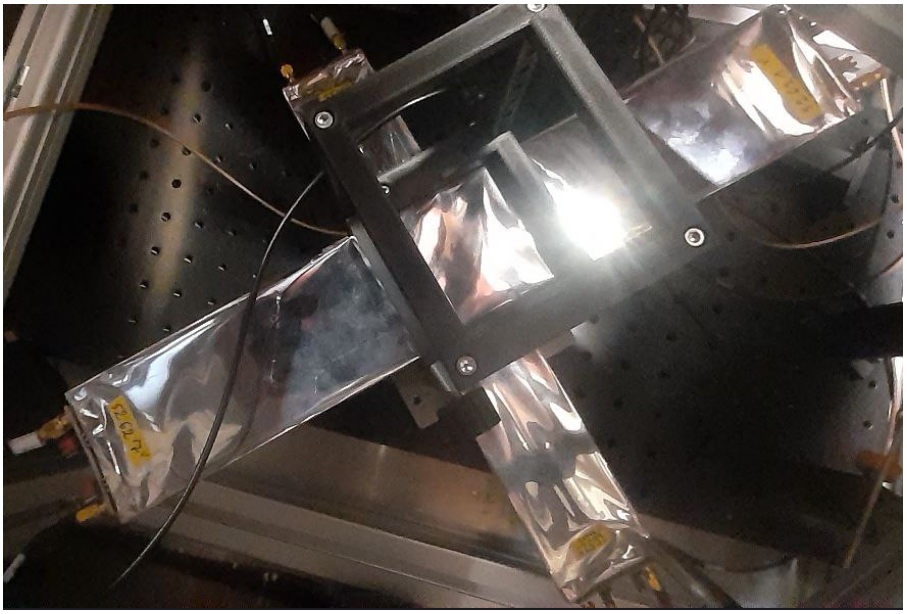

Figure 6.16: Cosmic setup used to perform the MIP calibration seen from above. A 3D printed frame allows to ensure a stable angle and distance between the two scintillators. Each bar is readout on both sides using a SiPM.

6.2.3.3 Influence of shaping time

As expressed in Section D.0.1.2, the shaping time cuts certain frequencies off. This can be seen as advantageous as it limits the used dynamic range provided the shaping time is short enough. The effects of the DT5202's amplifier and shaper are not precisely known, as a result, evaluation of the used shaping time can lead to an improvement in the readout electronics dynamic range by limiting the required bandwidth.

This evaluation was done using direct laser irradiation on a S14160-6050HS at a fixed low light level using HG mode, so that PE counts could well be observed. It was performed for the shaping times available within the provided software, namely {12.5, 25, 37.5, 50, 75, 87.5} ns. The measurement was done for 5 min per shaping time at a laser frequency of 1 kHz and an external triggering from the laser with the results being shown in Figure 6.19.

It observed that the PE spectrum is smeared and displaced considerably for any shaping time above 12.5 ns. This implies that high frequency noise is considerably increased and largely has a frequency between $\frac{1}{\omega_c} =$

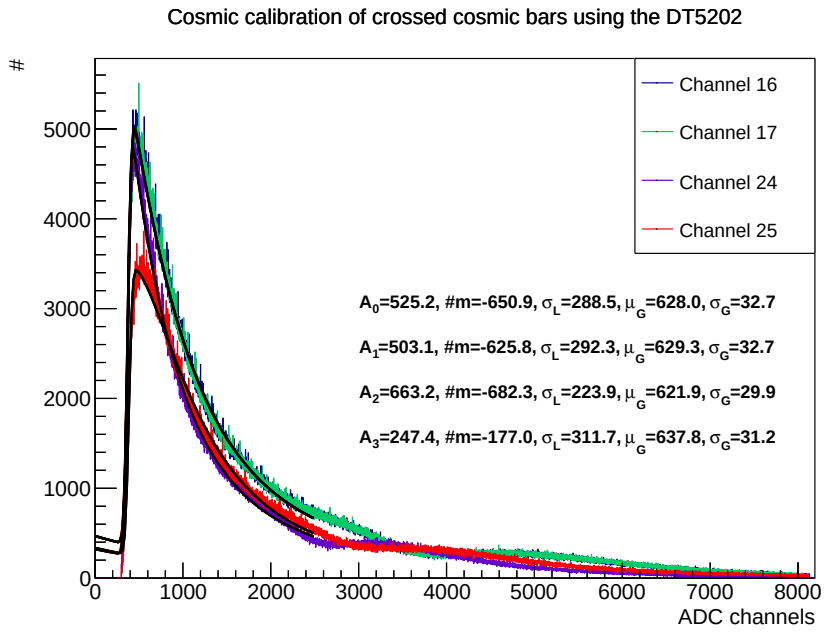

Figure 6.17: MIP calibration from the fit of a convolution of a Landau and a Gaussian onto the HG branch of the DT5202 for $G_{\mathrm{HG}} = 0$. It is noted that one channel in particular has much lower efficiency than the others, perhaps due to lower SiPM performance at this voltage. The bump around 3000 ADC is understood to originate from a bug in the electronic implementation.

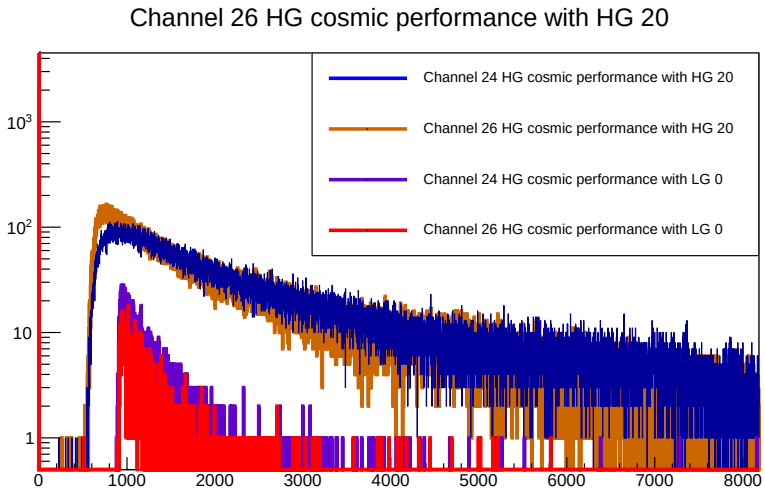

Figure 6.18: Example transition between HG and LG in cosmics radiation.

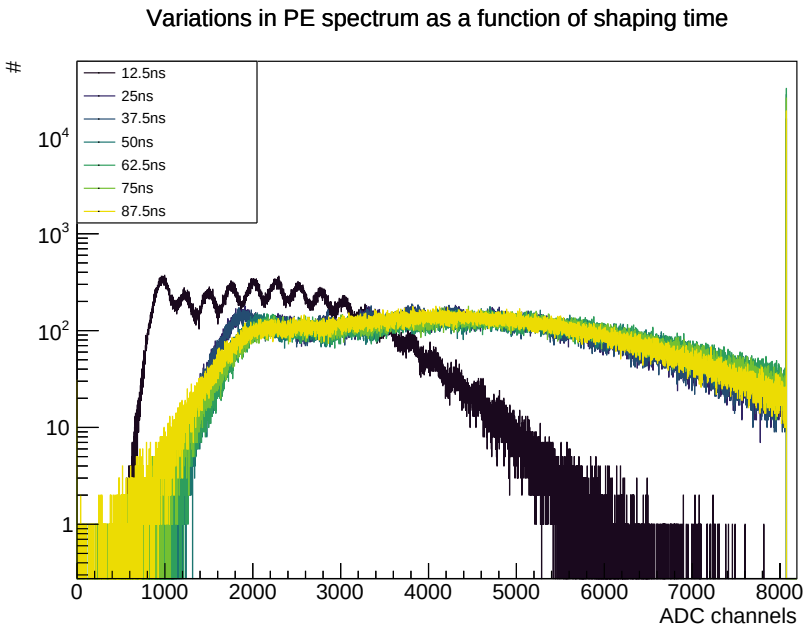

Figure 6.19: Digitised output of the DT5202 as a function of shaping time.

40 MHz and 80 MHz with small amount between 40 MHz and 26.7 MHz. Operation at lower shaping times, particularly 12.5 ns is therefore preferred as it allows better observation of PE spectrum and restricts the absolute signal size.

6.2.3.4 Conclusion

The DT5202, while displaying good performance, possessing an effective gain switch being capable of reconstructing both PE spectra and MIP distributions with good resolution, is unsuited for use in the SHiP ECAL. This is due to its significant dead time but also to its insufficient dynamic range as well as other implementation bugs such as non-linearities observed in MIP responses. Nonetheless, the DT5202 is suitable for use in prototyping as it will allow to operate in triggered mode without loss in efficiency. Another limitation is the designed adapter board which, while suitable for prototyping, requires proper impedance matching and delay compensation along its longer lines for it to be optimally operable in an experimental setting.

6.2.4 The KLauS chip

The KLaus6b (Kanäle für die Ladungsauslese von Silizium-Photomultipliern) chip is an ASIC designed for the readout of the CALICE AHCAL [347] [391–393] using a 180 nm CMOS process. Is is designed around two gain branches both using a passive integrating circuit and a low-pass Sallen-Key filter. Only one of the two branches is digitised based on the input charge as determined through an adaptive gain-selection comparator. The digitisation is performed using a 10 bit SAR ADC with an option to use a 12 bit SAR ADC for low intrinsic gain SiPMs. The chip displays in addition very good timing resolution < 100 ps and 36 channels with its block diagram shown in Figure 6.20.

6.2.4.1 Analogue front end

The processing of analogue signals is done in the front end and consists of a regulated common-gate transimpedance amplifier as shown in Figure 6.21 followed by a charge integrator and pulse shaper for precise charge measurement similar to the TOFPET2.

The signal is buffered in the low-impedance input stage. It is then distributed to subsequent branches, with the input stage impedance given by $R_{\text{in}} = \frac{1}{g_{\text{m1}}}\left(1 - \frac{g_{\text{m1}}g_{\text{m3}}}{g_{\text{m2}}g_{\text{m4}}}\right)$, with $g_{\text{m}X}$ the transconductance of the corresponding transistor and $1 - \frac{g_{\text{m1}}g_{\text{m3}}}{g_{\text{m2}}g_{\text{m4}}} > 0$. Notably The SiPM bias voltage is an integral part of the input

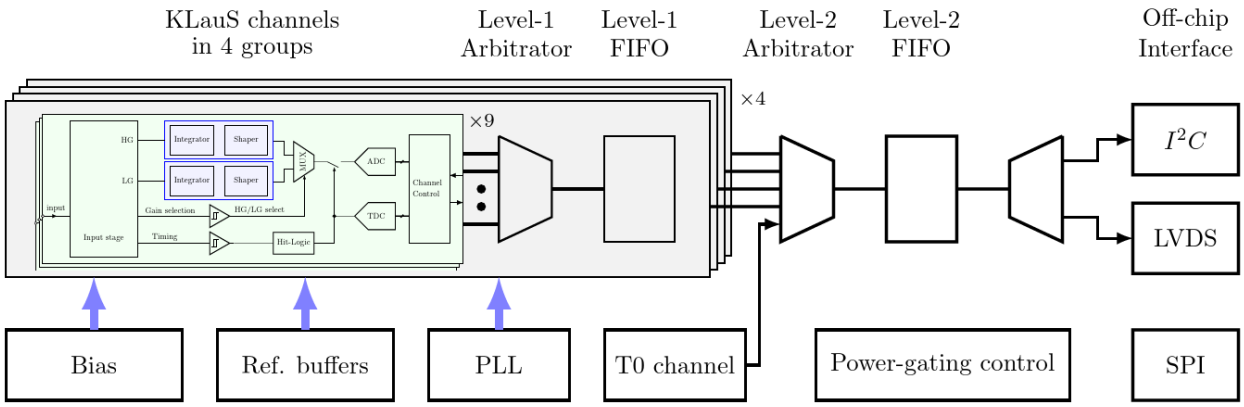

Figure 6.20: Block diagram of the KLauS chip [393].

stage, implying that the SiPM anode and cathode should be connected to the KLauS directly with the V_{DAC} being used to tune the effective SiPM bias itself within $\sim 2\,\mathrm{V}$.

Integration and shaping is done within the gain branches themselves, which can be tuned to cover different dynamic ranges using gain factors which are denominated HG11 (highest gain), HG17, LG160 and LG1200 (lowest gain) respectively in the following. All branches share the same ADC and underlying control logic. The buffered current input is integrated on a capacitor for a time constant $\tau_i C_i$ with a Sallen-Key shaper (see Appendix D.0.1.2). Two comparators are present for each channel, enabling the fast multiplexed gain selection and the very-low-threshold production of a trigger signal respectively. The chip also includes a digital hit logic circuit prior to the ADC conversion and an analogue monitor. The entire KLauS circuit is shown in Figure 6.21.

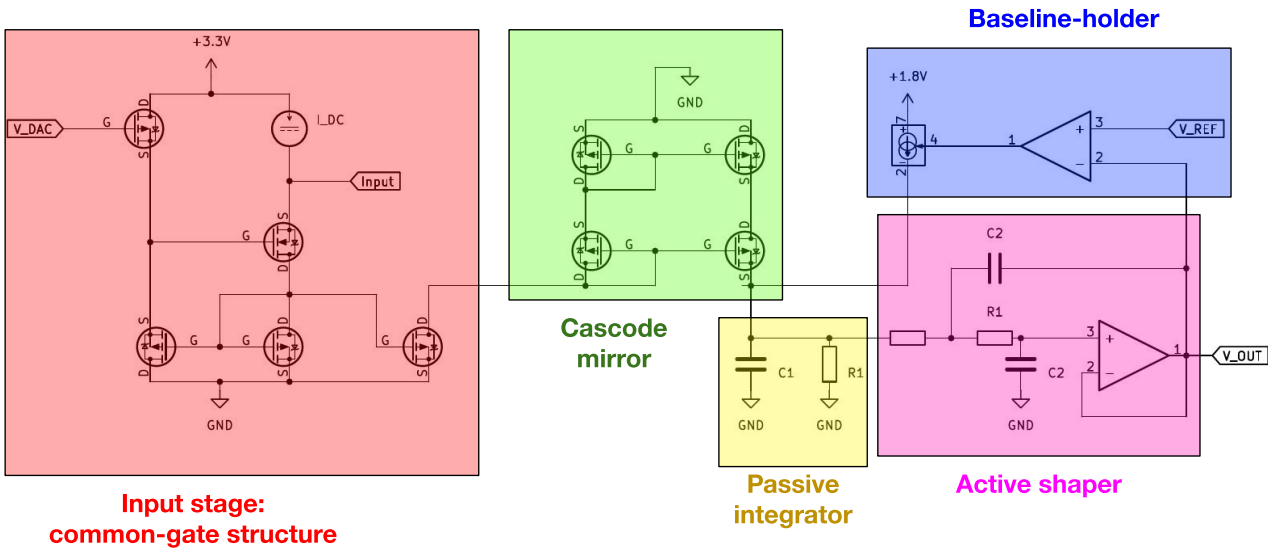

Figure 6.21: KLauS analogue circuit.

6.2.4.2 Digital circuit

The 10 bit ADC (with a pedestal located at $\sim$ 695 ADC counts due to the integration of the front end and ADC) is done using a successive approximation scheme (SAR, see Appendix D.0.2) and pictured in Figure 6.23. The ADC operates on the signal peak which is the only sampled point from the analogue output. A hold delay is implemented in order for peak finding to take place as shown in Figure 6.22. The data streams may be output wither through a slow I^2C bus or the faster LVDS interface with slow control being done through SPI. The chip can thus be controlled using a microcontroller, a microprocessor (such as a Raspberry Pi [394]) or an FPGA with up to 64 chips being theoretically controllable for a given bus.

In addition, the KLauS has a phase-lock loop (PLCC)-based TDC with a phase-frequency detector, a voltage-controlled ring oscillator, a clock buffer and a charge pump [393].

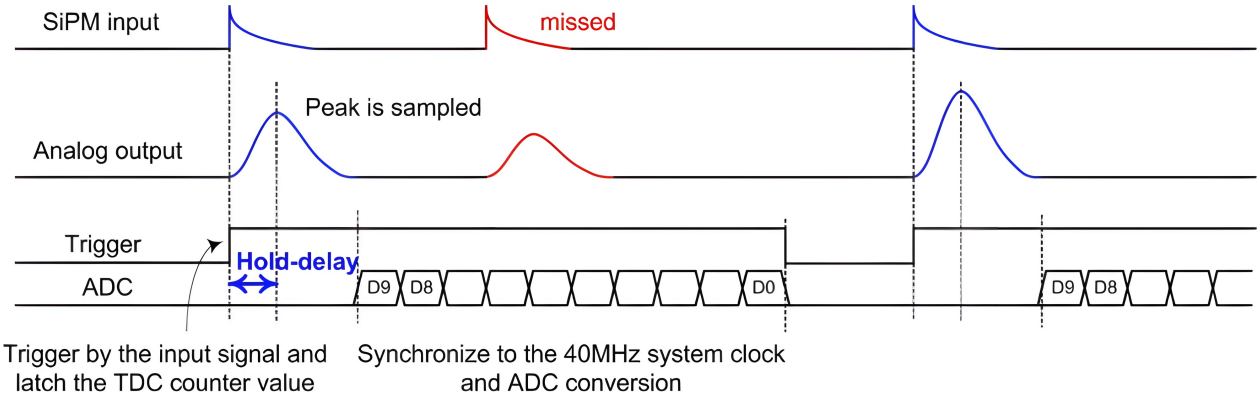

Figure 6.22: KLauS signal processing chain, time flows from left to right [395].

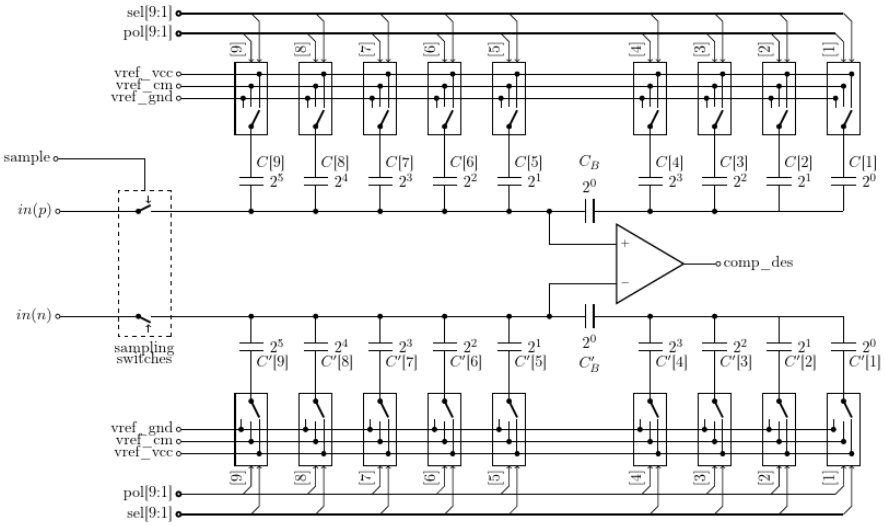

Figure 6.23: Block-level schematic of the KLauS 10-bit ADC [392].

6.2.4.3 Operation of the KLauS chip with high-capacitance SiPMs

KLauS operating conditions The KLauS chip is integrated onto a custom designed board designed by Konrad Briggl. It includes its powering, an HV LEMO connector supplying the base SiPM bias voltage, a LEMO connected to the chip's analogue monitor as well as 4 rows of double header connectors, each providing anode and cathode for a SiPM channel. An alternative board, replicating the capabilities of the first but modifying the powering scheme for more flexible operation was later designed and used to integrate the KLauS. It is pictured in Figure 6.24a. A custom adapter board was developed and used to connect SiPMs with two SMA connectors following schematics shown in Figure 6.24b.

The SiPMs are operated with $\sim 3\,\mathrm{V}$ overvoltage. Seeing as no significant loss nor noise increase is observed in the use of longer cables, connections are made with 3 m long SMA cables for bias and signal.

KLauS operation with small SiPMs The KLauS, with its low-capacitance FE amplfier, is well suited to the readout of small SiPMs using short cables. In those conditions it shows good resolution as shown in Figures 6.25 and 6.25 where the $1.3 \times 1.3\,\mathrm{mm}^2$ S13360-1325PE SiPM was exposed to various laser intensities corresponding to a few PE and is representative of the achieved resolution. The timing trigger threshold (TTT), used to place a threshold on signal amplitude [392], was varied as well which lead to a constant increase in the relative signal in each case.

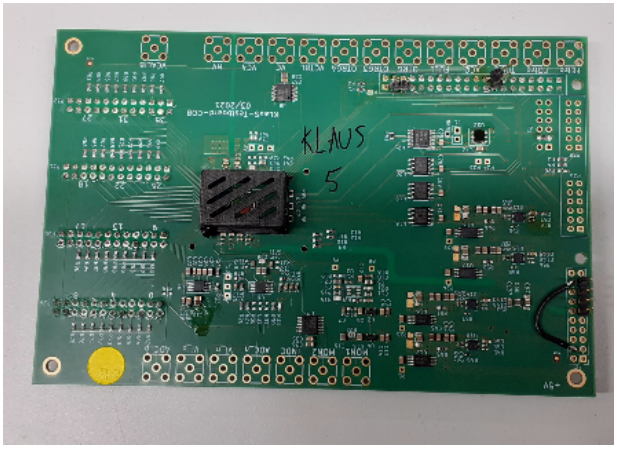

(a) Custom KLauS board designed and produced in Mainz. It replicates the Heidelberg board capabilities but implements a more flexible powering scheme.

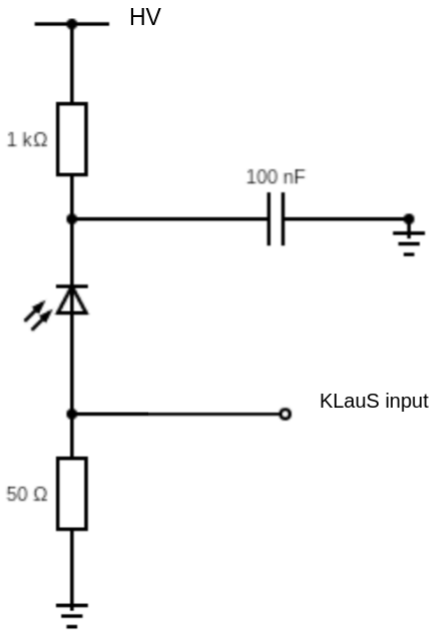

(b) Example SiPM circuit board. The HV is located on the pin of the first SMA connector with the signal input going onto the pin of the other SMA, the shieldings are grounded. This board model is used in the following studies. The top resistor is designated *base resistor* while the bottom one is called *pulldown resistor*.

Figure 6.24

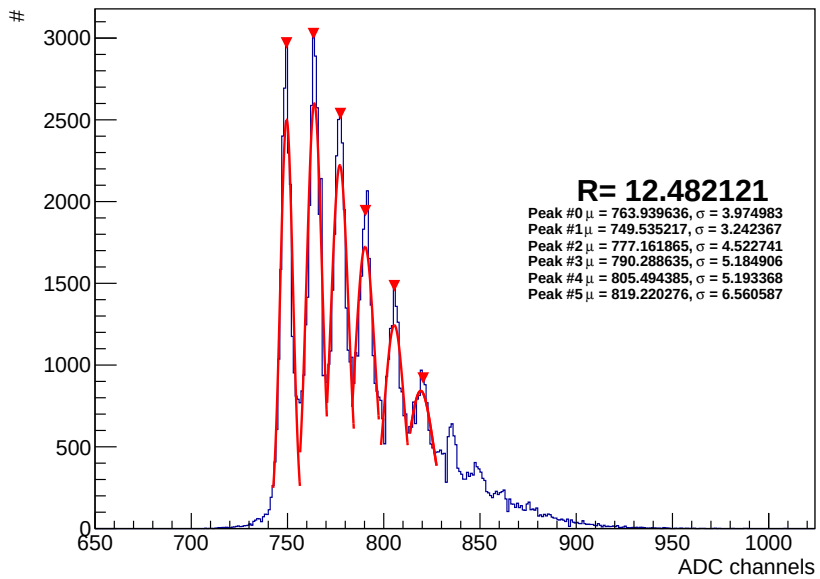

Figure 6.25: Single PE spectrum of a S13360-25PE SiPM exposed to low intensity laser irradiation on the KLauS chip in HG11.

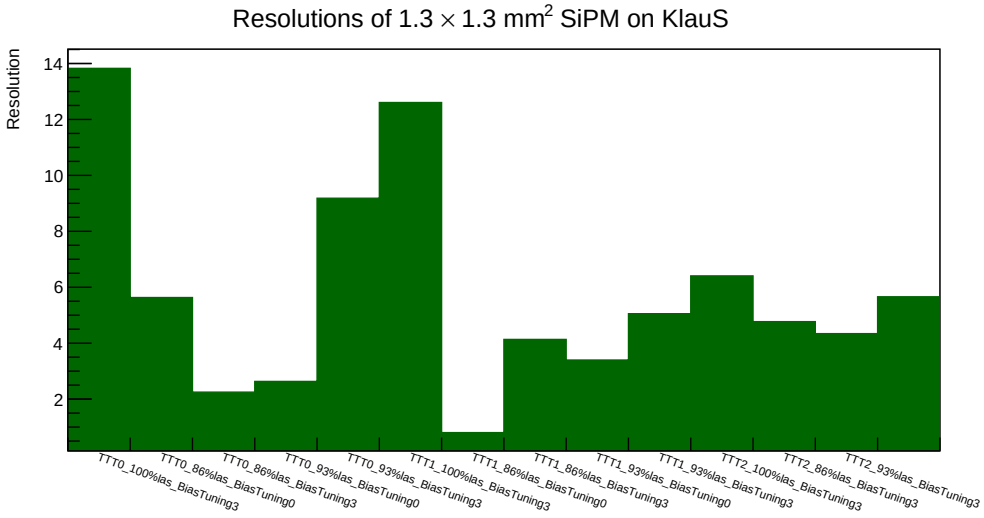

Figure 6.26: Resolutions achieved by the system using a single SiPM for different laser and TTT modes.

KLauS operation with large SiPMs While the KLauS may display good behaviour when operated with a small SiPM as input, unfortunately, large SiPMs, which display much larger capacitance, suffer from the KLauSes low-capacitance amplfier in three primary ways:

- Ballistic deficit, described in Section D.0.1.2
- Double integration: the mismatch in input capacitance leads to the capacitance pole being dominant over the OpAmp's internal pole. The capacitance can get charged and creates a step or tail which is also seen by the amplifier (see Appendix D.0.1.1). These slow components may linger and be processed by the Sallen-Key shaper. This mechanism leads to several peaks with decreasing amplitude being integrated. This is shown in Figure 6.27 (see also D.0.1.1).
- Noise increase: the larger capacitance mechanically leads to higher noise, smearing the photopeaks. This can be observed in Figure 6.28 for dark counts.

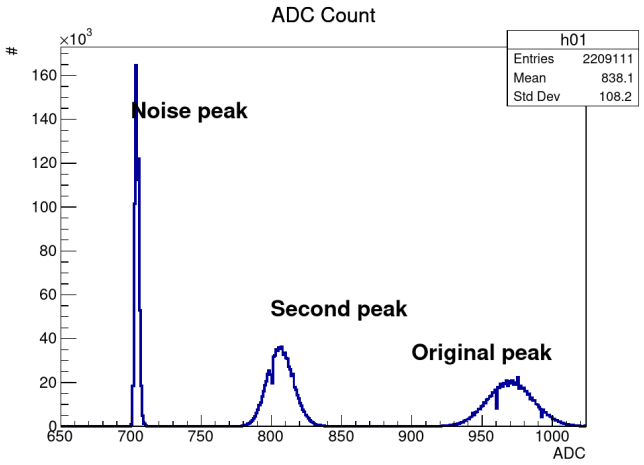

Figure 6.27: Double peak structure displayed by the KLauS HG 17 ADC when connected to a large SiPM.

The ballistic deficit, while problematic for timing applications, is not critical in the case of the SHiP ECAL which has much more moderate timing requirements than the chip's capabilities. The double peaking and noise increase however render any deployment of the KLauS using standard circuits in the ECAL impossible.

The condition for dual peaking to be caused by capacitance mismatch is that events from the second (smaller) peak consistently arrive after events in the first peak. Therefore, both peaks were looked at in time as shown in Figure 6.29.

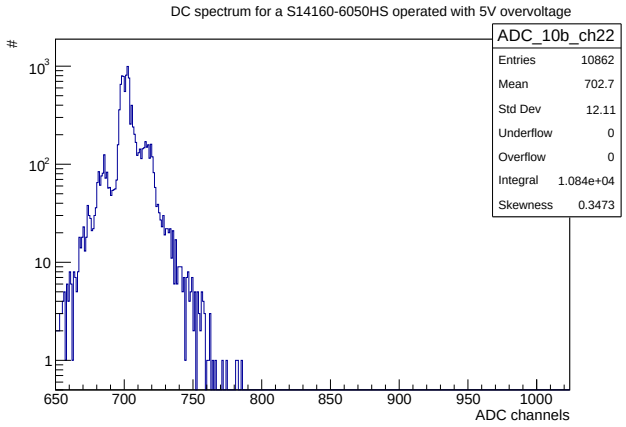

Figure 6.28: Dark count spectrum of a S14160-6050HS SiPM in HG11.

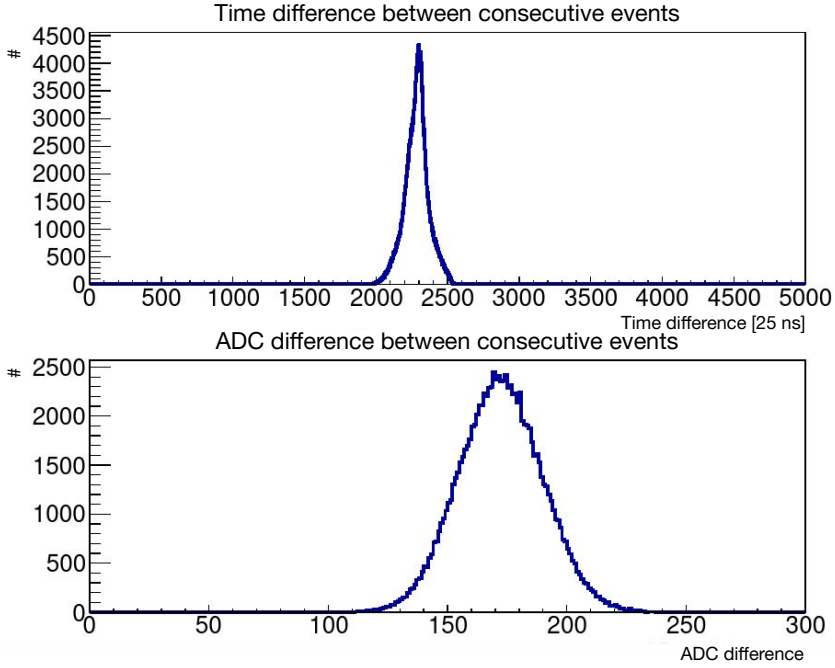

Figure 6.29: Time and HG17 ADC difference of event pairs (even and odd) in a 1 kHz laser irradiated data sample. Time units are provided in increments of 25 ns with positive difference indicating that the pulse from the second peak was integrated afterwards. ADC difference is between the first and second event.

Overwhelmingly, the pulses forming the smaller peak arrive $\sim 50\,\mu s$ after those from the first peak which is consistent with the signal capacitance mismatch at the amplifier considering the readout cycle of the shaper. Dual peaking is not caused by reflections as impedance is kept similar ($50\,\Omega$) at the SiPM output and KLauS input and similar tests were conducted by connecting two SiPMs to the same input for no change. This was also verified by varying pulldown resistance, cable length and input stage bias (ISB) which is shown in Figure 6.30.

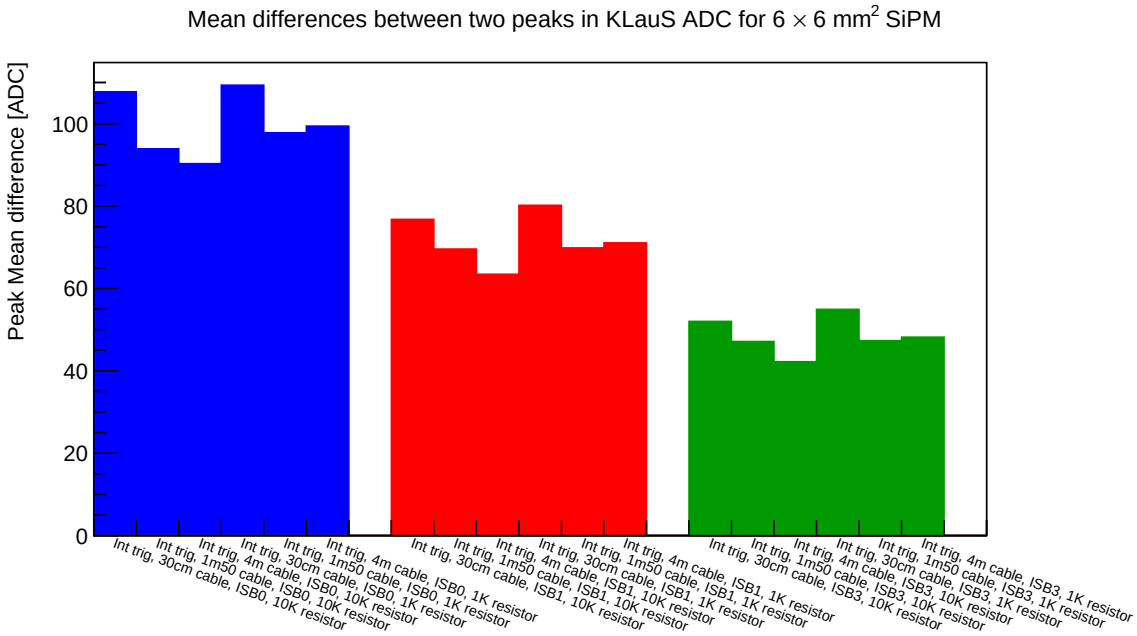

Figure 6.30: Variations in base resistance, cable length and input stage bias. Cable length and base resistance are observed to only play a weak role, smaller than the ADC difference itself.

Is it found that higher ISB leads to smaller distance between both peaks, with the second peak increasing in amplitude. This suggests that the amplifier's effective capacitance is decreasing with higher ISB settings. The base capacitor is also found to only have a weak influence on dual peaking, implying that corrective action should be focused onto the system capacitance.

Corrections to dual peaking Dual peaking, being caused by capacitive effects, is corrected by capacitive means. Two solutions have been evaluated in response to this issue: either an intermediate voltage-controlled preamplifier with high input capacitance and low output capacitance may be introduced, or the response function stability range may be extended through the use of an intermediate capacitor.

The introduction of an intermediate preamplifier, while functional and allowing to improve the achieved resolution as shown in Figure 6.31 remains problematic as the SiPM powering then becomes more complex. The amplifier itself also needs a dedicated powering scheme, complexifying the circuit. This eliminates the possibility to fine tune the SiPM's bias voltage through V_{DAC}. In addition, the amplifier gain has to remain close to 1 or below in order to retain dynamic range and minimise noise. These factors in addition to the time required to develop an optimal amplifier have led to this option not been pursued beyond evaluation. Common-drain MOSFET or BJT-based amplifiers or extra transimpedance amplfiers with a capacitor with $C \sim 10\,\mathrm{pF}$ in the feedback block are seen as promising solutions solutions to the KLauS amplifier instability problem.

If the powering scheme is to remain simple, the shaper peaking time would be increased. Alternatively the common-gate-stage would be modified by utilising for instance a full-cascode input stage instead as shown in Figure 6.32. Other possible solutions would include an active DC feedback can be added by directly adding a slow low-pass filter from the output back to the input or the addition of a DC restoration path done by adding a high-value resistor ($\sim 1\,\mathrm{M}\Omega$) between the amplifier's input and the ground. Both of those options may however induce distortions to the pulse shape. These options can however only be implemented at the ASIC design stage as the amplifier is engraved directly on the silicon and would need to be tested. The found alternative is the addition of a capacitor on the SiPM output line which allows to filter the slow DC signals and block the DC

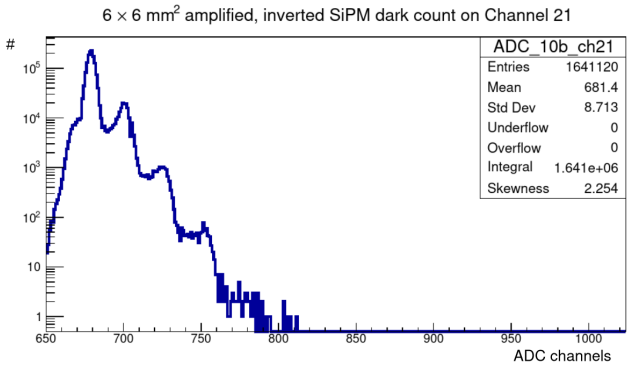

Figure 6.31: Amplified dark count pulse onto the KLauS HG17 using a custom charge-sensing amplifier.

capacitance from coupling to the amplifier input node. This effectively AC couple the KLauS chip. Since the exact specifications of the KLauS amplifier are not known, this was attempted with a great number of different capacitors (from 10 pF to 10 µF) in the circuit shown in Figure 6.33. Very small capacitors were found to have negligible effects on dual peaking with capacitors above 100 nF found to reduce it. The best performance was achieved with 220 nF capacitors with larger capacitors not being found to yield significant improvements.

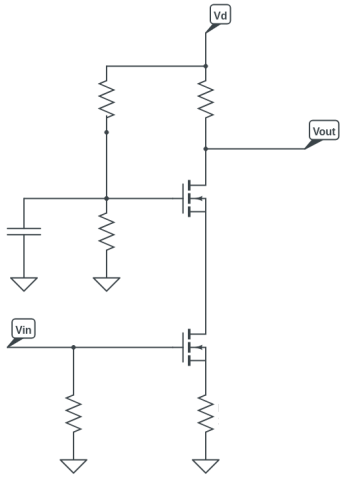

Figure 6.32: Proposed cascode amplifier configuration. Vin would be connected to the SiPM output, Vout is the output and Vd the amplifier bias.

The output has been found to match expected behaviour. The main limitation to this solution is the blocking of the DAC path which implies that single SiPM voltage cannot be fine-tuned. In addition the capacitor must be carefully selected for the used SiPM model. In addition, it is difficult to ensure that the secondary peaks are sufficiently damped as different operating conditions could cause dual peaking to resurface. This system however has the advantage of being easy to probe on an oscilloscope as well as using the KLauS ADC.

6.2.4.4 Conclusion

While the KLauS can be configured to partially fulfill the SHiP ECAL requirements, its 6b version is optimised for different purposes, namely small capacitance sensors and the overhead required to make it function flexibly is found to be too significant to justify its usage in the final design at this stage. In addition, the absence of a real parallel readout and the preference given to buffering via SRAM, usage of round-robin scheduling to allow fair and starvation-free readout across all channels and use of a second level FIFO structure for temporary rate surges reduces its relevance to the final detector in comparison to a real parallel readout. The exact rate limitations induced by these choices could not be evaluated in the laboratory with the existing DAQ structure as the data was transferred via I^2C, a very slow transmission bus which limits the maximum rate. It would have to be evaluated in real conditions at a test beam.

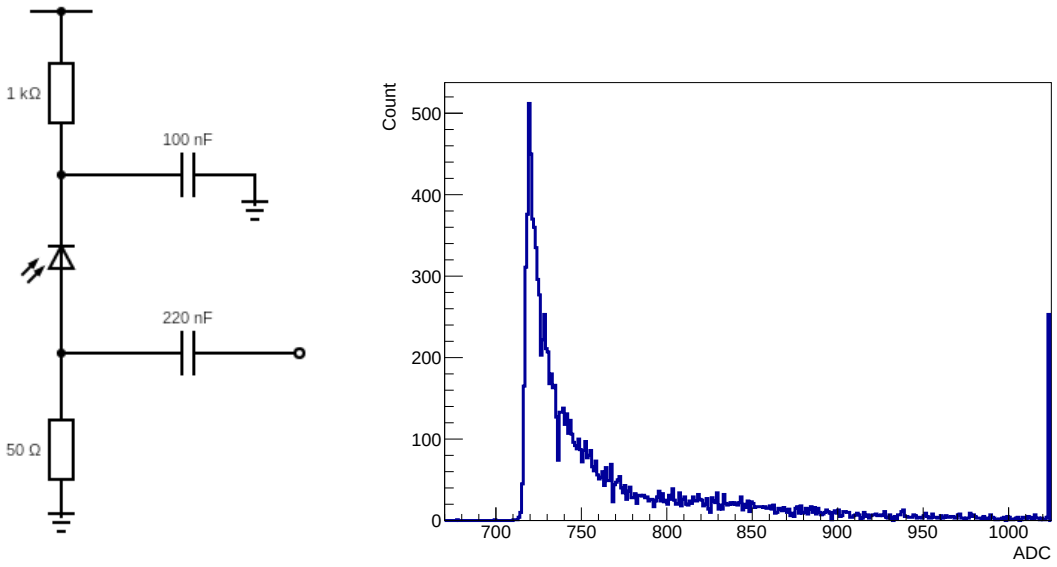

(a) Capacitor circuit found to be optimal.

(b) Cosmic signal distribution from one side of the scintillator bar given the optimised SiPM circuit.

Figure 6.33

6.2.5 Comparative evaluation of dynamic range for DT5702, DT5202 and KLauS chip

A definitive comparison of dynamic ranges has been made by exposing a single SiPM to the laser at 10 kHz (see Chapter 5) for different intensities in an otherwise fixed setup using three of the four evaluated readout systems evaluated in this work. The TOFPET2, having been evaluated in real conditions at SND@LHC was not tested of the sort as the readout hardware was not available in the laboratory.

The maximal achievable light intensity in the laboratory configuration was found to correspond to ~ 2500 PE. Each measurement has been done at the time of evaluation of its respective subsystem. The proportion of ADC used for each intensity was evaluated in each case based on a Gaussian fit of the ADC distribution. An offset of 695 has been applied to the KLauS whose ADC distribution begins at 695 ADC counts. The results of this evaluation are shown in Figure 6.34.

The KLauS is found to be the system with the largest dynamic range thanks to its 1:200 gain mode. It allows it to readout even heavily illuminated SiPMs which is deeply saturated and is, in combination with its reduced dead-time, found to be the most suitable system for the SHiP calorimeter system's readout amongst those evaluated. It could be used in the final detector, provided a new version capable of accepting higher capacitance, for instance through a suitable capacitor added to its transimpedance amplifier input with perhaps as a fully parallel readout being required as well.

6.3 Design and manufacturing of a flexible custom readout system using the KLauS chip

As the KLauS was found to be the chip most adequate towards fulfilling the SHiP calorimeter system's requirements among the systems evaluated, a scalable custom readout system was designed in order for many channels to be readout at the time. This has lead to the design, manufacturing and testing of the board shown in Figure 6.24a, that of a motherboard and that of corresponding SiPM boards. A study of cable effects is first performed followed by a discussion of motherboard design, a description of KLauS mezzanines and the SiPM boards are addressed. A review of the designed DAQ system concludes the section.

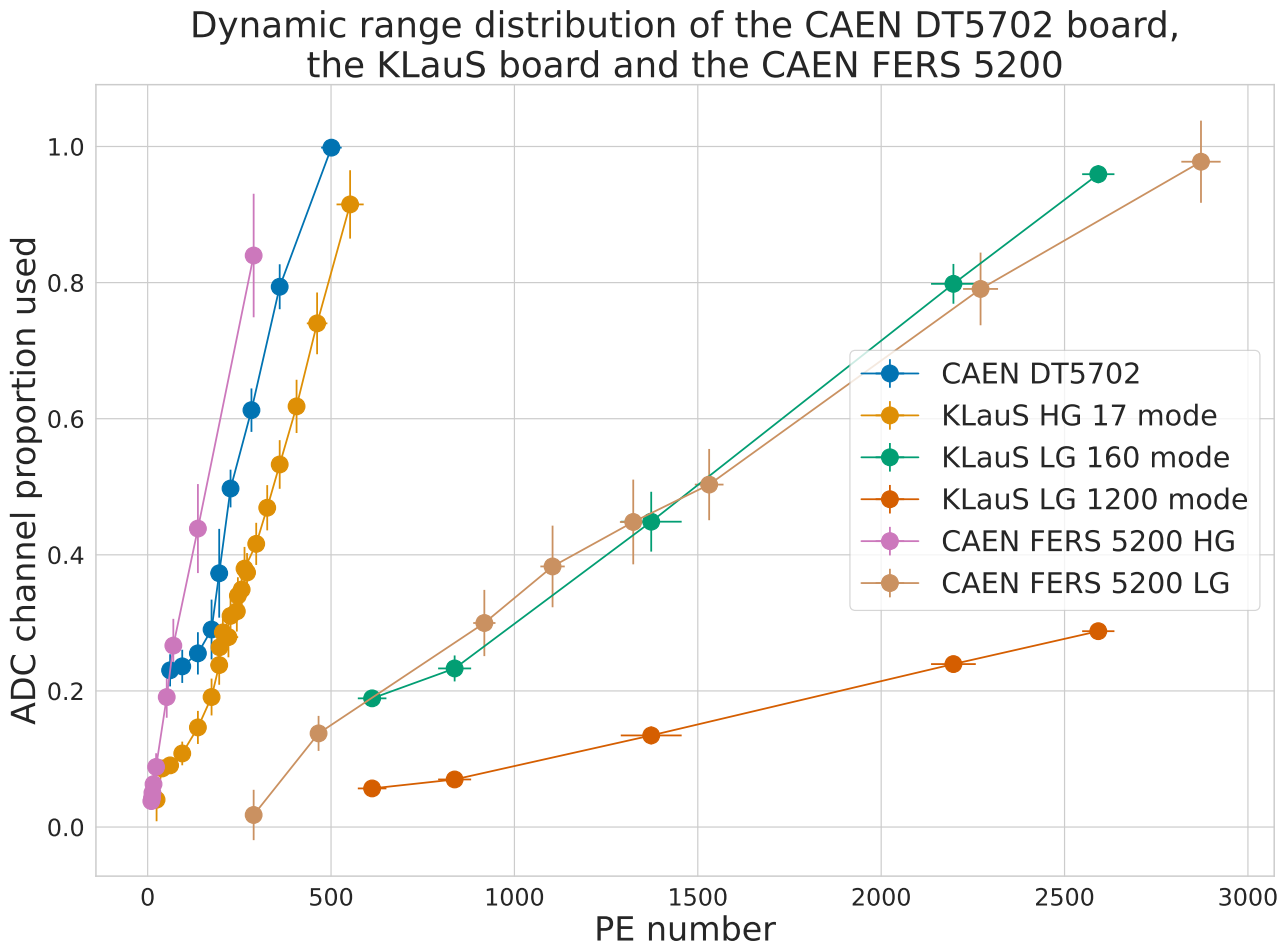

Figure 6.34: Dynamic range of the DT5702, DT5202 and KLauS chip. Saturation of the KLauS 1:200 branch could not be achieved for lack of sufficient coherent light input.

6.3.1 Study of coaxial cable effects

Cables lead to two unwanted effects: Attenuation of signals and an increase of noise. Those can both in principle be addressed through preamplification of the analogue signals. This solution however has key disadvantages: an adequate amplifier needs to be designed or selected, the amplifier complexifies the sensor board design with powering issues arising in particular such as displayed in Section 6.2.1. As a result, operating without preamplification is preferable, thus requiring low loss cables. For this purpose, coaxial cables are ideal and they are specially shielded to reduce electronic losses. The possibility of operation without preamplification is thus demonstrated by examining signal attenuation and noise increases in different lengths of SMA cables. Increases in noise from cables are kept dominant by operating at low 50 Ω impedance.

A key limitation of this measurement is the lack of different available lengths of cables with only 2 cable lengths (30 cm and 4 m), this was circumvented by interconnecting them through SMA-BNC-BNC-SMA connector sets. This connection scheme is lossy but by studying a constant amount of connections, it becomes possible to study only variations in cable length by connecting an analogue signal source on an oscilloscope. The results can be fitted and the amplitude loss and noise increase can thus be extracted as done in Figure 6.36.

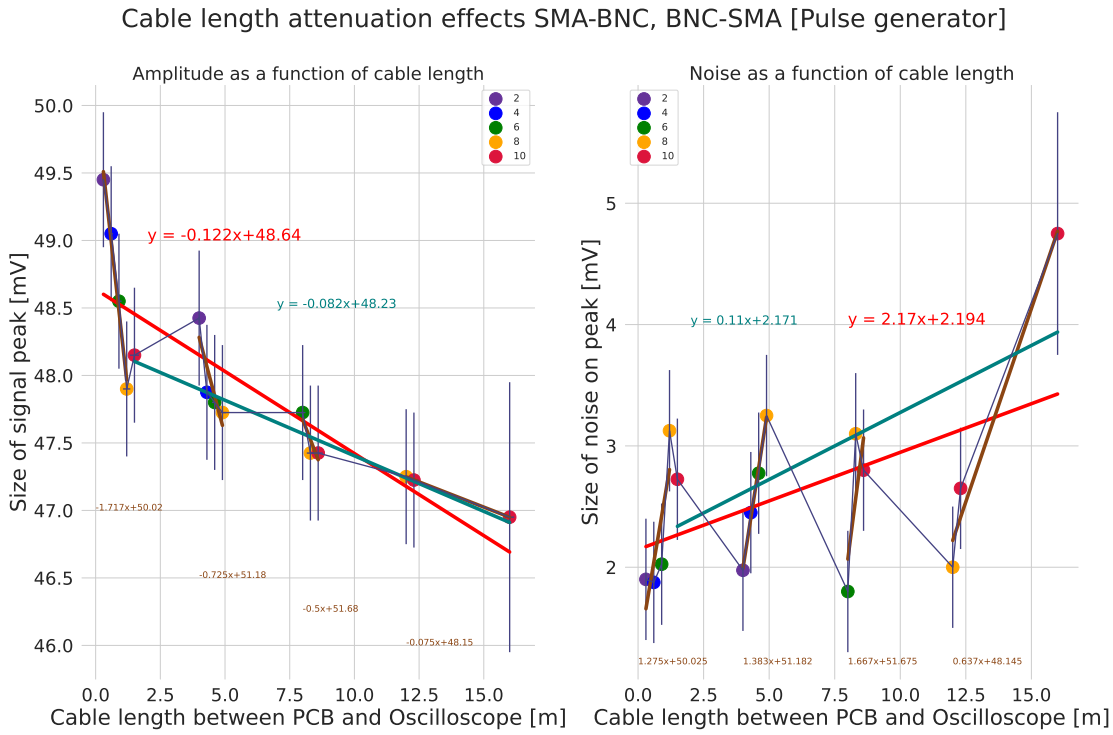

Figure 6.35: Amplitude loss and noise as a function of cable length for different interconnection counts, each color dot corresponds to a fixed interconnection count. The initial analogue signal is yielded by a SiPM irradiated by the laser for a 50 ± 0.5 mV output. The red fit lines correspond to a fit of all data whereas the teal line fit correspond to losses for 8 and 10 interconnections on the amplitude loss and noise side respectively. The brown fits correspond to losses over a set of short 30 cm length.

This measurement's systematics are fully correlated plus a factor of the amount of interconnections with the weight of the 2 and four interconnections being ignored as the datasets have only 2 data points each, yielding a final amplitude loss of $-0.078 \pm 0.004\,\mathrm{mV\,m^{-1}}$ for S14160-6050HS SiPMs illuminated with 263 PE using the laser. The noise increase on the other hand is similarly estimated to be $-0.071 \pm 0.042\,\mathrm{mV\,m^{-1}}$, consistent with 0 within measurement uncertainties.

This indicates that long coax cables may be used for experimental operation as losses are small and noise doesn't increase significantly. This is leveraged in the following system design with 3 m cables ultimately being used for prototyping. While this would increase the noise, this is mitigated by the dominant SiPM capacitance term as well as the AC coupling. This was also verified as being acceptable by examining the KLauS being coupled using short and long cable lengths to a S14160-6050HS SiPM illuminated with 312 PE on average using

the laser. This displays no significant noise increase as shown in Figure **??**.

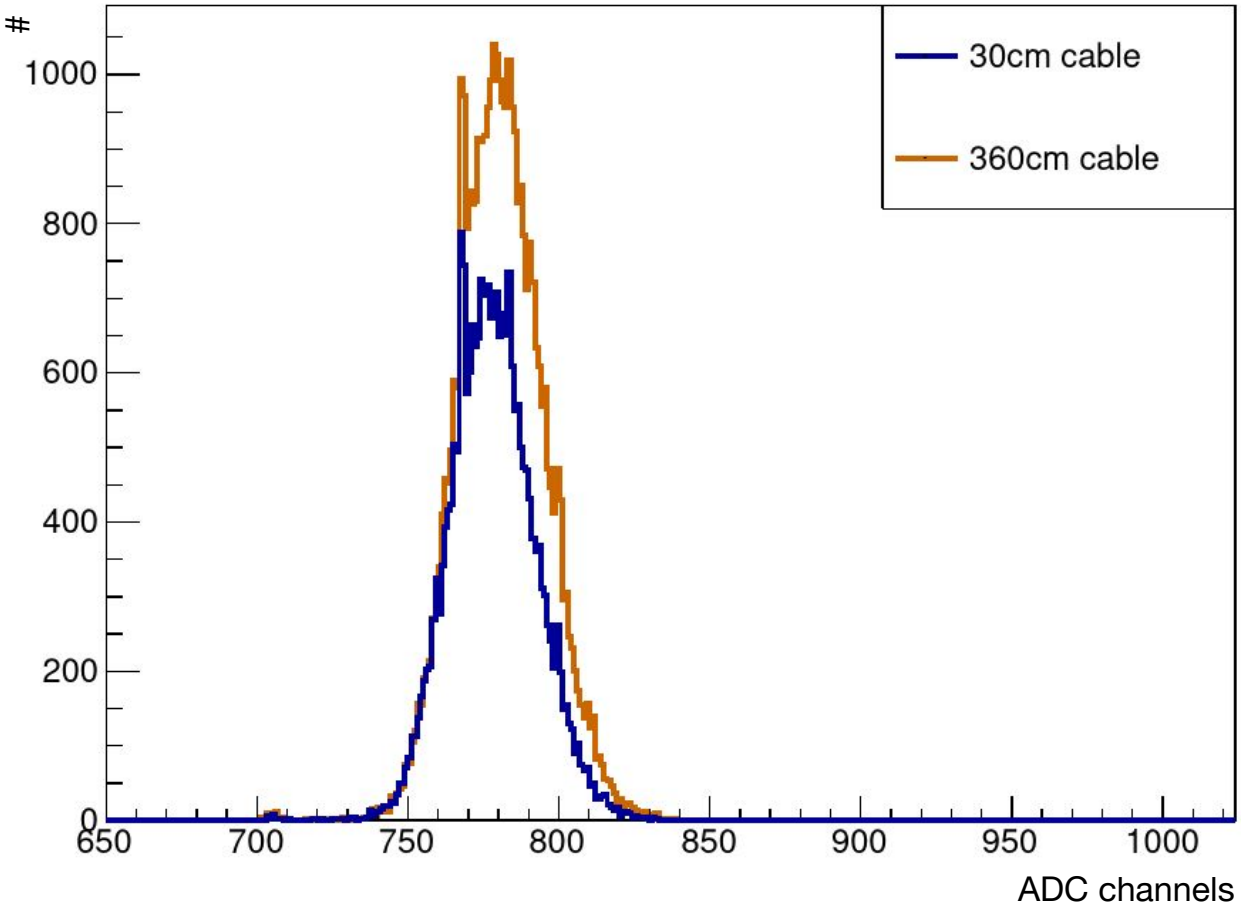

Figure 6.36: Signal comparison on the KLauS high gain 1 to 7 branch for 30 and 360 cm length connections.

6.3.2 Motherboard system design

6.3.2.1 Motherboard design and capabilities

The system is designed to allow the powering and readout of several hundreds of SiPMs while simultaneously controlling and reading out the corresponding KLauS chips with minimal inputs.

A single power line is required per board, with five inputs onto two 5-pin horizontal wire to board terminal block connectors. These take, from top to bottom +9 to +12 V input bias voltage (with lower voltages being preferred to limit board heating), +5 V, the SiPM bias voltage and two grounds. Only the first and one of the bottom two pins are required to be connected to allow for board operation, with the board having all services implemented to convert the 9 V input into all other required voltages.

The second block connector may be connected to that of another board, meaning that a single power supply is required to power the system with the only limitation being the maximum current and allowed voltage drop from the power supply.

The system is operated through a Raspberry Pi 4b (RPi) which is connected onto the side of the board. The Rpi is also powered via the board although it may also use an independent power supply to fit the user's needs. The power is divided from the initial 9 V using a set of powerful voltage regulators and large 100 µF capacitors, distributing the 5 V required by the KLauS and the Rpi and the SiPM bias voltage.

The motherboards can be chained via 40 pin flatband cables on the output bus, allowing the chaining of the Rpi's SPI bus used for slow control and I^2C buses used for data acquisition.

The board offers flexible capabilities which can be tuned through the use of jumpers and potentiometers. They are pictured in Figure 6.37. A review of the boards' assembly and the role of each jumper and potentiometer is given in Appendix E.

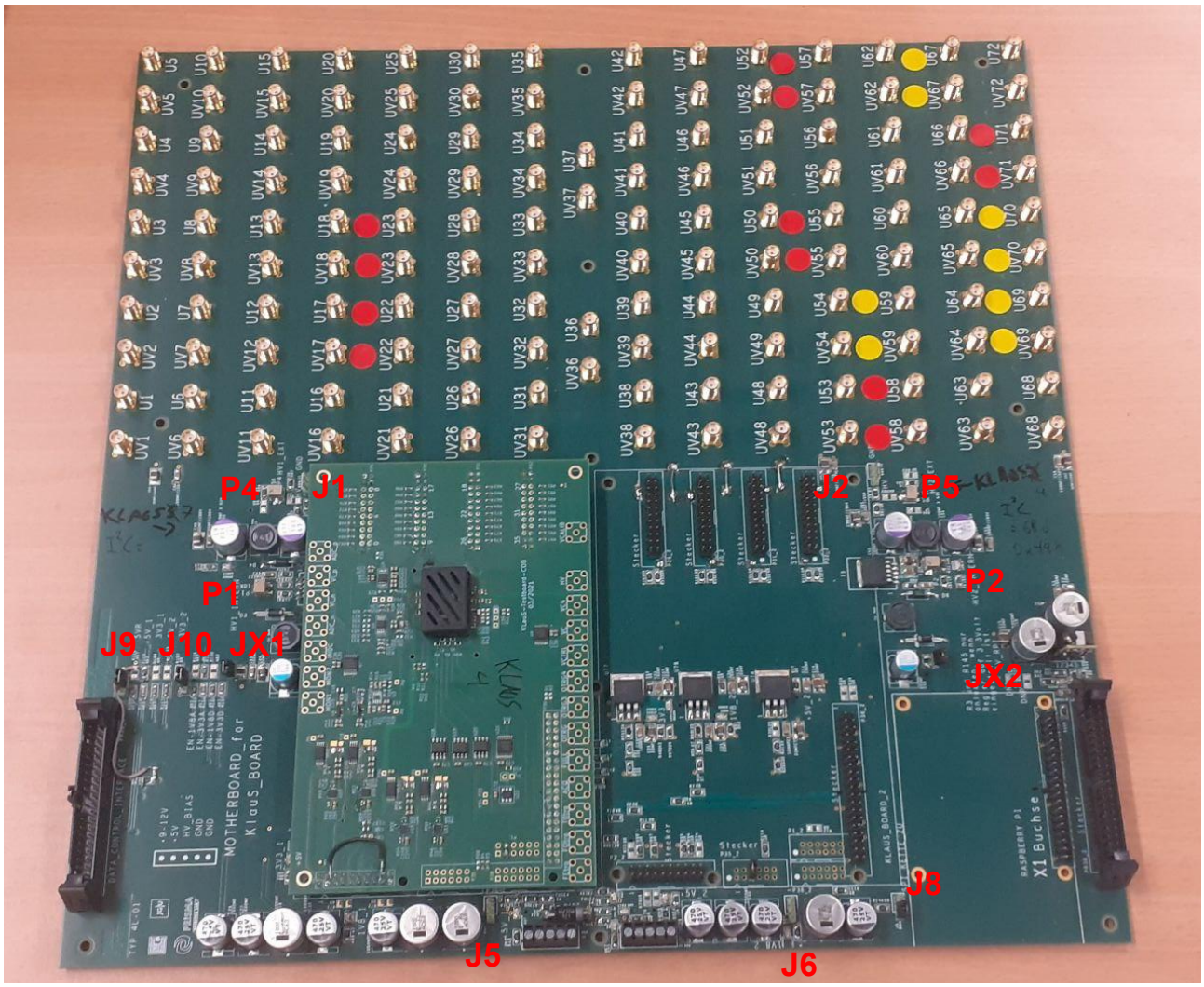

Figure 6.37: KLauS motherboard with relevant potentiometers (P) and jumpers (J).

The data and bias voltage are transmitted using 2 SMA cables per channel for stability and resilience, with the signal and positive HV being located onto the pins. The data transmission lines are meandered to equalise delays as shown in Figure 6.38. Some impedance differences are present on the board with far away channels displaying more irregular impedance behaviour than nearby ones as shown in TDR tests shown in Figure 6.39. These effects are however small and acceptable at the prototyping stage.

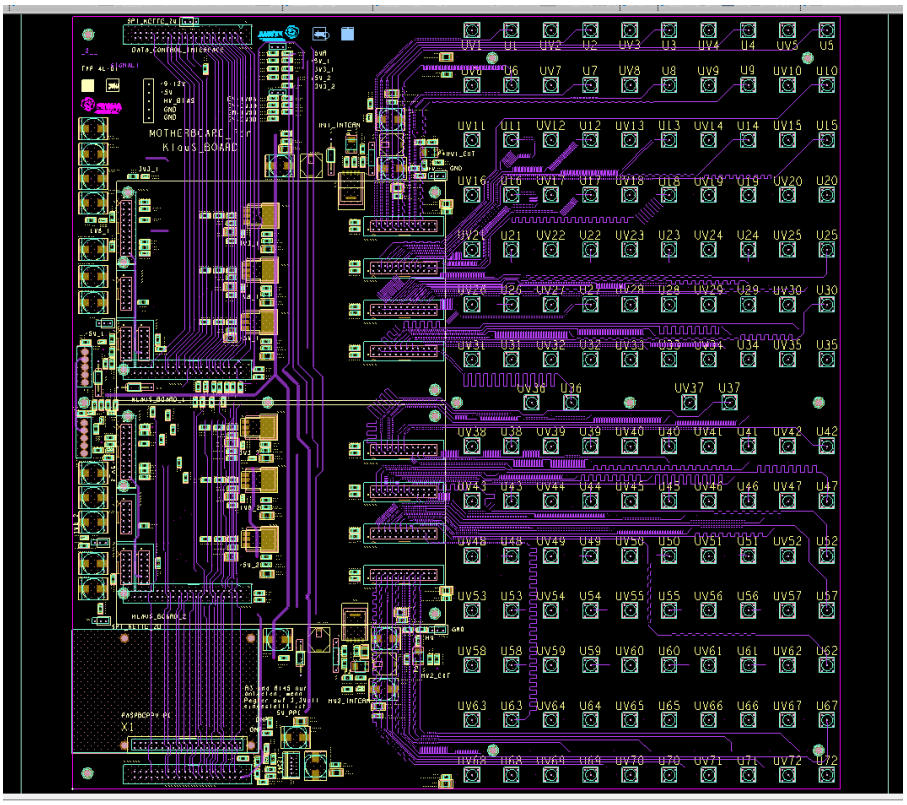

Figure 6.38: Signal traces of the KLauS motherboard's top layer, traces are similar on the back layer for channels using it. UV masks are bias voltage inputs whereas U masks are signal masks.

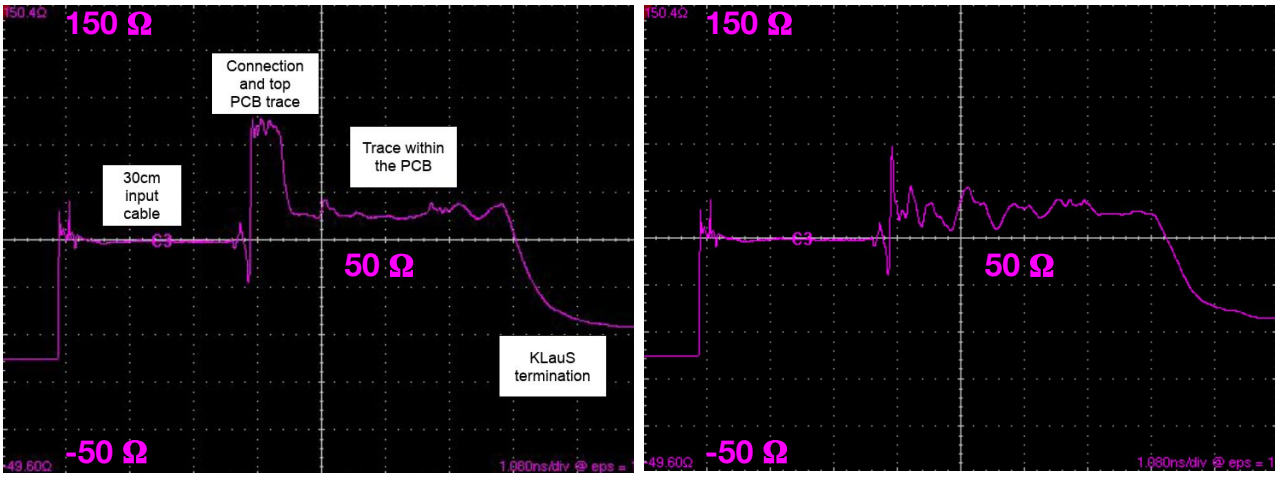

Figure 6.39: TDR test on channels 21 (left) and 30 (right).

KLauS mezzanines are mounted onto the motherboards using sets of header pins with the RPi connected through a short flatband cable to a set of header connectors on the right of the board.

6.3.2.2 KLauS mezzanine design

The KLauS mezzanine was designed to capitalise on the strengths of the original Heidelberg design while allowing flexible usage as a standalone or together with the motherboard. Two mezzanines can be slotted on

each motherboard, enabling 72 channels being readout at the time. The mezzanine powering circuit is adapted in consequence and uses a header pin connector to dispatch HV from the motherboard or from the external supply source. The HV is then distributed to the board's systems and fed into the KLauS itself. Each of the 36 channels is directly fed into the corresponding two pads through header pins (one anode and one cathode). Each motherboard was electrically tested on its own and together with a KLauS mezzanine and found to function reliably.

Nine KLauS mezzanines were assembled and tested independently. The assembly and test detail is provided in Appendix E.

6.3.3 SiPM board system design

6.3.3.1 SiPM board design

The S14160-6050HS SiPM boards are designed to allow SiPM operation with both the KLauS system and the DT5202 while minimising space usage. They as a result implement the circuit from 6.33a but allow to bypass the capacitors and resistors using a pair of jumpers and readout, making them compatible with the DT5202 through a swap in jumpers. When the board is oriented with the connectors facing the operator and with the jumpers at the top, placing both jumpers in the left position allows the signals to be readout by the KLauS or an oscilloscope with HV coming through the right SMA connector and signals collected on the left SMA connector. Placing both jumpers to the right allows readout by the DT5202 through the right SMA connected. This is done using the adapter board described in Section 6.2.3.1. A SiPM board is shown in Figure 6.40.

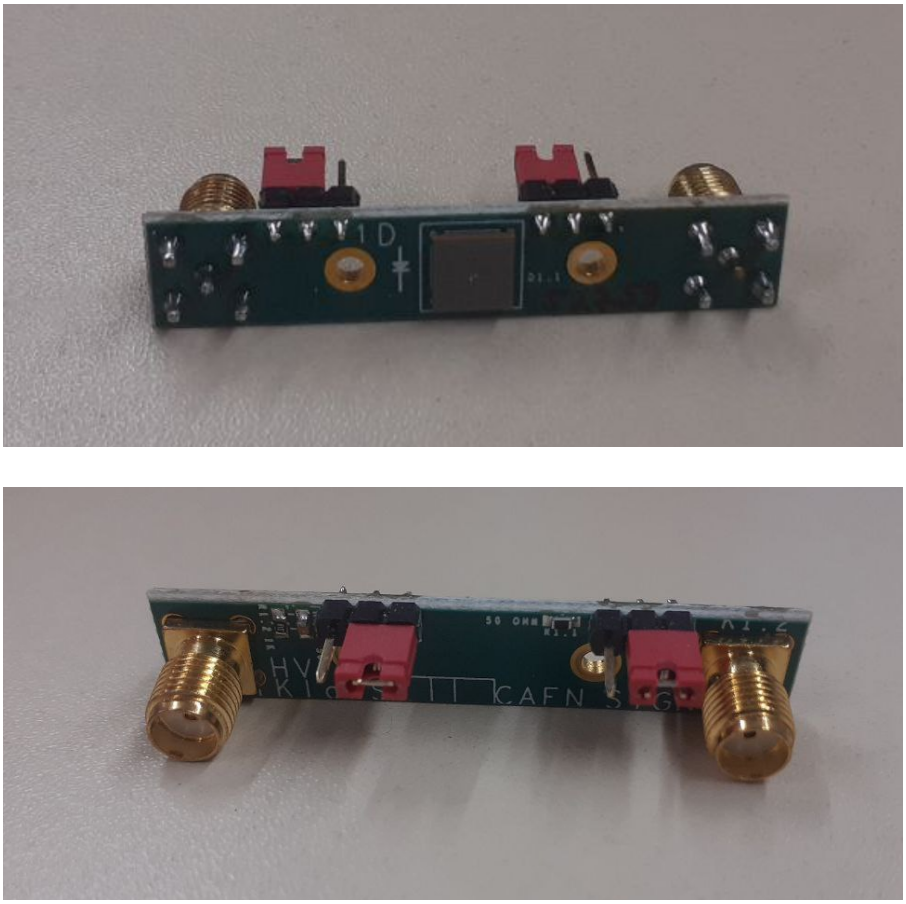

Figure 6.40: SiPM board front (left) and back (right) layers.

6.3.4 DAQ&Trigger architecture

The entire system is run triggerless with event building happening inside of the (master, see below) RPi which streams its data through an RJ45 cable over ethernet towards a DAQ PC. Critical are the slow control taking place over SPI and the data acquisition using I^2C which are described below.

6.3.4.1 SPI control configuration

The SPI bus is used alone for slow control of the KLauSes and has been shown to be able to control up to 4 KLauS chips. This implies that an extra RPi is required for each group of 4 chips. The reasons of the 4 chip limit are unknown as clock stretching was excluded by controlling the SPI pins on the motherboard using an oscilloscope until after 6 chips and current levels are stable also at this level.

Each KLauS is otherwise independently configured one at the time through the SPI bus.

6.3.4.2 I^2C DAQ configuration

The system was meant to run with a single RPi controlling the entire acquisition chain. The use of I^2C was however imposed by the use of the Heidelberg readout software meant to function with RPis. The key limitation of I^2C is its very low transmission speed which typically goes up to $400\,\mathrm{kbit\,s^{-1}}$. It is however possible to impose different speeds by modifying the I^2C baud rate configuration on the RPi within hardware limits. The efficiency of the system readout, defined as $\epsilon = \frac{N_{\mathrm{readout}}}{N_{\mathrm{pulse}}}$ is measured using a single SiPM connected to a KLauS channel and varying both the laser pulse frequency and the baud rate this is displayed in Figure 6.41. The KLauS readout architecture, relying on buffered serial transmission validates this approach for a single chip, even for all 36 channels. The efficiency is found to degrade above a baud rate of $1.4\,\mathrm{Mbit\,s^{-1}}$, likely due to hardware limitations, thus making $1.4\,\mathrm{Mbit\,s^{-1}}$ the optimal baud rate.

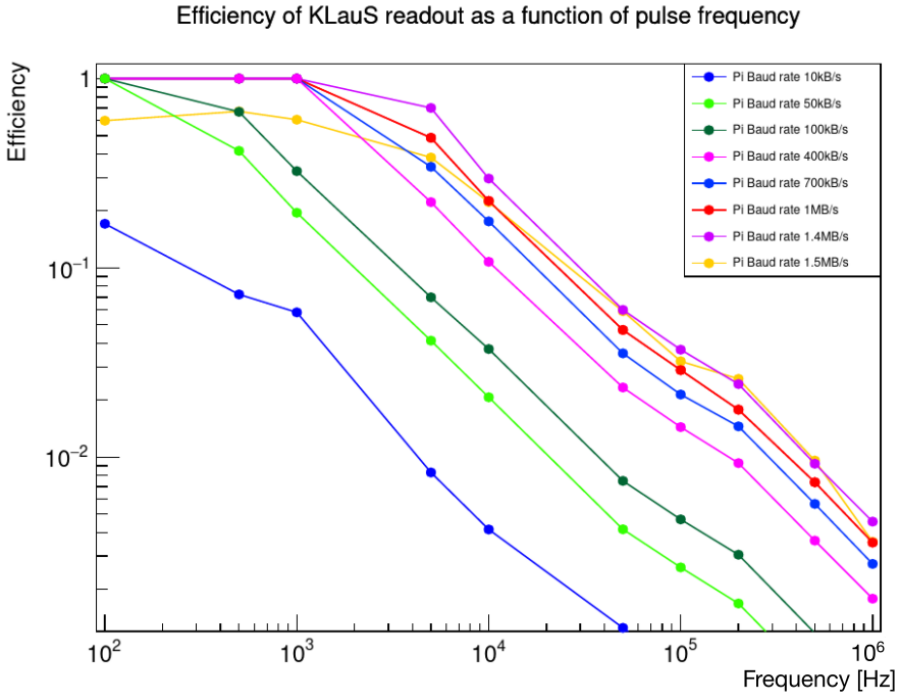

Figure 6.41: Readout efficiency as a function of laser pulse frequency for different baud rates.

While the I^2C baud rate may be made sufficient for a single chip but is found to significantly degrade efficiency for multiple chips as the I^2C saturates. As a response, extra I^2C buses were defined using free RPi pins, with the total I^2C bus count equalling the KLauS chip count thus enabling a full readout. The readout software was updated in consequence to merge the data, this is done by implementing a 100 ns processor hold time in the software, with the software accepting data from all I^2C buses after the first data packet arrives.

When running over multiple RPis, a master-slave system can be setup. In this case the master RPi reads data out from KLauS chips as normal and assigns timestamps to incoming events. Slave RPis are defined in addition, each reading out up to four KLauS chips. They send their events to the master using extra I^2C buses which are predefined, one per extra chip. These events are then integrated to the data structure by the master. The slave and master clocks, while sharing the same frequency, are however separated by a phase causing the clocks to be asynchronous and further subject to processor jitter. As a result, the master send a `RESYNC` signal every 10 ms to the slave using an extra I^2C bus. The slave then aligns its time to the `RESYNC` signal causing the slave to set its time to $t = n_{\texttt{RESYNC}} * 10\,\text{ms}$ with $n_{\texttt{RESYNC}}$ being the `RESYNC` signal count, stored in a `Long64_t` initialised to -1 and incremented with each `RESYNC`. The initial time $t_0 = 0$ for all slave RPis is therefore defined as the time of reception of the initial `RESYNC` signal from the master. The master RPi also counts emitted `RESYNC` signals meaning that data is only synchronisable after the first `RESYNC` signal and that the master RPi should begin data acquisition after all of the slaves. The difference in clock arrival time within the chain are assumed to be negligible. The system is shown in Figure 6.42

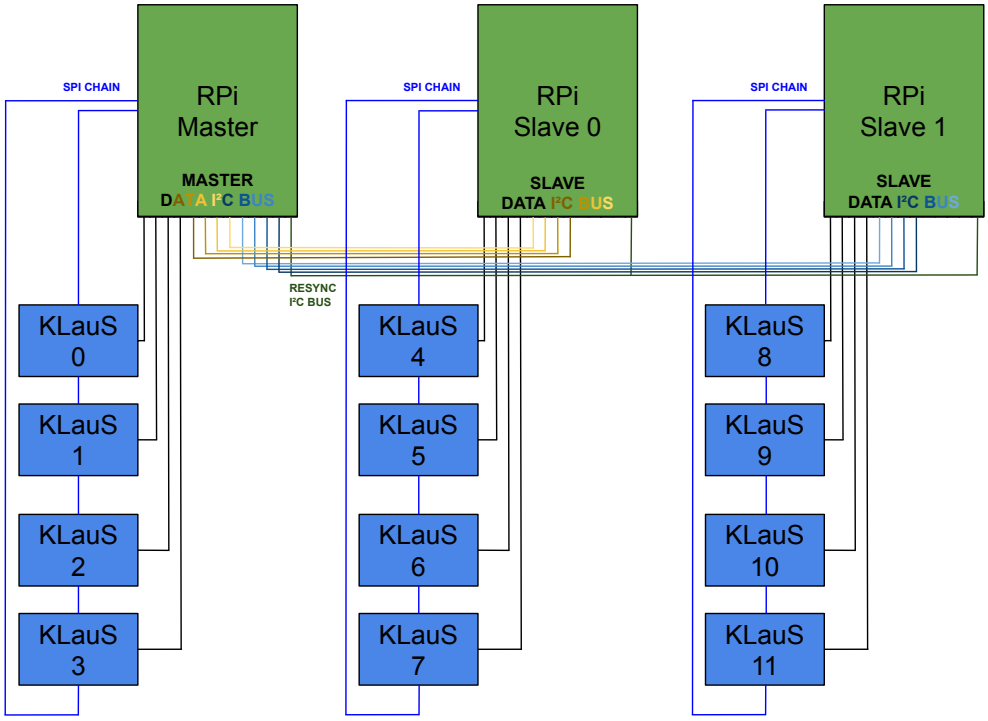

Figure 6.42: Schematic representation of the KLauS-based DAQ system.

6.3.5 Conclusion

The KLauS system is designed to operate over several hundreds of channels while limiting the development and cost of new integrations. This, while effective physically limits the maximum amount of channels to those of 12 KLauS chips, a consequence of the total amount of free pins on the master RPi. This system could be improved by creating a higher level of RPi with a "higher master" RPi reading out multiple master RPis. This system would quickly be limited by the transmittable data rate through I^2C however. A further level of improvement yet includes using the KLauSes LVDS bus which allows data transmission up to $160\,\text{Mbit}\,\text{s}^{-1}$, $\mathcal{O}(100)$ times more than the I^2C, this however requires the development of a new software and, while in-principle compatible with a RPi, would strongly benefit from the integration of an FPGA or a dedicated ASIC into the readout chain for control and operation of the entire chain. In addition, while the KLauS can accept an external trigger and while the SHiP calorimeter system will be run triggerless, an improvement to the system would be a mechanism for distributing an external trigger system.

This system can be scaled up to greater chip numbers, it would however require several levels of master and slave RPis with multiple slave RPis being concentrated by intermediate master RPis and those themselves sending their data through a different bus to a higher master Rpi.

Nonetheless, for data rates of $\mathcal{O}$(kHz) over $\sim$ 200 channels, this system can be run adequately and has been used in a test beam presented in Chapter 7.

Chapter 7

Technological prototype evaluation at test beams

Utilising the developments of Chapters 5 and 6, three test beams have been conducted:

- In March 2024 at DESY in Hamburg, to evaluate the KLauS readout system
- In September 2024 at PS at CERN, to evaluate particle identification capabilities and integration with thin scintillator layers
- In October 2024 at DESY in Hamburg, to evaluate integration with thin scintillator layers

These test beams were done using large custom-built prototypes running hundreds of channels. The data from each test beams is divided into runs which encapsulate different beam particle types, energies or electronic settings. Each run has $\sim$ 100000 events for a given configuration after noise and beam impurities are subtracted. The prototype basis is first explained and was identical in all test beams.

7.1 Prototypes and beam lines

7.1.1 Prototype basis

A basis of the beam lines used is provided thereafter with variations detailed in Sections 7.2, 7.3 and 7.4 respectively.

The prototype dark box was reused from the initial prototype of Section 5.1.1 with sensitive layers fixed to iron plates, each 4 mm thick on average. Sensitive layers are a mixture of wide $36 \times 6 \times 1\,\mathrm{cm}^3$ and thin $20 \times 1 \times 1\,\mathrm{cm}^3$ scintillator layers. The former utilises the optimised air interface described in Section 5.5.6 with the S14160-6050HS (large SiPMs for wide scintillator bars/layers) boards described in Section 6.3.3 established using a custom 3D printed piece. The latter utilise the small S13360-1325PE SiPMs (small SiPMs for small scintillator bars/layers)and rely on polystyrene extruded scintillator from Fermilab. Extra iron plates may be introduced into the prototype to create various configurations. High voltage (HV) and signals are provided and transmitted through SMA cables with the electronics below the dark box. The prototype is pictured in Figure 7.1.

7.1.2 Test beam infrastructure and line

Two different beam lines are used in the test beams: the DESY TB24 and line T9 at PS at CERN which are presented in turn.

Figure 7.1: TB1 prototype.

7.1.2.1 DESY TB24

The TB24 beam line [396] at the DESY test beam facility pictured in Figure 7.2, is capable of providing electrons extracted through Bethe-Heitler processes from the PETRA III synchrotron at energies from 1 to 6 GeV and frequencies dependent on the particle energies, ranging from ~ 1 k at 1 and 5 GeV to ~ 4 kHz at 3 GeV.

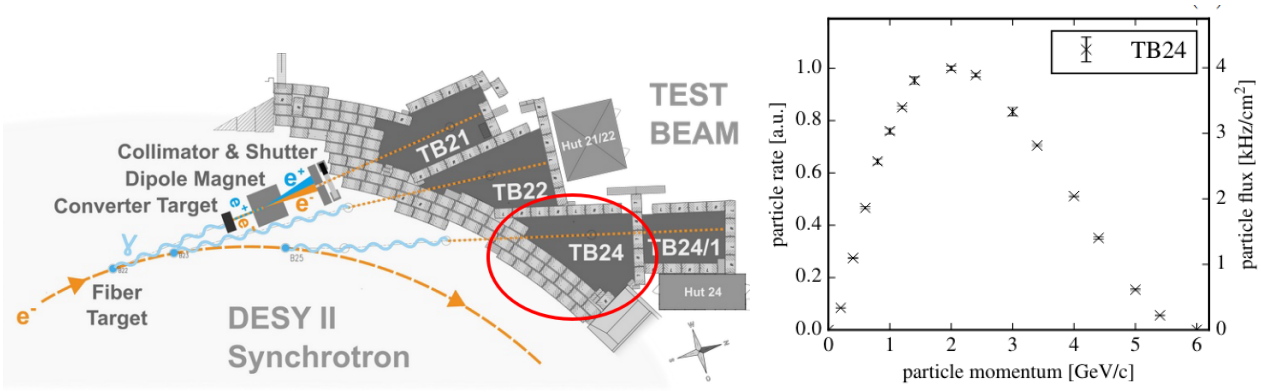

Figure 7.2: DESY test beam facility [397] and intensity as a function of particle momentum at TB24 [396].

7.1.2.2 CERN PS T9

The T9 beam line yields a secondary beam of different particles from protons extracted from the PS accelerator (see Figure 2.1). These protons impinge onto different targets and thus yield mixed beams with enriched hadron (particularly π^+) content using a low Z (copper or aluminium) target or electron content by adding 3 mm tungsten layer and an extra X_0 for photoconversion as shown in Figure 7.3. Alternatively, a beam shutter can be closed while a mixed hadronic beam is running, implying that only a μ (particularly μ^+) halo reaches the detector. The beam line is equipped with two trigger scintillators readout by a pair of PMTs, the scintillators are however placed at ~ 4 m from one another each, with cable length connecting the PMTs to the test beam area not being delay-adjusted, which had consequences on the data taking. The beam line topology is shown in Figure 7.3.

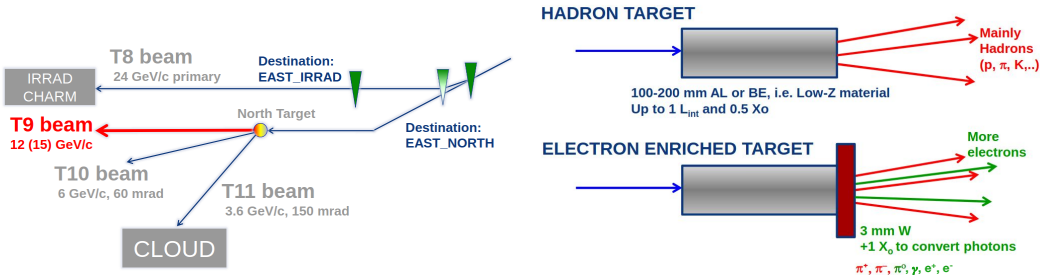

Figure 7.3: PS beam line topologie [398] (left) and secondary beam creation process [398] (right).

7.2 First test beam at DESY in March 2024

The first test beam (TB1) lead was held for one week in March 2024 and was principally meant to demonstrate the effectiveness of the readout electronics and DAQ scheme described in Section 6.3, as a result, the prototype was run in a wide variety of KLauS chip configurations with variations in gain mode (HG11, HG 17 and LG160, LG1200), input stage biases (setting 0,1,2 and 3), incoming electron energies (1 GeV, 3 GeV and 5 GeV) and timing trigger threshold (TTT, 1,2,3,4,5,6,7,10,20). It was done using the prototype in different configurations and was used to evaluate shower shape and energy reconstruction capabilities. The gain modes are denoted 160 (HG11 and LG160), 760 (HG17 and LG160), 1200 (HG11 and LG1200) and 7200 (HG17 and LG1200) in the following. Sensitive bar orientation is alternating between vertical and horizontal.

7.2.1 Prototype configurations, setup and calibration

7.2.1.1 Configuration

During TB1, the prototype was systematically used with a $\sim 70\,\text{cm}$ split in the calorimeter in order to mimic the SHiP calorimeter system's operating conditions, while varying the amount of passive material within the calorimeter. The main configuration tested was a sampling configuration, pictured in Figure 7.4. Only wide scintillator layers were used as sensitive layers in TB1.

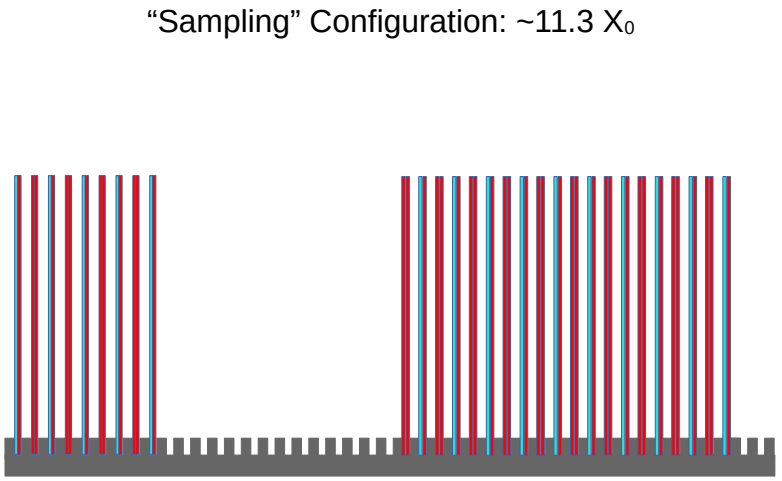

Figure 7.4: TB1's prototype configuration. All 15 sensitive layers are mounted onto a passive layer and are pictured in cyan. Purely passive layers are displayed in red.

There is a total of 15 sensitive layers within the prototype, categorised as L1-L15 from prototype front to back.

The readout electronics are based on a previous version of the setup described in 6.3.4 which chains the input IC^2 buses on a same motherboard. This has been found to result in frequent IC^2 bus saturation, causing losses in the KLauS L1 and L2 FIFOs, this has lead to the reviewed design of Section 6.3.4 which avoids bus chaining.

In addition, one KLauS chip was rendered inoperable during the first day of TB1, this was immediately noticed but could not be compensated as there was no backup well-functioning chip. As a result, two sensitive layers (L4 and L5) were rendered entirely passive. This was in part compensated using linear shower interpolation (see Section 7.2.2).

7.2.1.2 Calibration

Each used SiPM was intercalibrated using the laser to ensure an even response throughout the detector. This was done by exposing each SiPM to a constant light input from direct laser irradiation and tuning the bias voltage to ensure that each PE amplitude was similar to a reference SiPM within 0.5 PE, this is shown in Figure 7.5.

Each SiPM is MIP calibrated *a posteriori* using cosmics in the laboratory and pedestal corrected. Since it is not possible to run DAQ using both gain branches simultaneously on the KLauS, the HG-LG intercalibration was made in the laboratory for each channel using its dedicated SiPM with an $\frac{\text{HG}}{\text{LG}}$ ratio shown in Figure 7.6. The gain ratio allows to convert ADCs from LG into HG and therefore have a consistent energy response for both gains. They are done after substracting the ~ 695 ADC pedestal based on the corresponding noise run to bring the start of the distributions to 0 ADC and irradiating the SiPM to 3 light levels at 107, 511 and 990 average PE for 10 s. In each case, data is taken twice, forcing the gain mode to HG and LG respectively and taking a ratio of ADCs followed by an averaging of the ratios. The ratio discrepancies are found to be negligible.

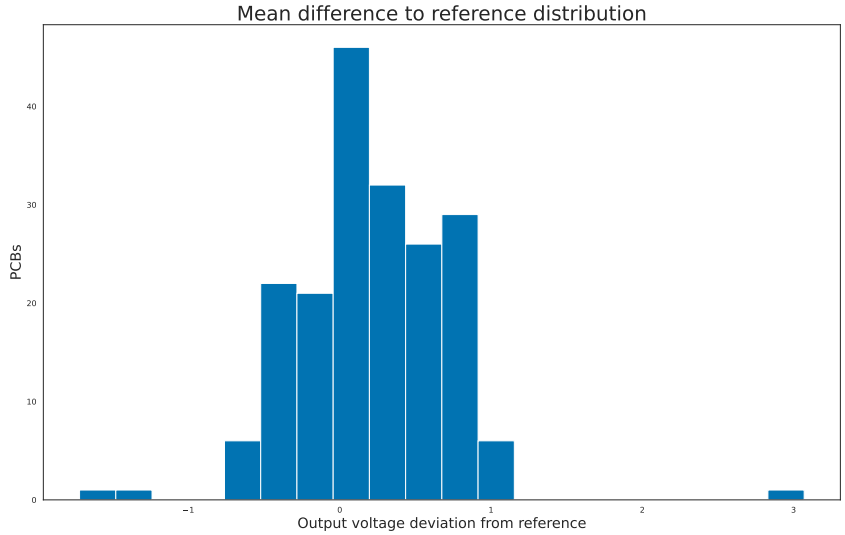

Figure 7.5: Output optimal bias voltage deviations.

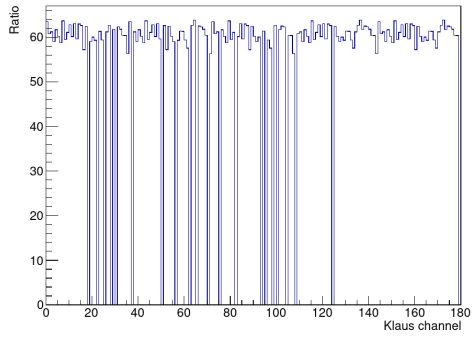

(a) Ratio of HG to LG in gain mode 160 after baseline correction.

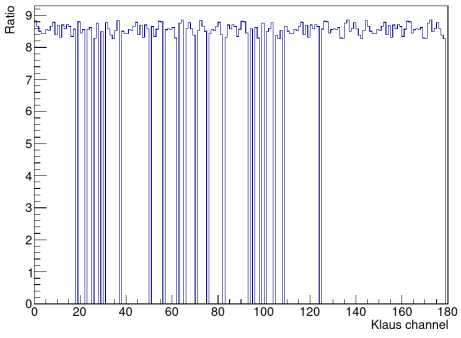

(b) Ratio of HG to LG in gain mode 760 after baseline correction.

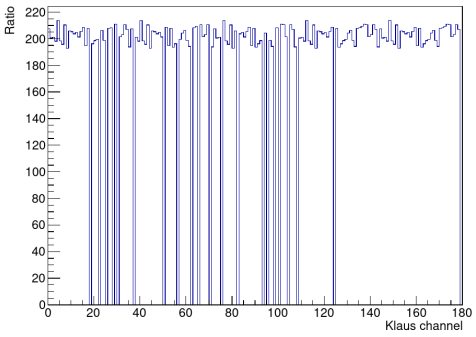

(c) Ratio of HG to LG in gain mode 1200 after baseline correction.

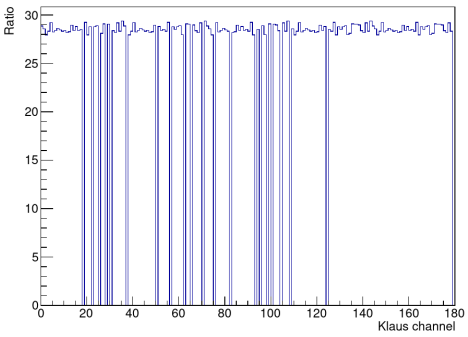

(d) Ratio of HG to LG in gain mode 7200 after baseline correction.

Figure 7.6

7.2.1.3 Analysis cuts

The common I^2C-based DAQ conjugated to the triggerless readout lead to instabilities in the data with large amounts of "empty" events especially at lower TTT values, corresponding to up to ~ 10 times the beam rate. These empty events are filtered using the cuts listed below.

- Noise cut (see below)
- Require data in at least on of the centre two strips of each of the first 3 layers to be above 1 MIP
- Require layers 7, 8 and 9 to all see more than 1 MIP across all bars each
- Require the total amount of MIPs not to exceed 500

Noise runs where the beam was off were taken for each HG configuration to evaluate and eliminate the pedestal such as shown in Figure 7.7. In those runs, a SiPM occasionally passes the TTT and causes an event across the I^2C bus used. As a result, all three I^2C buses are calibrated independently. The noise is eliminated using a 5σ cut on the right of the noise peak.

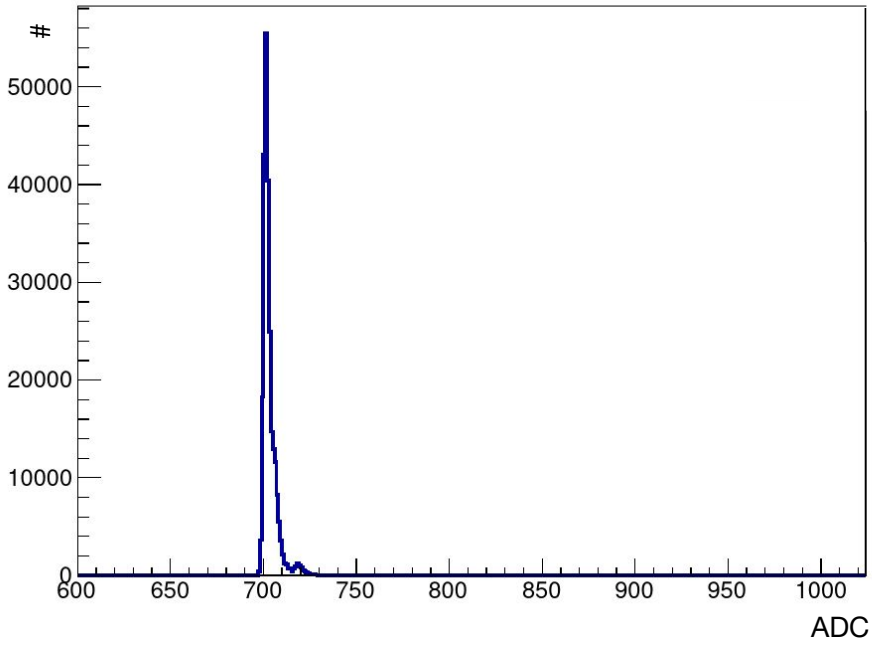

Figure 7.7: Example noise peak in channel 1 of KLauS 0 of RPi slave 0 in gain mode 760.

At higher values of TTT, no noise is recorded, the runs chosen for physics results are chosen with TTT=5 as they are the ones with the least noise while conserving the main noise peak which is valuable for pedestal compensation. It should be noted that noise levels are found to vary on a channel per channel basis but that the TTT level can only be set at the chip level. This leads to certain channels having higher noise levels than others even at those relatively low threshold levels. A lower threshold is generally preferred to maximise bandwidth.

7.2.2 Energy reconstruction

The shower energy can be reconstructed on an event-per-event basis. This is done by converting ADCs to MIP counts, providing a sampled energy deposition. The energy is reconstructed through:

$$E_{\text{reco}} = \frac{\sum_{\text{layer}=1}^{\text{layer}=15} E_{\text{loss,MIP}} \cdot N_{\text{MIPs,layer}}}{f_{\text{s}}} + c \tag{7.1}$$

Where $E_{\text{loss,MIP}}$ is the energy loss for a MIP in a sensitive layer, computed analytically from Equation 3.1 to be 1.785 MeV, $N_{\text{MIPs,layer}}$ is the MIP count in a given layer, f_{s} is the calorimetric sampling fraction and c is

a small adjustment parameter added by hand and used to compensate for the constant systematic uncertainty on the other parameters. It is found to be small $c < 5\,\%$ of the beam energy).

The energy reconstruction is only attempted in the sampling configuration as it is the only one with the stopping power required to perform sensible calorimetric reconstruction. In addition, techniques are used to compensate for the two missing layers as well as reconstructing leaking showers. The steps of energy reconstruction used here are therefore:

1. Take all ADC counts in an event
2. Convert ADC counts in each channel into MIP counts
3. Apply the cuts of Section 7.2.1.3
4. Adjust the MIP counts by taking the average each side of the double sided bar readout
5. Convert the adjusted MIP counts into energy by multiplying by 1.785 MeV
6. Scale for sampling fraction

7.2.2.1 Shower interpolation

The two fully passive L4 and L5 layers can be compensated for using linear interpolation. A "superlayer" L4+L5 is defined by linearly interpolating MIP counts between L3 and L6. The interpolated MIP count is assigned equally to both passive layers with the procedure being shown in Figure 7.8. This technique allows to compensate partially for the missing two layers by adding their interpolated energy to the total MIP count derived from the 13 other layers.

7.2.2.2 Leaking shower extrapolation

Leaking showers, such as pictured in the event displays of Figure 7.9 lead to underevaluation of shower energy. This can be compensated using shower extrapolation, provided the shower maximum is seen within the calorimeter strictly earlier than the final layer. Linear extrapolation is used here for simplicity, more advanced logarithmic decay modes also exist. The extrapolation ends at the last layer with positive extrapolated MIP counts with the sum of extrapolated MIPs being added to the total MIP count.

7.2.2.3 Energy resolution

Using the reconstruction techniques described above and after applying the cuts of Section 7.2.1.3, it is possible to reconstruct the energy of events. This is done for the runs using gain mode 760 and 7200 and TTT5 as shown in Figures 7.10 7.11.

Energy resolution is found to be around $18\,\%/\sqrt{\mathrm{E[GeV]}}$ with a better resolution being achieved when using gain mode 760, due to the better separation of the largely LG EM showers. The constant term is found to be small and quickly negligible, indicating a good prototype build. The noise term is found to be small as well, indicating that at the investigated energies, the relative thinness of the calorimeter does not constitute a significant downside given the compensatory extrapolation against leakage. Some minor saturation is found to affect the detector for LG=60 and not observed for LG=200 as shown in Figure 7.12.

7.2.3 TB1 Conclusion

The prototype has demonstrated its effectiveness as a calorimeter while running and displays an energy resolution around $18\,\%/\sqrt{\mathrm{GeV}}$ depending on the electronics configuration consistent with theory (see Section 7.5).

The KLauS-based readout electronics have demonstrated their effectiveness in running a large amount of channels in a triggerless fashion, with a large enough threshold (TTT=5), noise can be effectively suppressed. The I^2C bus being was however the main limit on the readout rate, this lead to the scheme described in Section 6.3.4. Furthermore the loss of two layers at the start of the test beam has highlighted a need for further investigation into the KLauS chip's reliability. Further improvements can be made on the motherboard's design in addition to the changes suggested in Chapter 6 to allow lower noise levels and thus a lowering of the TTT level.

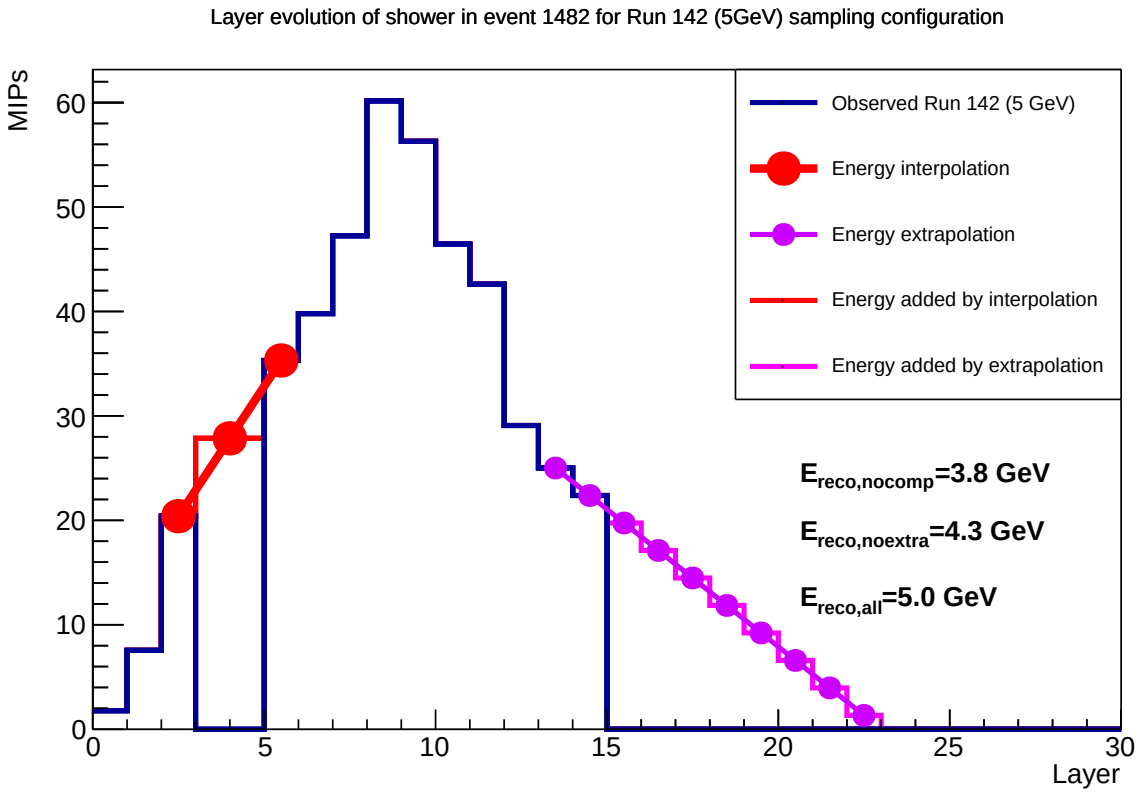

Figure 7.8: Interpolation and extrapolation procedures shown in a single event at 5 GeV. The energy without interpolation nor extrapolation ($E_{reco,nocomp}$) is evaluated at 3.8 GeV, the energy with interpolation only ($E_{reco,noextra}$) is evaluated at 4.3 GeV the energy with both extrapolation and interpolation ($E_{reco,all}$) is evaluated at 5.0 GeV.

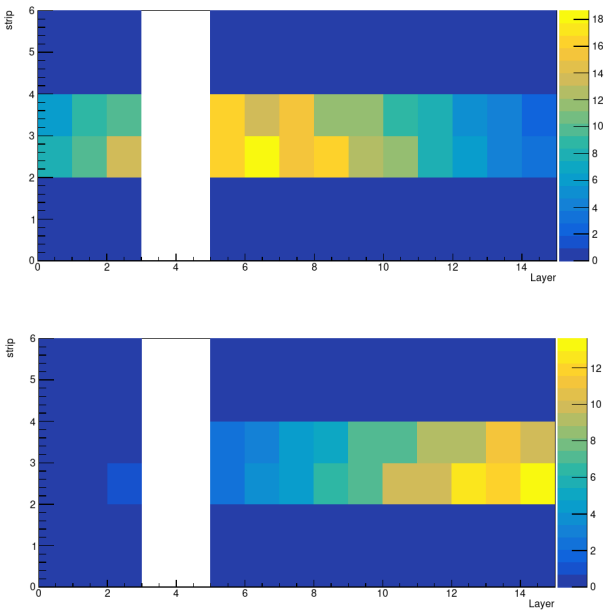

Figure 7.9: Event display of well contained (top) and leaking (bottom) 5 GeV event. Layers are shown as being all orientated in the same direction.

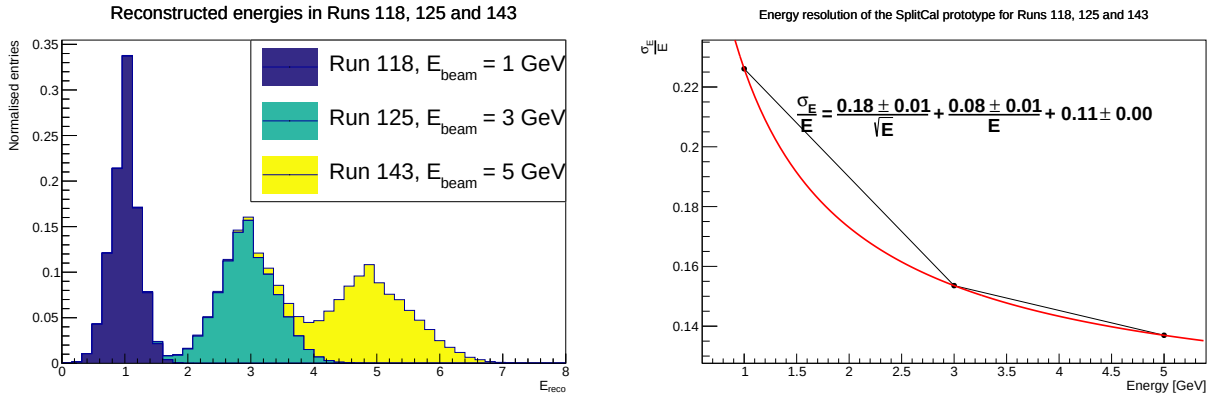

Figure 7.10: Reconstructed energies (left) and fitted resolution (red curve) (right) using gain 760.

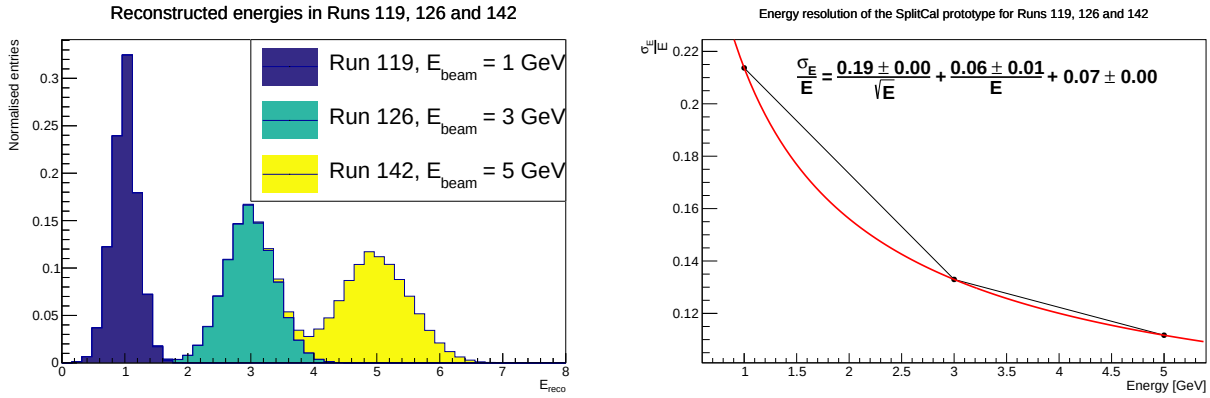

Figure 7.11: Reconstructed energies (left) and fitted resolution (red curve) (right) using gain 7200.

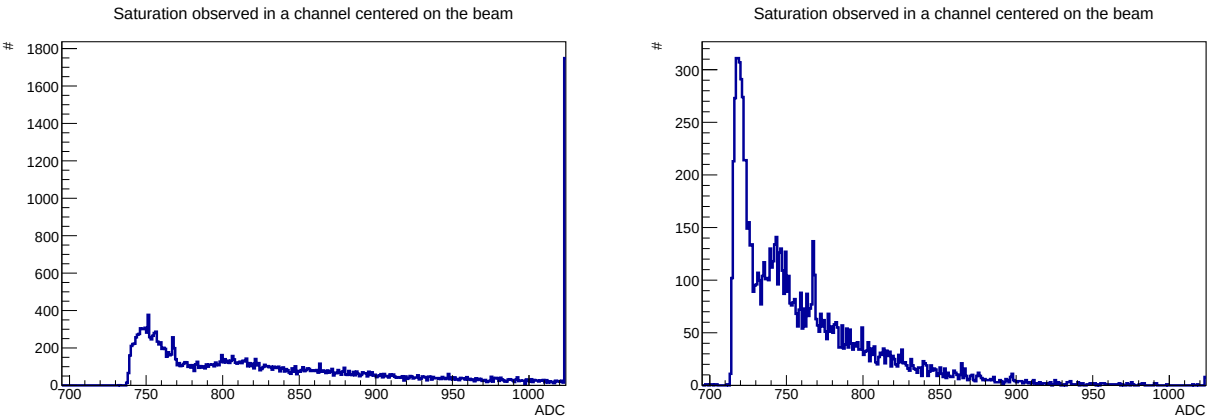

Figure 7.12: Saturation for LG=60 (left). Saturation is significant. Saturation for LG=200 (right). No saturation is observed. The same channel and same energy (5 GeV) is considered in both cases.

The triggerless operation demonstrated in this test beam will be used in the SHiP PID detector for the entirety of its 15 years of operation. The challenge of minimising noise was made clear in this test beam. The option of setting an individualised threshold per channel, rather than one per the entire chip as in implemented in the KLauS is seen as advantageous and would be beneficial for the final choice of ASIC used in the SHiP calorimeter system. The loss of bandwidth induced by the use of very low gain (LG200) has not been found to negatively affect the detector's energy resolution at those low energies, this remains to also be demonstrated for a broader energy range, where saturation is expected to be more problematic. This may be partially countered by lowering the SiPM overvoltage. The I^2C bus saturation issues noted during the test beam led to a DAQ architecture upgrade where chips on a same motherboard no longer share the same I^2C bus as is described in Section 6.3.4. The KLauS chip system could thus be used in the SHiP calorimeter system based on the rate distribution which remains to be determined from simulation of the final muon shield configuration (still to be determined at the time of writing). This would however necessitate a change in the KLauS chip, for instance the change in the input stage's topology towards a cascode input stage mentioned in Section 6.2.4.3. In addition, the test beam could only be conducted using electrons. Demonstration of the capability to perform PID requires beams with different particles, leading to a second test beam (TB2) being led at PS. Further developments are planned using similar DAQ architecture while also evaluating the CALOROC1b ASIC [399] which is a more natural fit to the SHiP calorimeter system as it integrates the cascode input, two gain switches and parallel readout, resulting in broader capacitance capabilities greater dynamic range and better resilience to rate variations.

7.3 Second test beam at CERN PS in September 2024

TB2 was held for one week at the Proton Synchrotron at CERN in September 2024 and focused on evaluating particle identification capabilities for the calorimeter prototype as well as angular resolution through the introduction of thin scintillator bar layers. This resulted in a modified prototype layout and the use of a different beam line.

7.3.1 Setup

7.3.1.1 Variation from base design and prototype configurations

In order to meet TB2's goals, the prototype's basis was altered with thin $20 \times 1 \times 1\,\mathrm{cm}^3$ scintillator bars. These bars were assembled in 9 layers of alternating orientation, each containing 20 bars. In addition 8 wide bar layers of TB1 are incorporated into the detector to mimic the SHiP ECAL's configuration. The detector was arranged in a split configuration similar to that of TB1 pictured in Figure 7.13.

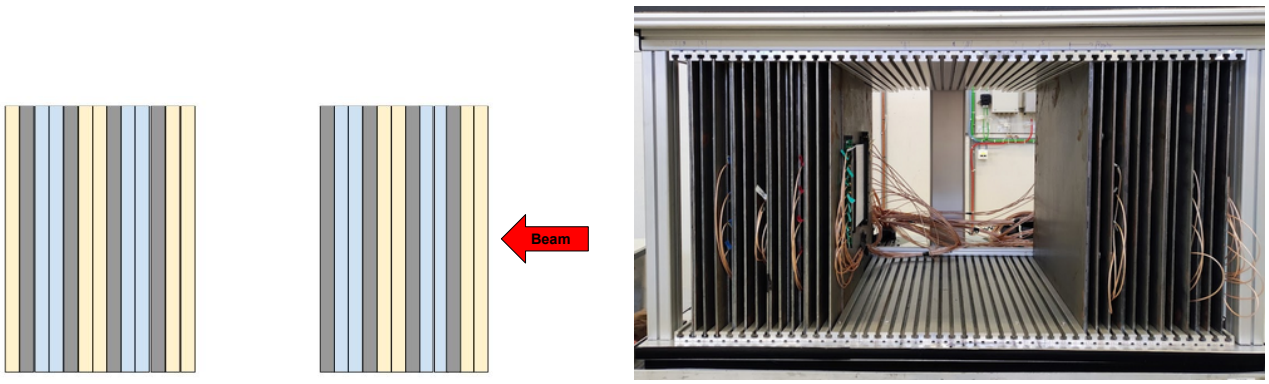

Figure 7.13: Illustration (left) and picture (right) of TB2's split configuration. The yellow rectangles represent thin bar layers, the blue bars represent the wide layers, the gray ones represent passive iron layers. Each sensitive layer is doubled with two iron layers.

7.3.1.2 Readout electronics, DAQ and trigger

The thin bar layers were developed independently and therefore require different readout electronics to the KLauS with four DT5702 modules being used (see Section 6.2.1) together with a DT5215 concentrator which synchronises the board clocks and provides a single ethernet data output from four optical links. The wide bars' SiPM boards had their circuit swapped using the jumpers embedded in their design.

The different readout electronics induced a change in operations mode as the DT5702 requires an external trigger to function adequately across all boards. The trigger scintillators from the T9 facility were used to that aim after a coincidence circuit made from a NIM crate, amplification units (which were later discarded), constant fraction discrimination units and a logic `AND` unit. The lack of delay compensation between the PMTs (see Section 7.1.2.2) was found to significantly affect the data rate which was partially compensated by moving the prototype crate back $\sim 3\,\mathrm{m}$ into the beam line (as far back as cable length and test beam area allowed) which increased the obtained particle rate. Nonetheless events quality was reduced with signals at the back of the detector being found to be integrated earlier than at the front. The setup is pictured in Figure 7.14. This reduces the beam arrival time before the trigger signal by 13 ns. Attempts were also made to modify the shaping time without any positive change being observed.

Figure 7.14: Prototype dark box after movement.

The large SiPMs are always operated at the lowest possible preamplfier gain whereas the small SiPMs use a gain of 50 for the HG and 40 for the LG in both HG and LG mode.

7.3.1.3 Calibration

Calibration was done channel per channel using muon halo runs, which allows to guarantee test beam conditions for the calibration runs which laboratory cosmic runs do not. This however has lead to an uneven channel exposition to the incoming muons with thus certain channels' calibration being overall worsened. The trigger issues are also suspected to have an effect on the calibration which lead to adaptations in the calibration procedure.

Most channels' events are binned in the 13 bit HG ADC and fitted using a Landau function with the Most Probable Value (MPV) being used as a MIP energy value. Due to low statistics for off axis channels, certain fits fail because of low signal statistics. For those channels, a second fit is attempted restricting the range to 400-3000 ADC, which is optically found to be acceptable. The channel for which the fit fails even under those conditions have their MIP peak assigned to the gaussian mean of a fit over all other MIP peak values for all channels as shown in Figure 7.15 for simplicity.

The ratio of HG to LG was performed directly on data using a combination of runs at all examined energies ($1, 3, 5\,\mathrm{GeV}$). Unlike in TB1, this was allowed by the possibility of simultaneous recording both branches' data. This was performed in two different ways.

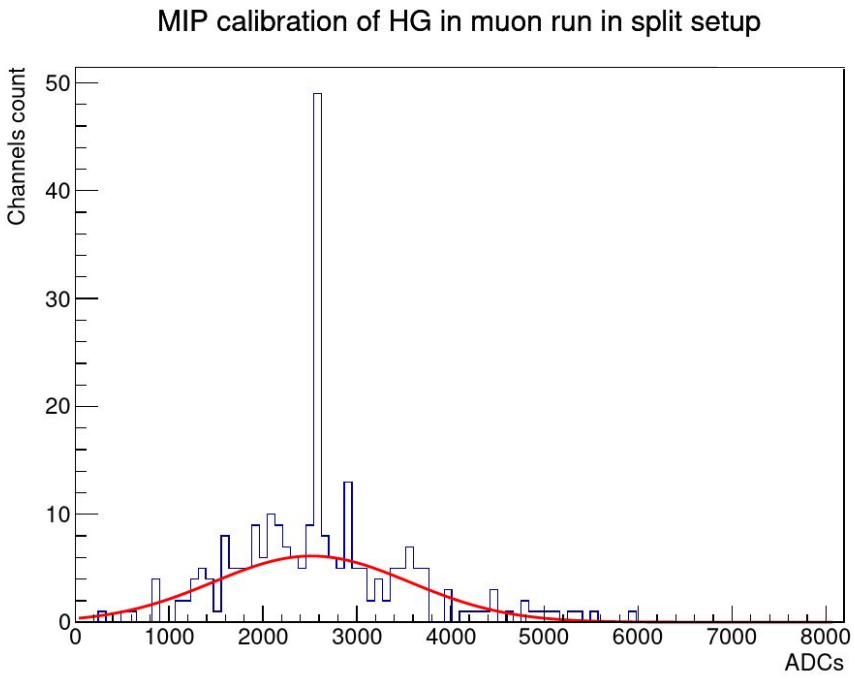

Figure 7.15: Calibration values of all channels, the red line represents the gaussian fit whose mean was used to assign MPV calibration peaks to channels for which the calibration fit couldn't converge for lack of statistics.

The first option was computing the HG/LG ratio for each channel by averaging the average of ratios in each event where $N_{\mathrm{ADC,LG}} \neq 0$ with the results shown in Figure 7.16. This solution suffers from uncertainties as ratios are found not to be constant for given channels. This is suspected to be linked to the trigger issues.

The second option entails fitting the distribution of HG to LG ADCs for each channel and using the slope as a conversion factor between gain modes as shown in Figure 7.17. While this solution was found to perform slightly worst however, particularly as certain channels displayed unstable behaviour, with energy resolution suffering as a result. This is in part attributed to the ratio instability among small SiPMs also shown as an example in Figure 7.17 which could perhaps be due to their smaller pixel counts inducing larger stochastic uncertainties.

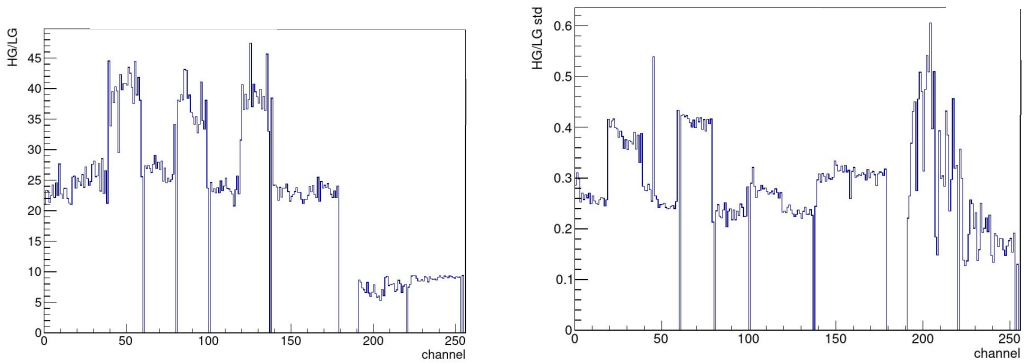

Figure 7.16: Mean ratio (left) and standard deviation ratio (right) of HG to LG for all channels in combination of $1, 3, 5\,\mathrm{GeV}$ e^+ run.

7.3.2 Energy reconstruction

Similarly to what was performed in Section 7.2.2, energy was reconstructed using Equation 7.1. Another energy reconstruction technique using only interpolation is also introduced.

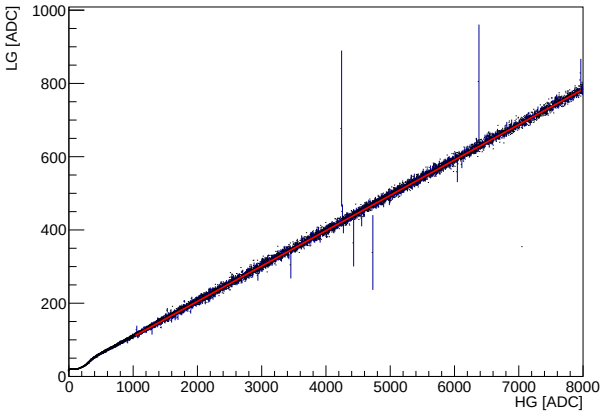

Figure 7.17: Fit of HG to LG distribution for a large SiPM channel in combination of $1, 35\,\text{GeV}$ e^+ run.

7.3.2.1 Simple energy reconstruction

The energy reconstruction is performed on $1, 3, 5\,\text{GeV}$ e^+ runs yielding the results shown in Figure 7.18 . Shower extrapolation is performed identically to TB1 for better energy estimation.

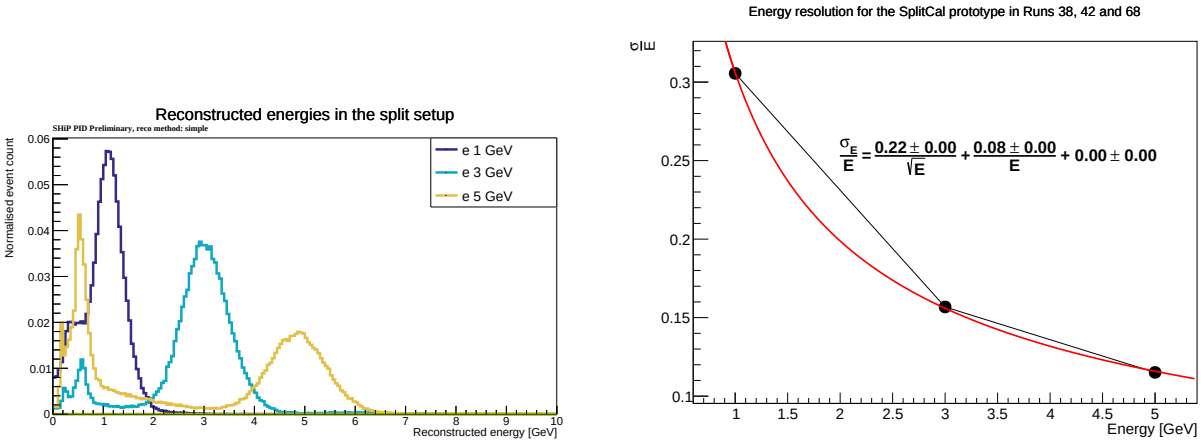

Figure 7.18: Energy reconstruction (left) and resolution using simple reconstruction based on Gaussian fits on each main energy peak (right) .

Despite the limitations intrinsic to the setup, particularly regarding the trigger, energy is found to be reconstructable with sharp peaks around the expected 1,3 and 5 GeV. The energy resolution is found to be significantly worst than in TB1, likely driven by the trigger issues. In addition, structures appear towards the lower end of the reconstructed energy distribution which are interpreted as events punching through the calorimeter, in particular π^+ and μ^+ linked to beam purity which are further examined in Section 7.3.3.

While energy reconstruction is feasible using this simple technique, interpolation as a full energy reconstruction technique for improved results as shown in the following.

7.3.2.2 Energy reconstruction by interpolation

As the SHiP ECAL prototype is a *sampling* calorimeter, it is thus possible to attempt a shower reconstruction purely based on interpolation working from the sampled points in the sensitive layers. The principle idea being to infer the shower development from the sampled sensitive layers. The shower showering dominantly in the amount of energy deposited in an iron plate is known (5.66 MeV per plate) allowing for:

$$\frac{N_{\text{MIPs,L1}} + N_{\text{MIPs,L2}}}{2} * N_{\text{plates,L2,L1}} * E_{\text{dep,MIP,plate}}, \tag{7.2}$$

where $N_{\text{MIPs,L1}}$ and $N_{\text{MIPs,L2}}$ are the MIP counts sampled on the sensitive layers preceding and succeeding the interpolation area, $N_{\text{plates,L2,L1}}$ is the number of iron plates between the two sensitive layers and $E_{\text{dep,MIP,plate}}$ is the expected energy deposition of a MIP in an iron plate, neglecting the Bethe-Heitler processes inside the scintillator. The principle is illustrated in Figures 7.19 7.21.

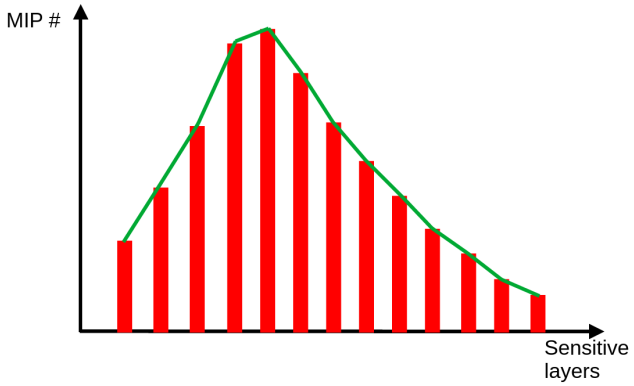

Figure 7.19: Principle of interpolation-based energy reconstruction: each red bar represents a sensitive layer with the green curve representing the interpolated longitudinal shower shape which is similar to the total shower energy.

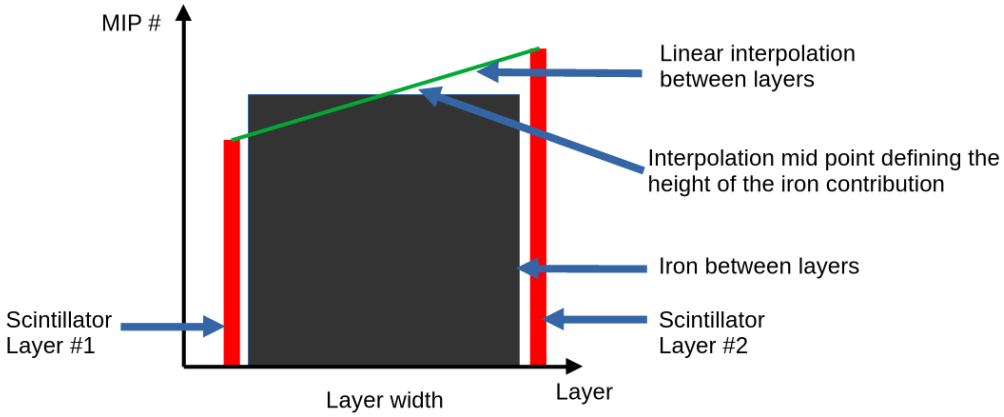

Figure 7.20: Principle of interpolation-based energy reconstruction: the material width of a layer represents the amount deposited by a MIP in said layer. Iron is denser, sees greater energy deposition and is thus wider.

Figure 7.21

This technique leads to better energy resolution as shown in Figure 7.22

Energy reconstruction having been conducted and the underlying principle of linear-interpolation-based reconstruction having been demonstrated, PID may be attempted.

7.3.3 Particle identification

PID, as expressed in Section 3.2.4 can be performed using various methods. In the case of TB2, $\frac{E}{p}$, one of the most common methods, cannot be applied as a result of the lack of spectrometer, preventing the evaluation of p, which may be done in future test beams common with the SST. More generally, the lack of HCAL and the relative thinness of the calorimeter in TB2 limits PID capabilities, in addition to the lack of beam purity and trigger delay. Nonetheless it is possible to perform PID in those conditions as well using the ratio of deposited energy in the back and front layers.

This is done by utilising three different beam types: positron beams, mixed hadron beams and mixed hadron runs having the beam shutter closed, inducing a muon halo. Of these run types, only the muon halo runs are expected to have $\sim$ 100% purity. Positron runs are expected to see their purity degrade at higher energies

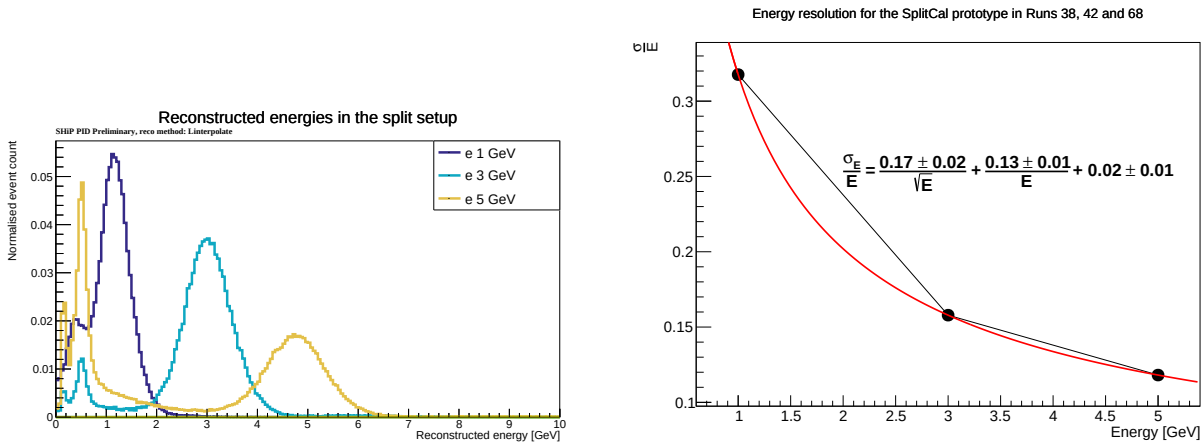

Figure 7.22: Energy reconstruction (left) and resolution using interpolation reconstruction based on Gaussian fits on each main energy peak (right).

whereas mixed hadron beams are expected to be primarily pions with a large proton fraction at higher energies and a large positron fraction at lower energies [400].

7.3.3.1 PID principles in TB2

The ratio of MIP counts in the back seven sensitive layers (B7/F2) to the front two layers was found to produce the best separation in this case, with examples for different runs shown in Figure 7.23. This metric is influenced by the trigger and thus may not apply equally well to other setups.

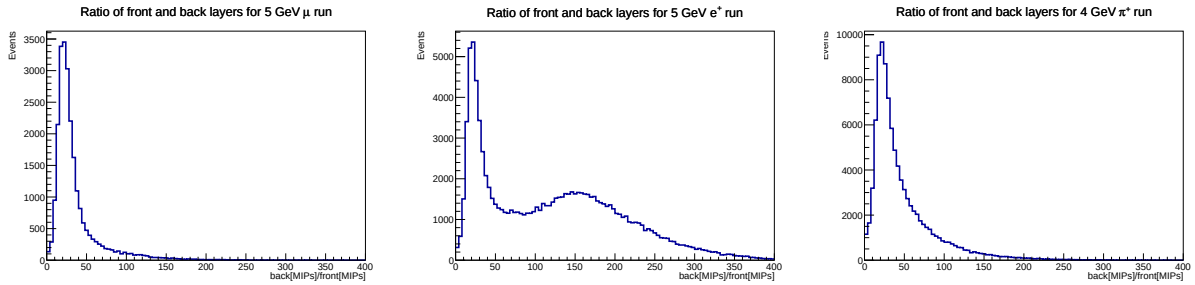

Figure 7.23: B7/F2 ratio for a 5.8 GeV muon run (left), a 5 GeV electron run (centre) and a 4 GeV pion run (right).

Three main characteristics are observed: in π^+ and μ^+ runs, the B7/F2 distributions display a single peak, this peak is narrower in the μ^+ case, likely due lower showering of muons and perhaps also to the greater beam purity of the associated runs. In the e^+ run case, a peak and a front are observed, the peak having an identical shape to that displayed in π^+ and μ^+ runs. It thus becomes possible to perform PID based on a cut applied to the initial peak of B7/F2, allowing a clean distinction between e^+ and the (primarily) π^+ or μ^+ component. The distinction of π^+ and μ^+ appears more complex in this context as only the peak width may be used with this metric, whose separation power is limited.

It should however be noted that the ratio, even for the very MIP-like muons, does not display a peak around $\frac{B7}{F2} = 3.5$ as expected. This is interpreted as being linked to the trigger issue, with signal peak integration being inconsistent across the detector. Nonetheless, this does not imperil the approach as the appearance of the structures of Figure 7.23 are consistent across particle runs, with evolutions following the expected particle purity.

7.3.3.2 PID of e^+ against π^+ and μ^+

The identification of e^+ events in the prototype can be made by placing a cut onto the B7/F2 value identified as having the same amount of (primarily) π^+ excess as e^+ signal. Using an e^+ run as data, this is done by

scaling the B7/F2 distribution of the π^+ run with the same energy as the e^+ one to the same amplitude as the B7/F2 initial peak. This is done using π^+ runs as they are expected to represent the dominant fraction of contamination in the e^+ runs. As no 5 GeV π^+ run could be recorded due to time constraints, the 5.8 GeV μ^+ muon run is used in lieu of a pion run for the 5 GeV e^+ study. The procedure is shown in Figure 7.24.

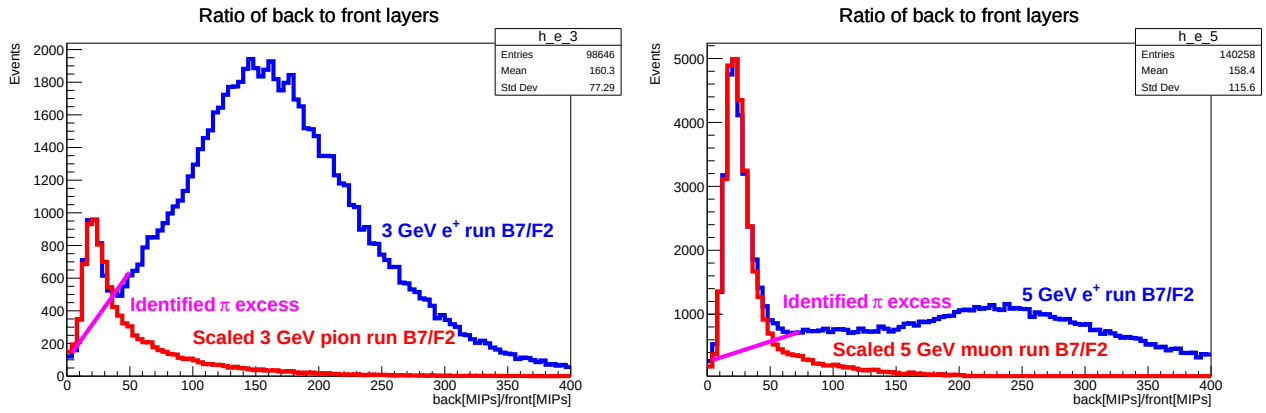

Figure 7.24: B7/F2 separation for a 3 GeV positron run (left) and 5 GeV pion run (right).

The excess is identified as appearing above a constant front of e^+ events, leading to a cut purity based on the B7/F2. This allows the determination of cut confusion matrix shown in Figure 7.25.

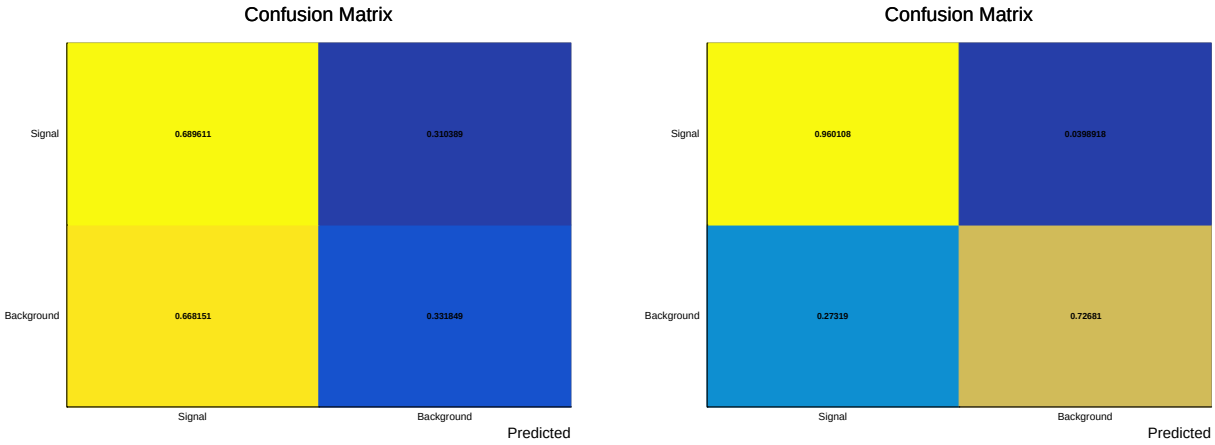

Figure 7.25: Confusion matrix of PID selection for 3 GeV e^+ (left) and 5 GeV e^+ signal (right).

This procedure is found to have limited effectiveness for the 1 GeV e^+ run as it is expected to have very high purity and thus displays a single peak at low B7/F2 as shown in Figure 7.26.

7.3.3.3 Conclusion

TB2 has allowed to evaluate a detector with a layout similar to the planned SHiP calorimeter system, just without gaseous detectors. It has allowed to determine particle energies using two separate techniques and verify the effectiveness of the DT5202 electronics for prototyping. Those, despite displaying some issues in terms of calibration and a requirement for a solid external trigger, have nonetheless demonstrated that they could be used. Two energy reconstruction methods were used: simple scaling and through linear interpolation. The latter appears to correct for some of the trigger issues that were observed and yields greater energy reconstruction, more in line with that observed in TB1.

The achieved energy reconstruction has further allowed to perform effective particle identification of positrons in a context of impure beams. Particle identification has not been attempted for hadron against muons as their characteristics were found not to be different enough in this ECAL-only test beam which would thus necessarily result in poor PID performance, as shown in Figure 7.27. Similar PID techniques will be used in the SHiP

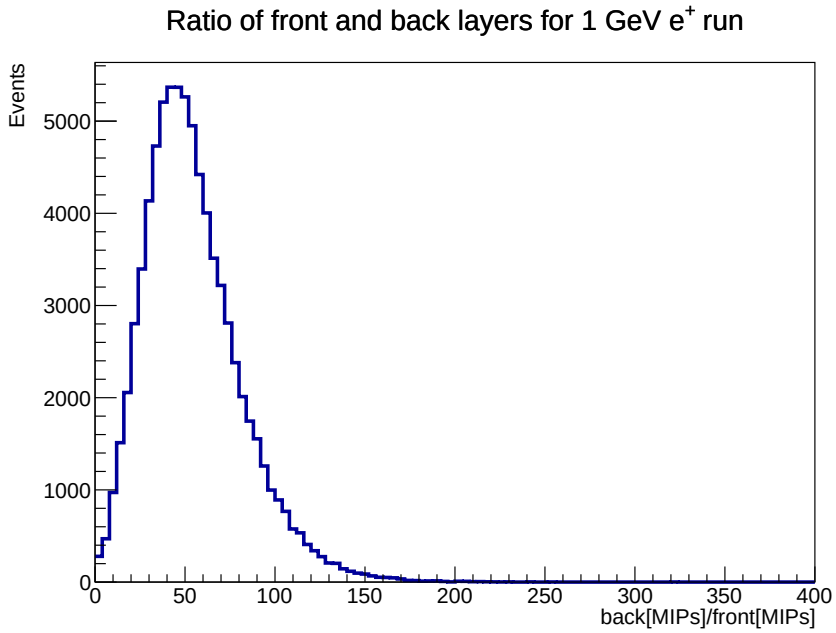

Figure 7.26: B7/F2 for the 1 GeV positron run.

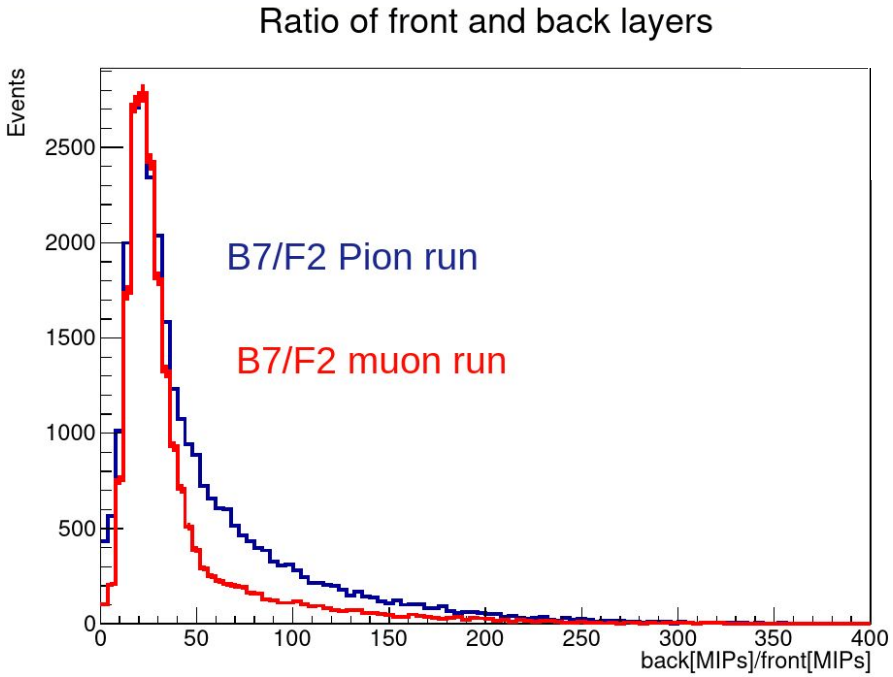

Figure 7.27: Distinction between hadronic and muon runs through $B7/F2$.

calorimeter system after comparison with Monte Carlo whereas π vs μ particle identification will be done with the help of a hadronic calorimeter.

Improvements are brought to this prototype through the implementation of an external trigger which features in the third test beam (TB3) as well as a hadronic section in a future test beam.

7.4 Third test beam at DESY

The third test beam (TB3) was held for one week in October 2024 and was dedicated to the study of calorimeter configuration and angular resolution. It was again performed at DESY using the same beamline to that of TB1. The used prototype was identical to the one of TB2, only using an external trigger scintillator built out of an EJ-200 scintillator tile connected to a large SiPM on a PCB from Section 6.3.3 operated in KLauS mode. The signal is sent to a discrete discriminator with a threshold allowing to filter out SiPM dark counts and the resulting signal is sent as an external trigger to the chained DT5202 system. This has been observed to significantly improve data quality. The trigger system is pictured in Figure 7.28. In the absence of a muon beam at DESY, calibration was done in laboratory using cosmics similarly to TB1. Operating conditions are otherwise similar to TB2.

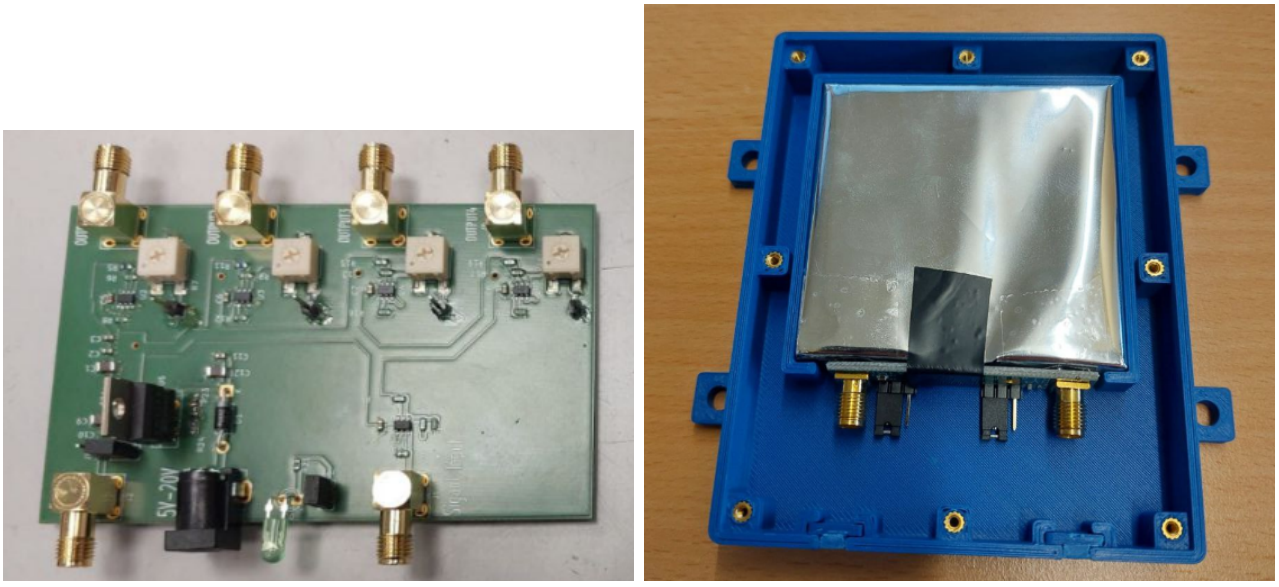

Figure 7.28: TB3 trigger fanout (left) and scintillator system (right). The discriminated trigger signals are distributed through the top four SMA connectors whereas the blue box is 3D printed and kept light tight with a similarly 3D printed cover.

Two configurations were examined in TB3, the split configuration, similar to that of TB2 and a long configuration which didn't include a split. Those are pictured in Figure 7.29.

7.4.1 Energy reconstruction

Energy reconstruction was again performed identically to TB2 using simple scaling and linear interpolation, this time for both the long and the split configuration.

The results are pictured in Figures 7.30, 7.31, 7.32 and 7.32

An improvement in energy resolution is noted compared to the otherwise identical TB2 conditions, particularly when using the simple scaling method, indicating that the issue there was indeed the trigger. Furthermore a degradation in the energy resolution is observed in the split configuration. This could be related to larger smearing of the shower due to distance. As shown in Section 4.1, this has a limited impact of the resolution of $X\gamma\gamma$ but does have an influence on the PID performance. Is suggests that some form of compromise between the different physics goals of the SHiP calorimeter system will have to be found.

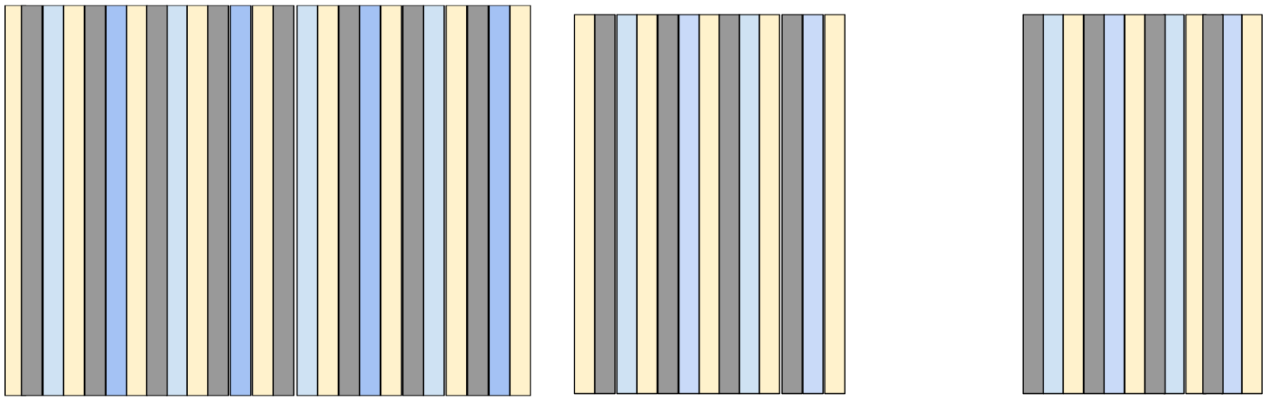

Figure 7.29: TB3 long (left) and split (right) configuration. The yellow rectangles represent thin bar layers, the blue bars represent the wide layers, the gray ones represent passive iron layers.

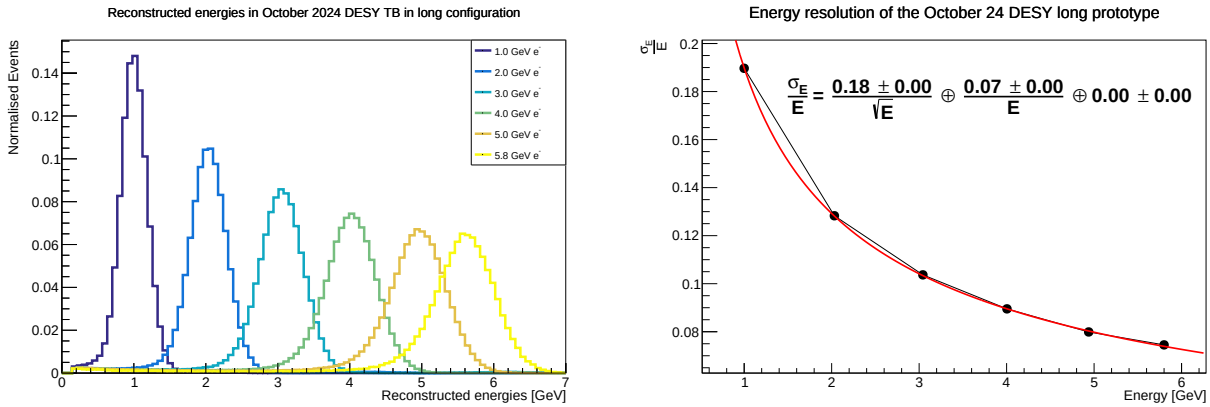

Figure 7.30: TB3 energy reconstruction (left) and resolution (right) in the long configuration using the simple scaling technique.

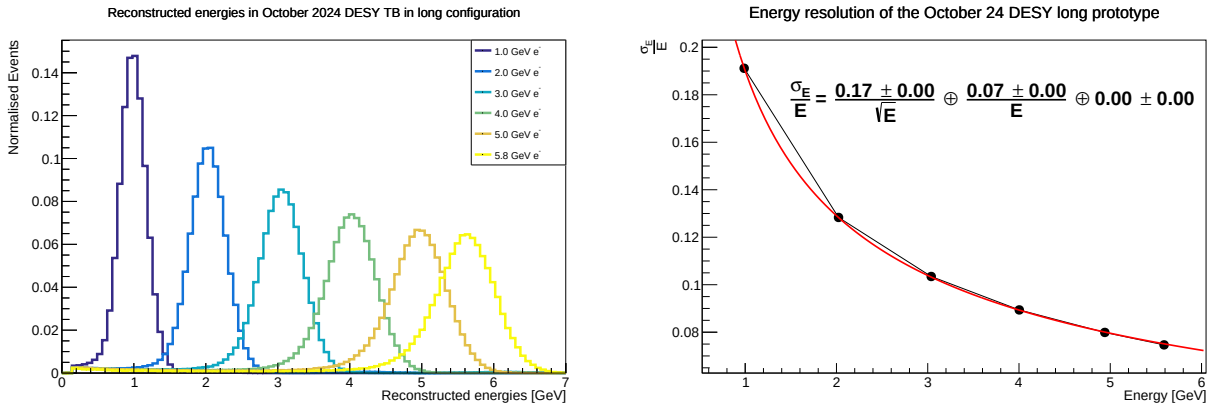

Figure 7.31: TB3 energy reconstruction (left) and resolution (right) in the long configuration using the interpolation technique.

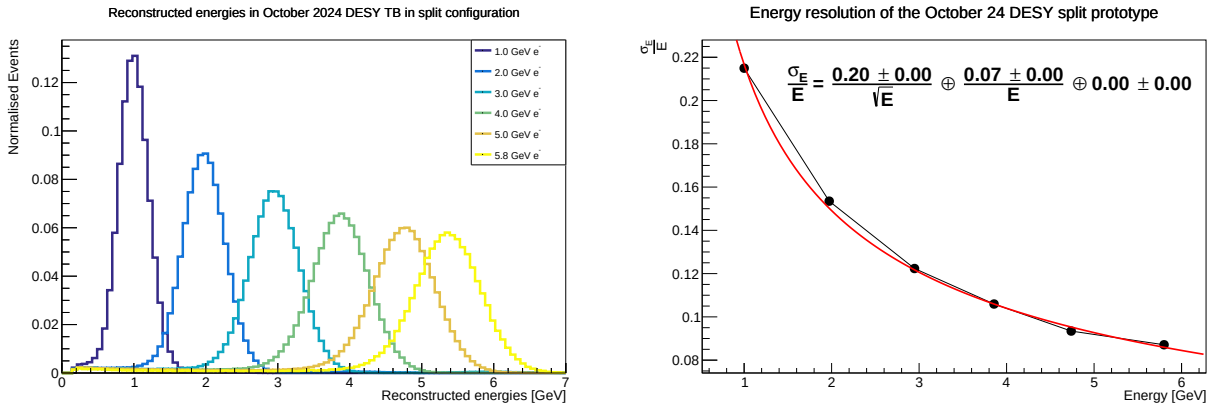

Figure 7.32: TB3 energy reconstruction (left) and resolution (right) in the split configuration using the simple scaling technique.

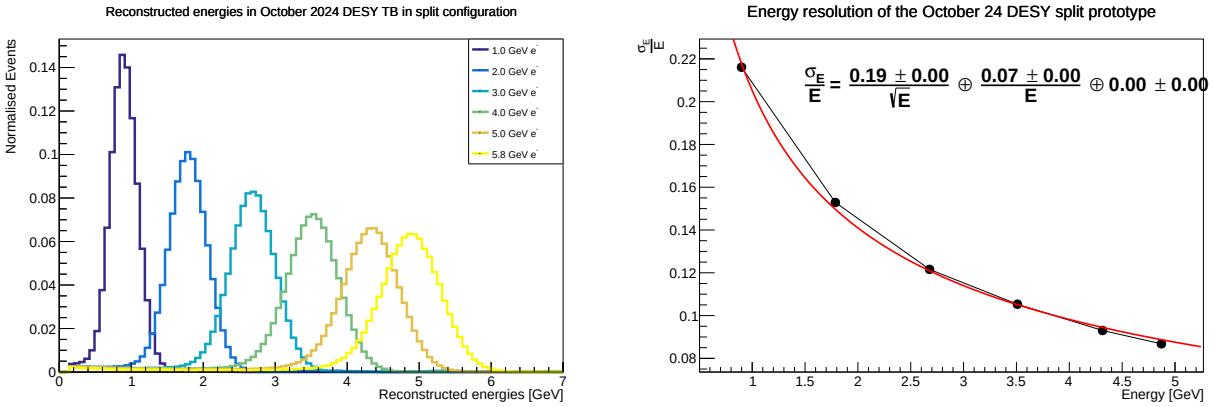

Figure 7.33: TB3 energy reconstruction (left) and resolution (right) in the split configuration using the interpolation technique.

7.4.2 TB3 Conclusion

TB3 has allowed to reproduce and validate energy reconstruction results from TB2 in a cleaner environment, leveraging an external trigger which has allowed for clean data taking using the DT5202. The achieved energy resolution is consistent with TB1. These energy reconstruction techniques will continue to be used and improved in the prototyping stage. The lack of beam particles other than e^- has prevented any PID from being done however.

While the improvement brought by the interpolation method is reduced, some weaker improvement is nonetheless observed, suggesting that the technique does indeed provide some benefit compared to simple scaling. This could be confirmed in a dedicated Monte Carlo study which perhaps could also include more advanced techniques, making use for instance of more realistic polynomial or exponential interpolation.

7.5 Conclusion

The set of test beams presented here have allowed to evaluate the triggerless, custom-built KLauS system in TB1, yielding an energy resolution which was further validated in TB2 and TB3. The system in question could be further improved with a new version using the LVDS bus for data readout to simplify the DAQ architecture and improve its flexibility and performance. Moreover, if the KLauS would be utilised in the SHiP calorimeter system, the FIFO-based readout would have to be validated at SHiP-like rates, which could not be achieved in TB1 given the slowness of the I^2C-based readout and the need to finalise the incoming particle rate studies for the SHiP calorimeter system. The issue of insufficient dynamic range was identified in TB1 with the extended LG1200 mode resolving the issue at those energies. The validity of this solution remains to be confirmed at SHiP energies which could be done by evaluating the same system at SPS.

TB2 has used the commercial DT5202 within the FERS-5200 readout system and has allowed to perform energy reconstruction introducing a more robust method using linear interpolation which has allowed to improve the energy performance despite the trigger issues encountered. This technique would now have to be validated in Monte Carlo studies. In addition, TB2 has seen effective particle identification in positron beams using the ratio of back to front layers. The used PID techniques will be the basis of those which will be utilised in future test beams and in the SHiP calorimeter system.

TB3, similarly to TB2 has used the FERS-5200 system and has allowed the validation of the results from both TB1 and TB2 using an external trigger. It indicates that the calorimeter split is detrimental to energy resolution, suggesting a need for optimisation between competing needs in the SHiP calorimeter system. It confirmed the added value of the interpolation technique an opened the way to new test beams at higher energy.

Overall the achieved energy resolution results in all test beams are consistent with an analytical calculation using Equation 3.18, estimated to be around $18\%/\sqrt{E[\text{GeV}}$ as shown in Figure 7.34. A further test beam (TB4) was held at SPS in May 2025 which will saw higher energy particles, different particle beams and the use of a novel custom-designed $5\lambda_a$ hadronic section in addition to an upgraded prototype to reach the full $20X_0$ SHiP calorimeter system's depth, both pictured in Figure 7.35 This will allow for a more complete evaluation of angular resolution and allow to perform PID in better conditions than in TB2 thanks to the use of an external trigger. The built ECAL prototype will also be used in future test beams until detector commissioning in 2030 to evaluate the currently under design new readout electronics based on the CALOROC1b as well as High Precision Layers based on gas detectors.

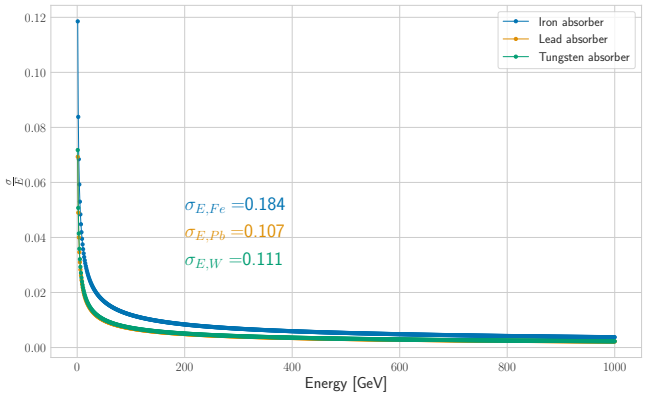

Figure 7.34: Sampling uncertainty for different materials using TB2/3-like sampling frequency.

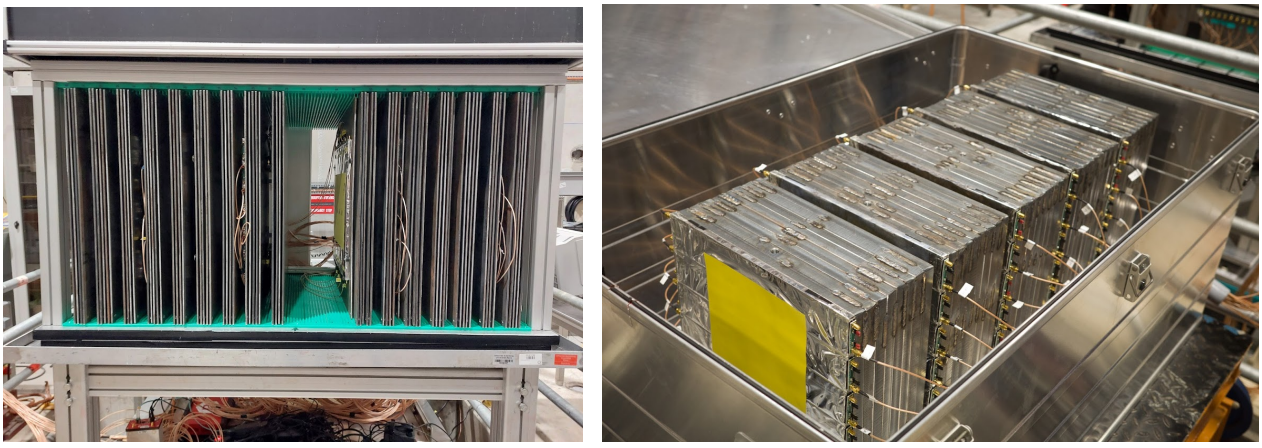

Figure 7.35: ECAL (left) and HCAL (right) prototype built and operated in TB4. The beam comes from the right.

Chapter 8

Calorimetry at SND@LHC

As exposed in Section 2.2, the SND detector pursues the observation of collider neutrino in an off-axis configuration. Both of its calorimeters, hadronic and electromagnetic have been studied in this work. First the experiment's HCAL (also called Mufilter) replica prototype was used to study hadronic showers in a test beam configuration for calibration, then its vertex detector and electromagnetic calorimeter with the development of calorimetric energy reconstruction in emulsions. The following focuses on techniques that can be used to tag the behaviour of hadronic showers in the HCAL and as the calorimetric energy reconstruction for electromagnetic showers as well as its uses to identify muon deep inelastic scattering and catastrophic bremstrahlung in the emulsion detector.

8.1 Studies of hadronic showers in the calibration of the SND hadronic calorimeter

The SND detector was built by the collaboration in 3 months between September 2021 and December 2021, making it the fastest experiment ever built at LHC. As a result, the HCAL calibration could not be done in advance and instead relied on test beams and Monte Carlo simulation [401]. Methods were developed in these studies of hadronic showers and were further used in the detector's calibration. The HCAL's upstream (US) stations are the main element being calibrated as the downstram (DS) stations principally serves in muon identification and tracking.

8.1.1 SND HCAL calibration

The principles of the SND HCAL calibration are exposed below followed by a description of the test beam which was used to calibrate the HCAL conducted in August 2023 at the H8 beam line at SPS.

8.1.1.1 Calibration procedure

Given that the detector from TI18 cannot be moved outside of the tunnel, a replica was built. While it shares characteristic with its TI18 counterpart, it remains different and thus is calibrated separately in a separate test beam (Section 8.1.1.2). There, after ensuring response uniformity throughout the US, the shower origin is tagged through a dedicated algorithm whose development is inspired by the studies conducted in Section 8.1.2 with the shower's transversal position also being evaluated. The shower profile can then be fitted through the equation

$$E_{\text{tot}} = k \times \text{QDC}_{\text{SciFi}} + \alpha \times \text{QDC}_{\text{US}}, \tag{8.1}$$

where k and α are calibration constants determined in fitting the QDC profiles of both detectors. The replica results are implemented in the Monte Carlo simulation, the output of which is then unfolded onto the SND HCAL US located in TI18.

The work conducted here has been dedicated to understanding hadronic showers primarily using Monte Carlo simulations which were then used for shower tagging [401].

8.1.1.2 Test beam setup

The test beam was conducted using a replica of the SND HCAL composed of five US planes and one DS plane. In addition, an instrumented iron target of variable thickness was positioned at the front of the HCAL, mimicking the emulsion target of TI18. The target is instrumented with eight SciFi planes of alternating orientation, each composed of 512 250 µm channels for a $13 \times 13\,\mathrm{cm}^2$ transversal profile. The iron target was composed of up to 3 iron walls, each 10 cm thick and $30 \times 30\,\mathrm{cm}^2$. The readout is largely identical to that in TI18 (see Section 2.2) with the system being entirely asynchronous and triggerless. The system was exposed to positive hadron beams (π^+ and proton) at 100 GeV, 140 GeV and 180 GeV and negative hadrons (primarily π^-) with 240 GeV and 300 GeV energies. A beam monitor (BM) was included but was not used in the final analysis. The test beam layout is shown in Figure 8.1.

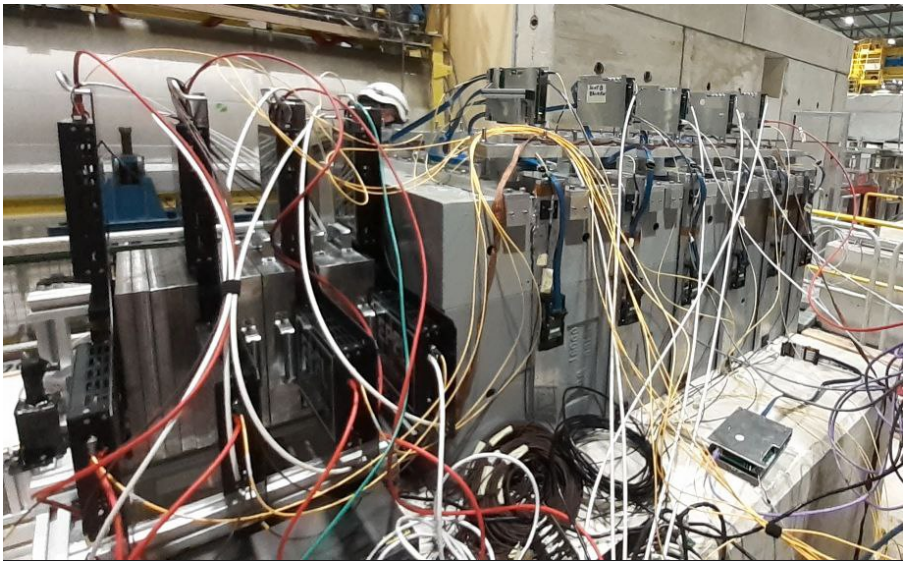

Figure 8.1: Test beam configuration, top graphic from [402].

8.1.2 Study of hadronic showers

Hadronic showers were studied under the lense of their transversal and longitudinal profile. This was done by implementing the test beam geometry into the SND collaboration's `sndsw` software [293] and using a particle gun of π onto the initial target plane with a charge corresponding to the particles obtained in the beam. This was done using a GEANT4 Monte Carlo simulation [297].

8.1.2.1 Shower analysis

The transversal and longitudinal profiles of hadronic showers are very varied (see Section 3.2.3) which can be problematic for shower reconstruction. While proper compensation for these characteristics requires a high

granularity calorimeter [403], characterisation of these variations is necessary to constrain the systematic uncertainties which contribute towards stochastic and constant calorimetric terms (see Section 3.2.1). Monte Carlo simulations are the preferred tool for these studies as it allows to evaluate realistic physics while having access to truth values.

90E_radius The study focuses on leakage and shower energy distribution, introducing a new metric called the 90E_radius. This metric represents the smallest transverse radius that contains 90 % of the shower's energy. Unlike the Moliere radius, which is a constant for all showers within a material, the 90E_radius is defined individually for each shower due to their diverse profiles.

The 90E_radius is defined by setting a shower weighted centre and then defining a radius equal to the detector's transversal size around it. This is done using visible particles' energy as origin in the transverse plane. This radius is then decreased in 5 mm increments until the smallest radius which still contains at least 90 % of the incoming particle's energy is identified. It should be noted that the 90E_radius is defined using the energy deposited within a sensitive plane and thus varies if the acceptance is varied.

The metric is utilised to investigate the transversal profile and breadth of showers from incoming hadrons in the HCAL, allowing to tag shower behaviour for in particular early and late showering pions or more exotic shower profiles.

8.1.2.2 Shower profile analysis

The variations in 90E_radius induced by π on target (PioT) were investigated at the different beam energies at each station (US1-US5) as well as within a cylinder of all SciFi and US stations. This is shown in Figures 8.2 and 8.3. The 90E_radius in SciFi is found to increase with energy and station, with many events having no radius at all as a result of pions punching-through the SciFi target. The 90E_radius peaks around 8 cm in the later SciFi stations which exceeds the detector's transversal size, indicating strong asymmetry in the induced showers. The combined 90E_radius applied to a cylinder through the detector is consistently larger than the single plane observation.

In the US, showers are found to also increase in size with increasing energy, the difference comes from their longitudinal evolution, with the 90E_radius peaking around 37 cm in US1 and US2 but reducing rapidely in the later stations, reaching an most probable non-zero value of around 26 cm in the DS. Many showers are also quenched entirely, leading to very small radii, especially further deep in the calorimeter. Similarly to SciFi, the 90E_radius shower cylinder (around 41 cm) is found to be close to the detector's transversal dimensions and consistently larger than the radius in any given plane, indicating strong transversal evolutions within the shower which cannot easily be tagged within the relatively low granularity SND HCAL.

The longitudinal evolution can however be directly evaluated by looking specifically at variations in 90E_radius between planes, these are shown for pion energies of 100 and 300 GeV in the HCAL in Figure 8.4. The remaining energies as well as the analogue evaluation in the SciFi can be found in Appendix F.

The distributions are well symmetric between US1 and US2 but gradually lose symmetry beyond, an effect which is mitigated at higher energies, indicating that showers are increasingly more homogeneous with increasing energies.

A significant cross-check is the station where the 90E_radius peaks, as it indicates the maximum transversal extension of the shower which is expected to relate to the station seeing the most particles. This was evaluated in the SciFi and US stations and is shown in Figure 8.5 and 8.6 for PioT energies of 100 and 300 GeV, the remainder being found in Appendix F.

Station US1 is found to have the largest showers, which motivated the installation of the best functioning planes as US1 and US2. These evaluations were also performed in the case where the target only is formed of 10 cm and 20 cm of iron and are shown in Appendix F.

Calorimeter unseen energy Transversal calorimeter leakage was investigated through the use of thin 1 mm air planes set over, under and onto the two sides of the target as well as a large air plane at the end of the target, used to evaluate the amount of energy exiting in the forward direction. The setup is shown in Figures 8.7. This allowed to investigate the total energy which doesn't reach the HCAL at all but is instead leaked and scattered out of the HCAL acceptance as shown in Figure 8.8 for 100 and 300 GeV π.

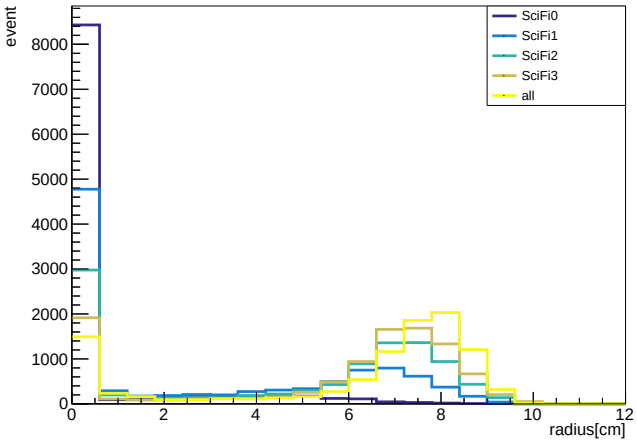

(a) 90E_radius in SciFi for 100 GeV PioT.

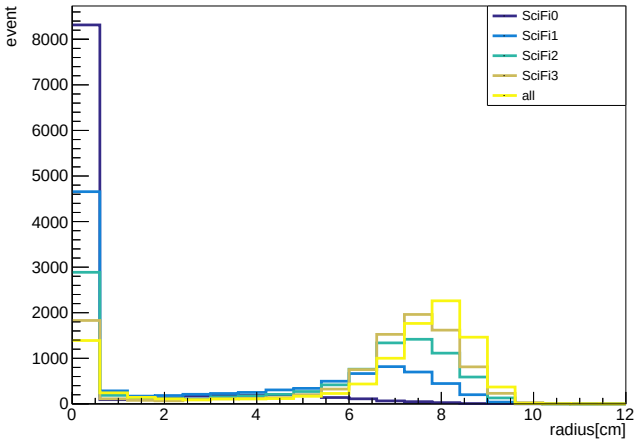

(b) 90E_radius in SciFi for 140 GeV PioT.

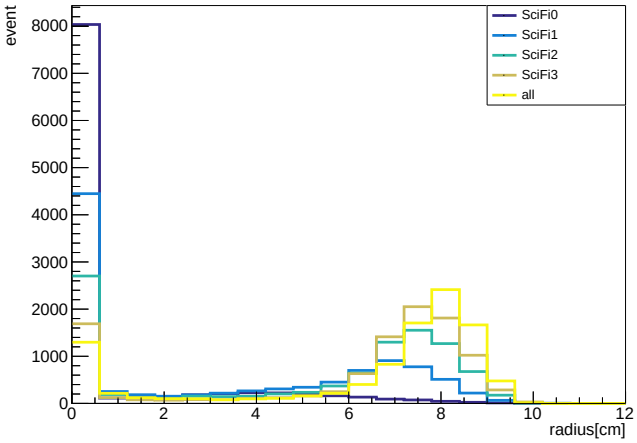

(c) 90E_radius in SciFi for 180 GeV PioT.

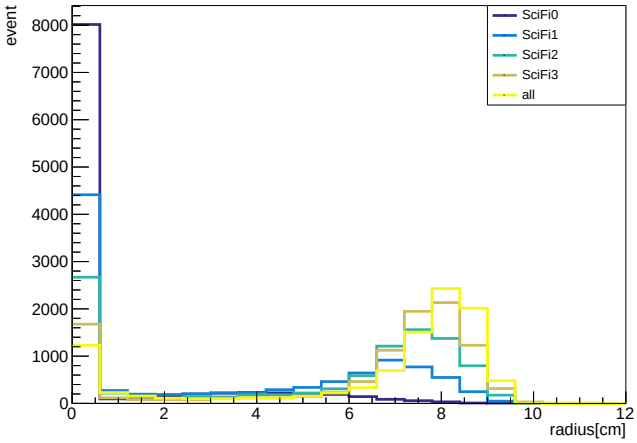

(d) 90E_radius in SciFi for 240 GeV PioT.

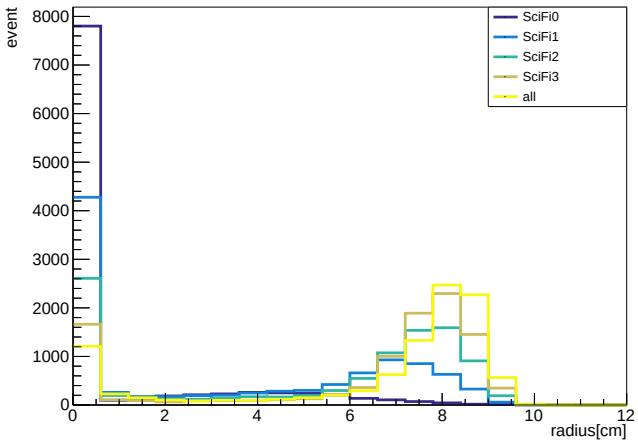

(e) 90E_radius in SciFi for 300 GeV PioT.

Figure 8.2

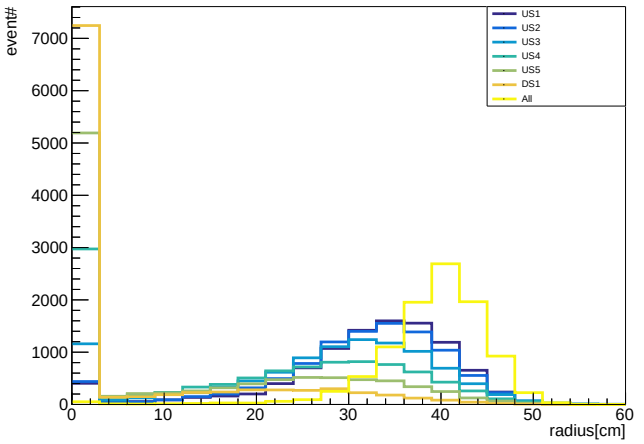

(a) 90E_radius in US for 100 GeV PioT.

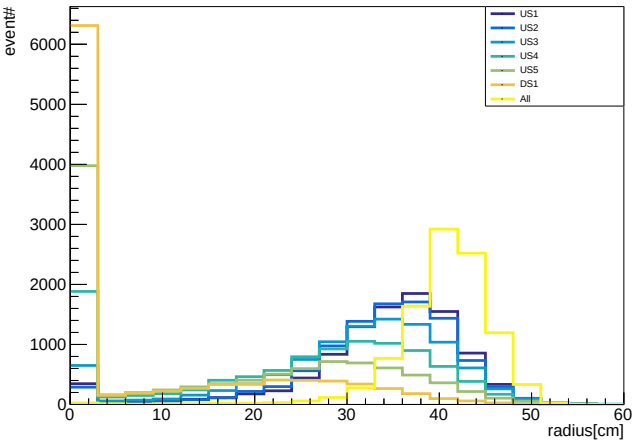

(b) 90E_radius in US for 140 GeV PioT.

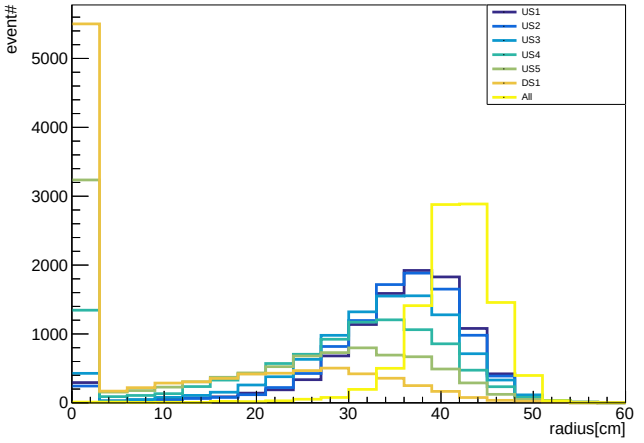

(c) 90E_radius in US for 180 GeV PioT.

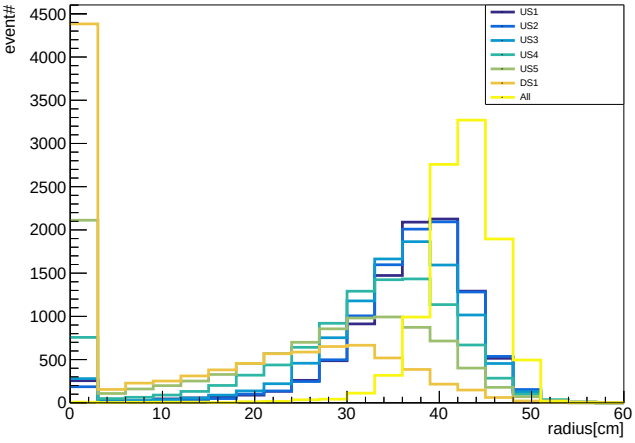

(d) 90E_radius in US for 240 GeV PioT.

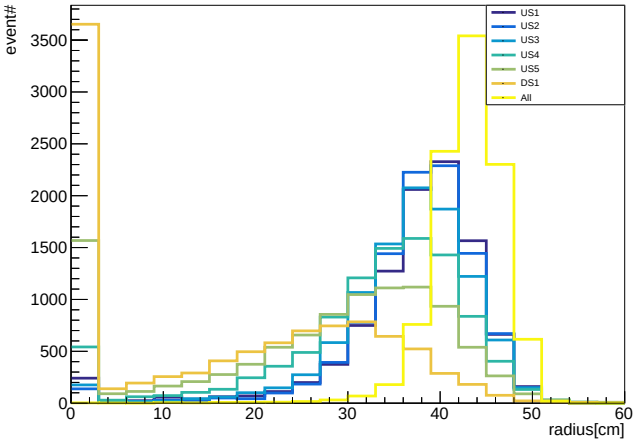

(e) 90E_radius in US for 300 GeV PioT.

Figure 8.3

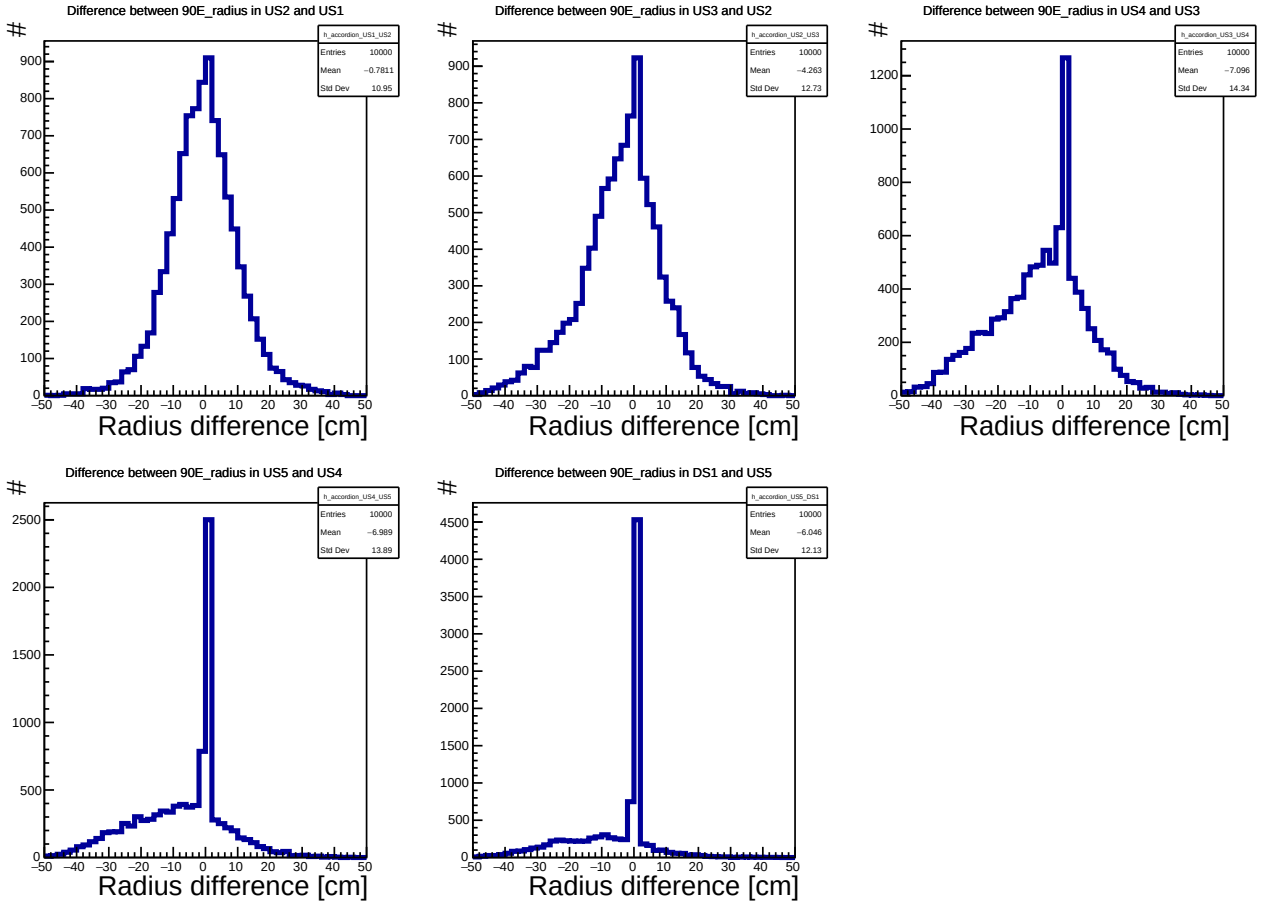

(a) Variations in 90E_radius in the HCAL in single events for 100 GeV impinging π^+

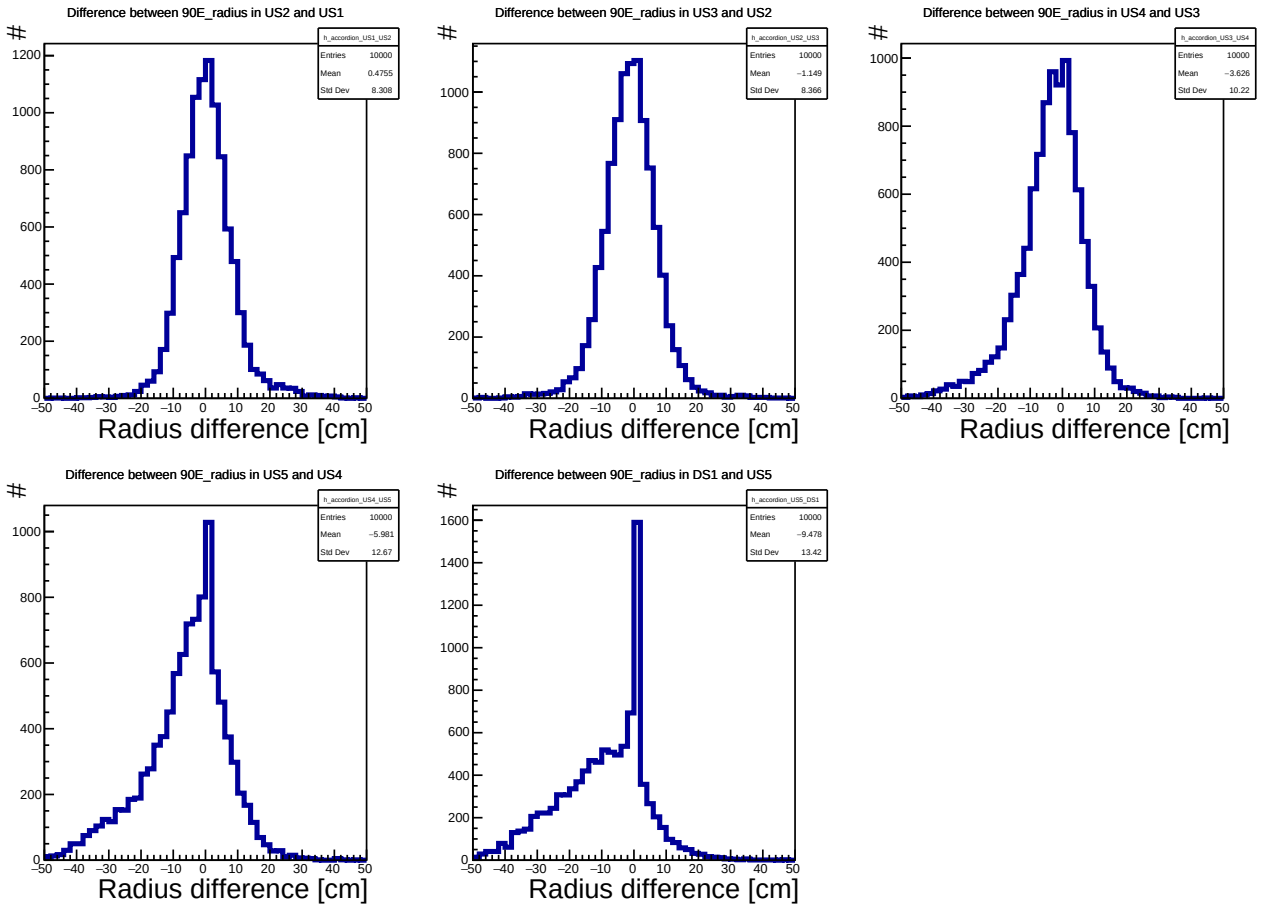

(b) Variations in 90E_radius in the HCAL in single events for 300 GeV impinging π^-

Figure 8.4

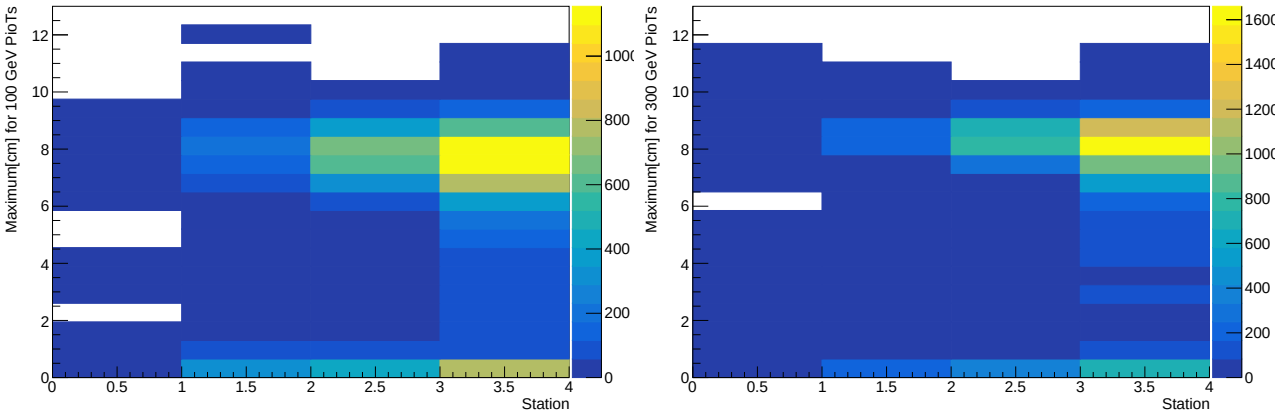

Figure 8.5: SciFi station with largest 90E_radius for 100 GeV (left) and 300 GeV incoming π^+.

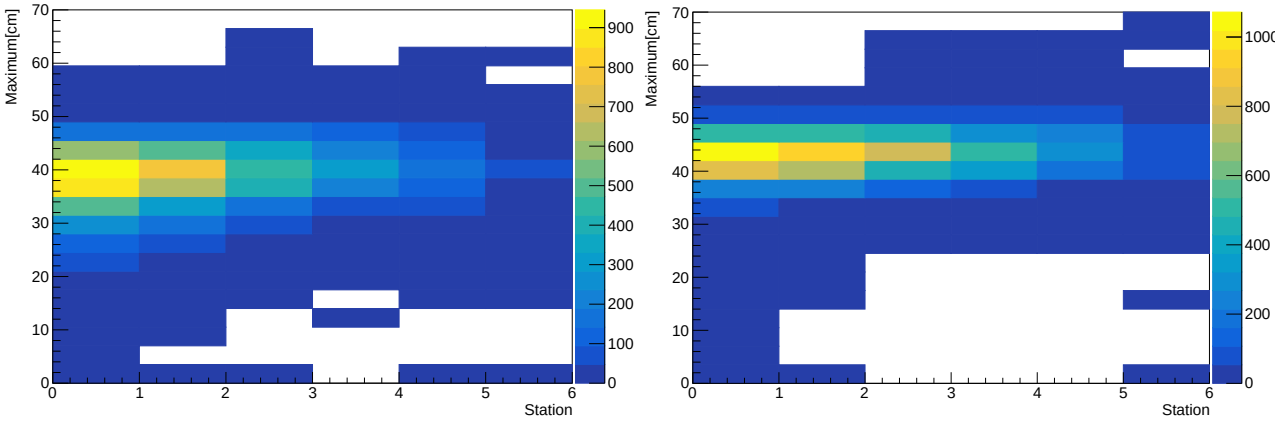

Figure 8.6: HCAL station with largest 90E_radius for 100 GeV (left) and 300 GeV (right) incoming π^+.

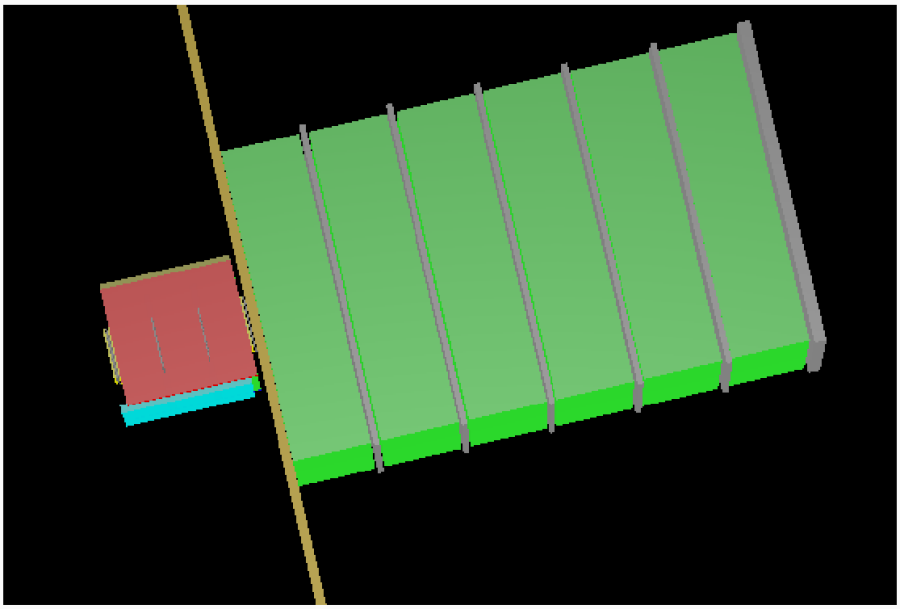

Figure 8.7: View of the GEANT4 setup. Two air layers around the target are shown in red and cyan with the yellow one being the front layer. The green regions represent the iron and the gray ones represent the sensitive layers.

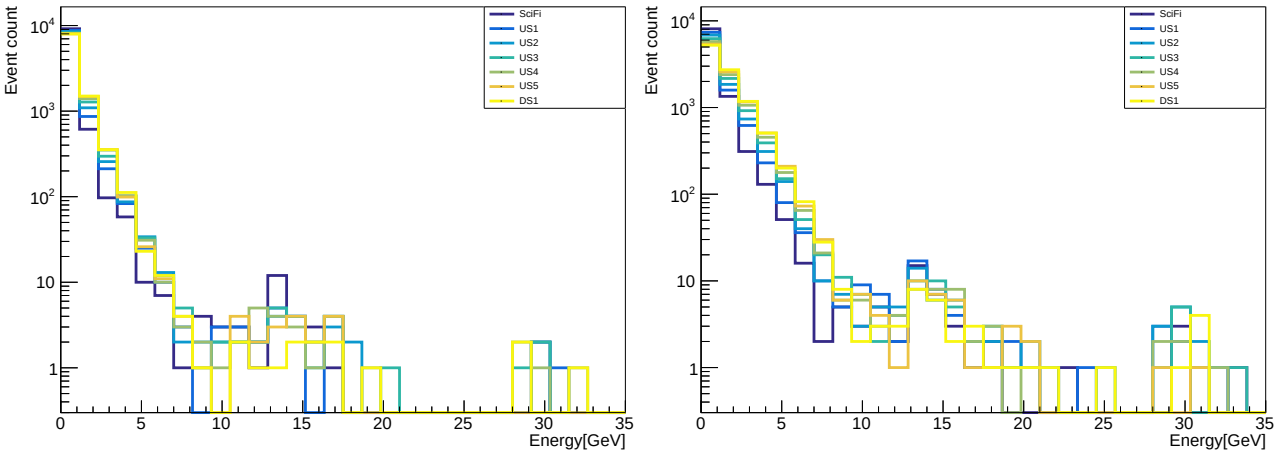

Figure 8.8: Energy not reaching the HCAL planes for 100 GeV (left) and 300 GeV (right) incoming π^+. The SciFi refers to the final SciFi station

While most of the event energy typically does reach the HCAL, over 10% of events have losses exceeding 2 GeV, a number which increases with PioT energy although they remain constant as a proportion of π energy. The primary source for these losses is transversal leakage. Therefore, the correlation between 90E_radius in sensitive planes and geometric planes is studied. This is modelled as 20 m sensitive air layers parallel to the HCAL stations shown in Figure 8.9 with the correlation being shown in Figures 8.10 and 8.14. The particle passing these air layers are recorded for π energies of 100 and 300 GeV in US1, US5 and all US stations combined. The figures relative to the remaining stations are found in Appendix F.

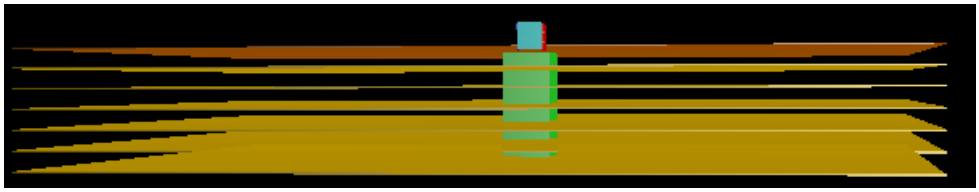

Figure 8.9: Sensitive air layers added to the GEANT4 geometry, the configuration is rotated clockwise for visibility.

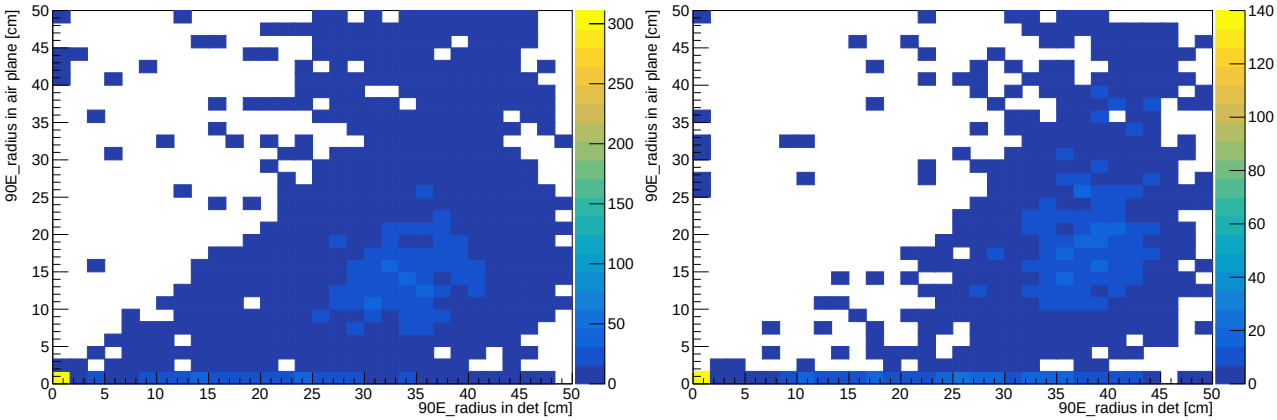

Figure 8.10: Correlation between 90E_radius in the air plane and in US1 for 100 GeV (left) π^+ and 300 GeV (right) π^-.

The correlation between 90E_radius is relatively poor, particularly for the further back stations and lower energies, indicating significant transversal shower development on the detector sides for leaked shower material so that the shower is significantly non-linear at large transversal extension but is more linear at small transversal extension. The lack of HCAL granularity does not motivate a more quantitative analysis.

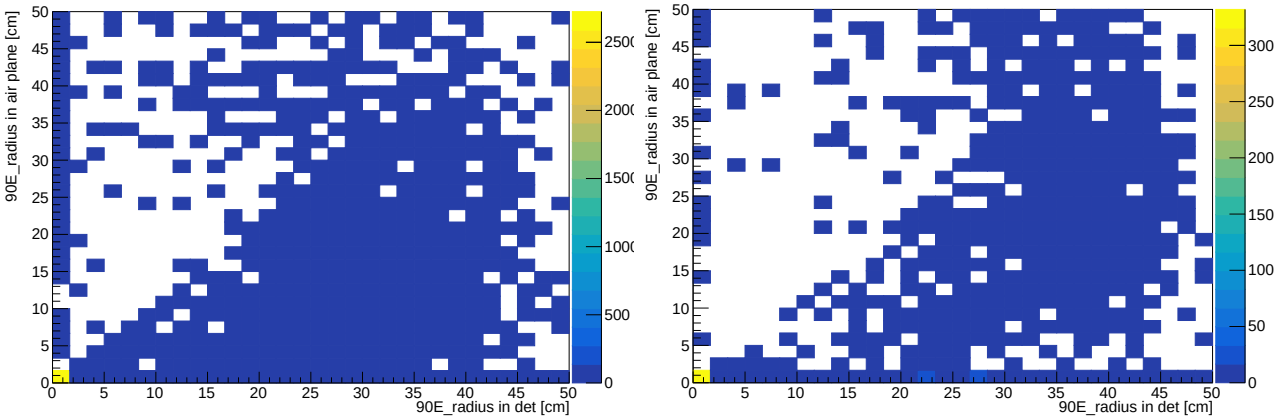

Figure 8.11: Correlation between 90E_radius in the air plane and in US5 for 100 GeV π^+ and 300 GeV π^-.

Figure 8.12

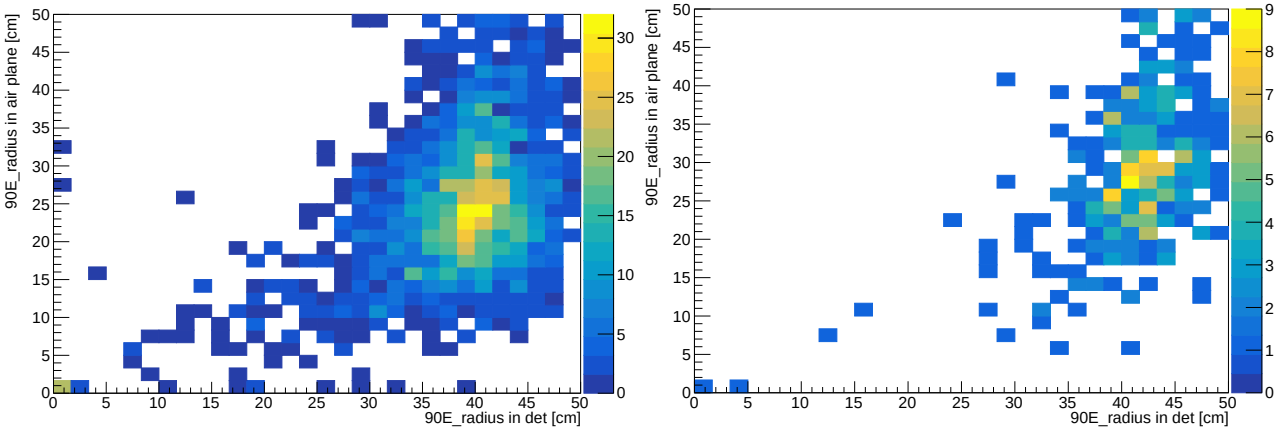

Figure 8.13: Correlation between 90E_radius in the air plane and in all stations for 100 GeV π^+ and 300 GeV π^-.

Figure 8.14

Centroid reconstruction in US using test beam data While the SND HCAL is a low granularity calorimeter, physical effects may be used to nonetheless reconstruct positions and even the shower directionality. This is done through in the following in a coordinate system shown in Figure 8.15.

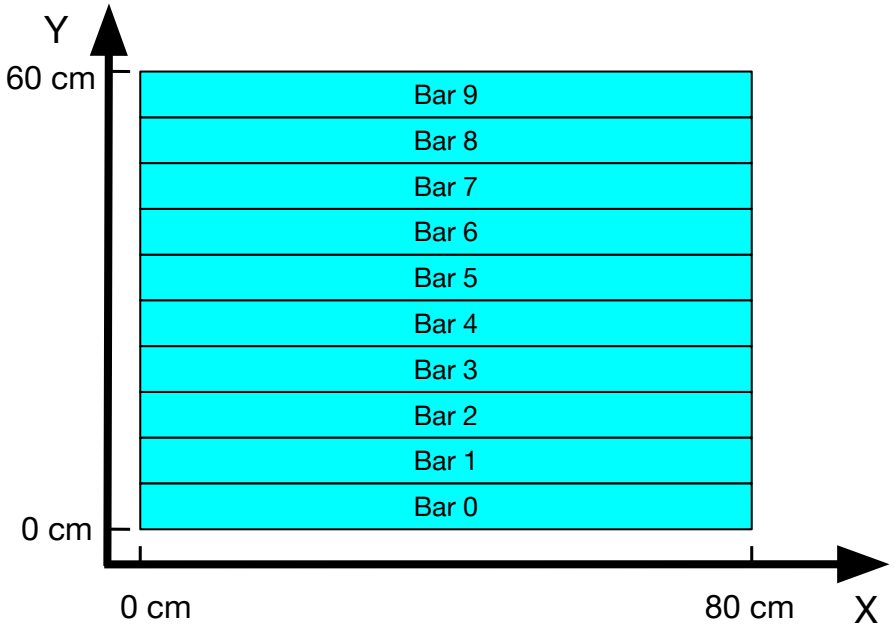

Figure 8.15: SND HCAL transverse view showing US bars and coordinate system.

Two effects are primarily investigated here: firstly the transversal width of the shower, investigated in Section 8.1.2.2, allow for multiple scintillator bars (~ 4) to typically see shower elements. This can be used to reconstruct a weighted average, a *centroid* corresponding to the Y-position centre of the shower through the formula $Y_{\text{centroid}} = \frac{\sum_{\text{bar}=0}^{\text{bar}=9} \times N_{\text{QDC}}}{N_{\text{QDC,tot}}}$. On the X axis, the scintillator attenuation length is known to be $\lambda_L = 3.6\,\text{m}$ [272], variations are hence expected at both ends of each US bar for asymmetric events. This allows for double sided reconstruction and was evaluated in data by examining the energy-calibrated QDCs in simulation and in a 100 GeV π^+ run. The centroid can effectively only be computed in the X-direction as all bars are placed horizontally, it is computed by taking all QDCs from both sides of the plane computing the weighted asymmetry through $X_{\text{centroid}} = \frac{\lambda_L}{2} \ln \frac{S2}{S1} + 40\,\text{cm}$ where S2 and S1 correspond to the signals from both scintillator sides. The centroid distributions for US1 are shown in Figure 8.16.

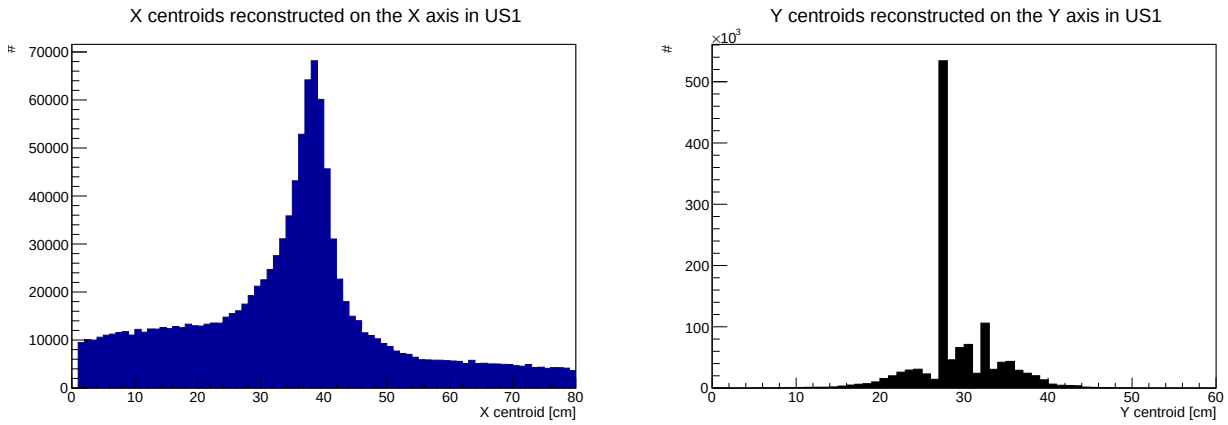

Figure 8.16: X-axis (left) and Y-axis (right) centroid distribution in US1 using 100 GeV π^+ test beam data.

The irregularities in Y can be attributed to the reconstruction which averages over bars, yielding to over-representation of certain bars in final state reconstruction. The offset in X can be attributed to the physical offset present in the testbeam whereas the asymmetry is largely attributed to the target and detector angle

relative to the beam. These centroid distributions yield up to 3D positions, one for each of the five US station plus one for the higher resolution DS station (up to 6 in total). This allows to fit a shower direction track through a simple 3D line fit through each point, the results of which are shown in Figure 8.17.

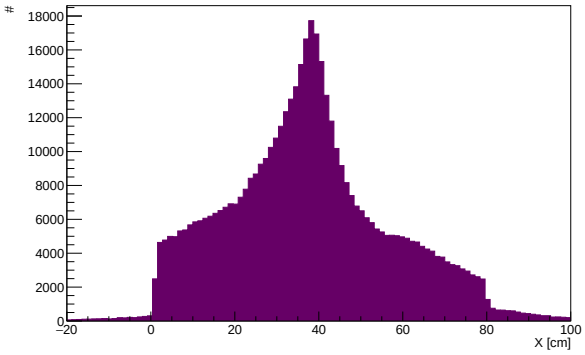

(a) X coordinate at $Z = 0$ distribution for shower direction tracks using 100 GeV π^+ test beam data.

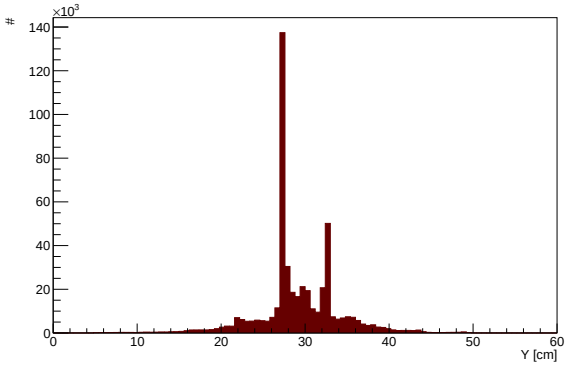

(b) Y coordinate at $Z = 0$ distribution for shower direction tracks using 100 GeV π^+ test beam data.

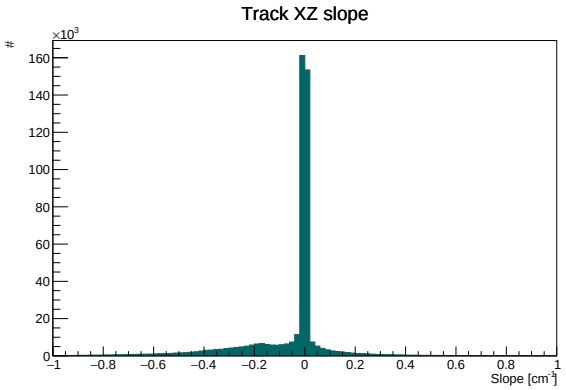

(c) XZ slope distribution for shower direction tracks using 100 GeV π^+ test beam data.

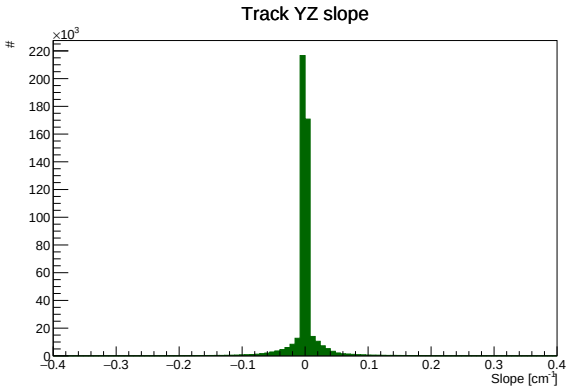

(d) YZ slope distribution for shower direction tracks using 100 GeV π^+ test beam data.

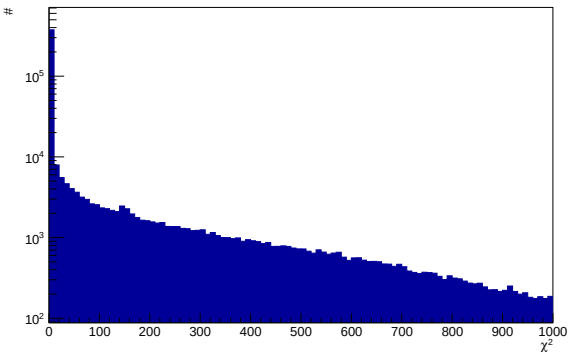

(e) χ^2 distribution for shower direction tracks using 100 GeV π^+ test beam data.

Figure 8.17: All tracks with $\chi^2 = 0$ corresponding to tracks with only two points are not shown.

The tracking procedure displays excellent behaviour overall with excellent resolution on the X and Y slopes and good resolution on the Y intercept. The X intercept resolution is found to be inferior showcasing the limit in the usage of the attenuation length for relatively short (80 cm) bars. Certain tracks are found to be very poor reflecting the chaotic nature of hadronic beams and typically display poorly behaved showers.

These shower direction tracks however offer a good ability to tag poorly behaved showers, where invisible transverse energy is significant or where transversal activity is strongly asymmetric, for instance due to electromagnetic components being prevalent in certain sections of the detector. These techniques can also be used to filter ambiguities discussed in Section 4.2.1.

8.2 SND emulsion detector calorimetry

At SND@LHC, ν_e are one of the most significant signals of SND@LHC as they can effectively be traced back to charm decays. ν_e mostly interact through CC in the detector and thus produce a $e^{\pm}$ which then goes on to shower electromagnetically in the detector. The tagging of these electromagnetic showers was explored in the emulsion detector, as well as that of their energy in Section 8.2.1.2. Together with other parameters these can be used to infer the energy of the incoming ν_e. However they are not the only source of electromagnetic showers in the emulsion detector, with forward muon DIS and catastrophic bremstrahlung being prominent sources of background. These were examined in Monte Carlo and data in Section 8.2.2 through the prism of calorimetry.

8.2.1 Electromagnetic shower reconstruction in emulsions

Emulsions, not measuring any amount of charge, are distinct from electronic detectors. Instead, segments are measured. Electromagnetic showers however have a constant $\sim \frac{1}{3}$ fraction of invisible photons, implying that unlike hadronic showers, there is strong linearity between particle amounts in the induced shower and incoming particle energy. The $e^{\pm}$ will manifest as segments within the emulsions and can thus be reconstructed as showers by tagging high density areas as is explained in Section 8.2.1.1 while the energy reconstruction procedure is provided in Section 8.2.1.2.

8.2.1.1 Shower tagging

As electromagnetic shower are very dense, particularly in tungsten which has $R_{\mathrm{M}} = 0.9327$, electromagnetic showers have been examined by stacking the data of all emulsion plates in one brick, which highlights "hot spots" as shown in Figure 8.18.

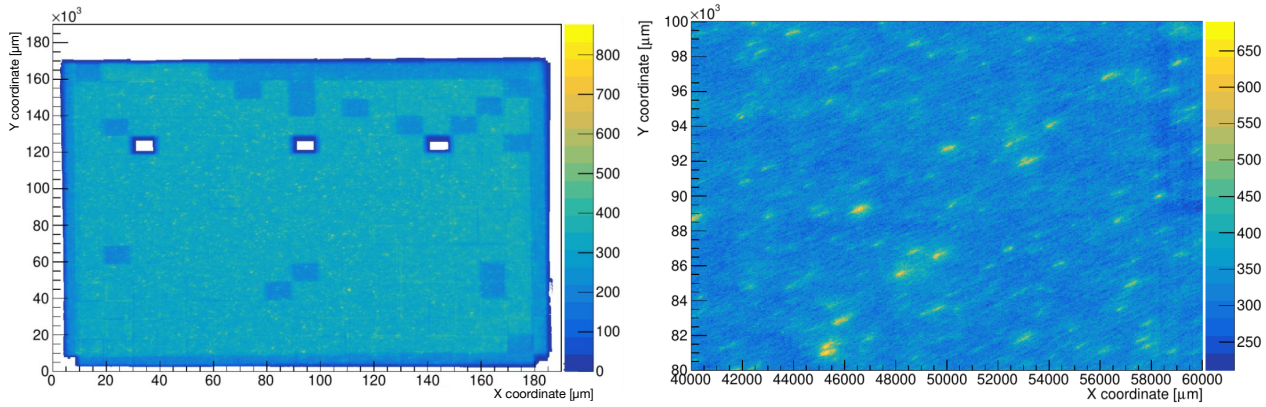

Figure 8.18: Overlay of all emulsion plates of brick 42 in Run 1 from July 2022 to September 2022 (left) and region between 40 mm and 60 mm in X and between 80 mm and 100 mm (right). "Hot spots" are clearly visible.

Hadronic showers are expected to be a negligible background as the length of the nuclear interaction constant implies much larger spatial extension which thus will not be tagged as high density showers. Hot spots are tagged through signal over background thresholds while the cluster centre is tagged through a specially developed technique dubbed *telescopic histograms*.

The telescopic histogram technique was devised to identify the centre of a tagged segment cluster while being resilient to local variations. It operates by rebinning the histogrammed segment distribution with a coarser binning and tagging the most populated one, then returning to a more finely binned distribution and repeating the process until a cluster centre is identified with appreciable resolution.

The algorithm takes a finely binned (for instance $10 \times 10\,\mu\mathrm{m}^2$ bins) histogram dubbed `h1` in the following. The histogram is rebinned with a certain rebinning factor f_r towards coarser binning (for example 5 for $50 \times 50\,\mu\mathrm{m}^2$ bins) dubbed `h2`. This is done recursively until a certain average bin population is achieved (such as one last time for $250 \times 250\,\mu\mathrm{m}^2$ bins in our example) yielding a total of n histograms up to `hn`. The most populated bin of `hn` is then identified and tagged, `hn-1` is then investigated within the corresponding bin limits

of the tagged `hn` bin (within 25 bins of `h2` in our example). This procedure is applied recursively until `h1` is reached, with the most populated bin in a given area being tagged and its centre being marked as cluster centre. The technique is illustrated in toy Monte Carlo in Figure 8.19. The procedure is found to be robust but loses precision with larger f_r. In SND@LHC emulsions, an $f_r = 5$ and $n = 3$ is found to yield good performance.

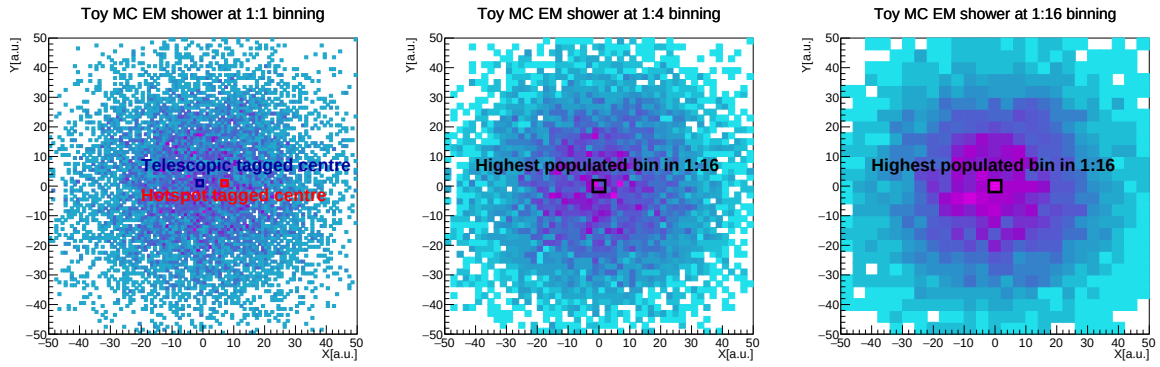

Figure 8.19: Telescopic histogram procedure. The procedure is more robust than simple most populated-bin tagging.

This technique is used to determine shower centres in electromagnetic showers in the following. It is found to be highly accurate, with energy reconstruction (see Section 8.2.1.2) performance using telescopic histograms cluster being almost identical to using MC true interaction point as shown in Figure 8.20.

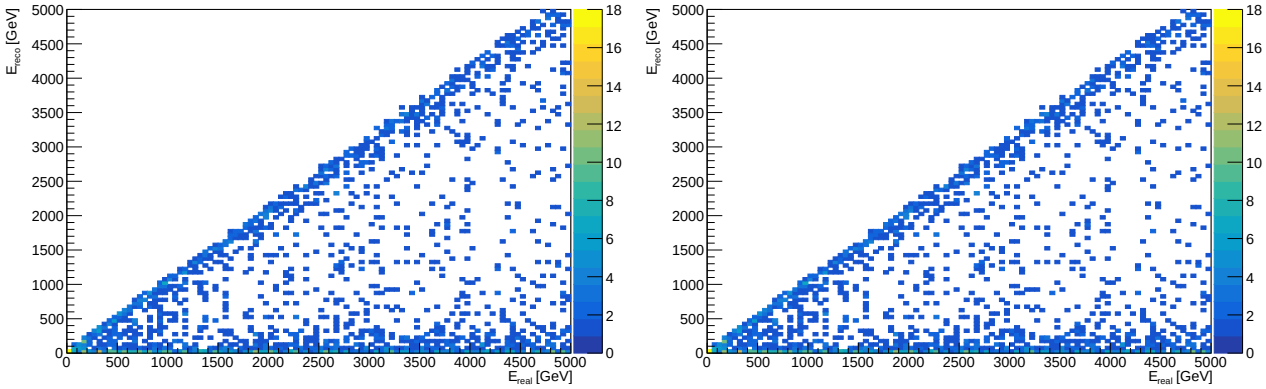

Figure 8.20: Relative energy resolution using Monte Carlo true event origin (left) and telescopic histogram event origin (right) as cluster centre. See Section 8.2.1.2 for details as to the reconstruction, a 1 mm cluster radius is used.

8.2.1.2 Shower energy reconstruction

The emulsion detector can be used as a very-high-granularity sampling calorimeter. It however does not measure charge or light yields the way the technologies described in Section 3.3 do, instead measuring particle counts directly through segments, the number of which are expected to be linear as a function of incoming particle energy as the invisible fraction of the EM shower due to γ is expected to be constant ($\frac{1}{3}$). It is possible to estimate the sampling resolution of the calorimeter (Section 3.2.2) for electromagnetic showers through Equation 3.18 as shown in Figure 8.21.

In addition, ν_e can interact anywhere within the emulsion brick and emulsion brick matching is extremely challenging due to the large distance and induced extrapolation error between walls. This implies that the distribution contain three primary components for any given brick:

- Showers taking place primarily in the brick, for those the energy reconstruction is easiest
- Showers leaking into or leaking out of the brick, for those the energy reconstruction is still possible in some cases but is more challenging

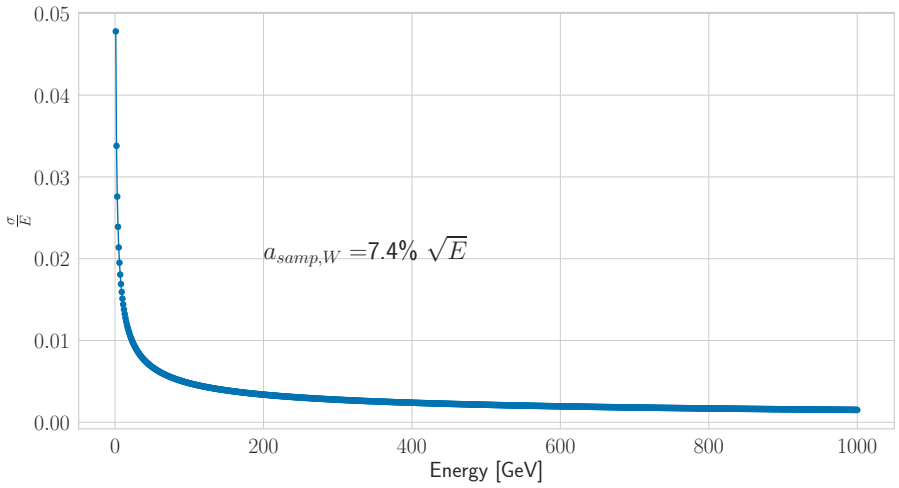

Figure 8.21: Sampling uncertainty for an SND ECC brick.

- Showers taking place primarily outside of the brick, for those reconstruction is done in the brick in question

These different cases were simulated in Monte Carlo by randomly distributing an e^- and π^0 particle gun with energies between 10 MeV and 5 TeV over the entire emulsion detector in the forward direction. The generation and particle counts as a function of incoming particle energy are shown in Figure 8.22. Electrons are produced in the more common ν_e CC interactions and are thus regarded as the main signal study with π^0 being used for reference in NC interactions.

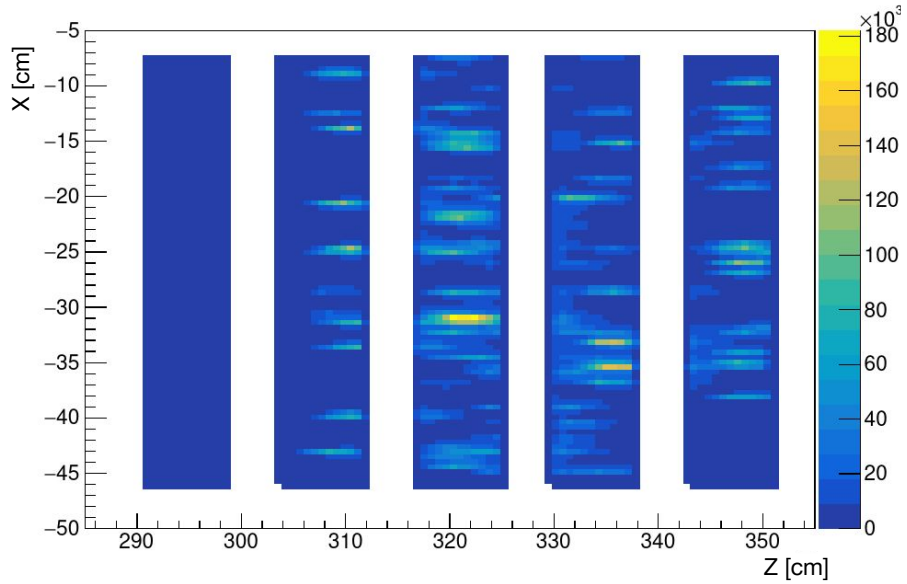

Figure 8.22: 100 π^0 XZ projection with energies between 10 MeV and 5 TeV generated all over the emulsion detector in the forward direction. The beam is oriented towards positive Z.

A distribution similar to that of Figure 8.23 emerges when the amount of segments in a given radius is computed, after tagging the cluster centre using telescopic histograms (see Section 8.2.1.1) has a corresponding equivalent with segments and tracks. The track requirements in this case are made voluntarily lose with only three segments being required in three consecutive plates with a $\chi^2 < 2.4$ after optimisations relating to the amount of plates that are typically traversed by an electron in an EM shower. The clusters are obtained by tagging centres in each of the 20 bricks independently and counting the amounts of segments and tracks in a 300 µm, 500 µm and 1 mm radius for segments and only 1 mm radius for tracks as the loss in stochastic resolution linked to the lack of tracks statistics. The events taking place outside of the showers, present at the bottom of the distributions are removed using a double sliced fit: the distribution profile is taken with and slice into

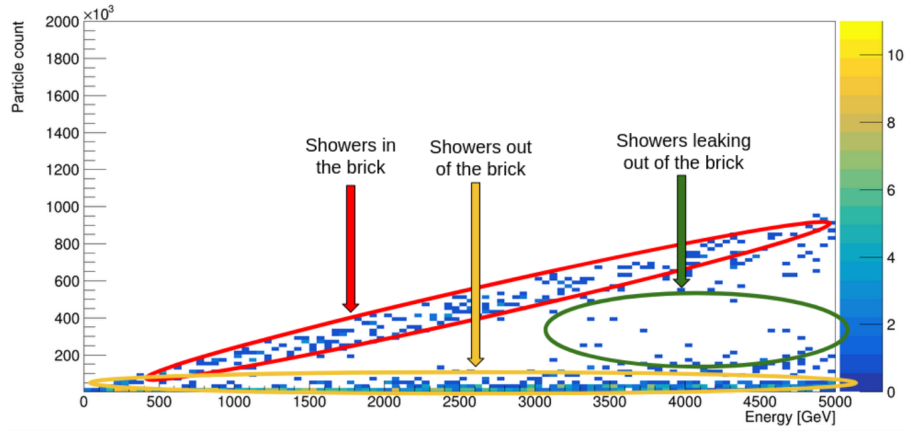

Figure 8.23: The three types of showers observed in a brick as seen in MC. "Empty" MC events taking place outside of the brick all together are also shown here.

N_{slice} energy slices of equal size. Each slice is then fitted with a gaussian distribution and the gaussian means alongside their corresponding fit errors are fitted with a linear function. After the first linear fit, all events taking values below the fitted function are ignored and the process is repeated once. The second linear fit slope is then used to calibrate the relationship between segment counts and the energy of incoming particles. The process is shown in Figures 8.24, 8.25, 8.27 for 1 mm radius.

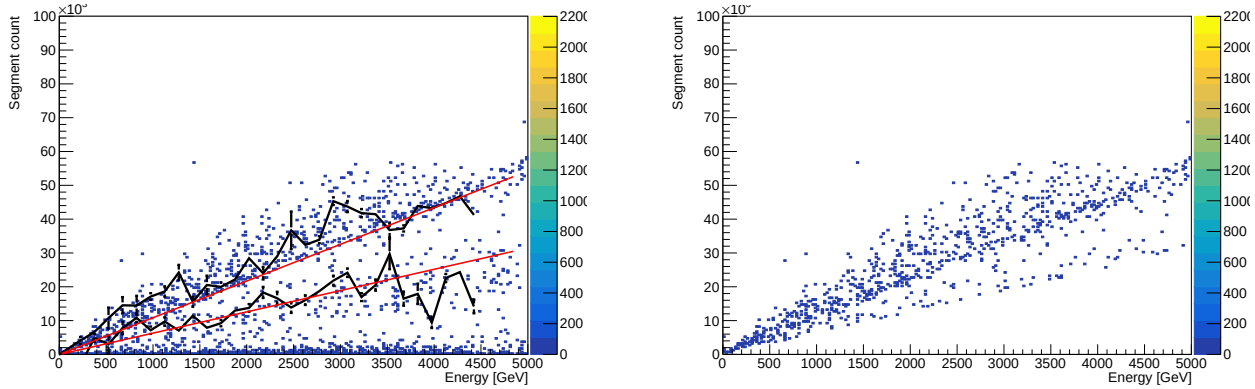

Figure 8.24: Full segment as a function of energy distribution for a 1 mm radius for 1000 π^0 using 30 slices (left) and for a 1 mm radius for 1000 π^0 using 50 slices after first fit cut. The bottom linear function (left) represents the first iteration while the top linear function represents the second function. The fitted slope is found to be 11.55 segments/GeV and 6.29 segments/GeV respectively.

The π^0 distribution is found to be more asymmetric than the e^- one which is interpreted as being caused by the $\gamma\gamma$ start of the shower which causes a greater width to the shower. The amount of slices used in the fit has significant influence on the result and the slice amount in each fit was fine-tuned to maximise fit performance. Nonetheless, the results are highly similar in both cases. The e^- samples were also examined using smaller radii of 500 and 300 µm which yield calibration constants of 10.14 and 8.77 segments/GeV respectively. As CC interactions are expected to be the primary source of ν_e interactions in the target, the electron sample is used to determine the resolution.

Utilising this calibration, it becomes possible to reconstruct EM shower energy which in ν_e interactions will depend on momentum transfer.

8.2.1.3 Energy resolution

Energy resolution is evaluated for the emulsion detector calorimeter through MC in two ways: first the resolution is evaluated for showers taking place at the start of the brick with incoming e^- impinging on the sensitive layer of the ECC. The shower is then maximally contained and the energy can thus be reconstructed as well as possible. The e^- were also generated all over the emulsion detector, leading to varying energy reconstructions depending on the origin point of the e^-, representing the randomness of ν_e interactions over the brick.

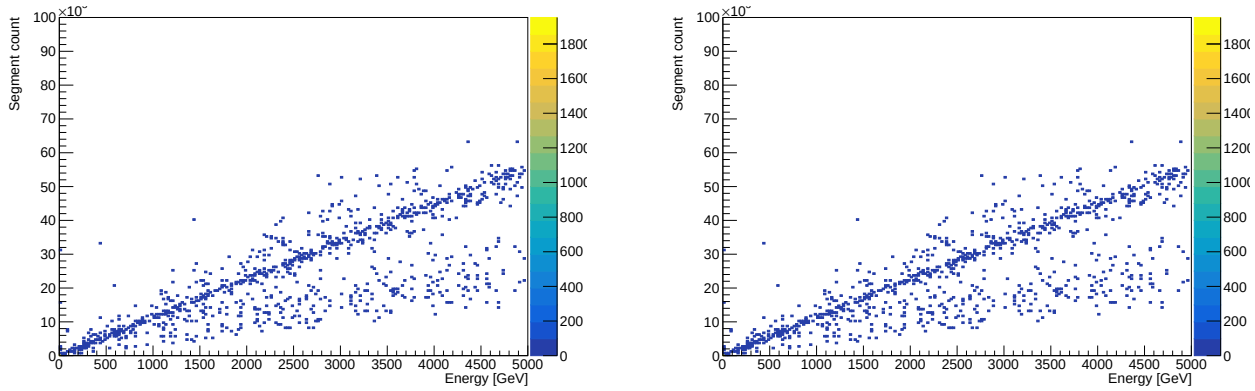

Figure 8.25: Full segment as a function of energy distribution for a 1 mm radius for 1000 e^- (left) and for 1000 π^0 (right). The fitted slope is found to be 11.70 segments/GeV and 2.96 segments/GeV respectively.

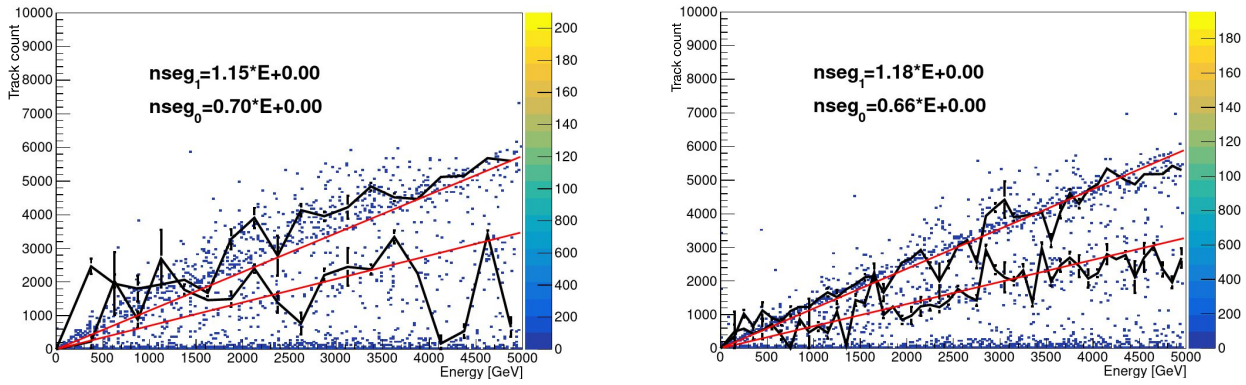

Figure 8.26: Full track as a function of energy distribution for a 1 mm radius for 1000 e^- (left) and 1000 π^0 (right). The bottom linear function represents the first iteration while the top linear function represents the second function.

Figure 8.27

Calorimetric energy resolution of the emulsion detector e^- were generated in samples of 1000 particles each at the start of brick 1 of wall 2 in the emulsion detector. Each sample had particles with energies of {10, 20, 50, 100, 200, 300, 400, 500, 600, 700, 800, 900, 1000} GeV such as to cover a large portion of the range of forwards LHC particles. Each particle energy was reconstructed using the calibration constant computed in Section 8.2.1.2 and each reconstructed energy distribution was fitted with a gaussian. The overall performance as a function of energy was then fitted to obtain the emulsion detector's calorimetric energy resolution for the different evaluated radii. The results are shown in Figures 8.28– 8.34.

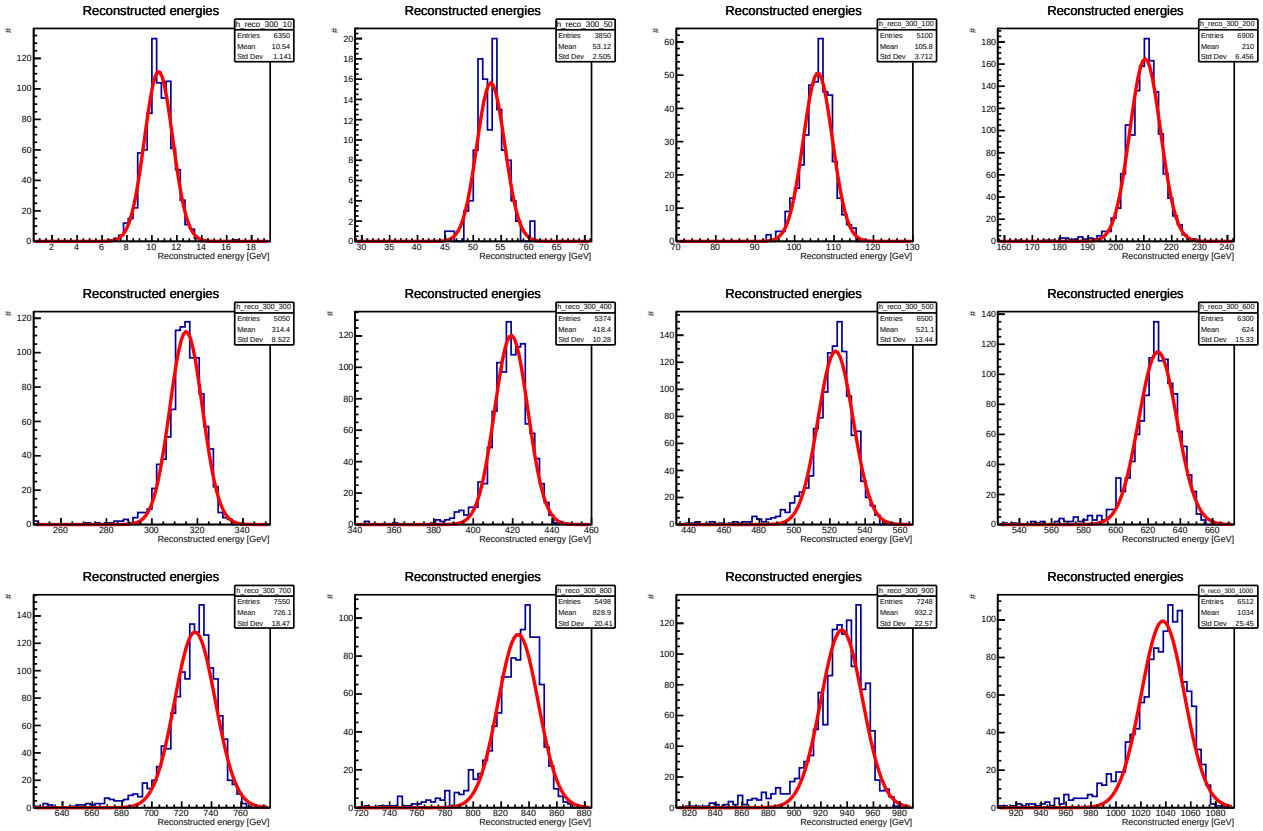

Figure 8.28: Fitted distributions of reconstructed energies using a 300 µm evaluation radius. The incoming electron energies are {10, 20, 50, 100, 200, 300, 400, 500, 600, 700, 800, 900, 1000} GeV from left to right and top to bottom.

The overall reconstruction is generally well centred on the expected value although they degrade at higher energies as a result of leakage. Energy resolution is found to improve with larger radii but remains considerably lower than the expected sampling uncertainty. This is expected to result from three primary factors:

1. The radius can only cover a fraction of all particles present in the shower, at the difference of a time differentiated EM shower which may be evaluated across the entire detector from a more conventional calorimeter such as the SHiP calorimeter system or its prototypes (see Chapters 3 and 7).
2. Furthermore, the emulsion detector suffers from poor efficiency, reaching a typical maximum of 95 %, this adds to the stochastic term and degrades the energy resolution.
3. Finally, the relative importance of each segment is not evaluated with the used technique, which could perhaps be improved upon using topological reconstruction capabilities of the high-position-resolution emulsion detector.

Calorimetric energy resolution as a function of shower starting point As a ν_e-induced shower may in principle start in any point of the emulsion detector, the energy resolution capabilities of the detector are examined as a function of shower starting point. This allows the rescaling of the energy reconstruction based on the identified starting point of the shower. This was done using the generation of e^- all across the detector similarly to what is shown in Figure 8.22. The longitudinal shower start is tagged by identifying the

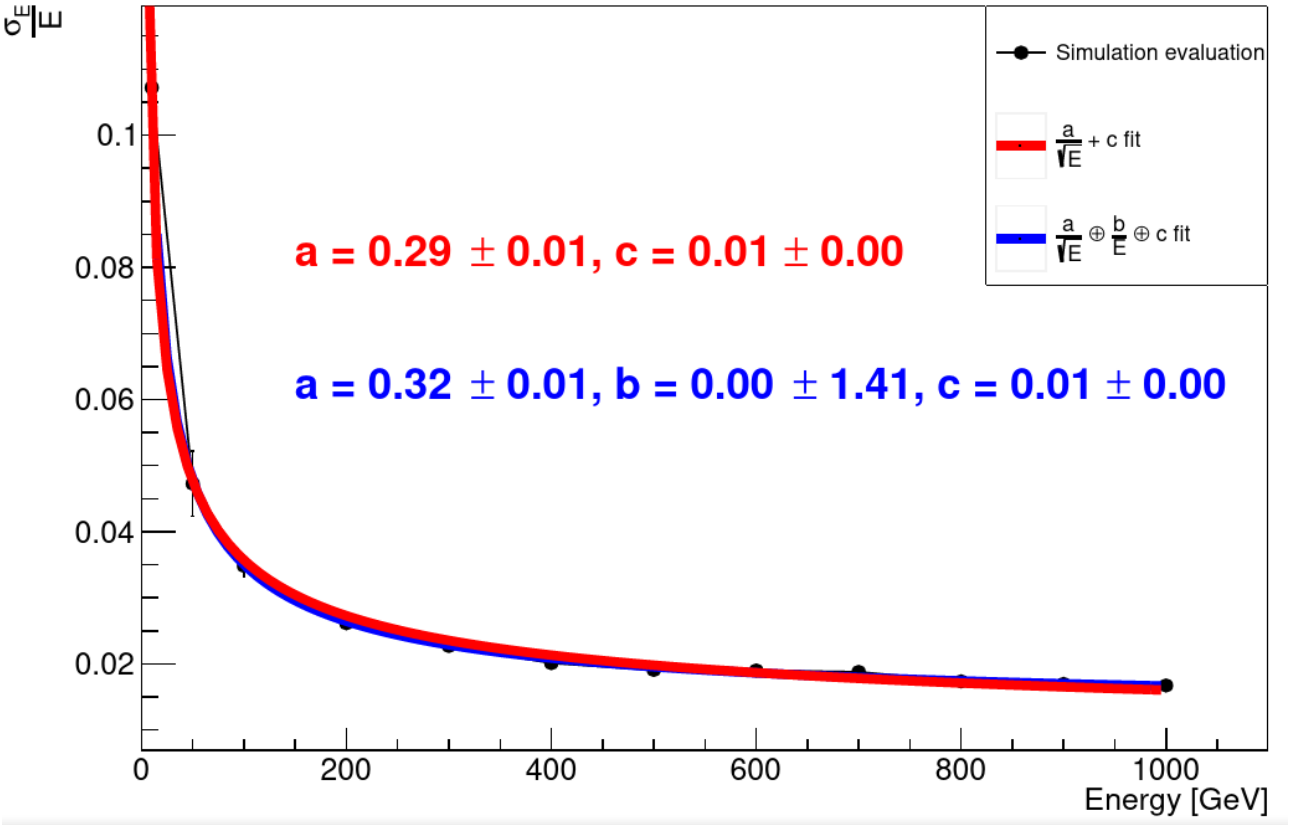

Figure 8.29: Energy resolution in emulsions using a 300 µm evaluation radius.

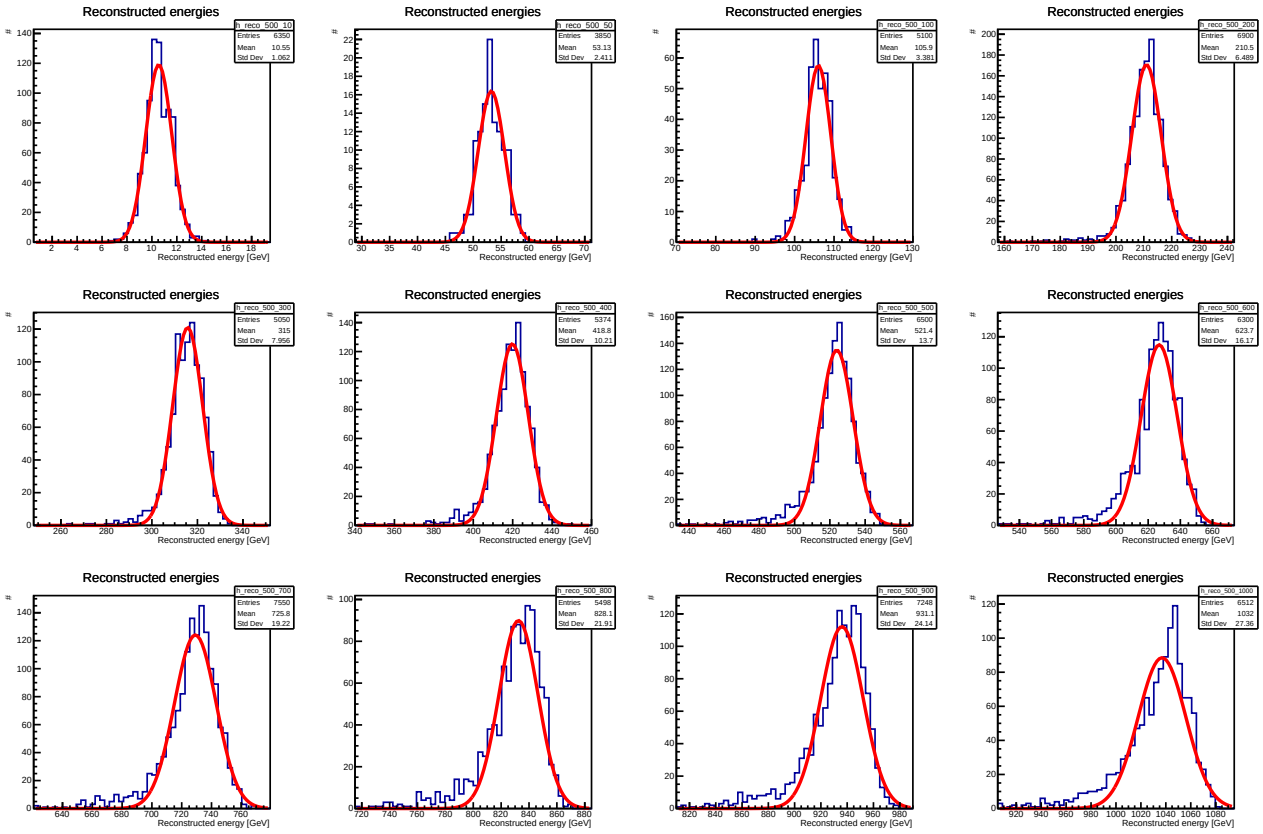

Figure 8.30: Fitted distributions of reconstructed energies using a 500 µm evaluation radius. The incoming electron energies are {10, 20, 50, 100, 200, 300, 400, 500, 600, 700, 800, 900, 1000} GeV from left to right and top to bottom.

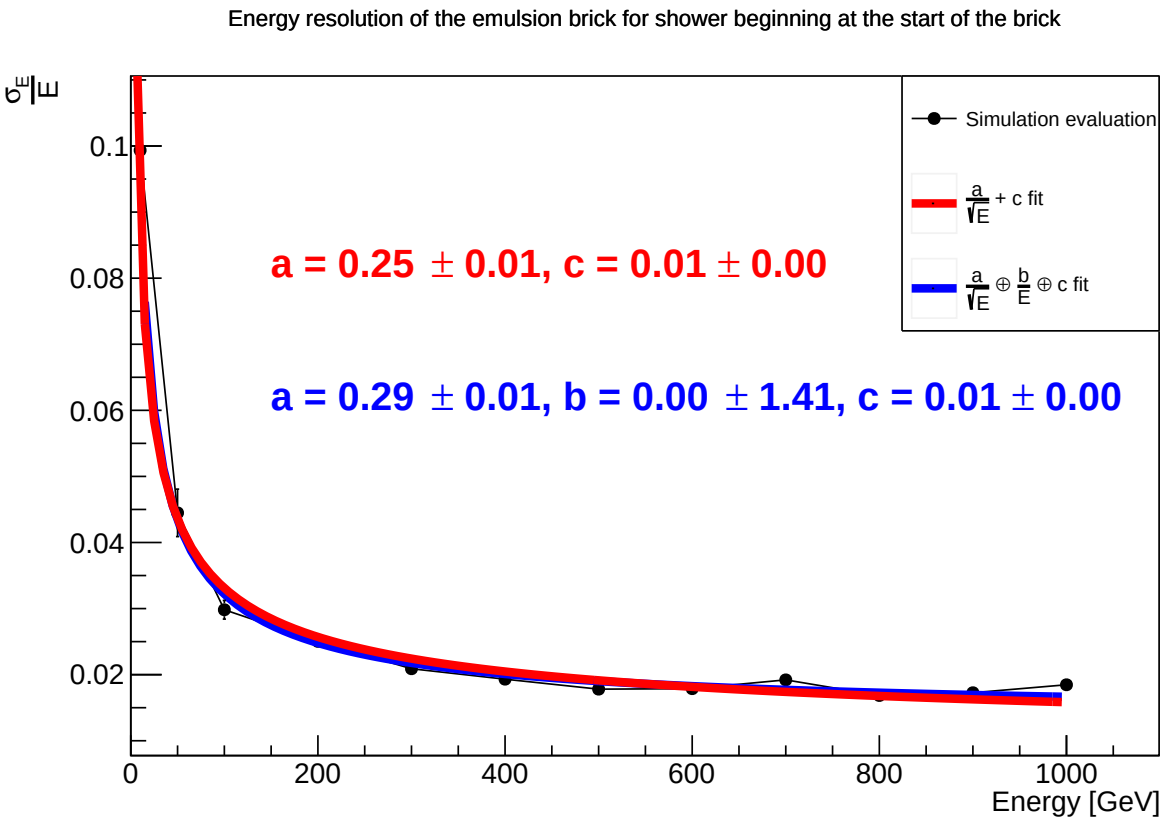

Figure 8.31: Energy resolution in emulsions using a 500 µm evaluation radius.

Figure 8.32

first layer containing at least 5% of the total shower segments within a 1 mm cluster radius. The energy is then reconstructed using the calibration constant determined in Section 8.2.1.3 for a 1 mm cluster radius. This is evaluated for each brick independently and concatenated with the results being shown as a function of distance from the start of the respective brick in Figure 8.35.

8.2.2 Calorimetric study of backgrounds to ν_e interactions

$\nu_e$interactions suffer from three primary backgrounds: μ deep inelastic scattering, μ catastrophic bremstrahlung and ν_μ deep inelastic scattering. The first two backgrounds were investigated in emulsions using Monte Carlo simulation.

8.2.2.1 Muon DIS background

Muon DIS scattering (muDIS), while an uncommon process, remains a significant background in the search for EM clusters because of the abundant muon flux as well its similar signature to EM showers, particularly when the primary interaction took place in the previous wall. The induced clusters are transversally very similar to those EM showers in particular. The amount of induced segments both in total and within a 1 mm cluster radius has been studied as a function of momentum transfer for 10^8 muDIS interactions. This large amount of generated muons is required as the `sndsw` generator is primarily conceived to simulate muDIS interactions in the rock preceding the detector rather than muDIS taking place within it. As a result, the event processor was tuned to ignore muDIS interactions taking place outside of the emulsion detector's acceptance, leading to an inflated initially generated events with $\sim$ 67000 muDIS interactions being conserved and used for analysis. An example muDIS shower is shown in Figure 8.36.

As muDIS constitute a background for EM showers despite not being purely EM processes, an evaluation of segment counts in muDIS interactions was performed. muDIS interactions however may have varying profiles based on the momentum transfer. Hence, the total segment count induced as a function of momentum transfer

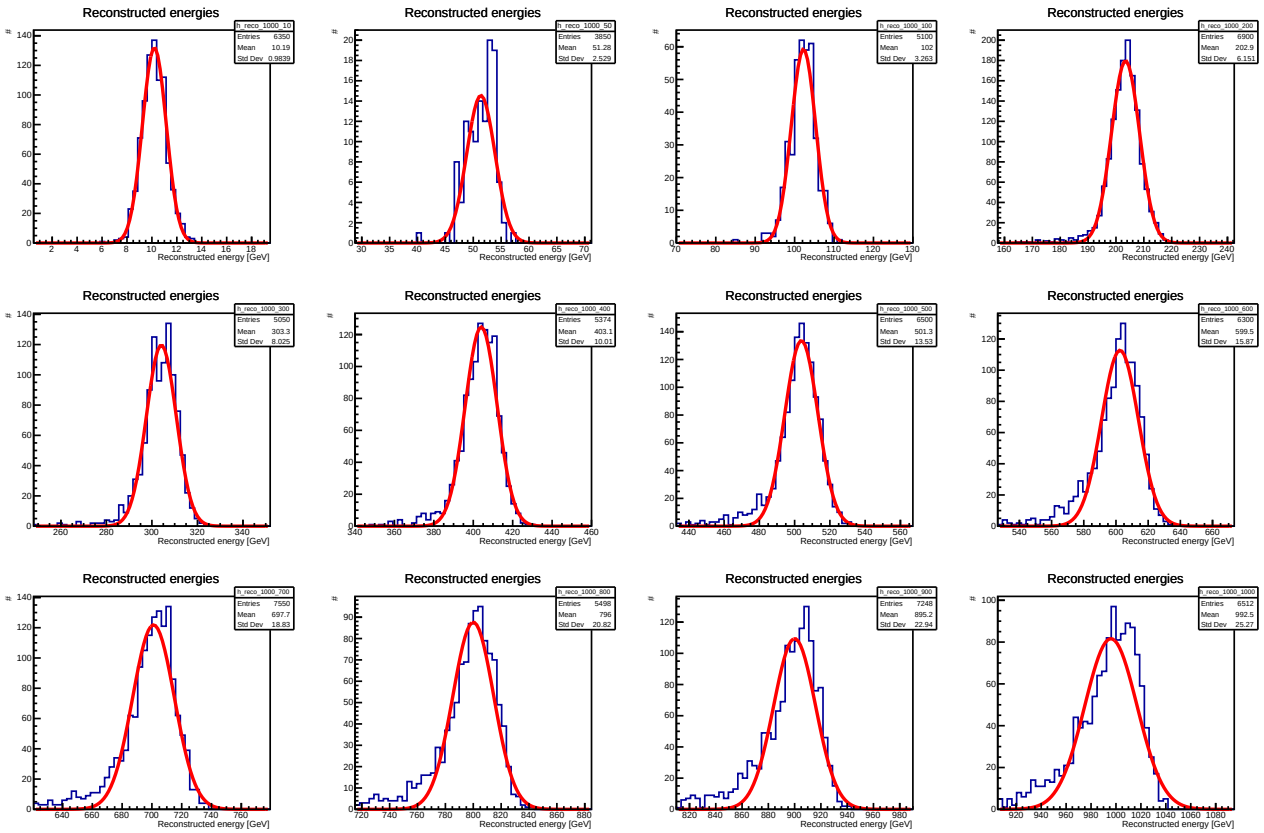

Figure 8.33: Fitted distributions of reconstructed energies using a 1 mm evaluation radius. The incoming electron energies are {10, 20, 50, 100, 200, 300, 400, 500, 600, 700, 800, 900, 1000} GeV from left to right and top to bottom.

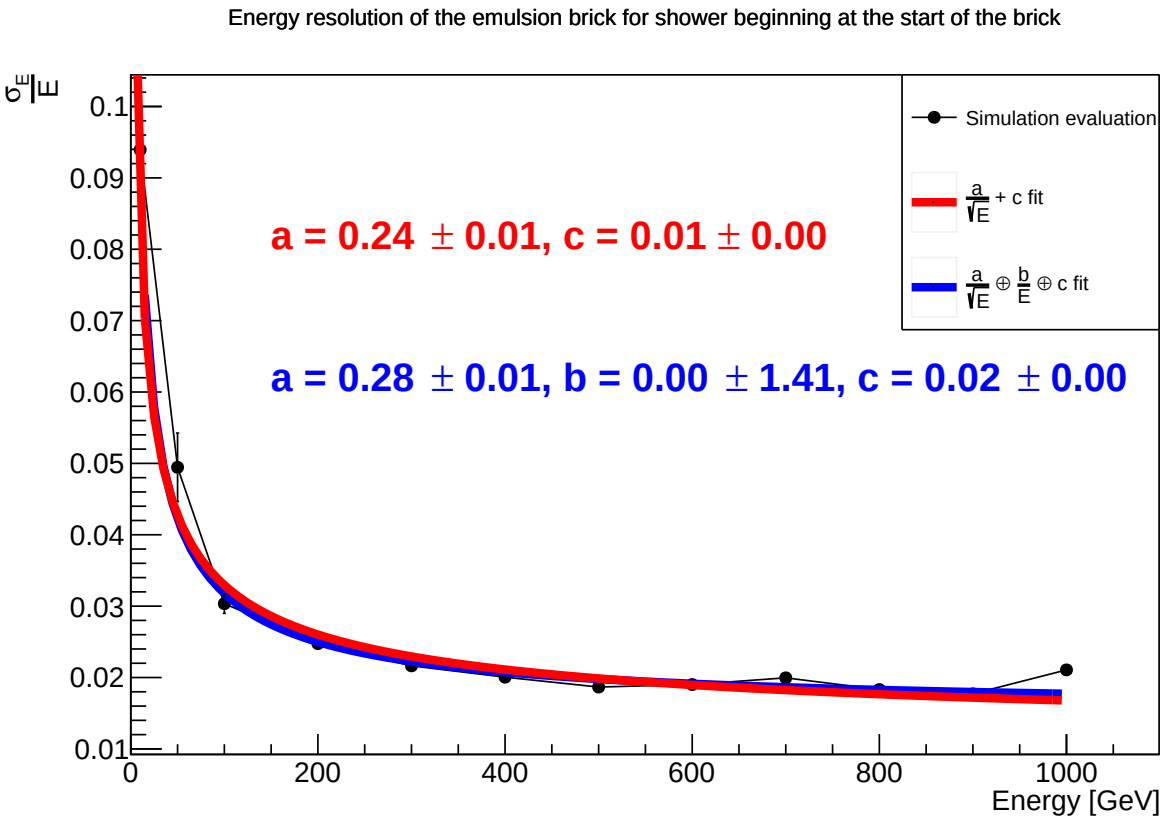

Figure 8.34: Energy resolution in emulsions using a 1 mm evaluation radius.

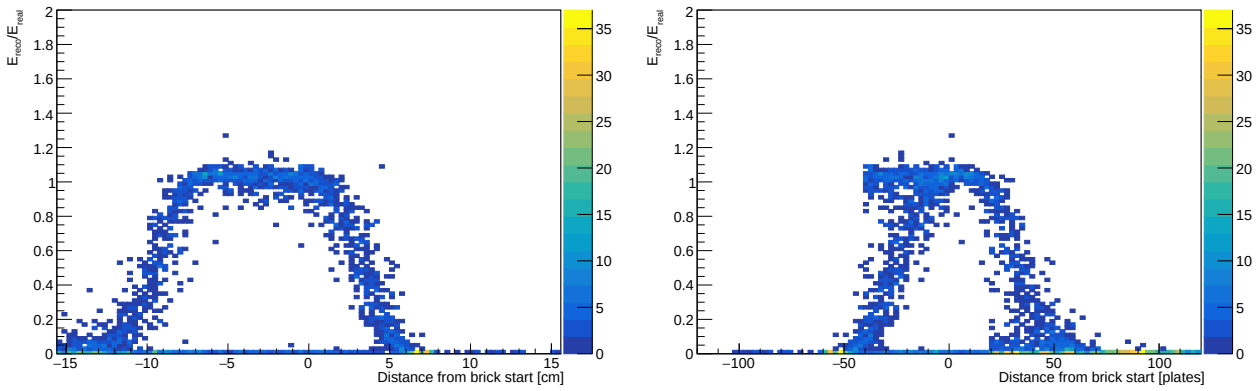

Figure 8.35: Energy reconstruction performance against distance (left) corrected for air distance (right) to considered brick start. Events situated in the first bin row are overwhelmingly events taking place outside of the considered brick.

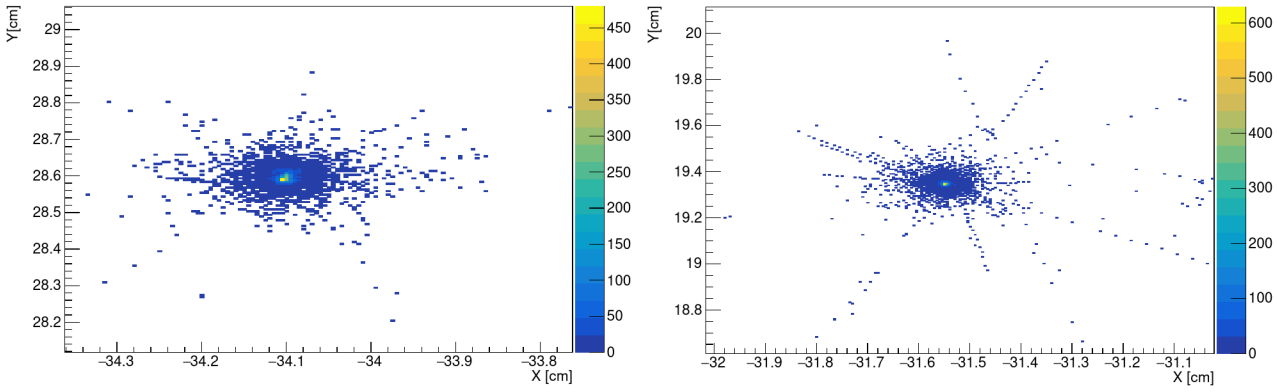

Figure 8.36: Examples of muDIS event stacked segments in the emulsion detector. The events are found to be well collimated and quite similar to electromagnetic showers.

was evaluated as well as that within 1 mm, 500 µm and 300 µm radii of the cluster centre and are shown in Figure 8.37.

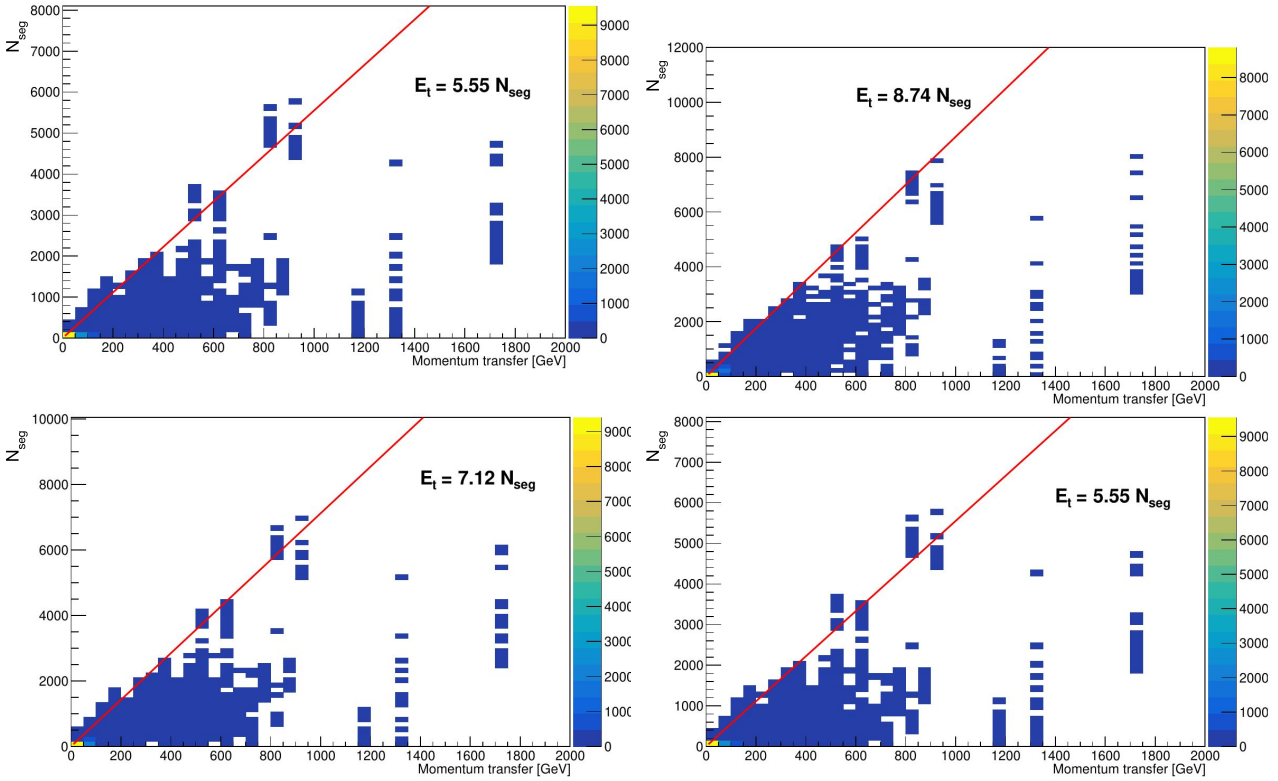

Figure 8.37: Total (top left), in a 1 mm radius (top right), in a 500 µm radius (bottom left) and in a 300 µm radius (bottom right) segment counts as a function of momentum transfer for muDIS interactions in emulsion.

The amount of segments for a given momentum transfer is found to vary significantly as a consequence of the exact process taking place. The maximum segment counts for each energy transfer bin were fitted and it was determined that muDIS leads to generally lower segment counts than electromagnetic showers with a ratio of $N_{\text{segmax,muDIS}}/N_{\text{seg}} \sim 0.7$. This implies that high-energy EM showers suffer from significantly reduced muDIS background with the exact energy cut remaining to be determined from a complete FLUKA simulation accounting for the energy of the muon flux and ensuing muDIS momentum transfer.

8.2.2.2 Muon catastrophic bremstrahlung background

Catastrophic muon bremstrahlung is a rare event which has a $\mathcal{O}(10^{-5})$ probability of occurring at energies $\sim 50\,\text{GeV}$ [342] which slowly increases with higher energies. It involves the muon losing all of its energy through bremstrahlung, forming a compact EM shower. This effect and its segment counts in different radii were studied in a MC sample of 10^5 muons passing through $1 \times 1\,\text{cm}^2$ of the emulsion detector, corresponding to the expected muon flux before a target change. This is displayed in Figure 8.38 and 8.39.

Certain muon events are found to display extremely large segment counts and are interpreted as catastrophic bremstrahlung. The smallness of the differences between the distribution as a function of initial and final energy imply that the amount of loss through bremstrahlung does not directly translate to a segment count per energy loss the same way that EM showers initiated by $e^{\pm}$ or π^0 do. Considering that the segment count for a standard electromagnetic shower is $\sim 10\,\text{GeV}^{-1}$ and that certain catastrophic bremstrahlung showers reach $N_{\text{seg}} \sim 16000 \rightarrow E_{\text{reco}} \sim 16\,\text{TeV}$, this constitutes a severe background which cannot easily be filtered through calorimetric methods, necessitating topological filters, particularly regarding the angle of the shower, these techniques are currently being studied to allow the filtering of this background.

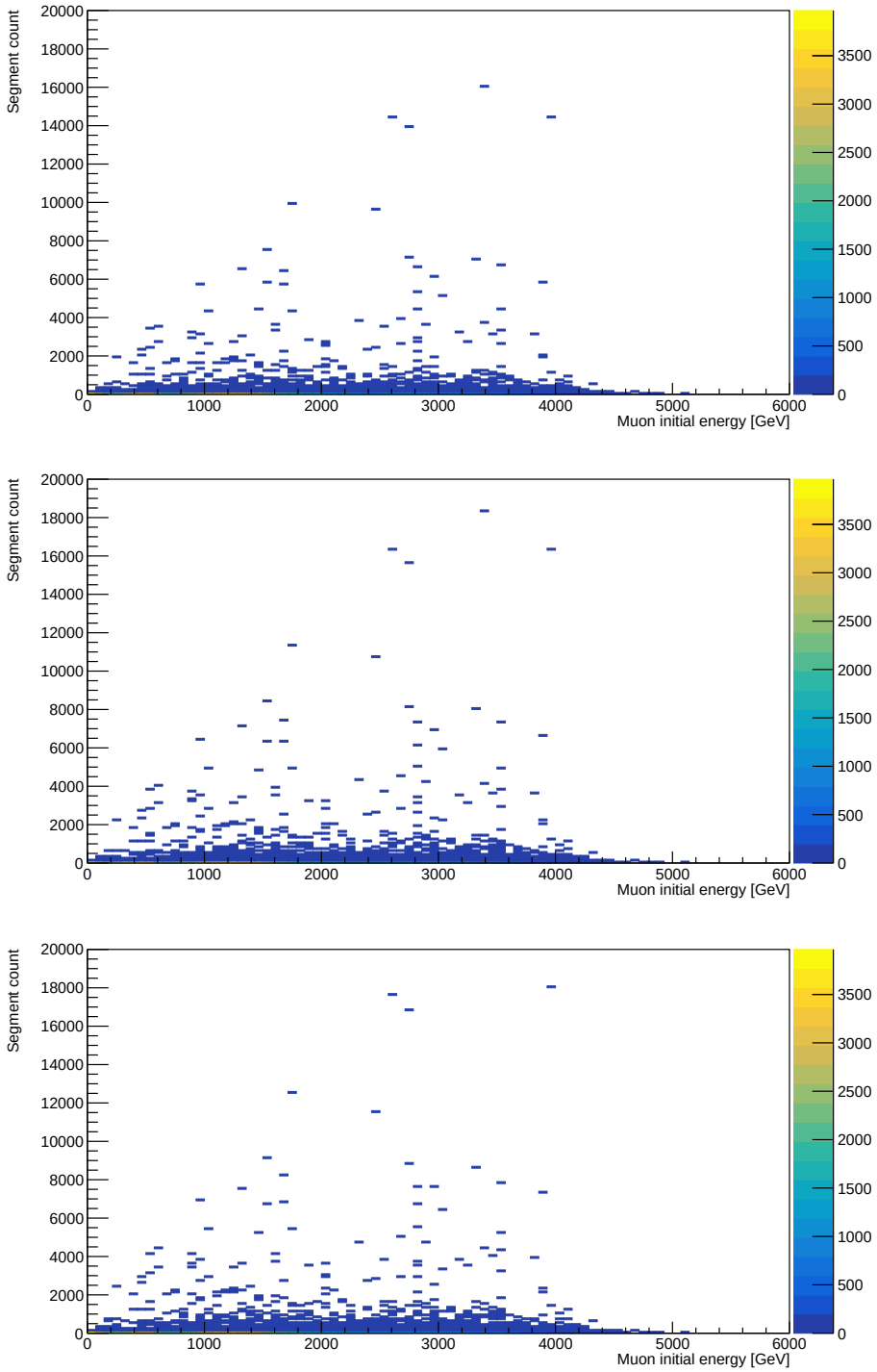

Figure 8.38: Segment counts from passing muons as a function of initial muon energy in a 300 µm radius (top), 500 µm radius (middle) and 1 mm radius (bottom).

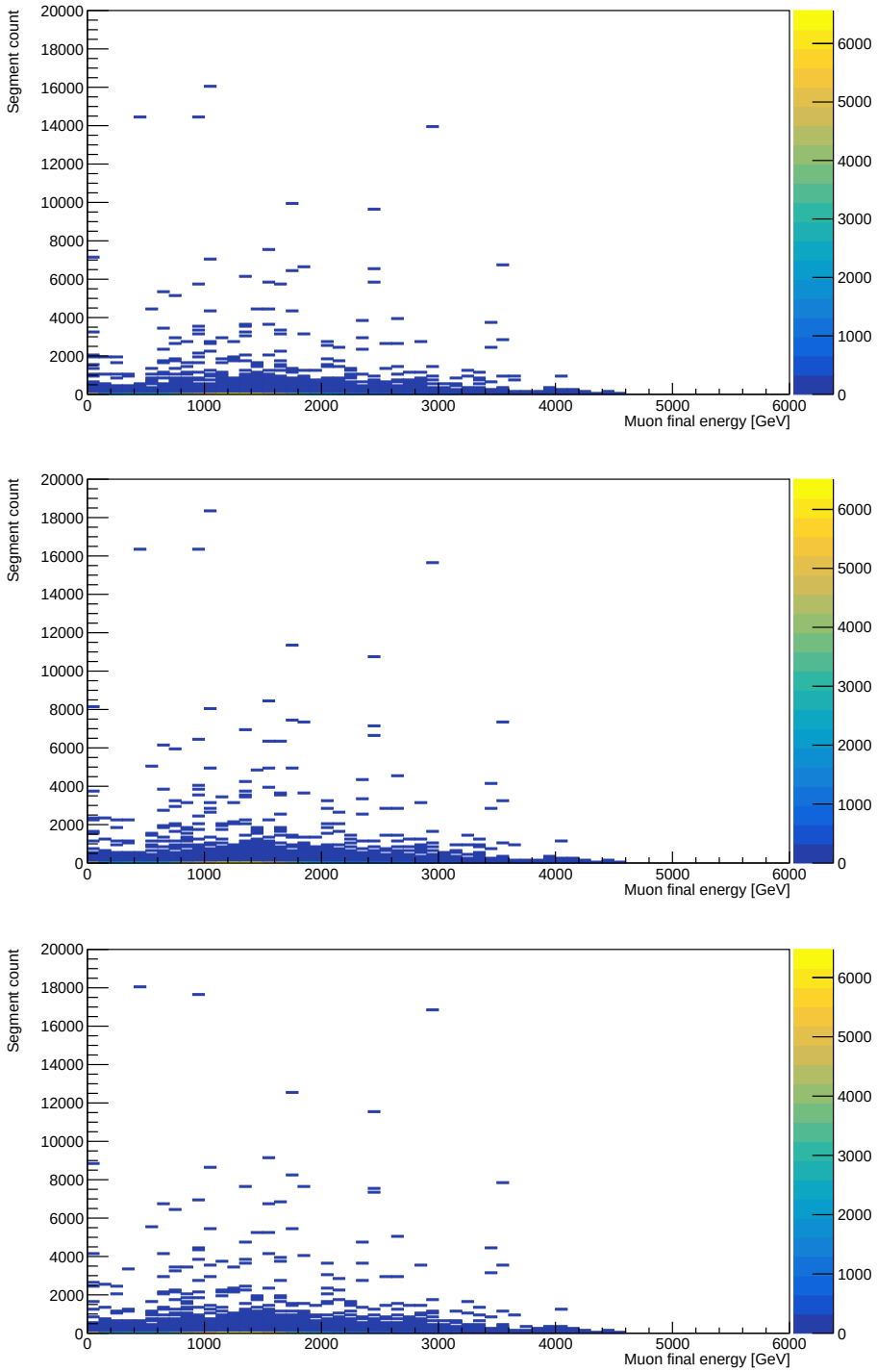

Figure 8.39: Segment counts from passing muons as a function of muon energy when it exists the detector in a 300 µm radius (top), 500 µm radius (middle) and 1 mm radius (bottom).

8.3 Conclusion

In this chapter, SND@LHC physics were carried out with particular investigation of hadronic showers in the HCAL and electromagnetic showers in the emulsion detector. A metric dubbed 90E_radius was defined and used to study both the transversal and longitudinal hadronic shower profile in a replica of the SND@LHC HCAL and instrumented target in test beam data. Furthermore, a centroid reconstruction and shower direction track algorithm was devised and implemented, which is now used in the hadronic calibration of the SND@LHC HCAL. Improvements to this centroid algorithm can be brought by carefully using timing information which is underway.

Calorimetric energy reconstruction was established in the emulsion detector for EM showers, allowing the determination of the energy of the intermediate particle in ν_e interactions which is crucial to their reconstruction and allows to the very clean reconstruction of charm production in the forward direction in the ATLAS experiment. Improvements to this energy reconstruction are expected from better use of the reconstructed shower topology and use of machine-learning techniques such as convolutional neural networks [404]. These techniques were also used to evaluate known backgrounds to $\nu_e$interactions, particularly muon deep inelastic scattering interaction and muon catastrophic bremstrahlung, with the later being expected to constitute a dominant source of background which can be in part filtered using cuts on spherocity :

$$S = \frac{\pi^2}{4}\left(\frac{\sum_i |\mathbf{p}_{Ti} \times \mathbf{n}|}{\sum_i \mathbf{p}_{Ti}}\right)^2, \tag{8.2}$$

which measures the transversal momentum p_T isotropy of the shower compared to the normal $\mathbf{n}$. The reconstruction also relies on realigning EM showers occurring at larger angles which are expected to have an enhanced ν_e origin then subtracting background using control regions. Nevertheless, the very large background amounts, particularly from catastrophic muon bremstrahlung, render reconstruction challenging and the final reconstruction remains underway.

Chapter 9

Conclusion

In this work, calorimetry in the forward detectors at the SHiP PID detector and at the SND@LHC SND HCAL and emulsion detector, was developed in both hardware and software.

The SHiP PID detector will combine good energy resolution, to achieve excellent particle identification capabilities and exceptional angular resolution to reconstruct shower directionality from neutral final states. The physics case for the SHiP calorimeter system was developed and requirements on its reconstruction capabilities, detector technologies, readout electronics and data acquisition were established.

The physics studies had a particular focus on $\gamma\gamma$ final states invariant mass reconstruction, which should be complemented by vertexing resolution studies which are necessary to ensure that the final state originates from the decay volume and to reject backgrounds from electromagnetic debris in particular. Furthermore, other channels, such as HNLs, Dark Photons, Dark axions should be investigated as well as they feature significant neutral final states which only the SHiP ECAL can observe, particularly at higher masses. Dedicated particle identification studies are also being done to demonstrate the detector's capabilities in general background rejection, particularly with regards to muons.

An extensive optimisation of the optical properties of scintillators and their coupling to SiPMs was carried out which extended to both software advances through the `Fibresim` framework and laboratory studies of means to improve light collection from $1 \times 6\,\mathrm{cm}^2$ cross section scintillators and WLS fibres. A simple optimised scintillator bar was established which allowed to double the amount of light collected from the references with more complex improvements being available for further upgrades. Further studies can be lead, particularly with regards to the value of a found optimised scintillator geometry together with WLS fibres traversing it. Moreover, the experimental determination of the output angular distribution of photons from WLS fibres is of key value, with a possible setup being proposed. The determination of the value of higher photon trapping efficiency against higher capture efficiency through different optical indices of optical cement when glueing the WLS fibres to the scintillator can also lead to better light output from the fibre. The `Fibresim` toolkit is being expanded to include greater precision in its photon distributions within the fibre with dependency on the input being accounted for as well as better accounting of the effects of phononics in SiPM response. In addition, quality of life upgrades such as an in-built analyser and a GUI are being implemented as well, with the code to be integrated into the `Fairship` software as a plugin for scintillator detectors.

Four different readout options for the SHiP calorimeter system's SiPMs were investigated with two of them being tested in test beams. A custom solution based on the KLauS chip from Heidelberg was designed, produced and evaluated along with a custom data acquisition scheme. While the chip was found not to be ideal for the SHiP calorimeter system, it was found to be a workable backup solution given a few design updates. A commercial DT5202 solution from CAEN was also evaluated and tested in test beams but was found not to be applicable outside of conceptual testing. A preferred solution, the CALOROC1b, was identified and is currently in production at the time of writing. A preliminary DAQ scheme for the SHiP calorimeter system was established with a focus on early digitisation of the signals with data processing, timestamping and slow and fast control being done on a single board per SHiP calorimeter module, ensuring full modularity of the design and compliance with SHiP DAQ standards.

A custom prototype was built using the optimised scintillator bars and these readout electronics with three test beams at DESY and PS@CERN having been conducted to evaluate it. These have validated the custom KLauS electronics and have yielded energy resolution consistent with expected sampling stochastics across all different beamlines. In addition $e^{\pm}$ particle separation capabilities were demonstrated. A higher energy energy

test beam at SPS is being performed at time of writing to evaluate a similar full 20 X_0 ECAL prototype and a $36 \times 36\,\mathrm{cm}^2$, $5\lambda_a$ HCAL prototype using the same scintillator bars and electronics. Further test beams are foreseen to evaluate the readout electronics and data acquisition systems which are currently under development, as well as the addition of GEM-based high precision layers into the ECAL to fully demonstrate the SplitCal concept.

The detector's final design will benefit from these studies which have identified the issue of SiPM saturation. This problem is particularly apparent for smaller SiPMs with few pixels. Indeed, large showers (see Section 6.1.1) yield a large amount of electrons which themselves translate to intense light yields. If each electron for such a shower is conservatively assumed to be a MIP and 10 PEs are assumed to be the light yield of each MIP in a thin scintillator bar which is coherent with observations, the expected light yield for a $\sim 200\,\mathrm{GeV}$ shower would be $\sim$ 180000 PE-equivalent in $\sim$ 3 bars or an average of $\sim$ 60000 PE per bar. The currently used S13360-1325PE SiPMs have 2668 pixels and SiPMs are known to suffer from noticeable saturation above $\sim 10\,\%$ of their total pixel count being fired. This implies that for saturation effects to remain limited in thin bars, $\sim$ 600000 pixels would be ideally be needed. Some of the best SiPMs on the market display $\sim$ 360000 pixel [405] and would be expensive to equip the entirety of the thin bars. As thin bars rely heavily on charge averaging to enable good reconstruction, SiPM saturation would make them tend towards their 1 cm intrinsic resolution. This implies that in order for thin bars to aid in resolving the shower directionality, they would preferentially placed at the beginning and the end points of the EM shower. HPLs would be placed at the shower maximum as their greater resolution makes them less effected by saturation, which they are regardless more likely to undergo as a result of their readout electronics [406]. The design implications are shown in Figure 9.1.

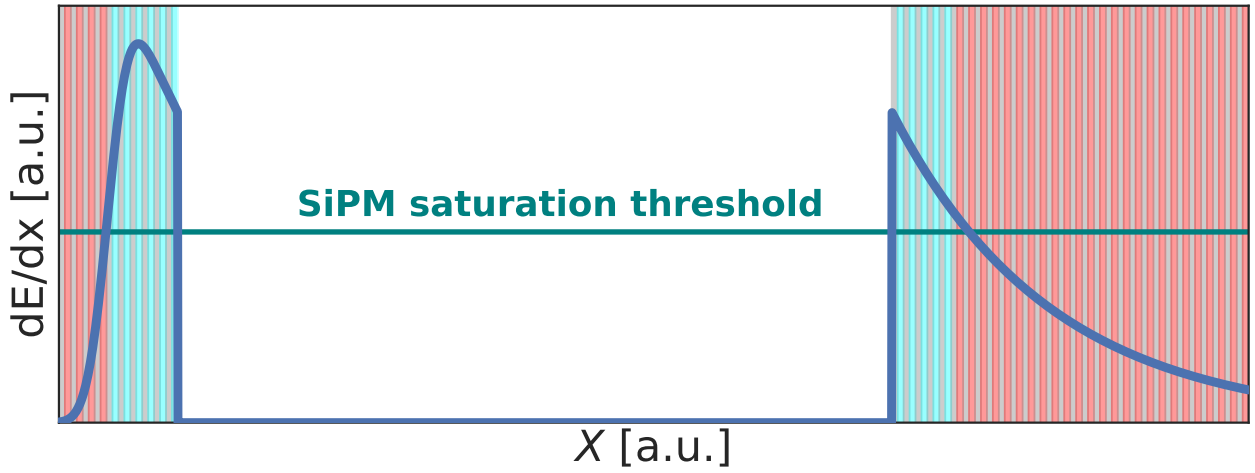

Figure 9.1: Schematic representation of the SplitCal. The blue curve represents energy loss induced by an electromagnetic shower which assumes the shower starts early. The teal represents the energy loss threshold above which the thin bar's SiPMs will saturate. As a result, the red bars are relevant positions for thin scintillator bar layers whereas the cyan ones are relevant positions for HPLs. The gray bars are passive material.

The uncertainty as to the photon showering location also suggests that increasing the depth of the calorimeter may be desirable to enable the reconstruction of particle energy.

Hadronic shower studies were performed at SND@LHC as part of the wider effort to calibrate the experiment's HCAL. This has lead to characterisation of shower profiles with the definition of a new metric, the 90E_radius which allows to evaluate both the transversal and longitudinal profile of hadronic showers. The low granularity of the HCAL was also in part compensated using the definition of centroids as defined in conventional trackers [296] which has contributed towards shower selection, necessary for detector calibration. The HCAL calibration is still ongoing at the time of writing and will allow to more effectively reject background in ν_e and ν_τ searches which will enable to observation of charm-induced events.

This work has also seen the establishment of electromagnetic calorimetry in emulsions which are now used in the search for collider ν_e in the SND@LHC emulsion detector together with the calorimetric background characterisations of muon deep inelastic scattering and catastrophic bremmstrahlung. Further improvements

in emulsion calorimetry are currently being developed, involving topological reconstruction of the shower and machine learning through convolutional and graph neural networks. The background studies are currently being refined with further metrics such as segment angles within the shower, allowing for the enhancement of signal while reducing the background. This will be used to observe charm decays in SND@LHC and hence enable refinements in QCD physics such as in low-x particle density functions.

Overall, this work has contributed to developing calorimetry in the forward direction and the SHiP calorimeter system, with many of the technologies, software packages, studies and techniques developed here being now used as the state of art for the continuous detector development of SHiP, both in its SND and downstream calorimeter.

Appendix A

Particle acceleration

A great deal of high-energy particle physics research is nowadays done through the use of particle accelerators, as they are the state-of-art mean in reaching high energies in a controlled environment. Particle accelerators have developed greatly since the first patent by Ernest Lawrence in 1932 [407] but generally function using the Lorentz force through the famous $\mathbf{F} = q \cdot (\mathbf{E} + \mathbf{v} \times \mathbf{B})$ (with q the charge, $\mathbf{E}$ the electrical field, $\mathbf{v}$ the velocity and $\mathbf{B}$ the magnetic field). Seeing as particle speed typically is often neighbouring the speed of light in high energy physics, the context dictates that magnetic fields are much more effective in accelerating particle than electrostatic accelerators. Accelerators usually accelerate particle beams which are in turn bent and focused at different stages of the accelerator through dipole and quadrupole magnets respectively. The accelaration function is fulfilled by so-called *Radiofrequency acceleration* (RF acceleration)[408] which function around the injection of radiofrequency voltage to create electric fields. For instance, the first RF linear accelerator from Rolf Widerröe in 1928 was based on a drift tube between two grounded electrodes connected to an RF source which delivered $E = 25\,\mathrm{keV}$ with $f = 1\,\mathrm{MHz}$ frequency. The RF source voltage V_{RF} may thus be increased through the number of gaps N which leads to an increase in the energy gain ΔE of a particle with charge q through $\Delta E = qNV_{\mathrm{RF}}$. The principle is shown in Figure A.1.

The longer drift tubes needed for higher frequencies and their antenna behaviour in those conditions are leading to high levels of radiation which constitutes the main limitations of this design. As such, modern accelerators see their efficiency further boosted by *Radiofrequency cavities* (RF cavities) which are conducting cylinders containing the aforementioned principle which reduces starkly the amount of radiated energy. The cylinder diameter, distance between the drift tubes and their own diameters are then set in such a way that synchronism $l_{\mathrm{N}} = \frac{v}{2f}$ is achieved for a given particle speed v.

Broadly speaking, two distinct types of accelerators geometries exist: the aforementioned linear accelerators and the circular accelerator. Linear accelerators [409] [410], using constant velocity and constant RF frequency are typically preferred in the case of light particles, particularly electrons, as accelerated particles mainly lose energy through *synchrotron radiation* which is a variant of *Bremsstrahlung radiation* in magnetic fields and characterized by the emission of photons by a charged particle and defined in natural units as:

$$\frac{\mathrm{d}\sigma_{\mathrm{rad}}}{\mathrm{d}E} = \frac{4\alpha^3}{m^2} Z^2 \frac{F(u,T)}{E}, \tag{A.1}$$

where $u = \frac{E}{\gamma m}$ is the ratio of the photon energy to the projectile energy, T is the kinetic energy of the particle while α is the EM fine-structure constant and E the energy of the particle. $F(u,T)$ can be fairly complex and is reviewed in [411]. The key characteristics of Equation A.1 is the dependence of the cross section on the inverse of the particle mass squared $\frac{1}{m^2}$, this explains that lighter particles are more susceptible to losing energy when bending and the maximum attainable energy is thus determined by their length and of course by their B-field intensity.

The other type of accelerator are synchrotrons which (typically) utilize changing velocity and variable RF frequency. As their name may imply, these accelerators seek to limit synchrotron radiation as the maximal momentum of their beams are impaired by it, consequence of their circular geometry. They are therefore particularly useful to accelerate heavy particles such as protons.

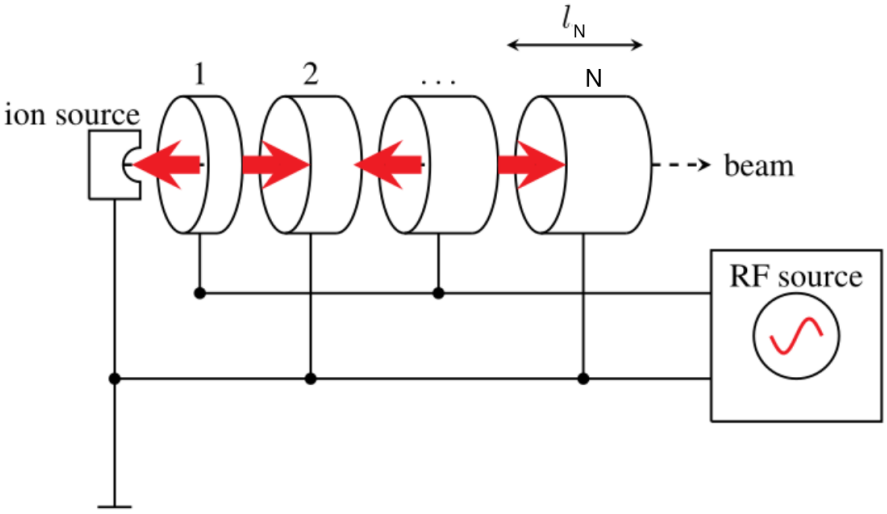

Figure A.1: Functioning principle of Wideröe's linear accelerator. The electric fields between the drift tubes accelerate the particles [408].

Appendix B

SHiP sensitivity to BSM models

The sensitivity of SHiP to BSM is fully complementary to collider experiments as explained in Section 2.3. This can be seen in Figure B.1:

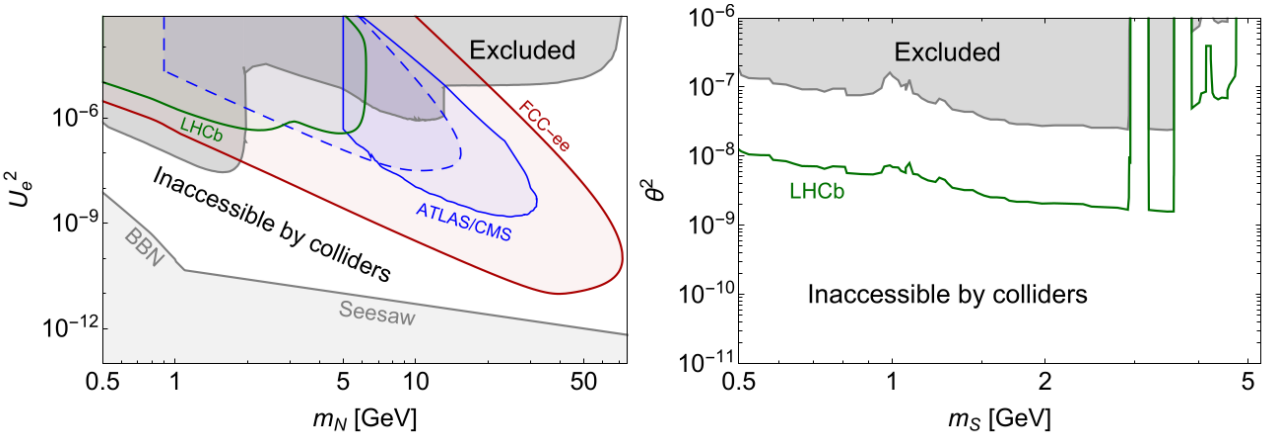

Figure B.1: Potential of current and future colliders for HNL searches (left) and dark scalar searches (right). Big Bang Nucleogenesis restricts the mass of any heavy right-handed neutrino [220]. Neutrino seesaw is defined when $U^2 = |U_{e-}|^2 + |U_{\mu-}|^2 + |U_\tau|^2$, whereas HNLs with total mixing below the seesaw line do not contribute to neutrino mass generation [26].

In light of this inability of collider experiments to probe the low GeV mass range, beam-dump experiments such as SHiP are particularly appropriate, as can be seen in Figure B.2:

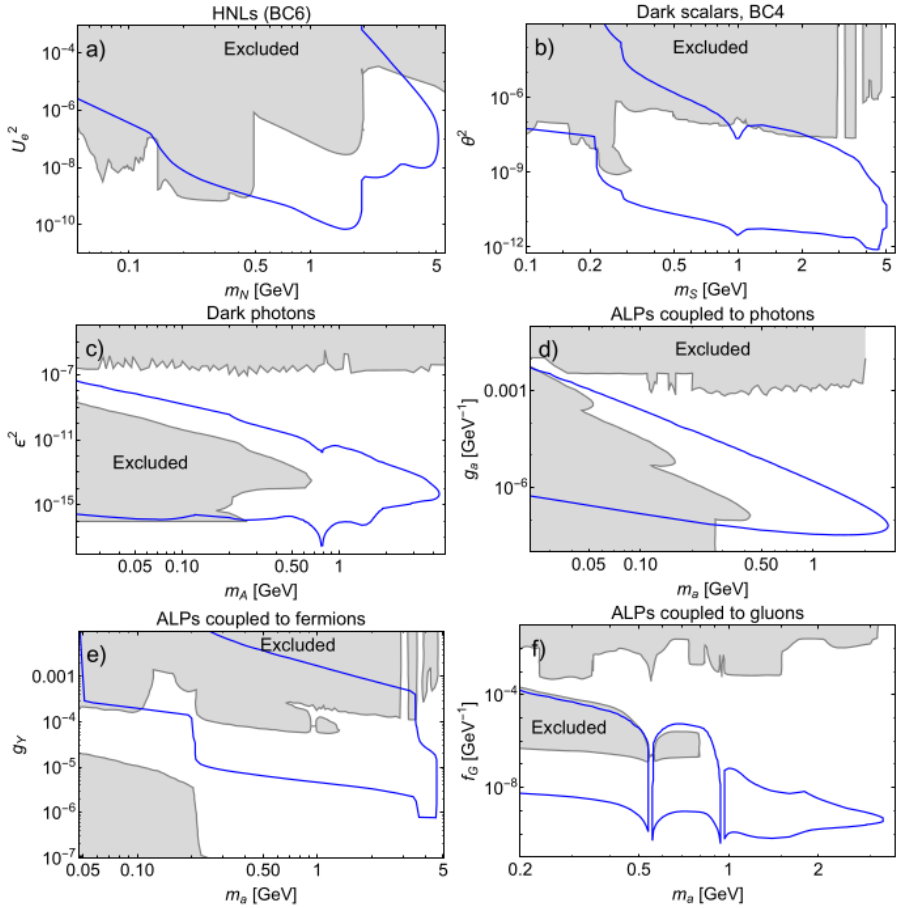

(a) SHiP sensitivity with 6×10^{20} PoT to different BSM channels: a) HNLs coupled to the electron neutrino flavour, b) dark scalars mixing with the Higgs boson and with $\mathrm{Br}(H \to SS) = 0$ (BC4), c) dark photons, and axion-like particles coupled to d) photons, e) fermions, and f) gluons [26].

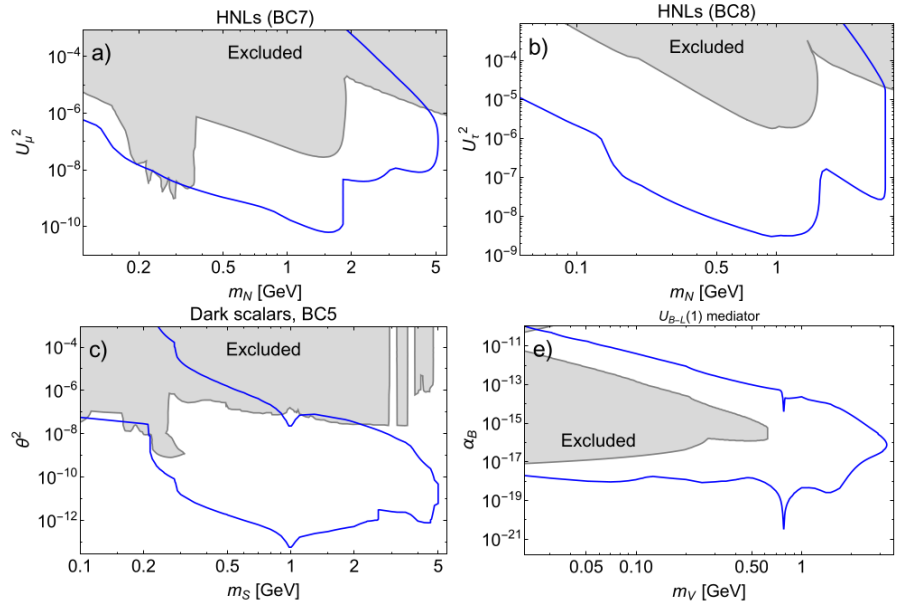

(b) SHiP sensitivity with 6×10^{20} PoT to different BSM channels: HNLs coupled to the muon a)or tau b) neutrino flavour, c) dark scalars mixing with the Higgs boson and with $\mathrm{Br}(H \to SS) = 0$ (BC5), d) and $U(1)$ mediator coupled to the anomaly-free combination of the baryon and lepton currents B−L [26].

Figure B.2

Appendix C

Complements to light optimisation

C.1 Foil optimisation result for each setup

The results for crumpled and smooth foils for a given set of three scintillators exposed to cosmics are shown in Figure C.1. Measurement details are found in Section 5.4.3.

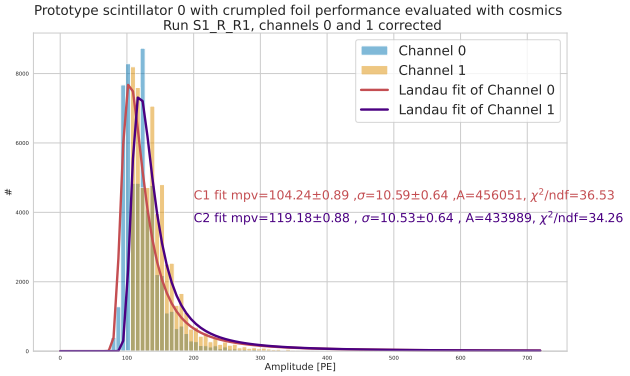

(a) Crumpled foil Scintillator 0.

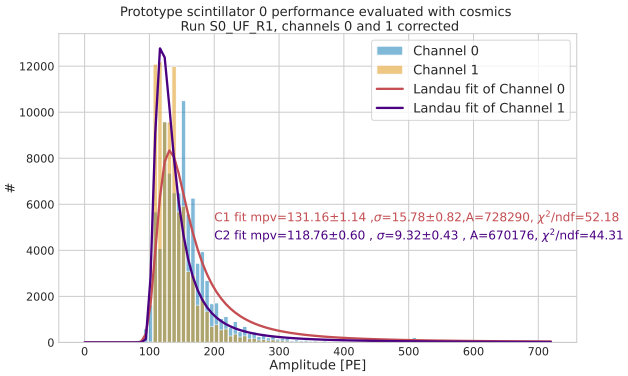

(b) Smooth foil Scintillator 0.

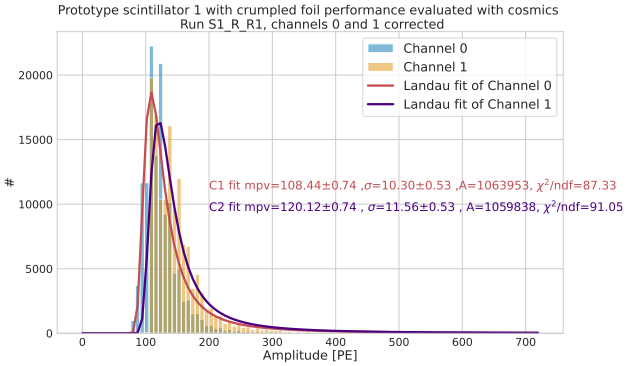

(c) Crumpled foil Scintillator 1.

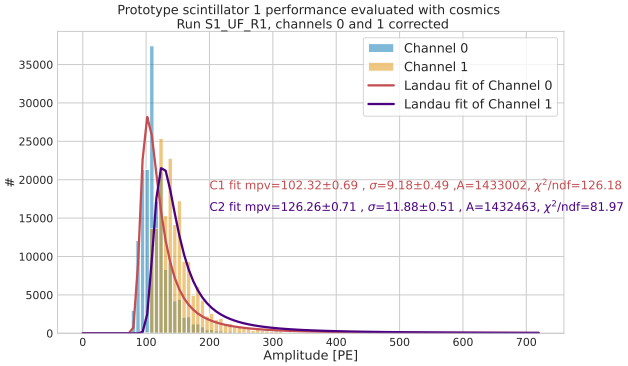

(d) Smooth foil Scintillator 1.

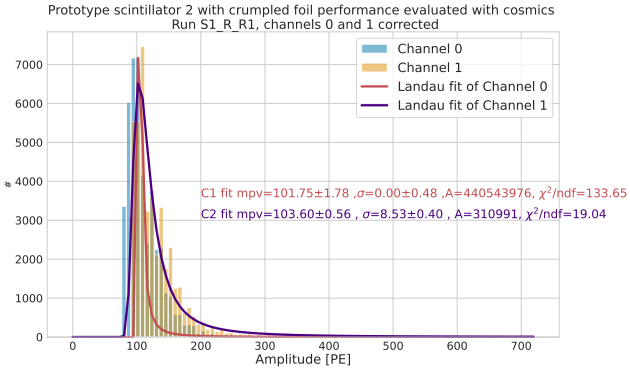

(e) Crumpled foil Scintillator 2.

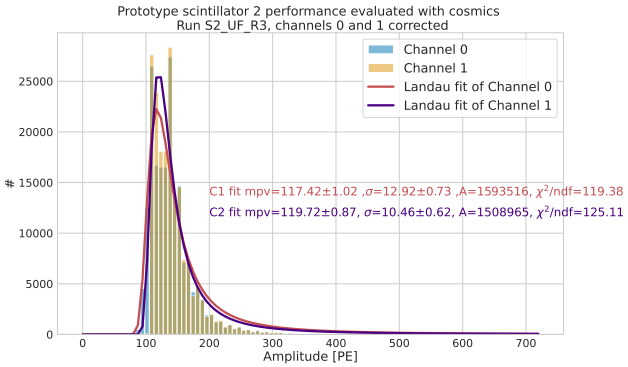

(f) Smooth foil Scintillator 2.

Figure C.1: Crumpled and smooth foil light output in all configurations.

C.2 Complements to fibre light output

Exposure of a SiPM at various distances from fibres directly irradiated by the laser yields the distributions shown in Figures C.2 and C.3 for round and square reflective walls respectively.

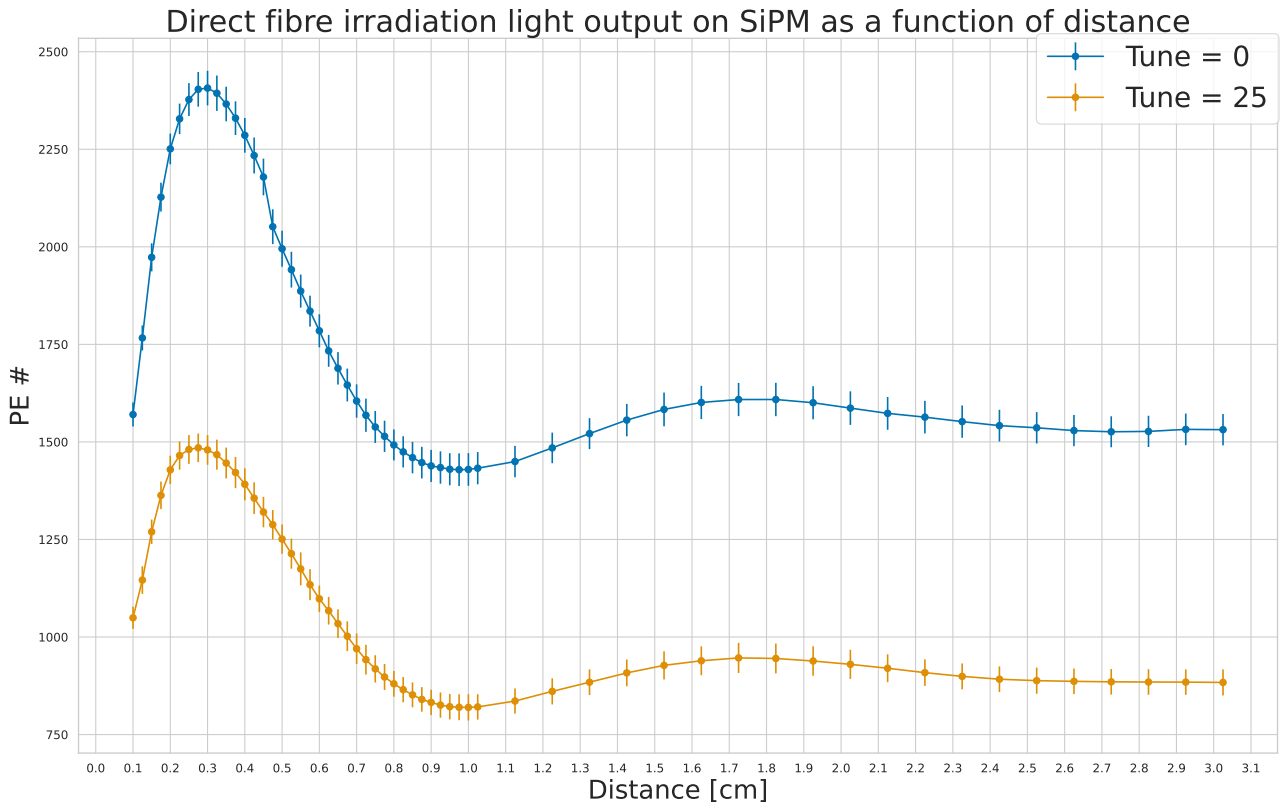

Figure C.2: Light distribution for directly irradiated SiPMs in round T2 for different laser intensities.

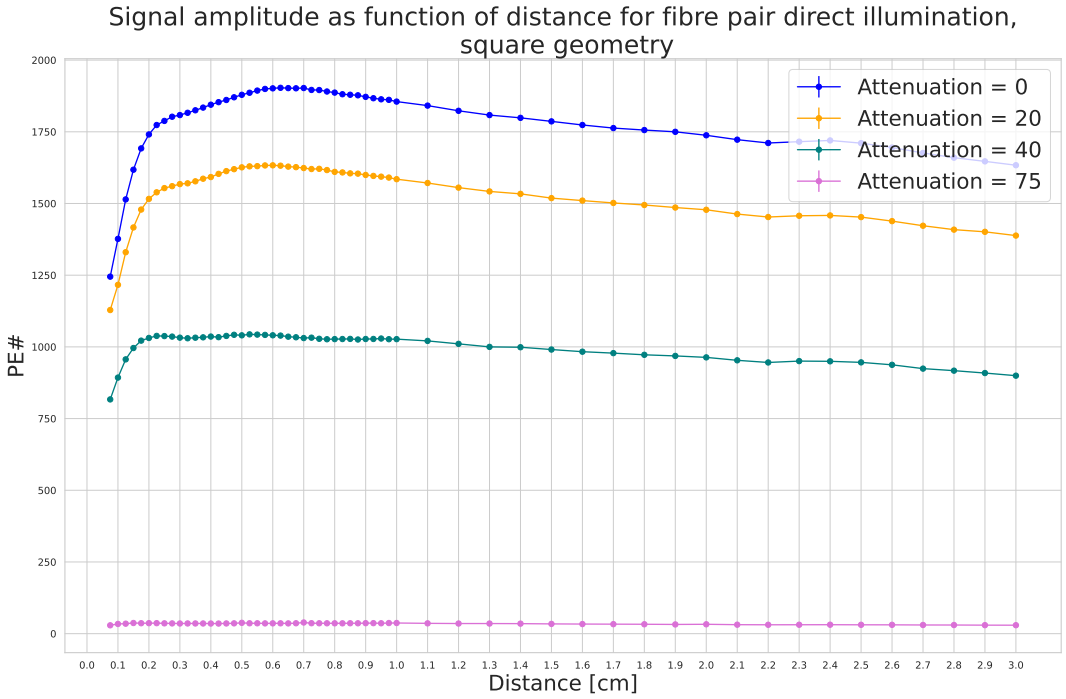

Figure C.3: Light distribution for directly irradiated SiPMs in square T2 for different laser intensities.

C.3 High optical setup performances

The ratios of both SiPMs sides explained in Section 5.5.4 are shown below.

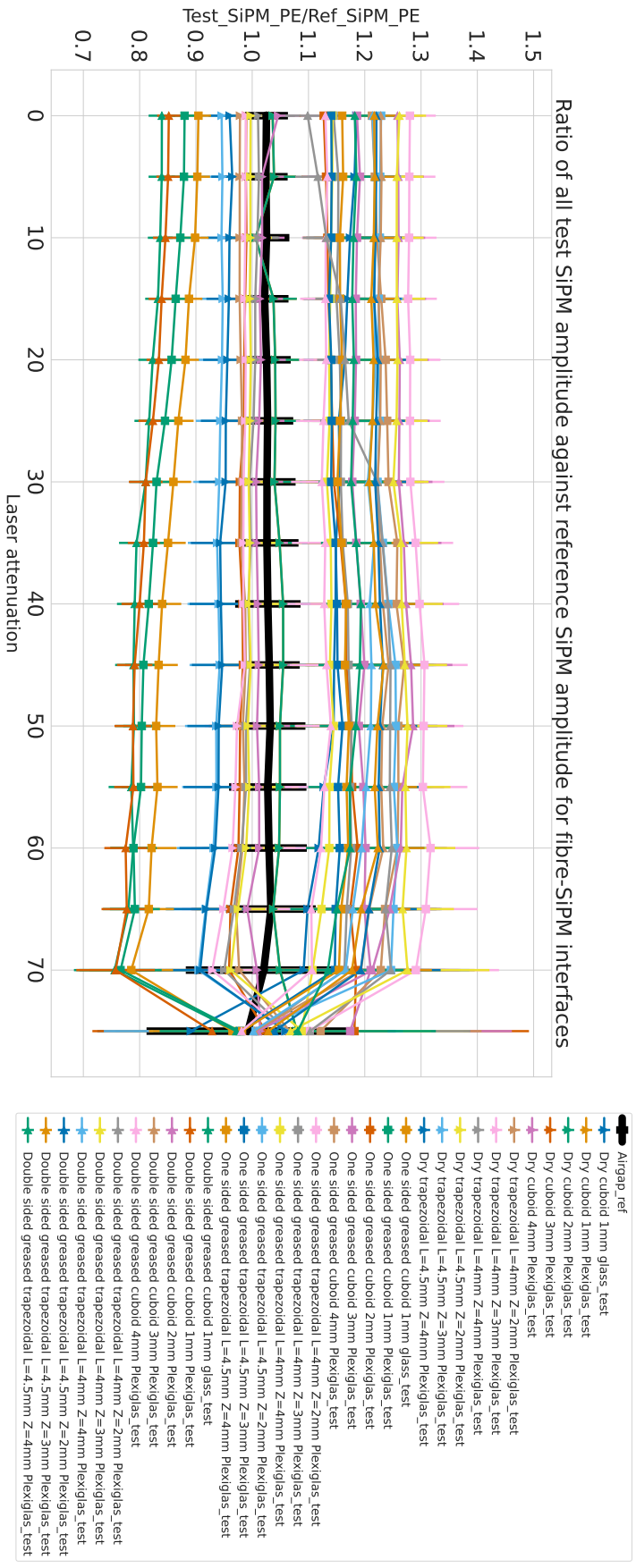

Figure C.4: Ratio of test SiPM amplitude to reference SiPM amplitude for different interfaces. For clarity, systematic error bars aren't shown. A summary of used setups is provided in Table 5.1

Appendix D

Contextualisation of readout electronics

This appendix is meant to offer the reader context towards to readout electronics as they relate to Chapter 6 in particular.

Readout electronics have three primary purposes:

1. The collection of an electrical charge yielded by the sensor, this is typically a short surge in current taking the form of a pulse.
2. A system response optimising the smallest detectable signal, event rate, time of arrival, the insensitivity to sensor pulse shape, and, particularly relevant in this case, the energy measurement
3. The digitisation of the signal and its storage for subsequent analysis

These three objectives can only rarely be optimised for simultaneously, leading to a compromise needing to be met, all at an acceptable price range.

D.0.1 Analogue electronics

Primary signals for (semiconductor) electronic sensors are commonly small, with a single electron converted onto a SiPM having a charge of $\mathcal{O}(10^{-19}\,\mathrm{C})$ which is further subject to statistical fluctuations as exposed in Sections 3.3.5 and 5.5.2. These, together with electronic noise, will further smear the signal preventing it from taking its ideal pulse shape as shown in Figure D.1. This determines the size of the minimal detectable signal. This thus often necessitates a primary gain G_p onto the sensor ($\mathcal{O}(10^6)$ for a SiPM, induced by the Geiger cascade) in order to allow the distinction of the signal.

This gain however also applies to sensor noise, which is determined by operating conditions (such as temperature) and importantly sensor capacitance. The signal to noise ratio (SNR) increases with decreasing capacitance with $\frac{V_s}{V_n} = \frac{Q_s}{V_n(C_d+C_i)}$, V_s and V_n being the signal and noise voltage amplitude respectively, while Q_s is the signal charge while C_d is the sensor capacitance and comes in addition to the amplifier capacitance C_i.

The signal typically manifests as a current pulse in time $i_s(t)$ with $E \propto Q_s = G_p \int_{t_0}^{t_f} i_s(t)\mathrm{d}t = \int_{t_0}^{t_f} I_s(t)\mathrm{d}t$, E being the energy deposition in the sensor, Q_s the total signal charge, t_o and t_f being the times of signal start and end respectively while $I_s(t)$ is the signal after primary amplification.

This shows that the reconstruction of Q_s, necessary to determine E requires some form of charge integration which can be done by either integrating the signal on the sensor capacitance, using an integrating amplifier (*charge-sensitive* amplifier), further amplifying the current pulse and using an integrating ADC (*charge-sensing* ADC, a *QDC*, see Section 2.2.3) or rapidly sampling and digitising the current pulse and use a numerical integration. These are typically integrated into a readout chain shown in Figure D.2.

D.0.1.1 Analogue signal integration

Amplifiers In a sensor volume such as the silicon bulk of a SiPM, charges are created and move towards their respective electrodes, if the amplifier, shown in Figure D.3 can be seen as having low resistance (low *impedance*), the discharge time constant $\tau = R_i(C_i + C_d)$ will be small and the amplifier will sense the signal current. If τ is large compared to the pulse duration however, the current pulse is integrated on the capacitance

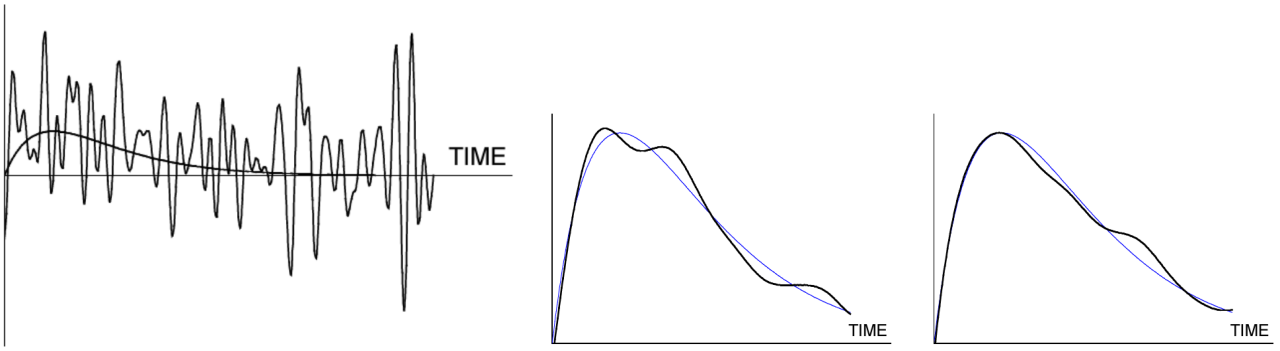

(a) Signal + noise for a signal to noise ratio of 1, the signal is undistinguishable. [412].

(b) Convolution of signal and noise at four different times given a signal to noise ratio of around 20. The blue curve represents the noiseless signal, the signal can easily be distinguished despite the noise [412].

Figure D.1

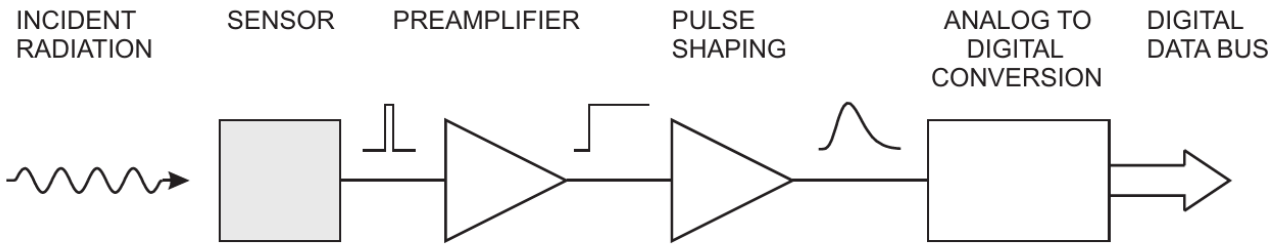

Figure D.2: Standard readout chain: radiation induces charge in the sensor, the analogue pulse of which is fed into a preamplifier, it then passes a shaper before being digitised in an analogue-to-digital converter.

and the induced voltage at the amplifier's input $V_i = \frac{Q_s}{C_d+C_i}$. The signal amplitude is hence dependent on sensor capacitance. The base unit for most amplifiers is the operational amplifier (OpAmp), shown in Figure D.4. It has three main characteristics:

- It has a high (open loop) gain $G_a \sim 10^5$ or more
- It possesses two voltage inputs V_+ and V_- and one output $V_o = G(V_+ - V_-)$
- It has very low input impedance and thus input current $I_{in} \sim 0$

Operational amplifiers attempt to minimise the difference between V_+ and V_-.

For a signal, the charge can be readout directly at the amplifier using a *charge-sensitive amplifier* (CSA) shown in Figure D.5.

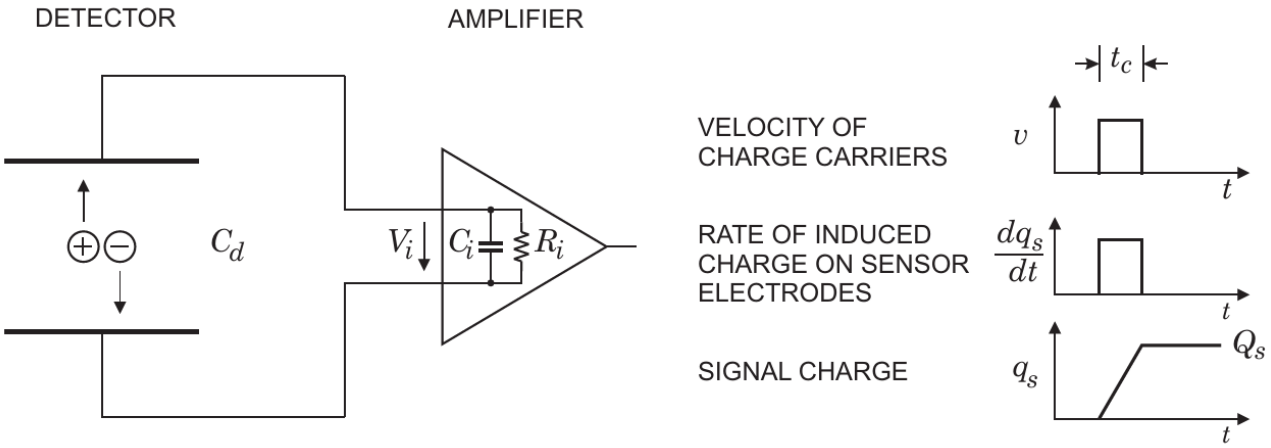

Figure D.3: Principles of charge collection and signal integration in an ionisation-based sensor [412].

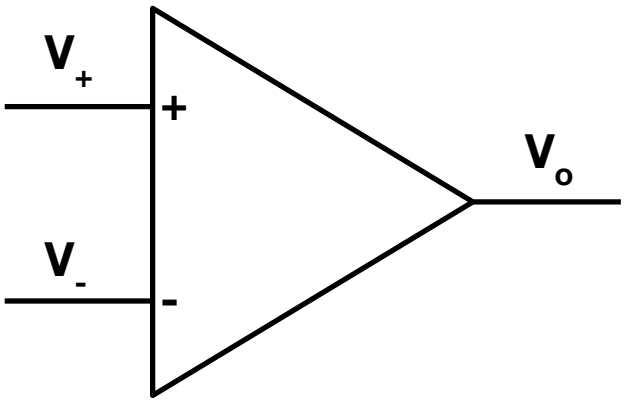

Figure D.4: OpAmp symbol, inputs and outputs. The gain is sometimes written A.

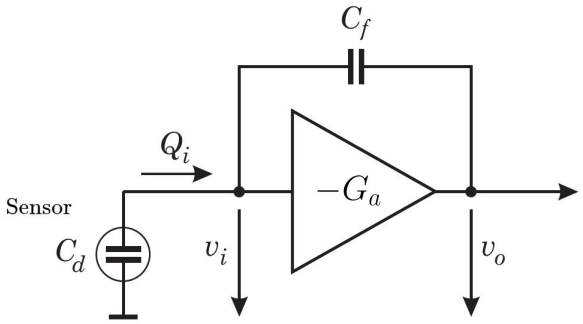

Figure D.5: Principles of a charge sensing amplifier: G_a is the amplifier gain, the input voltage v_i is amplified by $v_o = Z \cdot Q_i$ with Z the feedback (small) capacitor impedance. The feedback capacitor C_f is charged by the signal current implying $Q_f = Q_i$ [330].

In practice, CSAs have a time response, the signal charge is initially integrated on the sensor capacitance with subsequent charge being integrated on the amplifier capacitance. The gain element is commonly a field effect transistor (such as a MOSFET) or a bipolar transistor.

Another common amplifier is the transimpedance amplifier, pictured in Figure D.6a, they convert the charge into voltage which is then readout with $V_{texto} = -R_f I_{\text{in}}$.

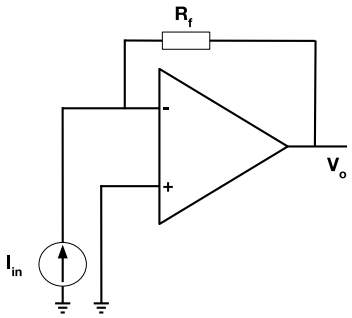

(a) Transimpedance amplifier.

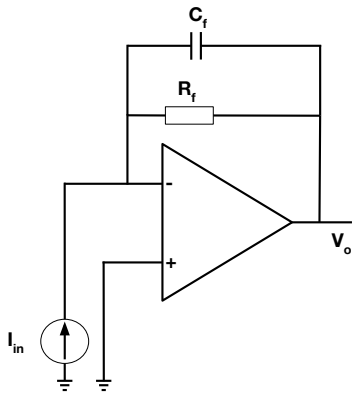

(b) Transimpedance amplifier with an extra capacitor in the feedback loop.

Response function The transfer function of an amplifier provides a description of how the amplifier output relates to the input as a function of signal frequency through a Laplace transform of its time response. It is defined by $H(f) = \frac{V_{\text{out}(f)}}{V_{\text{in}}(f)} = \frac{V_{\text{out}(s)}}{V_{\text{in}}(s)}$, with $s = 2j\pi f$ and j the imaginary constant. This is significant as it provides the amplifier gain as a function of frequency (the magnitude of $H(f)$), the phase shift (the argument of $H(f)$) as well as the bandwidth and stability range of the amplifier. For a transimpedance amplifier for

example, the response function will be $H(s) = \frac{V_o}{V} = \frac{A(s)}{1+A(s)B(s)}$ is the closed-loop gain of the amplifier with $A(s)$ the open loop gain of the amplifier (which is typically very large) and $B(s)$ the feedback factor of the resistor. It can be seen that AB cannot be allowed to be -1 as it would cause the response function to diverge and the amplifier to be unstable. This can be seen in the Bode plot shown in Figure D.7

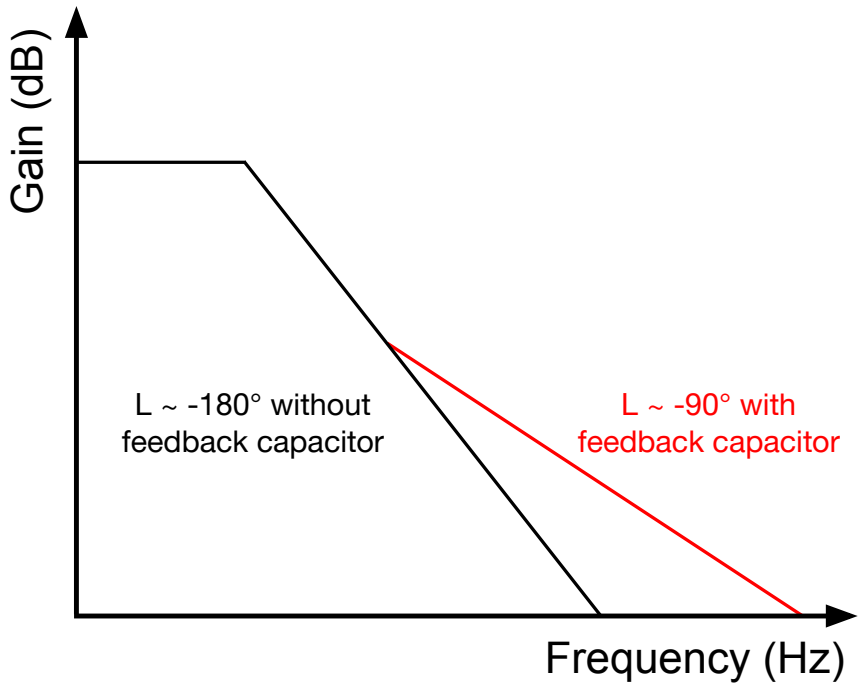

Figure D.7: Bode diagram of transimpedance amplifier. The gain loss L may be reduced by adding an adequate feedback capacitor.

The loop gain includes two poles: one from the op-amp's internal dominant pole (due to compensation), and another from the feedback resistor in combination with the sensor's capacitance C_T. If, at the frequency where $|AB| = 1$, the total phase shift approaches -180°, the feedback becomes positive and can induce oscillation. A loop gain that decreases steeply (e.g., $-40\,\mathrm{dB/decade}$) is more likely to accumulate such a phase shift. To mitigate this, a feedback capacitor is typically added in parallel with the resistor R_f as shown in Figure D.6b, introducing a zero that flattens the roll-off and shifts the phase toward -90°, thereby increasing the phase margin and ensuring stability.

This stability consideration is essential in the design of analog pulse shapers, where the transimpedance stage defines the signal's initial temporal response and must remain stable across the next stage of signal processing: the shaper's frequency range.

Distortions caused by DC components When interfacing a sensor with a regulated common-gate amplifier, the input capacitance of the sensor plays a critical role in signal integrity. The sensor's junction capacitance when directly coupled to the amplifier input, can inject slow transient components into the signal path if said capacitance is too large. These low-frequency artefacts arise due to the charge redistribution between the sensor capacitance and the amplifier's virtual ground node, especially in the presence of rapid current pulses. As the signal propagates through subsequent shaping stages, these slow components can manifest as secondary peaks or baseline distortions in the output waveform. This effect is particularly evident after digitisation, where the baseline has not fully recovered before the ADC samples the signal. Capacitors are a common way to filter these DC, low-frequency artefacts.

DC and AC coupling for ASICs The KLauS chip (see Section 6.2.4) is a DC-coupled ASIC whereas the CALOROC [399] is an AC-coupled ASIC. The DC-coupling has the advantage of well-preserving signal integrity even for slow components, the response to current pulses is also immediate which further contributes to effective peak finding for short-tailed signals, it also simplifies the power and biasing of the chip and allows

to easily evaluate the noise levels without extra calibration. This however also leads to high capacitance sensor (such as large SiPMs) coupling directly to the amplifier input, to suffer baseline shifts or slow tails which cause signal distortions in the shaping stage which leads to double peaking.

AC coupling on the other hand blocks baseline variations and DC offsets altogether, it also better isolates the detector capacitance from the amplifier output which induces fewer problem at the shaper, the biasing is also generally more flexible. This choice leads to a loss of DC information however: any slow baseline shifts or integral charge components below the high-pass corner frequency will be filtered. In addition, pulses may be distorted if the coupling capacitor and biasing resistor form a high-pass filter with a cutoff too close to the signal bandwidth this can lead to parts of the pulse being lost, leading to a more delicate tuning of ASIC components. Furthermore, noise levels are not as well defined as a function of threshold as a result of the AC cutoff.

Overall, both technologies may be used in the SHiP calorimeter system, the variations in capacitance render AC coupling more robust in this case, but with adequate modifications, DC coupling solutions may also function.

D.0.1.2 Signal shaping

The shaper has two primary goals: limiting the bandwidth (and thus the speed) of the signal in order to suppress noise while constraining the pulse width so that no overlap between pulses occur. This is done by inducing a lower and an upper frequency cutoff. These goals conflict with one another and thus a compromise must be found. The simplest shaper is a high pass filter-low pass filter (CR-RC) shaper is shown in Figure D.8.

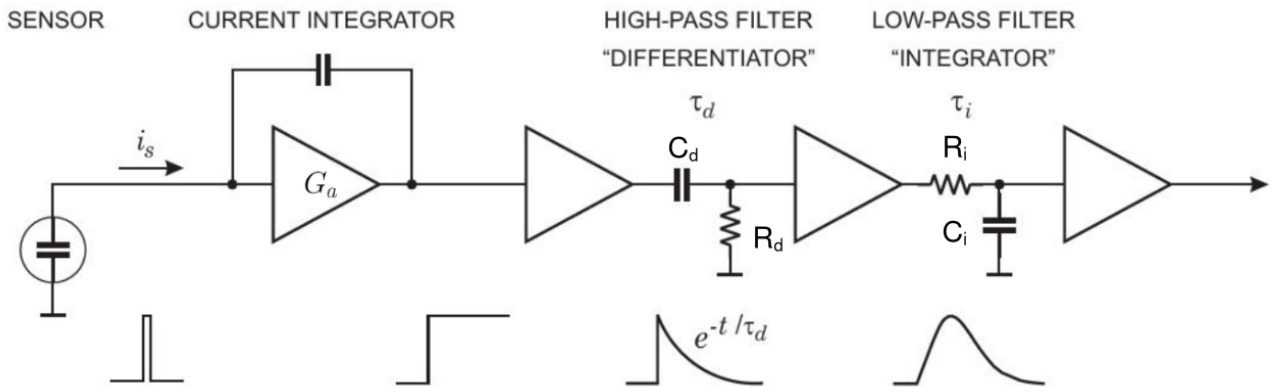

Figure D.8: Simple shaping system: integration is performed towards a slow decaying step function, a high pass filter (*differentiator*) limits the pulse width whereas a subsequent low-pass filter (*integrator*) reduces the high-frequency noise [412].

If $R_d = R_i$ and $C_d = C_i$, the induced time response or *shaping time* $\tau = \frac{1}{RC} = \frac{1}{\omega_c}$ with ω_c the signal cutoff frequency. These shapers commonly use a single $N = 1$ CR filter but M RC filters. The pulse shape described by its amplitude A is then described by:

$$A(t) = \frac{A_0}{M!}\left(\frac{t}{\tau}\right)^M e^{-\frac{t}{\tau}}. \tag{D.1}$$

The higher M, the more Gaussian the pulse shape which thus improves the double pulse resolution. Higher M shapers are however unwieldy, therefore CR-RC-CR shapers are often preferred as they have longer pulse shapes defined as:

$$A(t) = A_0\left[\frac{t}{\tau} - \frac{1}{2}\left(\frac{t}{\tau}\right)^2\right]e^{-\frac{t}{\tau}}. \tag{D.2}$$

This is favourable for high rates in order to minimise baseline fluctuations and undershoots. This longer pulse duration however, may induces *ballistic deficit*: if pulse rise time at the shaper input is longer than the high-pass constant of the shaper, the output amplitude of the shaper is trimmed by the preamplifier pulse's slow rise. This is due to the shaper's falling edge before the preamplifier's output maximum is reached: the shaper's bandwidth is too small, the preamplifier cannot follow the steep rising pulse edge. This effect is shown in Figure D.9.

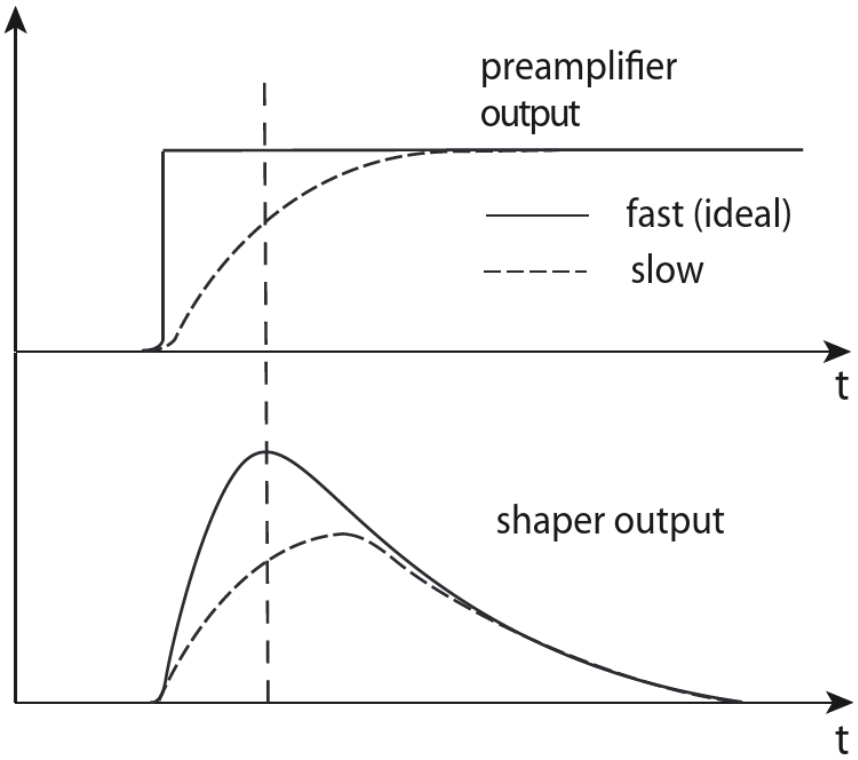

Figure D.9: Ballistic deficit for (a) a step function at the preamplifier output and the resulting shaper output (b) [412].

Sallen-Key topology shapers are an alternative to CR-RC-CR shapers, they function around operational amplifiers in a feedback configuration as shown in Figure D.10

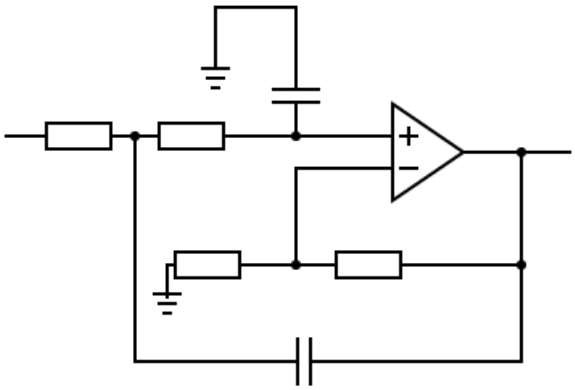

Figure D.10: Sallen-Key shaper topology.

D.0.2 Digital conversion

While signals are first processed on the analogue side, contemporary analyses are generally done on easy-to-store data, for which analogue signals, with their complex shapes, are ill-suited for. Analogue signals are as such digitised as part of the readout chain as shown in Figure D.2 and then processed as logical units which are easier to store and much more robust against distortions.

The digitisation of an analogue signal is done through an *Analogue-to-digital-converter* (ADC) which encodes a voltage proportional to either the incoming pulse area or the peak amplitude into a binary number called

the *code* counted in ADC channels/counts (often also referred to simply as ADC) and typically taking values between 0 and $2^n - 1$, with n the amount of bits available to the ADC. ADC require a clock which either affect the absolute digitisation rate or the bitwise digitisation rate. ADCs however systematically have a bit range n with the total number of available ADC values being 2^n with the least significant bit (LSB) corresponding to the smallest voltage variation the ADC is sensitive to. As an example, a 10-bit ADC with a reference voltage of 2048 mV will have an ideal resolution of $\sim 2\,\text{mV}$. The code suffers from a quantisation error $\delta = \frac{\text{LSB}}{\sqrt{12}}$. The SNR of an ADC on the other hand is defined as $\text{SNR}_{\text{ADC}} = 20\log_{10} 2^n\sqrt{12}$. Finally fluctuations are always present in the ADC which may modify the effective number of bits (ENOB) as $\text{ENOB} = n - \log_2\left(\frac{\text{RMS}_{\text{conv}}}{1/\sqrt{12}}\right)$.

Two ADC techniques are relevant in this work: *flash ADC* and *successive-approximation ADC* (SAR).

Flash ADC is conceptually simple: the voltage is applied in parallel to comparator inputs each having a different threshold voltage, with $2^n - 1$ comparators needed as shown in Figure D.11a. Since operations are done in parallel, flash ADC is particularly fast but suffers from a large needed footprint due to its relative circuit complexity in addition to a high power consumption and high cost.

SAR ADCs in comparison is a good compromise for most applications. The input voltage is successively approximated by comparing to available digital reference voltages starting with a midpoint voltage. The most significant bit (MSB) is then set to 0 or 1 depending on whether the input voltage is smaller or larger than the midpoint reference one. The input voltage is then compared to the midpoint voltage of either the larger voltage half or lower voltage half which sets the second most significant bit and so on until all bits have been set. An example of a SAR ADC architecture is shown in Figure D.11b. As an example, a very simple 3 bit ADC operating between 1 and 2 V would have 7 reference voltages $(1.125, 1.25, 1.375, 1.5, 1.625, 1.75, 1.875\,\text{V})$. If the input voltage has a value of $V_i = 1.7\,\text{V}$, $V_i > 1.5\,\text{V} \rightarrow \text{code} = 1XX$, $V_i < 1.75\,\text{V} \rightarrow \text{code} = 10X$, $V_i > 1.625\,\text{V} \rightarrow \text{code} = 101$.

The ADC counts can then be transmitted within a binary bitstream for processing and storage.

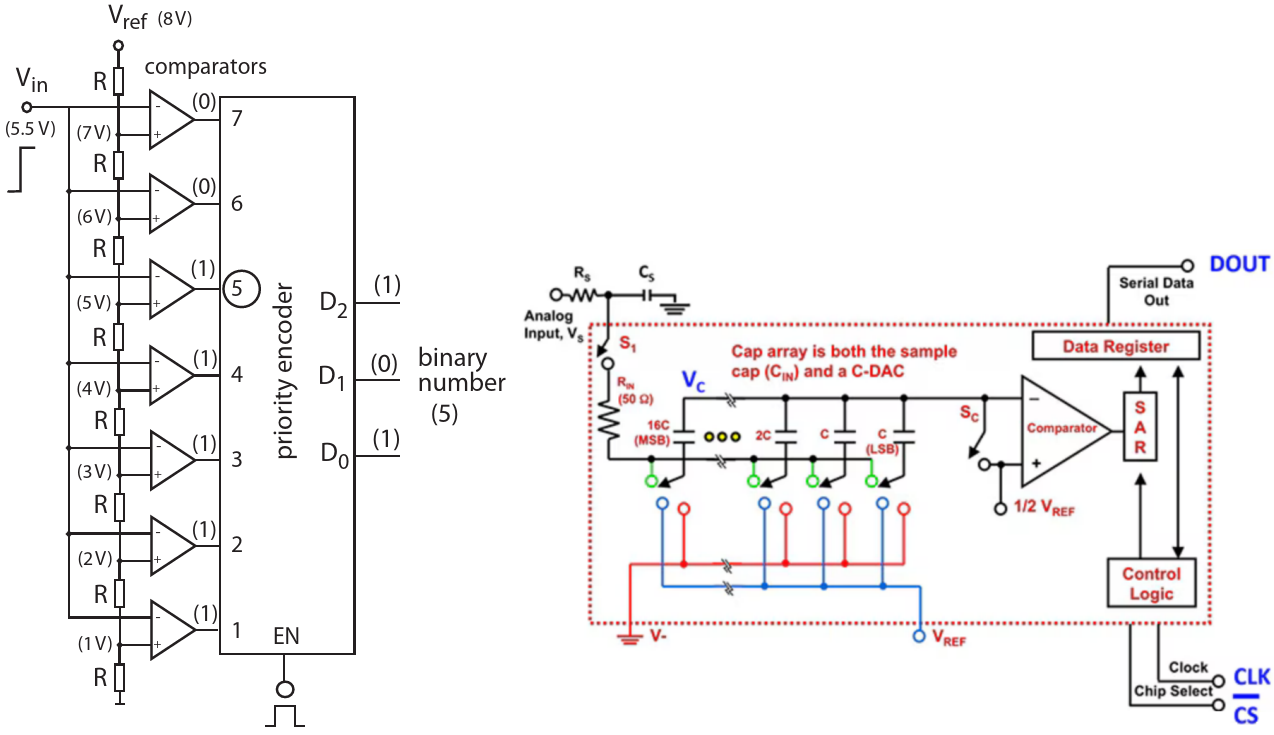

(a) Flash ADC block diagram. Each comparator has a threshold higher than its predecessor in the chain. A priority encoder finds the highest comparator (5 in this example) and delivers a code based on its inputs [330]

(b) Architecture of 4-bit SAR ADC. The capacitor array is digitally weighted: 16C, 8C, 4C, 2C and C [413].

.

Appendix E

Readout electronics manufacturing and operation

E.1 KLauS motherboard

The jumpers' and potentiometers' roles are detailed below, the board is always assumed to be positioned with SMA connectors at the top.

J1 and J2: modify the SiPM powering configuration. When in high position, allow for SiPMs to operated with two SMA connectors similar to the circuit shown in Figure 6.33a. When in low position, enable single connector operation as for the DT5202 with only the HV SMA connector being used.

P1 and P2: used to control and generate the bias voltage when J1/J2 are in low position

P4 and P5: used to regulate the voltage when J1 and J2 are in high position.

J5 and J6: used to close the SPI chain when the corresponding KlauS mezzanine is mounted onto the board.

J8 : used to close the SPI chain when the KlauS mezzanine is mounted onto the board.

J10 : enable/disable jumper , used to control the analogue/digital voltages of the KLauS, to be set high when the voltage at the end of the board chain is too low.

J9 : I^2C pullup, to be set only on the final board of the chain

JX1 and JX2: emergency stop for all respective KLauS systems

The control plane and readout plane grounds were originally separated but were connected to one another to reduce noise.

The motherboard was found to be too large to use a stencil printer. As a result, the solder paste covered stencil was superimposed by hand by aligning the stencil holes vertically. The parts were then mounted by hand and soldered in using a reflow oven. Four KlauS motherboards were manufactured and allows operation of KLauS mezzanine.

E.2 KLauS mezzanine

The KLauS mezzanines main components were mounted onto the PCB using a pick-and-place machine on top of the stencil dispensed solder paste then soldered into the reflow oven. The only exceptions to this were the header pins which were soldered by hand and the KLauS chip itself which was glued to the designated pads in arrays of 3×3 glue dots. The conductive glue were dispensed by a high-precision custom glue bot [414]. The glue was left to dry at 90 °C for 3 h in an oven.

The chip was then wire bonded to the board using aluminium wires. The system is normally protected by thermally conductive but electrically insulating paste. This solution was however found to be expensive and was substituted by a 3D-printed plastic casing consisting of a frame which was super-glued to the board and a

case which was meant to be removable and substitutable by the aforementioned paste. As a result, the case was glued to the frame using black silica which is hard enough to hold but removable for a future board upgrade if needed. The glueing, bonding and silica porcesses are shown in Figure E.1.

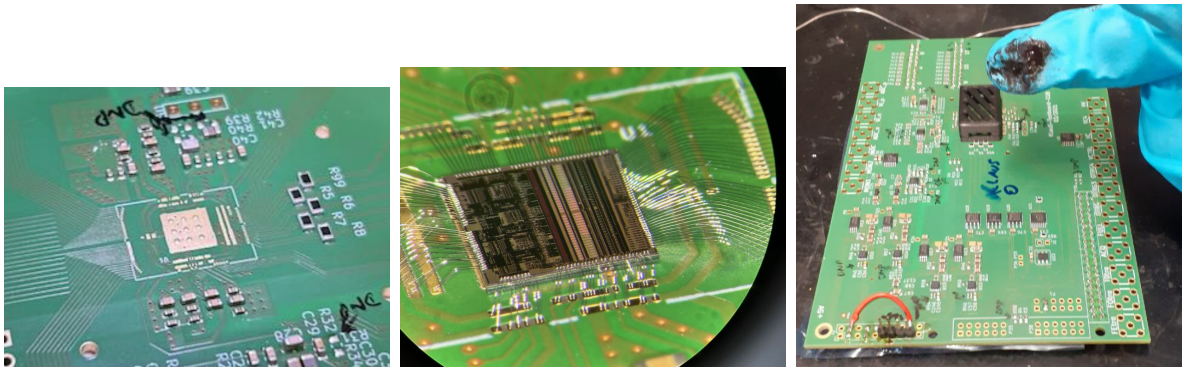

(a) Glue grid dispensed by the gluebot. (b) Wire bonded KLauS chip (c) Silica and casing of the KLauS mezzanine.

Figure E.1

Issues were noted with on multiple mezzanine boards, these were largely traced back to the chips themselves. The causes of these issues are unknown and could be caused by poor chip manufacturing quality or perhaps to the fact that the assembly operation were not performed inside of a clean room despite no indication that this was necessary being given by the designer in Heidelberg. The KLauS quality can be visualised in Figure E.2.

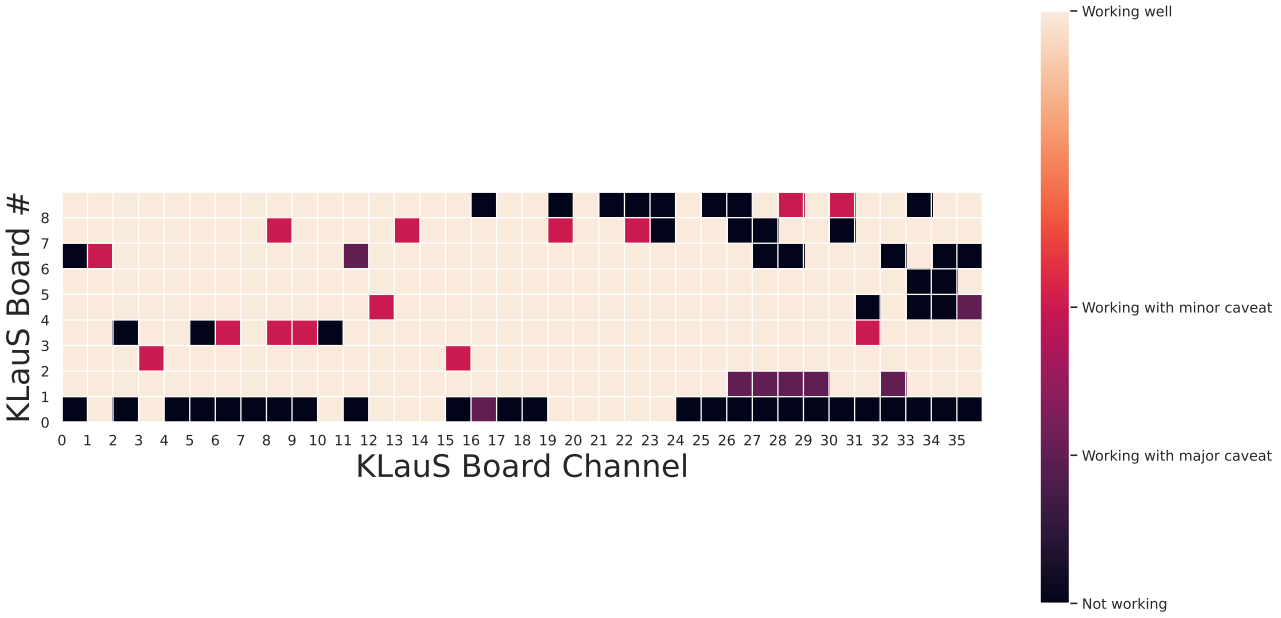

Figure E.2: KLauS mezzanine assembly quality minor caveats are evaluated not to be problematic for operation and manifest as higher noise which can be filtered by increasing the TTT. Major caveats are problematic for board operation and manifest as lowered efficiency or significantly higher noise.

E.3 SiPM board assembly

The SiPM boards were assembled as a panel of 25×8 with all resistors and capacitors placed onto the panel using the stencil-printer and the pick and place machine then soldered using the reflow oven. The SiPMs were placed by hand in a second step and then soldered the same way. The SMA connectors were soldered in by hand. The panel is shown in Figure E.3. The panel is broken up by hand in individual boards after the addition of resistors, capacitors and SiPMs. 192 SiPM boards were manufactured in total, leaving 8 slots empty as a result of SiPM availability.

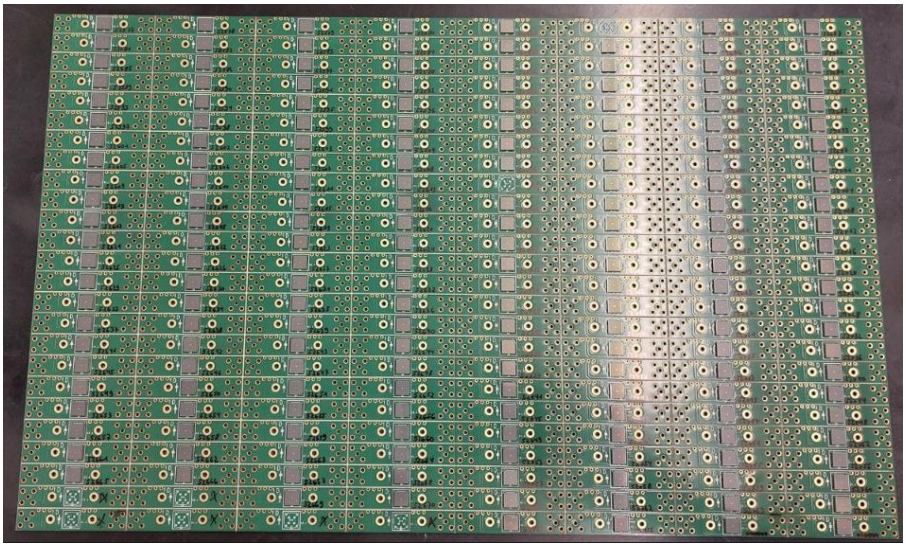

Figure E.3: SiPM boards panel prior to SMA soldering. Missing SiPMs purposely weren't added to the board for lack of sensors.

Appendix F

Complementary studies of hadronic showers in the SND HCAL

F.1 30 cm thick target studies

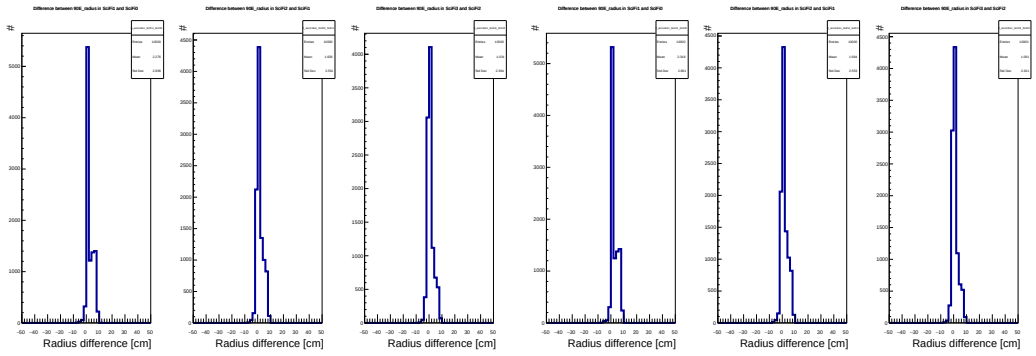

(a) Variations in 90E_radius in the HCAL in single events for 100 GeV impinging π

(b) Variations in 90E_radius in the HCAL in single events for 140 GeV impinging π

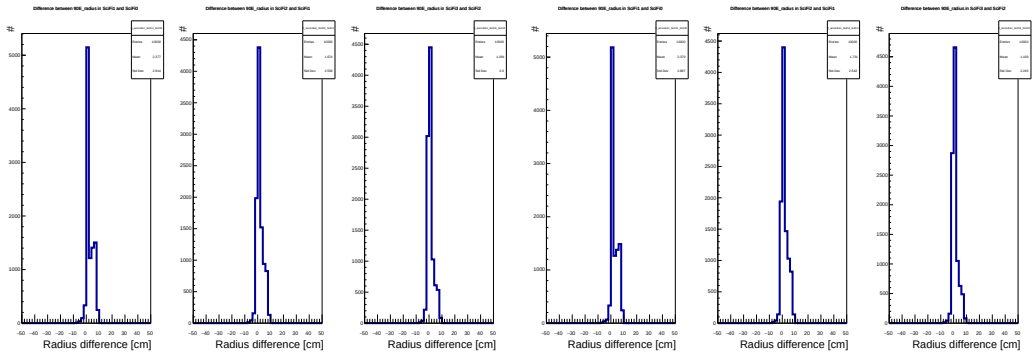

(c) Variations in 90E_radius in the HCAL in single events for 180 GeV impinging π

(d) Variations in 90E_radius in the HCAL in single events for 240 GeV impinging π

Figure F.1: Variations of 90E_radius in the SciFi with 30 cm target.

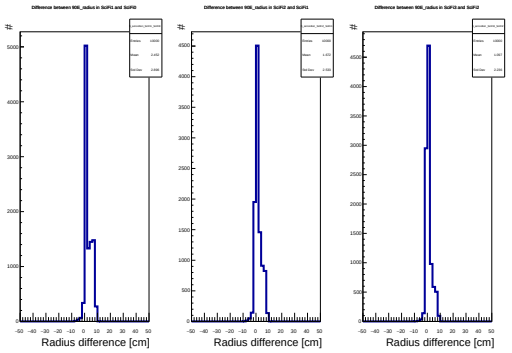

(a) Variations in 90E_radius in the HCAL in single events for 300 GeV impinging π

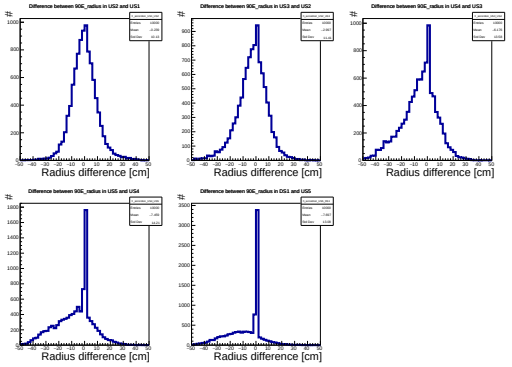

(b) Variations in 90E_radius in the HCAL in single events for 140 GeV impinging π

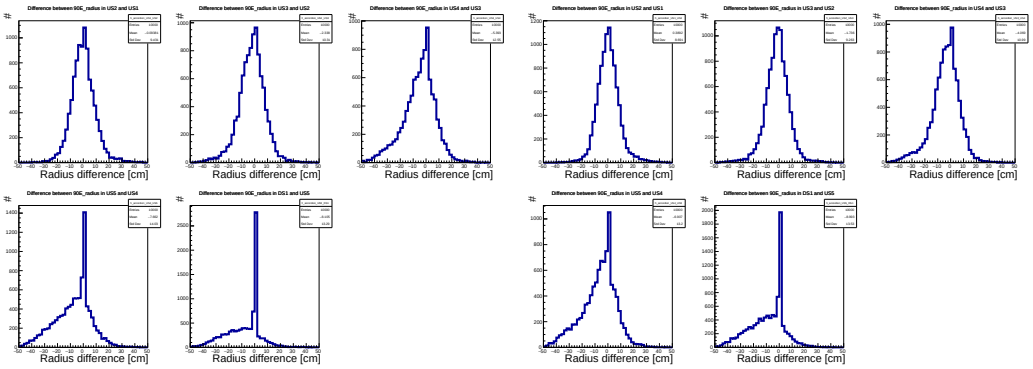

(c) Variations in 90E_radius in the HCAL in single events for 180 GeV impinging π

(d) Variations in 90E_radius in the HCAL in single events for 240 GeV impinging π

Figure F.2: Variations of 90E_radius in the HCAL with 30 cm target.

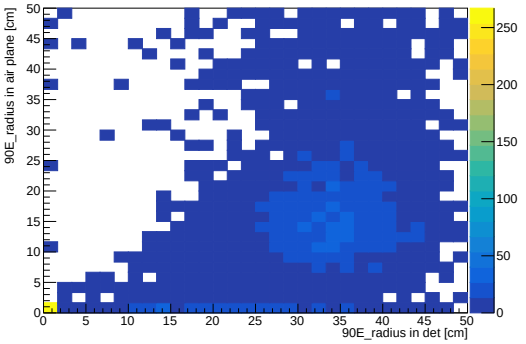

(a) Correlation between 90E_radius in the air plane and in US2 for 100 GeV π^+.

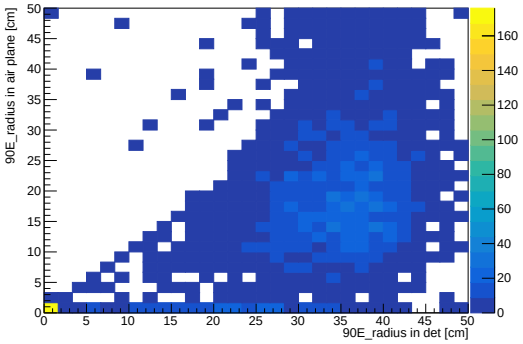

(b) Correlation between 90E_radius in the air plane and in US2 for 140 GeV π^+.

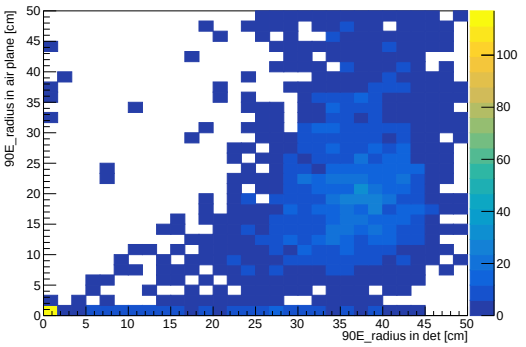

(c) Correlation between 90E_radius in the air plane and in US2 for 180 GeV π^+.

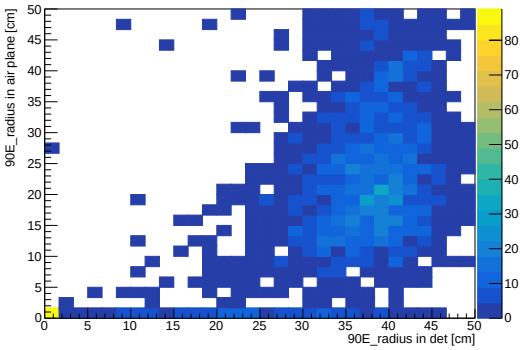

(d) Correlation between 90E_radius in the air plane and in US2 for 240 GeV π^-.

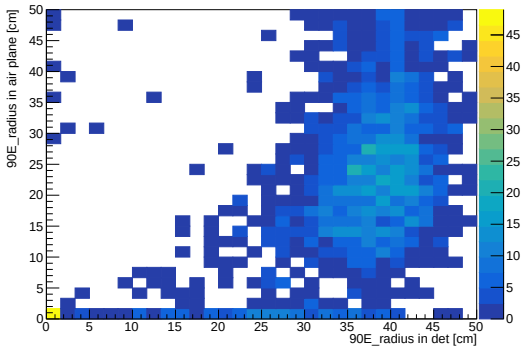

(e) Correlation between 90E_radius in the air plane and in US2 for 300 GeV π^-.

Figure F.3

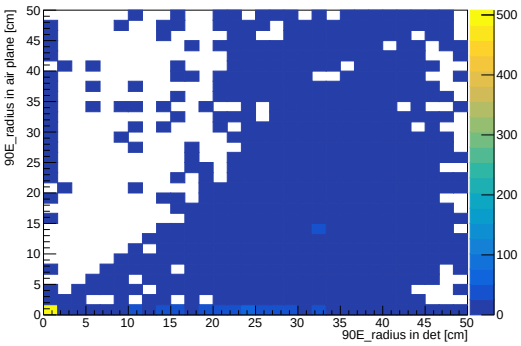

(a) Correlation between 90E_radius in the air plane and in US3 for 100 GeV π^+.

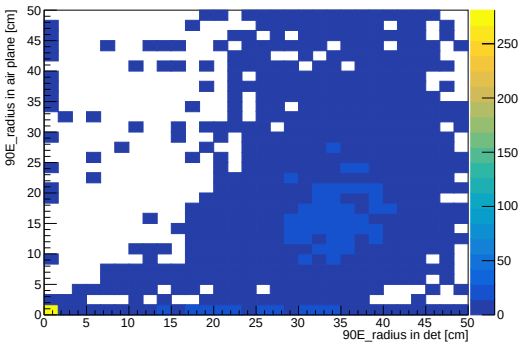

(b) Correlation between 90E_radius in the air plane and in US3 for 140 GeV π^+.

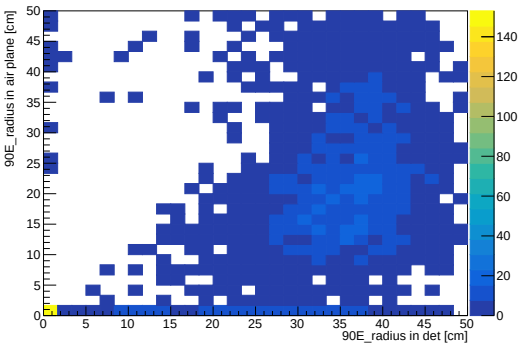

(c) Correlation between 90E_radius in the air plane and in US3 for 180 GeV π^+.

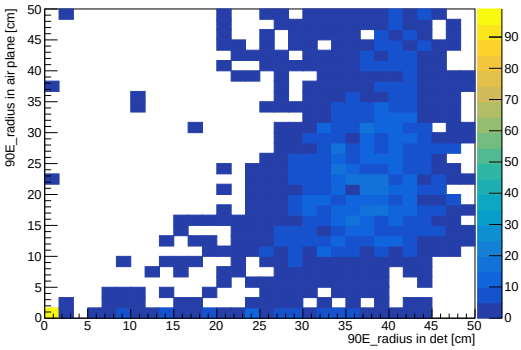

(d) Correlation between 90E_radius in the air plane and in US3 for 240 GeV π^-.

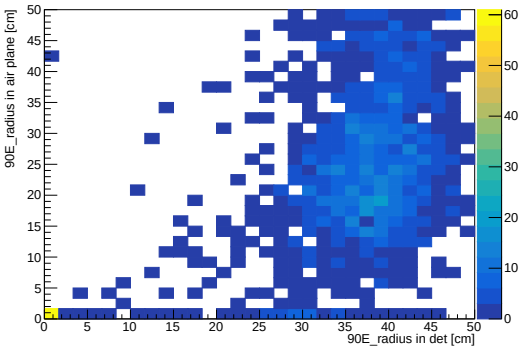

(e) Correlation between 90E_radius in the air plane and in US3 for 300 GeV π^-.

Figure F.4

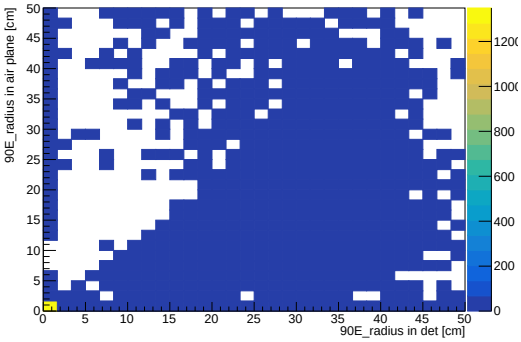

(a) Correlation between 90E_radius in the air plane and in US4 for 100 GeV π^+.

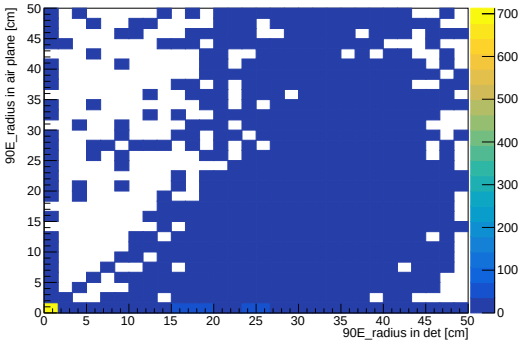

(b) Correlation between 90E_radius in the air plane and in US4 for 140 GeV π^+.

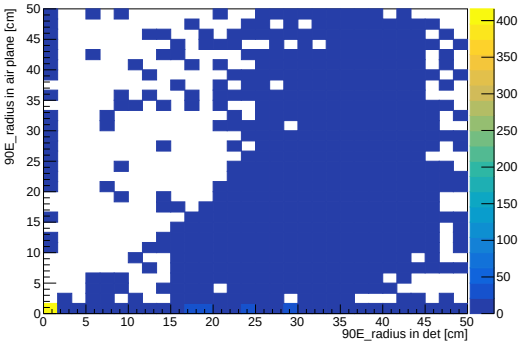

(c) Correlation between 90E_radius in the air plane and in US4 for 180 GeV π^+.

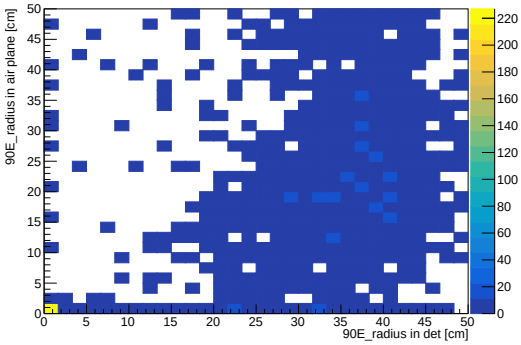

(d) Correlation between 90E_radius in the air plane and in US4 for 240 GeV π^-.

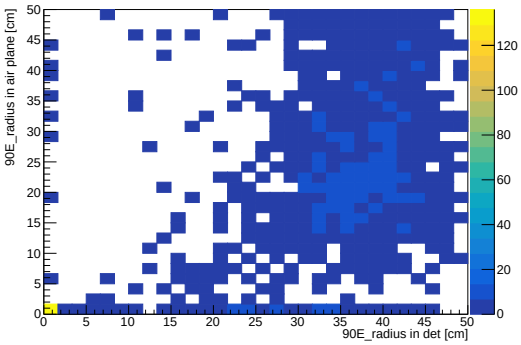

(e) Correlation between 90E_radius in the air plane and in US4 for 300 GeV π^-.

Figure F.5

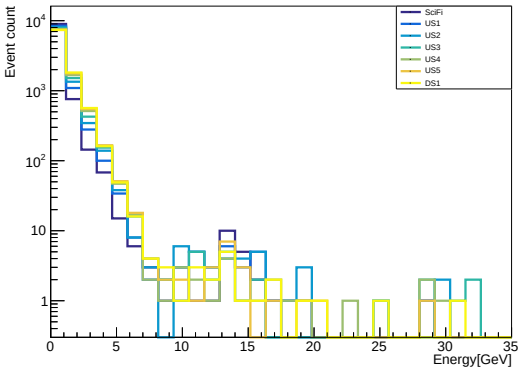

(a) 140 GeV π^+.

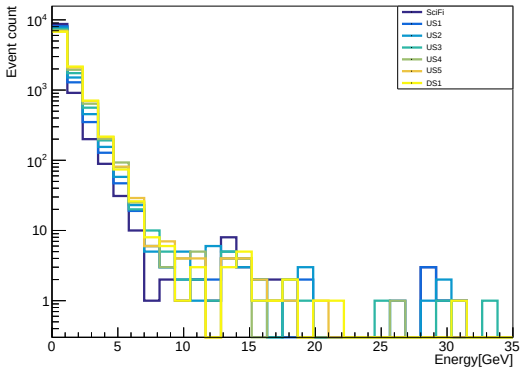

(b) 180 GeV π^+.

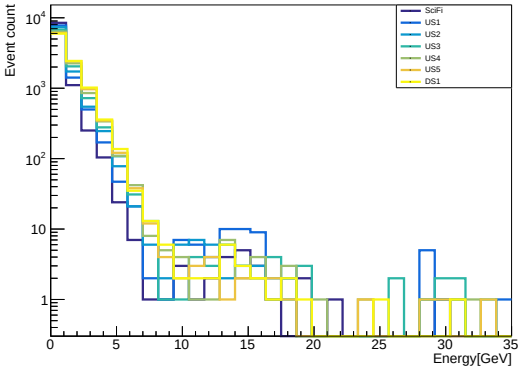

(c) 240 GeV π^+.

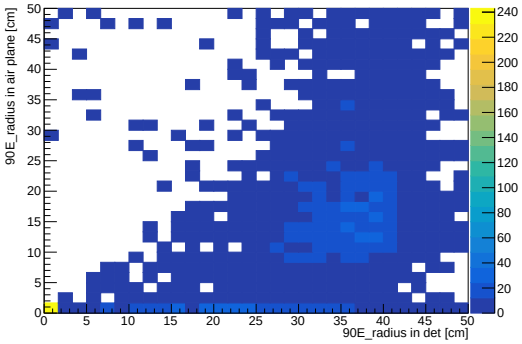

(a) Correlation between 90E_radius in the air plane and in US1 for 140 GeV π^+.

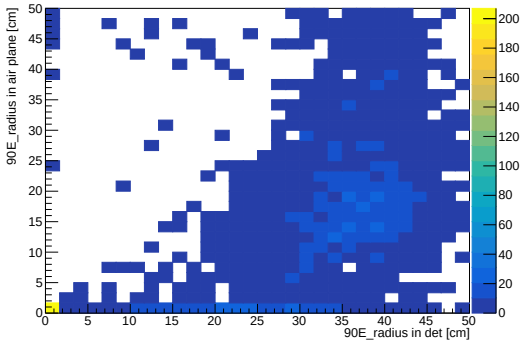

(b) Correlation between 90E_radius in the air plane and in US1 for 180 GeV π^+.

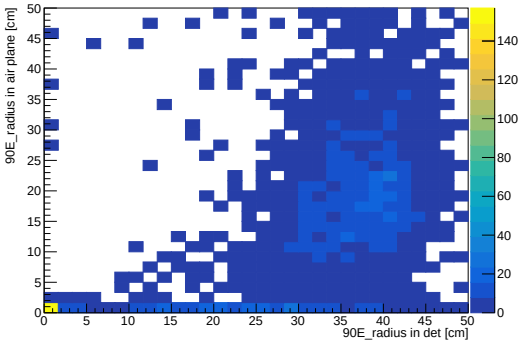

(c) Correlation between 90E_radius in the air plane and in US1 for 240 GeV π^-.

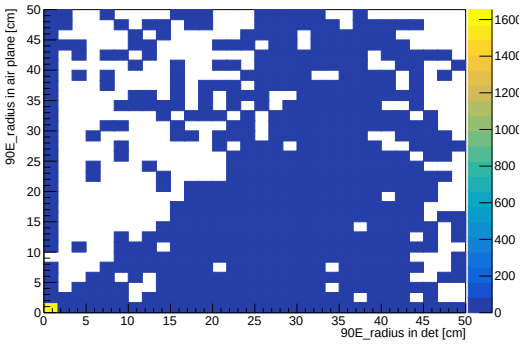

(a) Correlation between 90E_radius in the air plane and in US5 for 140 GeV π^+.

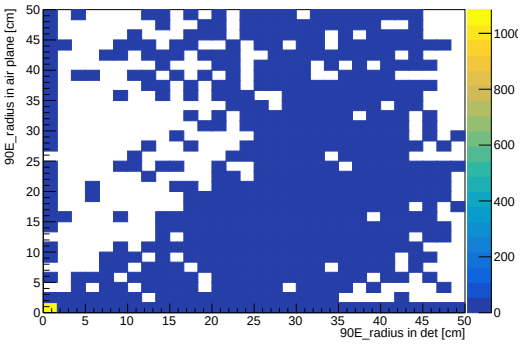

(b) Correlation between 90E_radius in the air plane and in US5 for 180 GeV π^+.

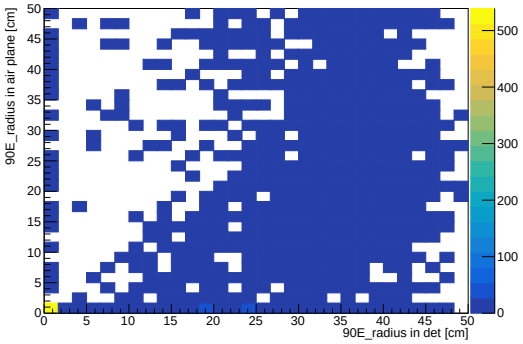

(c) Correlation between 90E_radius in the air plane and in US5 for 240 GeV π^-.

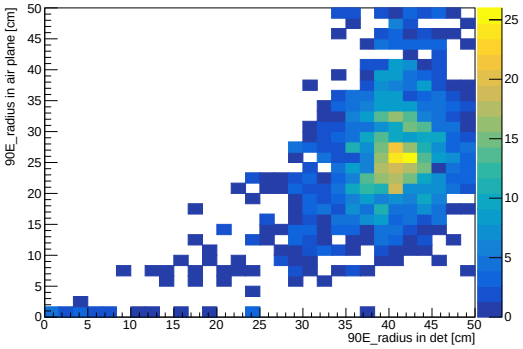

(a) Correlation between 90E_radius in the air plane and in all stations for 140 GeV π^+.

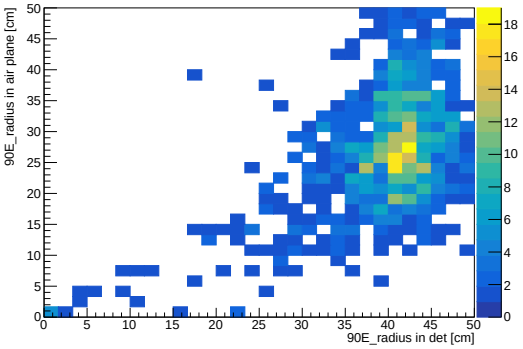

(b) Correlation between 90E_radius in the air plane and in all stations for 180 GeV π^+.

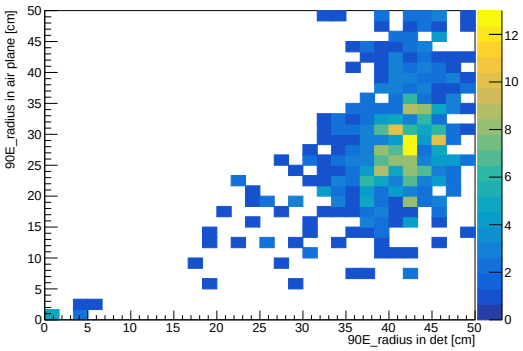

(c) Correlation between 90E_radius in the air plane and in all stations for 240 GeV π^-.

F.2 20 cm thick target studies

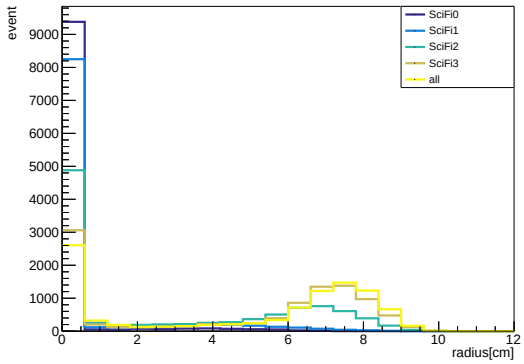

(a) 90E_radius in SciFi for 100 GeV PioT with a 10 cm target.

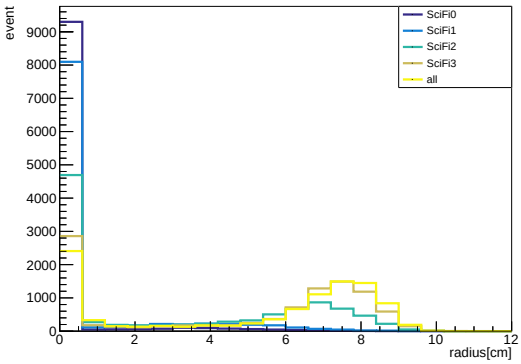

(b) 90E_radius in SciFi for 140 GeV PioT with a 10 cm target.

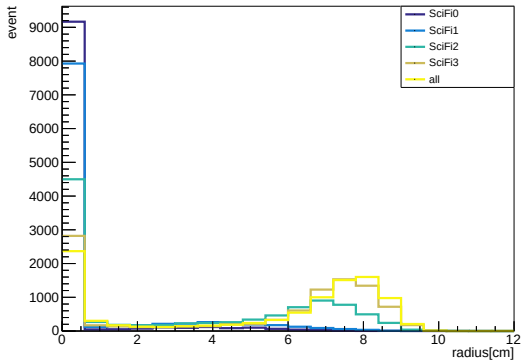

(c) 90E_radius in SciFi for 180 GeV PioT with a 10 cm target.

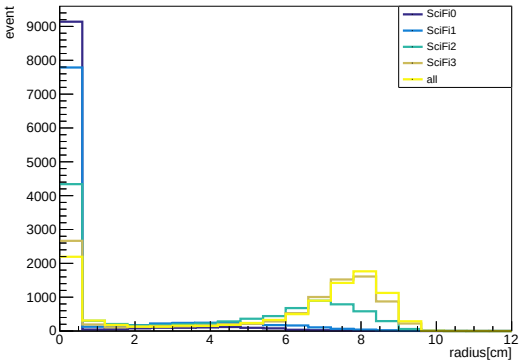

(d) 90E_radius in SciFi for 240 GeV PioT with a 10 cm target.

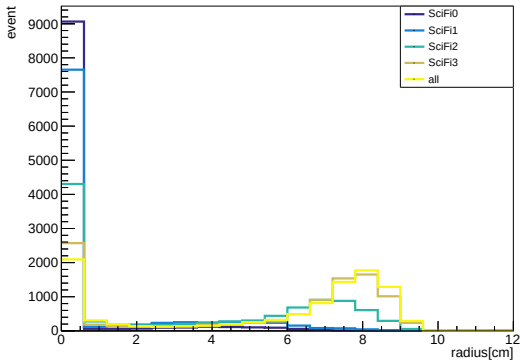

(e) 90E_radius in SciFi for 300 GeV PioT with a 10 cm target.

Figure F.10: 90E_radius in the SciFi with 30 cm target.

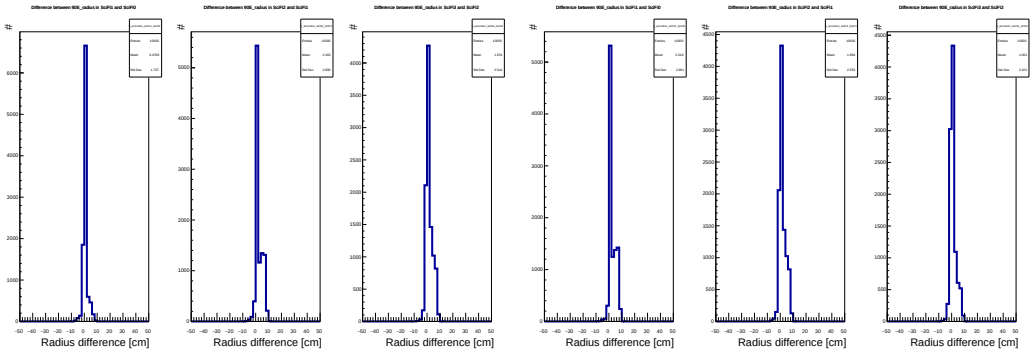

(a) Variations in 90E_radius in the SciFi in single events for 100 GeV impinging π

(b) Variations in 90E_radius in the SciFi in single events for 140 GeV impinging π

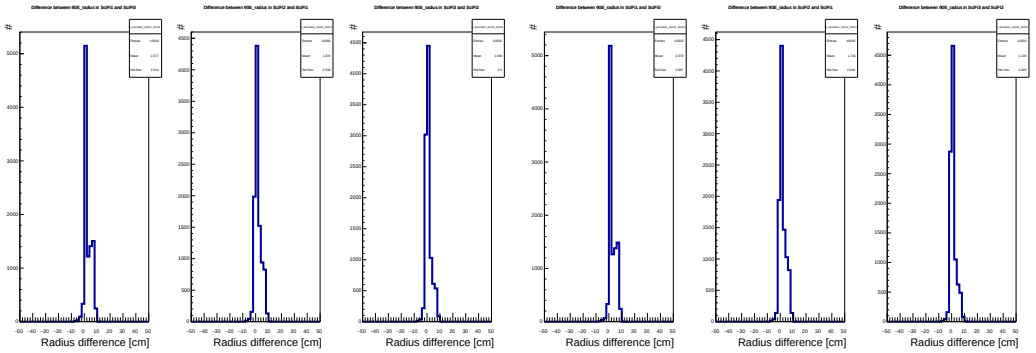

(c) Variations in 90E_radius in the SciFi in single events for 180 GeV impinging π

(d) Variations in 90E_radius in the SciFi in single events for 240 GeV impinging π

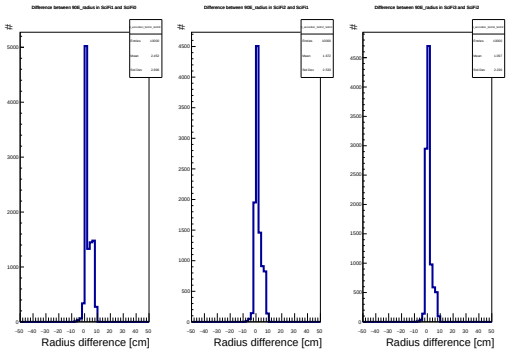

(e) Variations in 90E_radius in the SciFi in single events for 300 GeV impinging π

Figure F.11: Variations of 90E_radius in the SciFi with 30 cm target.

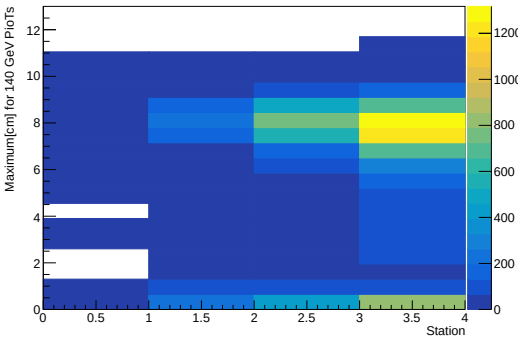

(a) SciFi station with largest 90E_radius with 140 GeV incoming π^+

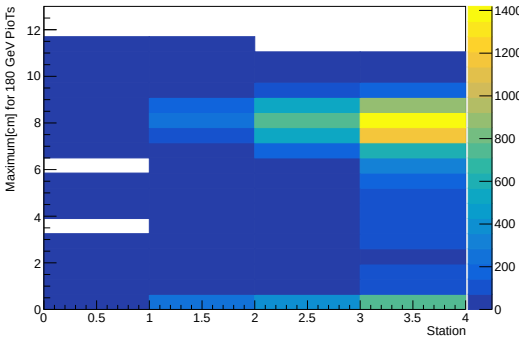

(b) SciFi station with largest 90E_radius with 180 GeV incoming π^+

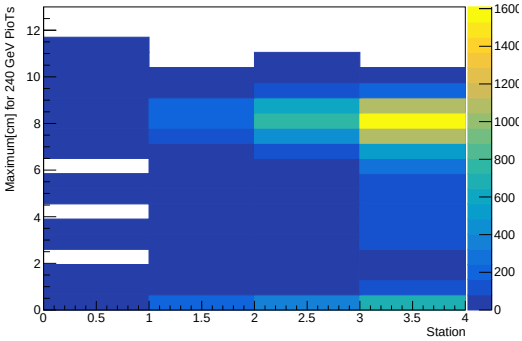

(c) SciFi station with largest 90E_radius with 240 GeV incoming π^+

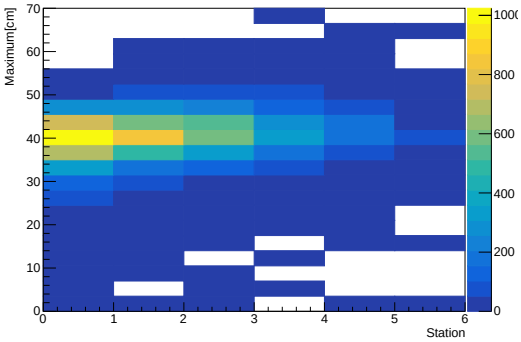

(a) HCAL station with largest 90E_radius with 140 GeV incoming π^+

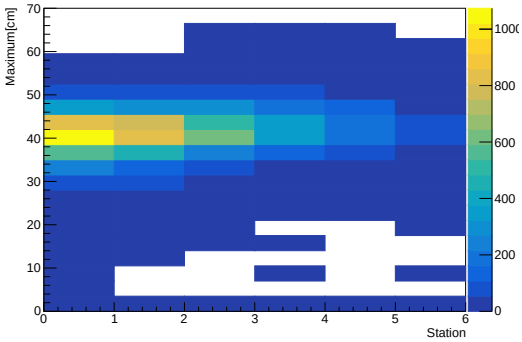

(b) HCAL station with largest 90E_radius with 180 GeV incoming π^+

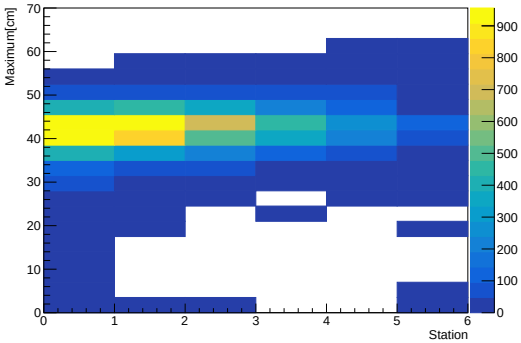

(c) HCAL station with largest 90E_radius with 240 GeV incoming π^+

Figure F.13

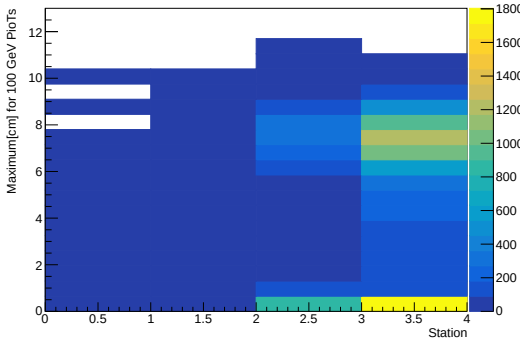

(a) SciFi station with largest 90E_radius with 100 GeV incoming π^+

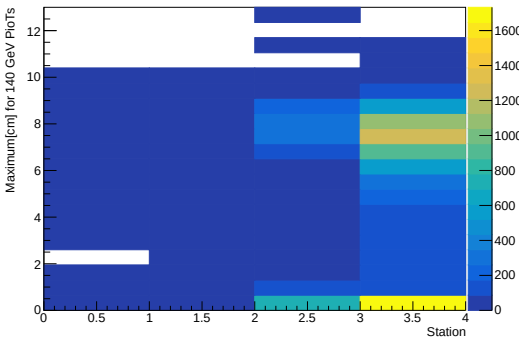

(b) SciFi station with largest 90E_radius with 140 GeV incoming π^+

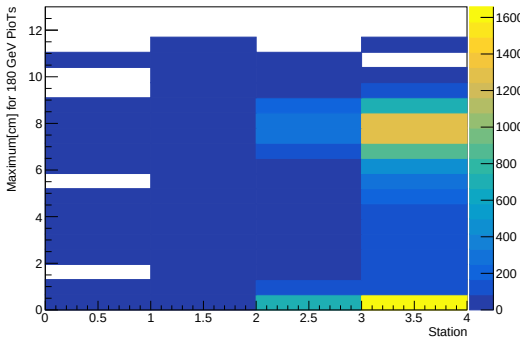

(c) SciFi station with largest 90E_radius with 180 GeV incoming π^+

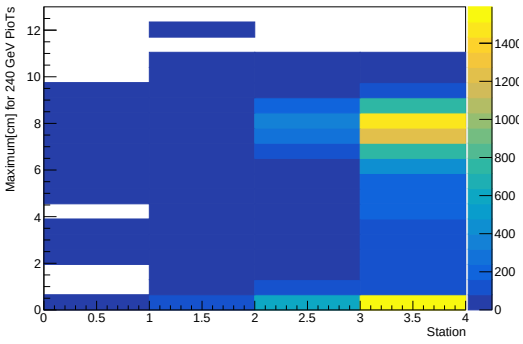

(d) SciFi station with largest 90E_radius with 240 GeV incoming π^+

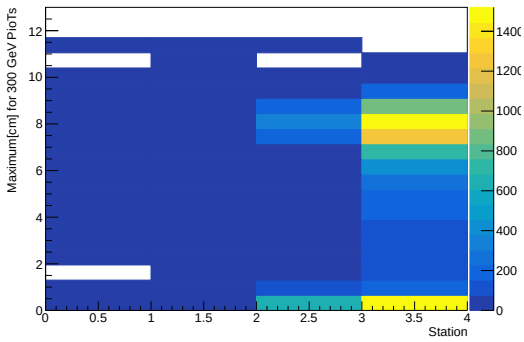

(e) SciFi station with largest 90E_radius with 300 GeV incoming π^+

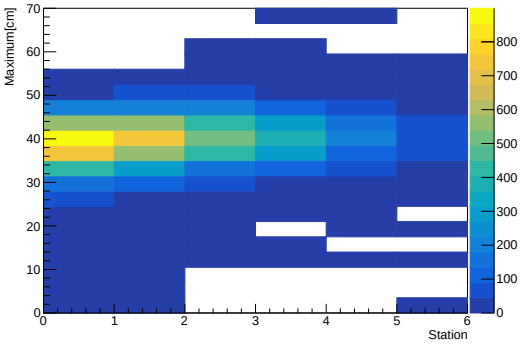

(a) HCAL station with largest 90E_radius with 100 GeV incoming π^+

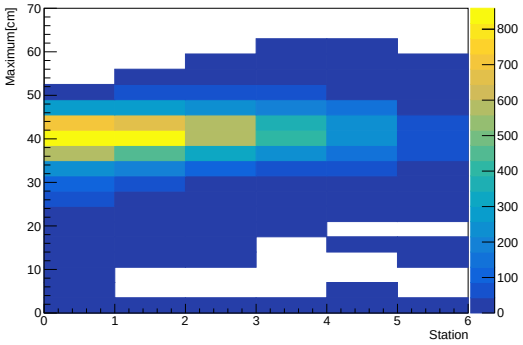

(b) HCAL station with largest 90E_radius with 140 GeV incoming π^+

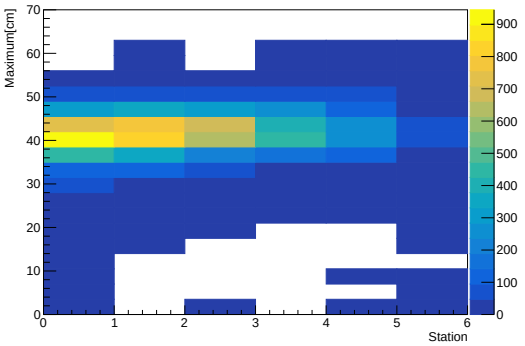

(c) HCAL station with largest 90E_radius with 180 GeV incoming π^+

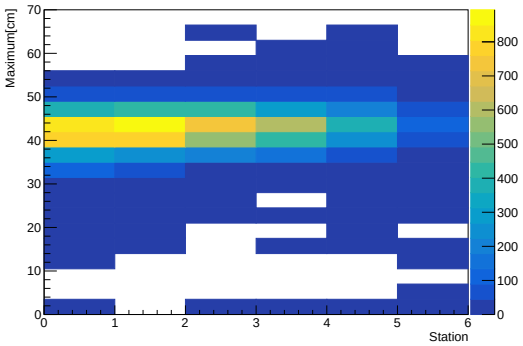

(d) HCAL station with largest 90E_radius with 240 GeV incoming π^+

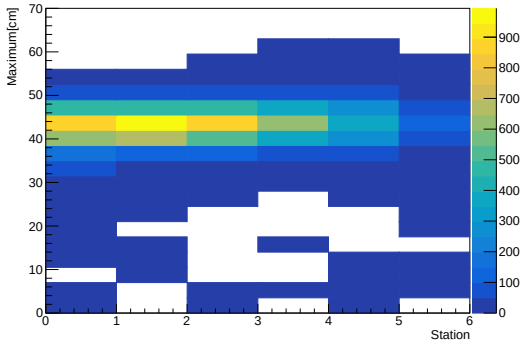

(e) HCAL station with largest 90E_radius with 300 GeV incoming π^+

Figure F.15

F.3 10 cm thick target studies

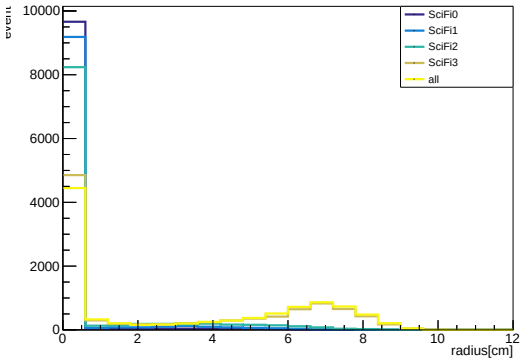

(a) 90E_radius in SciFi for 100 GeV PioT with a 10 cm target.

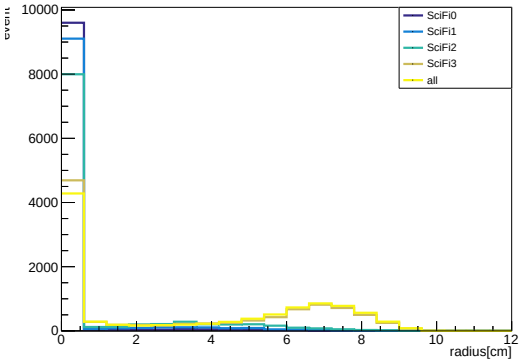

(b) 90E_radius in SciFi for 140 GeV PioT with a 10 cm target.

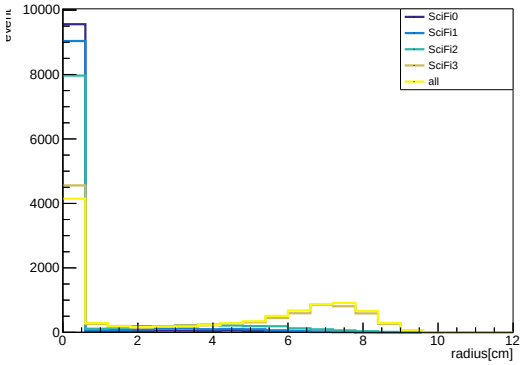

(c) 90E_radius in SciFi for 180 GeV PioT with a 10 cm target.

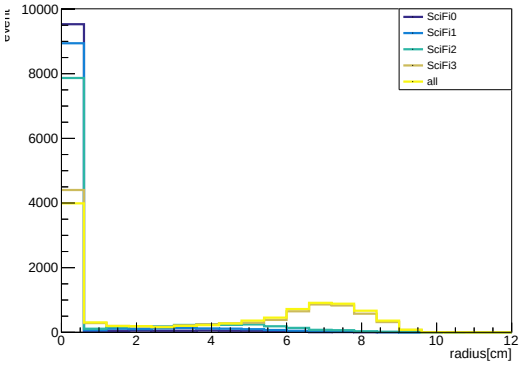

(d) 90E_radius in SciFi for 240 GeV PioT with a 10 cm target.

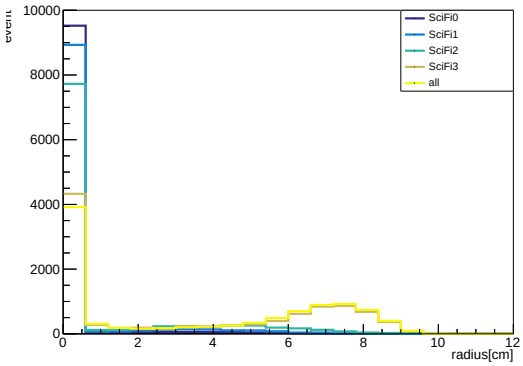

(e) 90E_radius in SciFi for 300 GeV PioT with a 10 cm target.

Figure F.16: 90E_radius in the SciFi with 30 cm target.

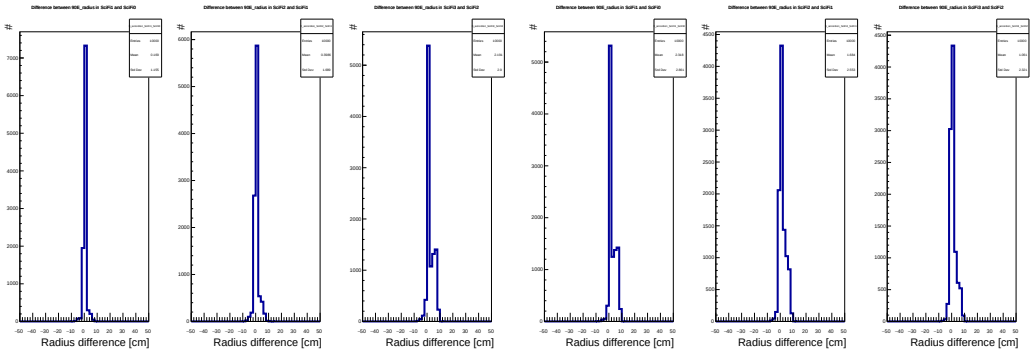

(a) Variations in 90E_radius in the SciFi in single events for 100 GeV impinging π

(b) Variations in 90E_radius in the SciFi in single events for 140 GeV impinging π

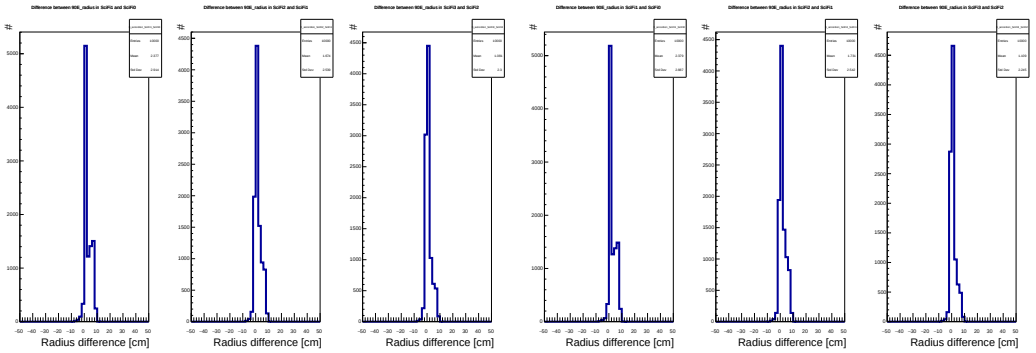

(c) Variations in 90E_radius in the SciFi in single events for 180 GeV impinging π

(d) Variations in 90E_radius in the SciFi in single events for 240 GeV impinging π

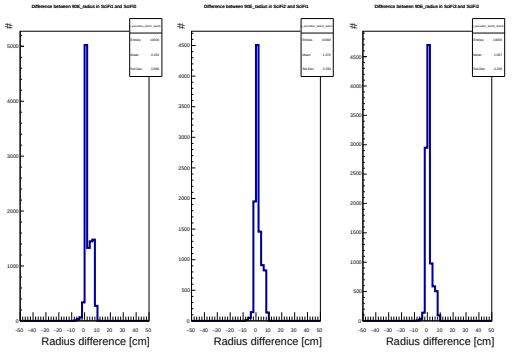

(e) Variations in 90E_radius in the SciFi in single events for 300 GeV impinging π

Figure F.17: Variations of 90E_radius in the SciFi with 30 cm target.

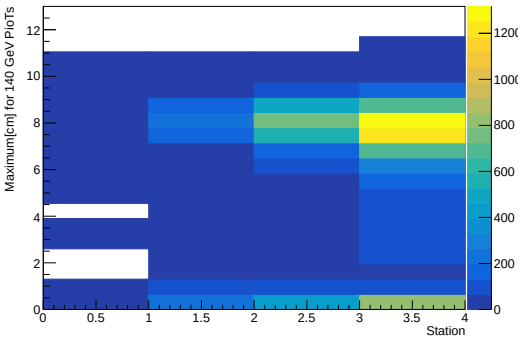

(a) SciFi station with largest 90E_radius with 140 GeV incoming π^+

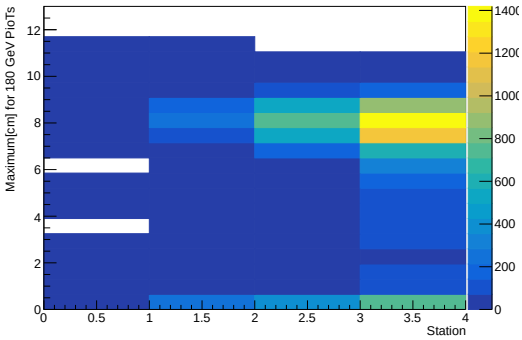

(b) SciFi station with largest 90E_radius with 180 GeV incoming π^+

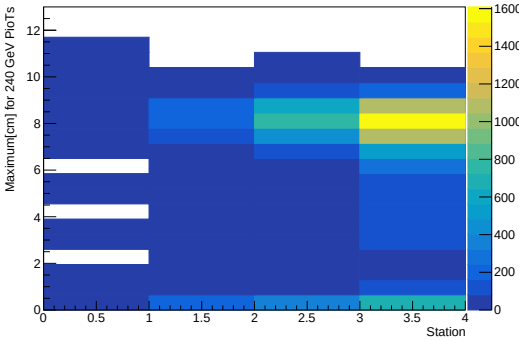

(c) SciFi station with largest 90E_radius with 240 GeV incoming π^+

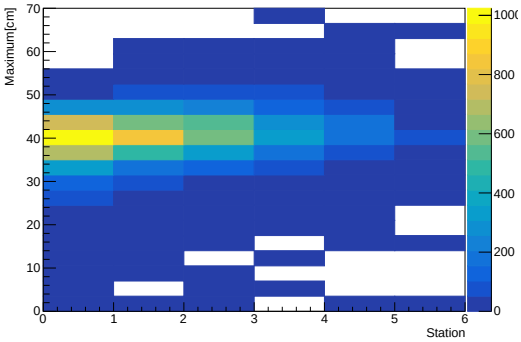

(a) HCAL station with largest 90E_radius with 140 GeV incoming π^+

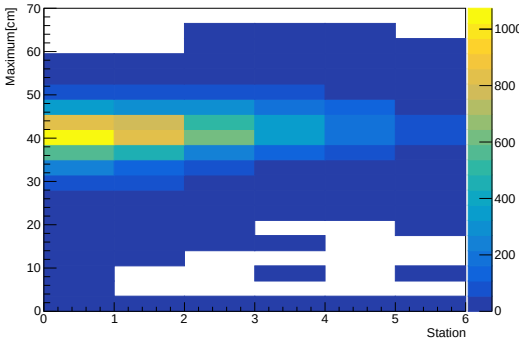

(b) HCAL station with largest 90E_radius with 180 GeV incoming π^+

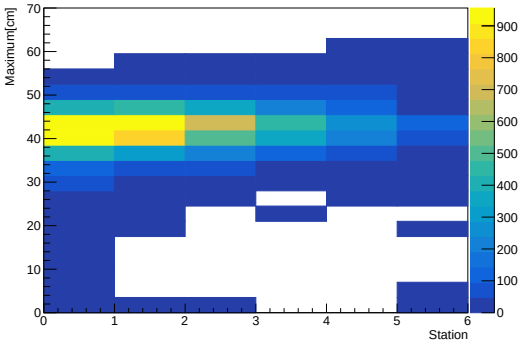

(c) HCAL station with largest 90E_radius with 240 GeV incoming π^+

Figure F.19

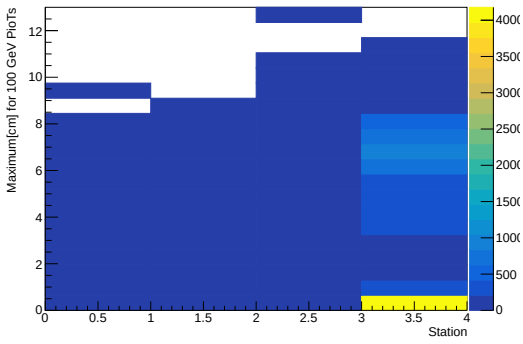

(a) SciFi station with largest 90E_radius with 100 GeV incoming π^+

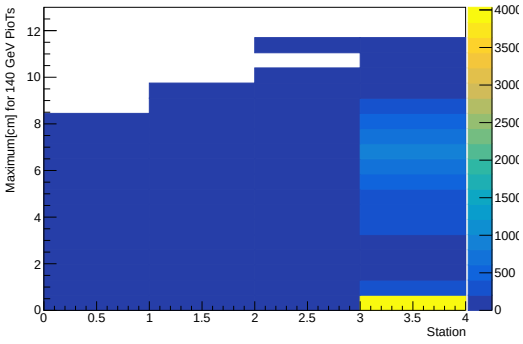

(b) SciFi station with largest 90E_radius with 140 GeV incoming π^+

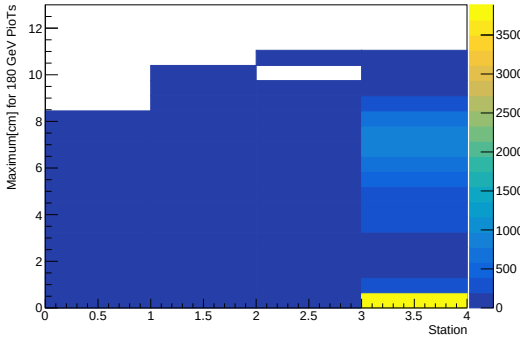

(c) SciFi station with largest 90E_radius with 180 GeV incoming π^+

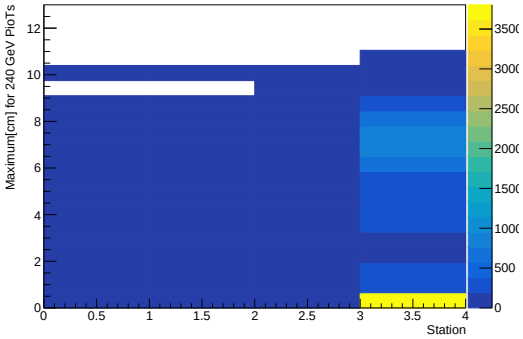

(d) SciFi station with largest 90E_radius with 240 GeV incoming π^+

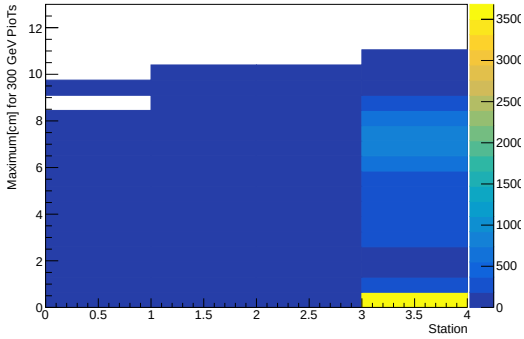

(e) SciFi station with largest 90E_radius with 300 GeV incoming π^+

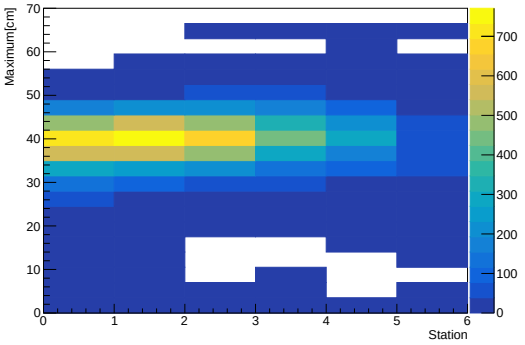

(a) HCAL station with largest 90E_radius with 100 GeV incoming π^+

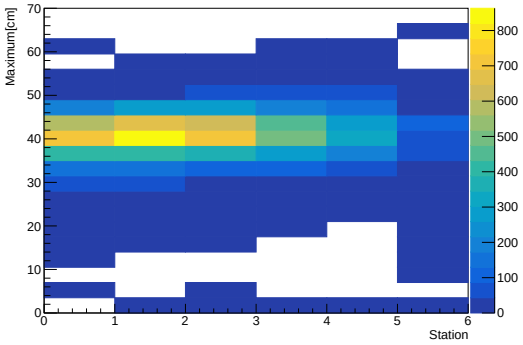

(b) HCAL station with largest 90E_radius with 140 GeV incoming π^+

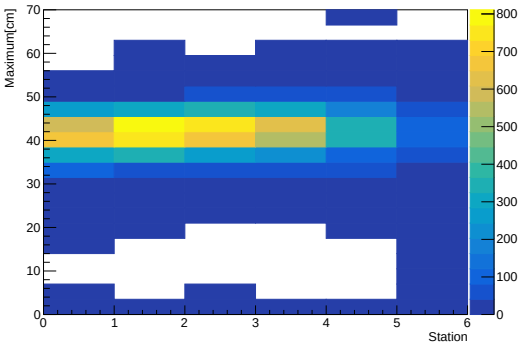

(c) HCAL station with largest 90E_radius with 180 GeV incoming π^+

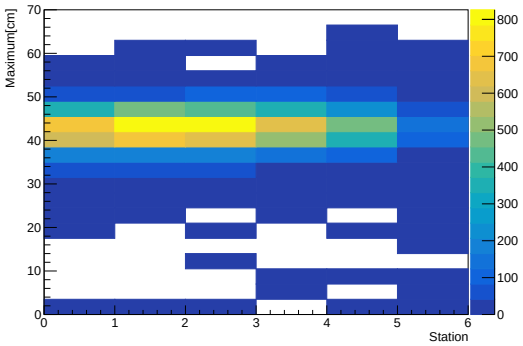

(d) HCAL station with largest 90E_radius with 240 GeV incoming π^+

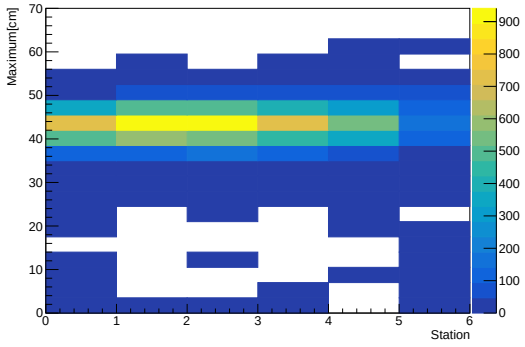

(e) HCAL station with largest 90E_radius with 300 GeV incoming π^+

Figure F.21

Bibliography

[1] D. P. Aguillard et al. 'Measurement of the Positive Muon Anomalous Magnetic Moment to 0.20 ppm'. In: *Phys. Rev. Lett.* 131 (16 2023), p. 161802. DOI: 10.1103/PhysRevLett.131.161802.

[2] X. Fan et al. 'Measurement of the Electron Magnetic Moment'. In: *Phys. Rev. Lett.* 130 (7 2023), p. 071801. DOI: 10.1103/PhysRevLett.130.071801.

[3] S. Chatrchyan et al. 'Observation of a new boson at a mass of 125 GeV with the CMS experiment at the LHC'. In: *Physics Letters B* 716.1 (2012), pp. 30–61. DOI: https://doi.org/10.1016/j.physletb.2012.08.021.

[4] G. Aad et al. 'Observation of a new particle in the search for the Standard Model Higgs boson with the ATLAS detector at the LHC'. In: *Physics Letters B* 716.1 (2012), pp. 1–29. DOI: https://doi.org/10.1016/j.physletb.2012.08.020.

[5] F. Englert and R. Brout. 'Broken Symmetry and the Mass of Gauge Vector Mesons'. In: *Phys. Rev. Lett.* 13 (9 1964), pp. 321–323. DOI: 10.1103/PhysRevLett.13.321.

[6] Peter W. Higgs. 'Broken Symmetries and the Masses of Gauge Bosons'. In: *Phys. Rev. Lett.* 13 (16 1964), pp. 508–509. DOI: 10.1103/PhysRevLett.13.508.

[7] G. S. Guralnik, C. R. Hagen and T. W. B. Kibble. 'Global Conservation Laws and Massless Particles'. In: *Phys. Rev. Lett.* 13 (20 1964), pp. 585–587. DOI: 10.1103/PhysRevLett.13.585.

[8] DESY. *Particle Physics 2011, Highlights and Annual Report*. Consulted on January 21st 2024. URL: https://www.desy.de/sites2009/site_www-desy/content/e410/e84441/e111138/DESY_PP_2011_ger.pdf.

[9] on behalf of the CDF Boris Tuchming and DØ collaborations. 'Tevatron Higgs Results'. In: *EPJ Web Conf.* 60 (2013), p. 02003. DOI: 10.1051/epjconf/20136002003.

[10] André de Gouvêa. 'Neutrino Mass Models'. In: *Ann. Rev. Nucl. Part. Sci.* 66 (2016), pp. 197–217. DOI: 10.1146/annurev-nucl-102115-044600.

[11] R. L. Workman et al. 'Review of Particle Physics'. In: *PTEP* 2022 (2022), p. 083C01. DOI: 10.1093/ptep/ptac097.

[12] Luigi Di Lella and Carlo Rubbia. 'The Discovery of the W and Z Particles'. In: *Adv. Ser. Direct. High Energy Phys.* 23 (2015), pp. 137–163. DOI: 10.1142/9789814644150_0006.

[13] S. Abachi et al. 'Observation of the top quark'. In: *Phys. Rev. Lett.* 74 (1995), pp. 2632–2637. DOI: 10.1103/PhysRevLett.74.2632.

[14] F. Abe et al. 'Observation of top quark production in $\bar{p}p$ collisions'. In: *Phys. Rev. Lett.* 74 (1995), pp. 2626–2631. DOI: 10.1103/PhysRevLett.74.2626.

[15] Yiming Abulaiti. *Status of searches for dark matter at the LHC*. Tech. rep. Geneva: CERN, 2022. URL: https://cds.cern.ch/record/2799299.

[16] J. Katharina Behr and Alexander Grohsjean. 'Dark Matter Searches with Top Quarks'. In: *Universe* 9 (2023), p. 16. DOI: 10.3390/universe9010016.

[17] G. Apollinari et al. 'High Luminosity Large Hadron Collider HL-LHC'. In: *CERN Yellow Rep.* 5 (2015), pp. 1–19. DOI: 10.5170/CERN-2015-005.1.

[18] E. Aprile et al. 'First Dark Matter Search with Nuclear Recoils from the XENONnT Experiment'. In: *Phys. Rev. Lett.* 131.4 (2023), p. 041003. DOI: 10.1103/PhysRevLett.131.041003.

[19] Jeff Chiles et al. 'New Constraints on Dark Photon Dark Matter with Superconducting Nanowire Detectors in an Optical Haloscope'. In: *Phys. Rev. Lett.* 128 (23 2022), p. 231802. DOI: 10.1103/PhysRevLett.128.231802.

[20] M. Filzinger et al. 'Improved Limits on the Coupling of Ultralight Bosonic Dark Matter to Photons from Optical Atomic Clock Comparisons'. In: *Phys. Rev. Lett.* 130 (25 2023), p. 253001. DOI: 10.1103/PhysRevLett.130.253001.

[21] Yasmine Sara Amhis et al. 'Averages of b-hadron, c-hadron, and τ-lepton properties as of 2021'. In: *Phys. Rev. D* 107.5 (2023), p. 052008. DOI: 10.1103/PhysRevD.107.052008.

[22] Roel Aaij et al. 'A study of *CP* violation in the decays $B^{\pm} \to [K^+K^-\pi^+\pi^-]_D h^{\pm}$ ($h = K, \pi$) and $B^{\pm} \to [\pi^+\pi^-\pi^+\pi^-]_D h^{\pm}$'. In: *Eur. Phys. J. C* 83.6 (2023). [Erratum: Eur.Phys.J.C 83, 672 (2023)], p. 547. DOI: 10.1140/epjc/s10052-023-11560-5.

[23] European Strategy Group. *2020 Update of the European Strategy for Particle Physics*. Tech. rep. Geneva, 2020. DOI: 10.17181/ESU2020.

[24] ECFA Detector R & D Roadmap Process Group. *The 2021 ECFA detector research and development roadmap*. Tech. rep. Geneva, 2020. DOI: 10.17181/CERN.XDPL.W2EX.

[25] *The High-Luminosity LHC Project. 298th Meeting of Scientific Policy Committee*. Tech. rep. 2016. URL: https://cds.cern.ch/record/2199189.

[26] R. Albanese et al. *BDF/SHiP at the ECN3 high-intensity beam facility*. Tech. rep. Geneva: CERN, 2023. URL: https://cds.cern.ch/record/2878604.

[27] D. Abbaneo et al. 'A Combination of preliminary electroweak measurements and constraints on the standard model'. In: (2001). eprint: hep-ex/0112021.

[28] D. Decamp et al. 'ALEPH: A detector for electron-positron annnihilations at LEP'. In: *Nucl. Instrum. Meth. A* 294 (1990). [Erratum: Nucl.Instrum.Meth.A 303, 393 (1991)], pp. 121–178. DOI: 10.1016/0168-9002(90)91831-U.

[29] P. A. Aarnio et al. 'The DELPHI detector at LEP'. In: *Nucl. Instrum. Meth. A* 303 (1991), pp. 233–276. DOI: 10.1016/0168-9002(91)90793-P.

[30] K. Ahmet et al. 'The OPAL detector at LEP'. In: *Nucl. Instrum. Meth. A* 305 (1991), pp. 275–319. DOI: 10.1016/0168-9002(91)90547-4.

[31] B. Adeva et al. 'The Construction of the L3 Experiment'. In: *Nucl. Instrum. Meth. A* 289 (1990), pp. 35–102. DOI: 10.1016/0168-9002(90)90250-A.

[32] S. Abachi et al. 'The D0 Detector'. In: *Nucl. Instrum. Meth. A* 338 (1994), pp. 185–253. DOI: 10.1016/0168-9002(94)91312-9.

[33] F. Abe et al. 'The CDF Detector: An Overview'. In: *Nucl. Instrum. Meth. A* 271 (1988), pp. 387–403. DOI: 10.1016/0168-9002(88)90298-7.

[34] Mark Thomson. *Modern Particle Physics*. 2013. ISBN: 978-1-107-03426-6.

[35] Francis Halzen and Alan D. Martin. *Quarks and Leptons, An Introductory Course in Modern Particle Physics*. 1984. ISBN: 0-471-88741-2.

[36] John D. Jackson. *Classical Electrodynamics*. 1999. ISBN: 0-471-30932-X.

[37] Bartel et al. 'New results on $e^-e^+ \to \mu^-\mu^+$ from the JADE detector at PETRA'. In: *Zeitschrift für Physik C Particles and Fields* (1985). DOI: 10.1007/BF01551792.

[38] G. 't Hooft and M. Veltman. 'Regularization and renormalization of gauge fields'. In: *Nuclear Physics B* 44.1 (1972), pp. 189–213. DOI: https://doi.org/10.1016/0550-3213(72)90279-9.

[39] Enrico Fermi. 'Tentativo di una teoria dell'emissione dei raggi beta'. In: *Ric. Sci.* 4 (1933), pp. 491–495.

[40] N. Boubarki. *Elements of Mathematics*. Chapters 7, 8 and 9. 1972. ISBN: 978-3-540-68851-8.

[41] Zhirayr Avetisyan. 'The structure of almost Abelian Lie algebras'. In: *International Journal of Mathematics* 33.08 (2022), p. 2250057. DOI: 10.1142/S0129167X22500574.

[42] C. N. Yang and R. L. Mills. 'Conservation of Isotopic Spin and Isotopic Gauge Invariance'. In: *Phys. Rev.* 96 (1 1954), pp. 191–195. DOI: 10.1103/PhysRev.96.191.

[43] F. Reines and C. L. Cowan. 'Detection of the free neutrino'. In: *Phys. Rev.* 92 (1953), pp. 830–831. DOI: 10.1103/PhysRev.92.830.

[44] C. L. Cowan et al. 'Detection of the free neutrino: A Confirmation'. In: *Science* 124 (1956), pp. 103–104. DOI: 10.1126/science.124.3212.103.

[45] Timo van Ritbergen and Robin G. Stuart. 'On the precise determination of the Fermi coupling constant from the muon lifetime'. In: *Nuclear Physics B* 564.3 (2000), pp. 343–390. DOI: https://doi.org/10.1016/S0550-3213(99)00572-6.

[46] Huayang Song, Hao Sun and Jiang-Hao Yu. 'Effective field theories of axion, ALP and dark photon'. In: *JHEP* 01 (2024), p. 161. DOI: 10.1007/JHEP01(2024)161.

[47] Steven Weinberg. 'Effective field theory, past and future'. In: *International Journal of Modern Physics A* 31.06 (2016), p. 1630007. DOI: 10.1142/S0217751X16300076.

[48] John F. Donoghue. 'General relativity as an effective field theory: The leading quantum corrections'. In: *Phys. Rev. D* 50 (1994), pp. 3874–3888. DOI: 10.1103/PhysRevD.50.3874.

[49] Carlo Alberto Gottardo. 'Search for charged lepton-flavour violation in top-quark decays at the LHC with the ATLAS detector'. Presented 26 Apr 2019. Bonn U., 2019. URL: https://cds.cern.ch/record/2676841.

[50] Kingman Cheung et al. 'Exploring interference effects between two ALP effective operators at the LHC'. In: (2024). eprint: 2404.14833.

[51] Rebeca Beltrán et al. 'Long-lived heavy neutral leptons from mesons in effective field theory'. In: *JHEP* 01 (2023), p. 015. DOI: 10.1007/JHEP01(2023)015.

[52] C. Antel et al. 'Feebly-interacting particles: FIPs 2022 Workshop Report'. In: *Eur. Phys. J. C* 83.12 (2023), p. 1122. DOI: 10.1140/epjc/s10052-023-12168-5.

[53] MURRAY GELL-MANN. 'Status of Weak Interactions'. In: *Rev. Mod. Phys.* 31 (3 1959), pp. 834–838. DOI: 10.1103/RevModPhys.31.834.

[54] Tsung-Dao Lee and CS Wu. 'Weak interactions'. In: *Annual Review of Nuclear Science* 15.1 (1965), pp. 381–476.

[55] C.Sbarra. *LEP II Boson cross sections and couplings*. 2000. URL: https://inspirehep.net/files/d614579761cde4b2abcb0ed22fef4894.

[56] F. J. Hasert et al. 'Observation of Neutrino Like Interactions Without Muon Or Electron in the Gargamelle Neutrino Experiment'. In: *Phys. Lett. B* 46 (1973), pp. 138–140. DOI: 10.1016/0370-2693(73)90499-1.

[57] W. D. Dau. 'UA1 results from pp collisions at $\sqrt{s} = 540$ GeV.' In: *International Cosmic Ray Conference*. Vol. 12. International Cosmic Ray Conference. 1983, pp. 71–90. URL: https://ui.adsabs.harvard.edu/abs/1983ICRC...12...71D.

[58] P. Bagnaia et al. 'Evidence for $Z^0 \to e^+e^-$ at the CERN $\bar{p}p$ Collider'. In: *Phys. Lett. B* 129 (1983), pp. 130–140. DOI: 10.1016/0370-2693(83)90744-X.

[59] M. Banner et al. 'Observation of Single Isolated Electrons of High Transverse Momentum in Events with Missing Transverse Energy at the CERN anti-p p Collider'. In: *Phys. Lett. B* 122 (1983), pp. 476–485. DOI: 10.1016/0370-2693(83)91605-2.

[60] S. L. Glashow. 'Partial Symmetries of Weak Interactions'. In: *Nucl. Phys.* 22 (1961), pp. 579–588. DOI: 10.1016/0029-5582(61)90469-2.

[61] Abdus Salam. 'Weak and Electromagnetic Interactions'. In: *Conf. Proc. C* 680519 (1968), pp. 367–377. DOI: 10.1142/9789812795915_0034.

[62] Steven Weinberg. 'A Model of Leptons'. In: *Phys. Rev. Lett.* 19 (1967), pp. 1264–1266. DOI: 10.1103/PhysRevLett.19.1264.

[63] S. Schael et al. 'Precision electroweak measurements on the Z resonance'. In: *Phys. Rept.* 427 (2006), pp. 257–454. DOI: 10.1016/j.physrep.2005.12.006.

[64] Victor Mukhamedovich Abazov et al. 'Measurement of the Effective Weak Mixing Angle in $p\bar{p} \to Z/\gamma^* \to \ell^+\ell^-$ Events'. In: *Phys. Rev. Lett.* 120.24 (2018), p. 241802. DOI: 10.1103/PhysRevLett.120.241802.

[65] Jens Erler and Matthias Schott. 'Electroweak Precision Tests of the Standard Model after the Discovery of the Higgs Boson'. In: *Prog. Part. Nucl. Phys.* 106 (2019), pp. 68–119. DOI: 10.1016/j.ppnp.2019.02.007.

[66] R. Casalbuoni et al. 'Vector and Axial Vector Bound States From a Strongly Interacting Electroweak Sector'. In: *Int. J. Mod. Phys. A* 4 (1989), p. 1065. DOI: 10.1142/S0217751X89000492.

[67] Antonio Dobado, Maria J. Herrero and Juan Terron. 'W+- Z0 signals from the strongly interacting symmetry breaking sector'. In: *Z. Phys. C* 50 (1991), pp. 465–472. DOI: 10.1007/BF01551458.

[68] E. Boos et al. 'Strongly interacting vector bosons at TeV e+ e- linear colliders'. In: *Phys. Rev. D* 57 (1998), p. 1553. DOI: 10.1103/PhysRevD.57.1553.

[69] A. S. Belyaev et al. 'Strongly interacting vector bosons at the CERN LHC: Quartic anomalous couplings'. In: *Phys. Rev. D* 59 (1999), p. 015022. DOI: 10.1103/PhysRevD.59.015022.

[70] F. Englert and R. Brout. 'Broken Symmetry and the Mass of Gauge Vector Mesons'. In: *Phys. Rev. Lett.* 13 (1964), pp. 321–323. DOI: 10.1103/PhysRevLett.13.321.

[71] Peter W. Higgs. 'Spontaneous Symmetry Breakdown without Massless Bosons'. In: *Phys. Rev.* 145 (1966), pp. 1156–1163. DOI: 10.1103/PhysRev.145.1156.

[72] G. S. Guralnik, C. R. Hagen and T. W. B. Kibble. 'Global Conservation Laws and Massless Particles'. In: *Phys. Rev. Lett.* 13 (1964), pp. 585–587. DOI: 10.1103/PhysRevLett.13.585.

[73] Yoichiro Nambu and G. Jona-Lasinio. 'Dynamical model of elementary particles based on an analogy with superconductivity. II.' In: *Phys. Rev.* 124 (1961), pp. 246–254. DOI: 10.1103/PhysRev.124.246.

[74] J. Goldstone. 'Field Theories with Superconductor Solutions'. In: *Nuovo Cim.* 19 (1961), pp. 154–164. DOI: 10.1007/BF02812722.

[75] Daniel Naegels. 'An introduction to Goldstone boson physics and to the coset construction'. In: 2021. arXiv: 2110.14504 [hep-th].

[76] T. P. Cheng, E. Eichten and Ling-Fong Li. 'Higgs Phenomena in Asymptotically Free Gauge Theories'. In: *Phys. Rev. D* 9 (1974), p. 2259. DOI: 10.1103/PhysRevD.9.2259.

[77] G. C. Branco et al. 'Theory and phenomenology of two-Higgs-doublet models'. In: *Phys. Rept.* 516 (2012), pp. 1–102. DOI: 10.1016/j.physrep.2012.02.002.

[78] Cássio Leite Vieira and Antonio Augusto Passos Videira. 'Carried by History: Cesar Lattes, Nuclear Emulsions, and the Discovery of the Pi-meson'. In: *Phys. Perspect.* 16 (2014), pp. 3–36. DOI: 10.1007/s00016-014-0128-6.

[79] M. Gell-Mann. 'Isotopic Spin and New Unstable Particles'. In: *Phys. Rev.* 92 (1953), pp. 833–834. DOI: 10.1103/PhysRev.92.833.

[80] T. Nakano and K. Nishijima. 'Charge Independence for V-particles'. In: *Prog. Theor. Phys.* 10 (1953), pp. 581–582. DOI: 10.1143/PTP.10.581.

[81] Murray Gell-Mann. 'Symmetries of Baryons and Mesons'. In: *Phys. Rev.* 125 (3 1962), pp. 1067–1084. DOI: 10.1103/PhysRev.125.1067.

[82] Nicola Cabibbo. 'Unitary Symmetry and Leptonic Decays'. In: *Phys. Rev. Lett.* 10 (1963), pp. 531–533. DOI: 10.1103/PhysRevLett.10.531.

[83] Makoto Kobayashi and Toshihide Maskawa. 'CP Violation in the Renormalizable Theory of Weak Interaction'. In: *Prog. Theor. Phys.* 49 (1973), pp. 652–657. DOI: 10.1143/PTP.49.652.

[84] Georges Aad et al. 'A precise measurement of the Z-boson double-differential transverse momentum and rapidity distributions in the full phase space of the decay leptons with the ATLAS experiment at $\sqrt{s} = 8$ TeV'. In: *Eur. Phys. J. C* 84.3 (2024), p. 315. DOI: 10.1140/epjc/s10052-024-12438-w.

[85] C. Giunti, C. W. Kim and U. W. Lee. 'Running coupling constants and grand unification models'. In: *Mod. Phys. Lett. A* 6 (1991), pp. 1745–1755. DOI: 10.1142/S0217732391001883.

[86] Adriano Di Giacomo. 'Confinement in QCD: novelties'. In: *Nucl. Part. Phys. Proc.* 324-329 (2023), pp. 90–93. DOI: 10.1016/j.nuclphysbps.2023.01.020.

[87] Gerard 't Hooft. 'On the Phase Transition Towards Permanent Quark Confinement'. In: *Nucl. Phys. B* 138 (1978), pp. 1–25. DOI: 10.1016/0550-3213(78)90153-0.

[88] Siegfried Bethke. 'Experimental tests of asymptotic freedom'. In: *Prog. Part. Nucl. Phys.* 58 (2007), pp. 351–386. DOI: 10.1016/j.ppnp.2006.06.001.

[89] David J. Gross and Frank Wilczek. 'Ultraviolet Behavior of Nonabelian Gauge Theories'. In: *Phys. Rev. Lett.* 30 (1973), pp. 1343–1346. DOI: 10.1103/PhysRevLett.30.1343.

[90] Stefan Scherer. 'Introduction to chiral perturbation theory'. In: *Adv. Nucl. Phys.* 27 (2003), p. 277.

[91] Yuri L. Dokshitzer. 'Calculation of the Structure Functions for Deep Inelastic Scattering and e+ e- Annihilation by Perturbation Theory in Quantum Chromodynamics.' In: *Sov. Phys. JETP* 46 (1977), pp. 641–653.

[92] Vladimir Naumovich Gribov and L N Lipatov. 'Deep inelastic ep scattering in perturbation theory'. In: *Sov. J. Nucl. Phys.* 15.4 (1972), pp. 438–450. URL: https://cds.cern.ch/record/427157.

[93] H. Abramowicz et al. 'Combination of measurements of inclusive deep inelastic $e^{\pm}p$ scattering cross sections and QCD analysis of HERA data'. In: *Eur. Phys. J. C* 75.12 (2015), p. 580. DOI: 10.1140/epjc/s10052-015-3710-4.

[94] Richard D. Ball et al. 'Parton distributions for the LHC Run II'. In: *JHEP* 04 (2015), p. 040. DOI: 10.1007/JHEP04(2015)040.

[95] F. D. Aaron et al. 'Combined Measurement and QCD Analysis of the Inclusive e+- p Scattering Cross Sections at HERA'. In: *JHEP* 01 (2010), p. 109. DOI: 10.1007/JHEP01(2010)109.

[96] Eric Drexler. *Summary of interactions between particles described by the Standard Model*. URL: https://upload.wikimedia.org/wikipedia/commons/a/a7/Elementary_particle_interactions_in_the_Standard_Model.png. 2014, Accessed on May 11th 2024.

[97] Babak Abi et al. 'Deep Underground Neutrino Experiment (DUNE), Far Detector Technical Design Report, Volume II: DUNE Physics'. In: (Feb. 2020). arXiv: 2002.03005 [hep-ex].

[98] Francis Halzen and Ali Kheirandish. 'Chapter 5: IceCube and High-Energy Cosmic Neutrinos'. In: *The Encyclopedia of Cosmology*. Ed. by Giovanni G. Fazi. 2023, pp. 107–235. DOI: 10.1142/9789811282645_0005. arXiv: 2202.00694 [astro-ph.HE].

[99] Y. Abe et al. 'Indication of Reactor $\bar{\nu}_e$ Disappearance in the Double Chooz Experiment'. In: *Phys. Rev. Lett.* 108 (2012), p. 131801. DOI: 10.1103/PhysRevLett.108.131801. arXiv: 1112.6353 [hep-ex].

[100] D. Abbaneo et al. 'Results and Perspectives from the First Two Years of Neutrino Physics at the LHC by the SND@LHC Experiment'. In: *Symmetry* 16.6 (2024), p. 702. DOI: 10.3390/sym16060702.

[101] Juan Rojo. 'Deep-Inelastic Scattering with LHC Neutrinos'. In: *31st International Workshop on Deep-Inelastic Scattering and Related Subjects*. July 2024. arXiv: 2407.06731 [hep-ph].

[102] Ferran Faura et al. 'The Strangest Proton?' In: *Eur. Phys. J. C* 80.12 (2020), p. 1168. DOI: 10.1140/epjc/s10052-020-08749-3. arXiv: 2009.00014 [hep-ph].

[103] A. De Roeck and R. S. Thorne. 'Structure Functions'. In: *Prog. Part. Nucl. Phys.* 66 (2011), pp. 727–781. DOI: 10.1016/j.ppnp.2011.06.001. arXiv: 1103.0555 [hep-ph].

[104] Sergey Alekhin et al. 'A facility to Search for Hidden Particles at the CERN SPS: the SHiP physics case'. In: *Rept. Prog. Phys.* 79.12 (2016), p. 124201. DOI: 10.1088/0034-4885/79/12/124201.

[105] C. Albright and C. Jarlskog. 'Neutrino production of M+ and E+ heavy leptons (I)'. In: *Nuc. Phys. B 84, pp. 467-492 ((1975))* ().

[106] G. Onengut et al. 'Measurement of charm production in antineutrino charged-current interactions'. In: *Phys. Lett. B* 604 (2004), pp. 11–21. DOI: 10.1016/j.physletb.2004.10.037.

[107] R. Schwienhorst et al. 'A New upper limit for the tau - neutrino magnetic moment'. In: *Phys. Lett. B* 513 (2001), pp. 23–29. DOI: 10.1016/S0370-2693(01)00746-8. arXiv: hep-ex/0102026.

[108] N. Aghanim et al. 'Planck 2018 results. VI. Cosmological parameters'. In: *Astron. Astrophys.* 641 (2020). [Erratum: Astron.Astrophys. 652, C4 (2021)], A6. DOI: 10.1051/0004-6361/201833910.

[109] Adam G. Riess et al. 'Observational evidence from supernovae for an accelerating universe and a cosmological constant'. In: *Astron. J.* 116 (1998), pp. 1009–1038. DOI: 10.1086/300499.

[110] Eric V. Linder. 'Exploring the expansion history of the universe'. In: *Phys. Rev. Lett.* 90 (2003), p. 091301. DOI: 10.1103/PhysRevLett.90.091301.

[111] A. G. Adame et al. 'DESI 2024 VI: cosmological constraints from the measurements of baryon acoustic oscillations'. In: *JCAP* 02 (2025), p. 021. DOI: 10.1088/1475-7516/2025/02/021.

[112] Yoshiaki Sofue and Vera Rubin. 'Rotation curves of spiral galaxies'. In: *Ann. Rev. Astron. Astrophys.* 39 (2001), pp. 137–174. DOI: 10.1146/annurev.astro.39.1.137.

[113] F. Zwicky. *Die Rotverschiebung von extragalaktischen Nebeln*. URL: https://ui.adsabs.harvard.edu/abs/1933AcHPh...6..110Z. Helvetica Physica Acta 6 (1933) 110.

[114] Edvige Corbelli and Paolo Salucci. 'The Extended Rotation Curve and the Dark Matter Halo of M33'. In: *Mon. Not. Roy. Astron. Soc.* 311 (2000), pp. 441–447. DOI: 10.1046/j.1365-8711.2000.03075.x.

[115] Richard Massey, Thomas Kitching and Johan Richard. 'The dark matter of gravitational lensing'. In: *Rept. Prog. Phys.* 73 (2010), p. 086901. DOI: 10.1088/0034-4885/73/8/086901.

[116] Douglas Clowe et al. 'A direct empirical proof of the existence of dark matter'. In: *Astrophys. J. Lett.* 648 (2006), pp. L109–L113. DOI: 10.1086/508162.

[117] Joachim Harnois-Déraps et al. 'Baryons, Neutrinos, Feedback and Weak Gravitational Lensing'. In: *Mon. Not. Roy. Astron. Soc.* 450.2 (2015), pp. 1212–1223. DOI: 10.1093/mnras/stv646.

[118] Ciaran O'Hare. *cajohare/AxionLimits: AxionLimits*. Version v1.0. 2020. DOI: 10.5281/zenodo.3932430. URL: https://cajohare.github.io/AxionLimits/.

[119] Wayne Hu, Rennan Barkana and Andrei Gruzinov. 'Cold and fuzzy dark matter'. In: *Phys. Rev. Lett.* 85 (2000), pp. 1158–1161. DOI: 10.1103/PhysRevLett.85.1158.

[120] Jae-Weon Lee. 'Galaxies with fuzzy dark matter'. In: *Journal of Korean Physical Society* 78.10 (2021), pp. 873–877. DOI: 10.1007/s40042-021-00077-3.

[121] Ilias Cholis et al. 'Orbital eccentricities in primordial black hole binaries'. In: *Phys. Rev. D* 94.8 (2016), p. 084013. DOI: 10.1103/PhysRevD.94.084013.

[122] Misao Sasaki et al. 'Primordial black holes—perspectives in gravitational wave astronomy'. In: *Class. Quant. Grav.* 35.6 (2018), p. 063001. DOI: 10.1088/1361-6382/aaa7b4.

[123] Anne M. Green. 'Primordial black holes as a dark matter candidate - a brief overview'. In: *Nucl. Phys. B* 1003 (2024), p. 116494. DOI: 10.1016/j.nuclphysb.2024.116494.

[124] Evan N. Kirby et al. 'Triangulum II. Not Especially Dense After All*'. In: *The Astrophysical Journal* 838.2 (2017). DOI: 10.3847/1538-4357/aa6570.

[125] Miguel A. Monroy-Rodríguez and Christine Allen. 'The End of the MACHO Era, Revisited: New Limits on MACHO Masses from Halo Wide Binaries'. In: *APJ* 790.2, 159 (2014), p. 159. DOI: 10.1088/0004-637X/790/2/159.

[126] Jacob D. Bekenstein. 'Relativistic gravitation theory for the MOND paradigm'. In: *Phys. Rev. D* (2004). [Erratum: Phys.Rev.D 71, 069901 (2005)]. DOI: 10.1103/PhysRevD.70.083509.

[127] Robert Monjo and Indranil Banik. 'Anomalous radial acceleration of galaxies and clusters supports hyperconical modified gravity'. In: (2024). arXiv: 2405.10019 [astro-ph.CO].

[128] Benoit Famaey and Stacy McGaugh. 'Modified Newtonian Dynamics (MOND): Observational Phenomenology and Relativistic Extensions'. In: *Living Rev. Rel.* 15 (2012), p. 10. DOI: 10.12942/lrr-2012-10.

[129] Oliver Schön. 'On Tensor Multi-Scalar Theories in a Post-Newtonian Setting'. PhD thesis. U. Tubingen, 2024. DOI: 10.15496/publikation-90502.

[130] David Benisty and Eduardo I. Guendelman. 'The Local Group as a test system for Modified Newtonian Dynamics'. In: *Phys. Dark Univ.* 30 (2020), p. 100708. DOI: 10.1016/j.dark.2020.100708.

[131] Fabio Iocco, Miguel Pato and Gianfranco Bertone. 'Testing modified Newtonian dynamics in the Milky Way'. In: *Phys. Rev. D* 92 (8 2015), p. 084046. DOI: 10.1103/PhysRevD.92.084046.

[132] David Vokrouhlický, David Nesvorný and Scott Tremaine. 'Testing MOND on small bodies in the remote solar system'. In: (2024). eprint: 2403.09555.

[133] Laurent Canetti, Marco Drewes and Mikhail Shaposhnikov. 'Matter and Antimatter in the Universe'. In: *New J. Phys.* 14 (2012), p. 095012. DOI: 10.1088/1367-2630/14/9/095012.

[134] Glennys R. Farrar and M. E. Shaposhnikov. 'Baryon asymmetry of the universe in the minimal Standard Model'. In: *Phys. Rev. Lett.* 70 (1993). [Erratum: Phys.Rev.Lett. 71, 210 (1993)], pp. 2833–2836. DOI: 10.1103/PhysRevLett.70.2833.

[135] Q. R. Ahmad et al. 'Direct evidence for neutrino flavor transformation from neutral current interactions in the Sudbury Neutrino Observatory'. In: *Phys. Rev. Lett.* 89 (2002), p. 011301. DOI: 10.1103/PhysRevLett.89.011301.

[136] Y. Fukuda et al. 'Evidence for oscillation of atmospheric neutrinos'. In: *Phys. Rev. Lett.* 81 (1998), pp. 1562–1567. DOI: 10.1103/PhysRevLett.81.1562.

[137] J. Schechter and J. W. F. Valle. 'Neutrino Masses in SU(2) x U(1) Theories'. In: *Phys. Rev. D* 22 (1980), p. 2227. DOI: 10.1103/PhysRevD.22.2227.

[138] J. Schechter and J. W. F. Valle. 'Neutrinoless Double beta Decay in SU(2) x U(1) Theories'. In: *Phys. Rev. D* 25 (1982), p. 2951. DOI: 10.1103/PhysRevD.25.2951.

[139] R. Arnold et al. 'Probing New Physics Models of Neutrinoless Double Beta Decay with SuperNEMO'. In: *Eur. Phys. J. C* 70 (2010), pp. 927–943. DOI: 10.1140/epjc/s10052-010-1481-5.

[140] V. Albanese et al. 'The SNO+ experiment'. In: *JINST* 16.08 (2021), P08059. DOI: 10.1088/1748-0221/16/08/P08059.

[141] A. Gando et al. 'Search for Majorana Neutrinos near the Inverted Mass Hierarchy Region with KamLAND-Zen'. In: *Phys. Rev. Lett.* 117.8 (2016). [Addendum: Phys.Rev.Lett. 117, 109903 (2016)], p. 082503. DOI: 10.1103/PhysRevLett.117.082503.

[142] M. Aker et al. 'Direct neutrino-mass measurement with sub-electronvolt sensitivity'. In: *Nature Phys.* 18.2 (2022), pp. 160–166. DOI: 10.1038/s41567-021-01463-1.

[143] A. Ashtari Esfahani et al. 'The Project 8 Neutrino Mass Experiment'. In: *Snowmass 2021*. 2022. eprint: 2203.07349.

[144] F. Couchot et al. 'Cosmological constraints on the neutrino mass including systematic uncertainties'. In: *Astron. Astrophys.* 606 (2017), A104. DOI: 10.1051/0004-6361/201730927.

[145] Mauricio Bustamante and Amy Connolly. 'Extracting the Energy-Dependent Neutrino-Nucleon Cross Section above 10 TeV Using IceCube Showers'. In: *Phys. Rev. Lett.* 122.4 (2019), p. 041101. DOI: 10.1103/PhysRevLett.122.041101.

[146] J. M. Pendlebury et al. 'Revised experimental upper limit on the electric dipole moment of the neutron'. In: *Phys. Rev. D* 92.9 (2015), p. 092003. DOI: 10.1103/PhysRevD.92.092003.

[147] B. Graner et al. 'Reduced Limit on the Permanent Electric Dipole Moment of $\mathbf{Hg}^{199}$'. In: *PRL* 116.16 (2016), p. 161601. DOI: 10.1103/PhysRevLett.116.161601.

[148] N. Yamanaka et al. 'Probing exotic phenomena at the interface of nuclear and particle physics with the electric dipole moments of diamagnetic atoms: A unique window to hadronic and semileptonic CP violation'. In: *Eur. Phys. J. A* 53.3 (2017), p. 54. DOI: 10.1140/epja/i2017-12237-2.

[149] Gerard 't Hooft. 'Symmetry Breaking Through Bell-Jackiw Anomalies'. In: *Phys. Rev. Lett.* 37 (1976), pp. 8–11. DOI: 10.1103/PhysRevLett.37.8.

[150] H. van Dam and M. J. G. Veltman. 'Massive and massless Yang-Mills and gravitational fields'. In: *Nucl. Phys. B* 22 (1970), pp. 397–411. DOI: 10.1016/0550-3213(70)90416-5.

[151] Steven Weinberg and Edward Witten. 'Limits on massless particles'. In: *Physics Letters B* 96.1 (1980), pp. 59–62. DOI: https://doi.org/10.1016/0370-2693(80)90212-9.

[152] Ryoyu Utiyama. 'Invariant Theoretical Interpretation of Interaction'. In: *Phys. Rev.* 101 (5 1956), pp. 1597–1607. DOI: 10.1103/PhysRev.101.1597.

[153] A.O. Barvinsky and G.A. Vilkovisky. 'The generalized Schwinger-DeWitt technique and the unique effective action in quantum gravity'. In: *Physics Letters B* 131.4 (1983), pp. 313–318. DOI: https://doi.org/10.1016/0370-2693(83)90506-3.

[154] Zvi Bern et al. 'Two-Loop Renormalization of Quantum Gravity Simplified'. In: *Phys. Rev. D* 95.4 (2017), p. 046013. DOI: 10.1103/PhysRevD.95.046013.

[155] David G. Boulware and Stanley Deser. 'String Generated Gravity Models'. In: *Phys. Rev. Lett.* 55 (1985), p. 2656. DOI: 10.1103/PhysRevLett.55.2656.

[156] Bryce S. DeWitt. 'Quantum Theory of Gravity. 1. The Canonical Theory'. In: *Phys. Rev.* 160 (1967), pp. 1113–1148. DOI: 10.1103/PhysRev.160.1113.

[157] Bryce S. DeWitt. 'Quantum Theory of Gravity. 2. The Manifestly Covariant Theory'. In: *Phys. Rev.* 162 (1967), pp. 1195–1239. DOI: 10.1103/PhysRev.162.1195.

[158] Don N. Page and C. D. Geilker. 'Indirect Evidence for Quantum Gravity'. In: *Phys. Rev. Lett.* 47 (14 1981), pp. 979–982. DOI: 10.1103/PhysRevLett.47.979.

[159] Kenneth Eppley and Eric Hannah. 'The necessity of quantizing the gravitational field'. In: *Found. Phys.* 7.1 (1977), pp. 51–68. DOI: 10.1007/BF00715241.

[160] B.Dewitt and G. ESPOSITO. 'An introduction to quantum gravity'. In: *International Journal of Geometric Methods in Modern Physics* 05.01 (2008), pp. 101–156. DOI: 10.1142/S0219887808002679.

[161] Athanasios Bakopoulos, Christos Charmousis and Nicolas Lecoeur. 'Compact objects in gravity theories'. In: *33rd Rencontres de Blois: Exploring the Dark Universe*. 2022.

[162] Irvin Martinez. 'Compact Objects from Spontaneous Symmetry Breaking'. In: (2023). eprint: 2301.09239.

[163] Eran Palti. 'The Swampland: Introduction and Review'. In: *Fortsch. Phys.* 67.6 (2019), p. 1900037. DOI: 10.1002/prop.201900037.

[164] Howard Georgi and S. L. Glashow. 'Unity of All Elementary-Particle Forces'. In: *Phys. Rev. Lett.* 32 (8 1974), pp. 438–441. DOI: 10.1103/PhysRevLett.32.438.

[165] Guido Altarelli. 'The Standard electroweak theory and beyond'. In: *Theoretical Advanced Study Institute in Elementary Particle Physics (TASI 98): Neutrinos in Physics and Astrophysics: From 10**(-33) to 10**(+28) cm*. 1998. arXiv: hep-ph/9811456.

[166] Leonard Susskind. 'Dynamics of Spontaneous Symmetry Breaking in the Weinberg-Salam Theory'. In: *Phys. Rev. D* 20 (1979), pp. 2619–2625. DOI: 10.1103/PhysRevD.20.2619.

[167] Gerard 't Hooft. 'Naturalness, chiral symmetry, and spontaneous chiral symmetry breaking'. In: *NATO Sci. Ser. B* 59 (1980), pp. 135–157. DOI: 10.1007/978-1-4684-7571-5_9.

[168] Sidney Coleman and Jeffrey Mandula. 'All Possible Symmetries of the S Matrix'. In: *Phys. Rev.* 159 (5 1967), pp. 1251–1256. DOI: 10.1103/PhysRev.159.1251.

[169] Rudolf Haag, Jan T. Łopuszański and Martin Sohnius. 'All possible generators of supersymmetries of the S-matrix'. In: *Nuclear Physics B* 88.2 (1975), pp. 257–274. DOI: https://doi.org/10.1016/0550-3213(75)90279-5.

[170] Christopher T. Hill and Elizabeth H. Simmons. 'Strong Dynamics and Electroweak Symmetry Breaking'. In: *Phys. Rept.* 381 (2003). [Erratum: Phys.Rept. 390, 553–554 (2004)]. DOI: 10.1016/S0370-1573(03)00140-6.

[171] Thomas G. Rizzo. 'Pedagogical introduction to extra dimensions'. In: *eConf* C040802 (2004), p. L013. arXiv: hep-ph/0409309.

[172] Howard Georgi. 'Unparticle physics'. In: *Phys. Rev. Lett.* 98 (2007), p. 221601. DOI: 10.1103/PhysRevLett.98.221601.

[173] R. Sekhar Chivukula and Howard Georgi. 'Composite Technicolor Standard Model'. In: *Phys. Lett. B* 188 (1987), pp. 99–104. DOI: 10.1016/0370-2693(87)90713-1.

[174] Krishna Rajagopal and Frank Wilczek. 'The Condensed matter physics of QCD'. In: *At the frontier of particle physics. Handbook of QCD. Vol. 1-3*. 2000, pp. 2061–2151. DOI: 10.1142/9789812810458_0043.

[175] Diptimoy Ghosh, Matteo Salvarezza and Fabrizio Senia. 'Extending the Analysis of Electroweak Precision Constraints in Composite Higgs Models'. In: *Nucl. Phys. B* 914 (2017), pp. 346–387. DOI: 10.1016/j.nuclphysb.2016.11.013.

[176] E. J. Salumbides et al. 'Constraints on extra dimensions from precision molecular spectroscopy'. In: *New J. Phys.* 17.3 (2015), p. 033015. DOI: 10.1088/1367-2630/17/3/033015.

[177] Stephen P. Martin. 'A Supersymmetry primer'. In: *Adv. Ser. Direct. High Energy Phys.* 18 (1998). Ed. by Gordon L. Kane, pp. 1–98. DOI: 10.1142/9789812839657_0001. arXiv: hep-ph/9709356.

[178] I. Hinchliffe et al. 'Precision SUSY measurements at CERN LHC'. In: *Phys. Rev. D* 55 (1997), pp. 5520–5540. DOI: 10.1103/PhysRevD.55.5520.

[179] Sophie Kadan. 'Searches for Supersymmetry (SUSY) at the Large Hadron Collider'. In: (2024). arXiv: 2404.16922 [hep-ex].

[180] R. Casalbuoni et al. 'A gravitino - goldstino high-energy equivalence theorem'. In: *Phys. Lett. B* 215 (1988), pp. 313–316. DOI: 10.1016/0370-2693(88)91439-6.

[181] Stanley D Deser and B Zumino. 'Broken supersymmetry and supergravity'. In: *Phys. Rev. Lett.* 38 (1977), p. 1433. DOI: 10.1103/PhysRevLett.38.1433.

[182] Kiwoon Choi. 'Goldstone supermultiplet as the messenger of supersymmetry breaking'. In: *Phys. Rev. D* 54 (1996), pp. 6591–6595. DOI: 10.1103/PhysRevD.54.R6591.

[183] Pierre Fayet and J. Iliopoulos. 'Spontaneously Broken Supergauge Symmetries and Goldstone Spinors'. In: *Phys. Lett. B* 51 (1974), pp. 461–464. DOI: 10.1016/0370-2693(74)90310-4.

[184] Taekoon Lee. 'Higher dimensional operator corrections to the Goldstino Goldberg-Treiman vertices'. In: *Eur. Phys. J. C* 13 (2000), pp. 365–369. DOI: 10.1007/s100520000256.

[185] Andrea Brignole, Ferruccio Feruglio and Fabio Zwirner. 'Aspects of spontaneously broken N=1 global supersymmetry in the presence of gauge interactions'. In: *Nucl. Phys. B* 501 (1997), pp. 332–374. DOI: 10.1016/S0550-3213(97)80767-5.

[186] K. O. Astapov and D. S. Gorbunov. 'Decaying light particles in the SHiP experiment. III. Signal rate estimates for scalar and pseudoscalar sgoldstinos'. In: *Phys. Rev. D* 93.3 (2016), p. 035008. DOI: 10.1103/PhysRevD.93.035008. arXiv: 1511.05403 [hep-ph].

[187] D. S. Gorbunov. 'Light sgoldstino: Precision measurements versus collider searches'. In: *Nucl. Phys. B* 602 (2001), pp. 213–237. DOI: 10.1016/S0550-3213(01)00122-5. arXiv: hep-ph/0007325.

[188] David E. Morrissey and Michael J. Ramsey-Musolf. 'Electroweak baryogenesis'. In: *New J. Phys.* 14 (2012), p. 125003. DOI: 10.1088/1367-2630/14/12/125003.

[189] Vanda Silveira and A. Zee. 'Scalar phantoms'. In: *Phys. Lett. B* 161 (1985), pp. 136–140. DOI: 10.1016/0370-2693(85)90624-0.

[190] Daniel Feldman, Boris Kors and Pran Nath. 'Extra-weakly Interacting Dark Matter'. In: *Phys. Rev. D* 75 (2007), p. 023503. DOI: 10.1103/PhysRevD.75.023503.

[191] Z. Chacko, Hock-Seng Goh and Roni Harnik. 'The Twin Higgs: Natural electroweak breaking from mirror symmetry'. In: *Phys. Rev. Lett.* 96 (2006), p. 231802. DOI: 10.1103/PhysRevLett.96.231802.

[192] Matthew J. Strassler and Kathryn M. Zurek. 'Echoes of a hidden valley at hadron colliders'. In: *Phys. Lett. B* 651 (2007), pp. 374–379. DOI: 10.1016/j.physletb.2007.06.055.

[193] John March-Russell et al. 'Heavy Dark Matter Through the Higgs Portal'. In: *JHEP* 07 (2008), p. 058. DOI: 10.1088/1126-6708/2008/07/058.

[194] Timothy Cohen et al. 'Asymmetric Dark Matter from a GeV Hidden Sector'. In: *Phys. Rev. D* 82 (2010), p. 056001. DOI: 10.1103/PhysRevD.82.056001.

[195] David Curtin et al. 'Exotic decays of the 125 GeV Higgs boson'. In: *Phys. Rev. D* 90.7 (2014), p. 075004. DOI: 10.1103/PhysRevD.90.075004.

[196] Martin Wolfgang Winkler. 'Decay and detection of a light scalar boson mixing with the Higgs boson'. In: *Phys. Rev. D* 99.1 (2019), p. 015018. DOI: 10.1103/PhysRevD.99.015018.

[197] Hsin-Chia Cheng, Lingfeng Li and Ennio Salvioni. 'A theory of dark pions'. In: *JHEP* 01 (2022), p. 122. DOI: 10.1007/JHEP01(2022)122.

[198] Howard Georgi. 'A Model of Soft CP Violation'. In: *Hadronic J.* 1 (1978), p. 155.

[199] M. A. B. Beg and H. -S. Tsao. 'Strong P, T Noninvariances in a Superweak Theory'. In: *Phys. Rev. Lett.* 41 (1978), p. 278. DOI: 10.1103/PhysRevLett.41.278.

[200] Ann E. Nelson. 'Naturally Weak CP Violation'. In: *Phys. Lett. B* 136 (1984), pp. 387–391. DOI: 10.1016/0370-2693(84)92025-2.

[201] Stuart Samuel. 'Does the Yang-Mills theory solve the strong CP problem by itself?' In: *Mod. Phys. Lett. A* 7 (1992), pp. 2007–2016. DOI: 10.1142/S0217732392001737.

[202] F. L. Bezrukov and Y. Burnier. 'Towards a solution of the strong CP problem by compact extra dimensions'. In: *Phys. Rev. D* 80 (2009), p. 125004. DOI: 10.1103/PhysRevD.80.125004.

[203] R. D. Peccei and Helen R. Quinn. 'CP Conservation in the Presence of Instantons'. In: *Phys. Rev. Lett.* 38 (1977), pp. 1440–1443. DOI: 10.1103/PhysRevLett.38.1440.

[204] R. D. Peccei and Helen R. Quinn. 'Constraints Imposed by CP Conservation in the Presence of Instantons'. In: *Phys. Rev. D* 16 (1977), pp. 1791–1797. DOI: 10.1103/PhysRevD.16.1791.

[205] Jihn E. Kim. 'Light Pseudoscalars, Particle Physics and Cosmology'. In: *Phys. Rept.* 150 (1987), pp. 1–177. DOI: 10.1016/0370-1573(87)90017-2.

[206] Mikhail A. Shifman, A. I. Vainshtein and Valentin I. Zakharov. 'Can Confinement Ensure Natural CP Invariance of Strong Interactions?' In: *Nucl. Phys. B* 166 (1980), pp. 493–506. DOI: 10.1016/0550-3213(80)90209-6.

[207] Mark Srednicki. 'Axion Couplings to Matter. 1. CP Conserving Parts'. In: *Nucl. Phys. B* 260 (1985), pp. 689–700. DOI: 10.1016/0550-3213(85)90054-9.

[208] Michael Dine, Willy Fischler and Mark Srednicki. 'A simple solution to the strong CP problem with a harmless axion'. In: *Physics Letters B* 104.3 (1981), pp. 199–202. DOI: https://doi.org/10.1016/0370-2693(81)90590-6.

[209] A. R. Zhitnitsky. 'On Possible Suppression of the Axion Hadron Interactions. (In Russian)'. In: *Sov. J. Nucl. Phys.* 31 (1980), p. 260.

[210] Stephon Alexander, Tucker Manton and Evan McDonough. 'The Field Theory Axiverse'. In: (2024). arXiv: 2404.11642 [hep-ph].

[211] John March-Russell, James Unwin and Stephen M. West. 'Closing in on Asymmetric Dark Matter I: Model independent limits for interactions with quarks'. In: *JHEP* 08 (2012), p. 029. DOI: 10.1007/JHEP08(2012)029.

[212] Afiq Anuar et al. *ALP-ine quests at the LHC: hunting axion-like particles via peaks and dips in $t\bar{t}$ production*. Tech. rep. 2024. URL: https://cds.cern.ch/record/2900407.

[213] Anne Mareike Galda, Matthias Neubert and Sophie Renner. 'ALP - SMEFT interference'. In: *JHEP* 06 (2021), p. 135. DOI: 10.1007/JHEP06(2021)135.

[214] H. Primakoff. 'Photo-Production of Neutral Mesons in Nuclear Electric Fields and the Mean Life of the Neutral Meson'. In: *Phys. Rev.* 81 (5 1951), pp. 899–899. DOI: 10.1103/PhysRev.81.899.

[215] V. M. Budnev et al. 'The Two photon particle production mechanism. Physical problems. Applications. Equivalent photon approximation'. In: *Phys. Rept.* 15 (1975), pp. 181–281. DOI: 10.1016/0370-1573(75)90009-5.

[216] Babette Döbrich et al. 'ALPtraum: ALP production in proton beam dump experiments'. In: *JHEP* 02 (2016), p. 018. DOI: 10.1007/JHEP02(2016)018.

[217] Lucian Harland–Lang, Joerg Jaeckel and Michael Spannowsky. 'A fresh look at ALP searches in fixed target experiments'. In: *Physics Letters B* 793 (2019), pp. 281–289. DOI: https://doi.org/10.1016/j.physletb.2019.04.045.

[218] S. D. Drell and Tung-Mow Yan. 'Massive Lepton Pair Production in Hadron-Hadron Collisions at High-Energies'. In: *Phys. Rev. Lett.* 25 (1970). [Erratum: Phys.Rev.Lett. 25, 902 (1970)], pp. 316–320. DOI: 10.1103/PhysRevLett.25.316.

[219] Sang Hui Im and Kwang Sik Jeong. 'Freeze-in Axion-like Dark Matter'. In: *Phys. Lett. B* 799 (2019), p. 135044. DOI: 10.1016/j.physletb.2019.135044.

[220] Takehiko Asaka and Mikhail Shaposhnikov. 'The νMSM, dark matter and baryon asymmetry of the universe'. In: *Phys. Lett. B* 620 (2005), pp. 17–26. DOI: 10.1016/j.physletb.2005.06.020.

[221] K. N. Abazajian et al. 'Light Sterile Neutrinos: A White Paper'. In: (2012). arXiv: 1204.5379 [hep-ph].

[222] A. Aguilar et al. 'Evidence for neutrino oscillations from the observation of $\bar{\nu}_e$ appearance in a $\bar{\nu}_\mu$ beam'. In: *Phys. Rev. D* 64 (2001), p. 112007. DOI: 10.1103/PhysRevD.64.112007.

[223] A. A. Aguilar-Arevalo et al. 'Significant Excess of ElectronLike Events in the MiniBooNE Short-Baseline Neutrino Experiment'. In: *Phys. Rev. Lett.* 121.22 (2018), p. 221801. DOI: 10.1103/PhysRevLett.121.221801.

[224] Andre de Gouvea. 'See-saw energy scale and the LSND anomaly'. In: *Phys. Rev. D* 72 (2005), p. 033005. DOI: 10.1103/PhysRevD.72.033005.

[225] G. Mention et al. 'The Reactor Antineutrino Anomaly'. In: *Phys. Rev. D* 83 (2011), p. 073006. DOI: 10.1103/PhysRevD.83.073006.

[226] Steven Weinberg. 'Baryon and Lepton Nonconserving Processes'. In: *Phys. Rev. Lett.* 43 (1979), pp. 1566–1570. DOI: 10.1103/PhysRevLett.43.1566.

[227] Samuel Brieden, Héctor Gil-Marín and Licia Verde. 'Model-agnostic interpretation of 10 billion years of cosmic evolution traced by BOSS and eBOSS data'. In: *JCAP* 08.08 (2022), p. 024. DOI: 10.1088/1475-7516/2022/08/024.

[228] Kyrylo Bondarenko et al. 'Phenomenology of GeV-scale Heavy Neutral Leptons'. In: *JHEP* 11 (2018), p. 032. DOI: 10.1007/JHEP11(2018)032.

[229] Alexey Boyarsky et al. 'Improved big bang nucleosynthesis constraints on heavy neutral leptons'. In: *Phys. Rev. D* 104.2 (2021), p. 023517. DOI: 10.1103/PhysRevD.104.023517.

[230] Nashwan Sabti, Andrii Magalich and Anastasiia Filimonova. 'An Extended Analysis of Heavy Neutral Leptons during Big Bang Nucleosynthesis'. In: *JCAP* 11 (2020), p. 056. DOI: 10.1088/1475-7516/2020/11/056.

[231] James M. Cline, Matteo Puel and Takashi Toma. 'A little theory of everything, with heavy neutral leptons'. In: *JHEP* 05 (2020), p. 039. DOI: 10.1007/JHEP05(2020)039.

[232] Stefano Vergani et al. 'Explaining the MiniBooNE excess through a mixed model of neutrino oscillation and decay'. In: *Phys. Rev. D* 104.9 (2021), p. 095005. DOI: 10.1103/PhysRevD.104.095005.

[233] Paulo Areyuna C., Jilberto Zamora-Saa and Alfonso R. Zerwekh. 'Dark Matter in the Vector Scotogenic Model'. In: (2024). arXiv: 2403.04030 [hep-ph].

[234] Henri Ruegg and Marti Ruiz-Altaba. 'The Stueckelberg field'. In: *Int. J. Mod. Phys. A* 19 (2004), pp. 3265–3348. DOI: 10.1142/S0217751X04019755.

[235] B. L. Combridge. 'Associated Production of Heavy Flavor States in p p and anti-p p Interactions: Some QCD Estimates'. In: *Nucl. Phys. B* 151 (1979), pp. 429–456. DOI: 10.1016/0550-3213(79)90449-8.

[236] Atakan Akmete. 'Sensitivity of the SHiP Experiment to Hidden Particles at the CERN SpS'. MA thesis. Middle East Tech. U., Ankara, 2020.

[237] Peter Adshead, Kaloian D. Lozanov and Zachary J. Weiner. 'Dark photon dark matter from an oscillating dilaton'. In: *Phys. Rev. D* 107.8 (2023), p. 083519. DOI: 10.1103/PhysRevD.107.083519.

[238] Marco Fabbrichesi, Emidio Gabrielli and Gaia Lanfranchi. 'The Dark Photon'. In: (2020). DOI: 10.1007/978-3-030-62519-1.

[239] Hartmut Wittig. 'Progress on $(g-2)_\mu$ from Lattice QCD'. In: *57th Rencontres de Moriond on Electroweak Interactions and Unified Theories*. 2023. arXiv: 2306.04165 [hep-ph].

[240] Jihn E. Kim. 'Weak Interaction Singlet and Strong CP Invariance'. In: *Phys. Rev. Lett.* 43 (1979), p. 103. DOI: 10.1103/PhysRevLett.43.103.

[241] Kunio Kaneta, Hye-Sung Lee and Seokhoon Yun. 'Portal Connecting Dark Photons and Axions'. In: *Phys. Rev. Lett.* 118.10 (2017), p. 101802. DOI: 10.1103/PhysRevLett.118.101802.

[242] Patrick deNiverville and Hye-Sung Lee. 'Implications of the dark axion portal for SHiP and FASER and the advantages of monophoton signals'. In: *Phys. Rev. D* 100.5 (2019), p. 055017. DOI: 10.1103/PhysRevD.100.055017.

[243] Alexey Boyarsky et al. 'Searches for new physics at SND@LHC'. In: *JHEP* 03 (2022), p. 006. DOI: 10.1007/JHEP03(2022)006. arXiv: 2104.09688 [hep-ph].

[244] T. Aaltonen et al. 'A Search for dark matter in events with one jet and missing transverse energy in $p\bar{p}$ collisions at $\sqrt{s} = 1.96$ TeV'. In: *Phys. Rev. Lett.* 108 (2012), p. 211804. DOI: 10.1103/PhysRevLett.108.211804. arXiv: 1203.0742 [hep-ex].

[245] A. H. Abdelhameed et al. 'First results from the CRESST-III low-mass dark matter program'. In: *Phys. Rev. D* 100.10 (2019), p. 102002. DOI: 10.1103/PhysRevD.100.102002. arXiv: 1904.00498 [astro-ph.CO].

[246] Ewa Lopienska. 'The CERN accelerator complex, layout in 2022. Complexe des accélérateurs du CERN en janvier 2022'. In: (2022). General Photo. URL: https://cds.cern.ch/record/2800984.

[247] Michał Czakon, Paul Fiedler and Alexander Mitov. 'Total Top-Quark Pair-Production Cross Section at Hadron Colliders Through $O(\alpha_S^4)$'. In: *Phys. Rev. Lett.* 110 (2013), p. 252004. DOI: 10.1103/PhysRevLett.110.252004.

[248] 'LHC Machine'. In: *JINST* 3 (2008). Ed. by Lyndon Evans and Philip Bryant, S08001. DOI: 10.1088/1748-0221/3/08/S08001.

[249] G. Aad et al. 'The ATLAS Experiment at the CERN Large Hadron Collider'. In: *JINST* 3 (2008), S08003. DOI: 10.1088/1748-0221/3/08/S08003.

[250] S. Chatrchyan et al. 'The CMS Experiment at the CERN LHC'. In: *JINST* 3 (2008), S08004. DOI: 10.1088/1748-0221/3/08/S08004.

[251] K. Aamodt et al. 'The ALICE experiment at the CERN LHC'. In: *JINST* 3 (2008), S08002. DOI: 10.1088/1748-0221/3/08/S08002.

[252] A. Augusto Alves Jr. et al. 'The LHCb Detector at the LHC'. In: *JINST* 3 (2008), S08005. DOI: 10.1088/1748-0221/3/08/S08005.

[253] Michael Tino and Michael Kobel. 'Determination of muon reconstruction efficiencies in the ATLAS detector using a tag & probe approach in $Z \to \mu\mu$ events'. In: (2011). URL: https://www.researchgate.net/publication/241772118_Determination_of_muon_reconstruction_efficiencies_in_the_ATLAS_detector_using_a_tag_probe_approach_in_Z_events.

[254] A. De Rujula and R. Ruckl. 'Neutrino and muon physics in the collider mode of future accelerators'. In: *SSC Workshop: Superconducting Super Collider Fixed Target Physics*. May 1984, pp. 571–596. DOI: 10.5170/CERN-1984-010-V-2.571.

[255] A. De Rújula, E. Fernández and J.J. Gómez-Cadenas. 'Neutrino fluxes at future hadron colliders'. In: *Nuclear Physics B* 405.1 (1993), pp. 80–108. ISSN: 0550-3213. DOI: https://doi.org/10.1016/0550-3213(93)90427-Q. URL: https://www.sciencedirect.com/science/article/pii/055032139390427Q.

[256] François Vannucci. *Neutrino physics at LHC/SSC*. Tech. rep. Paris: Paris 6. Lab. Phys. Nucl. Théor. Hautes Enérg., 1993. URL: https://cds.cern.ch/record/253670.

[257] N. Beni et al. 'Physics Potential of an Experiment using LHC Neutrinos'. In: *J. Phys. G* 46.11 (2019), p. 115008. DOI: 10.1088/1361-6471/ab3f7c. arXiv: 1903.06564 [hep-ex].

[258] N. Beni et al. 'Further studies on the physics potential of an experiment using LHC neutrinos'. In: *J. Phys. G* 47.12 (2020), p. 125004. DOI: 10.1088/1361-6471/aba7ad. arXiv: 2004.07828 [hep-ex].

[259] Roel Aaij et al. 'Test of lepton universality in beauty-quark decays'. In: *Nature Phys.* 18.3 (2022). [Addendum: Nature Phys. 19, (2023)], pp. 277–282. DOI: 10.1038/s41567-023-02095-3. arXiv: 2103.11769 [hep-ex].

[260] K. Kodama et al. 'Observation of tau neutrino interactions'. In: *Phys. Lett. B* 504 (2001), pp. 218–224. DOI: 10.1016/S0370-2693(01)00307-0. arXiv: hep-ex/0012035.

[261] N. Agafonova et al. 'OPERA tau neutrino charged current interactions'. In: *Sci. Data* 8.1 (2021), p. 218. DOI: 10.1038/s41597-021-00991-y.

[262] Abbaneo et al. *AdvSND, The Advanced Scattering and Neutrino Detector at High Lumi LHC Letter of Intent*. Tech. rep. Geneva: CERN, 2024. URL: https://cds.cern.ch/record/2895224.

[263] P. Migliozzi G. De Lellis and P. Santorelli. 'Charm physics with neutrinos'. In: *Phys. Rept.399 227* (). [Erratum: Phys. Rept.411,323(2005)].

[264] Richard D. Ball et al. 'Parton distributions from high-precision collider data'. In: *Eur. Phys. J. C* 77.10 (2017), p. 663. DOI: 10.1140/epjc/s10052-017-5199-5.

[265] Rhorry Gauld and Juan Rojo. 'Precision determination of the small-x gluon from charm production at LHCb'. In: *Phys. Rev. Lett.* 118.7 (2017), p. 072001. DOI: 10.1103/PhysRevLett.118.072001. eprint: 1610.09373.

[266] C. Ahdida et al. 'SND@LHC'. In: (Feb. 2020). arXiv: 2002.08722 [physics.ins-det].

[267] G. Acampora et al. 'SND@LHC: the scattering and neutrino detector at the LHC'. In: *JINST* 19.05 (2024), P05067. DOI: 10.1088/1748-0221/19/05/P05067. arXiv: 2210.02784 [hep-ex].

[268] Marco Dalavalle. *Collider Neutrinos, Standard Model at the LHC*. Consulted on October 11$^{\text{th}}$ 2024. 2024. URL: https://indico.cern.ch/event/1346940/contributions/5785341/attachments/2853412/4990010/SM@LHC2024_marcodallavalle.pdf.

[269] S. Polityko et al. 'The bremsstrahlung of muons at extremely high energies with LPM and dielectric suppression effect'. In: *Nuclear Instruments and Methods in Physics Research Section B: Beam Interactions with Materials and Atoms* 173.1 (2001), pp. 30–36. ISSN: 0168-583X. DOI: https://doi.org/10.1016/S0168-583X(00)00114-2.

[270] Rüdiger Voss. 'Deep-inelastic scattering with muons'. In: *Physics Reports* 403-404 (2004), pp. 3–18. ISSN: 0370-1573. DOI: https://doi.org/10.1016/j.physrep.2004.08.006.

[271] R. Albanese et al. 'Measurement of the muon flux at the SND@LHC experiment'. In: *Eur. Phys. J. C* 84.1 (2024), p. 90. DOI: 10.1140/epjc/s10052-023-12380-3. arXiv: 2310.05536 [hep-ex].

[272] Consulted on August 4$^{\text{th}}$ 2024. URL: https://eljentechnology.com/products/plastic-scintillators/ej-200-ej-204-ej-208-ej-212.

[273] Vanessa Nadig et al. 'Evaluation of the PETsys TOFPET2 ASIC in multi-channel coincidence experiments'. In: *EJNMMI Physics* (2021). DOI: 10.1186/s40658-021-00370-x.

[274] Antonio Iuliano. 'Event reconstruction and data analysis techniques for the SHiP experiment'. Presented 03 Jun 2021. Università degli Studi di Napoli Federico II, 2021. URL: https://cds.cern.ch/record/2776128.

[275] C. Ahdida et al. 'Reconstruction of 400 GeV/c proton interactions with the SHiP-charm project'. In: *Eur. Phys. J. C* 84.6 (2024), p. 562. DOI: 10.1140/epjc/s10052-024-12655-3.

[276] 'LHCb Tracker Upgrade Technical Design Report'. In: (Feb. 2014).

[277] Suekiti Kinoshita. 'The Photographic Action of the α-Particles emitted from Radioactive Substances'. In: *Proc. R. Soc. 83A: 432–458* (1910).

[278] Andrey Alexandrov et al. 'Super-resolution imaging for the detection of low-energy ion tracks in fine-grained nuclear emulsions'. In: *Sci. Rep.* 13.1 (2023), p. 22813. DOI: 10.1038/s41598-023-50208-y. arXiv: 2304.03645 [astro-ph.IM].

[279] 'Technical Design Report for the ATLAS Inner Tracker Pixel Detector'. In: (2017). DOI: 10.17181/CERN.FOZZ.ZP3Q.

[280] M. Mager. 'ALPIDE, the Monolithic Active Pixel Sensor for the ALICE ITS upgrade'. In: *Nucl. Instrum. Meth. A* 824 (2016). Ed. by Maria Giuseppina Bisogni et al., pp. 434–438. DOI: 10.1016/j.nima.2015.09.057.

[281] Brian Batell et al. 'Discovering dark matter at the LHC through its nuclear scattering in far-forward emulsion and liquid argon detectors'. In: *Phys. Rev. D* 104 (3 2021), p. 035036. DOI: 10.1103/PhysRevD.104.035036.

[282] G.C. Farnell and L.R. Solman. 'The Role of Gold in Sulphur-Plus-Gold Sensitization'. In: *The Journal of Photographic Science* 24.5-6 (1976), pp. 203–204. DOI: 10.1080/00223638.1976.11737894.

[283] Akitaka Ariga et al. *Particle Physics Reference Library, Nuclear Emulsions*. Chapter 9. ISBN: 9783030353179. DOI: 10.1007/978-3-030-35318-6.

[284] T. Nakamura et al. 'The OPERA film: New nuclear emulsion for large-scale, high-precision experiments'. In: *Nucl. Instrum. Meth. A* 556 (2006), pp. 80–86. DOI: 10.1016/j.nima.2005.08.109.

[285] C. Amsler et al. 'A new application of emulsions to measure the gravitational force on antihydrogen'. In: *JINST* (2013). DOI: 10.1088/1748-0221/8/02/P02015.

[286] Valeri Tioukov. *Emulsion analysis status and prospects*. 2016. URL: https://indico.cern.ch/event/580015/contributions/2366634/attachments/1376679/2090722/vt_EmulsionScanning_2016.pdf.

[287] A. Alexandrov et al. 'A new fast scanning system for the measurement of large angle tracks in nuclear emulsions'. In: *JINST* 10.11 (2015), P11006. DOI: 10.1088/1748-0221/10/11/P11006.

[288] V. Tyukov et al. 'The FEDRA Framework for emulsion data reconstruction and analysis in the OPERA experiment'. In: *Nucl. Instrum. Meth. A* 559 (2006). Ed. by J. Blumlein et al., pp. 103–105. DOI: 10.1016/j.nima.2005.11.214.

[289] Consulted on January 7$^{\text{th}}$ 2024. URL: https://www.hamamatsu.com/jp/en/product/optical-sensors/mppc/mppc_mppc-array/S13552.html.

[290] Consulted on January 7$^{\text{th}}$ 2024. URL: https://www.hamamatsu.com/jp/en/product/optical-sensors/mppc/mppc_mppc-array/S14160-3010PS.html.

[291] Giovanni De Lellis. *The SND@LHC experiment at CERN*.

[292] Consulted on September 6th 2024. URL: https://ttc.web.cern.ch/.

[293] Consulted on September 6th 2024. URL: https://github.com/SND-LHC/sndsw.

[294] Consulted on September 6th 2024. URL: https://github.com/ShipSoft/FairShip.

[295] Consulted on September 6th 2024. URL: https://fairroot.gsi.de/.

[296] Matei Climescu. 'Simulation of a silicon pixel tracker in a 400 GeV proton on thick target experiment to measure the charm production cross section'. Presented 02 Oct 2019. Bonn U., 2020. URL: https://cds.cern.ch/record/2718975.

[297] Consulted on September 7th. URL: https://geant4.web.cern.ch/.

[298] S. Agostinelli et al. 'GEANT4–a simulation toolkit'. In: *Nucl. Instrum. Meth. A* 506 (2003), pp. 250–303. DOI: 10.1016/S0168-9002(03)01368-8.

[299] C Ahdida et al. 'New Capabilities of the FLUKA Multi-Purpose Code'. In: *Front. Phys.* 9 (2022), p. 788253. DOI: 10.3389/fphy.2021.788253. URL: https://cds.cern.ch/record/2806210.

[300] Giuseppe Battistoni et al. 'Overview of the FLUKA code'. In: *Annals Nucl. Energy* 82 (2015), pp. 10–18. DOI: 10.1016/j.anucene.2014.11.007.

[301] Torbjorn Sjostrand, Stephen Mrenna and Peter Z. Skands. 'PYTHIA 6.4 Physics and Manual'. In: *JHEP* 05 (2006), p. 026. DOI: 10.1088/1126-6708/2006/05/026.

[302] Stefan Roesler, Ralph Engel and Johannes Ranft. 'The Monte Carlo event generator DPMJET-III'. In: *International Conference on Advanced Monte Carlo for Radiation Physics, Particle Transport Simulation and Applications (MC 2000)*. Dec. 2000, pp. 1033–1038. DOI: 10.1007/978-3-642-18211-2_166.

[303] Christian Bierlich et al. 'A comprehensive guide to the physics and usage of PYTHIA 8.3'. In: *SciPost Phys. Codeb.* 2022 (2022), p. 8. DOI: 10.21468/SciPostPhysCodeb.8.

[304] Costas Andreopoulos et al. 'The GENIE Neutrino Monte Carlo Generator: Physics and User Manual'. In: (2015). arXiv: 1510.05494 [hep-ph].

[305] R. Albanese et al. 'Observation of Collider Muon Neutrinos with the SND@LHC Experiment'. In: *Phys. Rev. Lett.* 131.3 (2023), p. 031802. DOI: 10.1103/PhysRevLett.131.031802. arXiv: 2305.09383 [hep-ex].

[306] W. Bonivento et al. 'Proposal to Search for Heavy Neutral Leptons at the SPS'. In: (Oct. 2013). arXiv: 1310.1762 [hep-ex].

[307] M. Anelli et al. 'A facility to Search for Hidden Particles (SHiP) at the CERN SPS'. In: (Apr. 2015). arXiv: 1504.04956 [physics.ins-det].

[308] Ahdida et al. *SHiP Experiment - Comprehensive Design Study report*. Tech. rep. Geneva: CERN, 2019. URL: https://cds.cern.ch/record/2704147.

[309] Aberle et al. *BDF/SHiP at the ECN3 high-intensity beam facility*. Tech. rep. Geneva: CERN, 2022. URL: https://cds.cern.ch/record/2839677.

[310] Aberle et al. *Study of alternative locations for the SPS Beam Dump Facility*. Tech. rep. The report is an update of the Comprehensive Design Study of the SPS Beam Dump Facility (CERN-PBC-REPORT-2019-005; CERN-2020-002), complementing the BDF/SHiP proposal. Geneva: CERN, 2022. arXiv: 2204.03549. URL: https://cds.cern.ch/record/2802785.

[311] H. S. Subramania. 'A Study of inclusive production of open charm particles at HERA-B energies using (1020) as a tag'. In: (2005). Accessed on October 5th 2024. URL: https://lss.fnal.gov/archive/other/thesis/subramania.pdf.

[312] A. Akmete et al. 'The active muon shield in the SHiP experiment'. In: *JINST* 12.05 (2017), P05011. DOI: 10.1088/1748-0221/12/05/P05011. arXiv: 1703.03612 [physics.ins-det].

[313] Maksym Ovchynnikov. *Muon DIS: recent updates*. Sept. 2024. URL: https://indico.cern.ch/event/1448055/contributions/6133463/attachments/2939825/5164537/SHiP_collaboration_meeting_talks__03_10_2024_%20(3).pdf.

[314] Iaroslava Bezshyiko. *Neutrino Background studies for SHiP*. Sept. 2024. URL: https://indico.cern.ch/event/1448055/contributions/6133461/attachments/2939669/5164189/NB-Oct2024-1.pdf.

[315] A. Brignoli et al. 'Performance of Prototypes with Different Reflector Materials for the SHiP Liquid Scintillator Surrounding Background Tagger'. In: (Mar. 2025). arXiv: 2503.10250 [physics.ins-det].

[316] Milind Vaman Diwan. 'Liquid Scintillators; Technology and Challenges'. In: (Aug. 2024). arXiv: 2408.01820 [physics.ins-det].

[317] Benjamin Bastian-Querner et al. 'The Wavelength-Shifting Optical Module'. In: *Sensors* 22.4 (2022), p. 1385. DOI: 10.3390/s22041385. arXiv: 2112.12258 [astro-ph.IM].

[318] J. Alt et al. 'Performance of a first full-size WOM-based liquid scintillator detector cell as prototype for the SHiP Surrounding Background Tagger'. In: *JINST* 19.05 (2024), P05024. DOI: 10.1088/1748-0221/19/05/P05024. arXiv: 2311.07340 [physics.ins-det].

[319] Amalia Ballarino et al. 'Chapter 6A: Cold powering of the superconducting circuits'. In: *CERN Yellow Rep. Monogr.* 10 (2020). Ed. by I. Béjar Alonso et al., pp. 129–137. DOI: 10.23731/CYRM-2020-0010.129.

[320] Lucie Baudet. *Spectrometer Magnet Status*. Consulted on October 6th 2024. 2024. URL: https://indico.cern.ch/event/1448055/contributions/6133500/attachments/2939384/5164709/241003_30thSHiPCollabMeeting_SpectrometerMagnet_Status_Final.pdf.

[321] N. I. Azorskii et al. 'New type of drift tubes for gas-discharge detectors operating in vacuum: Production technology and quality control'. In: *Phys. Part. Nucl. Lett.* 14.1 (2017), pp. 144–149. DOI: 10.1134/S1547477117010071.

[322] E. Delagnes et al. 'Reaching a few picosecond timing precision with the 16-channel digitizer and timestamper SAMPIC ASIC'. In: *Nucl. Instrum. Meth. A* 787 (2015). Ed. by Rémi Barbier et al., pp. 245–249. DOI: 10.1016/j.nima.2014.12.042.

[323] S. Gómez et al. 'FastIC: a fast integrated circuit for the readout of high performance detectors'. In: *JINST* 17.05 (2022), p. C05027. DOI: 10.1088/1748-0221/17/05/C05027.

[324] Michael Jonker. 'Readout Control Specifications for the Front-End and Back-End of SHiP'. In: (2016). URL: https://cds.cern.ch/record/2162870.

[325] D. Breton and J. Maalmi. *Electronics status and plans: report to collaboration meeting*. Consulted on October 6th 2024. 2024. URL: https://indico.cern.ch/event/1448055/contributions/6133245/attachments/2940246/5165275/SHiP_Electronics_Oct_2024_report.pdf.

[326] Maurice Garcia-Sciveres and Norbert Wermes. 'A review of advances in pixel detectors for experiments with high rate and radiation'. In: *Rept. Prog. Phys.* 81.6 (2018), p. 066101. DOI: 10.1088/1361-6633/aab064.

[327] A. Gabrielli et al. 'The silicon vertex detector of the Belle II experiment'. In: *Nucl. Instrum. Meth. A* 1064 (2024), p. 169401. DOI: 10.1016/j.nima.2024.169401.

[328] Matteo Giovannetti. 'New resistive gaseous detectors for high energy physics and beyond'. No public link available at the time of writing. University of Tor Vergata, 2023. URL: https://pubblicazioni.dsi.infn.it/tesi/gettesi.php?filename=533499.pdf.

[329] Maria Teresa Camerlingo. 'Analysis of the $W(H) \to (W)\, W\, W^*$ channel and validation of resistive Micromegas detectors for the ATLAS experiment'. University of Rome 3, 2022. URL: http://www.matfis.uniroma3.it/Allegati/Dottorato/TESI/MTCAMERLINGO/CamerlingoMT_34cycle_thesis_vFin_v2.pdf.

[330] Norbert Wermes and Hermann Kolanoski. *Particle Detectors*. 2020. ISBN: 978-0198858362.

[331] R:Wigmans. *Calorimetry*. 2017. ISBN: 9780198786351.

[332] Claus Grupen and Boris Schwartz. *Particle Detctors*. 2008. ISBN: 9781009401531.

[333] Luca Giannessi et al. 'Review of Recent Photocathode Advancements'. In: *JACoW* FEL2022 (2023), WEAI1. DOI: 10.18429/JACoW-FEL2022-WEAI1.

[334] S. Palestini. 'The liquid krypton calorimeter for experiment CERN-NA48'. In: *Nucl. Instrum. Meth. A* 367 (1995). Ed. by W. Bartl et al., pp. 263–266. DOI: 10.1016/0168-9002(95)00645-1.

[335] F. Nessi-Tedaldi. 'Overview of PbWO-4 calorimeter in CMS'. In: *Nucl. Instrum. Meth. A* 408 (1998). Ed. by P. Schlein, pp. 266–273. DOI: 10.1016/S0168-9002(98)00321-0.

[336] Hua-Qiao Zhang. 'The ATLAS Liquid Argon calorimeter: Overview and performance'. In: *J. Phys. Conf. Ser.* 293 (2011). Ed. by Yifang Wang, p. 012044. DOI: 10.1088/1742-6596/293/1/012044.

[337] Henri Videau. 'The Aleph Pictorial Electromagnetic Calorimeter: A High Granularity Gaseous Calorimeter Operated in a High Magnetic Field'. In: *Nucl. Instrum. Meth. A* 225 (1984), p. 481. DOI: 10.1016/0167-5087(84)90090-5.

[338] Bruno Rossi. *High Energy Particles*. 1st edition, Prentice-Hall. 1952.

[339] E. Longo and I. Sestili. 'Monte Carlo Calculation of Photon Initiated Electromagnetic Showers in Lead Glass'. In: *Nucl. Instrum. Meth.* 128 (1975). [Erratum: Nucl.Instrum.Meth. 135, 587 (1976)], p. 283. DOI: 10.1016/0029-554X(75)90679-5.

[340] Erwin Hilger. 'THE ZEUS URANIUM SCINTILLATOR CALORIMETER FOR HERA'. In: *Nucl. Instrum. Meth. A* 257 (1987). Ed. by E. Borchi, P. G. Pelfer and P. G. Rancoita, p. 488. DOI: 10.1016/0168-9002(87)90952-1.

[341] M. Abbrescia et al. 'The IDEA detector concept for FCC-ee'. In: (Feb. 2025). arXiv: 2502.21223 [physics.ins-det].

[342] Riccardo Aliberti. 'Particle Identification with Calorimeters for the Measurement of the Rare Decay $K^+ \to \pi^+\nu\bar{\nu}$ at NA62'. Presented 21 Jan 2019. Mainz U., 2018. URL: https://cds.cern.ch/record/2671696.

[343] J.M. Bauer. 'The BaBar Electromagnetic Calorimeter: Status and Performance Improvements'. In: *IEEE Nuclear Science Symposium Conference Record, 2005*. Vol. 2, pp. 1038–1042. DOI: 10.1109/nssmic.2005.1596430. URL: http://dx.doi.org/10.1109/NSSMIC.2005.1596430.

[344] Toyoko J. Orimoto. 'The CMS Electromagnetic Calorimeter: Construction, Commissioning and Calibration'. In: *PoS* EPS-HEP2009 (2009), p. 129. URL: https://cds.cern.ch/record/1283254.

[345] A. M. Magnan. 'HGCAL: a High-Granularity Calorimeter for the endcaps of CMS at HL-LHC'. In: *JINST* 12.01 (2017). Ed. by Pietro Govoni et al., p. C01042. DOI: 10.1088/1748-0221/12/01/C01042.

[346] DongWook Kim et al. 'A dose verification method for proton therapy by using a plastic scintillation plate'. In: *J Korean Phys Soc* 55.2 (2009), pp. 702–708.

[347] Antoine Laudrain. 'The CALICE AHCAL: a highly granular SiPM-on-tile hadron calorimeter prototype'. In: *J. Phys. Conf. Ser.* 2374.1 (2022), p. 012017. DOI: 10.1088/1742-6596/2374/1/012017.

[348] P. Annis et al. 'Tracking with capillaries and liquid scintillator'. In: *Nucl. Phys. B Proc. Suppl.* 61 (1998). Ed. by E. Borchi et al., pp. 390–395. DOI: 10.1016/S0920-5632(97)00592-6.

[349] Bastian Kessler. *Development of Wavelength-shifting Fibers with high Photon Capture-Rate*. Consulted on November 11th 2024. 2024. URL: https://butler.physik.uni-mainz.de/icecube/thesis/.

[350] 'Intelligent PMTs versus SiPMs'. In: (2013). Consulted on November 3rd. URL: https://indico.cern.ch/event/249875/contributions/546201/attachments/432321/599951/lecture_infieri_Puill.pdf.

[351] K. Abe et al. 'Hyper-Kamiokande Design Report'. In: (May 2018). arXiv: 1805.04163 [physics.ins-det].

[352] M. Grodzicka et al. 'Effective dead time of APD cells of SiPM'. In: *2011 IEEE Nuclear Science Symposium Conference Record*. 2011, pp. 553–562. DOI: 10.1109/NSSMIC.2011.6154111.

[353] Ketek GmbH: SiPM Technology. Version: 2015. URL: http://www.ketek.net/products/sipm-technology/.

[354] York Haemisch et al. 'Fully Digital Arrays of Silicon Photomultipliers (dSiPM) – a Scalable Alternative to Vacuum Photomultiplier Tubes (PMT)'. In: *Phys. Procedia* 37 (2012). Ed. by Ted Liu, pp. 1546–1560. DOI: 10.1016/j.phpro.2012.03.749.

[355] Consulted on November 16th. URL: https://www.onsemi.com/pub/collateral/and9782-d.pdf.

[356] Josue Daniel Jaramillo Arroyave. *EventCalc: An Event Generator for the SHiP Experiment at CERN*. Aug. 2024.

[357] Yehor Kyselov and Maksym Ovchynnikov. 'Searches for long-lived dark photons at proton accelerator experiments'. In: (Sept. 2024). arXiv: 2409.11096 [hep-ph].

[358] A. Lai et al. 'New measurements of the eta and K0 masses'. In: *Phys. Lett. B* 533 (2002), pp. 196–206. DOI: 10.1016/S0370-2693(02)01573-3.

[359] Phi Chau. 'Optimierung von hochauflösenden Sampling-Kalorimetern mit szintillatorbasierter SiPM-Auslese'. PhD thesis. Mainz U., 2022. DOI: 10.25358/openscience-7043.

[360] Walter M. Bonivento. 'Studies for the electro-magnetic calorimeter SplitCal for the SHiP experiment at CERN with shower direction reconstruction capability'. In: *JINST* 13.02 (2018), p. C02041. DOI: 10.1088/1748-0221/13/02/C02041.

[361] Michael et al. Tytgat. 'The Triple-GEM Project for the Phase 2 Upgrade of the CMS Muon System'. In: *PoS* TIPP2014 (2014), p. 065. DOI: 10.22323/1.213.0065.

[362] W. Bertozzi et al. 'Focal Plane Instrumentation: A Very High Resolution MWPC System for Inclined Tracks'. In: *Nucl. Instrum. Meth.* 141 (1977), pp. 457–476. DOI: 10.1016/0029-554X(77)90639-5.

[363] Hartmut F. W. Sadrozinski, Abraham Seiden and Nicolò Cartiglia. '4D tracking with ultra-fast silicon detectors'. In: *Rept. Prog. Phys.* 81.2 (2018), p. 026101. DOI: 10.1088/1361-6633/aa94d3. arXiv: 1704.08666 [physics.ins-det].

[364] Sebastian Ritter and Matei Climescu. *Calorimeters report from test beam*. 2024. URL: https://indico.cern.ch/event/1481729/contributions/6256102/.

[365] Stefan Kormannshaus. 'Measuring the direction of electromagnetic showers using MicroMegas detectors'. University of Mainz, 2018.

[366] Eduardo Cortina Gil et al. 'The Beam and detector of the NA62 experiment at CERN'. In: *JINST* 12.05 (2017), P05025. DOI: 10.1088/1748-0221/12/05/P05025. arXiv: 1703.08501 [physics.ins-det].

[367] Kuraray, private communication.

[368] Consulted on January 7th 2024. URL: https://www.hamamatsu.com/content/dam/hamamatsu-photonics/sites/documents/99_SALES_LIBRARY/ssd/s13360_series_kapd1052e.pdf.

[369] Rainer Wanke. *Calorimeter status and plans*. Consulted on January 5th 2025. 2019. URL: https://indico.cern.ch/event/799276/timetable/#20190313.detailed.

[370] Consulted on May 11th 2025. URL: https://www.rohde-schwarz.com/products/test-and-measurement/oscilloscopes/rs-rto6-oscilloscope_63493-1079745.html?change_c=true.

[371] Matthew Loyd et al. 'Accelerated aging test of new plastic scintillators'. In: *Nuclear Instruments and Methods in Physics Research Section A: Accelerators, Spectrometers, Detectors and Associated Equipment* 949 (2020), p. 162918. ISSN: 0168-9002. DOI: https://doi.org/10.1016/j.nima.2019.162918.

[372] Consulted on January 27th 2025. URL: https://docs.broadcom.com/doc/AFBR-S4N66C013-NUV-HD-Single-Silicon-Photo-Multiplier-DS.

[373] Yuriy Popovych. Private, Communication. 2022.

[374] Matei Climescu. Consulted on February 9th 2025. URL: https://gitlab.cern.ch/mclimesc/fibresim.

[375] Mirco Deckenhoff. 'Scintillating Fibre and Silicon Photomultiplier Studies for the LHCb upgrade'. PhD thesis. Dortmund U., Dec. 2015. DOI: 10.17877/DE290R-16897.

[376] Simon Nieswand. 'Measurement of the exit characteristics of light from optical multimode plastic fibres'. MA thesis. RWTH Aachen U., Dec. 2014.

[377] Q. Weitzel et al. 'Measurement of the response of Silicon Photomultipliers from single photon detection to saturation'. In: *Nuclear Instruments and Methods in Physics Research Section A: Accelerators, Spectrometers, Detectors and Associated Equipment* 936 (2019), pp. 558–560. ISSN: 0168-9002. DOI: https://doi.org/10.1016/j.nima.2018.10.074.

[378] Jun'ichi Kanasaki et al. 'Ultrafast dynamics in photoexcited valence-band states of Si studied by time- and angle-resolved photoemission spectroscopy of bulk direct transitions'. In: *Phys. Rev. B* 97 (3 Jan. 2018), p. 035201. DOI: 10.1103/PhysRevB.97.035201.

[379] Consulted on February 19th 2025. URL: https://eljentechnology.com/products/accessories/ej-560.

[380] Nikolai Beev. 'Analog-to-digital conversion beyond 20 bits'. In: (2018), p. 8409543. DOI: 10.1109/I2MTC.2018.8409543. URL: https://cds.cern.ch/record/2646282.

[381] Mirosław Firlej et al. 'An ultra-low power 10-bit, 50 MSps SAR ADC for multi-channel readout ASICs'. In: *JINST* 18.11 (2023), P11013. DOI: 10.1088/1748-0221/18/11/P11013. URL: https://cds.cern.ch/record/2882887.

[382] D. Thienpont and C. de la Taille. 'Performance study of HGCROC-v2: the front-end electronics for the CMS High Granularity Calorimeter'. In: *JINST* 15.04 (2020), p. C04055. DOI: 10.1088/1748-0221/15/04/C04055.

[383] Maksym Ovchynnikov. *Impact on sensitivity with background*. Dec. 2024. URL: https://indico.cern.ch/event/1481729/contributions/6256116/attachments/2989807/5266352/SHiP_collaboration_meeting_talks__19_12_2024_%20(3).pdf.

[384] Dina Reda Eldamak. *How to Choose the Best CMOS Technology for Your Application*. 2022. arXiv: 2212.11587 [eess.SY].

[385] Consulted on March 6th 2025. URL: https://www.weeroc.com/read_out_chips/citiroc-1a/.

[386] Consulted on August 11th 2024. URL: https://www.caen.it/download/.

[387] *Enclustra, Mercury SA1*. Consulted on August 4th 2024. URL: https://www.enclustra.com/en/products/system-on-chip-modules/mercury-sa1/.

[388] Consulted on March 9th 2025. URL: https://www.petsyselectronics.com/web/public/products/1.

[389] Matei Climescu. May require an RLP account to access. URL: https://gitlab.rlp.net/mclimesc/caen-janus-mainz.

[390] Scott B. Jones, Jon M. Wraith and Dani Or. 'Time domain reflectometry measurement principles and applications'. In: *Hydrological Processes* 16.1 (Jan. 2002), pp. 141–153. DOI: 10.1002/hyp.513.

[391] K. Briggl et al. 'KLauS: a low power Silicon Photomultiplier charge readout ASIC in 0.18 UMC CMOS'. In: *JINST* 11.03 (2016), p. C03045. DOI: 10.1088/1748-0221/11/03/C03045.

[392] Konrad Briggl. 'Silicon Photomultiplier Readout Electronics for Imaging Calorimetry Applications'. PhD thesis. U. Heidelberg (main), 2018. DOI: 10.11588/heidok.00024088.

[393] Zhenxiong Yuan. 'A Low-Power Silicon-Photomultiplier Readout ASIC for the CALICE Analog Hadronic Calorimeter'. PhD thesis. U. Heidelberg (main), 2020. DOI: 10.11588/heidok.00028659.

[394] Consulted on March 29rd 2024. URL: https://www.raspberrypi.com/products/raspberry-pi-4-model-b/specifications/.

[395] Konrad Briggl. Personal communication.

[396] R. Diener et al. 'The DESY II test beam facility'. In: *Nuclear Instruments and Methods in Physics Research Section A: Accelerators, Spectrometers, Detectors and Associated Equipment* 922 (2019), pp. 265–286. DOI: https://doi.org/10.1016/j.nima.2018.11.133.

[397] Norbert Meyners Ralf Diener and Marcel Stanitzki. *The DESY II Test Beam Facility*. Consulted on March 29rd 2024. 2023. URL: https://indico.cern.ch/event/1232761/contributions/5321961/attachments/2629758/4548431/2023.04_DESY2-TBF.pdf.

[398] Johannes Bernhard. *The T9 Secondary Beam at CERN*. Consulted on March 29rd 2024. 2023. URL: https://indico.cern.ch/event/700446/contributions/2873562/attachments/1719056/2774358/blfs2018_beams.pdf.

[399] Frederic DULUCQ. Consulted on March 23rd 2024. Oct. 2024. URL: https://indico.in2p3.fr/event/33456/contributions/144322/attachments/87589/132218/FD_241010_CALOROC_EIC_FR.pdf.

[400] Dipanwita Banerjee. Personal communication.

[401] D. Abbaneo et al. 'Studies of Hadronic Showers in SND@LHC'. In: (Apr. 2025). arXiv: 2504.01716 [physics.ins-det].

[402] Marco Gaetano Dallavalle. Consulted on April 17th 2025. URL: https://indico.cern.ch/event/1263276/contributions/5543228/attachments/2708449/4702625/Summer2023TestBeam_ASummary_fromMDVNotes.pdf.

[403] C. Adloff et al. 'Hadronic energy resolution of a highly granular scintillator-steel hadron calorimeter using software compensation techniques'. In: *JINST* 7 (2012). DOI: 10.1088/1748-0221/7/09/P09017.

[404] N. Akchurin et al. 'Perspectives on the Calibration of CNN Energy Reconstruction in Highly Granular Calorimeters'. In: (Aug. 2021). arXiv: 2108.10963 [physics.ins-det].

[405] Consulted on January 7th 2024. URL: https://www.hamamatsu.com/eu/en/product/optical-sensors/mppc/mppc_mppc-array.html.

[406] *The VMM3a User's Guide*. Tech. rep. CERN, 2022. URL: https://cds.cern.ch/record/2807691.

[407] Ernest Lawrence. *Method and apparatus for the acceleration of ions*. Accessed on 03.06.24. 1932. URL: https://patents.google.com/patent/US1948384A/en.

[408] Frank Gerigk. 'Cavity types'. In: *CERN Accelerator School: Course on RF for Accelerators*. Nov. 2011. arXiv: 1111.4897 [physics.acc-ph].

[409] T. K. Charles et al. 'The Compact Linear Collider (CLIC) - 2018 Summary Report'. In: 2/2018 (Dec. 2018). Ed. by P. N. Burrows et al. DOI: 10.23731/CYRM-2018-002. arXiv: 1812.06018 [physics.acc-ph].

[410] Philip Bambade et al. 'The International Linear Collider: A Global Project'. In: (Mar. 2019). arXiv: 1903.01629 [hep-ex].

[411] H. W. Koch and J. W. Motz. 'Bremsstrahlung Cross-Section Formulas and Related Data'. In: *Rev. Mod. Phys.* 31 (4 1959), pp. 920–955. DOI: 10.1103/RevModPhys.31.920.

[412] Helmut Spieler. *Analog and Digital Electronics for Detectors*. Consulted on March 4th 2025. URL: https://www.desy.de/~garutti/LECTURES/ParticleDetectorSS12/spieler.pdf.

[413] Consulted on May 11th 2025. URL: https://www.digikey.de/de/articles/analog-basics-part-1-sar-analog-to-digital-converters.

[414] Lars Weinstock et al. *Glueing and Assembly Robot for the P2 Tracking Detector - The Gluebot*. To be published. 2025.